Title
Morphology of mountain river channels: autogenetic organization and deterministic controls

Author
Wiener, Jason Scott

Publication Date
2022

Peer reviewed|Thesis/dissertation

Morphology of mountain river channels: autogenetic organization and deterministic controls

By

JASON WIENER
DISSERTATION

Submitted in partial satisfaction of the requirements for the degree of

DOCTOR OF PHILOSOPHY

in

Hydrologic Sciences

in the

OFFICE OF GRADUATE STUDIES

of the

UNIVERSITY OF CALIFORNIA

DAVIS

Approved:

Gregory B. Pasternack, Chair

Douglas M Thompson

Samuel Sandoval Solis

Committee in Charge

2022

ACKNOWLEDGMENTS

I first wish to acknowledge that completing my PhD, which has culminated in the drafting of this dissertation was not an easy road. It was accomplished over a period of seven years, which included some of my life's highest highs, lowest lows, and many turns and undulations along the way. A big part of that journey was making peace with the time that it took, which admittedly is on the longer side of what it takes for some, but those seven years are what it took me. I can, and will qualify the time by noting that those seven years included the births of my two sons, Alfred and Edward, after each of which I took a few months' time off for bonding and simply to be present in those unique and challenging moments; it included a global pandemic during which I retreated from work to be Alfie and Eddy's primary caregiver during those first months of greatest uncertainty; it included a quarter of planned leave due to financial reasons; it included innumerable days off to serve as caregiver during daycare closures, mental health days, vacations, and days spent sitting on the couch watching cartoons with a sick child; it include many decisions to often not work long hours and be present in the in-between hours to have more time with my family; it included time to reorient myself after switching from my original degree objective of a Masters to that of a Doctorate; it included more than one period where my mental health was impacted; it included time to get into therapy and begin the process of rebuilding myself and regaining a portion that was lost; it included time to provide service as a member on the Environmental Counsel of Sacramento, which took away from time working but reaped benefits worth that lost time; and it included 10 quarters as a Teaching Assistant (TA), times that were tremendously rewarding but significantly slowed the process. I mention all this to make a point to those who may end up reading this and especially to those who may find it helpful, which is this: It takes the time that it takes, be

accepting, be proud of what you've accomplished, and be thankful to those who helped you on the journey. Toward this end, I have a list of folks to thank that rivals the length of this quite lengthy dissertation.

First, and foremost I thank my dear wife, Kate Landman for her unwavering and unconditional support. Without you I would and could not have accomplished this, nor would my life be so bright. I love you honey more than my words can express. I will never stop trying for you. My youngest, Eddy is but three and my eldest, Alfie is but five as I write this. While I've learned to never underestimate children, I don't know if they can fully comprehend the impact they've had on my life. My dear boys, you were my anchors, you made me never give up, you drove me to breaking points I didn't know I had, but brought me back. The dissertation is dedicated to you. I love you both, always.

Next, I must thank my colleague and advisor, Gregory Pasternack whose mentorship, support, and willingness to take a chance helped lead to the achievements captured in this text, those unable to be written, and those yet to come. Greg, your guidance and feedback were always invaluable. Your steadfastness that the work adhere to the scientific method always pushed me, albeit often begrudgingly, to make the work better. You saw what I could do, made me achieve that and more, and had the patience, albeit often begrudgingly on your end, to let me get there my own way. The skills and lessons you've imparted will be instrumental in all the next steps of my life's journey. I look forward to collaborating in the future and finishing all the unfinished work we started.

I would also like to thank my other committee members, Douglas Thompson and Samuel Sandoval Solis. Your time and care with reviews vastly improved the work. Doug, your critical thinking always challenged me to dig deeper, connect lines of inquiry, and support every

supposition. It was delightful to work with you on this effort. Sam, your advice that the best thinking doesn't happen in a lab or in front of a computer has wrung true and served me many times as a good excuse to get away from a screen and go for a hike, and for that I am in debt.

I'd like to thank Thomas Harter and Peter Hernes for having their doors open (literally and figuratively), and the conversations and friendships this simple gesture enabled. I'd like to thank HSGG faculty members Majdi Abou Nam, Helen Dahlke, Isaya Kisekka, Holly Oldroyd, Parmod Pandey, Sarah Yarnell, and Daniele Zaccaria for their friendships and the many conversations shared in hallways, meetings, seminars, classrooms, around campus, and around town. I'd like to thank the rest of the HSGG faculty for their teaching and support along the way.

I'd like to thank the hydrologic science, plant science, earth and planetary science, environmental science and policy, sociology, and science and society departments for hiring me as a TA, Dr. Susan Pike for her friendship and financial support as a GSR, Dr. Laura Foglia and Larry Walker and Associates for financial support, and UAW 2865 for advocating and creating better working conditions for Academic Student Employees. This dissertation was also financially supported by Yuba Water Agency (Award #201503808) and by the USDA National Institute of Food and Agriculture, Hatch project number CA-D-LAW-7034-H.

I'd like to thank my many lab mates over the years, Luke Tillman, Matt Weber, Joni Gore, Scott Burman, Nina Li, Sean Luis, Pete Moniz, Arielle Gervasi, Kenny Larrieu, Sierra Phillips, Muwei Zheng, Sebastian Schwindt, Colin Byrne, Herve Guillon, Romina Diaz-Gomez, Anzy Lee, Chelsea Hopkins, Xavier Nogueira, Yuiko Chino, Paulo Silva, and Rachel Wright. Similarly, I'd like to thank all my fellow HSGG student colleagues I've had the pleasure to engage with. You are all brilliant, and I will cherish the innumerable 'science chats', times we escaped to go grab a bite or a drink, time spent on the river, and your friendship and support. Rest assured I will always

be a call or email away to provide a citation for any topic.

Finally, I want to thank all my friends and family, especially my parents, siblings, and in-laws for always believing in and supporting me. It's done, so please enjoy.

ABSTRACT

In alluvial rivers, whose bed and banks are made up of mobile sediment, river geometry generally adjusts to just mobilize the most resistant material lining the channel. In essence, such rivers are freely formed by sediment transport processes (e.g. erosion, deposition, transport, storage). In laterally confined coarse-bedded rivers where adjustment of channel planform and gradient are more restricted this is not always the case, resulting in channel morphologies characterized by resistant boundaries and large substrates, and predominance of other modes of adjustment such as changes in bed roughness. While study of mountain river geomorphology and hydraulics has increased in last 30 years, there remains room for methodological advancement and basic science exploration, especially given availability of technological innovations in data collection, modeling, and data analysis. Thus, the goals of this dissertation were: (i) to advance methods for geomorphic and hydraulic assessment suited to mountain river settings; and (ii) improve foundational understanding of mountain river channel morphology, geomorphic processes, and process-morphology linkages. Using a 13.2-km segment of the mountainous Yuba River (Northern California) as a test bed river study site, three chapters present this work:

In Chapter 1, a procedure was developed to map sub-meter resolution large bed elements (LBEs) from a 3D point-cloud and test the hypothesis that element configurations were organized to maximize flow resistance. The procedure, which involved applying a ground classification algorithm to produce a roughness surface model and extracting LBEs with a marker controlled watershed algorithm, resulted in mapping 42,176 LBEs in the study site. Scale and discharge-dependent LBE concentration and spacing metrics quantified for multiple laterally and/or hierarchically nested spatial domains and classified using three flow-resistance based

hydrodynamic regimes confirmed nearly all segment- and reach-scale LBE concentrations corresponded to a state of maximum resistance. However, disparities between concentration and spacing metrics left open questions about resistance maximization as an extremal model of geomorphic adjustment. Finer scale analyses demonstrated spatial variability of LBE configurations, but identified maximum resistance act as an attractor state toward which conditions converge. Lastly, lateral variability of LBE metrics had implications for discharge-dependent resistance.

Chapter 2 couples sub-meter resolution 2D hydrodynamic modeling with LBE mapping from Chapter 1 to present novel distributions of LBE relative submergences at multiple spatial scales and explores the dynamism of this hydraulic property across discharges and spatial domains (e.g. segment and reaches). Analysis confirmed the rate at which statistical and parametric properties changed between discharge-dependent LBE relative submergence datasets were statistically equivalent between study reaches, which we term 'process-based similarity'. One interpretation of this consistent scaling is that it represents a dynamic equilibrium in channel adjustment toward a critical state that minimizes the variance of how resistance changes with discharge between reaches. The presented ability to account for more complete representation of bed-surface heterogeneity and the joint-distribution of local flow depths has far reaching implications. For instance, accounting for relative submergence distributions in resistance equations could improve prediction and address the limitation that a 1:1 relation exists between mean depth and mean velocity present in most resistance equations. Observation of discharge-dependent dynamism of LBE height distributions also calls into question the practice of holding roughness coefficients constant, and the ability to map individual LBEs provides a sensible method for parameterizing spatially variable roughness lengths scales.

Finally, Chapter 3 presents an investigation into local topographic controls and morphodynamic processes involved in formation and/or persistence of morphological unit scale fluvial landforms (MU) and addresses five scientific questions about mountain river MUs and their hydro-morphological (HM) variables. The study applies a rigorous top-down classification followed by bottom-up analysis experimental design whereby a standard method involving meter-scale 2D hydrodynamic modeling and a baseflow hydraulics decision tree were used to classify and map nine spatially explicit baseflow in-channel MU types in the study site. Discretizing the study site into cross-sectional polygons a total of 2539 cross-sections were identified as being dominated by a single MU type and a diverse set of 18 HM variables, representing an array of possible hydraulic and geomorphic controls on MU formation and/or maintenance, were measured at these cross-sections. Cumulatively, study results develop holistic descriptions of HM variable conditions where certain MUs and/or groups of MUs occurred, interpret processes involved in the formation/persistence of these MU types, and provide inference on how HM variables exert deterministic control.

TABLE OF CONTENTS

Page

LIST OF FIGURES

Page

LIST OF TABLES

Page

LIST OF APPENDICIES

Page

CHAPTER 1. SCALE DEPENDENT SPATIAL STRUCTURING OF MOUNTIN RIVER LARGE ELEMENTS MAXIMIZES FLOW RESTISTANCE

1.1 Abstract

Macro-roughness elements such as boulders and bedrock outcrops, collectively referred to as large bed elements (LBEs), are key features influencing hydrodynamics and morphodynamics in mountain rivers. Where LBEs are abundant and account for a substantial portion of total flow resistance, existing geomorphic theory, previous physical experiments, and limited field observations support the theory that LBE configurations adjust to maximize flow resistance. However, methods to explicitly map individual features along entire river segments are lacking, thus limiting analysis of LBE spatial structure in boulder-bedded rivers. In addressing these gaps, this study sought to develop a procedure for mapping LBEs from 3D point-clouds, explore LBE spatial structure in a real boulder-bedded river, and test the hypothesis that LBE configurations were organized to maximize flow resistance. The mapping procedure applied a ground classification algorithm to produce a roughness surface model, from which LBEs were extracted by a marker controlled watershed algorithm. Implementing the procedure, 42,176 LBEs were mapped in 13.2-km of the mountainous Yuba River (Northern California). Scale and discharge-dependent LBE concentration and spacing metrics were quantified for multiple laterally and/or hierarchically nested spatial domains and classified to differentiate three flow-resistance based hydrodynamic regimes: isolated roughness, wake interference, and skimming flow. Of these regimes, wake interference corresponds to a state of maximum resistance, so hypothesis testing involved determining if this regime was dominant. Results confirmed 25 of 28 segment- and reach-scale LBE concentrations were in the wake interference regime. However, spacing metrics

classified 24 of these same spatial domains in the skimming flow regime. Herein, concentration metrics quantify LBE density in a given spatial area, whereas spacing metrics represent LBE proximity to one another. While comparison of segment and reach-scale regime classifications by each metric concluded concentration was superior to spacing for regime classification purposes, these disparities leave open questions about this extremal model of geomorphic adjustment. Lastly, lateral variability of metrics across the river corridor had implications for discharge-dependent resistance.

1.2 Introduction

Macroroughness riverbed elements such as boulders and bedrock outcrops differentiate mountain rivers from most lowland gravel-or-sand bedded rivers (Bathurst, 1978; Grant et al., 1990). Collectively referred to herein as large bed elements (LBEs), these features have a primary influence on hydraulic, hydrodynamic, and morphodynamic properties of mountain river channels as well as secondary effects on adjacent landscape processes (Table A1.1). In laterally confined coarse-bedded rivers where adjustment of channel planform and gradient are more restricted, extremal hypothesis, regime theory, physical experiments, and field observations support the theory that channels adjust bed roughness to maximize flow resistance, as this corresponds to a state of maximum stability (Abrahams et al., 1995; Adams, 2020; Church et al., 1998; Davies & Sutherland, 1983; Eaton & Church, 2009; Eaton et al., 2020; Wohl & Merritt, 2008).

Where LBEs are abundant, such as in bedrock or boulder-bedded rivers, the latter defined as those with $D_{50} \geq 64$ mm (*sensu* Bathurst, 1982), LBEs account for a substantial portion of total flow resistance (Chen et al., 2019). Links between LBE spatial structure metrics, such as LBE concentration and spacing, and flow resistance mean that such metrics can serve as a proxy for bed roughness adjustment and address whether LBEs are configured to maximize flow resistance

(Bathurst, 1978; Canovaro et al., 2007; Ferro, 1999; Papanicolaou & Tsakiris, 2017). However, study of this phenomenon, and the spatial structure of LBEs in natural river segments with abundant LBEs are still largely absent (Adams, 2020; Williams et al., 2019). This absence arises in part due to variability in how LBEs are defined and limited availability of continuous and comprehensive segment-scale LBE datasets (Benda, 1990; Grant & Swanson, 1995; Shobe et al., 2016).

Existing definitions of LBEs or macroroughness elements vary considerably in the peer-reviewed literature (Table A1.2), but typically reference fixed lengths or scaled measures of grain diameter including but not limited to $D > 0.5$ m, $D \approx$ bankfull flow depth, and D_{90} (D is grain size diameter and the subscript is the percent of grains finer). While arguably of equal import to the processes describe in the paragraph above (Gippel et al., 1996), the inclusion of large woody materials (LWM) in LBE definitions has been variable or unclear (Table A1.2). Inconsistent definitions complicate LBE mapping, and the interpretation and comparison of LBE related study findings between rivers. Alternate metrics, such as surface roughness that can account for LWM, coupled with algorithmic mapping procedures offer opportunity to provide more consistent, transferable LBE mapping approaches across rivers. However, automated methods to map these features in natural environments from remotely sensed data products remain limited (Carbonneau et al., 2004; Resop et al., 2012).

To address these gaps, we developed a semi-automated procedure for mapping LBEs from three-dimensional (3D) point clouds obtained via an airborne laser system. We then used results to explore the spatial structure of LBEs in a real boulder-bedded mountain river and address three specific scientific questions including whether LBEs were configured to maximize flow resistance. In the following sections, we first present background on LBE mapping (1.2.1), discuss factors

influencing LBE spatial structure (1.2.2), review hydrodynamic influences of LBEs (1.2.3), and finally present the questions of this study (1.2.4). Through objectively and systematically mapping LBEs, this study generated a large LBE dataset to test hypotheses providing insight into the spatial structure of LBEs in a real mountain river at multiple scales.

1.2.1 Mapping LBEs in river corridors

In-situ LBE mapping has been done manually with global positioning system (GPS) or total station survey equipment (Valle & Pasternack, 2006). Unfortunately, it may not be possible to map LBEs at all where access is limited or dangerous, which is a common situation in mountain rivers. Further, mapping all LBEs would be time consuming if hundreds-to-thousands of LBEs exist within a survey area, which may be the case at reach (~10^2-10^3 channel widths) and segment scales (~10^3-10^4 widths). Field survey methods for LBEs are also subject to the same problem of surveyor bias that occurs with mapping morphological units.

Remote sensing techniques for studying river sedimentology have a history spanning over four decades (Piégay et al., 2020). Broadly, we divide remote sensing approaches into those based on imagery and those based on topographic data. Many image-based techniques have proven capable of predicting grain-size information from images (e.g., Butler et al., 2001; Purinton & Bookhagen, 2019; Warrick et al., 2009). However, methods often focus on predicting representative grain size metrics (D_{50} or D_{84}), and do not facilitate mapping individual grains like LBEs. Software, such as Detert and Weitbrecht's (2012) '*BaseGrain'* and Purinton and Bookhagen's (2019) '*PebbleCounts'*, that include this capability have limited testing in mountain rivers with heterogeneous surface roughness's that complicate grain mapping (Pearson et al., 2017), and appear difficult to apply beyond the reach scale due to computational and input data requirements. Alternately, LBEs are commonly manually digitized from aerial images (Chen et

al., 2019; Finnegan et al., 2019). All image-based methods have limited ability to map submerged LBEs, require high-resolution imagery (<<1 m pixels) to ensure mapping accuracy (Carbonneau et al., 2004), and do not explicitly measure particle heights (i.e. planimetric two-dimensional [2D] mapping only).

Remote sensing of river topography likewise offers opportunities for studying river sedimentology and potential to overcome the 2D limitations of image-based methods (Brasington et al., 2012; Hodge et al., 2009). Generically, these approaches involve developing statistical models between measured sedimentological characteristics and topographic metrics, such as roughness height (Gomez, 1993) or the standard deviation, semi-variance, skewness, or kurtosis of detrended bed elevations within a submeter convolution kernel (Aberle & Smart, 2003; Schneider et al., 2015). Common topographic data sources include airborne or terrestrial laser systems (ALS and TLS, respectively) or photogrammetric techniques such as structure-from-motion (SfM). Factors relevant to LBE mapping such as resolution (point density), spatial coverage, accuracy, post-processing requirements, and cost vary widely between methods (Tomsett & Leyland, 2019). For example, while TLS and SfM produce greater point densities than ALS, (~10,000 pts/m^2 compared to ~10's pts/m^2 [Brasington et al., 2012]), they have greater time and labor requirement and may not be feasible in inaccessible mountain regions or for segment-scale applications (Piégay et al., 2020; Tomsett & Leyland, 2019). A caveat of nearly all image- and topographic-based grain-size prediction approaches is reliance on statistical models calibrated with site-specific field measurements. When models are applied outside the systems in which they're developed it is common for predictions to perform poorly on novel data (Pearson et al., 2017).

To our knowledge, Resop et al. (2012) provide the best example of semi-automated

mapping of LBEs in a natural setting. Using TLS, they applied a series of image-processing algorithms to a 2-cm digital terrain model (DTM) to segment and map individual boulders (>256 mm) along 100 m of a boulder-bedded river. Their approach, derived from methods for mapping tree canopies, performed well at mapping the location and shape of boulders compared to field measurements. A multi-step un-validated GIS approach to map boulders in the mountainous South Yuba River from a combination of terrestrial ALS, bathymetric sonar, and GPS survey data is also presented by Pasternack and Senter (2011). Overall, remote sensing offers potential for new and continued research in river sedimentology including mapping LBEs.

1.2.2 Organization of LBEs in river corridors

In natural channels, LBE spatial structure, defined as the number, size, and arrangement of LBEs, evolves as landscapes are acted upon by hillslope, glacial, volcanic, tectonic, fluvial, and biogeomorphic forces that together produce three key processes: supplying LBEs to the channel or exhuming them; weathering and attrition of LBEs; and LBE transport, deposition, and storage (Table A1.1). Hillslopes and low-order tributaries (1^{st}-3^{rd} order) are the main source delivering new LBEs to the channel network through landslide related processes (Benda, 1990; Hewitt, 2002; Hungr et al., 2001). Once in the river corridor, LBEs can remain immobile or only intermittently mobile for periods lasting 10^2-10^6 years (e.g. Williams et al., 2019). On the other hand, observations support that LBEs up-to several meters in size may still be transported downstream more frequently ($<10^2$ year recurrence intervals) (Grant et al., 1990; Molnar et al., 2010). In-channel LBEs also provide feedback on landscape evolution due to their ability to mediate incision, shape channel morphology, and influence sediment storage and transport (Golly et al., 2019; Hassan & Reid, 1990; Madej, 2001; Shobe et al., 2016). In-turn, these feedbacks, and associated changes to LBE spatial structure and channel boundaries, modify flow resistance. Applying the

simplifying assumption that channel adjustments are such that when resistance is low relative to hydraulic forces the channel boundary will adjust to increase hydraulic resistance and visa-versa, these feedbacks enable trajectories of LBE mediated channel adjustment toward conditions of maximum resistance while leaving room for more complex oscillations and non-equilibrium behavior (Chin & Phillips, 2007; Eaton & Church, 2009; Ferguson et al., 2019; Wohl & Merritt, 2008).

1.2.3 LBE influence on hydraulics and hydrodynamics

Protrusion of LBEs into a flow-field exert resistance on the fluid via frictional shear (Bathurst, 1978) and pressure fluctuations (Einstein & Barbarossa, 1952), colloquially termed skin friction and form drag, respectively. In boulder-bedded rivers, form resistance from LBEs can account for a substantial portion (>90%) of total flow resistance (Chen et al., 2019). When an array of LBEs is present, as is the case in natural channels, the superpositioning of vortices further affects resistance, wake and turbulent flow structures, and flow-field recovery (Canovaro et al., 2007; Fang et al., 2017).

Morris (1959) classified these combined effects into three basic hydrodynamic regimes: isolated roughness, wake interference, and skimming flow. Isolated roughness occurs when macroroughness feature spacing is large enough that wakes do not interact and the flow recovers before engaging the next downstream feature. Wake interference occurs when the wake from one feature extends to the next downstream feature and the flow never recovers. Lastly, skimming flows occur when features are close enough to form pockets of trapped highly irregular flow patterns with a relatively smooth flow structure above.

Morris's hydrodynamic regimes may be interpreted in terms of flow resistance (Fang et al., 2017; Papanicolaou & Tsakiris, 2017). When LBEs are widely spaced, such as in the isolated

regime, total form resistance due to LBEs can be estimated as the sum of drag on individual LBEs (Gippel et al., 1996). As more LBEs occupy the flow-field, the resistance relationship becomes non-linear typically reaching a peak in resistance followed by a decrease that eventually plateaus regardless of the presence of additional LBEs. The initial transition from linear to non-linear behavior is hypothesized to indicate a regime shift from isolated roughness to wake interference, wherein resistance reaches its peak. The subsequent decrease in resistance and plateau region are associated with conditions of skimming flow where resistance is proportionally high but not at a maximum (Canovaro et al., 2007; Ferro, 1999). Thus, the wake interference regime has been assumed to broadly correspond with conditions of maximum flow resistance.

Morris's hydrodynamic regimes have served as a basis in many physical experiments describing how LBEs influence the flow-field and flow resistance (e.g., Canovaro et al., 2007; Ferro, 1999; Papanicolaou & Tsakiris, 2017). In these studies, Morris's regimes have been represented using LBE concentration (Γ), which varies in how it is calculated but is defined here as the ratio of planform LBE area to wetted channel area; and/or non-dimensional spacing (λ_*), typically calculated as the distance (λ) between LBEs divided by the diameter of the upstream LBE (D_c). Strong correspondence in the above referenced studies between these LBE spatial structure metrics and flow resistance measurements allows a direct link connecting metrics with Morris's regimes and conditions associated with maximum resistance. Conceptually, provided availability of a census of LBEs, these same LBE spatial structure metrics may be extended to classify Morris's regimes in natural settings and test the degree that conditions associated with maximum resistance are present at multiple spatial scales.

1.2.4 Scientific questions

The sections above highlight three scientific questions concerning the mapping and spatial

structure of LBEs in natural channels. First, can ALS data be used to accurately map sub-meter-scale resolution LBEs along entire river segments? Second, are LBEs configured to maximize flow resistance, and if so at what typical spatial scales (segment, reach, and cross-section) does this occur? Third, does LBE spatial structure vary laterally to provide differential discharge-dependent roughness?

1.3 Study River Segment

The field site was a confined 13.2-km segment of the mountainous Yuba River (Northern California) draining 1853 km^2 of the western Sierra Nevada range (Figure 1.1). It is comprised of a low sinuosity, boulder-bedded, 5^{th} order mountain river confined within a steep-walled bedrock and forested hillside canyon, which is common among rivers draining the western slope of the northern Sierra Nevada range (Guillon et al., 2020). The river has a mean bed slope of 1.96% but exhibits localized variability, with many 10 – 100 m long ($10^0 – 10^1$ widths) stretches having slopes exceeding 10%. Like many bedrock-confined rivers, the study site lacks a contiguous floodplain having only localized areas supporting accumulation of alluvium at major tributary junctions, meander bends, or other areas of local valley widening (Fryirs et al., 2016). Despite this ambiguity, a previously reported morphologically determined bankfull discharge (Q_{bf}) of 10.7 m^3/s (YCWA, 2013) was used to enable comparison of metrics across sites respective of scale. For analytical purposes, the study site was delineated into six geomorphic reaches on the sole basis of channel-bed slope breaks (Figure 1.2).

Based on limited sedimentological data, bed substrates alternate between bedrock and alluvial sections (YCWA, 2013). Alluvial substrate, where present, is a heterogeneous mixture of materials dominated by coarse fractions (medium gravel/cobbles and larger). Contemporary sources of coarse clastic materials result from hillslope process, exhumation of boulders or

bedrock, historic hydraulic mining activities, and in-channel stores. Uniformly steep hillslopes are present along the study site with large areas exceeding 0.8 m/m, a regional slope threshold identified by Hurst et al. (2012) for producing landslides and scree cones. Curtis et al. (2005) also found mass wasting processes to dominate over other erosional processes (e.g. surface erosion), thus providing a relatively abundant supply of LBEs for delivery to the valley-bottom. Review of aerial imagery (Google Earth®) from 1957 to present shows landslides, debris flows, and rock falls throughout the study site. Quaternary glaciation present in the easternmost portions of the Yuba basin did not extend to the study site, however it is plausible that outwash deposits remain.

The region's alluvial-sediment processes are also affected by anthropogenic influences. New Bullards Bar (NBB) Dam is a 196.6 m high concrete arch dam on the North Yuba River near Dobbins, CA. Closed in 1969, the dam is a complete barrier to bedload transport into the study site passing only wash load. Two additional dams, Log Cabin Dam and Our House Dam, situated upstream of the study site in the Middle Yuba watershed, also act as partial barriers to downstream sediment transport.

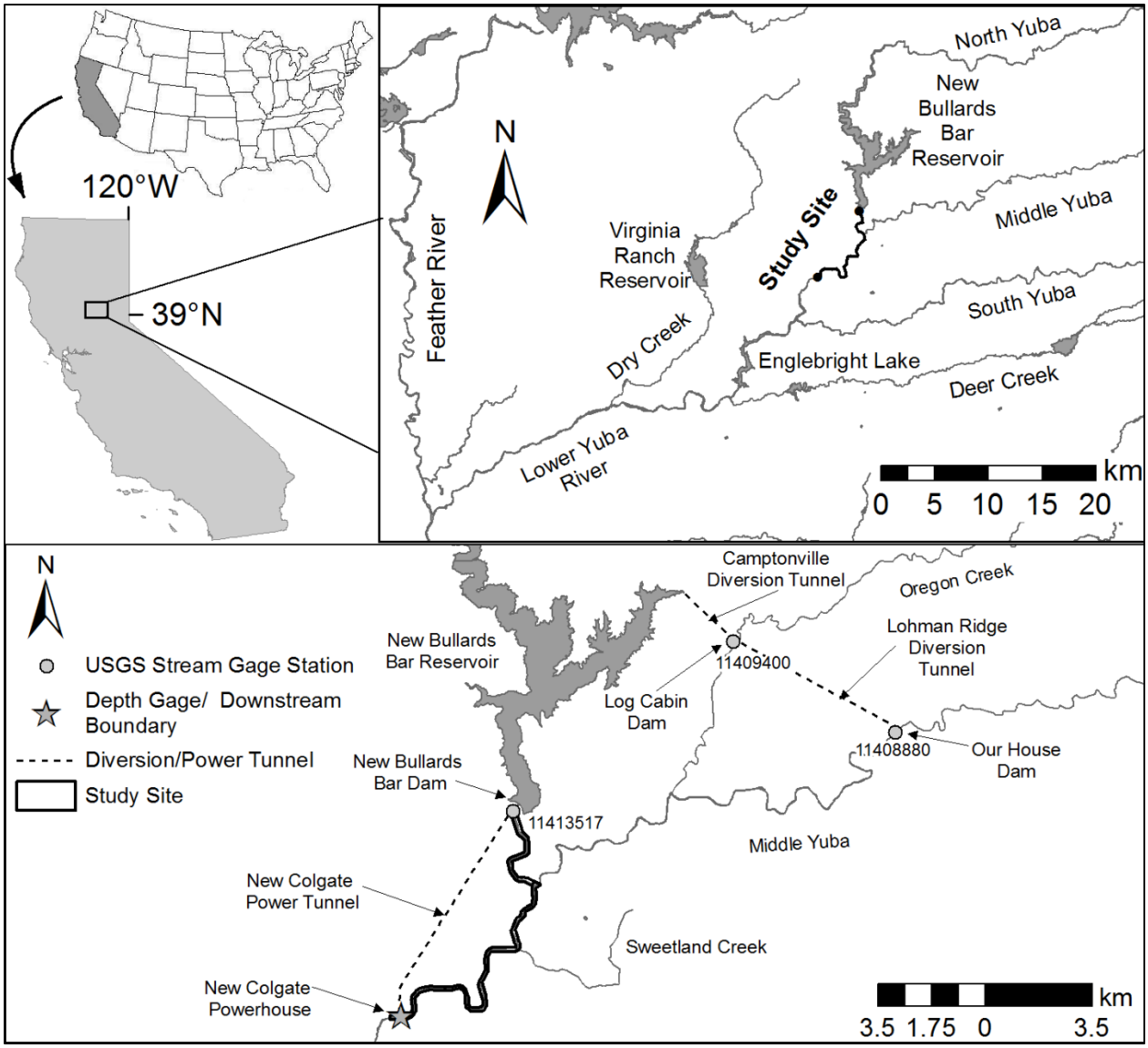

Figure 1.1. Map of study site, tributaries, gages, and infrastructure facilities, Yuba River, CA.

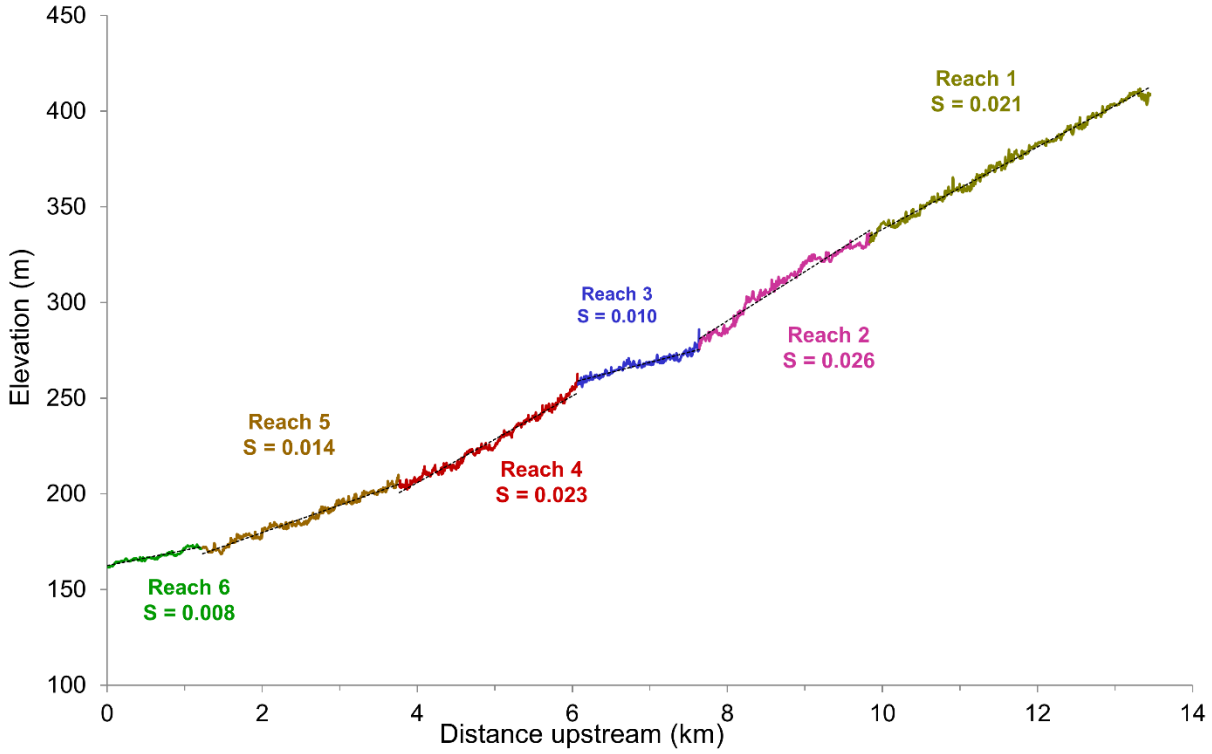

Figure 1.2. Longitudinal profile showing the extent and slope (m/m) of geomorphic reaches.

1.4 Methods

The three scientific questions were answered in order, as they build on each other. To address the first study question, a field campaign and remote sensing survey were carried out to collect topo-bathymetric point clouds and locate real LBEs in the study river segment (sections 1.4.1-1.4.2). A procedure for mapping LBEs along river channels from ALS 3D point-cloud data was developed, tested, and applied to map LBEs in a real boulder-bedded mountain river (section 1.4.3). Question 1 was answered using performance metrics comparing predicted LBEs to observed LBEs, using two different analyses (section 1.4.3). Next, to address the second question, LBE data were coupled with results from a 2D hydrodynamic model (section 1.4.4) to define LBE spatial structure metrics within multiple discharge-dependent portions of the river corridor (section 1.4.5). Specifically, Γ and λ_* values were calculated at segment, reach, and cross-sectional (0.1

width) scales. These were then compared to thresholds associated with Morris's wake interference regime from the literature to test the hypothesis that LBEs were organized to maximize flow resistance at these three spatial scales, as indicated by LBE spatial structure metrics corresponding with the wake interference regime. Finally, the third question regarding lateral distribution of LBE structure and flow resistance was answered by quantifying differences in LBE spatial structure metrics for different incremental inundation corridors, as defined in section 1.4.5.1.

Because this study has many detailed methods and additional results, supplementary materials are provided in APPENDIX 1. References to "Text A", "Table A", and "Figure A" followed by a number refer to locations in APPENDIX 1 where that item can be located.

1.4.1 Topo-bathymetric mapping

Between September 27-29, 2014 ALS data were collected within the study site by a professional surveying firm (Quantum Spatial, https://www.quantumspatial.com/) using a Riegl VQ-820-G bathymetric sensor system and a Leica ALS50 Phase II system (near infrared) mounted in a Cessna Grand Caravan. The initial ground classified point density was 2.3 pts/m^2. Following a process to address ground misclassification errors, this density was increased to 13.9 pts/m^2 (Text A.1.3.1). ALS collection was conducted during a period of low discharge estimated at 1.19 m^3/s at the downstream study site boundary. This discharge is exceeded 89.4% of the time based on the period October 1968 – February 2016 (Wiener & Pasternack, 2016a).

ALS data were supplemented with boat-based bathymetric observations, imagery-derived bathymetric estimates (*sensu* Legleiter et al., 2004), and systematically placed augmented points (*sensu* Valle & Pasternack, 2006). Single beam echo sounding data was collected by kayak between July 8 and 9th 2015 during low-flow conditions (0.89 m^3/s) using an Ohmex Sonarmite. The boat's 3D position was tracked using a Trimble 5800 Real Time Kinematic (RTK) GPS tied

to a local base station. Average boat-based point density was 0.53 pts/m^2.

Through verification and merging of individual datasets, an extremely detailed and accurate topographic map was created (Text A.1.3.1; Wiener & Pasternack, 2016b). The final bare Earth mapping included > 21 million points at an average point-spacing of 0.25 m (~ 16 pts/m^2). Points were used to create a 0.46 m x 0.46 m resolution raster (bare Earth DTM), the final map product used in the study.

1.4.2 Observed LBE dataset

For the purpose of parameterizing and assessing the study's LBE mapping approach an observed LBE dataset consisting of independently mapped LBEs was generated within a portion of the study segment from high-resolution aerial imagery. Imagery was collected for the downstream 1.2 km of the study site on September 20, 2016 using a DJI Phantom 3 Professional quadcopter uncrewed aerial vehicle equipped with on-board GPS, camera, and camera gimbal. The discharge on this day was estimated at 1.02 m^3/s (a low flow) at the downstream boundary Images were processed and a 2.6 cm resolution composite orthomosaic photograph was generated using Agisoft Photoscan Professional version 1.3 (Photoscan) following methods described by Carey et al. (2019). No terrain products were produced from the captured images.

The composite orthomosaic photograph, which contained numerous visible LBEs, was georeferenced to align with the study's ALS data. Next, LBEs visible in the orthomosaic photograph were manually digitized. Selecting which LBEs to digitize was done by randomly panning to different portions of the orthomosaic and digitizing all LBE that were clearly visible and differentiable from the bare earth and water. Digitizing was capped at a single 8-hour day effort. A total of 1194 digitized LBEs overlapping the region of topographic data collection (section 1.4.1) served as the LBE dataset (LBE_o) (Figure 1.3).

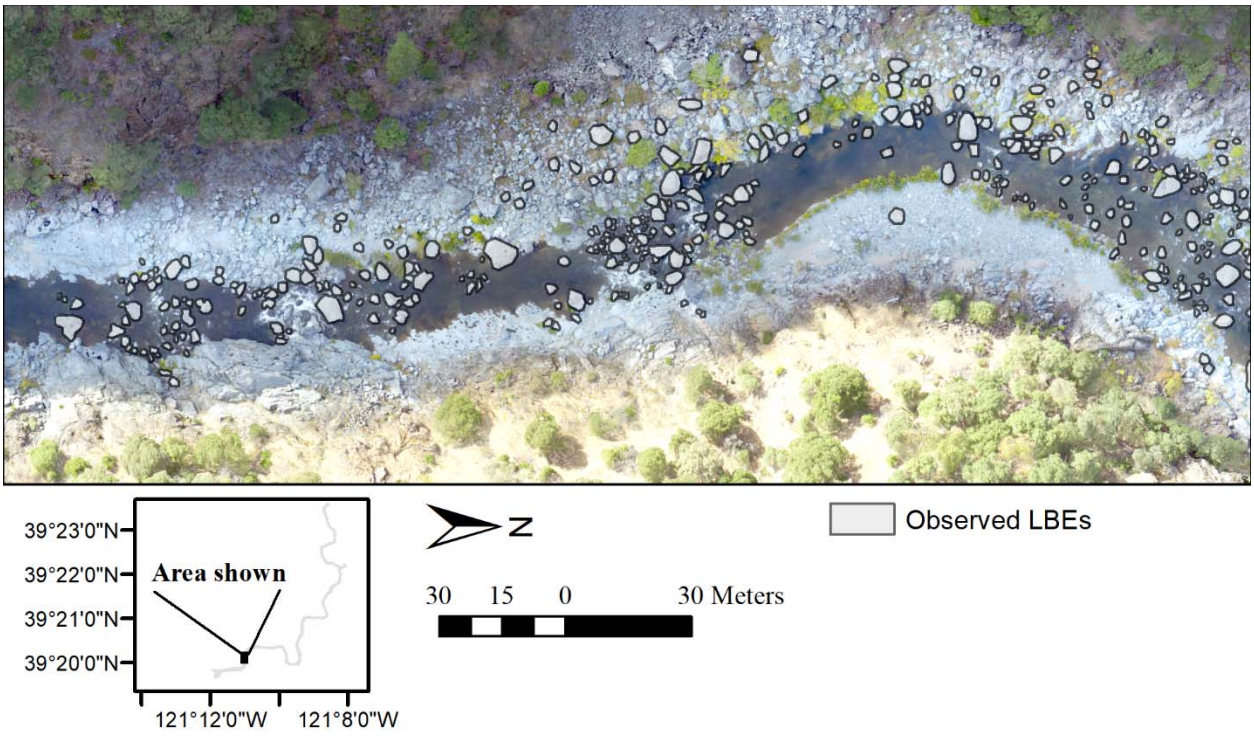

Figure 1.3. Portion of orthomosaic with manually digitized large bed elements (LBE_o) outlined by black lines. Only a portion of visible LBEs were digitized.

1.4.3 LBE mapping

For this study, we do not propose a universal definition for LBEs. Instead we developed and applied a novel procedure (Figure 1.4) for mapping terrain features, in this case sub-meter scale LBEs, from 3D topographic point clouds. The procedure takes into consideration existing LBE definitions, site-specific sedimentology, and establishing consistent methods for parameter specification to aid transferability of the mapping procedure. The procedure comprised two main steps, generating a roughness surface model (RSM) and extracting LBEs from the RSM. To answer the first scientific question the accuracy of both steps required independent and step-wise assessment. Therefore, multiple RSMs were generated, and then multiple approaches were used to extract LBEs from the best performing RSM. In each step, test metrics were used to compare RSM and extraction results and LBE observations and identify the best outcomes. The best performing

outcomes were vetted against benchmark values reported by Kaartinen et al. (2012) and Marconi et al. (2019) to determine if they met scientific norms to be considered accurate representations.

1.4.3.1 Roughness surface model generation and testing question 1

A RSM is the vertical difference between 'complete' and 'smoothed' DTMs. The RSM concept is similar to that of a canopy height model, a common product for mapping tree-crowns (Chen et al., 2006; Popescu & Wynne, 2004). Here, the complete DTM is the bare earth DTM described in section 1.4.1 and the smoothed DTM is essentially the bare earth DTM stripped of large roughness features, which methodologically differs from detrending the bare earth DTM. When these surfaces are differenced, the intent is for LBEs to 'stick-out' of the resulting RSM, as this allows them to be extracted in the second step of the mapping procedure.

Absent a unanimously accepted method for creating smoothed DTMs, a series of smoothed DTM point clouds and associated rasters were generated using the open source 'lasground_new.exe' ground classification algorithm (Isenburg, 2016), which applies an adaptive TIN approach to iteratively classify ground points from an unclassified point cloud based on six user defined parameters. This approach was selected as it proven to be effective at correctly classifying ground points in areas of variable terrain (Zhang & Whitman, 2005), is parametrically flexible, and its parameters (Table 1.1; Text A.1.3.3) can be related to measurements meaningful to mapping terrain features. The algorithm was run using the bare Earth 3D point cloud and a range of parameter values informed by physically based metrics (Table 1.1), such as site specific representative grain sizes, as inputs, to produce 14 unique smoothed DTM rasters (Table A1.3). Smoothed DTM rasters were then assessed heuristically based on visual observations of: (i) removal of clearly discernable LBEs; and (ii) retaining topographic characteristics of the original ground surface such as slope breaks, small-scale terrain undulations, and meso-scale terrain

features. Based on this qualitative assessment, six smoothed DTMs were selected for further processing and evaluation (Table A1.3).

The first of these processing steps involved subtracting each smoothed DTM raster from the complete DTM raster to produce six unique RSM rasters. Next, a binary threshold approach was used to map discrete sets of preliminary LBEs from each RSM. This was done by assigning a random selection of 70% of the LBE_o data to a 'training' dataset and then calculating the average RSM value of all raster cells located along the exterior boundary of each LBE_o polygon in the training set for each RSM, independently. Threshold values above which a RSM pixel was considered LBE were determined by taking the average of these sets of values for each RSM, respectively (Text A.1.3.3).

Sets of preliminary LBEs were evaluated by comparing predicted LBE polygons with the remaining 30% of the LBE_o data ('test data') using four performance metrics: producers accuracy (PA), producers overlap (PO), a modified Jaccard similarity index (MJI) and missed-to-excess ratio (MER). The four metrics were chosen to balance sensitivity to omission (i.e. missing a real LBE) and commission (i.e. mapping an erroneous LBE) errors, whereby PA and PO were considered to penalize omission and be less sensitive to commission compared to MJI and MER, which penalize commission while allowing omission (Shao et al., 2019). Jaccard index (JI) and PA are common metrics in classification exercises whereas PO and MER were devised for this study. PA, PO, and MJI all range from 0-1 and MER ranges from 0-∞. Higher values of all metrics indicate better mapping accuracy but not necessary better precision. Metrics were formulated to control for the situation where an LBE was predicted but missed in the observed dataset. Details, including numerical formulations, are provided in APPENDIX 1 (Text A.1.3.3).

Metrics were calculated for each preliminary LBE dataset and then independently rescaled

from 0-1 using standard normalization techniques. The arithmetic mean of normalized values was used as a global performance metric to select the best ground classification algorithm parameter set and associated RSM ('preferred RSM'). Once identified, performance metrics of the preferred RSM were evaluated to determine if it could support accurate LBE extraction.

1.4.3.2 LBE extraction and accuracy testing for question 1

The procedure's second step involved extracting LBEs from the preferred RSM and testing the accuracy of the extraction, as the second and more important test to answer question 1. The threshold technique described in section 1.4.3.1 offered one option for LBE extraction. However, while this simple and efficient method was considered reasonable for evaluating ground classification algorithm parameters to select the preferred RSM, both preliminary LBE mapping assessment and extensive research on tree-canopy mapping indicated alternative LBE extraction methods could improve mapping accuracy (Kaartinen et al., 2012). Drawing from forestry research, five LBE extraction approaches were identified for testing: (i) RSM with vertical threshold; (ii) Gaussian filtered RSM with vertical threshold; (iii) RSM with marker-controlled watershed segmentation (MCWS) algorithm and constant window size; (iv) RSM with MCWS and variable window size; and (v) Gaussian filtered RSM with MCWS and constant window size. Comparing tree-crown mapping algorithms, Kaartinen et al. (2012) demonstrated that MCWS performed equally well or outperformed more computationally expensive and parametrically complex approaches not tested in this study.

Approaches differed in regard to computational expense, number of parameters, and implementation. To evaluate mapping performance, multiple parameter sets were tested for each approach. Each parameter set was used to generate a set of predicted LBEs for the area covering the LBE_o dataset. Parameter values for each approach were either data-driven (i.e., derived from

the LBE_o data) or selected from a range of reasonable physically meaningful values (i.e., LBE heights). To constrain parameter spaces only data-driven calculations were used for approaches (ii-v). Ultimately, 12, 6, 10, 2, and 14 parameter sets were specified for approaches (i-v), respectively, resulting in a total of 44 LBE datasets (LBE_p), each a distinct mapping of LBEs (Table A1.4). Details of each approach and rationale for parameter selection are provided in APPENDIX 1 (Text A.1.3.3).

Once mapped, LBE_p datasets were assessed for accuracy using the same performance metrics as in step one, but compared to the entire LBE_o dataset. In addition to this internal comparison, PA and MJI scores were also evaluated against benchmark values from forestry research. Kaartinen et al. (2012) report PA values from past studies between 0.40-0.93 and found matching rates, a metric similar to PA, between 0.28-0.66 (median of 0.56) when benchmarking 32 tree-extraction algorithms. For MJI, JI scores from Marconi et al. (2019) were used for comparison. Their values ranged between 0.056-0.340 (median of 0.167).

The suite of performance metrics and summary global performance metric were informative, but had limitations in identifying a best approach and single parameter set. For one thing, the LBE_o data did not constitute a complete set of all LBEs, therefore the ability to optimize parameters was unrealistic. Further, the metrics did not address all mapping issues or errors such as over- or under-segmentation. Thus, metrics were coupled with visually based qualitative assessment of mapping performance covering the entire study segment to select one approach and parameter set used to generate LBEs for whole study segment (‘preferred dataset’).

Mapping performance of the preferred dataset was considered accurate if PA and MJI scores exceeded the median benchmark values provided above. However, LBEs from the preferred dataset were still not without uncertainty, which could influence answering study questions 2 and

3. Therefore, two additional steps were taken to filter out uncertain LBEs (Text A.1.3.3). First, LBEs were removed where the majority of topographic data was from imagery-derived bathymetric estimates or augmented points (section 1.4.1; Text A.1.3.1). Second, LBE polygons were removed where topographic data resolution and/or topographic variability were relatively low, presuming these would result in poor LBE predictions. This was accomplished by comparing lidar point densities and mean standard deviation in elevations ($\overline{\sigma_z}$) within LBE_o and LBE_p polygons from the preferred dataset to set thresholds for these metrics below which LBE_p polygons were removed. The final set of LBE polygons was used for all further analysis in this study. The minimum LBE polygon size was a single raster cell (0.46 m x 0.46 m). D_c values for each LBE were set as the max RSM value within each polygon.

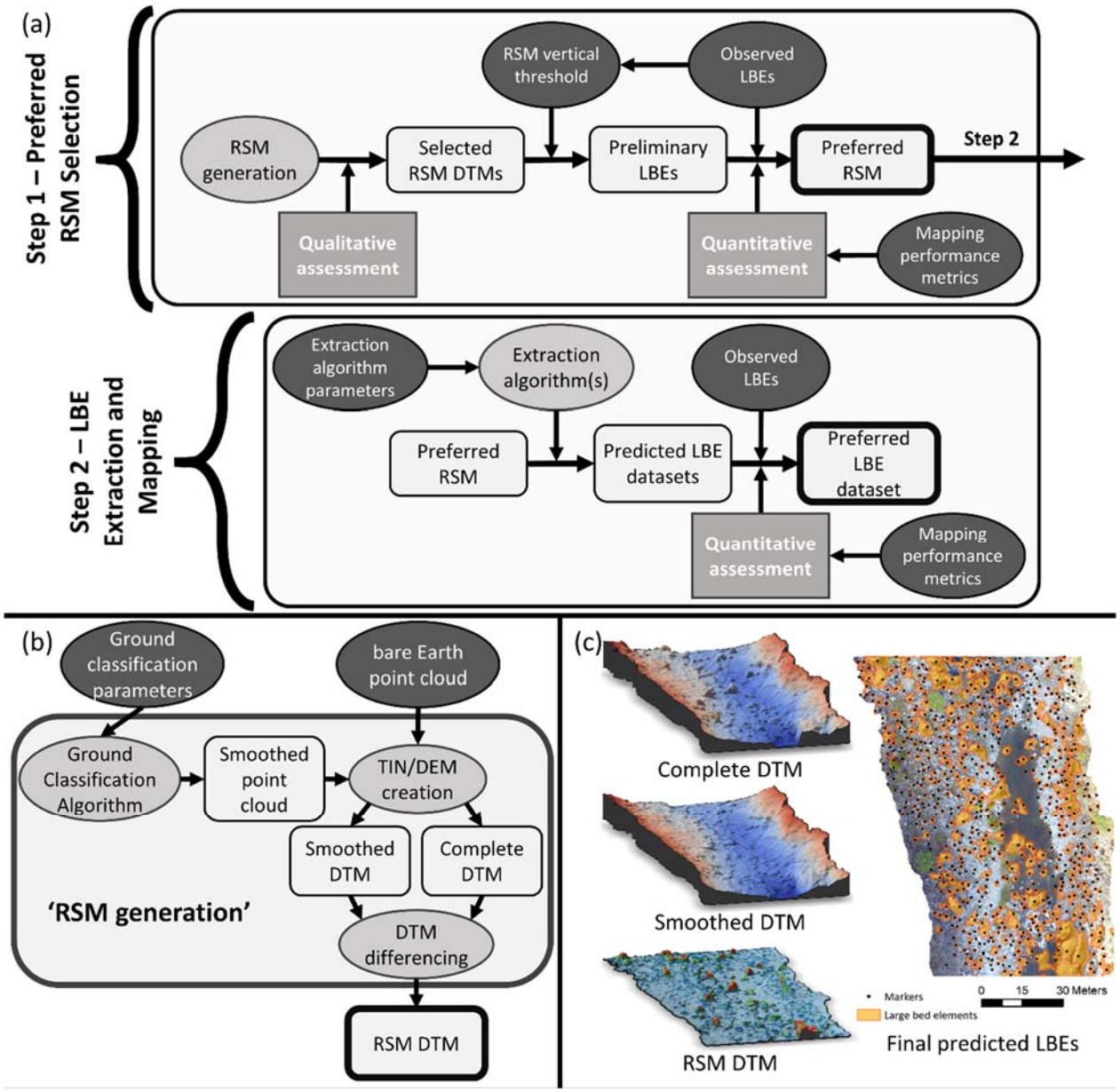

Figure 1.4. (a) Flowchart depicting simplified large bed element (LBE) mapping procedure with (b) detail of 'RSM generation' process and (c) oblique views of example complete, smoothed, and roughness surface model (RSM) digital terrain models (DTMs) from a small portion of the study site with resultant final predicted LBEs. In (a) and (b) light-gray rounded rectangles with dark text are output data, gray ovals with dark text are processing steps, dark-gray ovals with white text are input parameters or input data, and gray rectangles with white text are assessment steps. Arrows indicate directionality and interactions that generate new outputs or inform process steps/inputs. Key outputs from step 1 (preferred RSM) and step 2 (preferred LBE dataset) are outlined in bold.

Table 1.1. Ground classification algorithm parameter descriptions, range used in study, and details for large bed element (LBE) mapping[†].

Parameter	Description[‡]	Range used in study (m)	Information used to select range	LBE mapping details[‡]
Step	Window size used to select points to be iteratively classified.	1.52-4.57	DTM/RSM raster cell size	Controls removal of cohesive terrain features such that features larger than the window-size are preserved in ground classification (Zhang & Whitman, 2005). Recommend setting larger than planform diameter of average LBEs but less than maximum LBE diameter and/or scale of dominate terrain features. Length of ~3-9 raster cells used to set range in this study.
Bulge	Specifies how much the TIN is allowed to bulge up when including points as it is getting refined.	0.03-0.30	Preliminary testing and user manual	Typically 1/5-1/10 step size, smaller values recommended for creating a smoothed DTM.
Spike	Threshold at which points forming spikes above the coarsest TIN get removed.	0.03-0.50	Representative grain sizes and minimum LBE heights from previous studies	Length scale(s) collectively control if points are classified as ground or removed based on how much points extend below or protrude above an otherwise smooth but variable bed surface. Estimated D_{50} (0.128-0.256 m) and D_{16} (0.032-0.064 m) values (YCWA, 2013), and two representative LBE sizes for boulders from the Udden-Wentworth scale (Wentworth, 1922), 0.256 m and 0.5 m, used to set range in this study.
Down-spike	Threshold at which points forming spikes below the coarsest TIN get removed.	0-0.50		
Offset	The maximal offset up to which points above the current ground estimate get included.	0.03-0.50		
Intensity	Specifies the search level for initial ground point classification.	extra-hyper	Preliminary testing and user manual	Use intense search setting (hyper, ultra, extra) for steep, hilly terrains and simplified search settings (fine, coarse) for flat terrains.

[†]Acronyms in table are as follows: digital terrain model (DTM), roughness surface model (RSM), triangular irregular network (TIN), and D is grain size diameter and subscript is percent of grains finer.
[‡]See http://lastools.org/ for more details

1.4.4 Two-dimensional hydrodynamic modeling

Wetted areas were required to assess the discharge-dependent LBE spatial structure in

different portions of the channel. Wetted areas were generated from steady-state hydrodynamic simulations performed at ~ 1-m resolution using the free, public, 2D model, Sedimentation and River Hydraulics—Two-Dimensional model (SRH-2D) v. 2.2 (Lai, 2008). This is a proven code capable of simulating hydraulic conditions in mountain rivers with abundant LBEs (Brown & Pasternack, 2014; Strom et al., 2016). Simulations were run for four discharges (1.54, 10.73, 82.12, and 343.6 m^3/s) from an approximate baseflow to a ~ 3.5-yr flood. Model development, parameterization, and performance assessment are thoroughly documented in APPENDIX 1 (Text A.1.3.4). The 2D model performed comparably to similar published models (e.g. Lisle et al., 2000; Pasternack et al., 2006).

1.4.5 LBE spatial analysis

Having extracted a set of accurate LBE polygons from ALS point clouds, four subsets of the data were made comprising the set of final LBE polygons that intersected with the wetted area polygon of each simulated discharge. In this manner, discharge served to hierarchically nest spatial domains, since lower discharge wetted areas were always located within higher discharge wetted areas. These data are referred to herein as 'discharge-dependent LBE datasets'. From these data, LBE spatial structure was characterized in terms of concentration (Γ) and spacing (λ) metrics to answer questions 2 and 3. Specifically, metrics were used to classify segment, reach and cross-sectional spatial domains according to Morris' hydrodynamic regimes to assess if LBEs were configured to maximize flow resistance, per question 2. Concentrations were also analyzed by lateral distribution per question 3.

1.4.5.1 Spatially stratified LBE concentrations

Each LBE is a polygon with a plan view (2D) area. To geospatially quantify Γ, it is defined as the areal proportion of LBE polygons within any larger domain. In this study, the larger domain

varied depending on the analysis.

For question 2, the larger domain was the river's wetted area at a given discharge clipped to different portions of the study segment depending on the analysis scale. First, Γ was computed at the segment scale four times, once per discharge investigated (section 1.4.4) by clipping the LBE polygons with a wetted area polygon. This yielded four segment-scale wetted area Γ values. In addition, 24 more reach-scale wetted area Γ values were computed by clipping each discharge's segment-scale wetted area and the LBE polygons with the individual polygon for each of the six geomorphic reaches. The final segment- and reach-scale spatially stratified dataset consisted of 28 Γ values. Lastly, longitudinal Γ profiles were generated for the full extent of each wetted area at abutting 3-m wide, cross-sectional polygons stationed along the river corridor (Text A.1.3.5). Cross-sectional Γ values were calculated by dividing the area of LBE within each cross-sectional polygon by the polygon's area. This cross-sectional analysis provides the resolution of LBE patterns needed to evaluate local topographic, hydraulic, and morphodynamic factors compared to what is possible with averages at segment and reach scales.

To answer question 3, the four segment-scale wetted areas were used to create three incremental inundation corridor polygons. Incremental inundation corridor is defined as the river's terrain that is dry at a lower discharge and wet at a higher discharge (Figure 1.5). LBE polygons were clipped by each incremental inundation corridor polygon and Γ was computed for each of these three domains. These domains isolate analysis to the series of adjacent, non-overlapping regions of the river corridor that become successively inundated and geomorphically active with increasing discharge. In addition, each segment-scale incremental inundation corridor was clipped by the geomorphic reach polygons, once again yielding 28 domains (4 flows times six reaches plus 4 whole-segment flow areas) for testing.

1.4.5.2 LBE spacing calculations

Next, LBE-to-LBE spacings were used to further evaluate LBE spatial structure and as a second test of whether LBEs were organized to maximize flow resistance. First, longitudinal (streamwise) distances between upstream and downstream LBEs (λ^l) were estimated using a channel-oriented, path-based approach (Figure 1.6; Text A.1.3.5). Distances were non-dimensionalized (λ_*^l) by dividing each λ^l by the D_c value of the upstream LBE. Because multiple paths could emanate from each upstream LBE, LBEs could have multiple λ_*^l values. Thus, a single spacing value ($\widehat{\lambda_*^l}$) was calculated for each LBE as the median of all λ_*^l values. Next, each LBE was assigned to the discharge-dependent cross-section containing the LBE polygon's centroid. Finally, $\widehat{\lambda_*^l}$ values for all LBEs originating in each cross-section were averaged yielding one spacing value per cross-section per discharge ($\overline{\lambda_*^l}$).

1.4.5.3 Hydrodynamic regime and flow resistance inferences

All Γ and $\overline{\lambda_*^l}$ values were framed according to Morris's (1959) hydrodynamic regimes to evaluate spatial patterns and the dynamic percentage of channel in each regime, and test for conditions that maximize flow resistance at the designated spatial scales. Synthesizing multiple studies, bounds for Γ regime classification were set such that $\Gamma < 0.08$ (e.g. 8% percent of spatial domain) corresponded to the isolated roughness regime, Γ values between 0.08-0.30 to the wake interference regime, and $\Gamma > 0.30$ were classified as skimming flow (Canovaro et al., 2007; Fang et al., 2017; Ferro, 1999; Nowell & Church, 1979; Papanicolaou et al., 2001). Regime classification for $\overline{\lambda_*^l}$ used spacing thresholds reported by Papanicolaou and Tsakiris (2017), where $\overline{\lambda_*^l} > 6 \cdot D_c$ corresponded to the isolated roughness regime, $\overline{\lambda_*^l}$ values between $2\text{-}6 \cdot D_c$ to wake interference, and $\overline{\lambda_*^l} < 2 \cdot D_c$ to skimming flow (also see Gippel et al., 1996; Tan & Curran, 2012).

Since $\overline{\lambda_*^l}$ calculations were done at the cross-sectional scale and it was desirable to have segment- and reach-scale spacing based regime classifications, individual $\widehat{\lambda_*^l}$ values in each discharge-dependent segment and reach domain were classified using the same $\overline{\lambda_*^l}$ regime thresholds as above. Domains were then classified as the single regime having the highest percentage of classified $\widehat{\lambda_*^l}$. In this manner each spatial domain was assigned a regime classification using both Γ and a spacing metric ($\overline{\lambda_*^l}$ or $\widehat{\lambda_*^l}$). Conditions of maximum flow resistance were assumed to correspond to the wake interference regime (section 1.2.3). Thus, this criterion was used to test if LBEs were configured to maximize flow resistance for each metric for each spatial domain as appropriate to answer question 2. Cross-section regime classifications were further used to characterize local spatial variability, or lack thereof, in tendencies to maximize flow resistance.

Lastly, regime predictions from segment- and reach-scale Γ and $\widehat{\lambda_*^l}$, and cross-sectional Γ and $\overline{\lambda_*^l}$ values were compared for consistency in the form of confusion matrices showing the number of regimes classified similarly and how regime classifications differed between metrics, if this occurred. To interrogate metric appropriateness, LBE counts and median LBE areas were calculated at each channel cross-section. These metrics are also linked to local flow resistance (e.g. Canovaro et al., 2007; Gippel et al., 1996) and serve as an independent check on the ability of Γ and $\overline{\lambda_*^l}$ to characterize LBE spatial structure. These data were stratified by classification regime for each metric, Γ and $\overline{\lambda_*^l}$, independently, and statistical distributions were heuristically compared. Interpretation was that less overlap in distributions between regimes for the same metric was an indicator of better classification accuracy, since regimes correspond to different levels of flow resistance (Fang et al., 2017). Cross-sectional LBE counts and median LBE area data were also compared between sections classified the same and differently by each metric to help explain potential discrepancies in cross-section classifications (Text A.1.3.5).

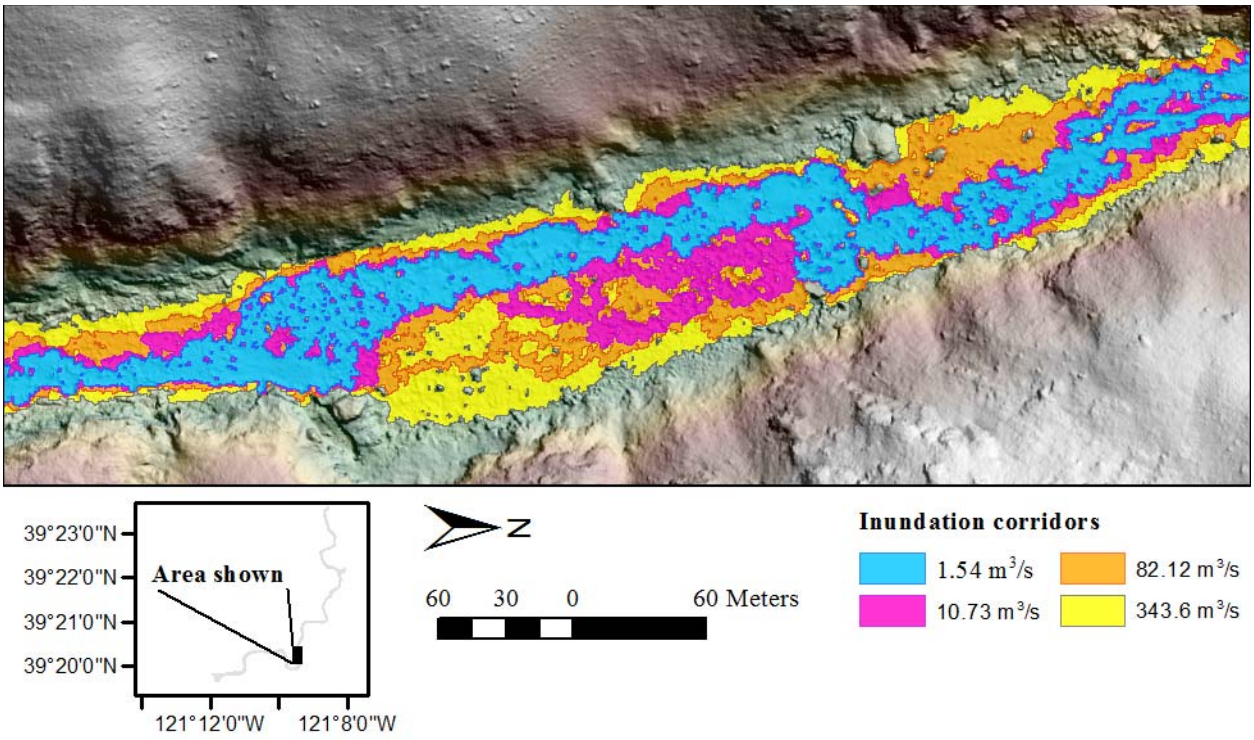

Figure 1.5. Typical output from 2D model simulations showing the baseflow wetted area (blue) and the subsequent incremental inundation corridors occurring as strips between successive higher discharges. For example, pink is the incremental inundation corridor between 1.54 and 10.73 m^3/s. Flow is from right to left.

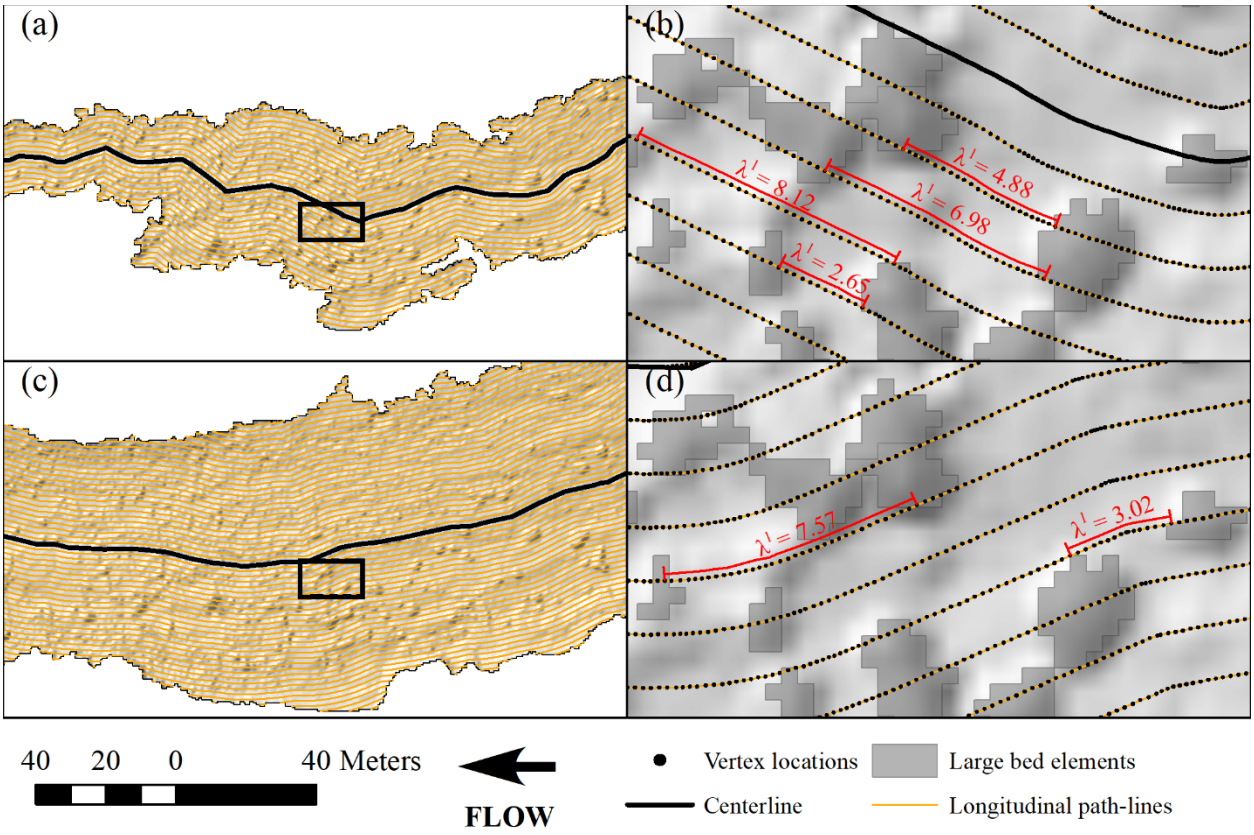

Figure 1.6. Arbitrary portion of the study segment illustrating path approach for large bed element-to-large bed element (LBE-to-LBE) spacing analysis depicting set of offset longitudinal path-lines for (a) 1.54 m^3/s and (c) 343.6 m^3/s discharge simulations. (b) and (d) depict zoomed in views of the inset boxes shown in panels (a) and (c) showing path-lines, LBEs, and densified vertices used in calculating non-dimensional LBE spacing ($\boldsymbol{\lambda_*^l}$) values. Example longitudinal LBE spacing (λ^l) measurements along path-lines between upstream and downstream LBEs are depicted in red in panel (b) and (d).

1.5 Results

1.5.1 Question 1 results (LBE mapping)

Qualitative assessment of the 14 smoothed DTMs determined certain ground classification parameter sets performed better than others (Table A1.3). Generally, larger step sizes (~3 and 4.5 m), smaller spike and offset values (0.128 m [D_{50}] and 0.064 m [D_{16}] versus 0.5 m), and intermediate down-spike values (0.128 m, 0.256 m, and 0.15 m) were best at filtering-out LBEs while maintaining character of the overall terrain. Ultimately, the study site's estimated D_{50} (0.128

m) was identified as the best measure for the spike and offset parameters, together with a slightly larger value of ~2·D_{50} (0.256 m) for the down spike parameter.

Quantitative assessment of preliminary LBEs mapped from the best six smoothed DTMs found P-LBE-10 to perform best, making the associated RSM the preferred RSM (Table A1.11). Preliminary LBEs from this RSM had the best global performance metric and second best MJI (0.183), MER (0.014), and PA (0.836) scores. PA scores for all six preliminary LBE datasets were between 0.794-0.864 and MJI scores were between 0.107-0.212. These values are near the high end of the benchmark values reported by Kaartinen et al. (2012) and Marconi et al. (2019), indicating an accurate representation of observations.

Comparing performance metrics between extraction approaches, there were within-approach and between-approach differences, with no one approach being best for all metrics. Correlations between performance metrics were also weak ($r < |0.57|$), thus supporting the use of multiple performance metrics. Selective results from the five LBE extraction approaches are presented in Table 1.2 with complete results for all 44 LBE_p datasets in Table A1.12. Between approaches, Gaussian filtered RSMs generally resulted in lower PA scores but higher PO scores, suggesting filtering produced fewer predicted LBEs but those that were mapped had good correspondence with coincident observed LBEs. One issue encountered with Gaussian filtering was rescaling of RSM values, as this complicated attempts to use physically-based metrics for parameter selection. With regard to PO, MJI, and global performance metrics, MCWS approaches (iii – v) performed better than vertical threshold approaches (i and ii). Trends for MER scores were not consistent, but vertical threshold approaches appeared to outperform MCWS approaches. No distinction was present between MCWS and vertical threshold approaches for PA performance as variation was more strongly controlled by within-approach parameters. Within approaches, larger

parameter values for marker detection and feature extraction in the MCWS algorithm (Text A.1.3.3.2) and larger vertical thresholds acted to reduce the spatial extent of LBE mapping. All else being equal, this had the effect of decreasing PA and PO scores and increasing MJI and MER scores. The interpretation here is that more constrained LBE mapping reduced commission errors at the expense of creating omission errors. Overall, tested approaches performed comparatively well as all datasets exceeded the selected MJI benchmark of 0.164, and 40 of 44 datasets exceeded the PA benchmark of 0.56. However, since MCWS approaches consistently performed best, they are recommended over vertical threshold approaches when mapping LBEs or similar landscape features.

Based on performance metrics and visualizing predicted LBE polygons, the MCWS-V-2 dataset from approach (iv), RSM with MCWS and variable window size, was selected as the preferred LBE dataset. Values for the main MCWS parameters controlling the minimum RSM value for a pixel to be considered a marker (minimum marker RSM height) and the minimum RSM value for a pixel to be included in the segmentation (minimum crown RSM height) for the MCWS-V-2 dataset were scaled to ~$2.4 \cdot D_{50}$ (0.312 m) and ~$2.1 \cdot D_{50}$ (0.272 m), respectively (Text A.1.3.3.2; Table A1.12). This dataset had the 27th best PA score (0.756), 33rd best PO score (0.720), 7th best MJI score (0.45), and 3rd best MER score (0.086) but had the 3rd best global performance metric score, thus representing a balance between accuracy and precision that favored avoidance of commission errors over excess prediction. PA and MJI scores also exceeded the specified benchmark thresholds, thus this dataset's LBE mapping was considered satisfactory. Qualitatively this dataset also performed well with regard to LBE segmentation. For instance, while datasets MCWS-C-6 and MCWS-C-8 from approach (iii), RSM with MCWS and constant window size, had better global performance metric scores, visualization found resulting LBEs were over-

segmented (Figure 1.7). Notably, no approach was able to discern boulders from bedrock outcrops or fully decouple individual boulders from boulder clusters, meaning, at times, clusters were aggregated into individual polygons.

Like many predictive sedimentological models there is potential for overfitting parameter values of the MCWS-V-2 dataset to the LBE_o data used for calibration and validation that could result in poor mapping performance when applied to the study segment as a whole. However, since the main MWCS parameters only define minimum RSM threshold values for what constitutes an LBE, mapping performance was consistent across the RSM and would only be impacted if the definition of an LBE substantially changed between reaches. Based on expert opinion, the set of observed LBEs was assumed representative of LBEs in the study site, and thus presumed suitable for specifying parameters to be applied to all study reaches. The fact that LBEs were mapped in varying abundances throughout the study site with only small areas lacking any LBEs is taken as reasonable support of this assumption. Qualitative assessment of mapped LBEs over the whole of the study segment and the fact that MCWS parameters were not set to optimize performance metrics also reduced potential overfitting.

Prior to filtering, MCWS-V-2 mapped a total of 46,471 individual LBEs in the study site. Of these, 302 LBEs (0.6%) were completely removed and an additional 497 LBEs (1.0%) were partially removed due to uncertainty in topographic source data. After this initial filtering, an additional 2,722 LBEs (5.9 %) did not meet the identified lidar point density criteria (>2.9 pts/m2) and 3,081 LBEs (6.7%) did not meet the $\overline{\sigma_z}$ criteria (>0.03 m) resulting in 3,993 more LBEs (8.6%) being removed, leaving 42,176 polygons in the final LBE dataset (Text A.1.3.3.2). Geometrically the final set of LBE polygons had D_c values (i.e., heights) ranging from the minimum of 0.312 m to 19.7 m and areas ranging from 0.2 to 234.4 m^2 (Figure 1.8). Filtering and the tendency to favor

low commission over omission errors meant the final mapping underestimated the total number of LBEs. Lastly, while focus was on mapping boulders and bedrock outcrops, LWM would be included in the final dataset if features met parametric mapping criteria, though previous surveys suggest low densities of LWM in the study site (YCWA, 2013).

Table 1.2. Selected performance metrics of predicted large bed element datasets with best and worst global performance score for each mapping approach. Maximum values for each metric are highlighted in light-gray and bolded and minimum values are italicized. Preferred dataset in red font[†].

ID	PA	PO	MJI	MER	Global Performance (Normalized mean)
(i) RSM with vertical threshold					
V-1	**0.894**	0.774	0.269	0.030	0.445
V-11	0.669	*0.659*	0.371	**0.086**	0.521
(ii) Gaussian filtered RSM with vertical threshold					
GV-1	0.760	0.705	0.333	0.054	0.458
GV-3	*0.611*	0.779	*0.246*	0.051	*0.352*
(iii) RSM with MCWS and constant window size					
MCWS-C-8	0.798	0.715	**0.464**	0.083	**0.738**
MCWS-C-10	0.809	0.828	0.392	0.025	0.581
(iv) RSM with MCWS and variable window size					
MCWS-V-1	0.760	0.715	0.460	0.083	0.714
MCWS-V-2	0.756	0.720	0.450	0.086	0.718
(v) Gaussian filtered RSM with MCWS and constant window size					
GV-MCWS-C-3	0.712	0.810	0.436	0.057	0.674
GV-MCWS-C-14	0.780	**0.874**	0.339	*0.020*	0.535

[†]Acronyms in table are as follows: producers accuracy (PA), producers overlap (PO), modified Jaccard similarity index (MJI), missed-to-excess ratio (MER), roughness surface model (RSM), and marker controlled watershed segmentation (MCWS).

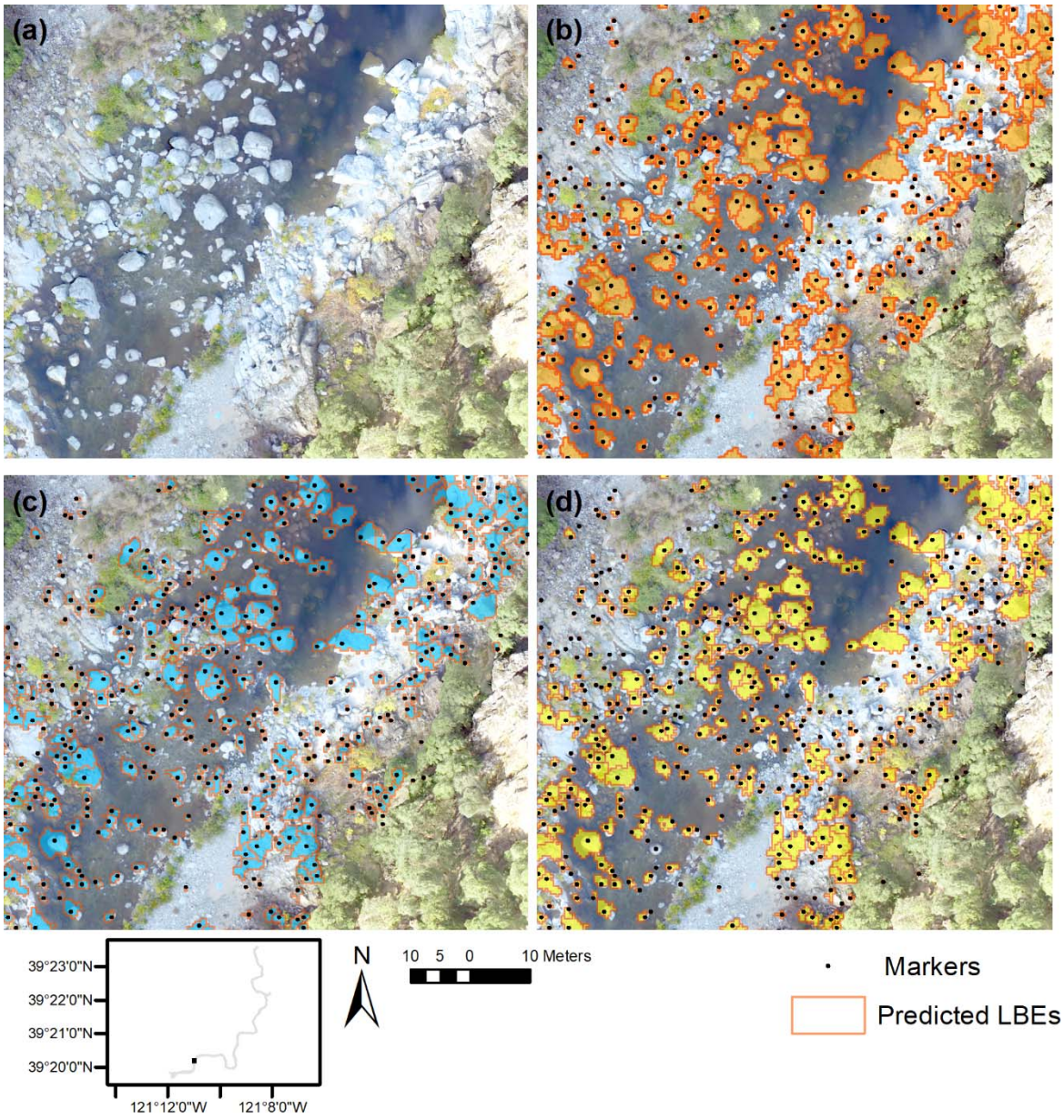

Figure 1.7. Comparison of large bed element (LBE) segmentation performance among algorithms. (a) uncrewed aerial system image, (b) MCWS-V-2, (c) MCWS-C-6, and (d) MCWS-C-8. Note tendency for greater polygon segmentation in panels (c) and (d). MCWS-V-2 (b) was selected as the preferred LBE dataset.

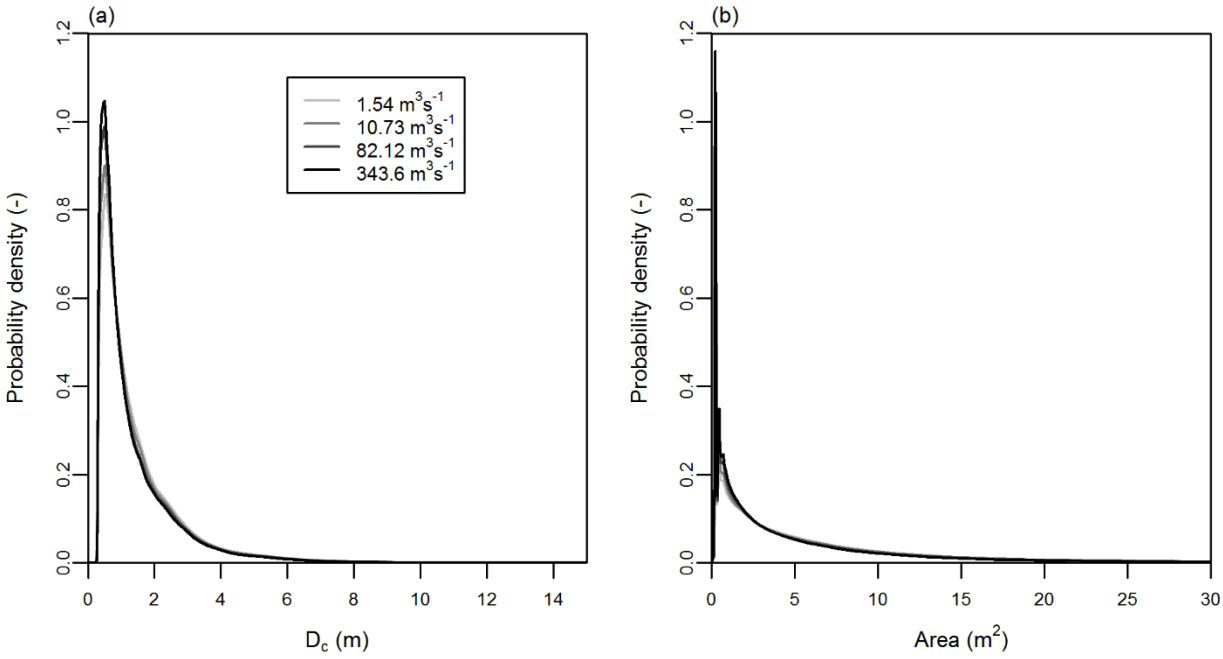

Figure 1.8. Overlain kernel densities of large bed element (LBE) (a) diameter (D_c), and (b) area probability densities for the four discharge-dependent LBE datasets. Note x-axis of both panels have been truncated for visual purposes.

1.5.2 LBE concentrations

LBEs were present individually and in clusters throughout the river corridor. Visually speaking, LBEs conformed to a variety of morphological configurations. Clustered LBEs appeared in seemingly random as well as organized arrangements often forming transverse orientations and step-like structures. Reticulate configurations were discernable but more difficult to identify (Figure 1.9).

At the segment scale, Γ of each wetted area monotonically increased from 18.2% at baseflow to 26.5% at flood-flow (Table 1.3). The trend indicates that as discharge increased the rate at which new LBE area was inundated (e.g. within the wetted area) exceeded the rate that new portions of the river corridor became inundated. This was facilitated by increasingly higher Γ values in each incremental inundation corridor (Table 1.3) and meant that, on a per-wetted-area

basis, increasingly higher Γ existed along channel margins.

Reach-scale results also found wetted area Γ to increase with discharge, although Reach 6 had nearly uniform values across discharges (Table 1.3). Changes in reach-scale wetted area Γ were also strongly influenced by inundation corridor Γ values, such that higher inundation corridor Γ generally resulted in greater increases in wetted area Γ between discharges (Figure A.1.9). A Pearson bivariate correlation of 0.86 between the differences in reach-scale wetted area Γ between subsequent discharges and inundation corridor Γ values supports this interpretation. Across discharges, reaches showed consistent trends in relative Γ magnitude. For instance, while each reach's wetted area Γ values varied with discharge, ranking values at any given discharge resulted in the same ordering across all discharges. As such, Reach 2 always had the highest wetted area Γ, whereas Reach 6 was always lowest. This consistent ordering suggests possible reach-scale wetted area Γ dependencies on hillslope and fluvial geomorphic, topographic, and geometric factors influencing LBE supply, storage, and/or transport.

Cross-sectional Γ trends for each wetted area varied spatially and with discharge (Figure 1.10). Mainly, the increased granularity of these results highlight Γ spatial variability and tendencies for semi-oscillatory and more irregular LBE patterns. Longitudinally, Γ profiles were characterized by constant high-frequency oscillations of varying amplitude and non-constant low-frequency fluctuations Figure 1.10). The non-parametric Mann-Kendall test indicated slight, but non-trivial ($p < 0.05$), decreasing downstream trends in all profiles. Comparison of all possible profile combinations found relatively high correlations ($r > 0.8$). Key features recurring throughout the profiles were sequences of LBE clustering as indicated by rising limbs in the profiles, which peaked or temporarily plateaued, and subsequently declined along diffusive style decay pathways. These patterns were emphasized after processing profiles with a 130 m (5 widths) centered

moving-window mean filter.

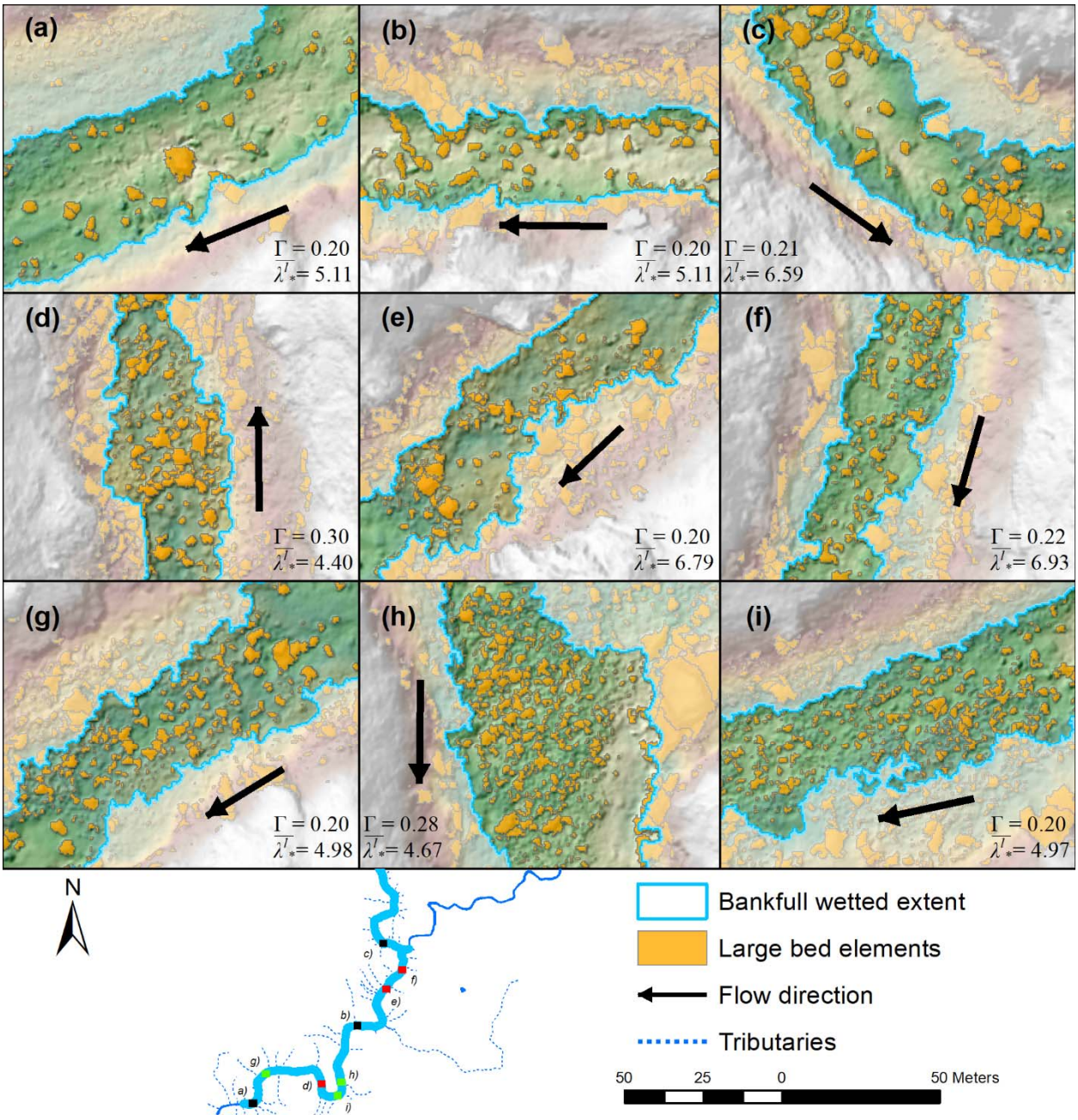

Figure 1.9. Typical configurations of clustered and individual large bed elements (LBEs) within the study site's bankfull channel overlain on shaded detrended relief that include (a-c) low concentration, isolated and clustered LBEs; (d-f) moderate concentration, transverse and step structures; and (g-i) high-concentration mixtures of steps, transverse structures and possible reticulate formations. LBEs outside the bankfull channel are partially transparent. Representative LBE concentration (Γ) and cross-sectionally averaged non-dimensional LBE spacing ($\overline{\boldsymbol{\lambda}^{\boldsymbol{l}}_{*}}$) values for each panel are shown. These values were calculated by averaging bankfull cross-sectional Γ and $\overline{\boldsymbol{\lambda}^{\boldsymbol{l}}_{*}}$ values for all cross-sections present in each panel.

Table 1.3. Discharge-dependent large bed element concentration (Γ) within each simulated wetted area and inundation corridor for study segment and reaches. Values between 0.08-0.30 are within the wake interference regime and are highlighted in gray.

Reach	Wetted area Γ				Incremental inundation corridor Γ		
	Simulated discharge (m^3/s)				Discharges bounding inundation corridor (m^3/s)		
	1.54	10.73	82.12	343.6	1.54 - 10.73	10.73-82.12	82.12-343.6
Segment	0.182	0.211	0.242	0.265	0.321	0.329	0.348
1	0.161	0.181	0.212	0.236	0.257	0.301	0.340
2	0.230	0.269	0.310	0.332	0.411	0.428	0.414
3	0.191	0.218	0.255	0.286	0.346	0.368	0.386
4	0.225	0.261	0.288	0.304	0.372	0.369	0.364
5	0.150	0.178	0.207	0.235	0.295	0.300	0.328
6	0.089	0.098	0.099	0.102	0.167	0.102	0.114

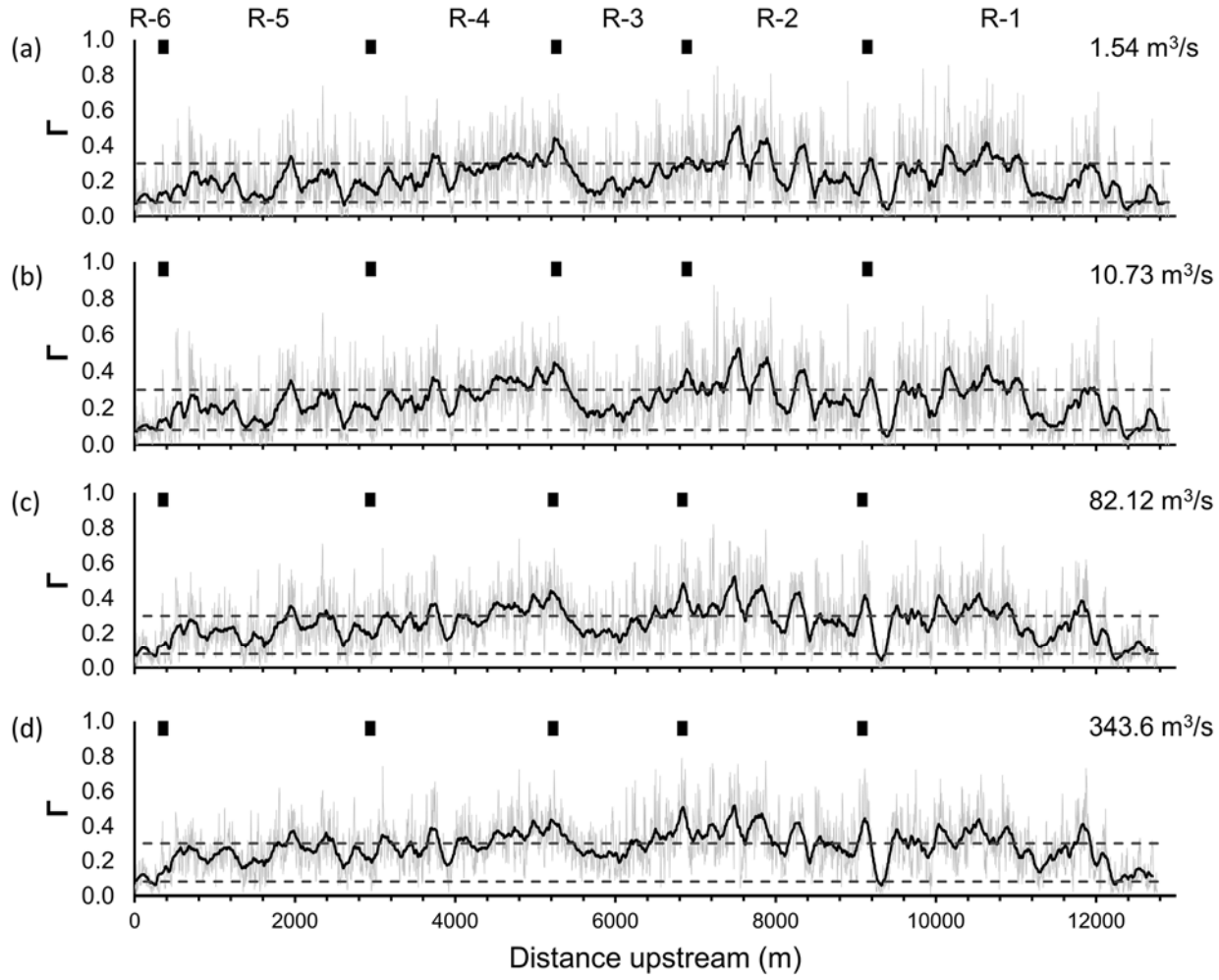

Figure 1.10. Longitudinal profiles of cross-sectional large bed element (LBE) concentration (Γ) values for each discharge-dependent LBE dataset. Light-gray lines are values at each cross-section. Black lines are moving average within a 130 m centered moving window. Dashed horizontal lines are thresholds for Morris's (1959) hydrodynamic regimes at 0.08 and 0.30, respectively. Black vertical markers at top show reach breaks.

1.5.3 LBE spacings

Discharge-dependent streamwise spacing metrics (λ^l, λ_*^l, and $\widehat{\lambda_*^l}$) spanned a wide range but always had positively skewed distributions showing a strong tendency for closely spaced LBEs (Figure A.1.10). The $\widehat{\lambda_*^l}$ results, which were for individual LBEs, depict clear clustering trends (Figure A.1.10), whereas $\overline{\lambda_*^l}$ longitudinal profiles, which depict spacing averaged at the cross-

sectional scale, illustrate greater variability in spacing behavior (Figure 1.11). For instance, $\overline{\lambda_*^l}$ profiles were quite erratic, and like Γ profiles, exhibited high-and-low frequency oscillations of varying amplitudes and consistencies.

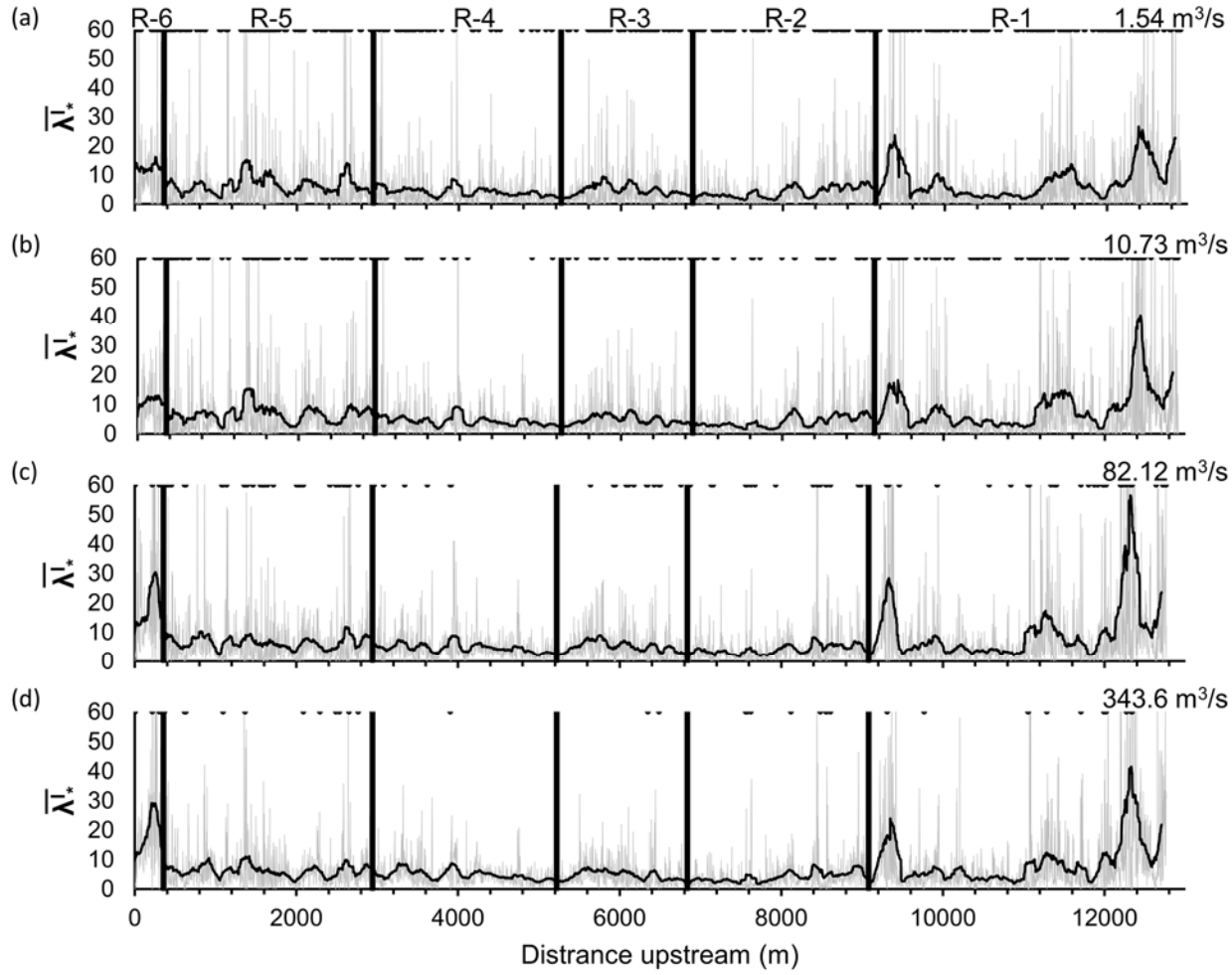

Figure 1.11. Longitudinal profiles of discharge-dependent cross-sectionally averaged non-dimensional large bed element spacing ($\overline{\boldsymbol{\lambda_*^l}}$) values. Light-gray lines are values at each cross-section. Black lines are moving average within a 130 m centered moving window. Dark dots along top of plot are cross-sections with zero values. Vertical black bars show reach breaks. Note the y-axis range is limited to 0-60 for visual purposes despite higher values occurring.

1.5.4 Question 2 results (maximum resistance)

Segment scale wetted area Γ values were all in the range of values associated with Morris's (1959) wake interference regime (Table 1.3). At the reach scale, 21 of 24 wetted area Γ results

were also within the wake interference regime, signifying LBEs in these spatial domains were predominantly configured to maximize flow resistance. Similarly, cross-sectional Γ values found wake interference to be the most common regime in all segment scale wetted areas and in 18 of 24 reach-scale wetted areas (Figure 1.12). Across discharges and spatial domains between 42-66% of cross-sections were classified in either isolated roughness or skimming flow regimes, thus demonstrating localized divergences from the wake interference regime. At higher discharges the proportion of cross-sections classified as wake interference and/or skimming flow increased as the proportion classified as isolated roughness decreased. Longitudinal profiles of cross-sectional Γ show oscillations were commonly around the thresholds of the wake interference regime (Figure 1.10).

Classifying segment- and reach-scale domains based on percentages of classified $\widehat{\lambda_*^l}$ values found that with the exception of Reach 6, which was always in the isolated flow regime, all domains were in the skimming flow regime (Table 1.4). On the other hand, percentages of classified cross-sectional $\overline{\lambda_*^l}$ values found that while skimming flow was the most prevalent regime in the segment-scale baseflow wetted area, wake interference was most prevalent in the wetted areas of the three higher discharges (Figure 1.13). In the study reaches, 8 of 24 wetted areas had the highest percentages of cross-sectional $\overline{\lambda_*^l}$ values in wake interference regime, 10 had the most in the skimming flow, and six had the most in the isolated flow regime (Figure 1.13). At higher discharges the proportion of cross-sections classified as wake interference and isolated roughness generally increased.

Trends in $\widehat{\lambda_*^l}$ and $\overline{\lambda_*^l}$ values contrast with results using Γ, which found LBE density to increase in these same domains. The differences are not mutually exclusive and could result from presence of high-density clusters of LBEs being relative widely spaced along channel margins as

larger portions of the river-valley were included in the calculations, compared to more closely spaced, lower density LBE clusters in the baseflow channel. Sensitivity to the spacing thresholds used to characterize the regimes certainly exists, however these results support that LBEs were closely spaced and structured to maximize resistance at certain scales and in certain portions of the river corridor. Further, like cross-sectional Γ values, oscillations in $\overline{\lambda_*^l}$ longitudinal profiles were commonly around the thresholds of the wake interference regime (Figure 1.11). In this sense the wake interference regime may represent an attractor state toward which conditions, on aggregate, converge.

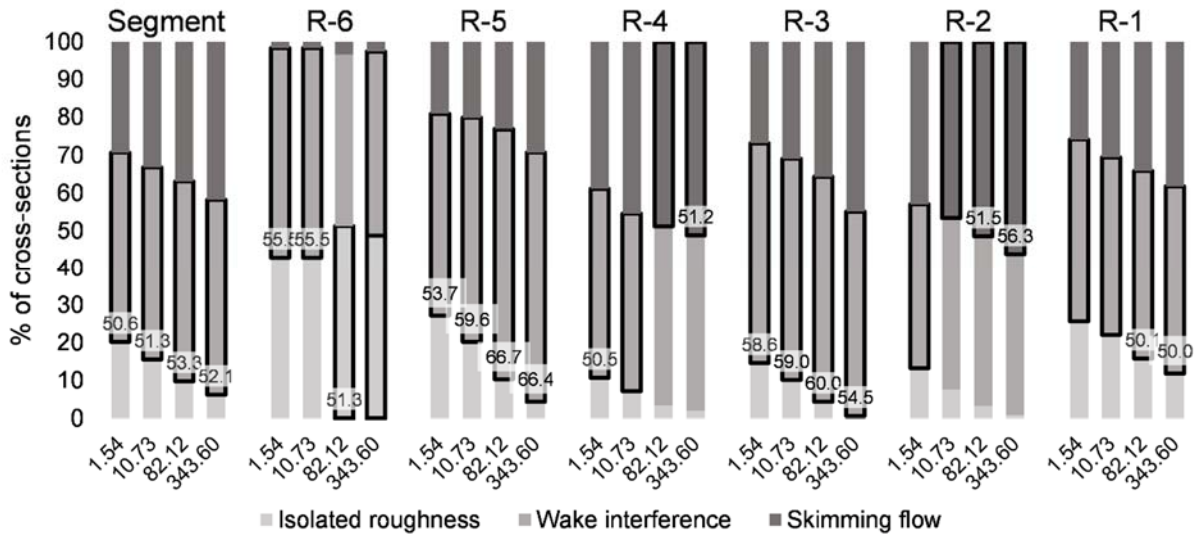

Figure 1.12. Percentages of cross-sectional large bed element (LBE) concentration (Γ) values by spatial domain classified according to Morris's (1959) hydrodynamic regimes for each discharge-dependent LBE dataset. Bars highlighted bold are the dominate regime for each flow. Labeled bars had majority (>50%) of cross-sections in one regime. Reaches are ordered from left to right moving upstream consistent with Figure 1.10.

Table 1.4. Percentage of individual non-dimensional large bed element (LBE) spacing ($\widehat{\lambda_*^l}$) values classified according to Morris's (1959) hydrodynamic regimes for each discharge-dependent LBE dataset. For each domain and flow the regime with the highest percentage of classified $\widehat{\lambda_*^l}$ is highlighted in gray and bolded. Abbreviations are such that: IF – isolated roughness; WI – wake interference; and SF – skimming flow.

Reach	Simulated discharge (m^3/s)											
	1.54			10.73			82.12			343.6		
	IF	WI	SF	IF	WI	SF	IF	WI	SF	IF	WI	SF
Segment	23.68	28.39	**47.93**	24.25	28.94	**46.81**	25.47	28.81	**45.72**	26.25	28.35	**45.40**
1	29.14	26.91	**43.94**	29.07	27.60	**43.33**	28.50	27.78	**43.72**	28.98	26.20	**44.81**
2	17.33	24.96	**57.71**	16.95	26.79	**56.26**	17.13	26.34	**56.53**	18.01	26.51	**55.48**
3	21.75	29.83	**48.42**	22.80	29.77	**47.44**	23.91	30.74	**45.36**	23.64	29.41	**46.95**
4	17.54	30.73	**51.72**	19.19	31.14	**49.67**	22.41	30.77	**46.82**	24.16	31.44	**44.40**
5	26.42	29.85	**43.73**	28.14	30.36	**41.50**	29.53	29.68	**40.80**	29.61	29.27	**41.12**
6	**52.81**	29.21	17.98	**55.97**	23.63	20.40	**57.89**	24.26	17.85	**60.95**	22.59	16.46

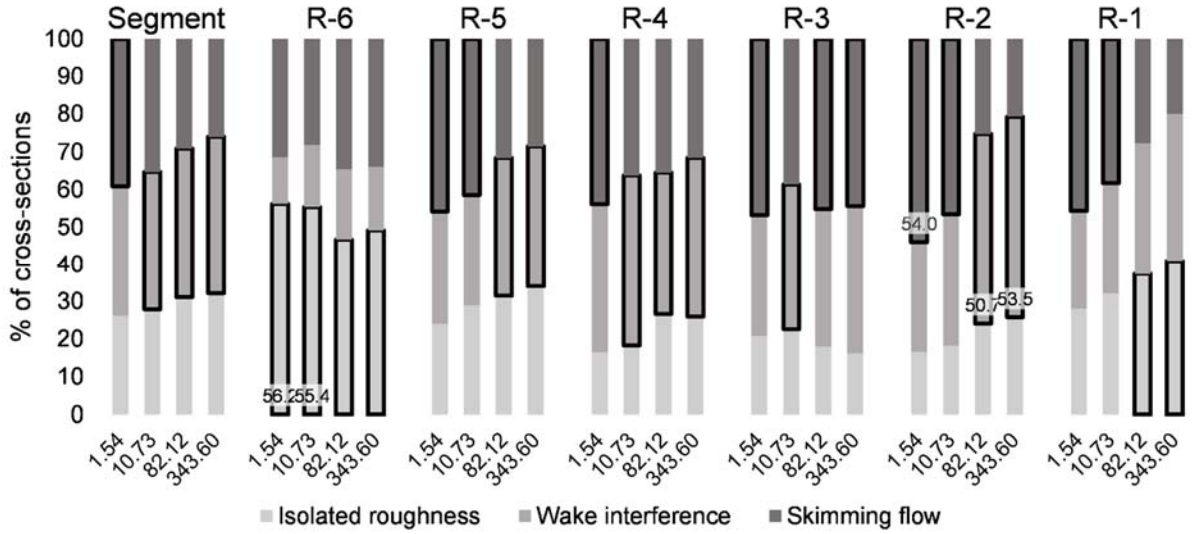

Figure 1.13. Percentages of cross-sectionally averaged non-dimensional large bed element (LBE) spacing ($\overline{\lambda_*^l}$) values within the study segment and each reach classified according to Morris's (1959) hydrodynamic regimes for each discharge-dependent LBE dataset. Bars highlighted bold are the dominate regime for each flow and study domain. Labeled bars had majority (>50%) of cross-sections in one regime. Reaches are ordered from left to right moving upstream consistent with Figure 1.11.

1.5.5 Comparing hydrodynamic regimes from concentration and spacing metrics

Numerous tests performed for question 2 using Γ and spacing metric results require reconciliation. Comparison of segment and reach-scale regime classifications by Γ and $\widehat{\lambda_*^l}$ found only 3 domains were classified the same by each metric. The two most common classification discrepancies were Γ-based wake interference sections classified as isolated and skimming flow regimes according to $\widehat{\lambda_*^l}$ values (Table 1.5). Comparison of all cross-sections found only 44% were classified the same by each metric. The three most common classification discrepancies were Γ-based wake interference sections classified as isolated and skimming flow regimes according to $\overline{\lambda_*^l}$ values, and Γ-based skimming flow sections classified as wake interference by $\overline{\lambda_*^l}$ (Table 1.5). This resulted in greater portions of the study site classified as skimming flow according to $\overline{\lambda_*^l}$ and $\widehat{\lambda_*^l}$ compared to Γ. As mentioned in section 1.5.4, uncertainty in regime thresholds could explain some of the disparity between methods. Adjusting $\overline{\lambda_*^l}$ thresholds to maximize the percent of cross-sections classified the same, with the constraint that wake interference was within the range of $1 \leq \overline{\lambda_*^l} \leq 10$, improved the percent predicted the same by both metrics to 51% and resulted in the following thresholds: isolated roughness for $\overline{\lambda_*^l} > 10$, wake interference for $3 \leq \overline{\lambda_*^l} \leq 10$, and skimming for $\overline{\lambda_*^l} < 3$. Higher $\overline{\lambda_*^l}$ values for the upper bound of the wake interference regime continued to improve consistency between metrics, but values greater than 10 for this threshold are not supported by the literature (Canovaro et al., 2007; Tan & Curran, 2012).

One issue that emerged when using $\overline{\lambda_*^l}$ values to classify cross-sections was if only one or a few LBEs were present per section, and all $\widehat{\lambda_*^l}$ values were small (i.e., <2), the section would be classified as skimming flow despite few LBEs being present. At the other extreme, a lack of downstream LBEs would identify a section with potentially high LBE concentrations in the isolated roughness regime. This issue was highlighted by results of comparing distributions of

cross-sectional LBE counts and median LBE areas classified by Γ and $\overline{\lambda_*^l}$, which found distributions of these metrics were more distinct and generally increased when progressing from isolated flow to skimming flow for Γ classified regimes, whereas distributions were more uniform between $\overline{\lambda_*^l}$ classified regimes (Text A.1.4.4; Figure A.1.11; Figure A.1.12). Several patterns also emerged when comparing LBE count and median LBE area distributions of similarly classified cross-sections with those having classification discrepancies (Figure A.1.13 and Figure A.1.14). For instance, LBE counts of sections classified as wake interference by Γ but as isolated roughness or skimming flow by $\overline{\lambda_*^l}$ were lower than for similarly classified sections (i.e. both in wake interference regime). This is reasonable for isolated roughness regime classification discrepancies, but unexpected for sections classified in the skimming flow regime. Since median LBE areas were lower for $\overline{\lambda_*^l}$-based isolated roughness sections and higher for $\overline{\lambda_*^l}$-based skimming flow sections compared to similarly classified sections, this suggests $\overline{\lambda_*^l}$-based isolated roughness classification discrepancies might have been driven by lower numbers of smaller LBEs with longer downstream spacings compared to similarly classified sections, and that $\overline{\lambda_*^l}$-based skimming flow classification discrepancies might have been driven by lower numbers of larger LBEs with shorter downstream spacings (Text A.1.4.4). In light of these issues and the established relationship between Γ and flow resistance (e.g. Canovaro et al., 2007; Nitsche et al., 2011), Γ is taken as a more reliable metric for the resistance based regime classification of natural channel cross-sections employed in this study.

Table 1.5. Confusion matrix of the number of domains classified into each of Morris's (1959) hydrodynamic regimes using (a) segment- and reach-scale large bed element (LBE) concentration (Γ) (rows) and individual non-dimensional large bed element (LBE) spacing ($\widehat{\lambda_*^l}$) (columns) values, and (b) cross-sectional Γ (rows) and cross-sectionally averaged non-dimensional LBE spacing ($\overline{\lambda_*^l}$) (columns) values. Numbers along diagonals were classified the same by both metrics. Abbreviations are such that: IF – isolated roughness; WI – wake interference; and SF – skimming flow.

(a) Segment and reach scale (n = 28)		$\widehat{\lambda_*^l}$ IR	WI	SF
	IR	0	0	0
Γ	WI	4	0	21
	SF	0	0	3

(b) Cross-section scale (n = 16,832)		$\overline{\lambda_*^l}$ IR	WI	SF
	IR	1346	435	387
Γ	WI	3411	3320	1997
	SF	866	2344	2726

1.5.6 Question 3 results (lateral LBE structure)

Wetted area and incremental inundation corridor Γ values served as indicators for how LBE spatial structure varied laterally in the study segment. In contrast with the results for question 2, the vast majority, 23 of 28, incremental inundation corridor Γ values were classified in the skimming flow regime, and only 5 were in the wake interference regime. Incremental inundation corridor Γ values always exceeded wetted area Γ values for the same domain. As described in section 1.5.2 this meant that on a per-area basis more LBEs were located along channel margins than in the baseflow and representative bankfull channels (Table 1.3). Within the same domain, changes in incremental inundation corridor Γ values were variable, at times increasing (Segment and Reaches 1, 3, and 5), decreasing (Reach 4), or fluctuating (Reaches 2 and 6) as discharge increased. Together, these results indicate LBE spatial structure varied laterally, thus providing differential discharge-dependent roughness in the study segment.

1.6 Discussion

1.6.1 Mapping LBEs in a mountain river

The study's semi-automated mapping procedure facilitated a systematic census of LBEs within a 13.2-km mountain river. Using open-source software and operations that could be

implemented in any GIS, the procedure is transferable across rivers with the caveat that parameterization will likely be site-dependent. Accurate mapping of LBEs from ALS data is valuable as these systems are capable of covering broader spatial ranges than other topographic-based remote sensing methods (Tomsett & Leyland, 2019). Compared to imagery-based methods, mapping LBEs from 3D point cloud data also had the benefit of retaining heights that LBEs protruded above a smoothed bed, which could be useful for ecological, hydraulic, and hazard analysis (Brasington et al., 2012). The mapping procedure also allows for mapping of LWM or other sources of macroroughness, as inclusion of such features is only constrained by topographic data resolution and algorithm parameters. The study's 0.46 m DTM resolution and the site's lack of LWM likely precluded extensive mapping of LWM as LBEs. However, given adequate data resolution, parameters could be tuned to map a ranged of desired roughness features captured by the unique RSM generation process.

The finding that all tested LBE extraction approaches performed well, based on most LBE_p datasets exceeding PA and MJI benchmarks for matching tree-crowns, is motivating given all approaches were parametrically simple and computationally efficient at the segment scale. Still, some approaches outperformed others as demonstrated by the range of PA scores (0.416-0.901). Importantly, high PA values alone may be misleading, as simply mapping more LBEs results in higher PA scores. For example, several LBE_p datasets with high PA scores had relatively low MJI and MER scores, justifying the need for multiple performance metrics (Table A1.12). Further cross-comparison of findings was constrained by absence of studies reporting performance metrics for LBE mapping. However, aspects of mapping performance were still interrogated and found the primary factors controlling mapping performance were: (i) parameter selection for smoothed DTM creation; (ii) approach for LBE extraction; and (iii) extraction algorithm parameterization.

Establishing physical and/or consistent data-driven methods for setting ground classification parameters as part of RSM generation is relevant for transferability of the LBE mapping procedure. As described in section 1.4.3.1, four physically based length scales informed the range of several key parameters tested and found D_{50} was best for parameterizing the algorithm's spike and offset parameters, and ~$2 \cdot D_{50}$ was best for the down spike parameter. These parameters can roughly be thought of in terms of controlling which grains should be included in the RSM and which should be removed. The outcome of this study was that grains ~D_{50} in height were retained in the RSM, and those larger were removed. This common sedimentological length scale provides a physical basis for parameter selection but further applications are required to evaluate its transferability or universality for smoothed DTM creation in other systems.

Approaches for LBE extraction varied in terms of mapping accuracy and ease of implementation. Performance metrics and heuristic assessment found approach (iv), MCWS with a variable window size, produced the best set of predicted LBEs. Generally, MCWS approaches (iii-v) outperformed vertical threshold approaches (i-ii) for mapping LBEs or similar landscape features, however, mapping performance typically varied more within-approaches having different parameters than between approaches having similar parameters (sections 1.4.3.2 and 1.5.1; Text A.1.3.3.2).

Similar to the smoothed DTM creation process, consistent methods for parametrizing feature extraction algorithms aid transferability of the LBE mapping procedure. Data-driven parameter calculations in this study were simple to implement in any GIS, only requiring a RSM and a small set (10^2-10^3) of observed LBEs. Observed LBEs could be digitized from imagery sources or field surveyed if necessary. Since MCWS approaches performed best, discussion is limited to methods for scaling the approach's minimum marker and minimum crown RSM height

input parameter values (see section 1.5.1 and Text A.1.3.3 for details). Calculated minimum RSM values for a pixel to be considered a marker for the top five performing MCWS approaches scaled between ~2.4-3.3·D_{50} (0.312-0.423 m). Holding other parameters constant, there was little difference in global performance metric scores for this range of values, suggesting, sensitivity to this parameter was low. In the sense this parameter controls the minimum height defining roughness elements it bears resemblance to Nikuradse's (1933) equivalent sand-grain roughness, k_s, which is typically related to characteristic grain sizes through various scaling relationships. The k_s parameter is ubiquitous in hydraulic resistance equations and is often scaled by multiplying D_{50} by a factor greater than unity based on understanding that the largest particles present dominate flow resistance (e.g. Powell, 2014). Marker RSM values in this study fall within the broad range of k_s scaling relationships, but are lower than what has been recommended for coarse-bedded rivers (e.g., 5-7·D_{50}) (Powell, 2014; Weichert, 2006). RSM values do not have a 1:1 correspondence with grain sizes as the former represents topographic offsets from a variable but smooth bed surface, which could account for why the minimum RSM value range was smaller than typical D_{50} scaling of k_s values. The smaller D_{50} scaling for minimum RSM values may simply serve to retain a range of smaller LBEs in the mapping procedure than what is considered in resistance equations with larger k_s values. Estimates of the minimum RSM for pixels to be included in the segmentation process, essentially a control on the lateral extent of LBE mapping, for the top five performing MCWS approaches scaled between ~1.5-2.1·D_{50} (0.192-0.272 m). These values were between ~0.61-0.87·minimum RSM values. Mapping performance was more sensitive to this parameter, and higher values had better global performance metric scores. These improvements diminished when values were above ~1.3·D_{50} (0.169 m) (Table A1.4 and Table A1.12). Further applications are required to evaluate the robustness of these scaling ranges for MCWS based LBE mapping in

other systems.

Beyond performance metrics, visualization noted differences in each approach's ability to distinguish individual LBEs versus aggregate features (i.e., over- and under-segmentation). Vertical threshold approaches appeared less capable of segmenting abutting LBEs, whereas MCWS methods performed better in this regard, as segmentation was an implicit part of the extraction algorithm. Depending on one's goals, some amount of LBE under-segmentation may be acceptable. For instance, mapping particle clusters and/or coarse bedforms such as channel steps are of interest in many studies (Hassan & Reid, 1990; Wittenberg & Newson, 2005). Alternately, over-segmentation can serve to differentiate complex LBE forms into discrete sections, provided each section has a peak identifiable by the marker algorithm. This could be applied toward the study of LBE granular structures, the differential sculpting of complex bedrock features, and/or allow classification of different cluster types, as a few examples.

1.6.2 LBE lateral spatial structure and resistance

Analyzing LBE spatial structure metrics made it possible to gain insight into LBE organization in the study site at multiple spatial scales. A notable pattern that emerged from quantifying Γ within wetted areas and incremental inundation corridors of discharges ranging from baseflow (1.54 m^3/s) to a 3.5-yr flood event (343.6 m^3/s) was that on a per-area basis more LBEs were located along channel margins than in the baseflow and representative bankfull channels (Table 1.3). This was true for the segment as a whole and within each reach, confirming it was neither scale-dependent nor only a localized phenomenon.

One explanation for higher Γ along channel margins is preferential deposition of hillslope derived LBEs in these areas rather than in the bankfull channel portion of the valley bottom. Benda (1990) made this observation in the Oregon Coast Range where boulders from debris flows were

deposited before the flow front, thus leaving various disconnected fans, levees, and/or terraces above channel bottoms. Depositional patterns (e.g. size, shape, and location) of wasting events are influenced by sedimentological and morphological hillslope properties and often differentiate by movement type (Hungr et al., 2001). For instance, pre-frontal boulder deposition is common among debris floods and rock avalanches, whereas coarse materials tend to be present at the front of landslides and debris flow deposits (Hewitt, 2002; Hungr et al., 2001). The site's high potential for mass wasting processes (Curtis et al., 2005), provide abundant possibilities to supply LBEs to the study site's valley-bottom. However, the degree to which various modes of wasting and associated depositional mechanics are responsible for observed lateral Γ patterns remain unclear, and theory suggests fluvial transport amongst other factors play a role. For example, mass movements are often conceptualized as being randomly located along rivers (e.g. Ouimet et al., 2007), which contrasts with the distinct sequences of high- and low-density LBE clusters in the baseflow and bankfull channels (Figure 1.10) and more diffuse and uniformly distributed LBEs along high flow channel margins (Table 1.3). Redistribution of channel margin LBEs to more uniformly paved configurations during historic high magnitude discharges offers one plausible explanation. The fact that LBEs were comprised of boulders, boulder clusters, and bedrock outcrops could mean Γ differences were simply due to the presence of exposed bedrock surfaces along channel margins. Weathering and attrition leading to more rapid breakdown of baseflow and bankfull channel LBEs could also account for a portion of lateral Γ differences (Attal, 2017).

While Γ values were highest along margins it is relevant to reiterate that baseflow and bankfull channel Γ values were still relatively high, often at levels conceptualized to maximize flow resistance, thus necessitating supply of LBEs to these portions of the valley bottom as well. Tight hillslope-channel coupling *(sensu* Whiting & Bradley, 1993) theoretically supports

deposition of hillslope derived materials in the bankfull channel. Conceptually, channel margins could act as interim storage locations for LBEs to enter the channel through destabilization processes occurring during infrequent high magnitude discharges (Golly et al., 2019). This is one of many fluvial-hillslope feedbacks known to modulate LBE delivery and depositional processes (Shobe et al., 2016). In addition to destabilizing channel margins, infrequent high magnitude discharges also promote disturbance and transport of bankfull channel LBEs and coarse-bedforms, which are thought to re-organize during smaller more frequent flood events, often achieving oscillatory or semi-oscillatory patterns similar to those observed in the study sites baseflow and bankfull channels (Grant et al., 1990). The study site's largest recorded flood occurred in 1997 at a magnitude of 2165.6 m^3/s. It is assumed this ~ 34-yr flood was capable of mobilizing LBEs several meters in size but the geomorphic work performed relative to the above processes and detangling relative roles of hillslope and fluvial processes driving lateral Γ differences require additional study.

Regardless of explanatory factors, the nested Γ sequence along the study site's river corridor confirmed LBE spatial structure did vary laterally and provides the means for differential roughness as an increasing density of macroroughness features are encountered as discharges increase. This structuring has potential implications toward the commonly held convention that average resistance decreases as discharge increases, as is the case in lower gradient channels with well-defined banks and less abundant LBEs (Powell, 2014). In confined river canyons with abundant LBEs that lack a clear bankfull channel, the discharge-resistance relation response may differ from convention depending on relative contributions of resistance from LBEs versus changing hydraulic conditions (Bathurst, 1978; Pagliara et al., 2008). Hypothetically, if resistance borne by LBEs in incremental inundation corridors increases faster than the amount lost from

increasing width-to-depth ratios and mid-channel LBEs becoming highly submerged (i.e. flow depth to D_c ratio ~10 [*sensu* Weichert, 2006]) and no longer contributing much resistance it is possible for spatially averaged resistance to increase, remain constant, or only minimally decrease up to a point these relationships no longer hold (Abu-Aly et al., 2014; Cassan et al., 2017). In the study site, the latter condition would certainly occur when the river canyon is inundated and LBEs submerge faster than new LBEs are encountered. Ferguson et al. (2019) found a similar scenario in a relatively smooth, trapezoidal, bedrock channel where resistance initially increased with discharge due to increased sidewall roughness, before subsequently decreasing. Notably, increased LBE submergence in the study site's baseflow and bankfull channels at higher discharges would result in substantial resistance heterogeneity along channel cross-sections, potentially necessitating variable roughness length scales along different portions of the channel margins such as proposed by Ferguson et al. (2019).

1.6.3 Segment and reach resistance maximization

The question of whether LBEs were configured to maximize flow resistance was answered using LBE concentrations (Γ) and LBE-to-LBE spacing (λ_*^l) metrics at multiple spatial scales. At segment and reach scales, 25 of 28 wetted area Γ values corresponded to Morris's (1959) wake interference regime which served as a hydrodynamic process-based mechanism for maximizing resistance. On the other hand, based on percentages of classified $\widehat{\lambda_*^l}$ values no discharge-dependent segment or reach scale domains corresponded to the wake interference regime (Table 1.4). Between metrics, there is reason to accept Γ is more reliable for this analysis (section 1.5.5), therefore the remainder of this section focuses on that metric with the understanding that $\widehat{\lambda_*^l}$ results contribute uncertainty to the supposition that LBEs were configured to maximize resistance. Interestingly, segment- and reach-scale Γ results did not document any cases of isolated roughness.

The three Γ values not classified in the wake interference regime had concentrations of 0.31, 0.33, and 0.304, respectively (Table 1.3). These are just outside the regime's specified range (0.08-0.30) but are within a broader range of values reported in the literature that may still serve to maximize resistance. For example, in 394 runs in a flume with three macroroughness element configurations (random, transverse stripe, and longitudinal strip), Canovaro et al. (2007) found flow resistance was maximized at macroroughness concentration of ~30%. Similarly, Pagliara et al. (2008) found friction factor increased for macroroughness concentrations up to ~30%, the maximum concentration of their 197 experimental runs in a fixed-bed flume with randomly patterned elements. Powell (2014) reviewed multiple studies, including those above, and reported resistance was maximized at macroroughness concentrations between 20-40%. Other experiments, such as those by Nowell and Church (1979) who found resistance maximized at a macroroughness density of 8.3%, support the possibility of resistance maximizing at lower concentrations. The range of Γ corresponding to maximum resistance in these studies contribute uncertainty to the study's simplifying assumption that the wake interference regime always corresponds to maximum resistance. However, in the absence of unifying Γ-resistance relations, the interpretation remains that discharge-dependent LBEs in the study segment and most reaches were configured to maximize or nearly maximize resistance.

Notably, omission and commission errors and over- and under-segmentation in the final LBE dataset would affect Γ and $\widehat{\lambda_*^l}$ values and associated regime classifications. Regarding Γ, omissions would result in underestimation effects that could be partly balanced by commission errors, whereas over- and under-segmentation wouldn't effect this metric. Assuming a 25% maximum omission rate (i.e. 25% increase in Γ), which is reasonable according to PA performance (Table 1.2), 5 of the 25 segment- and reach-scale Γ values in the wake interference regime would

switch to the skimming flow regime. However, all baseflow domains would remain in the wake interference regime and most Γ values would remain below 0.4. For $\widehat{\lambda_*^l}$, omissions would also generate underestimation effects, while commission and over- and under segmentation could have opposite effects due to creating more closely abutting LBEs.

Comparative Γ measurements from other mountain rivers are somewhat lacking, but a few are available in the scientific literature. Resop et al. (2012) mapped 31.8% areal cover of boulders (> 0.256 mm diameter) within a 2nd order, cobble-boulder forested Appalachian mountain stream. Boulder (> 0.5 m) concentrations reported by Nitsche et al. (2011) for 14 steep mountainous reaches in the European Alps were between 0-40%. Other reporting posits that large particles generally occupy 2-50% of the bed area in coarse-bedded rivers (Wittenberg & Newson, 2005). Outside natural rivers, the mobile-bed flume experiments of Church et al. (1998) and Hassan and Church (2000) found reticulate structures of "stone cells" to occupy 10-25% of final stable bed configurations. These experiments were conducted both with and with-out sediment feed under various flow conditions, typically in the range producing partial transport. Eaton et al. (2020) proposed a morphologic stability criteria for laterally confined gravel-bed streams of immobile grains occupying 20% of the areal proportion of the bed. Together, these findings provide some support that macroroughness features in mountain rivers occur within the wake interference regime. Still, inconsistencies in how LBE/macroroughness features are classified and quantified, the complexity of processes involved in how LBEs are supplied to and stored in channels, potential Γ dependencies with other morphometric properties, the need to potentially account for other sources of roughness (e.g. spill and vegetative roughness), and the continuously evolving nature of LBE distributions mean more study is needed to understand the wake interference regime as an attractor state for maximizing resistance toward which natural channels evolve (Molnar et al.,

2010). Further, the idea that LBEs organize to maximize resistance fundamentally requires both an active supply of LBEs in the landscape, which itself depends on several factors including but not limited to regional lithology, climate, vegetation, tectonics, and age of the landscape (Attal, 2017; Neely & Dibase, 2020); and a river style where roughness is the primary mode of channel adjustment, which is only true for certain river styles (Brierley & Fryirs, 2005; Fryirs et al., 2016). Notably, both these limiting conditions are present in the study site.

The positive relationship between channel slope and Γ, is a good example of one previously documented morphometric dependency (Grant & Swanson, 1995; Nitsche et al., 2012). Recent study on this topic posits a negative autogenic feedback exists between Γ, channel slope, and hillslope processes such that following a change in base level, river incision acts to steepen adjacent hillslopes, thereby increasing LBE delivery to channels (Shobe et al., 2016). The physical protection and resistance provided by LBEs mediate further channel incision, ultimately allowing for occurrence of overly steep channel slopes compared to equilibrium profiles expected by landscape evolution modeling theory. Like the works cited above, results from this study also found positive relationships between reach-averaged slope and Γ (Figure 1.14). More detailed analysis of the relationship between LBEs and morphometric properties, such as slope, is enticing but beyond the scope of this effort.

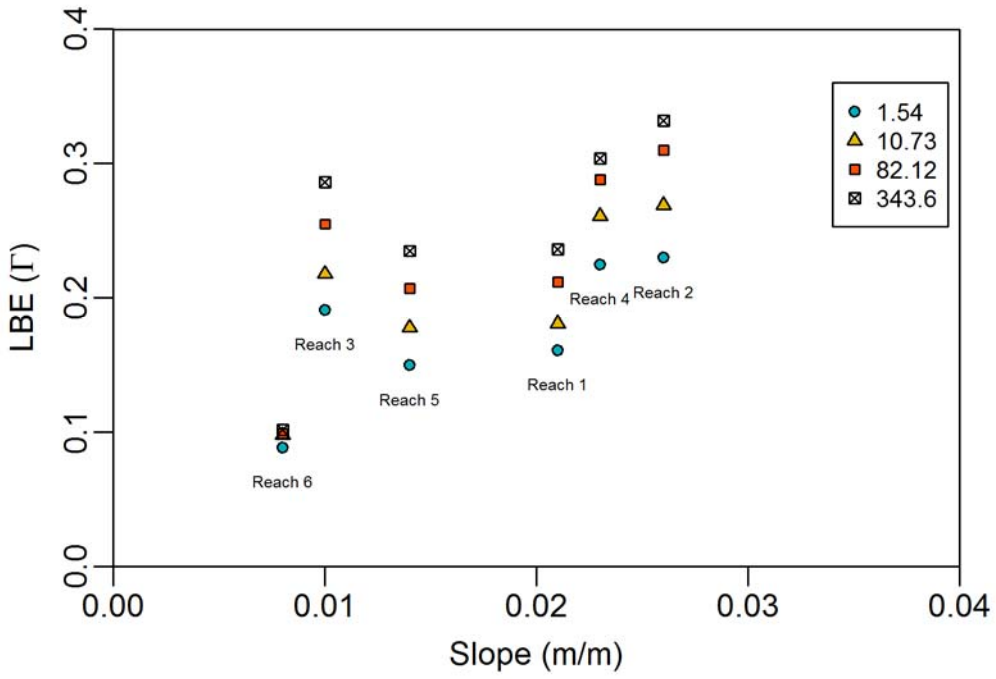

Figure 1.14. Reach scale large bed element (LBE) concentration (Γ) versus reach averaged slope for each discharge-dependent LBE dataset. Discharges in legend are in m^3/s.

1.6.4 Cross-section resistance maximization

Unlike previous efforts aggregating Γ at larger spatial scales (Nitsche et al., 2011), this study included both Γ and $\overline{\lambda_*^l}$ calculations at river cross-sections (10^{-1} width). This granularity highlighted spatial variability of Γ and $\overline{\lambda_*^l}$, and associated Morris regimes, in the study site. For $\overline{\lambda_*^l}$, this is also the first time we aware of this type of LBE spacing metric being calculated in a natural setting at any scale. In many mountain rivers the expectation that all cross-sections would conform to a single hydrodynamic regime such as the wake interference regime is unrealistic. This type of uniform, plane-bed channel morphology contrasts with both the diversity of river styles present in mountainous regions as well as the tendency for bedform development (Brierley & Fryirs, 2005; Grant et al., 1990). This divergence was exemplified by the oscillatory nature of the study site's Γ

and $\overline{\lambda_*^l}$ profiles (Figure 1.10; Figure 1.11), which includes definitive bedforms (Wiener & Pasternack, 2019). Nevertheless, the tendency for oscillations to be centered about the wake interference regime supports the notion that portions of the channel must be attracted to this state, which is compatible with theory for regular to semi-regular coarse bedforms patterns to maximize resistance and promote channel stability (Abrahams et al., 1995; Madej, 2001). In this regard there may be interest to use Γ and/or $\overline{\lambda_*^l}$ as more basic units of geomorphic analysis in addition to or in lieu of more traditional metrics involving channel unit classification (Adams, 2020; Grant et al., 1990).

Discrepancies in cross-sectional Γ and $\overline{\lambda_*^l}$ based regime classifications highlighted potential uncertainties in thresholds used to classify regimes and potential issues using $\overline{\lambda_*^l}$ for classifying Morris's hydrodynamic regimes in natural rivers. While Γ was taken as a more reliable metric for the purposes of this study, spacing metrics like $\overline{\lambda_*^l}$ and $\widehat{\lambda_*^l}$ still have utility in describing hydraulic properties in natural channels as they correspond with flow disruption and recovery length scales (Bathurst, 1978; Tan & Curran, 2012). Spacing metrics can also be used to address open questions of whether clustering mechanisms dominate over dispersive mechanisms in the longitudinal spacing of LBEs in mountain rivers (Madej, 2001). Taken together, the study's concentration and spacing metrics form scale-dependent phase-spaces providing more complete representations of a river channel's LBE spatial structure (Figure A.1.15). For instance, if a river has Γ in the wake-interference regime and $\overline{\lambda_*^l}$ in the skimming regime, as was often the case for baseflow conditions in the study site, this suggests individual LBEs are present in closely spaced clusters (i.e., low $\overline{\lambda_*^l}$), but that the clusters are widely spaced (i.e., relatively low Γ). Visualizing discharge-dependent metric trajectories on phase-spaces can aid in describing how LBE spatial structure and resistance change as different portions of the river corridor become inundated. Lastly,

it is reasonable to posit that data plotting in discrete regions of a Γ-λ phase-space could discriminate different channel morphologies and/or where different modes of channel adjustment such as planform, gradient, or bed roughness would likely dominate (Eaton & Church, 2009).

1.6.5 Resistance maximization as an attractor state

Results of the study found LBEs in the study segment and several other mountain rivers were often present in spatial configurations associated with maximizing flow resistance. However, findings do not address the question of how and why channels might adjust toward a state of maximum flow resistance. The why of this question remains part of a set of open questions on landscape evolution and fluvial morphodynamics that are outside the scope of the effort. However, acceptance of the extremal/regime theory hypothesis that channels adjust their boundaries to maximize flow resistance provides a limited answer, even if the validity of this hypothesis remains open (Eaton & Church, 2009).

How LBE configurations might evolve to maximize flow resistance can be explored through conceptual trajectories of landscape adjustment under the assumption that channels adjustment their boundary conditions to increase hydraulic resistance when resistance is low relative to hydraulic forces and visa-versa. Firstly, if LBEs are present in configurations above those associated with maximum flow resistance high LBE densities covering the channel bed would reduce incision (Shobe et al., 2016; Sklar & Dietrich, 2004). This would be expected to reduce hillslope LBE supply through reduced upslope propagation of hillslope steepening and increased hillslope stability (Attal et al., 2015; Shobe et al., 2016). During periods of reduced supply, other factors such as attrition, weathering, and transport could serve to reduce LBE configurations. Where LBE supply remains high, a cyclical feedback of resistance induced deposition creating more planar beds and thus more transportable LBEs could develop LBE

configurations that oscillate between maximize resistance and those exceeding this condition (i.e., skimming flow) (Eaton et al., 2020; Wohl & Merritt, 2008).

Alternately, LBE configurations lower than those that maximize flow resistance can drive feedbacks increasing LBE supply, deposition, or other adjustments that increase resistance. For instance, with less LBE cover incision processes would increase leading to greater hillslope LBE supply (Shobe et al., 2016). Lower resistance also means channels are less stable during floods, which can lead to hillslope destabilization that increases LBE supply, and increased LBE transport (Ferguson et al., 2019; Golly et al., 2019; Wohl & Merritt, 2008). The latter may be counterintuitive, but can promote bedform development through jamming type interactions and/or armor development that can then increase resistance through exhumation, increased deposition, and/or reduced transport of LBEs supplied by hillslopes (Wohl & Merritt, 2008). Though simplified, these feedbacks provide reasonable trajectories of LBE mediated channel adjustment toward conditions of maximum resistance while leaving room for more complex oscillations and non-equilibrium behavior.

1.7 Conclusions

In a recent commentary on the importance of larger-than-average particles, Williams et al. (2019) stated the need to, "appraise the presence, sources, distribution and role of large grain deposits in contemporary riverscapes." In this study we present and use a semi-automated procedure to systematically map LBEs at the segment scale within a mountain river from 3D point-cloud data. The suite of performance metrics employed found application of a MCWS algorithm to return the best LBE prediction results amongst tested methods, with performance comparable to efforts from the field of forestry for mapping tree-crowns. To allow transferability of the procedure, effort was taken to rely on physical or data-driven techniques for parameter selection.

The study site's D_{50} served as a reference scale for mapping algorithm parameters, but further application is required to understand the universality or range of appropriate scaling factors. Ultimately, given the availability of a 3D point cloud, reasonable LBE mapping was proven to be easily implementable across a variety of spatial scales. This could prove valuable toward improving sediment transport predictions (Yager et al., 2007) and habitat characterizations (Gippel et al., 1996) in mountain rivers where accurate accounting of LBEs is critical (Piégay et al., 2020).

Following mapping, novel exploration of LBE spatial structure was conducted using LBE concentrations and streamwise LBE-to-LBE spacing metrics for multiple laterally and/or hierarchically nested spatial domains at multiple spatial scales. Greater LBEs concentrations along channel margins compared to baseflow and representative bankfull channels provided the foundation for an untested conceptualization for spatially averaged resistance to increase, remain constant, or only minimally decrease with discharge, which differs from current conventional understanding. Segment- and reach-scale LBE configurations supported the hypothesis that LBEs were often organized to maximize flow resistance on the basis of the hydrodynamic flow regimes originally proposed by Morris (1959), however conflicting results, uncertainty in regime thresholds and the assumption that the wake interference regime always corresponds to maximum resistance, and uncertainty regarding the relative role of fluvial versus other geomorphic mechanisms driving LBE organization leave open questions about this extremal model of geomorphic adjustment. Analysis of river cross-sections demonstrated the spatial variability of LBE configurations, but findings also served to reinforce that the wake interference regime may act as an attractor state toward which conditions converge but from which there is freedom to deviate in response to dynamic forces shaping the LBE landscape (Phillips, 1999). Further study of LBEs in other mountain rivers at multiple spatial scales is required to better understand the

regularity and mechanisms by which LBEs are structured to maximize resistance and variability around the wake interference regime. Nevertheless, the fact that LBEs were often configured to maximize resistance as well as documenting differential patterns in the lateral spatial structure of LBEs in the river corridor may have practical applications for synthetic river design and guiding river management or restoration actions such as designing LBE configurations or having reach scale LBE concentrations in the wake interference regime as a process-based goal.

1.8 References

Aberle, J., & Smart, G. M. (2003). The influence of roughness structure on flow resistance on steep slopes. *Journal of Hydraulic Research, 41*(3), 259-269. doi:10.1080/00221680309499971

Abrahams, A. D., Li, G., & Atkinson, J. F. (1995). Step-Pool Streams: Adjustment to Maximum Flow Resistance. *Water Resources Research, 31*(10), 2593-2602. doi:10.1029/95wr01957

Abu-Aly, T. R., Pasternack, G. B., Wyrick, J. R., Barker, R., Massa, D., & Johnson, T. (2014). Effects of LiDAR-derived, spatially distributed vegetation roughness on two-dimensional hydraulics in a gravel-cobble river at flows of 0.2 to 20 times bankfull. *Geomorphology, 206*(Supplement C), 468-482. doi:https://doi.org/10.1016/j.geomorph.2013.10.017

Adams, D. L. (2020). Toward bed state morphodynamics in gravel-bed rivers. *Progress in Physical Geography: Earth and Environment,* 44(5):700-726. doi:10.1177/0309133320900924

Attal, M. (2017). Linkage Between Sediment Transport and Supply in Mountain Rivers. In D. Tsutumi & J. B. Laronne (Eds.), *Gravel-Bed Rivers*.

Attal, M., Mudd, S. M., Hurst, M. D., Weinman, B., Yoo, K., & Naylor, M. (2015). Impact of change in erosion rate and landscape steepness on hillslope and fluvial sediments grain size in the Feather River basin (Sierra Nevada, California). *Earth Surf. Dynam., 3*(1), 201-222. doi:10.5194/esurf-3-201-2015

Bathurst, J.C., (1978). Flow resistance of large-scale roughness. *J. Hydraul. Div*. ASCE 104, 1587–1603.

Bathurst, J.C., (1982). Flow resistance in boulder-bed streams. In: Hey, R.D., Bathurst, J.C., Thorne, C.R. (Eds.), *Gravel-bed Rivers*, Wiley, Chichester, pp. 443–462.

Benda, L. (1990). The influence of debris flows on channels and valley floors in the Oregon Coast Range, U.S.A. *Earth Surface Processes and Landforms, 15*(5), 457-466. doi:10.1002/esp.3290150508

Brasington, J., Vericat, D., & Rychkov, I. (2012). Modeling river bed morphology, roughness, and surface sedimentology using high resolution terrestrial laser scanning. *Water Resources Research, 48*(11). doi:10.1029/2012wr012223

Brierley, G. J., & Fryirs, K. A. (2005). The River Styles Framework. *Geomorphology and River Management: Applications of the River Styles Framework*. Malden, MA: Blackwell Publishing.

Brown, R. A., & Pasternack, G. B. (2014). Hydrologic and topographic variability modulate channel change in mountain rivers. *Journal of Hydrology, 510*(Supplement C), 551-564. doi:https://doi.org/10.1016/j.jhydrol.2013.12.048

Butler, J. B., Lane, S. N., & Chandler, J. H. (2001). Automated extraction of grain-size data from gravel surfaces using digital image processing. *Journal of Hydraulic Research, 39*(5), 519-529. doi:10.1080/00221686.2001.9628276

Canovaro, F., Paris, E., & Solari, L. (2007). Effects of macro-scale bed roughness geometry on flow resistance. *Water Resources Research, 43*(10). doi:10.1029/2006wr005727

Carbonneau, P. E., Lane, S. N., & Bergeron, N. E. (2004). Catchment-scale mapping of surface grain size in gravel bed rivers using airborne digital imagery. *Water Resources Research, 40*(7). doi:10.1029/2003WR002759

Carey, J. A., Pinter, N., Pickering, A. J., Prentice, C. S., & Delong, S. B. (2019). Analysis of Landslide Kinematics Using Multi-temporal Unmanned Aerial Vehicle Imagery, La Honda, California. *Environmental and Engineering Geoscience, 25*(4), 301-317. doi:10.2113/eeg-2228

Cassan, L., Roux, H., & Garambois, P. A. (2017). A Semi-Analytical Model for the Hydraulic Resistance Due to Macro-Roughnesses of Varying Shapes and Densities. *Water, 9*(9), 637.

Chen, Q., Baldocchi, D., Gong, P., & Kelly, M. (2006). Isolating individual trees in a savanna woodland using small footprint lidar data. *Photogrammetric Engineering and Remote Sensing, 72*, 923-932.

Chen, Y., DiBiase, R. A., McCarroll, N., & Liu, X. (2019). Quantifying flow resistance in mountain streams using computational fluid dynamics modeling over structure-from-motion photogrammetry-derived microtopography. *Earth Surface Processes and Landforms, 44*(10), 1973-1987. doi:10.1002/esp.4624

Chin, A., & Phillips, J. D. (2007). The self-organization of step-pools in mountain streams. *Geomorphology, 83*(3), 346-358. doi:https://doi.org/10.1016/j.geomorph.2006.02.021

Church, M., Hassan, M. A., & Wolcott, J. F. (1998). Stabilizing self-organized structures in gravel-bed stream channels: Field and experimental observations. *Water Resources Research, 34*(11), 3169-3179. doi:10.1029/98wr00484

Curtis, J. A., Flint, L. E., Alpers, C. N., & Yarnell, S. M. (2005). Conceptual model of sediment processes in the upper Yuba River watershed, Sierra Nevada, CA. *Geomorphology, 68*(3-4), 149-166. doi:10.1016/j.geomorph.2004.11.019

Davies, T. R. H., & Sutherland, A. J. (1983). Extremal hypotheses for river behavior. *Water Resources Research, 19*(1), 141-148. doi:10.1029/WR019i001p00141

Detert, M., & Weitbrecht, V. (2012). Automatic object detection to analyze the geometry of gravel grains – a free stand-alone tool. River Flow 2012, R.M. Muños (Ed.), Taylor & Francis Group, London, ISBN 978-0-415-62129-8, pp. 595-600.

Eaton, B. C., & Church, M. (2009). Channel stability in bed load–dominated streams with nonerodible banks: Inferences from experiments in a sinuous flume, *J. Geophys. Res*., 114, F01024, doi:10.1029/2007JF000902.

Eaton, B. C., MacKenzie, L. G., & Booker, W. H. (2020). Channel stability in steep gravel–cobble streams is controlled by the coarse tail of the bed material distribution. *Earth Surf. Process. Landforms*, 45: 3639– 3652. https://doi.org/10.1002/esp.4994.

Einstein, H. A., & Barbarossa, N. (1952). River channel roughness. *Trans ASCE* 117:1121–1132

Fang, H. W., Liu, Y., & Stoesser, T. (2017). Influence of Boulder Concentration on Turbulence and Sediment Transport in Open-Channel Flow Over Submerged Boulders. *Journal of Geophysical Research: Earth Surface, 122*(12), 2392-2410. doi:10.1002/2017jf004221

Ferguson, R. I., Hardy, R. J., & Hodge, R. A. (2019). Flow resistance and hydraulic geometry in bedrock rivers with multiple roughness length scales. *Earth Surface Processes and Landforms, 44*(12), 2437-2449. doi:10.1002/esp.4673

Ferro, V. (1999). Friction Factor for Gravel-Bed Channel with High Boulder Concentration. *Journal of Hydraulic Engineering, 125*(7), 771-778. doi:10.1061/(ASCE)0733-9429(1999)125:7(771)

Finnegan, N. J., Broudy, K. N., Nereson, A. L., Roering, J. J., Handwerger, A. L., & Bennett, G. (2019). River channel width controls blocking by slow-moving landslides in California's Franciscan mélange. *Earth Surf. Dynam., 7*(3), 879-894. doi:10.5194/esurf-7-879-2019

Fryirs, K. A., Wheaton, J. M., & Brierley, G. J. (2016). An approach for measuring confinement and assessing the influence of valley setting on river forms and processes. *Earth Surface Processes and Landforms, 41*(5), 701-710. doi:10.1002/esp.3893

Gippel, C. J., O'neill, I. C., Finlayson, B. L., & Schnatz, I. (1996). Hydraulic guidelines for the re-inroduction and management of large woody debris in lowland rivers. *Regulated Rivers: Research & Management, 12*(2-3), 223-236. doi:10.1002/(sici)1099-1646(199603)12:2/3<223::aid-rrr391>3.0.co;2-#

Golly, A., Turowski, J. M., Badoux, A., & Hovius, N. (2019). Testing models of step formation against observations of channel steps in a steep mountain stream. *Earth Surface Processes and Landforms, 44*(7), 1390-1406. doi:10.1002/esp.4582

Gomez, B. (1993). Roughness of stable, armored gravel beds. *Water Resources Research, 29*(11), 3631-3642. doi:10.1029/93wr01490

Grant, G. E., & Swanson, F. J. (1995). Morphology and Processes of Valley Floors in Mountain Streams, Western Cascades, Oregon. *Natural and Anthropogenic Influences in Fluvial Geomorphology* (J. Costa, A. Miller, K. Potter and P. Wilcock ed.).

Grant, G. E., Swanson, F. J., & Wolman, M. G. (1990). Pattern and origin of stepped-bed morphology in high-gradient streams, Western Cascades, Oregon. *GSA Bulletin, 102*(3), 340-352. doi:10.1130/0016-7606(1990)102<0340:PAOOSB>2.3.CO;2

Guillon, H., Byrne, C. F., Lane, B. A., Sandoval Solis, S., & Pasternack, G. B. (2020). Machine Learning Predicts Reach-Scale Channel Types From Coarse-Scale Geospatial Data in a Large River Basin. *Water Resources Research, 56*(3), e2019WR026691. doi:10.1029/2019wr026691

Hassan, M. A., & Church, M. (2000). Experiments on surface structure and partial sediment transport on a gravel bed. *Water Resources Research, 36*(7), 1885-1895. doi:10.1029/2000wr900055

Hassan, M. A., & Reid, I. (1990). The influence of microform bed roughness elements on flow and sediment transport in gravel bed rivers. *Earth Surface Processes and Landforms, 15*(8), 739-750. doi:10.1002/esp.3290150807

Hewitt, K. (2002). Styles of rock-avalanche depositional complexes conditioned by very rugged terrain, Karakoram Himalaya, Pakistan, in Evans, S.G., and DeGraff, J.V., eds., Catastrophic landslides: Effects, occurrence, and mechanisms: Boulder, Colorado, Geological Society of America Reviews in Engineering Geology, v. XV, p. 345-377.

Hodge, R., Brasington, J., & Richards, K. (2009). In situ characterization of grain-scale fluvial morphology using Terrestrial Laser Scanning. *Earth Surface Processes and Landforms, 34*(7), 954-968. doi:10.1002/esp.1780

Hungr, O., Evans, S. G., Bovis, M. J., & Hutchinson, J. N. (2001). A review of the classification of landslides of the flow type. *Environmental and Engineering Geoscience*; 7 (3): 221–238. doi: https://doi.org/10.2113/gseegeosci.7.3.221

Hurst, M. D., Mudd, S. M., Walcott, R., Attal, M., & Yoo, K. (2012). Using hilltop curvature to derive the spatial distribution of erosion rates. *Journal of Geophysical Research: Earth Surface, 117*(F2). doi:10.1029/2011jf002057

Isenburg, M. (2016). "LAStools - efficient LiDAR processing software" (version 160730, unlicensed), obtained from http://rapidlasso.com/LAStools.

Kaartinen, H., Hyyppä, J., Yu, X., Vastaranta, M., Hyyppä, H., Kukko, A., . . . Wu, J. C. (2012). An International Comparison of Individual Tree Detection and Extraction Using Airborne Laser Scanning. *Remote Sensing, 4*(4), 950-974.

Lai, Y. G. (2008). *"SRH-2D version 2: Theory and User's Manual Sedimentation and River Hydraulics – Two-Dimensional River Flow Modeling".* Retrieved from U.S. Department of the Interior, Bureau of Reclamation, Technical Service Center, Sedimentation and River Hydraulics Group. Denver, Colorado.: https://www.usbr.gov/tsc/techreferences/computer%20software/models/srh2d/index.html

Legleiter, C. J., Roberts, D. A., Marcus, W. A., & Fonstad, M. A. (2004). Passive optical remote sensing of river channel morphology and in-stream habitat; physical basis and feasibility. *Remote Sensing of Environment, 93*(4), 493-510. doi:http://dx.doi.org/10.1016/j.rse.2004.07.019

Lisle, T. E., Nelson, J. M., Pitlick, J., Madej, M. A., & Barkett, B. L. (2000). Variability of bed mobility in natural, gravel-bed channels and adjustments to sediment load at local and reach scales. *Water Resources Research, 36*(12), 3743-3755. doi:10.1029/2000wr900238

Madej, M. A. (2001). Development of channel organization and roughness following sediment pulses in single-thread, gravel bed rivers. *Water Resources Research, 37*(8), 2259-2272. doi:10.1029/2001wr000229

Marconi, S., Graves, S. J., Gong, D., Nia, M. S., Le Bras, M., Dorr, B. J., . . . Wang, D. Z. (2019). A data science challenge for converting airborne remote sensing data into ecological information. *PeerJ, 6*, e5843-e5843. doi:10.7717/peerj.5843

Molnar, P., Densmore, A. L., McArdell, B. W., Turowski, J. M., & Burlando, P. (2010). Analysis of changes in the step-pool morphology and channel profile of a steep mountain

stream following a large flood. *Geomorphology, 124*(1), 85-94. doi:https://doi.org/10.1016/j.geomorph.2010.08.014

Morris, H. (1959). Design methods for flow in rough channels. *Proc. ASCE, Journal of Hydraulics Division, 85*((HY7)), 43-62.

Neely, A. B., & DiBiase, R. A. (2020). Drainage area, bedrock fracture spacing, and weathering controls on landscape-scale patterns in surface sediment grain size. *Journal of Geophysical Research: Earth Surface, n/a*(n/a), e2020JF005560. doi:10.1029/2020jf005560

Nikuradse, J. (1933). "Tech. Rep. NACA Technical Memorandum 1292". In Stromungsgesetz in rauhren rohren, vDI Forschungshefte 361 (English translation: Laws of flow in rough pipes), Washington, DC, , USA: National Advisory Commission for Aeronautics. (1950)

Nitsche, M., Rickenmann, D., Kirchner, J. W., Turowski, J. M., & Badoux, A. (2012). Macroroughness and variations in reach-averaged flow resistance in steep mountain streams. *Water Resources Research, 48*(12). doi:10.1029/2012WR012091

Nitsche, M., Rickenmann, D., Turowski, J. M., Badoux, A., & Kirchner, J. W. (2011). Evaluation of bedload transport predictions using flow resistance equations to account for macro-roughness in steep mountain streams. *Water Resources Research, 47*(8). doi:10.1029/2011wr010645

Nowell, A. R. M., & Church, M. (1979). Turbulent flow in a depth-limited boundary layer. *Journal of Geophysical Research: Oceans, 84*(C8), 4816-4824. doi:10.1029/JC084iC08p04816

Ouimet, W. B., Whipple, K. X., Royden, L. H., Sun, Z., & Chen, Z. (2007). The influence of large landslides on river incision in a transient landscape: Eastern margin of the Tibetan Plateau (Sichuan, China). GSA Bulletin; 119 (11-12): 1462–1476. doi: https://doi.org/10.1130/B26136.1

Pagliara, S., Das, R., & Carnacina, I. (2008). Flow resistance in large-scale roughness condition. *Canadian Journal of Civil Engineering, 35*(11), 1285-1293. doi:10.1139/L08-068

Papanicolaou, A. N., Diplas, P., Dancey, C. L., & Balakrishnan, M. (2001). Surface Roughness Effects in Near-Bed Turbulence: Implications to Sediment Entrainment. *Journal of Engineering Mechanics, 127*(3), 211-218. doi:10.1061/(ASCE)0733-9399(2001)127:3(211)

Papanicolaou, A. N., & Tsakiris, A. G. (2017). Boulder Effects on Turbulence and Bedload Transport. In D. T. a. J. B. Laronne (Ed.), *Gravel-Bed Rivers*.

Pasternack, G. B., & Senter, A. E. (2011). 21st Century instream flow assessment framework for mountain streams. Retrieved from California Energy Commission, PIER. CEC-500-2013-059.: https://www.energy.ca.gov/2013publications/CEC-500-2013-059/CEC-500-2013-059.pdf

Pasternack, G. B., Ellis, C. R., Leier, K. A., Vallé, B. L., & Marr, J. D. (2006). Convergent hydraulics at horseshoe steps in bedrock rivers. *Geomorphology, 82*(1), 126-145. doi:https://doi.org/10.1016/j.geomorph.2005.08.022

Pearson, E., Smith, M. W., Klaar, M. J., & Brown, L. E. (2017). Can high resolution 3D topographic surveys provide reliable grain size estimates in gravel bed rivers? *Geomorphology, 293*, 143-155. doi:https://doi.org/10.1016/j.geomorph.2017.05.015

Phillips, J. D. (1999). Divergence, Convergence, and Self-Organization in Landscapes. *Annals of the Association of American Geographers, 89*(3), 466-488. doi:10.1111/0004-5608.00158

Piégay, H., Arnaud, F., Belletti, B., Bertrand, M., Bizzi, S., Carbonneau, P., . . . Slater, L. (2020). Remotely sensed rivers in the Anthropocene: state of the art and prospects. *Earth Surface Processes and Landforms, 45*(1), 157-188. doi:10.1002/esp.4787

Popescu, S. C., & Wynne, R. H. (2004). Seeing the Trees in the Forest. *Photogrammetric Engineering & Remote Sensing, 70*(5), 589-604. doi:10.14358/PERS.70.5.589

Powell, D. M. (2014). Flow resistance in gravel-bed rivers: Progress in research. *Earth-Science Reviews, 136*, 301-338. doi:https://doi.org/10.1016/j.earscirev.2014.06.001

Purinton, B., & Bookhagen, B. (2019). Introducing PebbleCounts: a grain-sizing tool for photo surveys of dynamic gravel-bed rivers. *Earth Surf. Dynam., 7*(3), 859-877. doi:10.5194/esurf-7-859-2019

Resop, J. P., Kozarek, J. L., & Hession, W. C. (2012). Terrestrial Laser Scanning for Delineating In-stream Boulders and Quantifying Habitat Complexity Measures. *Photogrammetric Engineering and Remote Sensing, 78*(4), 363-371.

Schneider, J. M., Rickenmann, D., Turowski, J. M., & Kirchner, J. W. (2015). Self-adjustment of stream bed roughness and flow velocity in a steep mountain channel. *Water Resources Research, 51*(10), 7838-7859. doi:10.1002/2015wr016934

Shao, G., Tang, L., & Liao, J. (2019). Overselling overall map accuracy misinforms about research reliability. *Landscape Ecology, 34*(11), 2487-2492. doi:10.1007/s10980-019-00916-6

Shobe, C. M., Tucker, G. E., & Anderson, R. S. (2016). Hillslope-derived blocks retard river incision. *Geophysical Research Letters, 43*(10), 5070-5078. doi:10.1002/2016gl069262

Sklar, L. S., & Dietrich, W. E. (2004). A mechanistic model for river incision into bedrock by saltating bed load. *Water Resources Research, 40*(6). doi:10.1029/2003wr002496

Strom, M. A., Pasternack, G. B., & Wyrick, J. R. (2016). Reenvisioning velocity reversal as a diversity of hydraulic patch behaviours. *Hydrological Processes, 30*(13), 2348-2365. doi:10.1002/hyp.10797

Tan, L., & Curran, J. C. (2012). Comparison of Turbulent Flows over Clusters of Varying Density. *Journal of Hydraulic Engineering, 138*(12), 1031-1044. doi:10.1061/(ASCE)HY.1943-7900.0000635

Tomsett, C., & Leyland, J. (2019). Remote sensing of river corridors: A review of current trends and future directions. *River Research and Applications, 35*(7), 779-803. doi:10.1002/rra.3479

Valle, B. & Pasternack, G. B. (2006). Field mapping and digital elevation modelling of submerged and unsubmerged hydraulic jump regions in a bedrock step-pool channel. Earth Surface Processes and Landforms 31:6:646-664.

Warrick, J. A., Rubin, D. M., Ruggiero, P., Harney, J. N., Draut, A. E., & Buscombe, D. (2009). Cobble cam: grain-size measurements of sand to boulder from digital photographs and autocorrelation analyses. *Earth Surface Processes and Landforms, 34*(13), 1811-1821. doi:10.1002/esp.1877

Weichert, R. (2006). "*Bed Morphology and Stability of Steep Open Channels"*. In Mitteilung 192, Zürich: Versuchsanstalt fürWasserbau, Hydrologie und Glaziologie (VAW), ETH. https://doi.org/10.3929/ethz-a-005135522

Wentworth, C. (1922). A Scale of Grade and Class Terms for Clastic Sediments. T*he Journal of Geology*, 30(5), 377-392. http://www.jstor.org/stable/30063207

Whiting, P. J., & Bradley, J. B. (1993). A process-based classification system for headwater streams. *Earth Surface Processes and Landforms, 18*(7), 603-612. doi:10.1002/esp.3290180704

Wiener, J., & Pasternack, G.B. (2016a). Accretionary Flow Analysis- Yuba River from New Bullards Bar to Colgate Powerhouse. Prepared for Yuba County Water Agency. University of California, Davis, CA. Retrieved from http://pasternack.ucdavis.edu/research/projects/ncrs/mountain-river-eco-geo

Wiener, J., & Pasternack, G.B. (2016b). 2014 Topographic Mapping Report- Yuba River from New Bullards Bar to Colgate Powerhouse. Prepared for Yuba County Water Agency. University of California, Davis, CA. Retrieved from http://pasternack.ucdavis.edu/research/projects/ncrs/mountain-river-eco-geo

Wiener, J.S., & Pasternack, G.B. (2019). Diversity and organization of mountain river morphological units challenge conceptions of riffle-pool, step-pool, and cascade channel types. Abstract EP51E-2129 presented at 2019 Fall Meeting, AGU, San Francisco, CA, 9-13 Dec.

Williams, R. D., Reid, H. E., & Brierley, G. J. (2019). Stuck at the Bar: Larger-Than-Average Grain Lag Deposits and the Spectrum of Particle Mobility. *Journal of Geophysical Research: Earth Surface, 124*(12), 2751-2756. doi:10.1029/2019jf005137

Wittenberg, L., & Newson, M. D. (2005). Particle clusters in gravel-bed rivers: an experimental morphological approach to bed material transport and stability concepts. *Earth Surface Processes and Landforms, 30*(11), 1351-1368. doi:10.1002/esp.1184

Wohl, E., & Merritt, D. (2008). Reach-scale channel geometry of mountain streams. *Geomorphology*, 93(3-4), 168-185. https://doi.org/10.1016/j.geomorph.2007.02.014

Yager, E. M., Kirchner, J. W., & Dietrich, W. E. (2007). Calculating bed load transport in steep boulder bed channels. *Water Resources Research, 43*(7). doi:10.1029/2006wr005432

Yuba County Water Agency. (YCWA). (2013). *Technncal Memorandum 1-1. Channel Morphology Upstream of Englebright Reservoir. Yuba River Development Project FERC Project No. 2246.* Retrieved from http://www.ycwa-relicensing.com/Technical%20Memoranda/Forms/AllItems.aspx

Zhang, K., & Whitman, D. (2005). Comparison of Three Algorithms for Filtering Airborne Lidar Data. *Photogrammetric Engineering & Remote Sensing*, 71(3), 313-324. doi:10.14358/PERS.71.3.313

CHAPTER 2. 'PROCESS-BASED SIMILARITY' REVEALED BY DISCHARGE-DEPENDENT RELATIVE SUBMERGENCE OF THOUSANDS OF LARGE BED ELEMENTS

2.1 Abstract

Relative submergence of macroroughness elements such as boulders and bedrock outcrops, or large bed elements (LBEs), collectively, is a primary control on hydraulics and morphodynamics in steep, coarse-bedded rivers. However, in practice, the property is typically represented by singular, often reach- or cross-section-averaged values that mask bed-surface heterogeneity and joint distributions of local flow depths. By coupling sub-meter resolution 2D hydrodynamic modeling with spatially explicit mapping of LBEs from a 13.2 km segment of a boulder-bedded mountain river, we present complete distributions of LBE relative submergences at multiple spatial scales and explore their dynamism across discharges. Through distribution fitting and statistical analysis of resultant discharge-dependent LBE relative submergence datasets, it was confirmed that segment- and reach-scale datasets exhibited similar statistical properties and were able to be drawn from the same type of distribution. Further, the rate at which statistical and parametric properties changed between discharge-dependent datasets were statistically equivalent between spatial domains, which we term 'process-based similarity'. Commonality in distribution type and the uniform between-discharge scaling relationships suggest mutual self-organizing processes associated with the size-frequency distribution, spatial arrangement, and submergence of LBEs were present between most domains. Implications of relative submergence distributions on estimating roughness coefficients, hydraulic resistance equations, and geomorphic processes are discussed.

2.2 Introduction

Morphology, defined here as the baseline landform topography and overlying structural elements, of relative high-gradient (≥1.5% channel slope), coarse-bedded ($D_{50} \geq 5$ mm) river channels typically includes predominantly immobile macroroughness features such as boulders and bedrock outcrops. Generally occupying 2-50% of the bed surface area (Wittenberg & Newson, 2005; Wiener & Pasternack, 2022), these large bed elements (LBEs) protrude from the bed-surface into the flow-field, often extending above the water surface over a range of discharges. Protrusion of LBEs into the flow exert resistance on the fluid (Robert, 1990), reduce energy available for sediment transport (Yager et al., 2007; Monsalve & Yager, 2017), influence the temporal and spatial structure of mean and turbulent flow characteristics (Lacey & Roy, 2008; Cooper et al., 2013; Groom & Friedrich, 2019), and influence the mosaic of physical habitat conditions (Kondolf et al., 1996; Crowder & Diplas, 2006).

The manner in which LBEs effect these same properties is strongly related to the degree of LBE relative submergence (h/D_c), where h is local flow depth and D_c is the diameter of the particle of interest, typically normal to an arbitrary datum representing the mean bed surface (Papanicolaou & Tsakiris, 2017). Standard practice is to quantify relative submergence using singular, often reach- or cross-section-averaged h and a single characteristic grain size (D_i), where the subscript i is the percent of grains finer (e.g. D_{50} and D_{84}) (Nitsche et al., 2011; Schneider et al., 2015; Ferguson et al., 2017). However, heterogeneity of LBE sizes and configurations present along the bed and banks of coarse-grained rivers means a variety of h/D_c values are likely present at any given discharge. Owing to limited availability of continuous and comprehensive segment-scale LBE datasets (Benda, 1990; Resop et al., 2012; Shobe et al., 2016) that are rarely if ever coupled with measurements of local flow depths, few if any studies document statistical distributions of

relative submergences for complete sets of LBEs present in natural rivers or how such distributions change with discharge. Accounting for such variability is critical for resolving local and spatially averaged flow hydraulics and sediment fluxes (Monsalve & Yager, 2017; Groom & Friedrich, 2019).

Thus, a main goal of this study was to document discharge-dependent distributions of h/D_c in different spatial domains (i.e. segment and river reaches) in a confined mountain river with abundant LBEs. These data were used to test two general hypotheses. First, based on studies documenting roughness height distributions of water-worked coarse-grained surfaces (natural or experimental) to be unimodal, positively skewed, and leptokurtic (Robert, 1990; Gomez, 1993; Hodge et al., 2009), it was hypothesized that h/D_c distributions would have these same properties (general hypothesis 1). Second, it was hypothesized that statistical properties of h/D_c distributions in a given spatial domain would change between discharges, specifically that the combination of depth changes at previously wetted and partly-to-fully submerged LBEs and new LBEs becoming wetted along expanding channel margins would cause h/D_c distribution variance to increase and central tendency measures such as mean and mode to remain relatively constant and/or increase (Aberle et al., 2010; Yochum et al., 2014; Wiener & Pasternack, 2022) (general hypothesis 2).

To accomplish the study's main goal and address these hypotheses, depth predictions from a two-dimensional (2D) hydrodynamic model were coupled with novel, spatially explicit mapping of LBEs from a confined, boulder-bedded river (i.e. $D_{50} \geq 64$ mm [*sensu* Bathurst, 1982]) with abundant LBEs to develop h/D_c distributions for a series of discharges. Acknowledging the potential for alternative behaviors beyond those hypothesized, changes in h/D_c distributions were also compared to six idealized evolutionary trajectories based on testable, statistical representations of discharge-dependent h/D_c distributions plausible for coarse-grained, partly-

confined to confined rivers. We begin by briefly reviewing concepts of surface roughness and relative submergence (2.2.1), present the six conceptual h/D_c distribution evolution styles (2.2.2), and finally present the questions of this study (2.2.3). Documenting spatially explicit h/D_c dynamics in this manner offers a novel approach for representing bed-surface heterogeneity with implications to the study of channel hydraulics and geomorphology.

2.2.1 Background

In coarse-grained natural rivers, bed roughness has predominately been quantified using four classes of methods: (i) characteristic particle-size approaches (Bunte & Abt, 2001); (ii) random-field approaches (Nikora et al., 1998; Aberle et al., 2010); (iii) statistical representations such as the standard deviation, skewness, or kurtosis of detrended bed-surface elevations within a sub-meter convolution kernel (Aberle & Smart, 2003; Yochum et al., 2012); and (iv) hybrid approaches combining aspects of the aforementioned approaches with additional metrics representing the size and/or spatial arrangement of roughness elements (Schlichting, 1936; Nitsche et al., 2012). Each class has strengths and weaknesses, review of which is outside the scope herein, and the question of how to measure bed roughness remains open for debate (Hodge & Hoey, 2016). Regardless, the result of applying these methods is typically generation of a single bed-roughness length-scale coefficient (Δ) for spatial domains ranging from grain patches to entire river reaches. While singular Δ values are practical, such as for use with spatially averaged hydraulic resistance equations (Powell, 2014), the fact remains they are composite approximations that mask significant heterogeneity of natural channel sediments (Furbish, 1987; Robert, 1990). Inclusion of multiple roughness length scales or other approaches that better represent spatially explicit topographic variability conjecturally offer potential to address such limitations (Smith, 2014; Ferguson et al., 2019).

Once determined, it is common practice for Δ values to be held fixed irrespective of stage (e.g. Nitsche et al., 2011; Yochum et al., 2012; Ferguson et al., 2017; see Aberle et al. [2010] and Abu-Aly et al. [2014] as exceptions). Fixing Δ ignores the discharge-dependent topographic variability of the portion of the bed in contact with the flow, which has implications for landscape evolution modeling, resistance estimates, and other applications (Ferguson et al., 2017). Theoretical and empirical correspondence between R/Δ, where R is hydraulic radius and Δ is parameterized from one of the methods described above (e.g., D_{50}, D_{84}, σ_z [standard deviation of detrended bed elevations], etc.) and common resistance coefficients (e.g., Manning's n or the Darcy-Weisbach friction factor f), has resulted in scaled relative submergence variables of this form being ubiquitous in hydraulic resistance equations (i.e. $\frac{1}{n} \propto \frac{1}{\sqrt{f}} \propto \frac{R}{\Delta}$). The most common functional relationships of these equations being of logarithmic or power-law forms (e.g. Powell, 2014). Notably, the assumption that $h \sim R$, which has minimal errors only for large width-to-depth ratios (>20), is regularly applied (Bathurst, 1985).

On the basis of such resistance equations, many workers document that total resistance values decrease monotonically as flow and depth increase (i.e. as relative submergence increases) (Powell, 2014). Universality of this norm remains debated, especially in boulder-bedded and bedrock-alluvial channels, and findings based on fixed roughness coefficients contribute added uncertainty (Abu-Aly et al., 2014; Hodge & Hoey, 2016; Cassan et al., 2017; Ferguson et al., 2017; Wiener & Pasternack, 2022). For instance, if Δ is fixed, discharge-dependent resistance estimates of many resistance equations simply reduce to being a function of local depth-discharge relationships. The underlying assumption is then that there exists a 1:1 correspondence between h and resistance for all systems with common Δ values. These factors, amongst others (e.g. Comiti et al., 2009; Yochum et al., 2012), contribute to scatter when comparing h/Δ versus hydraulic

resistance observations (Rickenmann & Recking, 2011) and why no single resistance equation is universally accepted for steep rivers with abundant LBEs and low relative submergence flows (Nitsche et al., 2012). By addressing discharge-dependent h/D_c distributions, this study provides new inference into the efficacy of fixing Δ and an approach that better represents bed-surface heterogeneity compared to singular Δ values.

Flow structures and sediment-transport patterns are also influenced by LBE submergence. Locally, LBEs induce pressure gradients that drive flow acceleration over and around elements followed by downstream deceleration and flow separation. These changes in momentum generate turbulence and large amounts of turbulent kinetic energy (Groom & Friedrich, 2019). The size and structure of LBE driven wakes and vortex structures are variable and difficult to predict. However, under idealized conditions, flows around isolated LBEs include a horseshoe vortex region extending ~0.5-1 D_c upstream and a downstream dual wake (primary and far wake) system extending up to ~7 D_c downstream (Shamloo et al., 2001; Tan & Curran, 2012). These structures result in characteristic patterns of scour and deposition that differ depending on submergence and can facilitate development of stable sediment patches (Shamloo et al., 2001; Monsalve & Yager, 2017).

A threshold value of 3.5 has been associated with shifts in depositional tendencies, wherein under high relative-submergence (HRS) conditions ($h/D_c > 3.5$), mobile particles preferentially deposit in wakes downstream of LBEs, and under low relative-submergence (LRS) conditions ($h/D_c < 3.5$) the probability of upstream deposition is heightened (Papanicolaou & Tsakiris, 2017). Threshold values for h/D_c have also been used to classify regimes where different resistance types (e.g. grain, form, spill) are believed to dominate (Bathurst, 1985) and to define scales for separating vertical velocity profiles into distinct layers with unique properties and governing functional

equations (e.g. Shamloo et al., 2001; Cooper et al., 2013). With these associations in mind, mapping spatially explicit LBE configurations and flow properties such as h/D_c can enable more detailed, localized, geomorphic and hydraulic analysis than permitted by spatially averaged values.

2.2.2 Styles of LBE relative submergence response to discharge

The evolution of river channel h/D_c distributions from one discharge to another involves two main processes: (i) depth changes at previously wetted, partly-to-fully submerged LBEs result in a new distribution of h/D_c values at just these LBEs; and (ii) new LBEs become wetted along the expanding channel margin and their distribution is convolved with the new distribution of previously wetted LBEs. For each change in discharge, these two processes occur in tandem to form unique sets of discharged-dependent h/D_c values. The manner of h/D_c distribution changes therein depends on discharge-dependent LBE spatial structure (i.e. location of LBEs in the river valley and which LBEs are wetted at different discharges) and hydrodynamics. In confined river canyons, several workers have documented higher LBE concentrations occurring along hillslope margins outside of valley bottom baseflow and/or bankfull channels (Benda, 1990; Sklar et al., 2020; Wiener & Pasternack, 2022). While the mechanisms for such configurations remain unclear, these circumstances provide conditions to initially hypothesize that h/D_c distributions in a given spatial domain (e.g. river reach) would remain nearly constant across a range of discharges as newly encountered, low submergence LBEs compensate for valley bottom LBEs that become increasingly submerged (Figure 2.1a). This contrasts somewhat with the expectations stated in the study's second general hypothesis, and notably, increased depths at previously wetted LBEs mean some degree of increase in the number of highly submerged particles and an increase in the right-tail of h/D_c distributions is unavoidable.

Statistical equivalency of discharge-dependent h/D_c distribution properties, such as

distribution type and statistical moments, are indicators that mechanisms conserving h/D_c scaling, such as those described above, are present between one or more discharges. This type of statistical self-similarity (Style 1) has been posited as an emergent property of dynamical systems with many interacting elements and extended spatial degrees of freedom, whereby internal dynamics and feedbacks result in system properties evolving toward a critical equilibrium state with self-similar distributions (Sornette, 2000). In fluvial geomorphology, statistical self-similarity has been related to the geometric properties of river networks and the size and spacing of aeolian, fluvial, glacial, and submarine landforms, but remains a controversial topic (Furbish, 1987; Baas, 2002; Ely et al., 2018). Variability in LBE configurations and channel morphology, expected increases in the right-tail of h/D_c distributions, and uncertainty of equilibrium state may conflict with the case for statistical self-similarity (Style 1). Therefore, five other conceptual discharge-dependent h/D_c distribution evolution Styles for partly-confined to confined rivers were theorized drawing on concepts of self-similarity and self-organized criticality (Sapozhnikov & Foufoula-Georgiou, 1999; Baas, 2002) (Figure 2.1).

Figure (b) depicts the case where h/D_c distributions in a given domain have similar central tendencies across discharges, but differ in shape as variance increases (Style 2). This trajectory follows from slight imbalances between how depth increases at previously wetted LBEs relative to the number of newly wetted, presumably low submergence, LBEs that contribute to heavier tails but maintain overall central tendency (Figure A.2.1a). This style is consistent with the study's second general hypotheses and could emerge in a river channel with several laterally nested floodplain-like alluvial surfaces hosting abundant LBEs, provided low-flow channel LBEs rapidly submerged simultaneous with the incremental shallow submergence of floodplain LBEs at successively greater discharges. This style reflects processes of increasing entropy, and divergence

toward greater hydrogeomorphic diversity around a steady attractor state (Chin & Phillips, 2007).

Figure 2.1**(**d) shows the case where distribution shape and variance in a given domain remain constant but central tendency increases with discharge (Style 3). Mathematically, this occurs if depth increases uniformly at all previously wetted LBEs and no new LBEs are encountered as discharges increase. This could be physically plausible for highly concave cross-sections (e.g. incised or canyon-confined channels) with LBEs relegated to the low-flow portions of the valley bottom, though the prospect of spatially uniform increases in depth is questionable in most rivers. In the context of rivers with hierarchically nested LBE non-uniformity (Pasternack et al., 2021; Wiener & Pasternack, 2022), conditions to achieve Style 3 generally require depths at previously wetted LBEs to increase at relatively uniform rates with magnitudes nearly equal to the shifts in central tendency (e.g. depth increases are normally distributed with low variance and means close to shift magnitudes), and depths at newly wetted LBEs to increase rapidly such that submergences are similar to the shifted distributions (Figure A.2.1b). This Style is comparable to simple stabilization of landscape patterns whereby self-organizing processes drive stability in pattern wavelengths, the pattern here being the shape and variance of discharge-dependent h/D_c distributions (Ely et al., 2018).

Figure 2.1**(**f) reflects the case where central tendency and variance are not conserved between discharge-dependent h/D_c distributions in a given domain, but distributions evolve such that rates at which parametric and certain statistical properties increase (i.e. slopes of property-discharge relationships) are equivalent between domains (Style 4). Unlike the within-domain conservation mechanisms of Style 1, this style involves statistical similarity across domains in the combined effects how depths change at each domain-specific set of previously wetted LBEs, and in the h/D_c values of newly wetted LBEs, and is referred to as ‘process-based similarity’. This style

reflects a mutualistic nature to how h/D_c distributions change across spatial domains similar to the phenomena of dynamic self-similarity (Sapozhnikov & Foufoula-Georgiou, 1999) and is indicative of universal autogenic dynamics (Ely et al., 2018). This style is also consistent with the study's second general hypothesis.

Styles 2-4 above all involve continuous, though not necessarily linear, changes in h/D_c distribution properties between discharges. Thresholds are a ubiquitous paradigm in fluvial geomorphology with utility for revealing activity of morphodynamic processes (Phillips, 2006; Pasternack et al., 2021), therefore it is valuable to consider these same Styles in the form of threshold type behaviors. Threshold Styles mimic the continuous Styles but involve small, gradual changes in h/D_c distribution properties over a narrow range of geomorphically-related discharges followed by dramatic shifts in distribution properties due to changes in inundated channel morphology. Figure 2.1(c and e) depict threshold type h/D_c evolution for Styles 2 and 3, referred as 2(b) and 3(b), respectively. Style 2(b), which involves stepped increases in variance, could occur in a valley with a triangular main channel cross-section and one or more side channels with variable LBE configurations. If LBE configurations in the main channel were laterally uniform, h/D_c distributions would remain relatively constant to the point where flows begin to inundate side channels. Rapid addition of the newly wetted LBEs with variable h/D_c values to the increasingly inundated main channel LBEs would drive the hypothetical stepped response. Style 3(b), which involves similar variances and stepped increases in central tendency, could occur in a confined valley with an inset, triangular, main channel with laterally uniform LBEs but few LBEs outside the main channel. Here, the threshold changes in h/D_c central tendency would be driven by non-linearity of the compound channel's stage-discharge relationship when stage exceeds the inset channel and flows onto the floodplain. These processes may repeat if multiple threshold are

present.

The Styles described in this section cover a range of h/D_c behaviors pertinent to partly-confined to confined rivers, but are not all-inclusive. Notably, as discharge increases the central tendency and variance of all h/D_c distributions are portrayed to increase or remain static, but are never theorized to decrease. For a river with a broad, well-defined floodplain having LBEs outnumbering those in the main channel, transition to out-of-bank flow could result in a decrease in h/D_c distribution central tendency. Certainly this and other Styles not included here are possible considering the diversity of global river morphology.

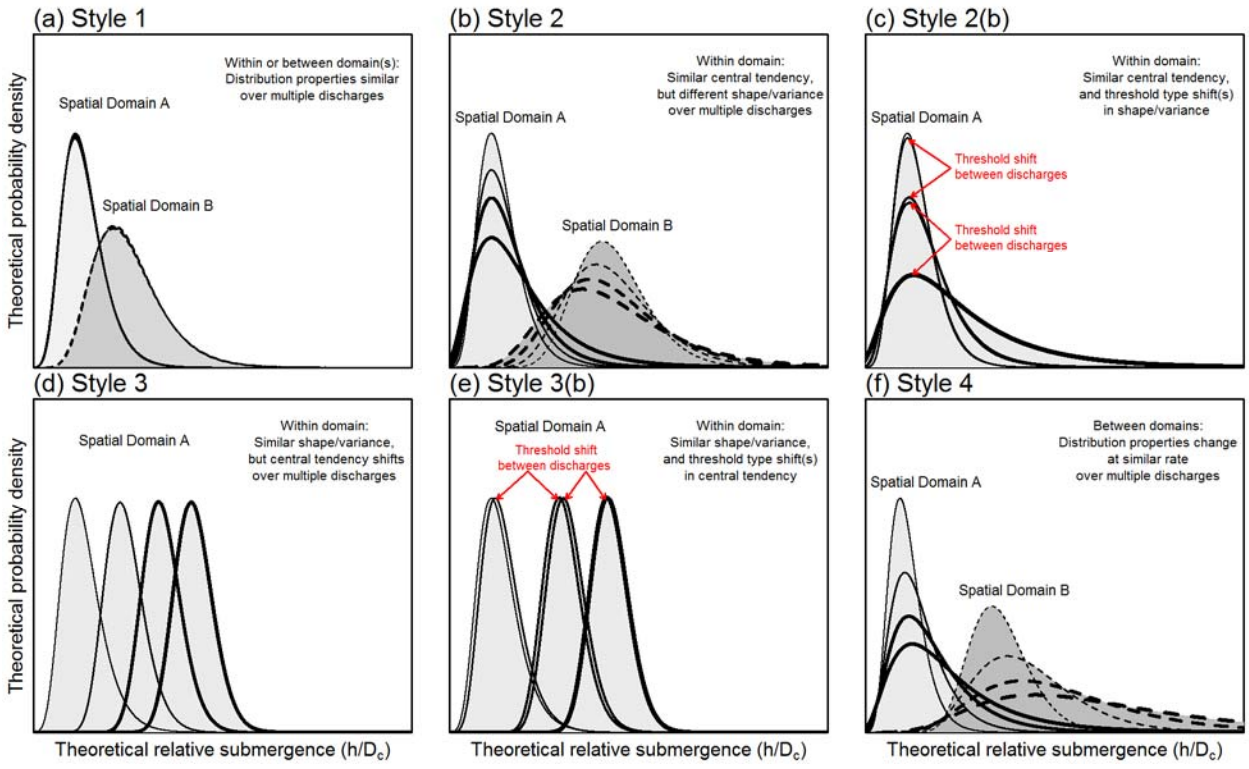

Figure 2.1. Conceptual representations of discharge-dependent h/D_c distribution dynamism. (a) Style 1 where distributions exhibit statistical self-similarity. (b) Style 2 wherein central tendency remains constant but variance increase with discharge. Two examples are provided where spatial domain A has constant modal values between discharges, and spatial domain B has constant means. (c) Style 2(b) which is similar to Style 2 but has h/D_c distributions that are nearly identical (represented by lines with considerable overlap) followed by distributions with threshold shifts in variance. (d) Style 3 wherein shape and variance are constant but central tendencies increase with discharge. (e) Style 3(b) which is similar to Style 3 but has threshold shifts in central tendency. (f) Style 4 wherein the rate of change of parametric and statistical properties are equivalent between domains. In each panel, increasing discharge is represented by increased line thicknesses. Different line styles represent h/D_c distributions for different domains. The number of discharge-dependent h/D_c distributions (lines) and domains shown are illustrative and differ between panels.

2.2.3 Scientific questions

The sections above highlight two scientific questions concerning documenting h/D_c distributions in natural channels. First, what are the discharge-dependent distributions of h/D_c in different spatial domains (i.e. segment and river reaches) in a confined mountain river with abundant LBEs? Second, within or between spatial domains, do discharge-dependent h/D_c

distributions exhibit statistical self-similarity (Style 1), or do behaviors match one or more of the study's other proposed Styles? The subsequent sections of this study document our approach to addressing these questions and the study's two general hypotheses. Lastly, the implications of accounting for h/D_c distributions on channel roughness, hydraulic resistance, and geomorphic processes are discussed.

2.3 Study River Segment

A 13.2-km segment of the mountainous Yuba River (Northern California) draining 1853 km^2 of the western Sierra Nevada range was used to test concepts (Figure 2.2). The study segment is comprised of a low-sinuosity, boulder-bedded, 5^{th}-order mountain river confined within a steep-walled bedrock and forested hillside canyon. The river here has a mean bed slope of 2%, but exhibits localized variability with many 10 – 100 m long (10^0 – 10^1 channel widths) stretches having slopes exceeding 10%. Multi-scale analysis required delineation of geomorphic reaches, thus the study segment was delineated into six geomorphic reaches on the sole basis of channel-bed slope breaks, which ranged from 0.8-2.6 % (Figure 2.3).

Based on limited sedimentological data, bed substrates alternate between bedrock and alluvial sections with estimates of larger boulders (> 512 mm) or bedrock covering over 60% of the channel (YCWA, 2013). Alluvial substrate, where present, is a heterogeneous mixture of materials dominated by coarse fractions (medium gravel/cobbles and larger). The presence of large bounders and the heterogeneity of sizes makes manual grain-size quantification difficult and labor intensive, if attempted. That said, Wolman (1954) pebble counts by YCWA (2013) consisting of sampling of a minimum of 100 pebbles along channel cross-sections within very limited portions of the study segment found average D_{50} values of 193 and 106 mm in the upstream and downstream most portions of the site, respectively, and a D_{84} value of 512 mm in both portions of the site.

Fluvial landforms present comprise a diverse suite of individual morphological units (Wiener & Pasternack, 2019) including cascades, step-pools, and riffle-pools, as well as forced and intermediate morphologies (Thompson et al., 2006).

Like many bedrock-confined rivers, the study segment lacks a contiguous floodplain having only localized areas supporting accumulation of alluvium at major tributary junctions, meander bends, or other areas of local valley widening. Remaining channel margins are comprised of coarse colluvium/alluvium and bedrock. Hydrodynamic modeling (section 2.4.3) found the limited number of alluvial surfaces (e.g. bars) to become inundated over a range of discharges. This non-uniformity corroborates evidence that bankfull discharge in mountain rivers be thought of as a range of recurring discharges (Radecki-Pawlik, 2002). Despite this ambiguity, it remains helpful for dimensional and comparative purposes to identify a single bankfull flow. A previously reported morphologically determined bankfull discharge of 10.73 m^3/s (YCWA, 2013) was used for this purpose. The associated segment-averaged bankfull wetted width and depth, estimated on the basis of hydraulic modeling, were 26 and 1.34 m, respectively.

Previous assessment to understand study segment morphology and hydro-morphodynamic controls has been conducted by Pasternack et al. (2021) and Wiener and Pasternack (2022). Geomorphic covariance structure analysis of study segment width and bed undulations by Pasternack et al. (2021) revealed a threshold stage of ~161 m^3/s above which landform structure was found to be organized and freely self-maintaining via flow convergence routing morphodynamics. Through mapping study segment LBEs (section 2.4.2) Wiener and Pasternack (2022) identified complex multi-scalar LBE organizational patterns often corresponding with Morris's (1959) wake interference regime that theoretically maximizes flow resistance for the channel. They also found LBE concentrations located along channel margins continuously

increased outside the baseflow and representative bankfull channels.

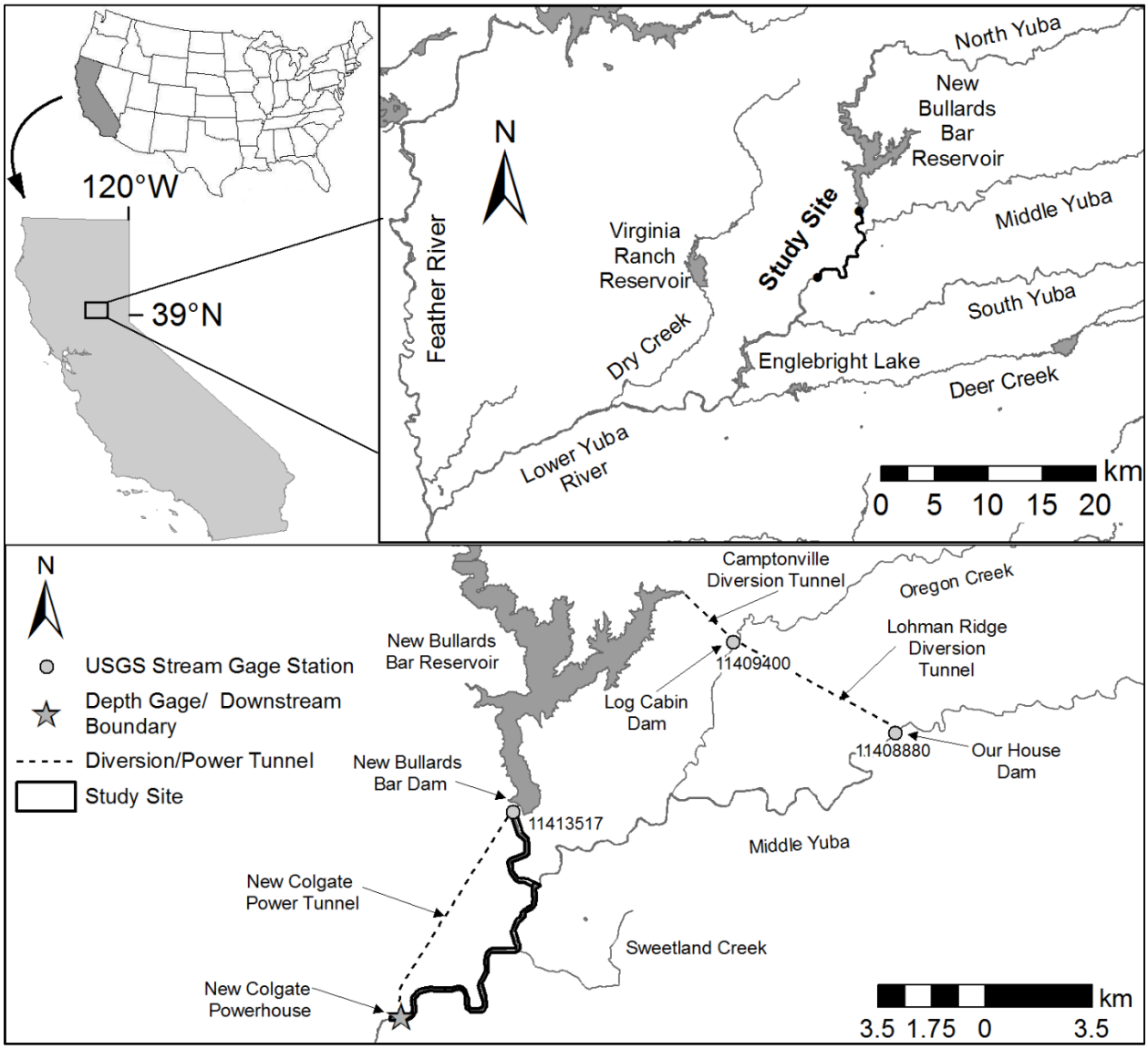

Figure 2.2. Map of study segment, tributaries, gages, and infrastructure facilities, Yuba River, CA.

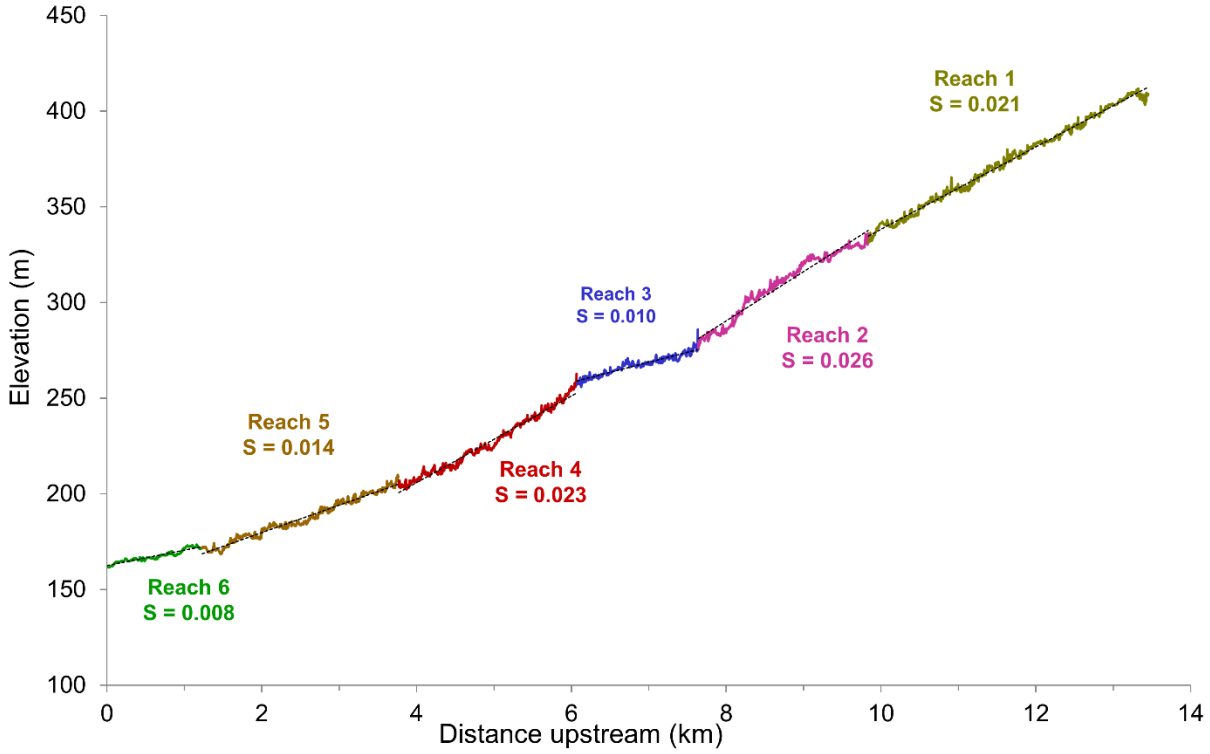

Figure 2.3. Longitudinal profile showing the extent and slope (m/m) of geomorphic reaches.

2.4 Methods

The two scientific questions and hypotheses were answered in order, as they build on each other. To address the first question, a field campaign and remote sensing survey were carried out to collect topo-bathymetric point clouds in the study river segment (section 2.4.1). Spatially explicit LBE data derived from the final topo-bathymetric point cloud (section 2.4.2) were coupled with results from a 2D hydrodynamic model (section 2.4.3) to estimate element-explicit relative submergence values for all LBEs, for discharges ranging from a representative baseflow condition to a valley-filling flood stage with an estimated 13.7-year recurrence interval (section 2.4.4). To address the second question, resulting h/D_c data were analyzed and fit by several common parametric distributions. Statistical and parametric properties of the data were compared using a hypothesis testing framework to address the study's two general hypotheses (section 2.4.5) and

test which of the envisioned h/D_c distribution evolution Styles best described h/D_c behavior in the study segment (section 2.4.6). Because this study has many detailed methods and additional results, supplementary materials are provided in APPENDIX 2. References to "Text A", "Table A", and "Figure A" followed by a number refer to locations in APPENDIX 2 where that item can be located.

2.4.1 Topographic and bathymetric mapping

Between September 27-29, 2014 Airborne Light Detection and Ranging (LiDAR) data were collected within the study segment by a professional surveying firm (Quantum Spatial, https://www.quantumspatial.com/) using a Riegl VQ-820-G bathymetric sensor system and a Leica ALS50 Phase II system (near infrared) mounted in a Cessna Grand Caravan. These data were supplemented with boat-based bathymetric observations, imagery-derived bathymetric estimates (*sensu* Legleiter et al., 2004), and systematically placed augmented points (Valle & Pasternack, 2006). Through verification and merging of each individual dataset, an extremely detailed and accurate topographic dataset was created (Wiener & Pasternack, 2022). The final bare Earth mapping included > 21 million points at an average point-spacing of 0.25 m (~ 16 pts/m^2). Points were used to create a 0.46 m x 0.46 m resolution digital terrain model (DTM) raster (bare Earth DTM), the final map product used in the study.

2.4.2 LBE mapping

Spatially explicit mapping of LBEs in the study segment was previously completed by Wiener and Pasternack (2022). Summarily, their procedure applied a ground classification algorithm to the study segment's bare Earth point cloud to create a 'smoothed' DTM raster. The smoothed DTM raster was differenced from the bare Earth DTM to generate a roughness surface model (RSM) raster. A marker-controlled watershed segmentation algorithm was used to extract

LBEs from the RSM. Mapping performance was comparable to or better than benchmark values from forestry research for mapping tree crowns, which is a reasonable proxy given the absence of performance metrics for mapping LBEs.

The study segment census yielded a total of 42,176 LBEs. Minimum LBE size was a single raster cell (0.46 m x 0.46 m). Mapping revealed LBEs to be present individually and in clusters throughout the river corridor in a variety of spatial configurations (Figure 2.4). The D_c value for each LBE was set as the max RSM within each polygon. In the final LBE map it was not possible to differentiate boulders from bedrock outcrops or fully decouple individual boulders from boulder clusters, meaning, at times, clusters were aggregated into individual polygons.

To spatially stratify LBEs within multiple discharge-dependent portions of the river corridor, LBE data were subset into five groups comprising the set of LBE polygons that intersected with each simulated discharge's wetted area polygon (section 2.4.3). LBE polygons that only partially intersected a wetted area polygon or only intersected the wetted area along their border were included in a group's set of LBEs. This allowed bank attached LBEs to be included in each subset as long as they were partially inundated. These subsets are referred to as 'discharge-dependent LBEs'. In this manner, discharge served to hierarchically nest spatial domains, because lower discharge wetted areas were always located within higher discharge wetted areas. Thus, discharge is often used in the context of a spatial reference throughout this study.

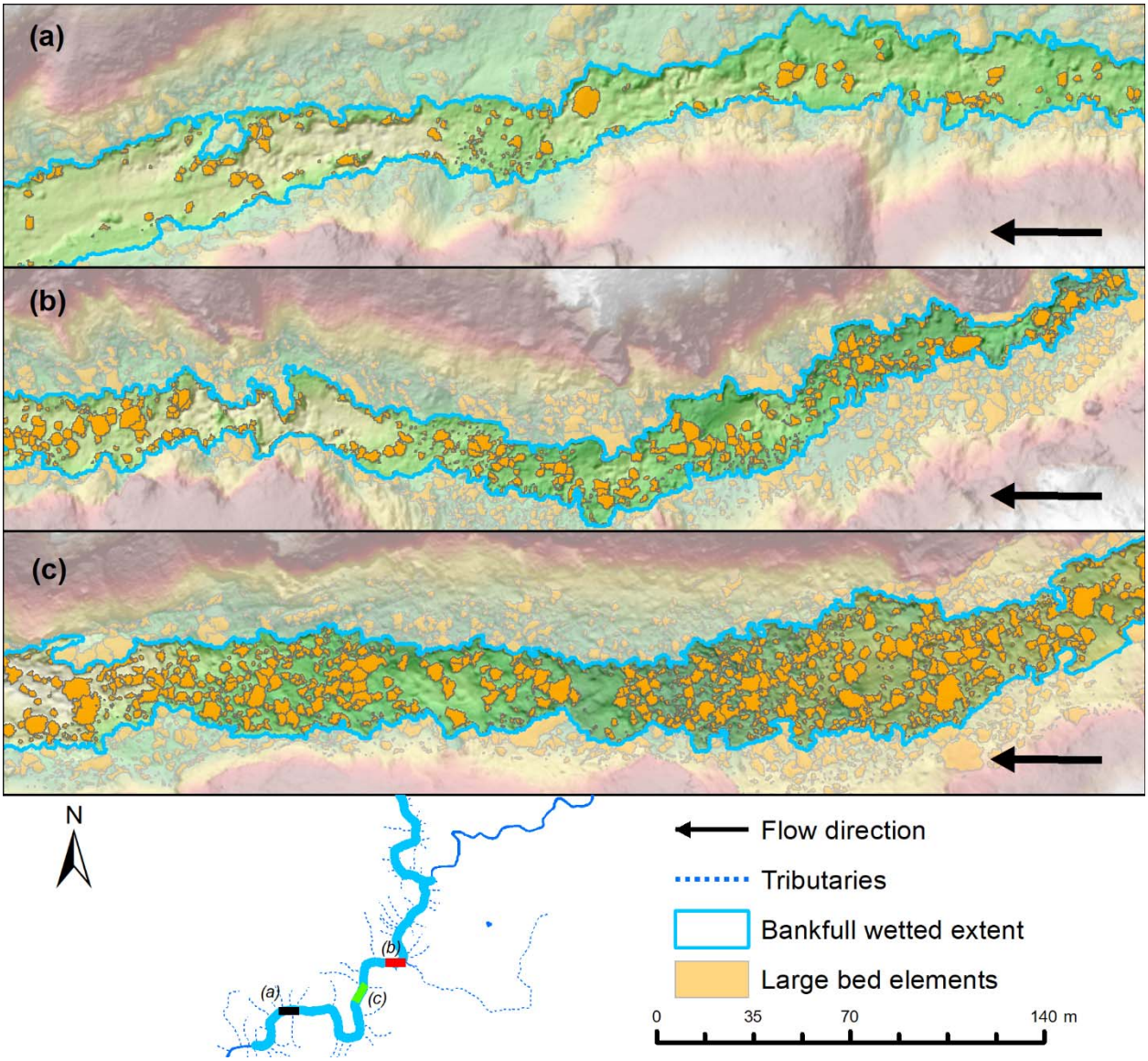

Figure 2.4. Typical configurations of LBEs within the study segment's bankfull channel overlain on shaded relief that include: (a) low concentration isolated and clustered LBEs, (b) moderate LBE concentrations with transverse and step structures, and (c) high LBE concentrations with mixtures of steps, transverse structures and possible reticulate formations. LBEs outside the bankfull channel are partially transparent. Polygon boundaries define individually mapped LBEs but may include clustered boulders as noted in text.

2.4.3 Two-dimensional hydrodynamic modeling

Steady-state hydrodynamics of the study segment were simulated at ~ 1-m resolution using the free, public 2D model known as Sedimentation and River Hydraulics—Two-Dimensional

model (SRH-2D) v. 2.2 (Lai, 2008). This is a proven code capable of simulating complex hydraulic conditions in mountain rivers (Brown & Pasternack, 2014; Strom et al., 2016). The decision to use 2D modeling represented a compromise between performance and accuracy compared to simpler 1D models and more complex 3D modeling (Benjankar et al., 2015). It also reflected the study's need for spatially explicit simulation of hydraulic conditions, specifically the delineation of wetted areas and flow-depth prediction aggregated at 10^0-10^2 m^2 scales. Simulations were run for five geomorphically or otherwise relevant discharges (1.54, 10.73, 82.12, 343.6, and 1184.6 m^3/s) from an approximate baseflow to an ~13.7-yr flood (Table 2.1). Detailed description of model development, parameterization, and performance assessment are presented by Wiener and Pasternack (2022). Depth prediction performance, which was most relevant to this study because it is used to compute relative submergence, is summarized below. This study does not investigate velocity.

Depth predictions were assessed using two tests and a suite of standard model performance metrics (Pasternack, 2011; Moriasi et al., 2007). First, deviations between observed and predicted water-surface elevations (WSEs) were assessed at 147,644 discrete point locations distributed throughout the 13.2-km domain. Observed WSE measurements were obtained as part of LiDAR data collection. Discharge during the period of LiDAR collection was estimated at 1.19 m^3/s. Simulation of this discharge was used to generate the set of predicted WSE values at the observation locations. The mean absolute deviation between measured and predicted WSE was 0.162 m. The majority (53%) of absolute deviations were less than the independently reported 0.117 m vertical accuracy uncertainty of the bathymetric LiDAR, which aligns with the expectation that 2D model WSE deviations should not exceed uncertainty in the topographic data (Pasternack, 2011; Brown & Pasternack, 2012).

For the second test, depth measurements made at 61 independent locations with a standard wading rod during a period of discharge of 3.51 m^3/s were compared to collocated model predictions for this same flow. Mean absolute deviation between measured and predicted depths was 0.092 m. The coefficient of determination (R^2) for predicted versus observed fixed-point depths was 0.80 ($p<0.001$) and the linear regression slope was 0.87 ($p<0.001$). These values are considered very good amongst 2D models (Brown & Pasternack, 2012) and certainly exceed recommended minimum norms for model performance (Pasternack, 2011). Among hydrologist-preferred metrics, depth predictions significantly outperformed standards for Nash-Sutcliffe efficiency, percent bias, and the root mean square error-observations standard deviation ratio. Overall, the 2D model met relevant modeling standards and performed comparably to similar models from published articles (Lisle et al., 2000; Pasternack et al., 2006).

Table 2.1. Simulated discharges.

Simulated discharge (m^3/s)	Approximate annual recurrence interval (years)	Segment averaged Froude number	Number of wetted LBEs	Description
1.54	1	0.11	13976	Representative baseflow taken as average of daily dry season (July 1 - September 31) flows at downstream boundary from 1930-2015.
10.73	1.06	0.18	17792	YCWA (2013) morphologically estimated bankfull flow.
82.12	1.59	0.28	24249	Flow observed to inundate several alluvial channel margins and with ~1.59-year recurrence, which nearly corresponds to most probable annual flood (Langbein, 1949).
343.6	3.46	0.35	31314	Maximum flow for which 2014-2015 boundary conditions were available
1184.6	13.7	0.39	39319	Boundary condition opportunistically collected for January 9, 2017 flood.

2.4.4 Relative submergence calculations

For an individual particle, relative submergence is typically defined as the ratio of the

approach flow depth (h) to particle height (D_c) (Papanicolaou & Tsakiris, 2017). In physical experiments and natural environments, the manner in which h and D_c are estimated varies widely, often involving spatial averaging or back-calculation of depths (Bathurst, 1985; Ferguson et al., 2017) and uncertainty about the bed-level datum from which to measure D_c (Aberle & Smart, 2003). For each LBE in this study, D_c was specified as described in section 2.4.2 and h was calculated as the arithmetic mean of model predicted depths added to RSM heights in all raster cells occupied by each LBE as well as cells within a one-cell buffer around the feature:

$$h = \frac{1}{q+r}\sum_{i=1}^{q}\sum_{j=1}^{r}\left((h_i + RSM_i) + (h_j + RSM_j)\right) \in \left\{h_i \middle| h_i > 0 \; and \; h_j \middle| h_j > 0\right\} \qquad \text{(EQ.1)}$$

where i is an index for cells where the LBE is present, j is an index for cells located within a one-cell buffer of the LBE, q is the number of LBE cells, and r is the number of buffer cells (Figure 2.5).

Using EQ. 1, h/D_c was calculated for each LBE at each simulated discharge. As study question 1 was interested in h/D_c distributions in different spatial domains over a range of discharges, results were hierarchically organized at reach and segment scales to generate a total of 35 discharge-dependent h/D_c datasets (i.e., wetted areas from the five discharge simulations for the entire segment [5 datasets] plus the same five wetted areas clipped to each of the six reaches [30 more datasets]). Organizing by discharge-dependent LBEs excluded 'dry' LBEs with h/D_c values of zero from each dataset. An additional four segment-scale datasets were generated for LBEs within the portions of the channel that became inundated between discharges, (i.e., incremental inundation corridor) (Figure 2.6). These subsets were generated the same as the discharge-dependent datasets (section 2.4.2) but using incremental inundation corridor polygons to select LBEs instead of wetted area polygons (Wiener & Pasternack, 2022). This domain isolates analysis to the series of nested, non-overlapping portions of the river corridor that become

successively inundated and geomorphically active with increasing discharge, and addresses how h/D_c distributions vary among just these discharge-dependent river margins.

The calculations described above provide reasonable proxies for field-based measurements of h and D_c that would otherwise be impossible to obtain under the range of simulated conditions for the number of LBEs considered in this study. These estimates are not without potential issues and uncertainty. To explore uncertainty, one alternative method for calculating h as well as an alternative for calculating D_c at each LBE were implemented (Text 1A.2.3.4). The alternative h metric, $\hat{h}$, was calculated as the maximum depth near each LBE according to:

$$\hat{h} = \max\{(h_i + RSM_i), (h_j + RSM_j)\} \in i\,\{1{:}\,q\}, j\{1{:}\,r\} \quad \text{(EQ.2)}$$

The alternate to D_c was to use the average RSM value within each LBE ($\overline{D}$). This generated a total of four possible relative submergence calculations reflecting sensible upper and lower bounds for each LBE for comparison.

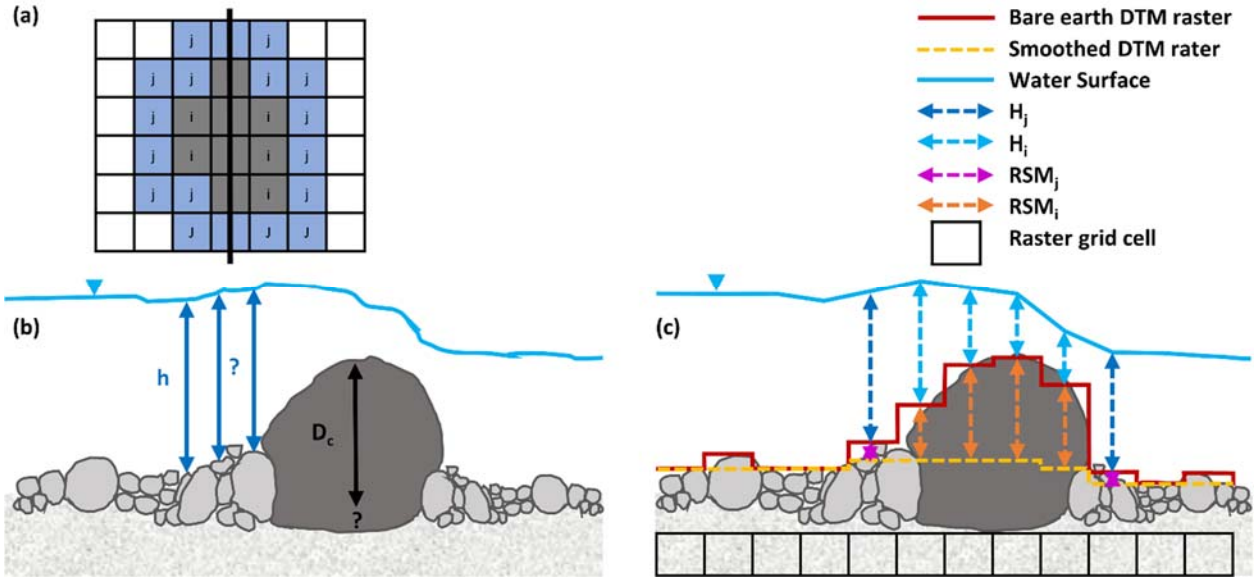

Figure 2.5. Conceptual illustration showing (a) plan-view of hypothetical LBE in gray with one-cell buffer region in blue and profile views along dark line in (a) of (b) natural conditions and (c) how natural conditions are represented in this study along with measurements needed for LBE relative submergence calculation. Note, question marks in (b) indicate uncertainty in how h and D_c should be measured under natural conditions.

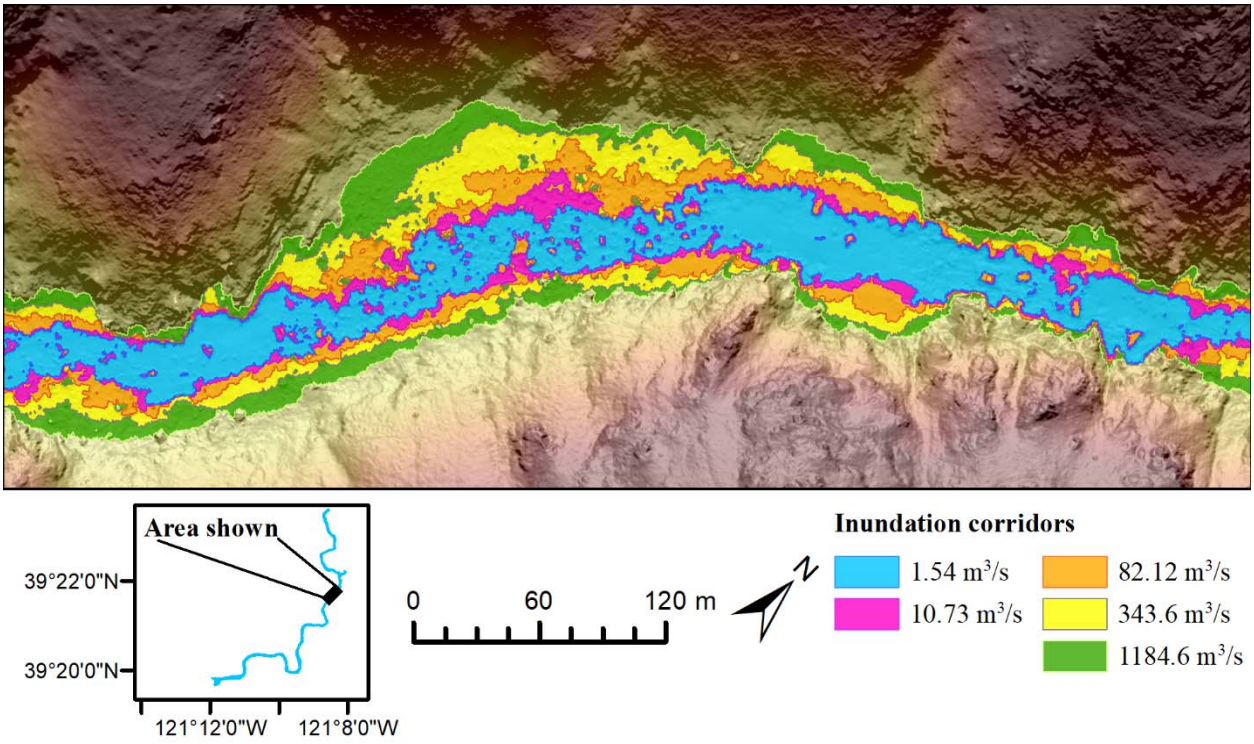

Figure 2.6. Typical output from 2D model simulations showing the baseflow wetted area (blue) and the subsequent incremental inundation corridors occurring as strips between successive higher discharges. For example, pink is the incremental inundation corridor between 1.54 and 10.73 m^3/s. Flow is from right to left.

2.4.5 LBE relative submergence general hypothesis testing

To test the study's two general hypotheses, the mean ($\bar{x}$), standard deviation (σ), mode (φ), coefficient of skewness (g), and kurtosis (β_2) were calculated for all 39 h/D_c datasets (Text 1A.2.3.5). Testing criteria for a dataset to be positively skewed and leptokurtic were $g>0.5$ and $\beta_2>3$, respectively. Unimodality was evaluated by visualizing h/D_c dataset probability densities. If over 66% of datasets were each unimodal, positively skewed, and leptokurtic we accepted general hypothesis 1.

In testing general hypothesis 2, regarding changes in h/D_c distribution statistical properties between datasets, measures of central tendency ($\bar{x}$ and φ) and variance of h/D_c datasets within a given domain (i.e. the study segment or a given reach) were compared either qualitatively, or using

non-parametric (e.g. Mann-Whitney U and Levene's tests) or appropriate parametric tests (e.g. Welch's t-test and F-test), whereby statistical equivalency was based on metrics being indistinguishable at a 95% confidence level. A positive test for this hypothesis in a given domain was based on two criteria. First, variance had to monotonically increase between discharge-dependent datasets and statistically equivalency of variance between datasets had to be rejected. Second, central tendencies had to be either statistically equivalent or if not statistically equivalent had to increase between discharge-dependent datasets. If either of these criteria were not met the test was rejected for that domain. Since modal values were derived from h/D_c histograms, if values between subsequent datasets were within one bin-width they were considered equivalent (Text 1A.2.3.5; Table A.2.1). General hypothesis 2 was accepted if positive tests were confirmed for the study segment as a whole and half the reaches.

2.4.6 LBE relative submergence distribution and styles analysis

In the first step toward h/D_c distribution Style hypothesis testing, data were fit with several parametric distributions (i.e. Normal, Log-normal, Weibull, Exponential, and Gamma) using maximum likelihood and method of moment estimators. All fitting was conducted using the 'fitdistrplus' R package (Delignette-Muller & Dutang, 2015). These distributions are common amongst natural phenomena and have been found to accurately describe the size, shape, or spacing of sedimentological and morphological attributes of fluvial bedforms (Van der Mark et al., 2008; Singh et al., 2012), submarine turbidites (Rothman et al., 1994), and other Earth surface landforms (Ely et al., 2018).

An initial requirement of all hypothesized Styles was that h/D_c distributions were from the same distribution type. Thus, fitted h/D_c distributions were evaluated on the basis of whether they were best fit by the same type of distribution within (i.e. between discharge-dependent datasets in

the same domain) and between spatial domains. Fits were compared using negative, log-likelihood values to select the best-fitting distribution for each dataset. Selected distributions were then evaluated with non-parametric or distribution-appropriate parametric goodness-of-fit tests (i.e. Anderson-Darling, Kolmogorov-Smirnov, and/or Shapiro-Wilk tests). Consistency in distribution type supports a common basis for coupling in the self-organizing processes driving: (i) LBE spatial arrangements and size-frequency distributions, and (ii) how spatially variable hydrodynamics act to submerge these features in the compared domains over the range of discharges (Baas, 2002, Hillier et al., 2016). Such inference is tentative, as multiple generative processes cannot be ignored as a means for arriving at a common set of distributions (Sornette, 2000).

If distributions in a given segment- and/or reach-scale domain were all of the same type, h/D_c behavior was tested relative to hypothesized Styles. Testing details for all Styles are summarized below and in Table 2.2, with additional details in supplemental materials (Text 1A.2.3.6). Broadly, distribution fitting parameters were compared between all discharge-dependent h/D_c datasets (i.e. 10 tests per parameter per domain) to assess equivalency using non-parametric or distribution appropriate parametric tests (e.g. likelihood-ratio tests, t-test, F-test), whereby statistical equivalency between distributions was based on all parameters being indistinguishable at a 95% confidence level. Statistical properties of raw h/D_c data (e.g. mean [$\bar{x}$], standard deviation [σ], mode [φ], coefficient of skewness [g], and kurtosis [β_2]) were also compared within domains either qualitatively, or using non-parametric (e.g. Mann-Whitney U and Levene's tests) or appropriate parametric tests (e.g. Welch's t-test and F-test), whereby statistical equivalency was based on measures of central tendency and variance being indistinguishable at a 95% confidence level (Text 1A.2.3.6). The above analyses were extended to multiple spatial domains for each of those best fit by the same distribution type, whereby fitting parameters and

statistical properties were compared between all relevant datasets.

Acceptance of the Style 1 hypothesis required statistical equivalency of all discharge-dependent h/D_c dataset properties within a given domain (i.e. distribution type, fitting parameters, and statistical properties), thus indicting that mechanisms, such as those hypothesized in section 2.2.2 that conserve h/D_c distribution scaling were present. Presence of statistical self-similarity across multiple domains would support even greater invariance of h/D_c distributions in the study segment. Acceptance of Style 2 in a given domain was based on central tendency being statistically equivalent between all discharge-dependent datasets and having to reject that variances were equal. Contrarily, Style 2 was rejected if central tendencies were not statistically equivalent between discharge-dependent datasets or any variances were statistically equivalent between datasets. Acceptance of Style 3 required variance to be statistically equivalent and rejecting that central tendencies were equal between datasets in a given domain. Style 3 was rejected if either of these criteria were not upheld.

Unlike Styles 1, 2, and 3, acceptance of Style 4 was based on statistical similarity in how discharge-dependent h/D_c distributions changed between domains. Style 4 testing first required that both central tendency and variance were not equivalent between discharge-dependent h/D_c datasets within compared domains (i.e. rejection of all previous Styles). Statistical models were then fit to obtain slopes for the rate that parametric and statistical properties in each domain changed with discharge. A positive test for Style 4 was based on two criteria: (i) data were reasonably fit (F-test, $p<0.05$) by the same type of model (e.g. linear, power-law, etc.); and (ii) statistical equivalency of modeled slopes between domains. Slope comparison was conducted using the approach of Paternoster et al. (1998) by employing a test statistic computed according to their equation 4 as follows:

$$Z = \frac{b_1 - b_2}{\sqrt{SEb_1^2 + SEb_2^2}} \quad \text{(EQ. 3)}$$

where b_1 and b_2 are regression slopes for the models being compared, SEb_1 and SEb_2 are standard errors of the regression slopes from the respective models, and Z is a test statistic that follows a *t*-distribution with degrees of freedom $(n_1 + n_2 - 4)$ with n_1 and n_2 equal to the number of samples in each dataset. The acceptance criteria for Style 4 was that $\bar{x}$, σ, and distribution parameter slopes would be equivalent (Text 1A.2.3.6).

Tests for threshold Styles 2(b), 3(b), and 4(b) involved a combination of the tests for Styles 1-4, whereby acceptance was based on two criteria. The first criteria was equivalency of all dataset properties between at least one set of successive discharges (i.e. same criteria as Style 1). Next, was that these data be preceded or followed by a dataset with a dramatic difference in relevant parameters (i.e. variance for Style 2(b) and central tendency for Style 3(b)). Given the stringency of Style 1 testing, acceptance of the first criteria was loosened such that datasets could have small, gradual changes in h/D_c distributions between discharges. Specifically, if the percent change in all h/D_c dataset properties were less than 5% between discharges, the set of discharges were considered similar and thus acceptable with this component of threshold Style behavior. In characterizing magnitudes of threshold shifts in distribution properties a separate set of non-dimensional metrics was developed by normalizing the percent change in h/D_c dataset properties between discharges by the percent change in averaged depth for the same spatial domain according to the general formulation:

$$\Phi_\Delta^* = \frac{\frac{\Phi_{k+1} - \Phi_k}{\Phi_k}}{\frac{\bar{h}_{k+1} - \bar{h}_k}{\bar{h}_k}}; \; \Phi = \{\bar{x}, \sigma, \varphi\} \quad \text{(EQ.4)}$$

where k is an index for discharge, $\bar{h}$ is domain averaged model predicted flow depth, and Φ_Δ^* is a generic non-dimensional metric for a h/D_c dataset property (Φ). Small (<1) or zero Φ_Δ^* values

illustrate cases of little or no change between discharges relative to changes in flow depth, whereas larger relative changes occur as Φ^*_Δ values exceed unity. A value of 1.2 was used as a threshold indicating dramatic shifts (*sensu* Wyrick et al., 2014). Thorough testing for threshold styles was partly limited by the number and relative magnitudes of simulated discharges. Lastly, the possibilities of accepting multiple Styles or rejecting all Styles in favor of alternative behaviors were left open.

Incremental inundation corridor h/D_c datasets served to isolate sets of LBEs along channel margins and were largely composed of those LBEs that became newly wetted between discharges. While h/D_c behavior in these domains was not tested relative to hypothesized Styles, data were analyzed for statistical self-similarity using the same set of tests.

Table 2.2. Testing details for styles of LBE relative submergence response to discharge.

Style	Description	Domain(s) compared	Acceptance criteria[†]	Example tests for statistical equivalency
1	Statistical self-similarity	within or between	Fitting parameters and statistical properties equivalent between all datasets.	likelihood-ratio test (Held & Bove, 2014) Welch's t-test F-test
2	Constant central tendency shifting variance	within	Central tendency equivalent between all datasets and rejection of equivalency of variance between all datasets.	Welch's t-test (central tendency) Mann-Whitney U test (central tendency) F-test (variance) Levene's test (variance)
2(b)	Constant central tendency threshold type shifting variance	within	Central tendency equivalent between all datasets. Statistical self-similarity between at least two successive datasets. Rejection of equivalency of variance in dataset preceding or following self-similar data accompanied by dramatic shift in σ_{Δ}^{*}.	
3	Constant variance shifting central tendency	within	Variance equivalent between all datasets and rejection of equivalency of central tendency between all datasets.	
3(b)	Constant variance threshold type shifting central tendency	within	Variance equivalent between all datasets. Statistical self-similarity between at least two successive datasets. Rejection of equivalency of central tendency in dataset preceding or following self-similar data accompanied by dramatic shift in $\bar{x}_{\Delta}^{*}$ or φ_{Δ}^{*}.	
4	Process-based similarity	between	Rejection of Styles 1, 2, 2(b), 3, and 3(b). Slope of discharge-dependent $\bar{x}$, σ, and distribution parameters equivalent between domains.	Equality of regression coefficients test (Paternoster et al., 1998)
4(b)	Threshold type process-based similarity	between	Rejection of Styles 1, 2, 2(b), 3, 3(b), and 4. Statistical self-similarity of at least two successive datasets in two or more domains for the same set of discharge-dependent data. Slope of discharge-dependent $\bar{x}$, σ, and distribution parameters equivalent for remaining non self-similar data between same domains.	

[†]Style rejected if any acceptance criteria not met.

2.5 Results

2.5.1 Question 1 (LBE relative submergence distributions) and general hypothesis results

Distributions of h/Dc values in 38 of 39 segment, reach, and incremental inundation corridor spatial domains were leptokurtic (β2>3) and had moderate-to-high positive skewness (g>0.5) (Figure 2.7; Figure 2.8; Figure 2.9; Table A.2.2; Table A.2.3). Only the dataset in Reach 6 associated with the largest discharge (1184.6 m3/s) was platykurtic (β2<3) and had moderate positive skewness (0<g<0.5). With the exception of the six reach-scale datasets associated with the largest discharge, Reach 6 LBEs within the 82.12 wetted area, and Reach 3 and Reach 6 LBEs within the 343.6 m3/s wetted area, the remaining 30 datasets were unimodal (Figure A.2.2). Altogether 28 of 39 datasets (72%) were unimodal, positively skewed, and leptokurtic, thus general hypothesis 1 was accepted with the caveat that not all datasets had these characteristics.

Despite these basic similarities, datasets showed clear differences with regard to distribution shape and other statistical properties. Across all segment- and reach-scale domains, higher discharges corresponded with monotonic increases in h/D_c dataset means and standard deviations, and decreases in skewness, kurtosis, α, and β values (Table A.2.2). Thus, the dominant trajectory was for squatter, wider, less positively skewed h/D_c distributions (Figure 2.7; Figure 2.8). Monotonic increases in h/D_c means and standard deviations also fulfilled part of the criteria for accepting general hypothesis 2. Consistent with the next set of acceptance general hypothesis 2 criteria, comparison of central tendencies using the non-parametric Mann-Whitney U test and variances using Levene's test (R Core Team, 2021; Fox & Weisberg, 2019) between subsequent discharge-dependent datasets in each domain required rejecting that these properties were equivalent above a 95% confidence level (p <<0.05) for all comparisons. Changes in modal values on the other hand were more variable. While modes tended to increase slightly between discharges,

decreases occurred on five occasions (Table A.2.2). Decreases were all within one bin-width of the preceding value, therefore trends in modal values were considered to either increase or remain relatively constant. While the modal decreases leave room for speculation, this fulfilled the final criteria for accepting general hypothesis 2.

Notably, the magnitude that h/D_c properties changed varied within and between domains, and especially across discharges. Visual inspection suggests there was greater similarity in data associated with the same discharge between domains (e.g. Reach 4, 1.54 m^3/s LBE data compared to Reach 5, 1.54 m^3/s LBE data) compared to similarity that occurred in the sequences of h/D_c values within any given domain. That said, the manner in which distribution shapes changed over the series of discharge-dependent datasets appeared comparable between spatial domains. These trends are evaluated further in the context of Style testing the next sections.

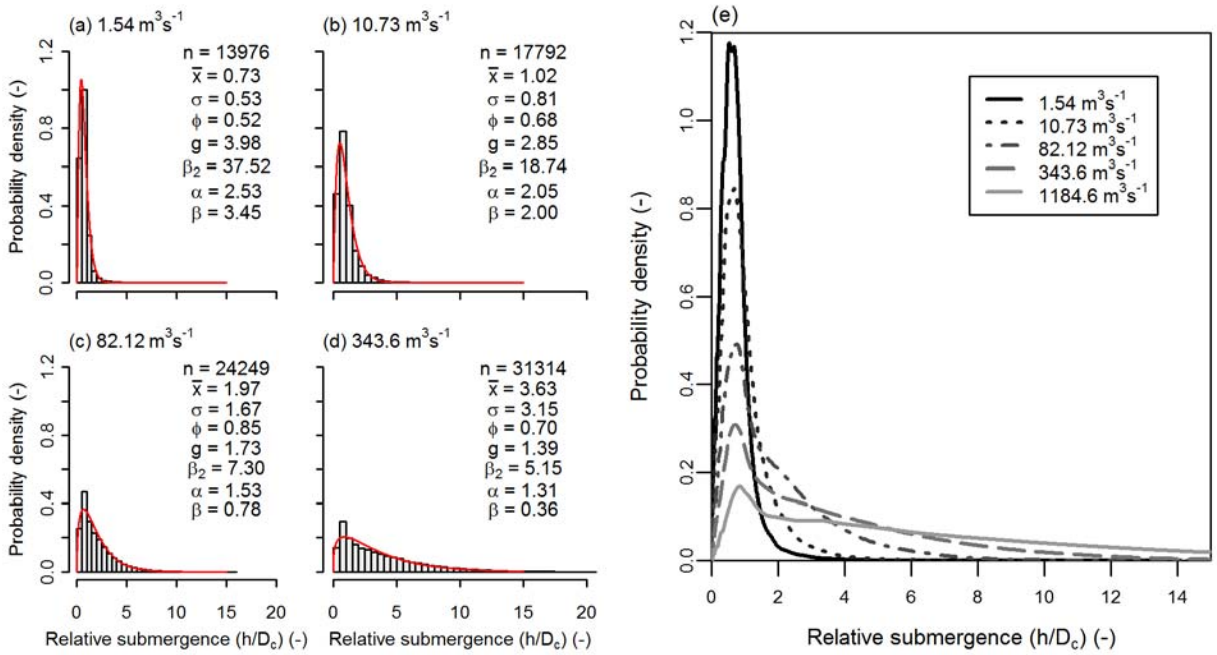

Figure 2.7. Histograms of (a-d) segment-scale h/D_c probability densities (bars) overlain with fitted gamma distribution (red lines) for discharge-dependent LBE datasets associated with 1.54, 10.73, 82.12, and 343.6 m^3/s and (e) kernel density of all segment-scale h/D_c probability densities overlain together. For panels a-d the count (n), mean ($\bar{x}$), standard deviation (σ), mode (φ), skewness (g), and kurtosis (β2) of each dataset is shown as well as the shape (α) and rate (β) parameters from fitted gamma distributions.

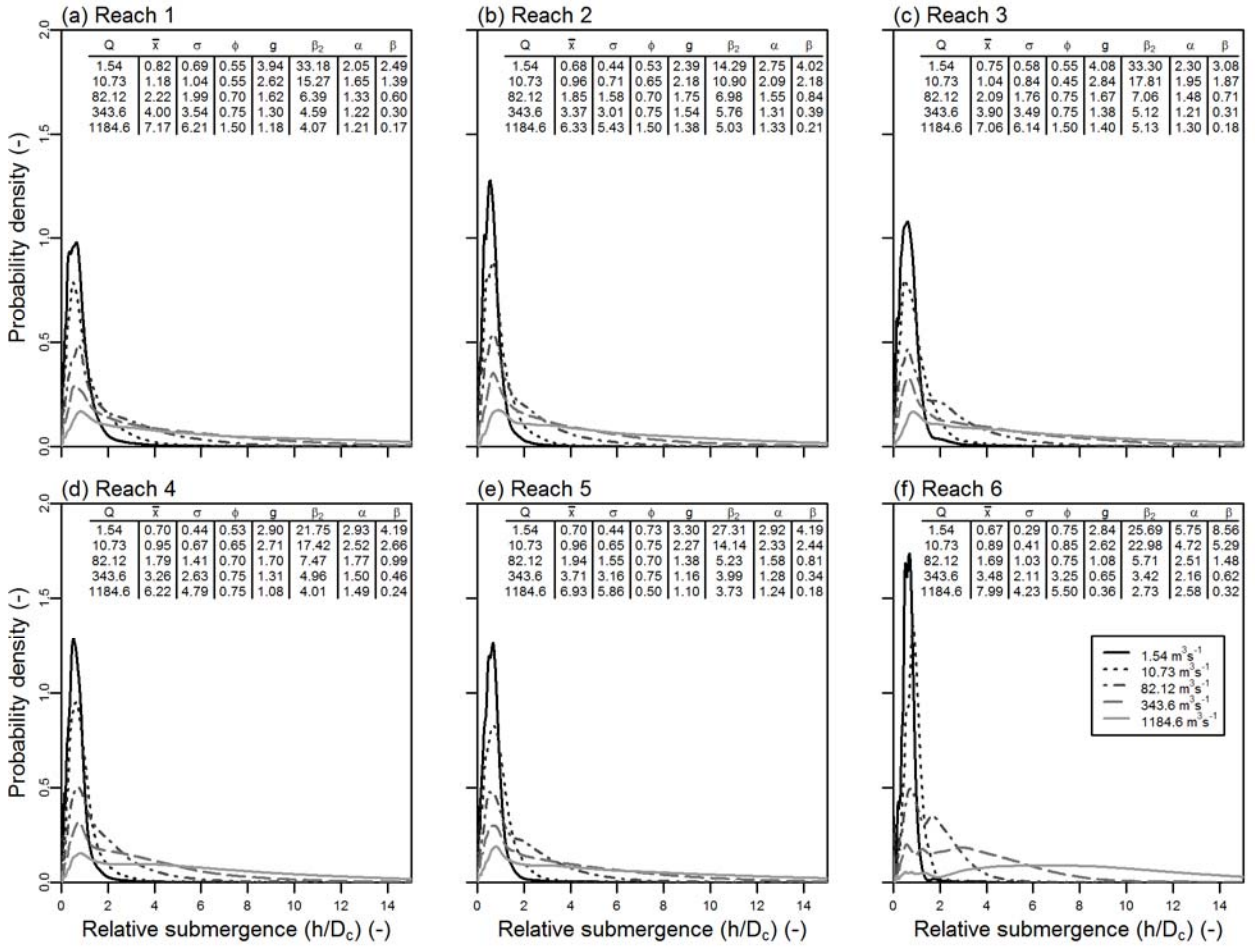

Figure 2.8. Overlain kernel densities of h/D_c probability densities for the five discharge-dependent LBE datasets within each geomorphic reach (a-f). Summary statistics and fitted gamma distribution parameters shown.

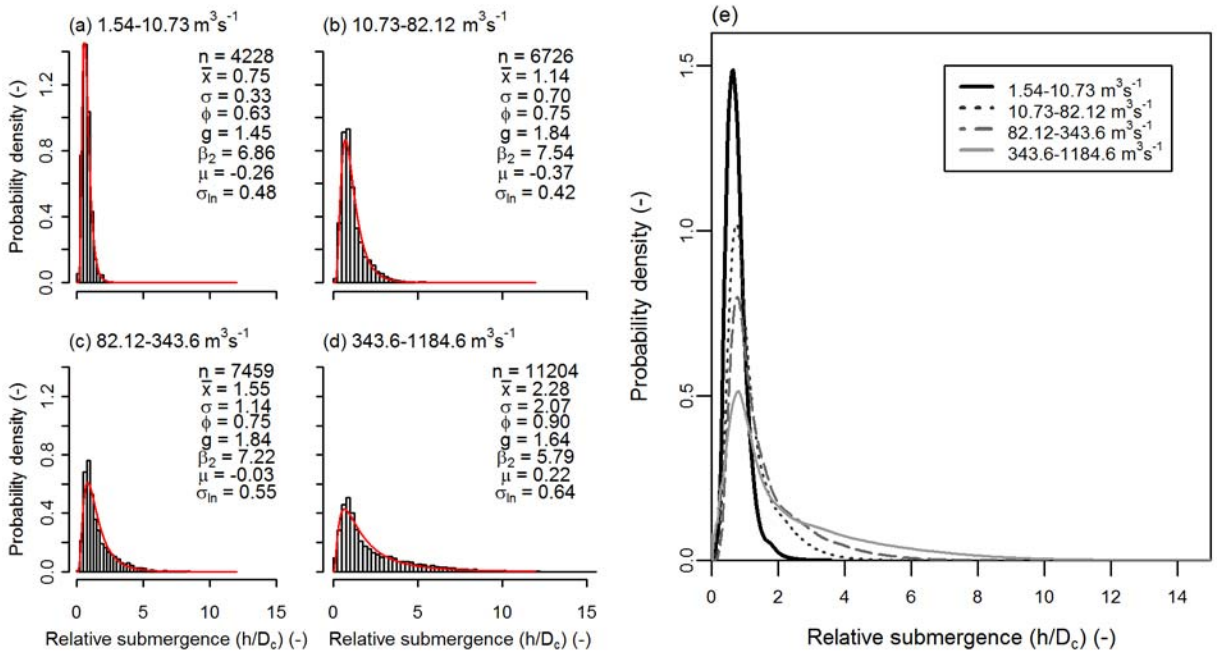

Figure 2.9. Histograms of (a-d) each incremental inundation corridor's h/D_c probability density (bars) overlain with fitted log-normal distribution (red lines) and (e) kernel density of all incremental inundation corridor probability densities overlain together. Summary statistics and fitted log-normal distributions parameters (μ and σ_{ln}) shown.

2.5.2 Question 2 results (distribution types and within domain style testing)

Acceptance criteria for all Styles required h/D_c datasets to be from the same distribution type. Distribution fitting found four of five segment-scale h/D_c datasets to be best fit by two-parameter Gamma distributions, and one best fit by a Weibull distribution (LBEs associated with the 1184.6 m^3/s wetted area) (Figure 2.7). This was supported by the Anderson-Darling goodness-of-fit test applied with Braun's (1980) correction to account for parameters being estimated from the data (Faraway et al., 2019), which concluded it was not possible to reject that the 1.54-343.6 m^3/s datasets were drawn from Gamma distributions and the 1184.6 m^3/s dataset from a Weibull distribution at the 95% confidence level ($p >> 0.05$). This test also supported that it was not possible to reject that the 1184.6 m^3/s dataset could be drawn from a Gamma distribution.

At the reach scale, 24 of 30 datasets were best fit by two-parameter Gamma distributions,

and six were best fit by Weibull distributions (i.e. Reach 1, 4, and 5 LBEs associated with 1184.6 m^3/s wetted area; Reach 6 LBEs associated with 82.12, 343.6, and 1184.6 m^3/s wetted areas) (Figure A.2.2). Goodness-of-fit testing confirmed it was not possible to reject these data were drawn from the aforementioned distributions above the 95% confidence level (corrected Anderson-Darling test*; p* >>0.05) and also supported it was not possible to reject that all datasets could be drawn from Gamma distributions at the 95% confidence level.

Acceptance of the Style 1 hypothesis required all discharge-dependent h/D_c dataset properties within a given domain to be statistically equivalent. Given nearly all segment- and reach-scale h/D_c datasets were best fit by or could reasonably be drawn from Gamma distributions, fitted parameters (i.e. shape [α] and rate [β]) were evaluated for statistical equivalency through pair-wise comparison of all unique dataset combinations using the likelihood-ratio-test of Krishnamoorthy et al. (2015). Within domain testing required rejecting that parameters were equal above a 95% confidence level for all comparisons, thus requiring rejection of the Style 1 hypothesis. These results also conflicted with the acceptance component of the three threshold Styles associated with gradual changes occurring between at least two successive h/D_c datasets (Table 2.2). Percent changes in h/D_c $\bar{x}$, σ, g, β_2, α, and β values between discharges, the second criteria used to indicate gradual behavior for threshold Style testing, exceeded the 5% test limit for all comparisons, and exceeded 5% for all but three φ comparisons (Table A.2.2). The absence of small, gradual changes between h/D_c datasets necessitated rejection of threshold Styles 2(b), 3(b), and 4(b) for the set of tested discharges. Percent change results provided additional support for rejecting Style 1, which unlike statistical tests were not biased by large LBE sample sizes. Non-dimensional metrics (Φ_{Δ}^{*}) calculated to test for dramatic shifts as part of assessing threshold Style behavior further demonstrated changes in h/D_c dataset properties were more continuous and

involved dramatic changes between discharges (Figure 2.10). All segment and reach scale $\bar{x}_{\Delta}^{*}$ and σ_{Δ}^{*} values exceeded 1.2, the specified threshold for dramatic shifts. Specifically, values above unity indicated changes in h/D_c dataset means and variances increased at rates more rapid than average flow depths increased. In contrast, φ_{Δ}^{*} values were predominantly below 1.2 and included both negative and zero values. Notably, simultaneous exceedances of both $\bar{x}_{\Delta}^{*}$ and σ_{Δ}^{*} above the shift threshold at each discharge also conflicted with acceptance criteria of Styles 2(b) of 3(b) that were based on shifts occurring for only one property at a time (Table 2.2).

Next, results of segment and reach datasets testing were evaluated on the basis of statistical equivalency of central tendency and variance relative to Style 2 and 3 acceptance criteria. Given datasets were not normally distributed, central tendencies were compared using the non-parametric Mann-Whitney U test and variances were compared using Levene's test (R Core Team, 2021; Fox & Weisberg, 2019). All within domain tests were rejected above a 95% confidence level (p <<0.05), thus requiring rejection of Styles 2 and 3. Though not explicitly part of the testing criteria, the relatively large percent changes in $\bar{x}$ and σ values and magnitude of $\bar{x}_{\Delta}^{*}$ and σ_{Δ}^{*} values described above further supported rejecting these Styles.

Comparison of between segment- and reach-scale domain h/D_c dataset properties for the purpose of determining if statistical self-similarity existed across multiple domains had mixed results. Only 19 of 150 possible α value comparisons could not be rejected as being equal above a 95% confidence level, and equality of β values was rejected for all comparisons (Figure A.2.3a). Comparison between reaches found only 36 α and 12 β values of the 425 possible pair-wise combinations for each variable could not be rejected as being equal (Figure A.2.3). Similar results occurred for tests assessing statistical equivalency of variance and central tendency between segment- and reach-scale h/D_c datasets (Text 1A.2.4.2; Figure A.2.4). These results indicate h/D_c

statistical self-similarity did not exist between spatial domains. Of the datasets with roughly equivalent h/D_c distribution properties, the vast majority were for LBEs associated with the same discharge (Text 1A.2.4.2). Therefore, greater similarity in h/D_c datasets existed between domains at the same discharge compared to similarity that occurred within any given domain over the range of tested discharges.

Results presented thus far demonstrate study segment h/D_c values exhibited discharge-dependent dynamism inconsistent with several hypothesized Styles in favor of more mutualistic changes. Covariation between the mean and standard deviation of geometry properties of Earth surface landforms have been previously reported by Ely et al. (2018) and Van der Mark et al. (2008). Ely et al. (2018) made this observation studying lengths and widths of multiple drumlin datasets, while Van der Mark et al. (2008) document that the heights, lengths, crest elevations, and trough elevations of fine-grained bedforms from field and flume experiments had such relations. Evaluating bivariate trends of h/D_c dataset properties identified several covarying relationships. For example, decreases in segment-scale Gamma distribution parameters α and β were marked by strong linear correlation (R^2 = 0.994, p = 0.003). This indicates there was a mutualistic and predictable nature to how values changed between discharges, with the caveat that analysis was based on only five data points (Figure 2.11a). The same pattern was observed in each reach independently, but only partially when looking at all reaches together as Reach 6 had somewhat distinct parameter values (Figure 2.11b). A strong linear correspondence was also present across discharges between h/D_c $\bar{x}$ and σ values, showing a connection between increasing spread and central tendency (Figure 2.11c-d). These results support that changes in parametric and statistical properties between domains were consistent, such as envisioned by Style 4. The nature of these changes are reviewed in greater detail next.

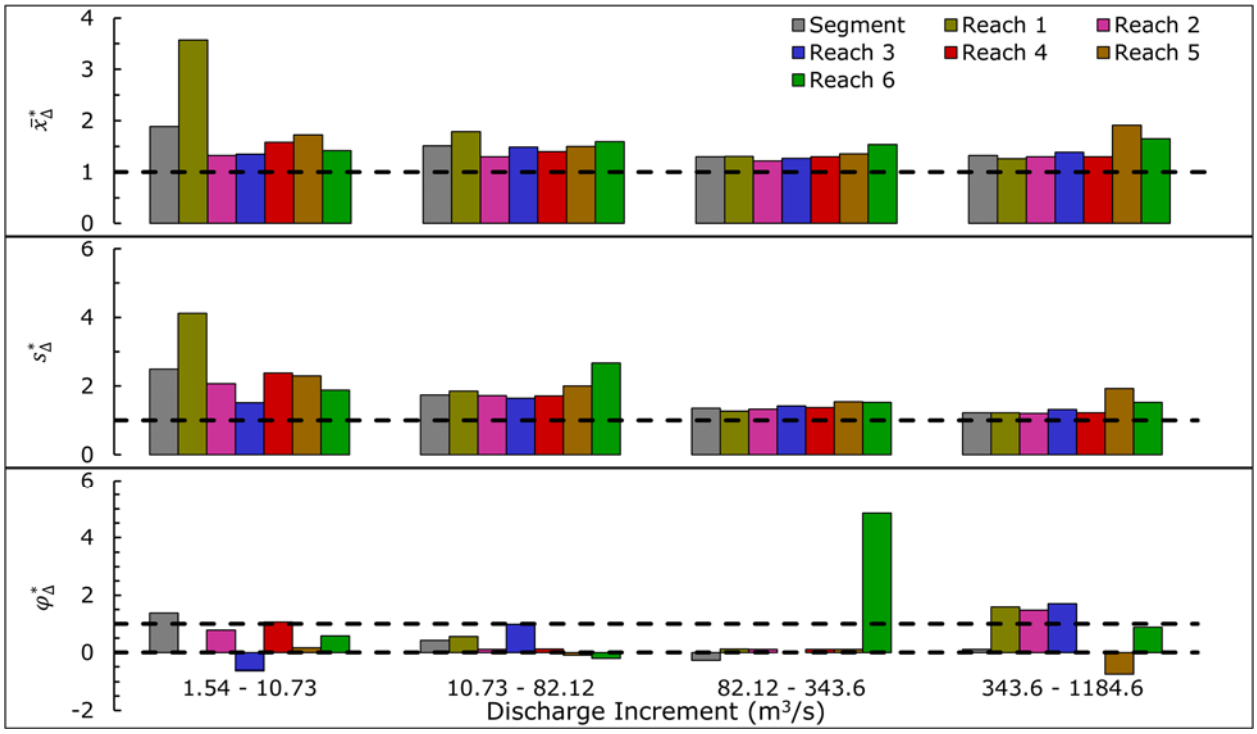

Figure 2.10. Segment- and reach-scale non-dimensional $\bar{\boldsymbol{x}}^*_\Delta$, $\boldsymbol{s}^*_\Delta$, and $\boldsymbol{\varphi}^*_\Delta$ values illustrating relative magnitudes of change in h/D_c distribution properties between datasets. Smaller values indicate less change between datasets. The horizontal dashed lines at 1.2 represent a threshold for dramatic shifts between datasets.

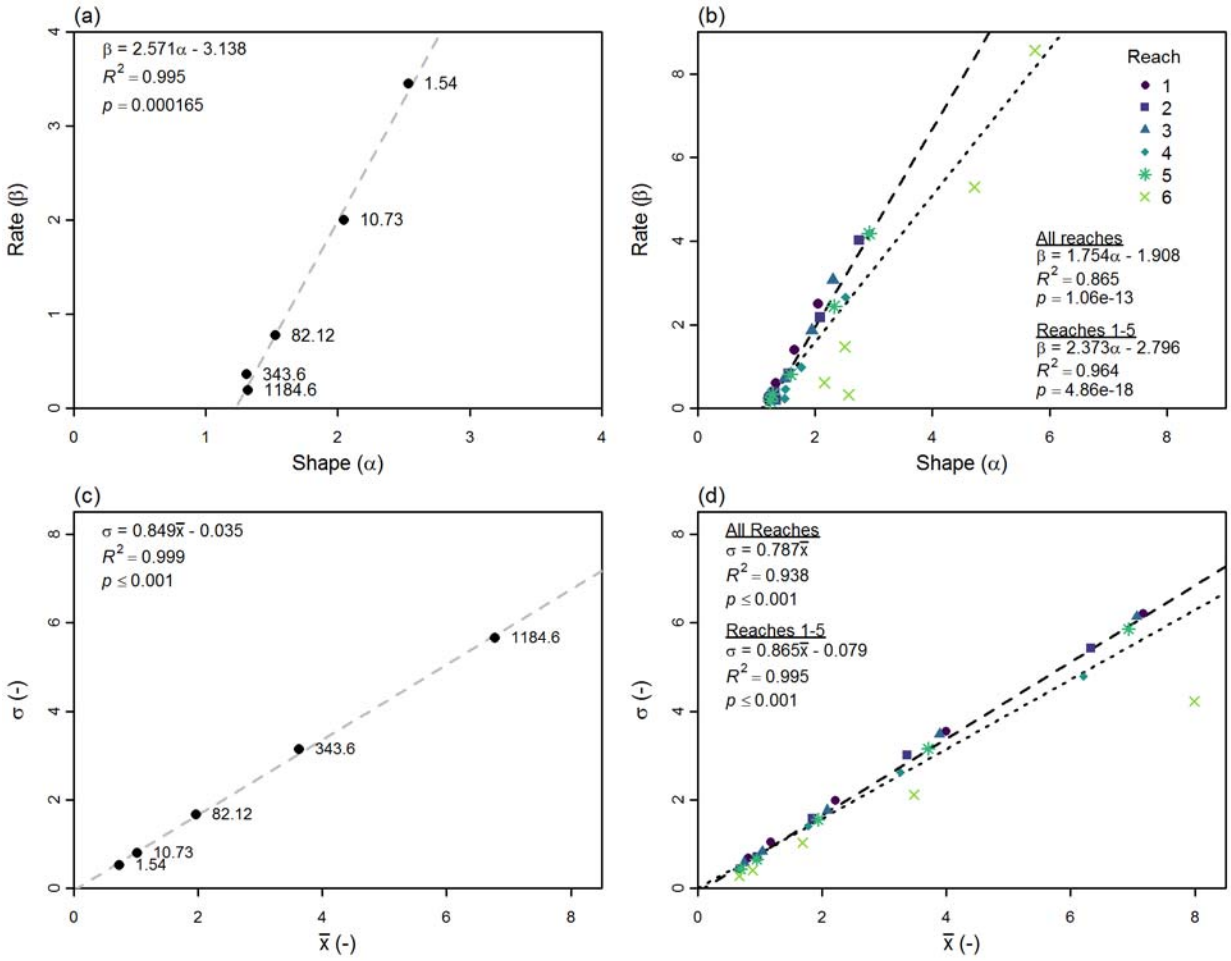

Figure 2.11. Scatter plots of (a) segment and (b) reach scale fitted Gamma distribution parameters (β vs α) for discharge-dependent h/D_c distributions and (c) segment and (d) reach scale standard deviation (σ) versus mean ($\bar{x}$) discharge-dependent h/D_c values. Gray dashed line in panels (a) and (c) are lines of best fit for segment data. Regression equations and statistics are shown in the upper left corners. Short and long dashed lines in (b) and (d) are lines of best fit for all reaches and for data from only reaches 1-5, respectively. Numbers next to segment points are discharge in m^3/s associated with the data point. Discharge decreases from top-right to bottom-left in (b) and from bottom-left to top-right in (d).

2.5.3 Between domain process-based similarity

Results presented in section 2.5.2 required rejection of Styles 1, 2, 3(b), 3, and 3(b). This was a necessary criteria of Style 4, which envisioned discharge-dependent h/D_c distributions to evolve consistently between domains, such that rates at which parametric and designated statistical properties changed were equivalent. Visually, relationships between h/D_c dataset parametric and

statistical properties versus discharge appeared to follow power-laws, therefore data in each domain were modeled by fitting linear models to log-transformed discharges and h/D_c dataset properties (i.e. $\bar{x}$, σ, φ, g, β_2, α, and β values), resulting in seven models per domain and 49 models total (Figure A.2.5). Model fitting was completed in the R programming language using ordinary least squares regression. With the exception of modal values, and the caveat that only five data points were used per model, models explained relatively large amounts of variance (i.e. adjusted-R^2 between 0.776 and 0.989 for $\bar{x}$, σ, g, β_2, α, and β models and between 0.183 and 0.858 for φ models) and thus were considered reasonably accurate. Further, with the exception of six of the seven models for modal values all slope coefficients were statistically significant (F-test, $p < 0.05$) (Table A.2.4).

Model slopes (i.e. power-law exponents) of each response metric were compared between all unique domains pairs using EQ. 3. Of the 84 relevant slope comparisons (21 per metric for $\bar{x}$, σ, α, and β), only the Segment and Reach 6 α-slope comparison was rejected for equivalency above a 95% confidence level ($|Z| \geq 2.776$). This meant that all other α slopes, and all $\bar{x}$, σ, and β slopes were considered equivalent between all pairs, consistent with the Style 4 acceptance criteria (Table 2.2). Of the additional 63 comparisons between φ, g, and β_2 slopes, 23 were rejected (Text 1A.2.4.3). This meant 20 of 21 unique domain pairs had roughly equivalent $\bar{x}$, σ, α, and β slopes and 7 of the 21 domain pairs had roughly equivalent slopes for all variables (Figure 2.12). Collectively, we view these results as indication of Style 4 being both reasonable and certainly the most representative Style for h/D_c distribution behavior in the study segment.

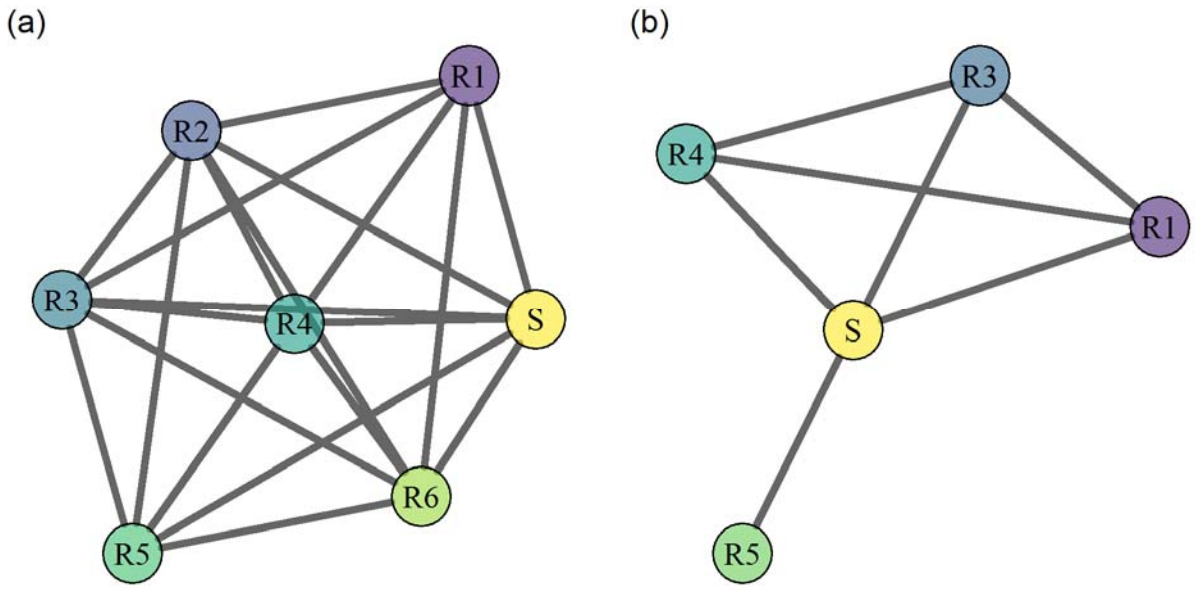

Figure 2.12. Network graphs showing spatial domains as nodes (colored circles) with connections (lines) to other domains indicating domains had equivalent slopes for (a) $\bar{x}$, σ, α, and β values, and (b) for all variables. 'S' and 'R' are shorthand for segment and reach, respectively. Domains that are absent did not have equivalent slopes with any other domains for specified variables.

2.5.4 Incremental inundation corridor relative submergence

All four incremental inundation corridor h/D_c datasets were best fit by Log-normal distributions, which was supported at the 95% confidence level by the corrected Anderson-Darling test (Figure 2.9). This finding was only corroborated for the 1.54-10.73 m^3/s corridor data when applying the Shapiro-Wilk test (Millard, 2013), which is considered a relatively powerful test for normally distributed data. Because data were best fit by log-normal distributions, central tendencies were compared with Welch's t-test and variances were compared using F-tests (R Core Team, 2021). Despite slightly stronger visual resemblances between datasets than those present when comparing datasets in other domains (Figure 2.7; Figure 2.8; Figure 2.9), all tests were rejected above a 95% confidence level (p <<0.05) suggesting h/D_c values of LBEs along the incrementally wetted channel margins were each statistically unique. Isolating the independent

sets of h and D_c values in each corridor found distributions of D_c values to exhibit greater similarly across the four corridors (Figure A.2.6). This was confirmed using the non-parametric overlapping index (Pastore & Calcagni, 2019), which found comparison of all possible sets of D_c values to have index values between 0.88-0.94 versus index values between 0.31-0.67 for h comparisons. The index varies from 0-1 for end-member conditions of no distribution overlap and perfect distribution overlap, respectively. This means variations in flow depths along channel margins played a larger role in differences between incremental inundation corridor h/D_c datasets compared to diversity in LBE heights.

2.5.5 Submergence trends and alternate calculations

Many hydrogeomorphic factors influence h/D_c distribution changes, however isolating the following three components of the data aided interpretation of several trends described in the previous results sections: (i) the number and (ii) h/D_c values at newly wetted LBEs at each discharge; and (iii) how depths change at previously wetted LBEs between discharges. An example of this scrutiny is provided in Figure 2.13(a-d), which depicts superimposed frequency histograms of segment-scale h/D_c values at the set of newly wetted LBEs with histograms of h/D_c changes that occurred at each set of previously wetted LBEs for each change in discharge (Text 1A.2.4.5). It is clear that depth increases at previously wetted LBEs drastically overshadow addition of new, low-submergence LBEs and drive trends to less positively skewed h/D_c distributions with higher mean h/D_c values. This was quantitatively supported by independently calculating the difference in the mean of each h/D_c dataset resulting solely from the addition of newly wetted LBEs ($\Delta\bar{x}_n$) versus the mean difference due to depth changes at previously wetted LBEs ($\Delta\bar{x}_p$), which confirmed the latter always exceeded the former (Figure 2.13[a-d]) (Text 1A.2.4.5). Though not depicted, the same results were found at the reach-scale. More minor trends, such as isolated

decreases in modal values were also partly explained by variability in the relative magnitude of the independent dataset components depicted in Figure 2.13(a-d). For instance, addition of a large number of newly wetted, very low submergence LBEs between 82.12-343.6 m^3/s, simultaneous with only moderate depth increases at previously wetted LBEs were assumed responsible for the observed decrease in modal values between the two datasets (Figure 2.7). A final observation regarding the influence of changing flow depths versus LBE configurations on h/D_c results was that the distribution of segment-scale D_c values remained relatively constant across discharges even with the addition of new LBEs, whereas flow depths at LBEs were, unsurprisingly more dynamic (Figure 2.13[e-n]). Overlap indexes comparing all possible segment-scale D_c datasets varied between 0.81-0.96 versus between 0.13-0.70 for h comparisons. The same pattern was true for all reach-scale datasets (Text 1A.2.4.5). This result corroborates those above that study segment h/D_c distribution changes were more strongly influenced by the magnitude and variability of h changes at each successive set of previously wetted LBEs compared to configurations, heights, and flow depths at newly wetted LBEs.

Amidst near universal trends for increasing h/D_c values at higher discharges it is relevant to highlight that a substantial portion of LBEs remained emergent ($h/D_c<1$), below the LRS regime threshold ($h/D_c<3.5$), or below other thresholds used to differentiate bed morphology effects on hydraulic and sedimentological processes across discharges (Table 2.3). For instance, even at the highest simulated discharge, 10.5% of LBEs would be emergent and 40.2% would still influence hydraulics at the water surface (e.g. $h/D_c<3$, Cooper et al., 2013). It is also important to recall that conditions at LBEs within laterally nested, discharge-dependent portions of the river corridor did not change equally between discharges. For example, considering LBEs within the baseflow channel, only 1.4% of these features remained emergent across all discharges. A complete

accounting of the percent of LBEs intersecting each wetted area that exceeded relevant h/D_c thresholds at each higher discharge are included in Table A.2.5.

Compared to the alternative methods for calculating h and D_c (section 2.4.4), the preferred metric, h/D_c, yielded the lowest values, and thus may have a tendency for underestimation. Potential underestimation is expected to be relatively minimal as values across methods were comparable in magnitude. Regressing h/D_c values against the calculation method with the highest values, $\hat{h}/\overline{D}$, found a scaling factor of 1.38 minimized error between estimates, which serves as an expected value for the magnitude of uncertainty. Comparisons of h/D_c values with the other two calculation methods, $\hat{h}/D_c$ and $h/\overline{D}$, returned scaling factors of 1.09 and 1.26, respectively. Regardless of calculation method, discharge-dependent distributions of relative submergence were consistent in their shape and how they changed between datasets (Figure A.2.8). Ultimately, the h/D_c calculation method allowed reasonable approximation of relative submergence values for thousands of macroroughness features over 13 km of river spanning a range of discharges, for which there is scientific as well as practical value, such as mapping submerged hazards (Strom et al., 2017).

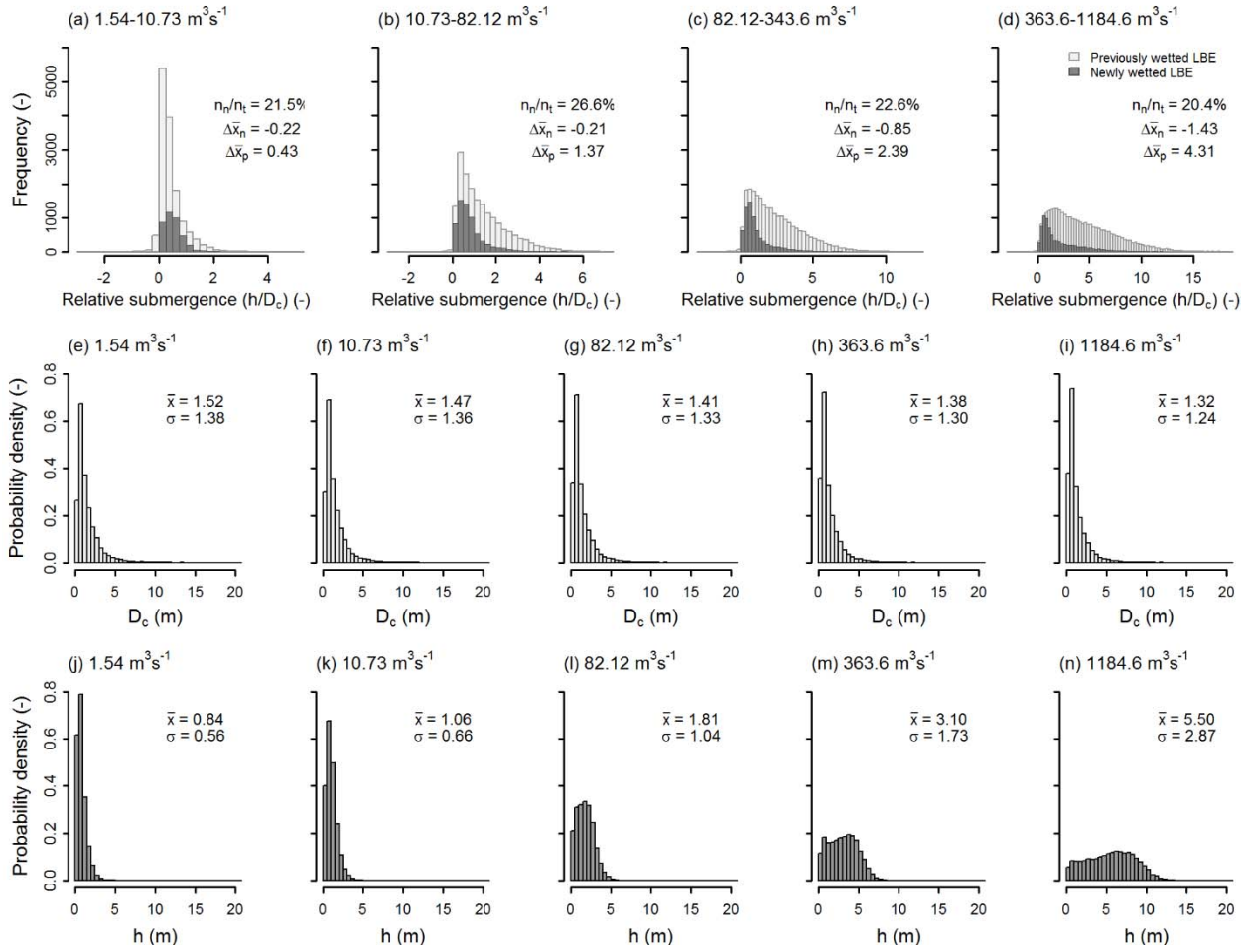

Figure 2.13. Frequency histograms of (a-d) segment-scale h/D_c values at LBEs that become newly wetted between each successive discharge (dark gray bars) superimposed with histograms of changes to h/D_c values that occurred at previously wetted LBEs between each discharge (light gray bars) and probability density histograms of (e-i) D_c values and (j-n) h values at LBEs within each segment-scale, discharge-dependent LBE dataset. The percentage of newly wetted LBEs (n_n) relative to the total number of LBEs (n_t) at each ending discharge (second number in header) are shown in (a). Differences in mean h/D_c dataset values due solely to the addition of newly wetted LBEs ($\Delta\bar{x}_n$) and those due solely to changes in h at previously wetted LBEs ($\Delta\bar{x}_p$) are also shown in (a). For (e-n) note greater similarity of D_c values between datasets compared to h values.

Table 2.3. Percentage of segment-scale h/D_c values exceeding certain thresholds at each discharge.

Simulated Discharge (m^3/s)	Threshold†					
	1	2	3	3.5	4	10
1.54	17.7	2.5	0.8	0.5	0.3	0.0
10.73	37.7	9.3	3.0	1.7	1.0	0.0
82.12	63.8	37.6	20.9	15.5	11.5	0.2
343.6	78.1	60.1	46.7	40.9	35.7	4.9
1184.6	89.5	77.9	68.7	64.1	59.8	24.2

†Thresholds correspond to following: 1 – Emergent vs submerged conditions; 2 – h at double LBE height; 3 – Approximate threshold flow depth where form-induced sublayer always extends to water surface (Cooper et al., 2013); 3.5 – Transition from LRS to HRS regime (Papanicolaou & Tsakiris, 2017); 4 – Transition from intermediate to small-scale roughness (Bathurst, 1985) and surface effects are negligible (Shamloo et al., 2001); and 10 – Threshold for applicability of canonical hydraulically rough boundary-layer theory (Katul et al., 2002).

2.6 Discussion

2.6.1 LBE relative submergence distributions and styles

In light of the questions and hypotheses posed by this study two initial takeaways were that results largely confirmed general hypothesis 1, that h/D_c distributions across multiple discharge-dependent spatial domains were unimodal, leptokurtic, and positively skewed (Figure 2.7; Figure 2.8; Figure 2.9) and that changes between h/D_c distributions over a series of discharges were primary as predicted by general hypothesis 2. Despite these basic similarities, both variability in h/D_c dataset properties and more complex evolutionary behaviors were observed.

In considering how h/D_c values would evolve, an initial hypothesis was that distributions would remain constant in any given spatial domain across discharges (Style 1). Despite segment- and reach-scale datasets being reasonably drawn from the same distribution type (Gamma), visual and statistical differences confirmed h/D_c distributions were not conserved. Thus, the Style 1 hypothesis was rejected. Statistical comparison within and between domains also required rejection of Styles 2 and 3, and conditionally rejecting threshold Styles 2(b), 3(b), and 4(b). Complete rejection of threshold style behavior was limited by the number of flow simulations, as

processes associated with these Styles could have been hidden between simulated discharges. However, propensity for continuous changes in h/D_c distribution properties did not favor these styles being present in the study segment. Ultimately, what did emerge was strong evidence for process-based similarity (Style 4) being the most appropriate behavioral model to explain h/D_c dynamics in the study segment.

The observation that reach-scale h/D_c distributions evolved in essentially the same manner between discharges, has theoretical and practical relevance. One broad interpretation of the consistent scaling is that common self-organizing processes associated with the size-frequency distribution, spatial arrangement, and submergence of LBEs were present between domains (Sapozhnikov & Foufoula-Georgiou, 1999; Hillier et al., 2016). Each of these properties involves complex feedbacks in the fluvial-hillslope system that are difficult to disentangle. However, if D_c is taken to represent the bed-roughness length-scale coefficient (Δ), and the set of h/D_c data are proportional to reach-averaged flow resistance, as is widely accepted (Powell, 2014), study results indicate that while individual reach-scale resistance magnitudes might differ, the rate of change in resistance with discharge between reaches were roughly equal. Interpreted in the context of regime theory and extremal hypotheses, this suggests a degree of mutual reach-scale channel adjustment and implies attraction to a common critical state (Adams, 2020; Eaton & Church, 2009). In laterally confined rivers, modification of bed resistance is both the most rapid and often only independent degree of channel adjustment available (Adams, 2020). Where bed resistance is dominated by LBEs, physical experiments, theory, and field measurements provide evidence that LBEs configurations self-organize toward conditions that maximize flow resistance as this promotes channel stability (Adams, 2020; Church et al., 1998; Eaton & Church, 2009). Consistent with these studies, previous analysis found 21 of 24 discharge-dependent reach-scale LBE datasets in the

study segment were configured to maximize flow resistance (Wiener & Pasternack, 2022). Recent experiments by Carollo & Ferro (2021) and boundary layer theory analysis of Cassan et al. (2017) applicable to rough bedded rivers indicate resistance is maximized when relative submergences are in the range ~0.55-1. If taken as a target, in order to keep the bulk of h/D_c values in this range as stage/discharge increases requires new low submergence LBEs be added in numbers that account for depth increases at previously wetted LBEs. This evolution is consistent with general hypothesis 2 and aligns better with Styles 1, 2, and 4 compared to Style 3. Looking at study segment mean and modal values h/D_c, only at the lowest discharges were mean values in the 0.55-1 range. On the other hand, with the exception of Reach 6 nearly all modal values were in this range. Thus, our interpretation of h/D_c process-based similarity in the study segment is that it represents a dynamic equilibrium in channel adjustment toward a critical state that minimizes the variance of how resistance changes with discharge between reaches (Wohl & Merritt, 2008). Lateral confinement, observed LBE configurations, and modal h/D_c value support that the critical state toward which reaches adjust coincides with one that maximizes flow resistance. Though further analysis is required, h/D_c process-based similarity and deviation therefrom could serve as a quantitative metric to assess the degree that a series of connected river reaches are in equilibrium (Sapozhnikov & Foufoula-Georgiou, 1999), or may simply indicate if such reaches differ in their primary mode of channel adjustability.

Similarity in the magnitude of reach-scale h/D_c dataset properties at the same discharge can also be used to make inference about channel adjustment (Wohl & Merritt, 2008; Schneider et al., 2015). For instance, the coefficient of variation (CV) of mean reach-scale h/D_c values ($\bar{x}$) were less than 10% at each distinct discharge (Table A.2.2). Using the logic at the beginning of the preceding paragraph and substituting $\bar{x}$ values in place of R/D_{84}, rough estimates of the Darcy-

Weisbach friction factor in each reach at each discharge can be made using the unbiased and widely used variable-power resistance equation of Ferguson (2007) (see section 2.6.3 and Text 1A.2.5.3 for equation). For the calculations, the assumption that $h \sim R$ is applied, which is simplifying, but not uncommon in practice (Bathurst, 1985), and reasonable given the comparative nature of the exercise. The CV of these resistance estimates do not exceed 16% between reaches for any given discharge. This is phenomenologically similar to the findings of Wohl and Merritt (2008), who found the range of bankfull flow resistance values (f) to be constant between geographically distributed mountainous steam reaches with different channel morphologies. They concluded such uniformity was consistent with the extremal hypotheses that channels were adjusted to maximize resistance.

Contrary to h/D_c process-based similarity at the segment- and reach-scale, greater self-similarity was observed between incremental inundation corridor h/D_c distributions. While these data bore greater visual resemblance to the Style 2 conceptualization (Figure 2.9), statistical testing did not confirm this or any other Style (i.e. central tendencies and variances were considered not statistically equivalent). Nonetheless, results indicated that independent sets of h and D_c values in each corridor were more constant between discharges than these same metrics were when considered for the entire river corridor (Figure A.2.6; Figure 2.13). Factors driving this similarity, especially the uniformity of D_c values along channel margins require additional exploration that is outside the scope of this effort (e.g. Sklar et al., 2020). However, it is logical to expect that the set of depths along incremental channel margins in a confined river canyon would be relatively shallow. Shallow depths together with near constant LBE D_c values explain the comparatively lower variance and lower overall magnitudes of h/D_c values in the incremental inundation corridors.

Lastly, of the reach-scale h/D_c datasets, the wider and lower gradient Reach 6 stood out in its evolutionary behavior. At the highest simulated discharge (1184.6 m^3/s) h/D_c values in this reach had near zero skewness and followed a more bell-to-uniform shaped distribution compared to the positively skewed, unimodal distributions in the five upstream reaches (Figure 2.8; Table A.2.2). This more uniform h/D_c distribution resulted from relatively low numbers of newly wetted LBEs being encountered simultaneous with large relative increases in depth at both previously wetted and newly wetted LBEs. These changes align with the canonical power-law form of channel width and depth hydraulic geometry relationships for an inundated U-shaped valley, whereby rates of channel width increase are low compared to rates of depth increase (Gonzalez & Pasternack, 2015). Convergence toward a uniform h/D_c distribution may be a common limiting state for confined river canyons at high discharges when the valley bottom is inundated and few new LBEs are encountered. Indeed, h/D_c distributions of the study's other reaches also appeared to evolve toward this limiting state. Presence of more V-shaped valley geometries with greater abundances of LBEs in these other domains may partly explain the slower trajectory toward uniform h/D_c distributions that could still occur at discharges higher than those simulated.

2.6.2 Evolution toward a relative submergence limiting-state

Evolution of h/D_c values toward uniform distributions may help explain field and experimental observations from bedrock-alluvial channels of reach-averaged flow resistance being stable at high discharges (Richardson & Carling, 2006; Hodge & Hoey, 2016; Ferguson et al., 2019). While empirical data and most resistance equations confirm the rate at which resistance decreases drastically diminishes with discharge (e.g. Powell, 2014), such observations contrast with the idea that resistance should continuously decrease as increasing stage drowns-out bed roughness. Mechanisms driving the decoupling of flow resistance from discharge have been

previously attributed to increasing sidewall roughness driving lateral and turbulent flow mixing and due to spatial variability of the flow-field being separated into a central core of high-velocity flow surrounded by marginal slack-water zones (Richardson & Carling, 2006; Hodge & Hoey, 2016). Boundary layer theory also supports that hydraulic roughness is independent of depth for h/D_c>10, which under certain simplifying assumptions (e.g. uniform flow) would lead to constant resistance (Katul et al., 2002; Cassan et al., 2017). If resistance is considered proportional to the set of h/D_c data, and resistance contributed by LBEs with h/D_c<10 vastly exceeds resistance contributed by LBEs with h/D_c>10, then evolution toward uniform h/D_c distributions with a constant lower h/D_c bound and finite upper h/D_c bound above 10 would result in resistance being constant.

To address the emergent question of whether the study segment's h/D_c distribution approaches a uniform distribution, study results were used to statistically model h/D_c distributions for flows higher than those initially tested. In doing so, the segment-scale, power-law relationship between discharge and β (Figure 2.14a) was used to initially calculate simulated β values for a range of discharges (see section 2.5.2; β -discharge model was selected over α-discharge model based on slightly better accuracy [R^2 = 0.988 versus 0.959]). Next, α values were predicted using the previously modeled β-α relationship (Figure 2.11a). Figure 2.14b shows the resulting series of simulated h/D_c gamma distributions using predicted parameters for discharges ranging between 1.1-4500 m^3/s, the upper bound of which has an ~500-year recurrence level.

The simulated data spotlight the transition from high frequencies of relatively low h/D_c values at low flows to more uniformly distributed values at higher flows, which match observations in the study segment. Technically, if α approaches unity and β approaches zero the Gamma probability density function equals zero for all values. For segment- and reach-scale h/D_c

distributions, the study found both conditions to be true as discharge increased (Figure 2.11). However, if it is assumed that β is asymptotic to zero, as indicated in the β-discharge relationship (Figure 2.14a), and α can be estimated using the statistical relationship in Figure 2.11a, then simulated h/D_c values for increasingly larger discharges always approach a uniform distribution with probabilities approximately equal to the increasingly smaller β values. Physically, this would suggest that at very high discharges there are few, but always nearly equal numbers of, low submergence LBEs along the channel margins and highly submerged LBEs in topographic lows, with a mix of h/D_c values between these extremes. As discussed above, the nearly uniform distribution of h/D_c values provides a preliminary theoretical means for resistance to become constant at higher discharges. Such theoretical stochastics require further investigation, but at present could be useful in guiding design of synthetic river channels, numerical simulations, or physical experiments with LBEs.

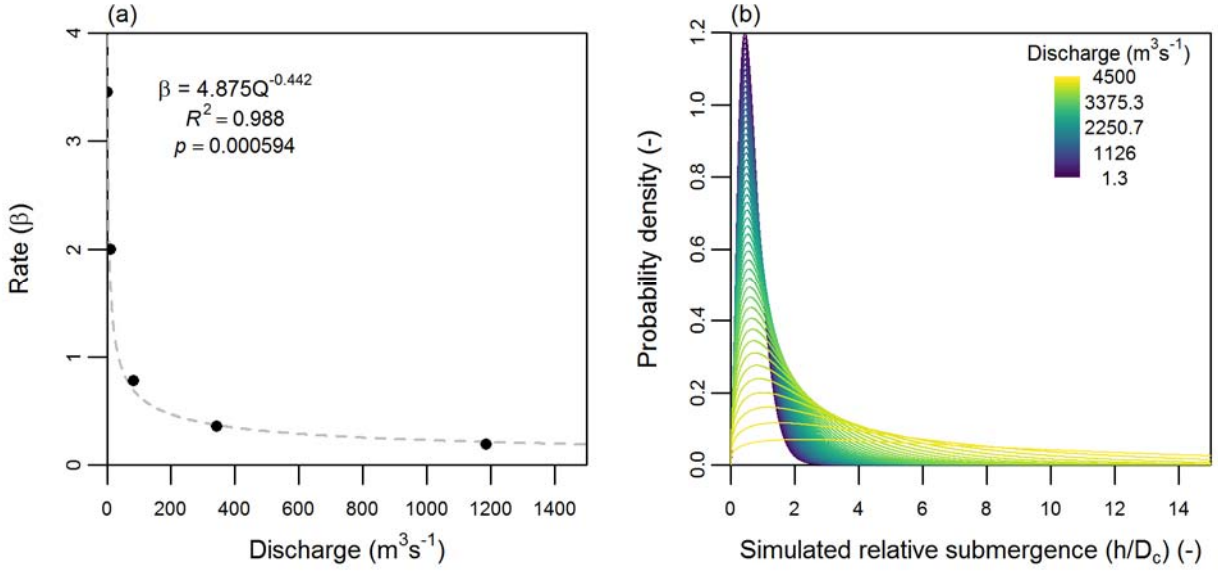

Figure 2.14. (a) Fitted Gamma distribution rate (β) parameters versus discharge (m^3/s) for segment-scale discharge-dependent h/D_c data and (b) simulated h/D_c distributions for discharges ranging between 1.3-4500 m^3/s.

2.6.3 Implications of relative submergence distributions

As discussed in section 2.6.1, a near-universal takeaway of this study was that distributions of h/D_c values were unimodal, leptokurtic, and positively skewed. We are not aware of h/D_c datasets for comparison, however, Hodge et al. (2009) found distributions of surface elevations in two gravel-cobble-bed English rivers were positively skewed. Additionally, Gomez (1993), Day (1976), and Aberle and Nikora (2006) independently found roughness heights to evolve toward skewed and leptokurtic distributions during armoring in gravel-bedded flumes, and several workers document heights of finer-grained bedforms such as dunes to follow distributions with similar characteristics (Van der Mark et al., 2008; Singh et al., 2012).

Coarse-bedded ($D_{50} \geq 5$ mm) rivers generally display skewed, often lognormal grain-size distributions (GSDs) (Bunte & Abt, 2001). Relationships between surface GSDs and roughness height distributions typically don't exhibit 1:1 correspondence as they are influenced by several factors such as imbalances in sediment supply-to-transport ratios that promote fining and development of planar beds or from heterogeneous packing, spacing, and clustering of grains (Kirchner et al., 1990; Gomez, 1993). Nonetheless, for armored beds, it is reasonable that roughness height distributions would follow the general form of surface GSDs as large particles protrude further into the flow (Kirchner et al., 1990; Gomez, 1993). A universal trend for skewed roughness height distributions has implications for random-field based approaches to roughness approximation. These methods generally rely on the assumption that bed elevations are homogenous and Gaussian distributed (Nikora et al., 1998), otherwise requiring higher-order structure functions when beds are anisotropic and non-Gaussian (i.e. skewed and leptokurtic) (Aberle & Nikora, 2006).

A fundamental limiting assumption of most reach-averaged resistance equations is that for

a given Δ value, a 1:1 relation exists between mean depth and mean velocity (Ferguson, 2007). Attempts to reduce scatter between observed and predicted resistance have typically involved the addition of variables (e.g. slope and LBE concentration) into resistance equations (Nitsche et al., 2012), the use dimensionless variables (Ferguson, 2007; Rickenmann & Recking, 2011), or partitioning approaches (David et al., 2011). David et al. (2011), for example, employed a drag force approach to estimate grain resistance by summing drag contributions from all individual large grains present in their study reach. These resistance estimates were always higher than those from typical resistance equations, but were still considered to underestimate grain resistance at low flows. The linearity assumption of such additive approaches is complicated by wake interactions that result in non-linear relations between LBE concentrations and resistance (e.g., Wiener & Pasternack, 2022).

Conceptually, the inclusion of multiple roughness length scales (Ferguson et al., 2019) or methods that better characterize bed roughness and depth heterogeneity, such as the discharge-dependent relative-submergence distributions presented in this study, could address the equifinality issues described above (Ferguson, 2012). To this end, a simple numerical example is introduced to demonstrate one way h/D_c distributions may be used to estimate resistance. For the example, the four resistance equations of Bathurst (1985), Ferguson (2007), Katul et al. (2002), and Thompson and Campbell (1979) (Bathurst, Ferguson, Katul, and T&C) were selected and solved traditionally and with a h/D_c distribution-based approach (see Text 1A.2.5.3 for equations). We focus on these four equations as they are widely referenced, apply to and provide unbiased solutions for coarse-bedded rivers with low submergence, provide solutions for the same common resistance coefficient (f), and beyond empirical coefficients only require input of h/D_{84} (i.e. $h \sim R$). Each equation uses D_{84} to parameterize Δ, consistent with the view that large particles dominate

flow resistance. While effectiveness of D_{84} and characteristic particle sizes in general in estimating resistance are the subject of controversy (Yochum et al., 2012), alternatives (e.g. σ_z most commonly) are not without drawbacks and have not always outperformed particle-size approaches in application (Schneider et al., 2015).

For the traditional approach each equation was solved for each reach at each simulated discharge using a single h/D_{84} value, as intended by their original formulation. Estimates of h were made by averaging model predicted depths over each reach. A constant D_{84} of 0.512 m obtained from previous sampling (YCWA, 2013) was used for all calculations. These were used to solve each equation for f, and are referred to as 'traditional–f' values. Next, the same resistance equations were solved for f, but this time numerically integrating over each reach-scale h/D_c dataset as input for h/D_{84} (Text 1A.2.5.3). These are referred to as 'integrated–f' values.

Comparison found integrated–f values were on average ~6.8 times larger than traditional–f values, which is not surprising given the range of lower submergence values present in the former (Figure 2.15a). Differences varied by equation, as integrated–f values computed using the Bathurst equation were on average ~16.1 times larger than traditional–f values, whereas integrated–f values were only ~3.1-4.3 times larger for the other three equations. Several workers have demonstrated popular resistance equations, including those referenced above, tend to underestimate resistance coefficients (n and f) in course-bedded rivers at low flows, resulting in velocity overestimation and shear-stress underestimation (e.g. Yochum et al., 2012; Ferguson et al., 2017). Notably, error trends are not universal, and a tendency for resistance under-prediction at lower relative submergence and over-prediction at higher relative submergence is well documented (Rickenmann & Recking, 2011).

At this time, it remains unclear if resistances calculated using the integrated approach

actually outperformed traditional estimates. However, the integrated approach does provide more complete representation of bed-surface heterogeneity and the joint-distribution of local flow depths. The approach also allows unique resistance value to be estimated for any given discharge and spatial domain and we believe it has potential for improving resistance estimation despite the greater input data requirements. For instance, for a given reach and given discharge, the integration approach provided a marginal degree of similarly collapse between equations as the CV of integrated–f values were reduced by ~2.9% compared to traditional–f CV values, which we interpret as a positive outcome. Additional analysis on these fronts is beyond the scope of this study, but could be an area of future research, especially given availability of improved methods for remotely-sensed depth measurements (Legleiter & Harrison, 2019).

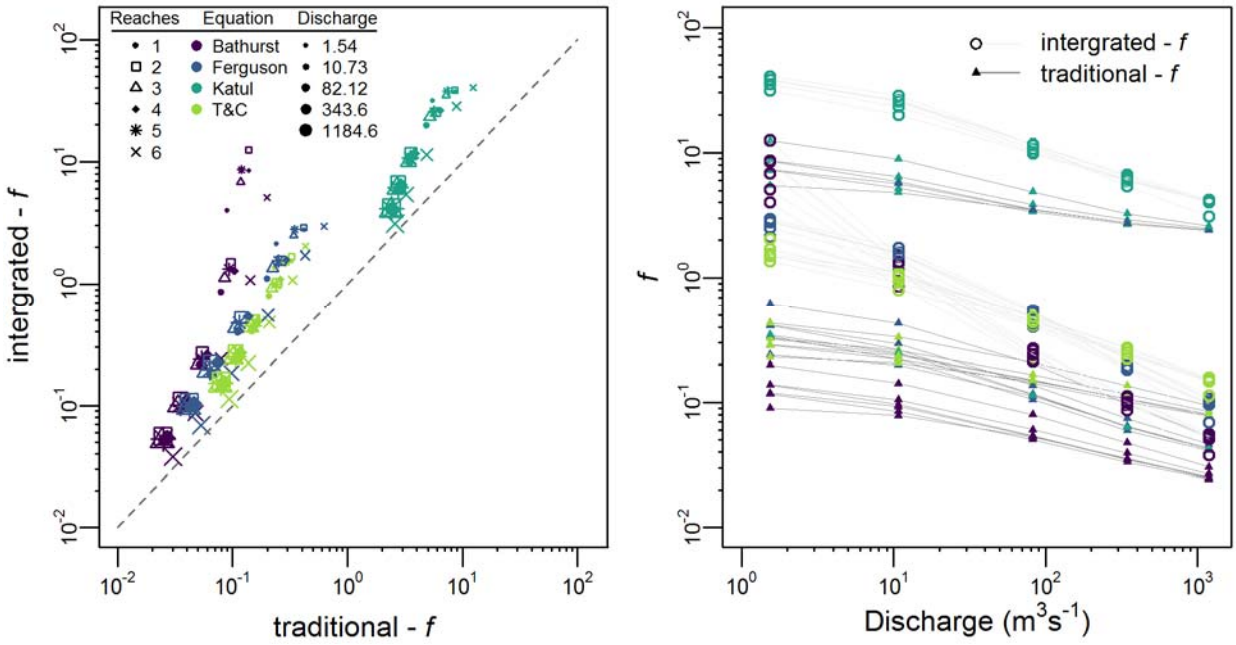

Figure 2.15. (a) Comparison of reach-scale Darcy-Weisbach friction factor (*f*) estimates made using h/D_{84} – *f* and h/D_c integrated– *f* calculation methods; and (b) calculated *f* versus discharge for all reaches. In (a) data from each reach are represented by unique symbols. Symbols are colored according to resistance equation and sized according to corresponding discharge simulation. Dashed gray line is the 1:1 line. In (b) symbols correspond to the method used to calculate *f* and are colored according to resistance equation.

2.6.4 Resistance trends and fixed roughness coefficients

Separate analysis in the study segment by Wiener and Pasternack (2022) found LBE concentrations increased with stage. Together with results from this study this has ramifications toward two conventions in engineering hydraulics: (i) that reach-average resistance decreases as discharge increases; and (ii) that Δ remain constant in a given domain regardless of discharge. To the first point, across all study domains, higher discharges corresponded with increased mean h/D_c values and less positively skewed h/D_c distributions as the drowning-out of LBEs in the channel center outweighed addition of low submergence LBEs along channel margins. This translated into monotonic decreases in reach-scale resistance based on the common equations referenced in section 2.6.3 (Figure 2.15b). These decreases are partly a result of the underlying assumptions of

these equations, which may be ill-specified for very low submergence conditions (h/D_c<1). For instance, at low stages, river flows diverge around emergent LBEs forming multiple flow paths (Reid & Hickman, 2008). Drag forces from LBEs are also drastically reduced when h/D_c<0.5 due to slower flow velocities and reduced frontal-area exposure (Lamb & Brun, 2017). As stage increases and LBEs become fully submerged, drag forces increase and momentum is extracted throughout the flow depth. The hydraulic efficiency and reduced momentum loss from LBEs at low stage support theory that resistance may initially increase as LBEs become fully submerged (Reid & Hickman, 2008; Cassan et al., 2017). As stage continues to rises and LBEs become further submerged, drag forces tend to stay relatively constant, but the portion of the velocity profile influenced by LBEs shrinks (Lamb & Brun, 2017). Thus, while drag forces may be large, the effect on mean velocity and total discharge often becomes negligible and a decrease or leveling off of resistance occurs (Lamb & Brun, 2017). This leveling off of resistance in main channel may be partly offset by new emergent LBEs along channel margins.

Study segment hydrodynamic simulation found an increasingly prominent and longitudinally connected central-core of high velocity flow became established at higher discharges. This core was surrounded by regions with lower velocities often forming recirculating zones along the channel periphery. The separation of the flow-field in this manner mirrors expected changes in resistance described above based on observed h/D_c conditions (Table 2.3; Table A.2.5). Namely, that as main channel LBEs became deeply submerged their resistance contribution became less impactful to velocities in the channel center, simultaneous with the central portion of the channel becoming progressively decoupled from resistance contributed from LBEs along channel margins. Ultimately, the manner in which variable conditions at LBEs distributed throughout a channel interact to influence average resistance remains a challenge and findings of

this study illustrate the importance of considering spatial variability in channel morphology and hydraulics (Hodge & Hoey, 2016).

On the second point regarding fixed Δ values, while changes in discharge-dependent D_c values were subtle (Figure 2.13; Figure A.2.6; Figure A.2.7), they would be ignored by a constant Δ, suggesting scrutiny of this common practice is required (Ferguson et al., 2019). Aberle et al. (2010) also found statistical moments of bed elevations (i.e., standard deviation, skewness and kurtosis) to depend on discharge in a low-gradient, sand-bedded river and Yochum et al. (2104) confirmed the same in several high-gradient coarse-bedded rivers. Using mean D_c values or another representative D_c percentile appears to be the simplest alternative for specifying discharge-dependent variable roughness. Isolating distributions of D_c values in incremental inundation corridors (Figure A.2.6) may also provide a sensible method for parameterizing spatially variable roughness lengths scales along different portions of the channel margins such as proposed by Ferguson et al. (2019). Interestingly, mean D_c values decreased slightly at higher discharges in all study domains, which could be an indication of reduced roughness. However, we posit that higher LBE concentrations along channel margins along with unaccounted sources of roughness and resistance provide the means for spatially averaged resistance to increase, remain constant, or only minimally decrease with discharge, a topic that remains the focus of continued study (Abu-Aly et al., 2014; Cassan et al., 2017; Ferguson et al., 2019).

2.6.5 Dynamism of local relative submergence

As stated by Groom and Friedrich (2019), "Understanding the spatial patterns and structure of flow properties across a bed has fundamental implications for geomorphic processes and local ecology." Thus far we have focused on LBE relative submergence conditions aggregated at segment and reach scales, however element-explicit h/D_c values produced by the methods

presented herein can be used to study submergence patterns and dynamics at many spatial scales, such as at individual LBE or clusters of elements. For discussion purposes, an example using element-explicit h/D_c values for more local-scale analysis is presented below. The example focuses on documenting h/D_c conditions that would be encountered by an arbitrary object traveling along a portion of the river's thalweg under different discharge conditions. While highly simplified, the object could be representative of a particle or organism, such as a fish or macroinvertebrate, moving along this dominate flowline. An arbitrary 520-m (~20 channel widths) portion of Reach 1 was selected as the domain of interest. Within the domain, the object's path was set as the baseflow thalweg and LBEs within 1 m of the thalweg were identified and assigned a longitudinal position along the thalweg, assuming these represent LBEs that interact with the object or visa-versa. Discharge-dependent h/D_c values at these LBEs were recorded and plotted longitudinally (Figure 2.16).

Firstly, it can be observed that numerous LBEs with variable h/D_c conditions would be encountered along the object's journey. If relevant h/D_c values are known (e.g. a range of h/D_c values that provide physical habitat for an aquatic organism of interest), inference may be drawn from the sets of encountered conditions. For instance, from the perspective of bedload particles traveling along the specified route, at discharges at or below 10.73 m^3/s, nearly all LBEs were in the LRS regime ($h/D_c<3.5$). This condition is associated with enhanced deposition of mobile bedload upstream of LBEs (Monsalve & Yager, 2017; Papanicolaou & Tsakiris, 2017). Thus, it may be inferred that there would be many opportunities for deposition and intermittent storage upstream of these LBEs. Monsalve & Yager (2017) also found LRS regime bedload deposition promoted cluster formation and increased stability of stoss-side sediment patches with little effect on wake GSD or bed elevations (see also Wittenberg & Newson, 2005). At higher discharges

($\geq$82.12 m^3/s), most encountered LBEs were in the HRS regime (h/D_c<3.5), which is associated with increased probability for mobile particle deposition in LBE wakes (Papanicolaou & Tsakiris, 2017). Notably, higher transport capacities and associated selective entrainment or equal mobility of the bed and increased potential for cluster destabilization and LBE mobilization during these higher discharges may limit depositional processes (Wittenberg & Newson, 2005). Patch stability at a given LBE, a feature of interest in river management (Kondolf et al., 1996), is likely enhanced by persistence of LRS or HRS regime conditions across a wide range of discharges that would be easy to track from the data. In the example, the few LBEs remaining in the LRS regime at high discharges may, for instance, harbor sediment patches and provide shelter from surrounding higher velocities and turbulent intensities important to aquatic organisms (Crowder & Diplas, 2006; Lacey & Roy, 2008). Lastly, while no attempt is made to track time and flow-dependent particle movements, as discharge cycles between periods of baseflow and flood the transition of LBEs between LRS and HRS regimes provide a plausible mechanism for intermittent, localized storage and transport as bedload particles hop-scotch downriver between locations that favor deposition. This stage-dependent LBE morphodynamic control may mediate sediment yield and facilitate observed long term storage (>10^3 of years) of theoretically highly mobile grains in mountain rivers (Faustini & Jones, 2003; Sutfin & Wohl, 2019).

Despite its simplicity, the example above yields high-level incite regarding how LBE relative submergence dynamics can lead to unique patterns for sediment storage and transport through mountain river systems and provide crucial environmental conditions for aquatic biota. It is acknowledged we have barely broached the surface of how element-explicit h/D_c values may be used in river science and management, but the hope is presenting these concepts can stimulate further research.

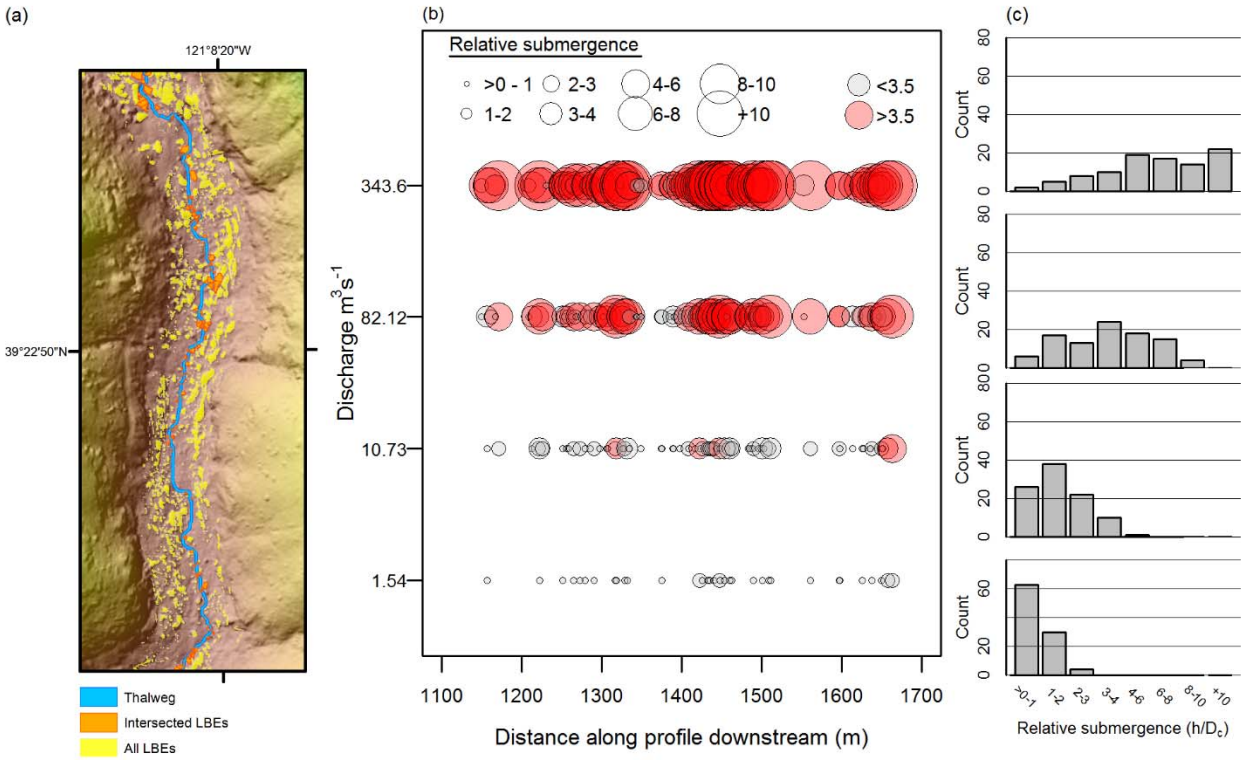

Figure 2.16. (a) Selected 520 m portion of Reach 1 used to illustrate discharge-dependent h/D_c conditions at each LBE encountered by object moving along the baseflow thalweg. (b) Longitudinal plots of LBE locations (circles) along the thalweg scaled (circle size) based on relative submergence and color coded as being in the LRS (gray) or HRS (red) regimes. Each row in (b) depicts h/D_c conditions at the same set of LBEs for the discharge depicted on the vertical axis. (c) Histograms of h/D_c values for each discharge, also stacked following the same order as in panel (b). Flow in (a) is from top to bottom. The object encounters 678 LBEs.

2.7 Conclusions

To our knowledge this is the first time complete distributions of h/D_c values have been presented and studied for a natural boulder-bedded river. In doing so we were able to document discharge-dependent h/D_c distributions at multiple spatial scale, address hypotheses regarding h/D_c behavior, and discuss the hydraulic and geomorphic implications of study results and accounting for h/D_c distributions more generally. Through fitting and statistical analysis of discharge-dependent h/D_c datasets we confirmed segment- and reach-scale data exhibited similar general statistical properties (i.e. positive skewness), were able to be drawn from the same type of

distribution, but also varied between spatial domains and across discharges. LBE height distributions were also all found to be positively skewed, highlighting the non-Gaussian nature of this property which has implications for how bed roughness is characterized. Dynamism of LBE heights, albeit only slight across discharges calls into question the practice of holding roughness coefficients constant, and highlights the need to uniquely represent this property across discharge conditions. Comparing solutions of four common hydraulic resistance equations found resistance estimates incorporating complete h/D_c distributions had higher resistance than those based on more standard singular h/D_{84} estimates, the latter of which has often been criticized for issues of underestimation. While untested, greater accounting in resistance equations of discharge-dependent relative submergence over larger portions of the riverbed could be relevant toward improved resistance estimation and help collapse scatter in existing h/Δ-channel resistance relationships (Schneider et al., 2015; Monsalve & Yager, 2017).

A key aspect of this study was analyzing the evolution of h/D_c between discharges. Results confirmed changes in study segment h/D_c distributions were predominately as hypothesized, such that in each domain variance in h/D_c values increased and central tendencies either increased or remained relatively constant over the series of tested discharges. Further analysis of these changes against six plausible evolutional Styles revealed statistical and parametric properties of study segment h/D_c distributions evolved consistently between discharges, between spatial domains, thus exhibiting what we term process-based similarity (Style 4). Applying study results to simulate h/D_c values at discharges beyond those tested showed continued evolution toward uniform conditions, which supported previous findings of resistance becoming constant at high discharges. While the universality of relative-submergence stochastics presented requires further testing, the unique distributions and discharge-dependent relationships can serve as an immediate reference for

studies wishing to better understand effects of h/D_c diversity on boulder-bedded rivers.

2.8 References

Aberle, J., & Nikora, V. (2006). Statistical properties of armored gravel bed surfaces. *Water Resources Research, 42*(11). doi:10.1029/2005WR004674

Aberle, J., Nikora, V., Henning, M., Ettmer, B., & Hentschel, B. (2010). Statistical characterization of bed roughness due to bed forms: A field study in the Elbe River at Aken, Germany. *Water Resources Research, 46*(3). doi:https://doi.org/10.1029/2008WR007406

Aberle, J., & Smart, G. M. (2003). The influence of roughness structure on flow resistance on steep slopes. *Journal of Hydraulic Research, 41*(3), 259-269. doi:10.1080/00221680309499971

Abu-Aly, T. R., Pasternack, G. B., Wyrick, J. R., Barker, R., Massa, D., & Johnson, T. (2014). Effects of LiDAR-derived, spatially distributed vegetation roughness on two-dimensional hydraulics in a gravel-cobble river at flows of 0.2 to 20 times bankfull. *Geomorphology, 206*(Supplement C), 468-482. doi:https://doi.org/10.1016/j.geomorph.2013.10.017

Adams, D. L. (2020). Toward bed state morphodynamics in gravel-bed rivers. *Progress in Physical Geography: Earth and Environment,* 44(5):700-726. doi:10.1177/0309133320900924

Baas, A. C. W. (2002). Chaos, fractals and self-organization in coastal geomorphology: simulating dune landscapes in vegetated environments. *Geomorphology, 48*(1), 309-328. doi:https://doi.org/10.1016/S0169-555X(02)00187-3

Bathurst, J.C., (1982). Flow resistance in boulder-bed streams. In: Hey, R.D., Bathurst, J.C., Thorne, C.R. (Eds.), Gravel-bed Rivers, Wiley, Chichester, pp. 443–462.

Bathurst, J. C. (1985). Flow Resistance Estimation in Mountain Rivers. *Journal of Hydraulic Engineering, 111*(4), 625-643. doi:doi:10.1061/(ASCE)0733-9429(1985)111:4(625)

Benda, L. (1990). The influence of debris flows on channels and valley floors in the Oregon Coast Range, U.S.A. *Earth Surface Processes and Landforms, 15*(5), 457-466. doi:10.1002/esp.3290150508

Benjankar, R., Tonina, D., & McKean, J. (2015). One-dimensional and two-dimensional hydrodynamic modeling derived flow properties: impacts on aquatic habitat quality predictions. *Earth Surface Processes and Landforms, 40*(3), 340-356. doi:10.1002/esp.3637

Braun, H. (1980). A Simple Method for Testing Goodness of Fit in the Presence of Nuisance Parameters. *Journal of the Royal Statistical Society. Series B (Methodological), 42*(1), 53-63.

Brown, R.A., & Pasternack, G. B. (2012). *Monitoring and assessment of the 2010-2011 gravel/cobble augmentation in the Englebright Dam Reach of the lower Yuba River, CA. Prepared for the U.S. Army Corps of Engineers, Sacramento District.* Retrieved from University of California at Davis, Davis, CA.: http://pasternack.ucdavis.edu/files/5313/7692/9028/EDRreport_20121215_FINAL.pdf

Brown, R. A., & Pasternack, G. B. (2014). Hydrologic and topographic variability modulate channel change in mountain rivers. *Journal of Hydrology, 510*(Supplement C), 551-564. doi:https://doi.org/10.1016/j.jhydrol.2013.12.048

Bunte, K., & Abt, S.R., (2001). Sampling surface and subsurface particle-size distributions in wadable gravel-and cobble-bed streams for analyses in sediment transport, hydraulics, and streambed monitoring. Gen. Tech. Rep. RMRS-GTR-74. Fort Collins,CO: U.S. Department of Agriculture, Forest Service, Rocky Mountain Research Station. 428 p.

Carollo, F.G., & Ferro, V. (2021). Experimental study of boulder concentration effect on flow resistance in gravel bed channels. *Catena*, 205. https://doi.org/10.1016/j.catena.2021.105458.

Cassan, L., Roux, H., & Garambois, P.A. (2017). A Semi-Analytical Model for the Hydraulic Resistance Due to Macro-Roughnesses of Varying Shapes and Densities. *Water, 9*(9), 637.

Chin, A., & Phillips, J. D. (2007). The self-organization of step-pools in mountain streams. *Geomorphology, 83*(3), 346-358. doi:https://doi.org/10.1016/j.geomorph.2006.02.021

Church, M., Hassan, M. A., & Wolcott, J. F. (1998). Stabilizing self-organized structures in gravel-bed stream channels: Field and experimental observations. *Water Resources Research, 34*(11), 3169-3179. doi:10.1029/98wr00484

Comiti, F., Cadol, D., & Wohl, E. (2009). Flow regimes, bed morphology, and flow resistance in self-formed step-pool channels. *Water Resources Research, 45*(4). doi:https://doi.org/10.1029/2008WR007259

Cooper, J. R., Aberle, J., Koll, K., & Tait, S. J. (2013). Influence of relative submergence on spatial variance and form-induced stress of gravel-bed flows. *Water Resources Research, 49*(9), 5765-5777. doi:https://doi.org/10.1002/wrcr.20464

Crowder, D. W., & Diplas, P. (2006). Applying spatial hydraulic principles to quantify stream habitat. *River Research and Applications, 22*(1), 79-89. doi:10.1002/rra.893

David, G. C. L., Wohl, E., Yochum, S. E., & Bledsoe, B. P. (2011). Comparative analysis of bed resistance partitioning inhigh-gradient streams, *Water Resour. Res.*, 47, W07507, doi:10.1029/2010WR009540

Day, T. J., (1976). Preliminary results of flume studies into the armouring of a coarse sediment mixture, Pap. 76-1C, pp. 277-287, Can. Geol. Surv., Ottawa.

Delignette-Muller, M. L., & Dutang, C. (2015). fitdistrplus: An R Package for Fitting Distributions. *2015, 64*(4), 34. doi:10.18637/jss.v064.i04

Eaton, B. C., & Church, M. (2009). Channel stability in bed load–dominated streams with nonerodible banks: Inferences from experiments in a sinuous flume, *J. Geophys. Res*., 114, F01024, doi:10.1029/2007JF000902.

Ely, J. C., Clark, C. D., Spagnolo, M., Hughes, A. L. C., & Stokes, C. R. (2018). Using the size and position of drumlins to understand how they grow, interact and evolve. *Earth Surface Processes and Landforms, 43*(5), 1073-1087. doi:10.1002/esp.4241

Faraway, J., Marsaglia, G., Marsaglia, J., & Baddeley, A., (2019). goftest: Classical Goodness-of-Fit Tests for Univariate Distributions. R package version 1.2-2. https://CRAN.R-project.org/package=goftest

Faustini, J. M., & Jones, J. A. (2003). Influence of large woody debris on channel morphology and dynamics in steep, boulder-rich mountain streams, western Cascades, Oregon. *Geomorphology, 51*(1), 187-205. doi:https://doi.org/10.1016/S0169-555X(02)00336-7

Ferguson, R. (2007). Flow resistance equations for gravel- and boulder-bed streams. *Water Resources Research, 43*(5). doi:10.1029/2006wr005422

Ferguson, R. I., Hardy, R. J., & Hodge, R. A. (2019). Flow resistance and hydraulic geometry in bedrock rivers with multiple roughness length scales. *Earth Surface Processes and Landforms, 44*(12), 2437-2449. doi:10.1002/esp.4673

Ferguson, R. I., Sharma, B. P., Hardy, R. J., Hodge, R. A., & Warburton, J. (2017). Flow resistance and hydraulic geometry in contrasting reaches of a bedrock channel. *Water Resources Research, 53*(3), 2278-2293. doi:10.1002/2016WR020233

Fox, J., & Weisberg, S. (2019). An R Companion to Applied Regression, Third edition. Sage, Thousand Oaks CA. https://socialsciences.mcmaster.ca/jfox/Books/Companion/.

Furbish, D. J. (1987). Conditions for geometric similarity of coarse stream-bed roughness. *Mathematical Geology, 19*(4), 291-307. doi:10.1007/BF00897840

Gomez, B. (1993). Roughness of stable, armored gravel beds. *Water Resources Research, 29*(11), 3631-3642. doi:10.1029/93wr01490

Gonzalez, R. L., & Pasternack, G. B. (2015). Reenvisioning cross-sectional at-a-station hydraulic geometry as spatially explicit hydraulic topography. *Geomorphology, 246*, 394-406. doi:https://doi.org/10.1016/j.geomorph.2015.06.024

Groom, J., & Friedrich, H. (2019). Spatial structure of near-bed flow properties at the grain scale. *Geomorphology, 327*, 14-27. doi:https://doi.org/10.1016/j.geomorph.2018.10.013

Held L., & Bové D. S. (2014). Frequentist Properties of the Likelihood. In: Applied Statistical Inference. Springer, Berlin, Heidelberg. https://doi.org/10.1007/978-3-642-37887-4_4

Hillier, J. K., Kougioumtzoglou, I. A., Stokes, C. R., Smith, M. J., Clark, C. D., & Spagnolo, M. S. (2016). Exploring Explanations of Subglacial Bedform Sizes Using Statistical Models. *PLOS ONE, 11*(7), e0159489. doi:10.1371/journal.pone.0159489

Hodge, R., Brasington, J., & Richards, K. (2009). Analysing laser-scanned digital terrain models of gravel bed surfaces: linking morphology to sediment transport processes and hydraulics. *Sedimentology, 56*(7), 2024-2043. doi:10.1111/j.1365-3091.2009.01068.x

Hodge, R. A., & Hoey, T. B. (2016). A Froude-scaled model of a bedrock-alluvial channel reach: 1. Hydraulics. *Journal of Geophysical Research: Earth Surface, 121*(9), 1578-1596. doi:https://doi.org/10.1002/2015JF003706

Katul, G., Wiberg, P., Albertson, J., & Hornberger, G. (2002). A mixing layer theory for flow resistance in shallow streams. *Water Resources Research, 38*(11), 32-31-32-38. doi:https://doi.org/10.1029/2001WR000817

Kirchner, J. W., Dietrich, W. E., Iseya, F., & Ikeda, H. (1990). The variability of critical shear stress, friction angle, and grain protrusion in water-worked sediments. *Sedimentology, 37*(4), 647-672. doi:10.1111/j.1365-3091.1990.tb00627.x

Kondolf, G. M., Vick, J. C., & Ramirez, T. M. (1996). Salmon Spawning Habitat Rehabilitation on the Merced River, California: An Evaluation of Project Planning and Performance. *Transactions of the American Fisheries Society, 125*(6), 899-912. doi:10.1577/1548-8659(1996)125<0899:SSHROT>2.3.CO;2

Krishnamoorthy, K., Lee, M., & Xiao, W. (2015). Likelihood ratio tests for comparing several gamma distributions. *Environmetrics, 26*(8), 571-583. doi:10.1002/env.2357

Lacey, R. W. J., & Roy, A. G. (2008). The spatial characterization of turbulence around large roughness elements in a gravel-bed river. *Geomorphology, 102*(3), 542-553. doi:https://doi.org/10.1016/j.geomorph.2008.05.045

Lai, Y. G. (2008). *"SRH-2D version 2: Theory and User's Manual Sedimentation and River Hydraulics – Two-Dimensional River Flow Modeling".* Retrieved from U.S. Department of the Interior, Bureau of Reclamation, Technical Service Center, Sedimentation and

River Hydraulics Group. Denver, Colorado.: https://www.usbr.gov/tsc/techreferences/computer%20software/models/srh2d/index.html

Lamb, M. P., & Brun, F. (2017). Direct measurements of lift and drag on shallowly submerged cobbles in steep streams: Implications for flow resistance and sediment transport, *Water Resour. Res.*, 53, 7607–7629, doi:10.1002/2017WR020883.

Langbein, W. B. (1949). Annual floods and the partial-duration flood series. *Eos, Transactions American Geophysical Union, 30*(6), 879-881. doi:https://doi.org/10.1029/TR030i006p00879

Legleiter, C. J., & Harrison, L. R. (2019). Remote Sensing of River Bathymetry: Evaluating a Range of Sensors, Platforms, and Algorithms on the Upper Sacramento River, California, USA. *Water Resources Research, 55*(3), 2142-2169. doi:https://doi.org/10.1029/2018WR023586

Legleiter, C. J., Roberts, D. A., Marcus, W. A., & Fonstad, M. A. (2004). Passive optical remote sensing of river channel morphology and in-stream habitat; physical basis and feasibility. *Remote Sensing of Environment, 93*(4), 493-510. doi:http://dx.doi.org/10.1016/j.rse.2004.07.019

Lisle, T. E., Nelson, J. M., Pitlick, J., Madej, M. A., & Barkett, B. L. (2000). Variability of bed mobility in natural, gravel-bed channels and adjustments to sediment load at local and reach scales. *Water Resources Research, 36*(12), 3743-3755. doi:10.1029/2000wr900238

Millard, S. P. (2014). EnvStats, an R Package for Environmental Statistics *Wiley StatsRef: Statistics Reference Online*.

Monsalve, A., & Yager, E. M. (2017). Bed Surface Adjustments to Spatially Variable Flow in Low Relative Submergence Regimes. *Water Resources Research, 53*(11), 9350-9367. doi:https://doi.org/10.1002/2017WR020845

Moriasi, D. N., Arnold, J. G., Van Liew, M. W., Bingner, R. L., Harmel, R. D., & Veith, T. L. (2007). Model Evaluation Guidelines for Systematic Quantification of Accuracy in Watershed Simulations. *Transactions of the ASABE, 50*(3), 885. doi:https://doi.org/10.13031/2013.23153

Morris, H. (1959). Design methods for flow in rough channels. Proc. ASCE, Journal of Hydraulics Division, 85((HY7)), 43-62.

Nikora, V. I., Goring, D. G., & Biggs, B. J. F. (1998). On gravel-bed roughness characterization. *Water Resources Research, 34*(3), 517-527. doi:10.1029/97wr02886

Nitsche, M., Rickenmann, D., Kirchner, J. W., Turowski, J. M., & Badoux, A. (2012). Macroroughness and variations in reach-averaged flow resistance in steep mountain streams. *Water Resources Research, 48*(12). doi:10.1029/2012WR012091

Nitsche, M., Rickenmann, D., Turowski, J. M., Badoux, A., & Kirchner, J. W. (2011). Evaluation of bedload transport predictions using flow resistance equations to account for macro-roughness in steep mountain streams. *Water Resources Research, 47*(8). doi:10.1029/2011wr010645

Papanicolaou, A. N., & Tsakiris, A. G. (2017). Boulder Effects on Turbulence and Bedload Transport. In D. T. a. J. B. Laronne (Ed.), *Gravel-Bed Rivers*.

Pasternack, G. B. (2011). *2D Modeling and Ecohydraulic Analysis*. Seatle, WA: Createspace.

Pasternack, G. B., Ellis, C. R., Leier, K. A., Vallé, B. L., & Marr, J. D. (2006). Convergent hydraulics at horseshoe steps in bedrock rivers. *Geomorphology, 82*(1), 126-145. doi:https://doi.org/10.1016/j.geomorph.2005.08.022

Pasternack, G. B., Gore, J., Weiner, J. (2021). Geomorphic covariance structure of a confined mountain river reveals landform organization stage threshold. *Earth Surface Processes and Landforms*. https://doi.org/10.1002/esp.5195.

Pastore, M., & Calcagnì, A. (2019). Measuring Distribution Similarities Between Samples: A Distribution-Free Overlapping Index. *Front. Psychol*. 10:1089. doi: 10.3389/fpsyg.2019.01089

Paternoster, R. Brame, R. Mazerolle, P, & Piquero A. (1998). Using the correct statistical test for the equality of regression coefficients. *Criminology, 36*(4), 859-866. doi:https://doi.org/10.1111/j.1745-9125.1998.tb01268.x

Phillips, J. D. (2006). Evolutionary geomorphology: thresholds and nonlinearity in landform response to environmental change, *Hydrol. Earth Syst. Sci.*, 10, 731–742, https://doi.org/10.5194/hess-10-731-2006.

Powell, D. M. (2014). Flow resistance in gravel-bed rivers: Progress in research. *Earth-Science Reviews, 136*, 301-338. doi:https://doi.org/10.1016/j.earscirev.2014.06.001

R Core Team (2021). R: A language and environment for statistical computing. R Foundation for Statistical Computing, Vienna, Austria. URL https://www.R-project.org/.

Radecki-Pawlik, A. (2002). Bankfull discharge in mountain streams: theory and practice. *Earth Surface Processes and Landforms, 27*(2), 115-123. doi:10.1002/esp.259

Reid, D.E., & Hickin, E.J. (2008). Flow resistance in steep mountain streams. *Earth Surface Processes and Landforms*, 33: 2211-2240. https://doi.org/10.1002/esp.1682

Resop, J. P., Kozarek, J. L., & Hession, W. C. (2012). Terrestrial Laser Scanning for Delineating In-stream Boulders and Quantifying Habitat Complexity Measures. *Photogrammetric Engineering and Remote Sensing, 78*(4), 363-371.

Richardson, K., & Carling., P.A. (2006). The hydraulics of a straight bedrock channel: Insights from solute dispersion studies, *Geomorphology*, 82(1–2), 98–125, doi:10.1016/j.geomorph.2005.09.022.

Rickenmann, D., & Recking, A. (2011). Evaluation of flow resistance in gravel-bed rivers through a large field data set. *Water Resources Research, 47*(7). doi:10.1029/2010wr009793

Robert, A. (1990). Boundary roughness in coarse-grained channels. *Progress in Physical Geography: Earth and Environment, 14*(1), 42-70. doi:10.1177/030913339001400103

Rothman, D. H., Grotzinger, J. P., & Flemings, P. (1994). Scaling in turbidite deposition. *Journal of Sedimentary Research, 64*(1a), 59-67. doi:10.1306/d4267d07-2b26-11d7-8648000102c1865d

Sapozhnikov, V. B., & Foufoula-Georgiou, E. (1999). Horizontal and vertical self-organization of braided rivers toward a critical state. *Water Resources Research, 35*(3), 843-851. doi:https://doi.org/10.1029/98WR02744

Schlichting, H. (1936). Experimentelle Untersuchungen zum Rauhigkeitsproblem. *Ingenieur-Archiv, 7*(1), 1-34. doi:10.1007/BF02084166

Schneider, J. M., Rickenmann, D., Turowski, J. M., & Kirchner, J. W. (2015). Self-adjustment of stream bed roughness and flow velocity in a steep mountain channel. *Water Resources Research, 51*(10), 7838-7859. doi:10.1002/2015wr016934

Shamloo, H., Rajaratnam, N., & Katopodis, C. (2001). Hydraulics of simple habitat structures. *Journal of Hydraulic Research, 39*(4), 351-366. doi:10.1080/00221680109499840

Shobe, C. M., Tucker, G. E., & Anderson, R. S. (2016). Hillslope-derived blocks retard river incision. *Geophysical Research Letters, 43*(10), 5070-5078. doi:10.1002/2016gl069262

Singh, A., Guala, M., Lanzoni, S., & Foufoula-Georgiou, E. (2012). Bedform effect on the reorganization of surface and subsurface grain size distribution in gravel bedded channels. *Acta Geophysica, 60*(6), 1607-1638. doi:10.2478/s11600-012-0075-z

Sklar, L. S., Riebe, C. S., Genetti, J., Leclere, S., & Lukens, C. E. (2020). Downvalley fining of hillslope sediment in an alpine catchment: implications for downstream fining of sediment flux in mountain rivers. *Earth Surface Processes and Landforms, 45*(8), 1828-1845. doi:10.1002/esp.4849

Smith, M. W. (2014). Roughness in the Earth Sciences. *Earth-Science Reviews, 136*, 202-225. doi:https://doi.org/10.1016/j.earscirev.2014.05.016

Sornette, D. (2000). *Critical Phenomena in Natural Sciences: Chaos, Fractals, Selforganization and Disorder: Concepts and Tools*.

Strom, M. A., Pasternack, G. B., Burman, S. G., Dahlke, H. E., & Sandoval-Solis, S. (2017). Hydraulic hazard exposure of humans swept away in a whitewater river. *Natural Hazards, 88*(1), 473-502. doi:10.1007/s11069-017-2875-6

Strom, M. A., Pasternack, G. B., & Wyrick, J. R. (2016). Reenvisioning velocity reversal as a diversity of hydraulic patch behaviours. *Hydrological Processes, 30*(13), 2348-2365. doi:10.1002/hyp.10797

Sutfin, N. A., & Wohl, E. (2019). Elevational differences in hydrogeomorphic disturbance regime influence sediment residence times within mountain river corridors. *Nature Communications, 10*(1), 2221. doi:10.1038/s41467-019-09864-w

Tan, L., & Curran, J. C. (2012). Comparison of Turbulent Flows over Clusters of Varying Density. *Journal of Hydraulic Engineering, 138*(12), 1031-1044. doi:doi:10.1061/(ASCE)HY.1943-7900.0000635

Thompson, C. J., Croke, J., Ogden, R., & Wallbrink, P. (2006). A morpho-statistical classification of mountain stream reach types in southeastern Australia. *Geomorphology, 81*(1), 43-65. doi:https://doi.org/10.1016/j.geomorph.2006.03.007

Thompson, S. M., & Campbell, P. L. (1979). Hydraulic of a large channel paved with boulders. *Journal of Hydraulic Research, 17*(4), 341-354. doi:10.1080/00221687909499577

Valle, B. L., & Pasternack, G. B. (2006). Field mapping and digital elevation modelling of submerged and unsubmerged hydraulic jump regions in a bedrock step-pool channel. *Earth Surface Processes and Landforms, 31*(6), 646-664. doi:10.1002/esp.1293

van der Mark, C. F., Blom, A., & Hulscher, S. J. M. H. (2008). Quantification of variability in bedform geometry. *Journal of Geophysical Research: Earth Surface, 113*(F3). doi:10.1029/2007jf000940

Wiener, J. S., & Pasternack, G. B. (2019). Diversity and organization of mountain river morphological units challenge conceptions of riffle-pool, step-pool, and cascade channel types. Abstract EP51E-2129 presented at 2019 Fall Meeting, AGU, San Francisco, CA, 9-13 Dec.

Wiener, J. S., & Pasternack, G. B. (2022). Scale dependent spatial structuring of mountain river large bed elements maximizes flow resistance. Unpublished.

Wittenberg, L., & Newson, M. D. (2005). Particle clusters in gravel-bed rivers: an experimental morphological approach to bed material transport and stability concepts. *Earth Surface Processes and Landforms, 30*(11), 1351-1368. doi:10.1002/esp.1184

Wohl, E., & Merritt, D. M. (2008). Reach-scale channel geometry of mountain streams. *Geomorphology, 93*(3), 168-185. doi:https://doi.org/10.1016/j.geomorph.2007.02.014

Wolman, M. G. (1954). A method of sampling coarse river-bed material. *Eos, Transactions American Geophysical Union, 35*(6), 951-956. doi:https://doi.org/10.1029/TR035i006p00951

Wyrick, J. R., & Pasternack, G. B. (2014). Geospatial organization of fluvial landforms in a gravel–cobble river: Beyond the riffle–pool couplet. Geomorphology, 213(Supplement C), 48-65. doi:https://doi.org/10.1016/j.geomorph.2013.12.040

Yager, E. M., Kirchner, J. W., & Dietrich, W. E. (2007). Calculating bed load transport in steep boulder bed channels. *Water Resources Research, 43*(7). doi:10.1029/2006wr005432

Yuba County Water Agency (YCWA) (2013). *Technncal Memorandum 1-1. Channel Morphology Upstream of Englebright Reservoir. Yuba River Development Project FERC Project No. 2246.* Retrieved from http://www.ycwa-relicensing.com/Technical%20Memoranda/Forms/AllItems.aspx

Yochum, S. E., Bledsoe, B. P., David, G. C. L., & Wohl, E. (2012). Velocity prediction in high-gradient channels. *Journal of Hydrology, 424-425*, 84-98. doi:https://doi.org/10.1016/j.jhydrol.2011.12.031

Yochum, S. E., Bledsoe, B. P., Wohl, E., & David, G. C. L. (2014). Spatial characterization of roughness elements in high-gradient channels of the Fraser Experimental Forest, Colorado, USA, *Water Resour. Res.*, 50, doi:10.1002/2014WR015587.

CHAPTER 3. HYDRO-MORPHOLOGICAL VARIABLE LINKAGES WITH MORPHOLOGICAL UNIT SCALE FLUVIAL LANDFORMS IN A BOULDER-BEDDED MOUNTAIN RIVER

3.1 Abstract

Fluvial landforms at the 1-10 bankfull channel-width scale, termed morphological units (MUs), are considered the building blocks of river systems, reflect distinct formative processes, and are valuable as a basic unit for assessing instream habitat or overall riverine health. To date, only limited treatment exists on MU typologies, governing hydro-morphological (HM) variables, and morphogenesis of spatially explicit MU locations for high gradient, coarse-bedded mountain rivers. This study addressed five scientific questions about mountain river MUs and their HM variables: (i) Do MU types have statistically unique combinations of HM variables? (ii) What HM variables are the strongest statistical discriminators of MU type? (iii) Are MU types located in portions of the river valley with expected assemblages of HM attributes? (iv) Are at-a-station hydraulic geometry variables better at discriminating/predicting MU types better than channel geometry variables? And, (v) what level of MU predictive capability can be achieved with HM variables? The testbed used to answer these questions was the confined 13.2-km segment of the high gradient, coarse-bedded, mountainous Yuba River (northern California). A meter-resolution, topo-bathymetric digital terrain model was produced from green and near-infrared airborne lidar, echo sounding, and limited depth-from-color estimation. Employing a standard method involving meter-scale 2D hydrodynamic modeling and a baseflow hydraulics decision tree, nine spatially explicit baseflow in-channel MU types were mapped. MU types included three pool unit types, alluvial step, steep plane bed (i.e. a passable riffle analog), and several transitional unit types.

Meanwhile, a set of 15 HM variables representing an array of possible hydraulic and geomorphic controls on MU occurrence were measured at river cross-sections where a single MU type was found to dominate. Selected HM variables included common (channel-bed slope; width-to-depth ratios) and novel (bankfull cross-section geometry index; baseflow-to-valley width ratio) ones. Combinations of multi-variate statistical analysis and heuristic assessment confirmed MU types had distinct HM variable assemblages and were located in portions of the river valley with expected assemblages of HM attributes based on scientific literature for each HM variable. Pairwise statistical analysis and a Random Forest machine learning algorithm determined baseflow width, baseflow-to-valley width ratio, bankfull width-to-depth ratio, and baseflow water surface slope had the greatest power to discriminate MU types and predict MU occurrence. The most parsimonious Random Forest model with ten HM variables as predictors achieved a median accuracy over 80% on 1000 sets of independent resampled MU test datasets. Taken together, study results provide a depth of geomorphic interpretation on local topographic controls and morphodynamic processes involved in MU formation as well as how HM variables exert fluvial control.

3.2 Introduction

Classification and mapping of riverine landforms at the 1–10 average bankfull channel widths ($\overline{W_{Bf}}$) or 'morphological unit' scale provides multifaceted benefits and is of broad interest to the river science community (Hawkins et al., 1993; Bisson et al., 2006; Belletti et al., 2017). While several terms exist describing this scale of fluvial landform (e.g. Wyrick et al., 2014; Wheaton et al., 2015), morphological unit (MU) is the preferred term for this study. Baseflow channel MUs (used interchangeably with MU herein) are defined following Wyrick et al. (2014) as discernible riverine landforms revealed by the combination of underlying topographic form and

hydraulics generated as water moves through the channel. MUs are considered the geomorphic building blocks of river systems reflecting distinct local form–process associations (Brierley & Fryirs, 2005; Belletti et al., 2017) and their study can aid in understanding relationships between river channel form and process (Lane & Richards, 1996; Wyrick & Pasternack, 2014).

The peer-reviewed scientific literature ('literature') contains a plethora of methods to classify and map MUs ranging from early efforts employing field-based, visual assessment of baseflow topographic and hydraulic indicators (Grant et al., 1990; Halwas & Church, 2002), to modern algorithmic, multi-dimensional approaches for automated MU mapping using variables derived from sources such as field measurements, remotely sensed meter-to-sub-meter scale digital terrain models (DTMs) and aerial imagery, and/or two-dimensional (2D) hydrodynamic model outputs (Wheaton et al., 2015; Mahdade et al., 2020; van Rooijen et al., 2021; Woodworth & Pasternack, 2022). A constant across all methods is the use of pre-specified hydro-morphological (HM) variables representing the size, shape, sedimentology, roughness, topography, optical properties, and/or hydraulics of the river corridor in a decision framework that classifies MU types and can be used to delineate MU polygons. Broadly, decision frameworks can be supervised (top-down) or unsupervised (bottom-up). Supervised frameworks involve pre-determined types of MUs with set or well-defined HM variable criteria (Wyrick et al., 2014; Wheaton et al., 2015). Variables and criteria in supervised frameworks often derive from conceptual models of MU form and function, which can be iteratively adjusted to reflect localized knowledge and landform diversity (Brierly et al., 2013). Unsupervised frameworks on the other hand are purely statistical and make no a priori assumption on the set of MUs. While unsupervised MU classification emerges from data-driven, bottom-up analysis of HM variable statistical similarity (dissimilarity) and/or clustering, heuristic decision making is typically required to define and describe the final number

of MU types (Helm et al., 2020; van Rooijen et al., 2021). Unsupervised approaches can also miss important but rare MU types (Wyrick et al., 2014).

Once mapped, MU spatial configurations can be analyzed to address fundamental landform questions (Grant et al., 1990; Wyrick & Pasternack, 2014; Kasprak et al., 2016; Woodworth & Pasternack, 2022). If both MU locations and independent HM variables measured at MU locations are available, bottom-up statistical analysis can be used to determine if MUs occur in riverscape settings with specific HM variable assemblages (Peterson & Rabeni, 2001; Wyrick & Pasternack, 2014; Lane et al., 2022). Building on the concept that MUs reflect distinct form-process associations, where HM variables have direct or inferential physical linkages to morphogenetic processes known to control MU formation and/or persistence (Caamaño et al., 2009; Thompson, 2012; Brown et al., 2016; Pasternack et al., 2018a), such variables can be used to test and compare the influence of such processes on channel morphology when provided with an independent set of landform locations (Montgomery et al., 1995; White et al., 2010; Thompson & Fixler, 2017; Pasternack et al., 2018b; Byrne et al., 2021). Development of MU process-morphology linkages with HM variables is often confounded by issues like process-blending (e.g. MU morphogenesis involving multiple processes or the same process operating at different spatial scales through a range of flow conditions), equifinality, complementary and/or conflicting influences between HM variables, uncertain or incomplete MU process-morphology understanding, and covariation amongst HM variables (e.g. Pasternack et al., 2018a; Palucis et al., 2017).

Nonetheless, HM variables with even tenuous MU process-morphology connections that serve as strong MU discriminators are relevant toward understanding factors influencing the geomorphic structure and organization of riverscapes. For example, extracting a variety of HM variables, Golly et al. (2019) derived a set of diagnostic morphological parameters to test several

models of step-formation against field observations of step morphology in a steep mountain stream. The quintessential work of Grant et al. (1990) similarly used MU-HM variable statistical relationships to provide insight into the morphogenesis of mountain river 'channel units'. Wyrick and Pasternack (2014) also found a diverse suite of MUs in a gravel-cobble river to be distinguished by HM variables suggesting some degree of deterministic control on MU locations.

While methods for MU classification and mapping are important (e.g. Wheaton et al., 2015), they have been addressed in many more publications compared to the topic of bottom-up MU-HM variable analysis, especially in high-gradient (≥1.5% channel slope), coarse-bedded (D_{50} ≥ 5 mm, where D is grain-size diameter and the subscript is percent of grains finer) natural rivers. Further, when performed, bottom-up MU-HM variable analysis has often been limited to a few HM variables, such as channel-bed slope and grain-size distribution (GSD) metrics (e.g. D_{50}, D_{84}) (Grant et al., 1990; Halwas & Church, 2002). These same variables are ubiquitous in many classification methods, thus introducing potential spurious outcomes if used in the classification process itself (Grant et al., 1990; Halwas & Church, 2002; Helm et al., 2020). Channel-bed slope and GSD metrics are linked to geomorphic processes via their relationship with sediment transport competence (Kasprak et al., 2016), but generally lack well-defined direct or inferential MU process-morphology links as to why they would control occurrence of certain MUs versus others (Golly et al., 2019). Channel-bed slope has also been posited to serve as only a rough indicator of MU occurrence (Montgomery et al., 1995), and distinct GSD metrics between MU types have been found to develop more as a response to MU formation rather than as a casual mechanism (Thompson & Fixler, 2017; Hassan et al., 2021). Such limitations highlight the need to study other HM variables in the context to which they control MU occurrence.

3.2.1 Scientific questions

Thus, this study sought fundamental insights into the relations among MU types and HM variables by answering five novel scientific questions. (i) Do MU types have statistically unique combinations of HM variables? (ii) What HM variables are the strongest statistical discriminators of MU type? (iii) Are MU types located in portions of the river valley with expected assemblages of HM attributes based on linkages between HM variables and process-based mechanisms that preferentially support and maintain certain MU assemblages? (iv) Are at-a-station hydraulic geometry (AHG) variables better at discriminating/predicting MU types better than channel geometry variables? And (v) what level of MU predictive capability can be achieved with HM variables, and what is the most parsimonious combination of HM variables for predicting MU types?

This study is novel in several regards. The steep, boulder-bedded canyon study segment presents a challenging setting for MU mapping and prediction, yet a unique, highly detailed dataset was obtained. The set of HM variables considered is broader than those from previous bottom-up studies. It includes variables that were expected to be predictive of MU occurrence based on past literature, and novel variables representing an array of possible hydraulic and geomorphic controls on MU formation and/or maintenance that have not been investigated before. Findings from addressing these questions are relevant for advancing basic understanding of fluvial landforms. They are also valuable for guiding river management and restoration activities, which often have the goal of creating specific MU configurations (Thompson, 2012; Helm et al., 2020).

In the next sub-section we begin by reviewing generalized MU types for coarse bedded rivers and list selected HM variables and the expectation of these variables for the generalized MU types. HM variables were drawn from previous studies documenting empirical discriminatory

properties and/or descriptive process-morphology linkages between MUs and HM variables. In this manner, we hypothesize that MU types will have unique combinations of HM variables on the basis of multi-variate statistical analysis. Similarly, on the basis that HM variable expectations for each MU are based on review of the literature (APPENDIX 3) we hypothesize that a combination of statistical and heuristic assessment will confirm MU types are located in portions of the river valley with expected assemblages of HM attributes.

3.2.2 Generalized MU types, selected hydro-morphological variables, and MU expectations for coarse-bedded rivers

A diversity of named in-channel MU types have been described for coarse-bedded rivers (Bisson et al., 1982; Grant et al., 1990; Hawkins et al., 1993; Church & Zimmermann, 2007; Wheaton et al., 2015). Despite differences in definitions and classification methods, commonalities allow simplification of MU types into five end-member groups based on relative combinations of collocated, low flow water depth and water speed (velocity) (Figure 3.1; APPENDIX 3). Pools, riffles, and steps are by far the most commonly referenced MUs in the literature, and are often defined using characteristics beyond low flow depth and water speed (Wheaton et al., 2015). The other two end-members contain less common MU types that function as transitional units between pools and riffles/steps.

Beyond MUs, river corridors are characterized by a suite of continuous hydraulic, geometric, sedimentological, and topographic conditions that can be measured at multiple spatial scales (Nardini et al., 2020). Once specific metrics and a spatial-scale of interest are defined, these hydro-morphological conditions form the basis to measure HM variables. MUs on the other hand occupy the river corridor at discrete, stage independent locations, and thus can be viewed as a discrete categorical variable. Once mapped, MUs can define the spatial scale to measure HM

variables, thereby reducing continuous riverscape conditions to discrete measurements that can provide multi-variate data detailing HM variable conditions at each MU type.

A total of 18 HM variables were considered and organized into the following 6 groups: channel-size variables, channel-shape variables, channel-obstruction/roughness variables, gradient variables, longitudinal change variables, and AHG exponent variables (Table 3.1. Summary of selected hydro-morphological (HM) variables.). Selected variables were those most relevant to MU types and morphogenetic processes occurring in coarse-bedded mountain rivers, those easy to obtain using basic survey methods or derive from digital terrain models (e.g. Golly et al., 2019), and were influenced by data available in a testbed river study segment (section 3.3). A comprehensive literature review of the selected HM variables including process-morphology linkages and relative expectations for the generalized set of MU types for each variable is provided in APPENDIX 3.

Hypothesized and testable expectations for each variable for the generalized set of MU types were developed from the literature (Table 3.2. Hypothesized hydro-morphological (HM) variable expectations for generalized morphological unit (MU) types[†].; APPENDIX 3). Several of the considered variables are stage dependent, and some variables are calculated at multiple stages (i.e. wetted width). This served two purposes. First, MU formation and attributes of low flow channel morphology are predominately driven by processes active during high flows (Grant et al., 1990; Wyrick & Pasternack, 2014; Thompson, 2018), thus inclusion of variables calculated at low flow often have potential to be good discriminators of MU type (Wyrick & Pasternack, 2014; Helm et al., 2020). Second, there is uncertainty regarding the stage at which morphogenetic processes are active and/or dominant in shaping channel morphology (Sawyer et al., 2010; Pasternack et al., 2018b, Thompson, 2018, Pasternack et al., 2021). In alluvial rivers, bankfull stage is regularly

viewed as determining channel geometry (Leopold & Wolman, 1957; Dunne & Jerolmack, 2020) and cited as the stage at which HM variables are determined (Wyrick et al., 2014; Helm et al., 2020). However, in mountain rivers, discharges necessary for shaping topographic structure, performing landform maintenance, and/or reorganizing bedforms or boulders may be significantly higher than bankfull (Turowski et al., 2013; Pasternack et al., 2021; Polvi, 2021). Thus, several HM variables are calculated at multiple stages including a representative baseflow stage, which corresponds to flows whose hydraulics reveal overlying landforms, a representative banfkull stage, which can be determined statistically or morphologically (Williams, 1978), and a representative formative stage corresponding to a stage known to maintain landforms or perform geomorphic work (Sawyer et al, 2010; Pasternack et al., 2021). In certain settings, such as low gradient alluvial rivers, bankfull and formative stages may be the same.

Taking these factors into consideration, each variable was identified a priori as being primarily for MU prediction or having stronger process-morphological linkages (Table 3.1. Summary of selected hydro-morphological (HM) variables.). High flow variables with process-linkages were viewed to serve as controls on MU occurrence. Alternately, because baseflow prediction variables describe MU morphology after formation, they are viewed as responses to formative processes, and more controlled by MU occurrence. Variables calculated at multiple stages but having the same expectations reflect uncertainty regarding the discharge at which a linked process may be active and the associated expectations would be relevant (Table 3.2. Hypothesized hydro-morphological (HM) variable expectations for generalized morphological unit (MU) types[†].). Potential correlation between HM variables is acknowledged, but was not viewed as reason to remove variables from consideration.

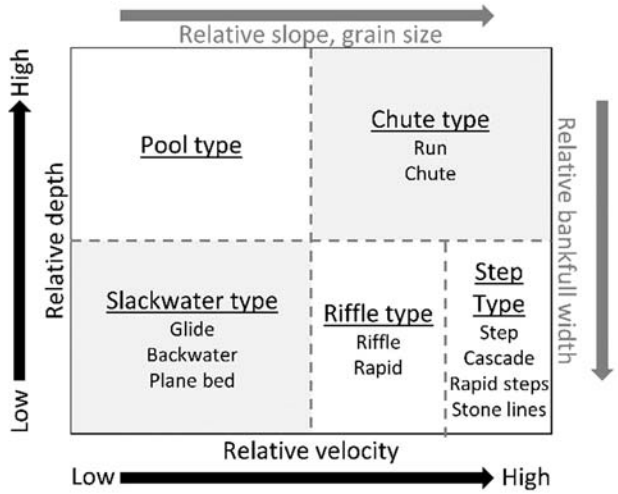

Figure 3.1. Generalized in-channel morphological unit (MU) end-members are dichotomized based on the primary axes of relative low flow depth and relative velocity shown in black. Alternative variables used to dichotomize these MU types are shown on the secondary axis in gray. Main end-members are underlined with units common to these end-members listed below. Not all MU end-members may be present across all river styles. Note that the horizontal and vertical dashed lines shown need be a constant value nor span the full range of the variable; dashed line could be rectangular step functions, sloped lines, or curves.

Table 3.1. Summary of selected hydro-morphological (HM) variables.

HM variable	Primary study purpose	Rationale/Process-morphology linkage	References
Channel-size variables			
Baseflow wetted width (W_{Bs}) (m)	MU prediction	Flow convergence routing[†]	Halwas & Church, 2002; Wyrick & Pasternack, 2014; Brown et al., 2016; Pasternack et al., 2018a; Golly et al., 2019
Formative wetted width (W_F) (m)	Process linkage	Jammed-state step formation; flow convergence routing[†]	
$Q_{13.7}$ wetted width ($W_{13.7}$) (m)			
Channel-shape variables			
Bankfull width-to-depth (W/h_{Bf}) (m/m)	Process linkage	Bar instability; bar formation	Florsheim, 1985; Furbish, 1998; Wilkinson et al., 2008; Wyrick & Pasternack, 2014; Carbonari et al., 2020
Formative width-to-depth (W/h_F) (m/m)	Process linkage		
Baseflow-to-valley width (W_{BS}/W_V) (m/m)	Process linkage	Hillslope sediment (dis)connectivity; entrenchment/confinement; flow convergence routing; jammed-state step formation; keystone step formation;	Wolman & Eiler, 1958; Whiting & Bradley, 1993; Grant & Swanson, 1995; White et al., 2010; Pasternack et al., 2018a; Golly et al., 2019
Bankfull cross-section geometry index (Θ) (-)	Process linkage	Flow convergence routing; flow resistance; channel stability; transport competence	Richards, 1976a; Dingman, 2007; White et al., 2010; Gonzalez & Pasternack, 2015; Pasternack et al., 2018a
Channel-obstruction/roughness variables			
Bankfull LBE concentration (Γ_{Bf}) (m^2/m^2)	Process linkage	Jammed-state step formation; keystone step formation; flow resistance; topographic steering; bar instability	Buffington et al., 2002; Church & Zimmermann, 2007; Harrison & Keller, 2007; Chartrand et al., 2011; Golly et al., 2019
Formative LBE concentration (Γ_F) (m^2/m^2)	Process linkage		
Gradient variables			
Baseflow bed-slope (S_{Bs}) (m/m)	MU prediction	Transport competence[‡]; flow resistance; topographic hydraulic effects (backwater)	Richards, 1976ab; Grant et al., 1990; Halwas & Church, 2002; Wyrick & Pasternack, 2014

HM variable	Primary study purpose	Rationale/Process-morphology linkage	References
Baseflow water surface slope (WSS_{Bs}) (m/m)	MU prediction	Flow resistance; topographic hydraulic effects (backwater)	Richards, 1976ab; Grant et al., 1990; Halwas & Church, 2002; Wyrick & Pasternack, 2014
$Q_{13.7}$ water surface slope ($WSS_{13.7}$) (m/m)	Process linkage	Transport competence	
Longitudinal change variables[§]			
Baseflow wetted width change (ΔW_{Bs}) (m/m)	MU prediction	Topographic hydraulic effects (backwater); flow convergence routing[†]	Grant et al., 1990; Pasternack et al., 2018a; Golly et al., 2019; Saletti & Hassan, 2020; Wang et al., 2021
Formative wetted width change (ΔW_F) (m/m)	Process linkage	Jammed-state step formation; keystone step formation; flow convergence routing	
Formative shear stress change ($\Delta\tau_F$) ($n \cdot m^{-2}/m$)	Process linkage	Keystone step formation; flow convergence routing	
At-a-station hydraulic geometry exponent variables[¶]			
Width exponent (*b*) (-)	Process linkage	Flow convergence routing; flow resistance; channel stability; transport competence	Richards, 1976a; White et al., 2010; Gonzalez & Pasternack, 2015; Pasternack et al., 2018a
Depth exponent (*f*) (-)	Process linkage		
Velocity exponent (*m*) (-)	Process linkage		

[†]Flow convergence routing process-morphology linkage is a dual-stage mechanism primary driven by conditions at higher flows (e.g. formative discharge).

[‡]Process-linkage based on correlation between S_{Bs} and WSS at higher flow stages.

[§]Change determined upstream of MU over distance of 2 times average bankfull width.

[¶]Based on hydraulics from baseflow-to-valley filling flood stage.

Table 3.2. Hypothesized hydro-morphological (HM) variable expectations for generalized morphological unit (MU) types[†].

Generalized MU	*Channel-size variables*			*Channel-shape variables*				*Channel-obstruction/roughness variables*	
	W_{Bs}	W_F	$W_{13.7}$	W/h_{Bf}	W/h_F	W_{Bs}/W_V	θ_3	Γ_{Bf}	Γ_F
Step-type	L	L[‡]	L[‡]	H	H	L	unconfined U-to-convex shaped	H	H
Riffle-type	L	H	H	H	H	L		H	H
Pool-type	H	L	L	L	L	H	confined U-shaped	L	L
Chute-type	L	L-I	L-I	L-I	L-I	L	confined U-to-rectangular shaped	L-I	L-I
Slackwater-type	I	I-H	I-H	I-H	I-H	I	V-to-rectangular shaped	I-H	I-H

Generalized MU	*Gradient variables*			*Longitudinal change variables*			*At-a-station hydraulic geometry exponent variables*		
	S_{Bs}	WSS_{Bs}	WSS_F	ΔW_{Bs}	ΔW_F	$\Delta\tau_F$	*b*	*f*	*m*
Step-type	H	H	Reduced differences in medians between units compared to WSS_{Bs}	Negative	Negative[‡]	Positive[‡]	H	H	L
Riffle-type	H	H		Negative	Positive	Negative	H	H	L
Pool-type	L	L		Positive	Negative	Positive	L	L	H
Chute-type	I-H	I-H		Near-zero	Near-zero	Near-zero	L-I	I	I-H
Slackwater-type	I	I		Near-zero	Near-zero	Near-zero	I	I-H	I

[†]Expectations defined and colored along fuzzy gradient: low (L), intermediate (I), and high (H); or as otherwise noted. Grey-scale color gradient goes from light-to-dark along low-to-high gradient. MU-HM variable pairs with multiple expectations, such as L-I or I-H, reflect higher uncertainty and potential for variable to span a wider range of values.

[‡]Dominant expectation listed but values at step units expected to be bimodal to represent both jammed-state (low W_F and $W_{13.7}$, negative ΔW_F, and positive $\Delta\tau_F$) and keystone (high W_F and $W_{13.7}$, positive ΔW_F, and negative $\Delta\tau_F$) formation models.

3.3 Study river segment

A 13.2-km segment of the mountainous Yuba River (Northern California) draining 1853 km^2 of the western Sierra Nevada range was used as the study testbed (Figure 3.2). The study segment is comprised of a low sinuosity, boulder-bedded, 5th order mountain river confined within a steep-walled bedrock and forested hillside canyon. The river here has a mean bed slope of 1.98% but exhibits localized variability with many 10 – 100 m long (10^0 – 10^1 channel widths) stretches having slopes exceeding 10%. The Yuba River watershed has an extensive history of human modification including hydraulic gold mining, land-use change, flow regulation and diversion, and channelization (YCWA, 2013). Presently, water resources in the vicinity of the study area are heavily regulated for flood protection, power generation, and water management. Detailed Yuba catchment hydrologic information is readily available (YCWA, 2012; Wiener & Pasternack, 2016).

The regions alluvial-sediment processes are also affected by anthropogenic influences. New Bullards Bar Dam, a 196.6 m high concrete arch dam on the North Yuba River near Dobbins, CA, serves as a complete barrier to bedload transport conveying only limited wash load. Log Cabin Dam and Our House Dam, both situated upstream of the study segment in the Middle Yuba watershed (Figure 3.2), also act as significant barriers to sediment transport (Curtis et al. 2005; YCWA, 2013). Sediment discontinuity has resulted in winnowing of finer sized materials in the study segment (YCWA, 2013). Based on limited sedimentological data, bed substrates alternate between bedrock and alluvial sections with estimates of larger boulders (> 512 mm) or bedrock covering over 60% of the channel (YCWA, 2013). Sediment storage capacity contrasts between sections, with bedrock sections lacking large storage capacity and the limited alluvium present commonly being restricted to deep pools, zones of low velocity, along intermittent bars, zones of

recirculating flow, or at major tributary junctions, meander bends, or other areas of local valley widening (Curtis et al., 2005; James, 2005). Where present, alluvial substrate is a heterogeneous mixture of materials dominated by coarse fractions (medium gravel/cobbles and larger). The presence of large boulders and the heterogeneity of sizes makes manual grain-size quantification difficult and labor intensive, if attempted. That said, Wolman (1954) pebble counts by YCWA (2013) within very limited portions of the study segment found average D_{50} values of 193 and 106 mm in the upstream and downstream most portions of the site, respectively, and a D_{84} value of 512 mm in both portions of the site.

Like many bedrock-confined rivers, the study segment lacks a contiguous floodplain. Hydrodynamic modeling (section 3.4.1) found the limited number of alluvial surfaces (e.g. bars) to become inundated over a range of discharges. This non-uniformity corroborates evidence that bankfull discharge in mountain rivers be thought of as a range of recurring discharges (Radecki-Pawlik, 2002). Despite this ambiguity, it remains helpful for dimensional and comparative purposes to identify a single bankfull flow and a previously reported morphologically determined bankfull discharge of 10.73 m^3/s (YCWA, 2013) was used for this purpose.

Previous geomorphological assessments to understand study segment morphology and hydro-morphodynamic controls have been conducted by Wiener and Pasternack (2019), Pasternack et al. (2021), and Wiener and Pasternack (2022). Based on reach averaged bed-slope, median grain size (D_{50}), W/h_{Bf}, and bankull relative roughness (h/D_{50}) reported by Wiener and Pasternack (2019) and YCWA (2013), the upstream most ~3.5 km of the study segment most closely aligns with Montgomery and Buffington's (1997) proposed 'step-pool' channel morphology, whereas the downstream most ~0.7 km would be classified 'pool-riffle' and the remainder of the segment would be considered 'plane-bed' (Buffington & Montgomery, 2013).

Geomorphic covariance structure (GCS) analysis of width and bed undulations by Pasternack et al. (2021) revealed a threshold stage of ~161 m^3/s above which study segment topographic structure was consistent with flow convergence routing morphodynamics. While this conceptually provides a mechanism for freely self-maintaining GCS landform organization, the authors found long intervals of the study segment where flow convergence routing was not active and landform organization was likely driven by other processes. Notably, landforms in their study, which were based on classification of detrended standardized bed elevations and estimates of standardized width, differ from the MUs that are the focus of this study.

Through mapping study segment macroroughness elements, Wiener and Pasternack (2022) identified complex multi-scalar roughness element organizational patterns often corresponding with Morris's (1959) wake interference regime that theoretically maximizes flow resistance for the channel. They also found roughness element concentrations located along channel margins continuously increased outside the baseflow and representative bankfull channels.

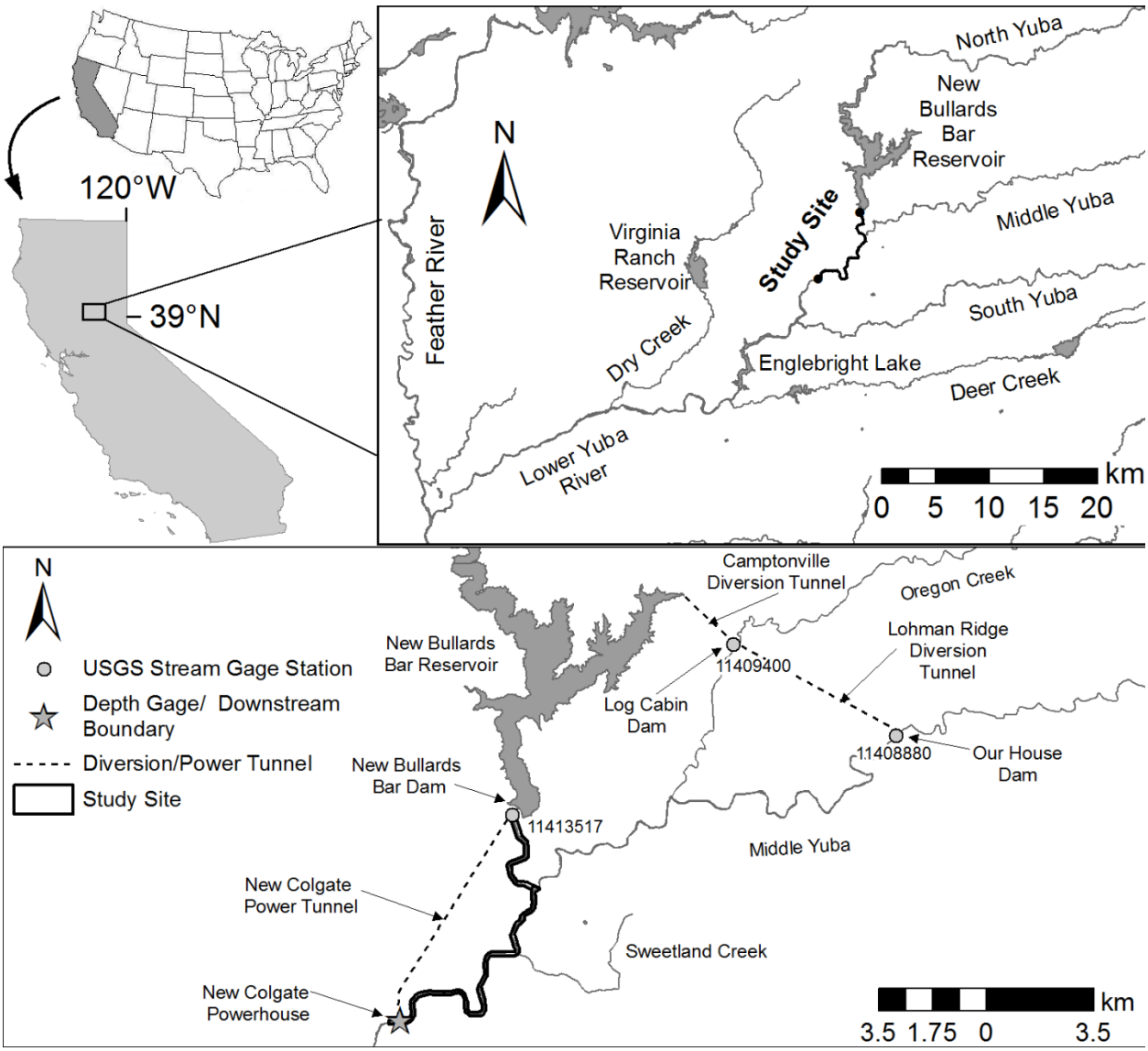

Figure 3.2. Map of study segment, tributaries, gages, and infrastructure facilities, Yuba River, CA.

3.4 Methods

3.4.1 Experimental design and data generation

The study's questions and hypotheses were answered in order using a rigorous but transparent experimental design (Figure 3.3). To answer the first question of whether MU types have unique combinations of HM variables, the top-down, supervised hydraulic method of Wyrick et al. (2014) was used to classify and map MUs within the study segment. Next, 15 of the 18 HM

variables were selected and measured at river cross-sections where a single MU type was found to dominate. The set of 15 HM variables did not include the three AHG variables based on potential for spurious correlation with the Wyrick et al. (2014) MU classification and mapping scheme (see section 3.4.3). A suite of statistical approaches were then used to test if MU types had unique combinations of HM variables (section 3.4.2.1), to evaluate the discriminatory power of individual HM variables (section 3.4.2.2), and test if MU types occurred in locations with expected HM variable attributes (section 3.4.2.3). Despite potential correlation, discriminatory ability of AHG variables were also evaluated and compared to other HM variables (section 3.4.3). Lastly, a machine learning algorithm (Random Forest) was used to develop and test models for MU occurrence prediction based on HM variables (section 3.4.4). Summaries of data sources, MU delineation, and HM variable calculations are provided below with extensive details in APPENDIX 3.

The first data source needed for MU classification and mapping, and determining HM variables was a topographic map. A 0.46 m x 0.46 m resolution DTM raster was created from airborne light detection and ranging (lidar) data, boat-based bathymetric observations, imagery-derived bathymetric estimates (e.g. Legleiter et al., 2004), and systematically placed augmented points (Valle & Pasternack, 2006) that together had an average density of ~ 16 pts/m^2. Next, steady-state hydrodynamics were simulated at ~ 1-m resolution using the Sedimentation and River Hydraulics—Two - Dimensional model (SRH - 2D) v. 2.2 (Lai, 2008). Simulations were run for four geomorphically or otherwise relevant discharges (1.54, 10.73, 161.0, and 1184.6 m^3/s) from an approximate baseflow to an ~13.7-yr flood (Table 3.3). Overall, the 2D model met relevant modeling standards and performed comparably to similar models from published articles (e.g. Lisle et al., 2000; Pasternack et al., 2006).

Using these data sources, MUs were delineated using the hydraulics - based landform classification method of Wyrick et al. (2014) (see also Wyrick & Pasternack, 2014; Woodworth & Pasternack, 2022). First, a supervised classification approach (i.e. decision tree) discriminated the river's bivariate baseflow depth-velocity phase-space into a set number of MUs with discrete bivariate ranges. Second, the phase-space classification was applied to 2D model depth and velocity rasters to classify each cell, which were agglomerated into contiguous MU patches. Final hydraulic thresholds delineated nine baseflow channel MU types covering the entire extent of the river's baseflow wetted area (Figure 3.4). This set of MU polygons were analyzed in the context of their abundance (counts and areal coverage), lateral diversity, adjacency probabilities, and longitudinal spacing using the methods of Wyrick and Pasternack (2014). These analyses were not specific to addressing study questions, but are useful for documenting MU organization and spatial patterns, which has value toward advancing understanding of mountain river fluvial morphology.

Because HM variables were designed to be measured at river cross-sections, the box counting procedure of Wyrick and Pasternack (2012) was used to generate a series of longitudinally abutting 3-m wide, baseflow cross-sectional polygons ('cross-sections') stationed along the river corridor. Baseflow cross-sections were assigned to a specific 'dominant' MU if at least 50% of a cross-sectional polygons area was occupied by a single MU types polygons. Cross-sections without a dominant MU were labeled as 'mixed'. Of the 4236 baseflow cross-sections, 2539 were found to be dominated by a single MU type (Table 3.4).

Lastly, values for 15 selected HM variables were determined directly at or numerically related to the same set of 4236 baseflow cross-sectional polygons used when defining dominant MUs (Table 3.5). While most HM variable calculations followed previous methods (Table 3.5), Θ_3 calculations were somewhat novel and warrant brief description. Θ3 values were derived by

fitting rescaled cross-sectional elevations (z_n) and cross-stream distances (x_n) determined at bankfull cross-sections with a power function of the form:

$$z_n = \theta_1(|x_n - \theta_2|)^{\theta_3} \quad \text{(EQ. 5)}$$

where $\{\Theta_i\}$ are three fitting parameters. The function is symmetrical about Θ_2, and can take on various shapes depending on combinations of Θ_1 and Θ_3 (Figure 3.5). The Θ_3 parameter primary determines the shape of the cross-section. For Θ_3=1, the equation produced a perfect V-shaped section. As Θ_3 increases above unity sections become increasingly concave-up (U-shaped) approaching a rectangular cross-section as Θ_3 goes to infinity, whereas for Θ_3 less than unity sections are convex. Despite its flexibility, Eq.5 only produces smooth, symmetric cross-section shapes. In this manner, cross-section models are unable to account for in-channel topographic variability associated with roughness features, bedforms, and channel asymmetries. The function may also have difficulty fitting multi-thread channels. Detailed calculation methods for all HM variable are described in APPENDIX 3.

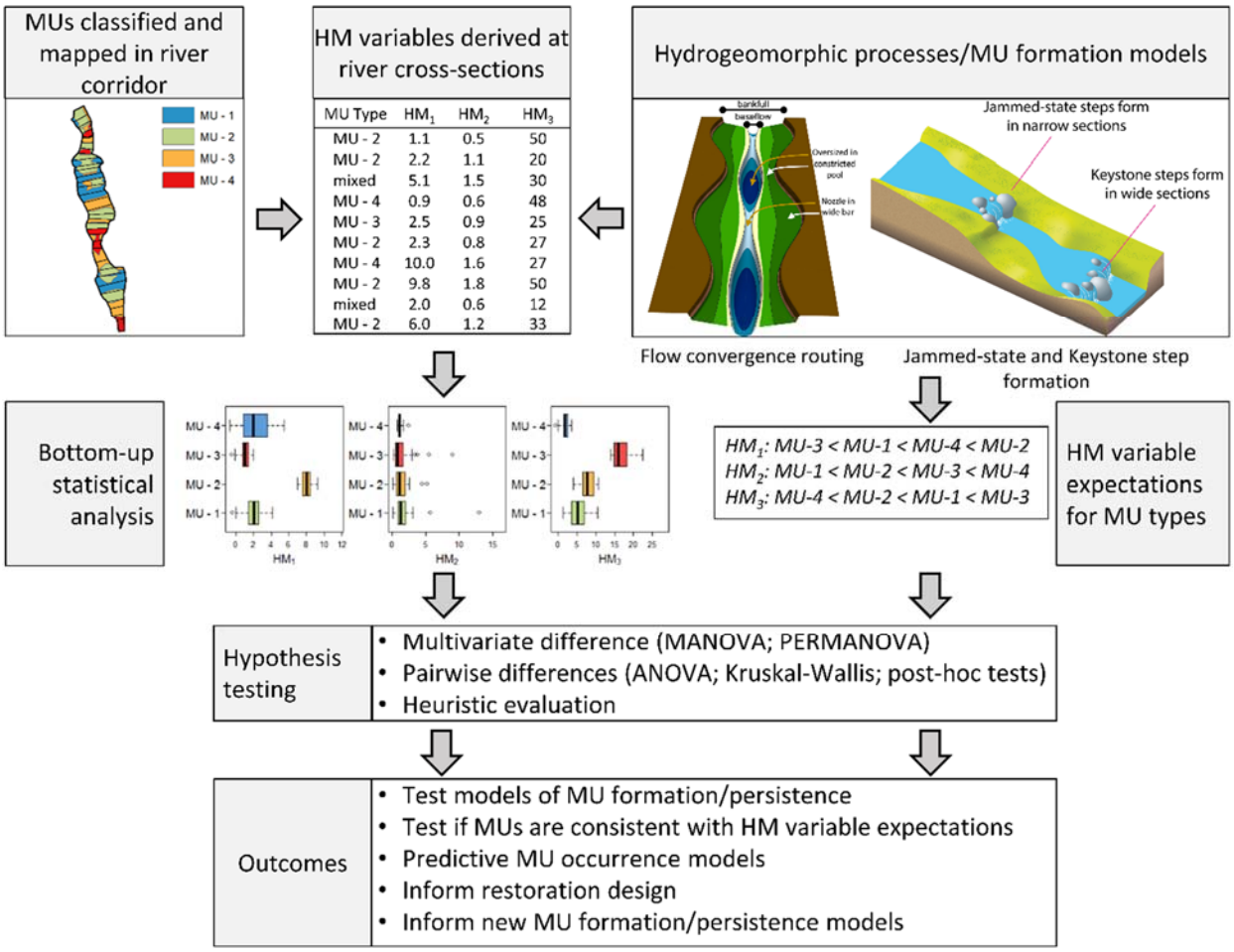

Figure 3.3. Conceptual experimental design. First 2D morphological units (MUs) are classified and mapped across the baseflow river corridor. Next hydro-morphological (HM) variables are extracted from the river corridor at cross-sections where individual MU types are found to dominate. Selected HM variables can include those with potential predictive capability of where MU types are likely to occur and/or process-morphology linkages with hydrogeomorphic processes and/or models associated with MU formation and/or persistence. Bottom-up statistical analysis is used to answer questions, test hypothesized HM variable expectations for classified MU types, and inform other outcomes. The hydrogeomorphic process of flow convergence routing and jammed-state and keystone step formation models are depicted as they have direct or inferential links to HM variables and strong associations with the formation of specific MUs. They are represented using graphical illustrations from Pasternack et al. (2018b) and Golly et al. (2019), respectively.

Table 3.3. Simulated discharges.

Simulated discharge (m^3/s)	Approximate annual recurrence interval (years)	Description
1.54	1	Representative baseflow taken as average of unimpaired daily dry season (July 1 - September 30) flows at downstream boundary from 1930-2015. Used for morphological unit delineation.
10.73	1.06	YCWA (2013) morphologically estimated bankfull flow.
161.0	2.37	Flow above which study segment was found to be freely self-maintaining via flow convergence routing morphodynamics and used herein as the 'formative' discharge (Pasternack et al., 2021).
1184.6	13.7	Maximum simulated flow based on boundary conditions collected for January 9, 2017 flood event. Used herein as the '$Q_{13.7}$' discharge.

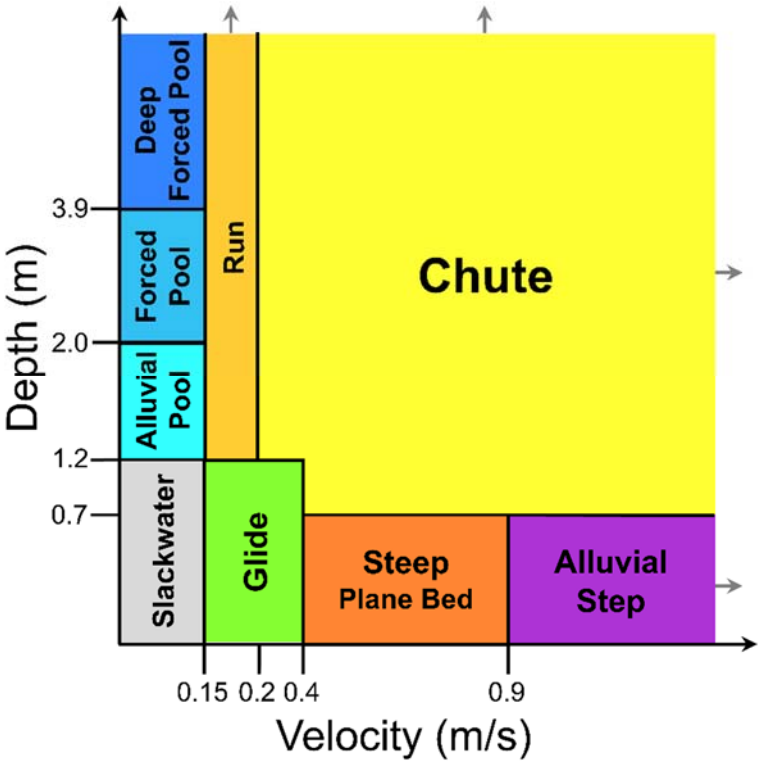

Figure 3.4. Phase-space plot of depth and velocity thresholds showing morphologic unit hydraulic domains.

Table 3.4. Cross-sections dominated by a single morphological unit (MU) type.

MU Type	Number of cross-sections
Alluvial Pool	87
Forced Pool	389
Deep Forced Pool	34
Slackwater	1360
Glide	207
Run	11
Steep Plane Bed	365
Alluvial Step	49
Chute	37
Sub-total	2539
Mixed	1697
Total	4236

Table 3.5. Summary of hydro-morphological (HM) variable calculations including data sources and reference for calculation method.

HM variable	Data source[†]	Method Reference
Baseflow wetted width (W_{Bs})	2D model baseflow wetted area	Wyrick & Pasternack, 2012; 2014
Formative wetted width (W_F)	2D model formative wetted area	Wyrick & Pasternack, 2012; 2014
$Q_{13.7}$ wetted width ($W_{13.7}$)	2D model $Q_{13.7}$ wetted area	Wyrick & Pasternack, 2012; 2014
Bankfull width-to-depth (W/h_{Bf})	2D model bankfulll wetted area; 2D model bankfull depth raster	Wyrick & Pasternack, 2012; 2014
Formative width-to-depth (W/h_F)	2D model formative wetted area; 2D model formative depth raster	Wyrick & Pasternack, 2012; 2014
Baseflow-to-valley width (W_{Bs}/W_V)	2D model baseflow wetted area; detrended digital terrain model (DTM)	White et al., 2010; Wyrick & Pasternack, 2012; 2014
Bankfull cross-section geometry index (Θ_3)	DTM	-
Bankfull LBE concentration (Γ_{Bf})	DTM	Wiener & Pasternack, 2022
Formative LBE concentration (Γ_F)	DTM	Wiener & Pasternack, 2022
Baseflow bed-slope (S_{Bs})	smoothed DTM; LBEs	Wyrick & Pasternack, 2012; 2014
Baseflow water surface slope (WSS_{Bs})	2D model baseflow water surface elevation (WSE) raster	Wyrick & Pasternack, 2012; 2014
Formative water surface slope (WSS_F)	2D model formative WSE raster	Wyrick & Pasternack, 2012; 2014
Baseflow wetted width change (ΔW_{Bs})	2D model baseflow wetted area	Wyrick & Pasternack, 2012; 2014; Golly et al., 2019
Formative wetted width change (ΔW_F)	2D model formative wetted area	Wyrick & Pasternack, 2012; 2014; Golly et al., 2019
Formative shear stress change ($\Delta\tau_F$)	2D model formative shear stress raster	Wyrick & Pasternack, 2012; 2014; Golly et al., 2019

[†]Source data obtained from Pasternack et al. (2021), Wiener and Pasternack (2022), or this study.

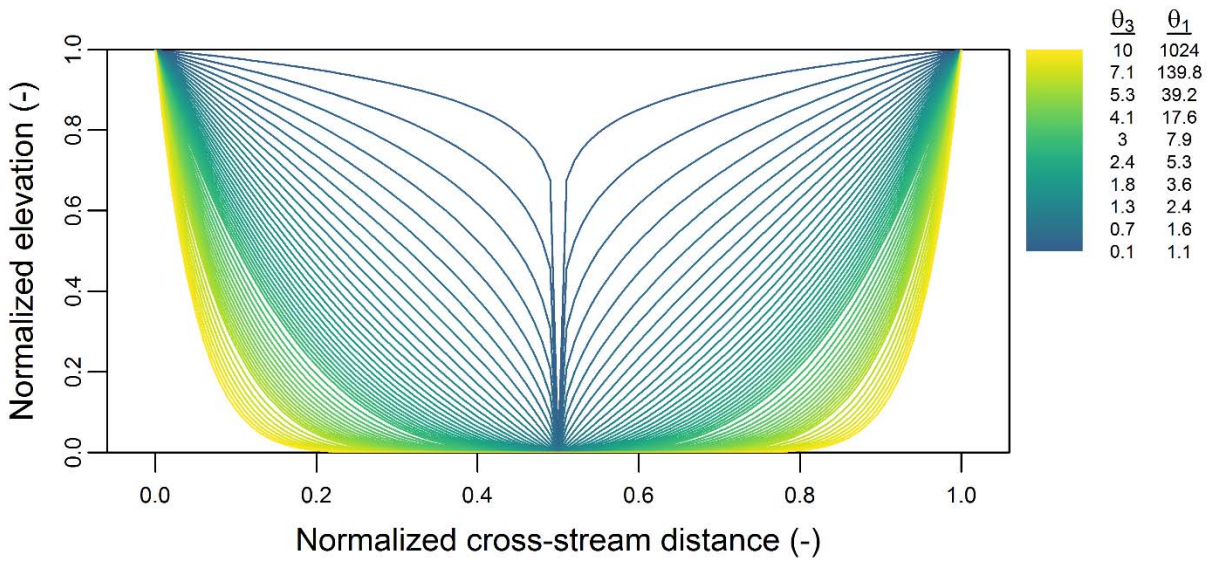

Figure 3.5. Example cross-sections generated by Eq. 5 [$z_n = \Theta_1(|x - \Theta_2|)^{\Theta_3}$], where z_n is normalized elevation and x is normalized cross-stream distance, with different combinations of Θ_1 and Θ_3, and a constant Θ_2 set equal to 0.5. Vertical exaggeration is 0.5.

3.4.2 Statistical analysis linking MUs and HM variables

The following subsections describe methods used to evaluate relationships between MUs and HM variables. They also explain how the first three study questions were answered.

3.4.2.1 Question 1: multivariate differences methods

To determine if MU types had statistically unique combinations of HM variables, differences in HM variables between all MU types were evaluated using PERMANOVA at an alpha of $p \leq 0.05$ (Anderson, 2001). As a further test, MU stratified HM variable assemblages were evaluated a posteriori by pairwise PERMANOVA adjusted for multiple inference following Holm (1979). A criteria of 27 of 36 pairwise tests being positive was taken as a threshold for upholding the hypothesis that MU types have unique HM variable combinations. This criteria corresponds to the case where each MU is similar to one other unique MU, but not more than that. To aid in visualizing MU similarity and provide initial inference on the strength of HM variables in

differentiating MUs, non-metric multidimensional scaling (NMDS) was used to collapse information from multiple dimensions into two NMDS dimensions and principal component analysis (PCA) was used to show the amount of variance in the data explained by each HM variable (APPENDIX 3).

3.4.2.2 Question 2: pairwise analysis methods

To investigate HM variable discriminatory power, pairwise analysis was performed using Welch's ANOVA and Games-Howell tests (Games et al., 1979; Peters, 2018). Initially, HM variables were tested independently between MUs at the 95% confidence level ($p \leq 0.05$) using Welch's ANOVA test (i.e. one test for each HM variable). This test also serves to compliment the pairwise PERMANOVA testing in addressing the question of if MU types had unique combinations of HM variables. A majority of positive tests (≥8) was taken as a secondary criteria for upholding the hypothesis that MU types have unique HM variable combinations.

Post-hoc analysis was performed using the Games-Howell (GH) test at the 95% confidence level ($\alpha = 0.05$) adjusted for multiple inference following Holm (1979). Variables were ranked based on the number of significant GH pairwise comparisons relative to the number of all possible MU combinations (i.e. 36 different combinations for 9 MU types) to determine which were the strongest discriminator of MU types. Following the approach of Lane et al. (2022), a variable was generally considered significant in discriminating MU types if more than 50% of differences between MU pairs (18) were significant above $\alpha = 0.05$. Lastly, the number of significant GH tests between each unique pair of MUs were quantified to evaluate HM variable similarity between MU pairings.

3.4.2.3 Question 3: heuristic expectation assessment methods

To address the question of whether MUs occurred in locations with expected assemblages

of HM attributes, distributions of HM variables for each MU were visualized using violin plots and evaluated heuristically in combination with HM variable summary statistics and results of the pairwise analysis (APPENDIX 3). Specifically, median HM variable values were stratified and ordered by MU type and used to determine if the sequence of ordered values followed the expectations listed in Table 3.2. A fuzzy classification was used to convert the ranked median HM variable values to the ordinal expectations in Table 3.2. Separate ordination schemes were needed to compare outcomes for Θ_3, WSS_F, ΔW_{Bs}, ΔW_F, and $\Delta\tau_F$ to expectations listed in Table 3.2 (APPENDIX 3). For each HM variable, the expected order was considered met if a supermajority 7 of 9 reclassified ranked MU outcomes corresponded to the hypothesized ordinal expectations. The overall hypothesis that MUs occurred in locations with expected HM attributes was upheld if the majority of HM variables (≥8) followed the expected order. A simple transference scheme was applied to map the final set of MU types to the most representative generalized MU type listed in Section 3.2.2 based on similar combinations of baseflow depth and velocity (Figure A.3.3).

3.4.3 Question 4: hydraulic topography variables as alternative to channel geometry index methods

Beyond the limitations of Eq. 5 described in Section 3.4.1, there are several reasons why Θ_3 may not perform well in terms of discriminating MU types. First, this study only mapped baseflow channel MUs, whereas Θ_3 represents the bankfull channel. It is plausible that bankfull geometry might control or predict features inside them (White et al., 2010), so it is worth testing, but ultimately that may not materialize. Second, hydraulically defined MUs simply may not be well differentiated by this proxy metric for cross-sectional geometry. Finally, MUs by any classification but especially by hydraulics may be sensitive to non-local effects that are not captured by cross-section geometry variables like Θ_3 (MacWilliams et al., 2006; Saletti & Hassan,

2020; Hassan et al., 2021). In light of these considerations and despite the potential for spurious correlation, we sought to explore the AHG geometry exponents, *b*, *f*, and *m*, as additional HM variables.

Following the hydraulic topography approach of Gonzalez and Pasternack (2015), *b*, *f*, and *m* exponents of the canonical hydraulic geometry equations for width, depth, and velocity were estimated at each cross-section (APPENDIX 3). Fitting leveraged results from additional 2D model simulations, yielding a total of eight discharges between 1.54 m^3/s and a valley-filling flood of 1184.6 m^3/s. Discriminatory power of the resulting three additional HM variables was assessed following the pairwise analysis approach described in Section 3.4.2.2 and compared to Θ_3 and other HM variables.

3.4.4 Question 5: random forest prediction models

Random Forest (RF) is a supervised machine learning algorithm that aggregates individual classification and regression trees built from random subsets of predictors into a less biased ensemble model (Breiman, 2001). The use of RF is widespread, and has proven effective in fluvial geomorphology for extrapolation of river classification to unmeasured stream intervals (Guillon et al., 2020; Donadio et al., 2021), for mapping fluvial and other Earth surface landforms (Rabanaque et al., 2021; Szabó et al., 2020; Woznicki et al., 2019), and for modeling the spatial pattern of GSD (Diaz-Gomez et al., 2021). To address the final study question regarding MU predictive capability a total of four RF models were developed using different combinations of HM variables as predictors. Description of each model, model development, and model testing are summarized below and detailed in APPENDIX 3.

Model development followed a consistent training-validation approach. Prior to model fitting, HM variables were rescaled using min-max normalization. Based on imbalances in the

number of cross-sections dominated by each MU type, stratified balanced partitioning was used to split data into datasets for model training and testing. A 75/25% split rate for each MU type was used to resample data to ensure at least two samples of each MU type made it into each training and testing dataset (i.e. only 11 sections were dominated by run). Resampling was repeated 1000 times for each model. For each resample, models were fit using the training dataset and validated using the testing data. Model performance was assessed using Matthews's correlation coefficient (MCC) and accuracy (i.e., ratio of number of accurately predicted classes to total classes). Overall model performance was based on the median MCC and accuracy from all resampling events. Hyperparameter tuning for each model followed a grid search approach with a similar validation approach as model development.

The first RF model included all 15 HM variables as predictors ('complete model'). A reduced predictor model was based on identification of the most parsimonious set of HM variables ('parsimonious model'). Predictors for the parsimonious model were identified through an intermediate step of fitting multi-nominal logistic regression models for all possible HM variable combinations (i.e., 32,767 models) on the complete MU dataset, and using AIC model selection to identify the most parsimonious combination (Burnham & Anderson, 2002). A third reduced predictor model was developed using only *b*, *f*, and *m* (section 3.4.3) as predictors ('AHG model'). A final 'null model' with no HM variables was developed for comparison purposes. All models were assessed using the same procedure described above.

The RF models described above were limited to predicting MU types for the ~ 60% of channel cross-sections having a single dominant MU type, therefore an independent test dataset was created and used to further assess model performance in a more difficult context that encompassed another portion of the study segment. Specifically, cross-sections previously

identified as mixed but having 30-50% of their area composed of a single MU type were identified and incorporated into a new dataset. These cross-sections had no dominant MU, but are considered to have a single "subdominant" MU. This dataset consisted of 1633 of the 1697 mixed cross-sections, and an additional ~39% of the total number of baseflow cross-sections (Table A.3.3). Instead of training new models on these data, the four models (complete, parsimonious, AHG, and null) trained on the cross-sections with a single dominant MU were applied to these sections and evaluated following the same procedure and performance metrics described above. The only difference was instead of training models on a portion of the dominant MU cross-sections, models were trained on the full dataset.

3.5 Results

3.5.1 Morphologic unit types

This study mapped and analyzed 4,285 MU polygons, yielding a large dataset to drive robust statistical inquiry. Analysis of this final set of processed MU polygons (i.e., the set of polygons comprising a continuous mapping over the entirety of the baseflow wetted area) confirmed the study segment to be comprised of complex, non-random patterns of unequally distributed fluvial landforms (Figure 3.6). The most aerially abundant MU was slackwater, occupying ~42% of the mapped extent (Table 3.6). The next two most abundant MUs were forced pool and glide. Deep forced pool, alluvial step, and chute had the least aerial abundance. Based on counts of individual MU polygons, slackwater and glide were still the most common units followed by alluvial pool, steep plane bed, and chute (Table 3.6). Forced pool and deep forced pool were the least common MUs by count.

Lateral distribution analysis found the study segment had, on average, ~ 5 MU types per cross-section. Even higher lateral diversity was common in locations of bifurcated flow (Figure

3.6). Based on visual assessment, several configurations appeared more common than others. Slackwater and glide polygons were regularly present along the channel margins. Pool unit polygons were often laterally sandwiched between slackwater with a succession to deeper pools toward the channel center. Units with higher baseflow water speeds exhibited similar transitions. Chute and steep plane bed polygons were each commonly located next to glide and slackwater units. The shallow and rapid flow of alluvial step unit polygons were found laterally adjacent to steep plane bed, glide, and slackwater units.

Adjacency probability results identified strong patterns of non-random collocation and avoidance between unit types (Table A.3.4). Contrary to traditional findings, pool units and high baseflow velocity units (i.e., steep plane bed, chute, and alluvial step) exhibited greater-than-random avoidances with one another. Instead, units including glide, run, and slackwater that were envisioned as entrances and exits to the pools and high baseflow velocity units, did act as transitions between such areas (Figure A.3.4). Groupings of collocated high baseflow velocity units as well as low baseflow velocity units could partly be an artifact of the classification method, but since these units reflect the spatial configuration of different topographic and hydraulic conditions, they still represent an objective depiction of landform organization.

Lastly, longitudinal spacing analysis of run, steep plane bed, alluvial step, chute, and aggregated pool units found unit-to-unit spacings were primarily uni-modally distributed with peaks between 2 and 5 average bankfull widths ($\overline{W_{Bf}}$) (Figure A.3.5). Alluvial step had the tightest mean spacing of $2.5 \cdot \overline{W_{Bf}}$. Chute, pool units, and run were all similarly spaced with mean values of 3.8, 3.9, and $4.0 \cdot \overline{W_{Bf}}$, respectively. Steep plane bed had the longest distance between units at a mean spacing of $6.4 \cdot \overline{W_{Bf}}$. Pool units, steep plane bed, run, and chute showed slight bi-modal spacing distributions with secondary peaks between 6-10$\cdot \overline{W_{Bf}}$. Similar mean and modal spacings

amongst pool, run, and chute units suggest units occur together in periodic sequences through the study segment as part of larger geomorphic unit couplets (Figure A.3.5). Since none of the units in the longitudinal analysis were typically found to have strong lateral adjacency tendencies, the chute-run portion of these couplets may be an important transition from steep plane bed and alluvial step units into pool units.

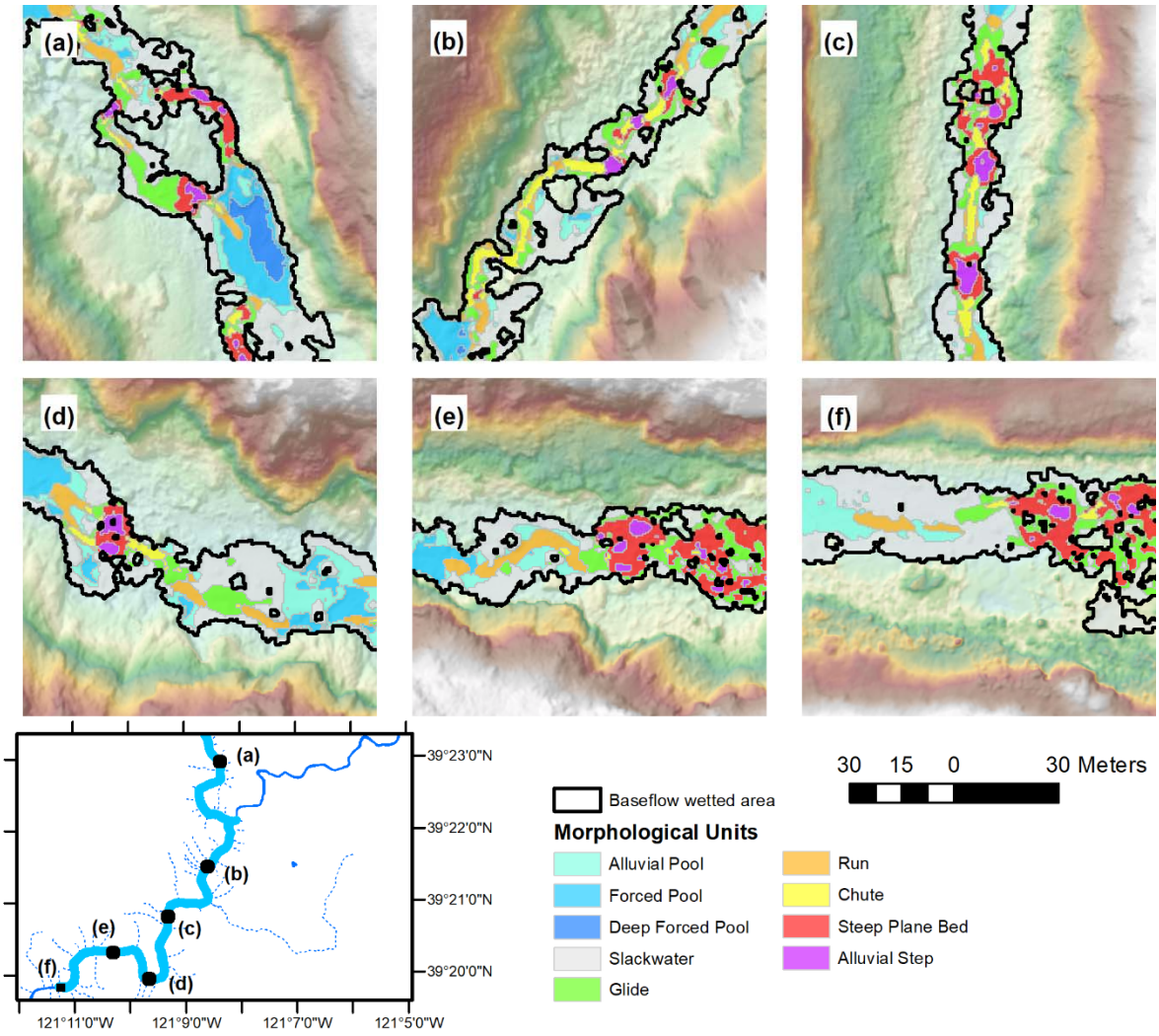

Figure 3.6. Example MU configurations overlain on detrended DTM illustrating typical lateral distributions and adjacencies. Flow directions are from top-to-bottom or left-to-right.

Table 3.6. Baseflow channel morphological unit (MU) polygon abundance metrics.

Morphological unit	Area (m^2)	Area (%)	Number (-)	Number (%)
Alluvial Pool	27617	11.7	581	13.6
Forced Pool	31088	13.2	176	4.1
Deep Forced Pool	4817	2.0	10	0.2
Slackwater	98496	41.8	1227	28.6
Glide	28964	12.3	840	19.6
Run	9242	3.9	308	7.2
Chute	7561	3.2	376	8.8
Steep Plane Bed	22951	9.7	511	11.9
Alluvial Step	4924	2.1	256	6.0
Total	235659	100	4285	100

3.5.2 Hydro-morphological variables

HM variables exhibited diverse ranges of values (Figure 3.7; Table A.3.5). After rescaling variables by subtracting the mean and dividing by the range, it emerged that variables had similar overall ranges but differing magnitudes of dispersion based on common dispersion measures such as standard deviation and inter-quartile range (Figure 3.7; Table A.3.5). Comparing unscaled variables, only 5 of 105 pairs of HM variables were highly correlated ($r > 0.7$): W_{Bs} and W_{Bs}/W_V, W_F and $W_{13.7}$, W_F and W/h_F, $W_{13.7}$ and W/h_F, and W/h_{Bf} and W/h_F (Figure A.3.6).

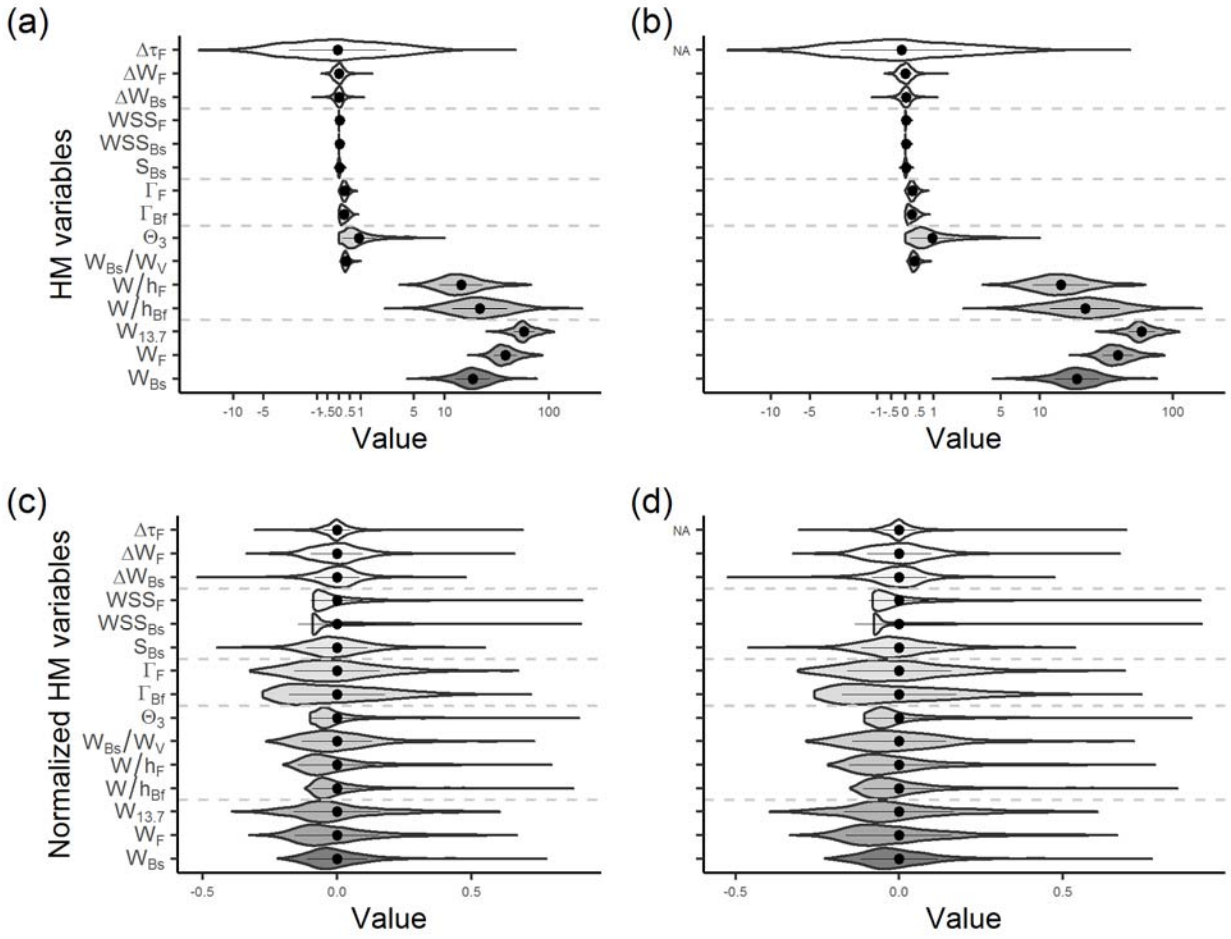

Figure 3.7. Violin plots of hydro-morphological (HM) variables at (a) all 4236 cross-sections and (b) at 2539 cross-sections with a dominant morphological unit (MU). Violin plots of normalized HM variables at (c) all 4236 cross-sections and (d) at 2539 cross-sections with a dominant MU. Note logarithmic x-axis in panels (a) and (b). Violins represent kernel density of each variable. Points in each violin are mean values and lines in each violin show one standard deviation from mean. Dashed gray lines separate the five groups of selected HM variables.

3.5.3 Morphological unit-hydro-morphological variable relations

Cross-sections dominated by a single MU had diverse and often unique ranges of HM variable values (Figure 3.8). Summary statistics of each HM variable for each MU type are provided in Table A.3.7. Example cross-sections fit by Eq. 5 for each MU type are presented in Figure 3.9. Notably, locations with highly irregular and complex topography were difficult to fit using the flexible albeit simple form of Eq 5. Results of analyses used to address the first three

study questions are presented in the following subsections.

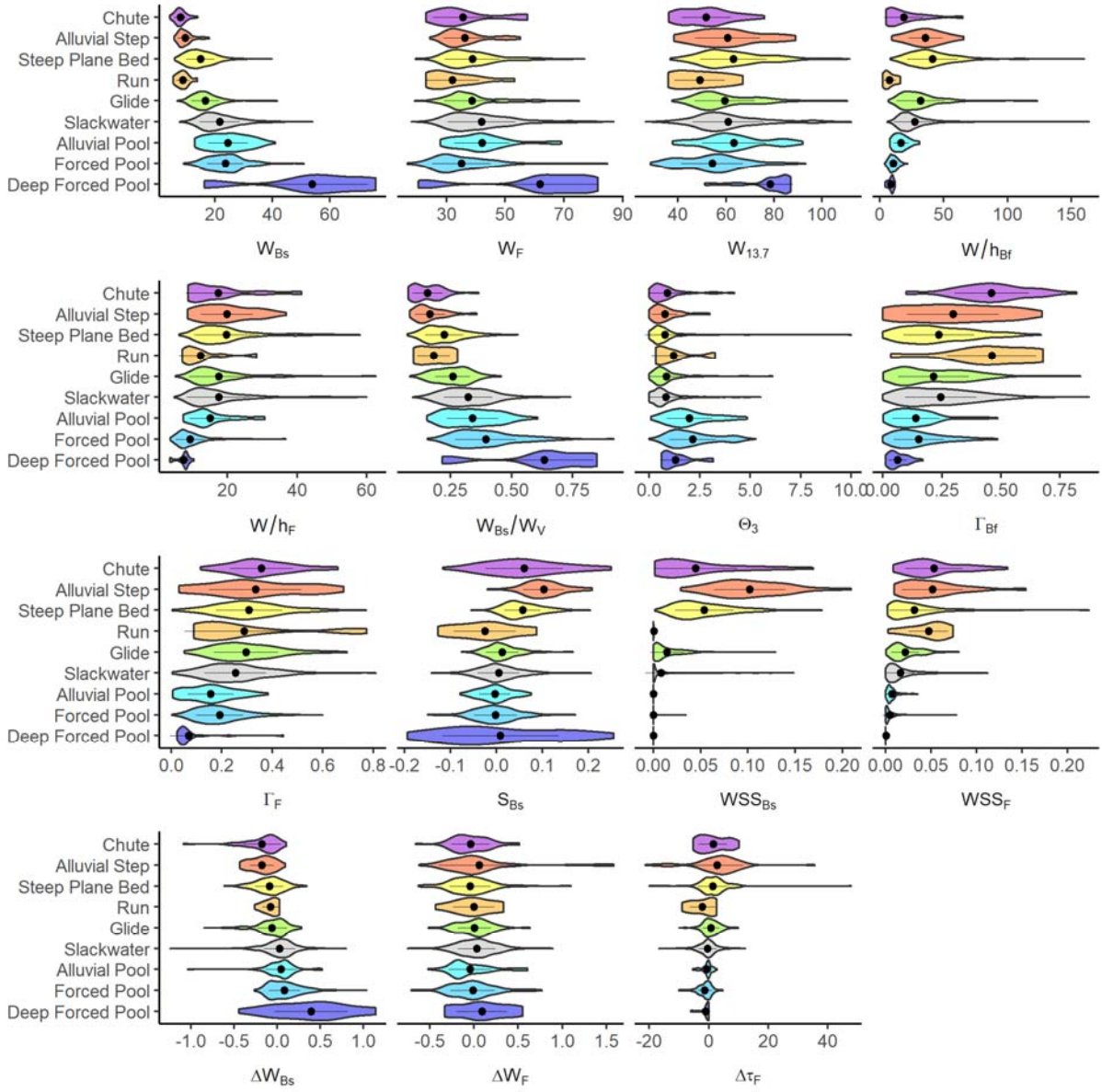

Figure 3.8. Violin plots of hydro-morphological (HM) variables by morphological unit (MU) type. Violins represent kernel density of each variable. Points in each violin are mean values and lines in each violin show one standard deviation from mean.

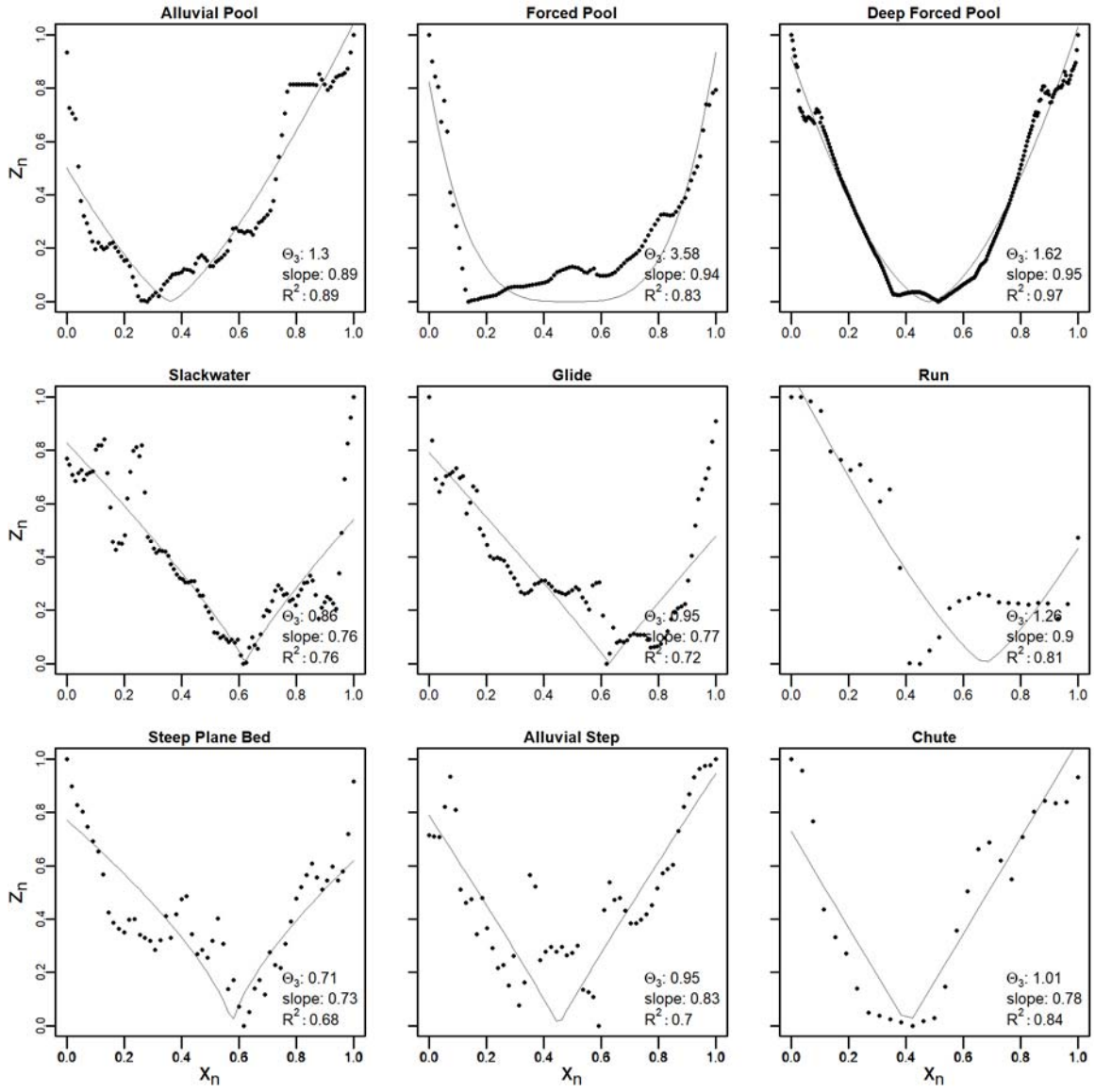

Figure 3.9. Example of a cross-section fit with Eq 5 for each morphological unit (MU) type. Points are observed values and line is predicted values from Eq 5, where z_n is normalized elevation and x_n is normalized cross-stream distance. Examples shown correspond to the cross-section with the 75% percentile slope metric for each MU. Goodness-of-fit metrics (slope and R^2) and bankfull cross-section geometry index (Θ_3) are shown.

3.5.3.1 Question 1: multivariate differences results

On the basis of the 15 selected HM variables, MU types were significantly different from one another (PERMANOVA; $p << 0.01$). Pairwise PERMANOVA tests indicated all 36 MU-MU

comparisons differed above a 95% confidence level ($p \leq 0.05$) according to unadjusted test results and after applying Holm's (1979) correction. This exceeded the criterion of 27 positive tests for upholding the hypothesis that MU types have unique HM variable combinations (section 3.4.2.1), but may not be surprising given the large number of HM variables.

Collapsing variables to the first two NMDS dimensions provided some degree of clustering in the data even if regions of overlap remained (Figure 3.10). Stress from the 2D NMDS analysis was 0.157, indicating a 'useable' ordination, but also that a higher-dimension solution could improve inference and potentially provide greater clustering/grouping in the data (Clarke, 1993). The first and second principle component axes explained 30.9 and 25.4% of the variance in the data, respectively (Figure 3.10). The first component was dominated by channel size and shape variables (i.e. wetted widths, width-to-depth ratios, and valley confinement [W_{Bs}/W_V]). The second principal component was dominated by gradient and channel-obstruction/roughness variables, which to some degree reflect mean velocity. This meant that moving from bottom-left to top-right in the NMDS ordination there is a shift from wider, lower gradient units in more valley confined settings to units with steeper gradients and greater LBE concentrations in areas with less valley confinement (Figure 3.10).

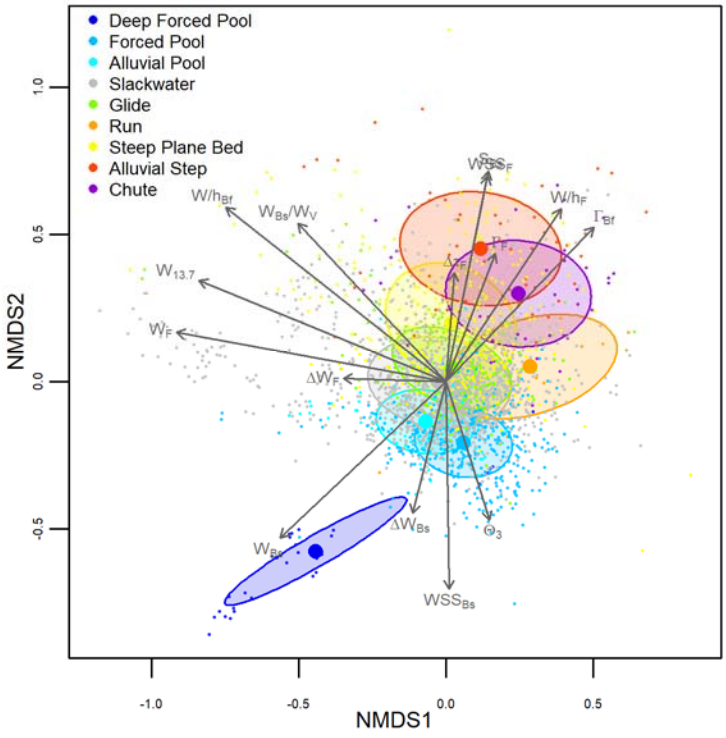

Figure 3.10. Plot of the first two non-metric multidimensional scaling (NMDS) dimensions. Large points are the mean NMDS values for the set of cross-sections dominated by each morphological unit (MU) type, small points are values for individual cross-sections dominated by a single MU type, and ellipses are one standard deviation from mean. Vectors represent the influence of hydro-morphological variables on the variance between MUs. Longer vectors explain more variance between MUs.

3.5.3.2 Question 2: pairwise analysis results

Welch's ANOVA test results indicated all HM variables were different between MUs ($p << 0.01$), which met the second criterion for upholding the hypothesis that MU types have unique HM variable combinations. Next, post-hoc analysis by pairwise GH tests determined HM variables differed in their ability to differentiate MU types (Table 3.7). Based on unadjusted p values, 12 HM variables exceeded the 18 pairs threshold to be considered a significant discriminator of MU occurrence. This dropped to eight HM variables when using adjusted p values. The maximum number of significant adjusted tests, 33 of 36 possible, was achieved by W_{Bs}, followed by W_{BS}/W_V,

WSS_{Bs}, WSS_F, and W/h_{Bf}, indicating MU types differed along the individual gradients of these variables more-so than the others. The least explanatory variable was ΔW_F, which after adjustment had only one significant test. Large dispersion and/or overlap of HM variable values across MU types likely influenced the ability of some HM variables, such as W_F, $W_{13.7}$, Θ_3, S_{Bs}, and $\Delta\tau_F$ to differentiate MU types according to the GH test (Figure 3.8).

Not all variables discriminated the same MU types from one another (Figure A.3.8). Numbers of significant adjusted GH tests also varied between different MU pairings, meaning some MUs had greater similarity to others based on HM variables (Table 3.8). The greatest number of differences were generally between high baseflow velocity units (i.e. steep plane bed and alluvial step) and pool units. The fewest number of differences were between run and most other MU types. Other similar pairings included: alluvial pool with forced pool, glide with run and the three high baseflow velocity units, and the high baseflow velocity units with one another. No MU pairing was found to have significant differences for all HM variables, and no pairings were found to have no differences in HM variables based on GH tests.

Table 3.7. Counts of significant morphological unit-morphological unit (MU-MU) differences based on Games-Howell test for each hydro-morphological (HM) variable applied at the 95% confidence level using unadjusted *p* values and values adjusted for multiple inference following Holm (1979). Bold numbers exceeded the 18 significant pairs needed to be considered a significant discriminator of MU occurrence. Variables in bold and highlighted in gray exceeded the 18 significant pairs for both unadjusted and adjusted *p* values.

HM variable	Number of significant tests unadjusted *p* value	Number of significant tests adjusted *p* value	Rank based on number of adjusted significant tests
Baseflow wetted width (W_{Bs})	**33**	**32**	1
Formative wetted width (W_F)	**18**	16	9
$Q_{13.7}$ wetted width ($W_{13.7}$)	**20**	15	10
Bankfull width-to-depth (W/h_{Bf})	**29**	**26**	5
Formative width-to-depth (W/h_F)	**19**	15	10
Baseflow-to-valley width (W_{Bs}/W_V)	**31**	**30**	2
Bankfull cross-section geometry index (Θ_3)	16	10	13
Bankfull LBE concentration (Γ_{Bf})	**26**	**22**	7
Formative LBE concentration (Γ_F)	**21**	**20**	8
Baseflow bed-slope (S_{Bs})	**19**	12	12
Baseflow water surface slope (WSS_{Bs})	**30**	**30**	2
Formative water surface slope (WSS_F)	**31**	**27**	4
Baseflow wetted width change (ΔW_{Bs})	**25**	**23**	6
Formative wetted width change (ΔW_F)	2	1	15
Formative shear stress change ($\Delta\tau_F$)	12	9	14

Table 3.8. Counts of significant morphological unit-morphological unit (MU-MU) differences based on adjusted and unadjusted Games-Howell tests for each hydro-morphological variable between each MU pairing. Unadjusted test results are shown in parenthesis next to adjusted results. Numbers in bold correspond to MU pairings with ≥8 significant differences in HM variables out of the possible 15 variables.

	Forced Pool	Deep Forced Pool	Slackwater	Glide	Run	Steep Plane bed	Alluvial Step	Chute
Alluvial Pool	5 (7)	**11 (12)**	7 (8)	**10 (11)**	4 (7)	**12 (12)**	**11 (12)**	**10 (11)**
Forced Pool		**10 (11)**	**13 (14)**	**14 (14)**	4 (5)	**14 (14)**	**11 (12)**	**9 (11)**
Deep Forced Pool			**11 (12)**	**12 (13)**	7 (7)	**12 (13)**	**11 (13)**	**10 (11)**
Slackwater				**8 (9)**	4 (5)	**12 (12)**	**8 (8)**	**8 (10)**
Glide					3 (6)	6 (7)	6 (6)	6 (8)
Run						3 (7)	3 (4)	1 (3)
Steep Plane bed							5 (6)	5 (6)
Alluvial Step								3 (5)

3.5.3.3 Question 3: heuristic expectation assessment results

Heuristic assessment found hypothesized MU expectations were met for 9 of 15 selected HM variables (Figure 3.8; Table 3.9). This exceeded the criterion of eight needed to accept the hypothesis that MUs occurred in locations with expected assemblages of HM attributes, but does mean expectations were not met for several variables. Of HM variables whose expectations were met, the complete set of expectations (9 of 9) were met for W_{Bs}, W/h_F, and W_{Bs}/W_v. Of the six HM variables where MU expectations were not met, W_F, $W_{13.7}$, Θ_3, and ΔW_F had 6 of 9 MU expectations met, while only 5 of 9 MU expectations were met for Γ_{Bf}, and $\Delta\tau_F$ (APPENDIX 3). While not included as part of the hypothesis testing criteria, expectations were also met for all three AHG exponent variables (Table 3.9). The total number of HM variable expectations met for each MU type ranged from 8 for run to all 18 for alluvial step (Table 3.9).

Table 3.9. Summary of whether hydro-morphological (HM) variables met hypothesized morphological unit (MU) expectations[†].

Generalized MU	Study segment MU[‡]	*Channel-size variables*						*Channel-shape variables*							
		W_{Bs}		W_F		$W_{13.7}$		W/h_{Bf}		W/h_F		W_{Bs}/W_V		Θ_3[¶]	
		E	R	E	R	E	R	E	R	E	R	E	R	E	R
Step-type	AS	L	3	L[§]	4	I[§]	6	H	8	H	9	L	1	unconfined U-to-convex shaped	V-shaped (convex)*
Riffle-type	SPB	L	4	H	6	H	7	H	9	H	8	L	4		V-shaped (convex)*
Pool-type	AP		8		8		8		5		4		7		U-shaped*
	FP	H	7	L	3	L	3	L	3	L	2	H	8	confined: U-shaped	U-shaped (rectangular)*
	DFP		9		9		9		2		1		9		U shaped (V-shaped)*
Chute-type	RN	L	2	L-I	1	L-I	1	L-I	1	L-I	3	L	3	confined: U-to-rectangular shaped	V-shaped
	CH		1		2		2		4		5		2		V-shaped (convex-to-U)
Slackwater-type	SL	I	6	I-H	7	I-H	5	I-H	6	I-H	6	I	6	V-to-rectangular shaped	convex (V-shaped)
	GL		5		5		4		7		7		5		V-shaped*
Expectation met		**9 of 9 - Yes**		6 of 9 - No		5 of 9 - No		**7 of 9 - Yes**		**9 of 9 - Yes**		**9 of 9 - Yes**		6 of 9 - No	

Generalized MU	Study segment MU[‡]	*Channel-obstruction/roughness variables*				*Gradient variables*					
		Γ_{Bf}		Γ_F		S_{Bs}		WSS_{Bs}		WSS_F	
		E	R	E	R	E	R	E	R	E	R
Step-type	AS	H	7	H	8	H	9	H	9	Reduced differences in medians between units compared to WSS_{Bs}	Sum of absolute differences in medians reduced by 50% compared to WSS_{Bs}
Riffle-type	SPB	H	5	H	7	H	8	H	8		
Pool-type	AP		2		2		4		3		
	FP	L	3	L	3	L	3	L	2		
	DFP		1		1		1		1		
Chute-type	RN	L-I	8	L-I	4	I-H	2	I-H	4		
	CH		9		9		7		7		
Slackwater-type	SL	I-H	6	I-H	5	I	5	I	5		
	GL		4		6		6		6		
Expectation met		5 of 9 -No		**8 of 9 - Yes**		**8 of 9 - Yes**		**8 of 9 - Yes**		**Yes**	

Generalized MU	Study segment MU‡	*Longitudinal change variables*††						*At-a-station hydraulic geometry exponent variables*						Expectation met (n=18)
		ΔW_{Bs}		ΔW_F		$\Delta \tau_F$		*b*		*f*		*m*		
		E	R	E	R	E	R	E	R	E	R	E	R	
Step-type	AS	(-)	(-)	(-)§	(~0) (- & bi-modal)	(+)§	(+) (bi-modal)	H	8	H	8	L	1	18
Riffle-type	SPB	(-)	(-) (~0)	(+)	(-) (~0)	(-)	(+) (~0)	H	6	H	9	L	2	15
Pool-type	AP		(+) (~0)		(~0) (-)		(-)		3		4		7	14
	FP	(+)	(+)	(-)	(~0)	(+)	(-)	L	2	L	3	H	8	16
	DFP		(+)		(~0) (+)		(-)		1		1		9	14
Chute-type	RN	(~0)	(-) (~0)	(~0)	(~0)	(~0)	(~0) (-)	L-I	7	I	2	I-H	6	8
	CH		(-)		(~0)		(+) (~0)		9		5		3	12
Slackwater-type	SL	(~0)	(+) (~0)	(~0)	(+) (~0)	(~0)	(-) (~0)	I	4	I-H	6	I	5	17
	GL		(-) (~0)		(~0)		(+) (~0)		5		7		4	16
Expectation met		**8 of 9 - Yes**		6 of 9 - No		5 of 9 - No		**7 of 9 - Yes**		**8 of 9 - Yes**		**8 of 9 - Yes**		

†Expectations (E) defined and colored along fuzzy gradient: low (L), intermediate (I), and high (H); or as otherwise noted. Grey-scale color gradient goes from light-to-dark along low-to-high gradient. MU-HM variable pairs with multiple expectations, such as L-I or I-H, reflect higher uncertainty and potential for variable to span a wider range of values. Results (R) are ordered median values from low (1) to high (9), or otherwise noted. Ranks are related to ordinal expectations and colored using the following overlapping fuzzy classification: low (1-4), low-intermediate (2-5), intermediate (4-6), intermediate-high (5-8), and high (6-9). Expectations and results of the same color indicate expectation was met.

[‡]Steep plane bed (SPB), alluvial step (AS), alluvial pool (AP), forced pool (FP), deep forced pool (DFP), run (RN), chute (CH), slackwater (SL), and glide (GL).

[§]Dominant expectation listed but values at step units expected to be bimodal to represent both jammed-state (low W_F and $W_{13.7}$, negative ΔW_F, and positive $\Delta\tau_F$) and keystone (high W_F and $W_{13.7}$, positive ΔW_F, and negative $\Delta\tau_F$) formation models.

[¶]Θ_3 values interpreted as follows: <1 convex, ~1 V-shaped, >1 U-shaped, and >2.5 rectangular. First results are based on two-sided t.test relative to unity, secondary result in parenthesis is additional heuristic interpretation based on distribution of data. Expectation upheld if either result met expectation and are marked with a * symbol.

[††]Grey-scale color gradient goes from light-to-dark along negative-to-positive gradient. First results are based on two-sided t.test relative to zero, secondary result in parenthesis is additional heuristic interpretation based on distribution of data.

3.5.4 Question 4: hydraulic topography variable results

Based on results in the sections above, it emerged that Θ_3 was only an intermediate discriminator of MU type relative to other HM variables (e.g. ranking 13 of 15 with 10 significant adjusted GH tests; Table 3.7). Further, MU types often had different Θ_3 values than expected (Table 3.9). Alternately, pairwise analysis found AHG exponents had among the strongest MU discriminatory ability compared to the 15 selected HM variables having 32, 16, and 26 significant adjusted GH tests for *b*, *f*, and *m*, respectively (Figure 3.11). This meant *b*, which reflects the rate that width increases with discharge (stage), tied for having the most discriminatory power of all HM variables. Results also generally aligned with hypothesized expectations across MU types (Table 3.9; APPENDIX 3).

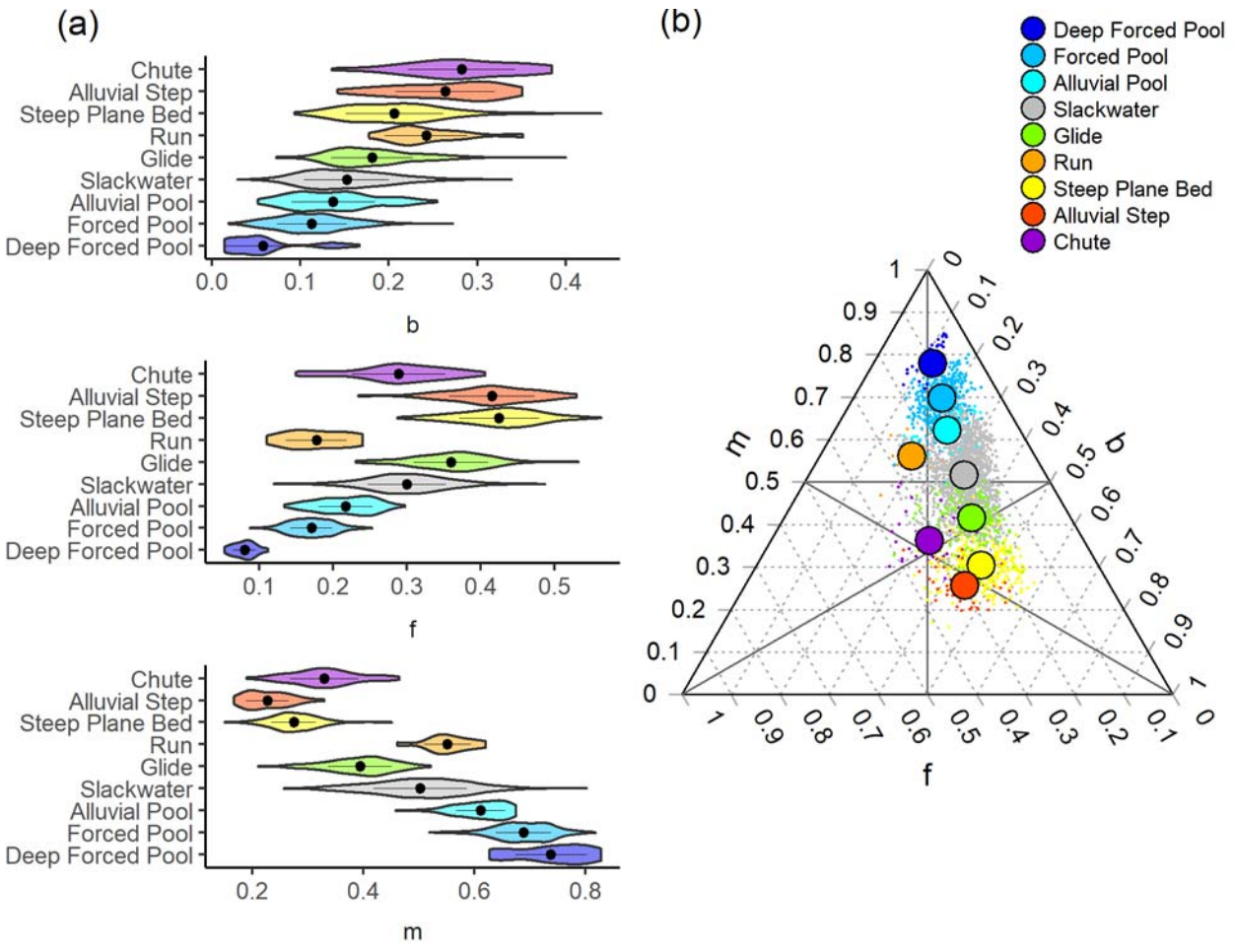

Figure 3.11. (a) Violin plots of at-a-station hydraulic topography exponents, *b-f-m*, for each morphological unit (MU). Violins represent kernel density of each variable. Points in each violin are mean values and lines in each violin show one standard deviation from mean. (b) Ternary diagram of *b-f-m* values for each MU cross-section (small points) and median *b-f-m* value for each MU across all cross-sections (large points). Lines in ternary diagram show conditions where $b=m$, $f=m$, $b=f$, and $b+f=m$, respectively. b, f, and m are exponents of the canonical hydraulic geometry equations for width, depth, and velocity, respectively.

3.5.5 Question 5: random forest model results

The complete RF model had a median MCC of 70.1% and median accuracy of 81.0% based on 1000 comparisons with testing data. Across resampling, Gini impurity varied but several HM variables emerged as consistently being important, including W_{Bs}, W/h_{Bf}, and WSS_{Bs} (Figure 3.12). These same variables were also identified as strong discriminators of MU type by pairwise analysis (section 3.5.3.2). Results of the AIC model selection found the most parsimonious model included the following ten predictors: W_{Bs}, W_F, $W_{13.7}$, W/h_{Bf}, W/h_F, Γ_{Bf}, Γ_F, WSS_{Bs}, ΔW_F, and Θ_3.

The parsimonious model had a median MCC of 69.5% and median accuracy of 80.5% on the testing data. Comparing models, the complete model offered only minor improvement over the parsimonious model. Both models provide substantial improvement over the null model's accuracy of 53.9% (MCC could not be computed for the null model as each class is not predicted).

The final RF model with the three AHG exponents, b, f, and m, had a median MCC of 71.1% and median accuracy of 81.6% on the test data. This slightly exceeded performance of the other RF models. However, it is unclear if such improvement is due to AHG exponents being better predictors or simply due to spurious correlation between these predictors and the MU classification system, which both derive from hydraulic measurements.

Misclassifications were similar between complete, parsimonious, and AHG RF models. The top four most common misclassifications were glide as slackwater, slackwater as steep plane bed, steep plane bed as glide, and alluvial pool as slackwater which, on average accounted for

between 35.5-57.7% of total test set misclassifications across models. Several other common errors included misclassifying glide sections as steep plane bed, alluvial step as steep plane bed, and forced pool as slackwater. Higher total misclassification rates among these pairings were somewhat influenced by imbalance in MU dominated cross-sections as there were simply more slackwater, steep plane bed, forced pool, and glide sections to be misclassified (Table 3.4). Other misclassifications were consistent with MU pairings that exhibited few differences in HM variables based on numbers of significant adjusted GH tests (Table 3.8).

Applying the complete model trained on the full set of dominant MU cross-sections to the subdominant MU cross-section dataset yielded a median MCC of 27.5% and median accuracy of 47.5%. The parsimonious model had median MCC and accuracy scores of 26.4% and 46.9%, respectively. These scores are on the same order as the median accuracy of the null model (45.8%), suggesting predictions from these models were comparable to random selection. This performance is surprising given that subdominant MU cross-sections had similar appearing HM variable distributions to those with a single dominant MU (Figure A.3.9). Median MCC and accuracy scores from the AHG model of 32.2% and 51.3% offered some improvement, but were still relatively low.

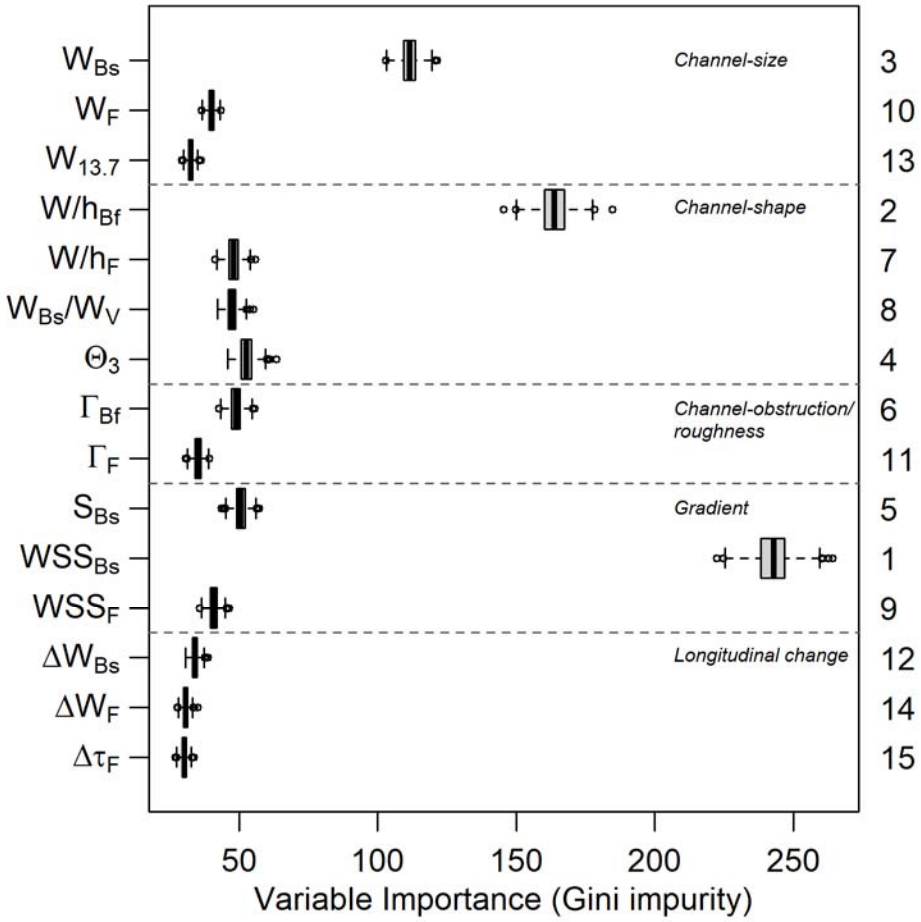

Figure 3.12. Boxplots of hydro-morphological (HM) variable importance from complete random forest model across 1000 resamplings. HM variables are organized by group and separated by dashed gray lines. Numbers along right axis are ranked importance values from highest (1) to lowest (15) according to mean Gini impurity.

3.6 Discussion

Using the top-down MU classification approach of Wyrick et al. (2014) a spatially explicit census of 4,285 individual MU polygons among nine baseflow MU types were mapped within a 13.2-km coarse-bedded, mountain river. Discretizing the study river segment into cross-sectional polygons a total of 2539 cross-sections were identified as being dominated by a single MU type and a diverse set of 18 HM variables were measured at these cross-sections. Bottom-up

multivariate (PERMANOVA) and pairwise (ANOVA; GH) statistical analyses supported our initial hypothesis that MU types had statistically unique combinations of 15 selected HM variables, and a combination of statistical and heuristic analyses supported our hypothesis that MU types occurred in portions of the river valley with expected assemblages of these same HM attributes. Cumulatively, study results can be used to develop holistic descriptions of HM variable conditions where certain MUs and/or groups of MUs occurred, interpret processes involved in the formation/persistence of these MU types, and provide inference on how HM variables exert deterministic control.

Notably, other factors such as lithology, vegetation, hillslope properties, non-local factors, and flow and sediment regimes known to influence channel morphology were not included as HM variables, so interpretations are given in the context of what was measured. Many of the HM variables are also unidimensional in nature, whereas processes involved in MU formation and maintenance (e.g. sediment routing, eddy formation with jet flow, vortex scour) are often multidimensional (Booker et al., 2001; Thompson, 2018; Hassan et al., 2021). Additionally, findings and discussion in the subsequent sections are focused on the ~60% of the channel where a single MU type was found to dominate. These locations can be viewed as strong representations of the form of each MU type, but means ~40% of the channel characterized by greater lateral MU diversity is not considered and would benefit from further inquiry. This may be an underlying disadvantage of 2D MU delineation schemes as applied in the context of this study, as many cross-sections will not have a dominant MU Type (Wyrick & Pasternack, 2014). However, all linear cross-section and longitudinal profile-based MU classification schemes result in portions of the channel being omitted from classification (e.g. Jarrett 1993; Helm et al., 2020) in addition to ignoring lateral variably.

3.6.1 Synthesis of hydro-morphological links with morphological unit spatial patterns

The study's three pool unit types consistently occurred in channel locations where W_{Bs} was comparatively high. At 161.0 and 1184.7 m^3/s these same locations had more variable or intermediate W_F and $W_{13.7}$ values (Figure 3.8; Table 3.9). This transition likely reflects backwater conditions created by downstream hydraulic controls (e.g. negative pool exit slopes, downstream topographic highs, downstream high LBE concentrations) becoming inundated at higher flows stages and resulting in more uniform flows widths (Richard, 1976; Caamaño et al., 2009). However, cross-sections dominated by alluvial pool and deep forced pool still occurred where W_F and $W_{13.7}$ tended to be highest. This meant alluvial pool and deep forced pool were often spatially nested in locations with similar relative multi-stage width conditions (e.g. wide-in-wide; Pasternack et al., 2021). In contrast, forced pool dominated cross-sections occurred where median W_F and $W_{13.7}$ were third lowest (narrowest), which was lower than median W_F and $W_{13.7}$ values at steep plane bed and alluvial step dominated cross-sections.

Conditions at alluvial pool and deep forced pool sections are somewhat counterintuitive to the dual-stage flow convergence routing mechanism for pool maintenance, whereas the high flow switch in width between forced pool and steep plane bed/alluvial step is in-line with the conceptualization that this width switch provides the means for pools to scour at higher discharge and maintain relief with adjacent riffle type MUs (MacWilliams et al., 2006; Thompson, 2011; Pasternack et al., 2018a). One explanation for why width conditions at alluvial pool and deep forced pool were inconsistent with the flow convergence routing mechanism could relate to the inability of the study's wetted width variables to capture pool asymmetries and other 2D or 3D flow patterns, which produce hydrodynamic conditions associated with high flow sediment routing involved in pool-riffle maintenance (Booker et al., 2001). Other HM variables also offer possible

explanations. All pool units occurred in confined valley settings (i.e. high W_{Bs}/W_v), and ΔW_F results indicate formative widths were typically constant or narrowing downstream toward the majority of pool dominated cross-sections functioning like a nozzle in concept (section 3.5.3.3). Together, these conditions would facilitate high-stage formation of jet flow and flow convergence associated with pool scour.

Among other HM variables, pool dominated cross-sections had the lowest median WSS_{Bs}, Γ_{Bf}, and Γ_F of all MUs, occurred in settings with comparatively low W/h_{Bf} and W/h_F, and had amongst the lowest S_{Bs} values (Figure 3.8; Table A.3.7). These findings were consistent with hypothesized expectations derived from past studies (Table 3.9; section 3.2.2). Further, although pool dominated cross-sections had the lowest median WSS_F, average percent increases between WSS_{Bs} and WSS_F at pool sections were only second to increases at run sections, which is consistent with findings of Richards (1976ab) amongst others (e.g. Thompson, 2018). Lastly, pool units occurred in locations where ΔW_{Bs} was mainly positive (upstream baseflow channel width increased toward unit), and where $\Delta\tau_F$ was typically negative or near-zero (upstream formative shear stresses decreased or were constant toward unit). Negative $\Delta\tau_F$ is interpreted as promoting depositional conditions that are contrary to expectations for maintenance of pool units at formative discharges. However, the metric does not account for overall magnitude of τ, and the cross-sectional averaging of τ may miss locations of peak τ associated with high-stage sediment routing through pool units (Strom et al., 2016). Longitudinal change metrics are also susceptible to the scale over which they are calculated (Golley et al., 2019; Nardini et al., 2020). The three change metrics, were calculated over a region $2 \cdot \overline{W_{Bf}}$ upstream of each dominant MU cross-section (Golley et al., 2019). Given, MU spacing results (section 3.5.1) this aligns with the typical spacing between alluvial step units and certain pool units, but may not be sufficient to represent conditions

approaching MUs with larger spacings and/or that dominate cross-sections wider than $\overline{W_{Bf}}$.

Cross-sections dominated by steep plane bed and alluvial step occurred in channel locations with HM attributes that were essentially the opposite of pool units. Such locations were comparatively narrow at baseflow and of intermediate width at formative discharge (e.g. nozzles nested in nozzles; Pasternack et al., 2021), and had comparatively high W/h_{Bf}, W/h_F, Γ_{Bf}, Γ_F, S_{Bs}, and WSS_F (Figure 3.8; Table 3.9). These unit's cross-sections had the highest median WSS_{Bs}, but unlike pool units, average percentage changes between WSS_{Bs} and WSS_F were not only the lowest among all MU types but tended to slightly decrease, indicative of a drowning out of topographic controls. Above the formative discharge, widths increased rapidly leading to steep plane bed and alluvial step dominated cross-sections having the third and fourth highest median $W_{13.7}$ values, respectively. According to longitudinal change variables ΔW_{Bs} was mainly negative (narrowing), ΔW_F was negative or near-zero (narrowing or constant), and $\Delta\tau_F$ tended to be positive (increasing).

An initial interpretation of ΔW_F and $\Delta\tau_F$ tendencies is that these locations would not be depositional at the formative discharge and that deposition would only occur at higher discharges, if ever under contemporary flow and sediment regimes that involve flow regulation, land use impacts, and altered sediment supply and transport processes (Turowski et al., 2013; Polvi, 2021; see section 3.6.3). Similarly, while comparatively narrow W_F values clash with expectations for steep plane bed to serve as a riffle analog under the guise of the flow convergence routing mechanism, the fact that these units occurred where $W_{13.7}$ was rapidly increasing and the valley was unconfined (i.e. low W_{Bs}/W_v) is consistent with evidence that stages much higher than bankfull may be required to initiate the dual-stage width switch in confined mountain rivers where LBEs are abundant and account for a substantial portion of total flow resistance (White et al., 2010; Pasternack et al., 2021; Wiener & Pasternack, 2022). Comparatively high Γ_{Bf} and Γ_F at steep plane

bed and alluvial pool dominated cross-sections also help explain the discrepancy with the flow convergence routing mechanism. High LBE concentrations serve to increase flow resistance, promote deposition or at least reduce energy available for sediment transport, and increase transverse velocities (e.g. Furbish, 1998; Wiener & Pasternack, 2022). Such increased flow resistance could compensate for the difference in mass and energy conservation typically achieved by flow widths at riffle type units exceeding pool units (Caamaño et al., 2009; Brown et al., 2016). For instance, de Almeida and Rodriguez (2011) found riffle crest coarsening increased entrainment thresholds and reduced riffle erosion, which together served to stabilize riffle locations. These same changes in sedimentological properties have been found to promote fine sediment deposition at riffles during infrequent large flood events (Chartrand et al., 2015; Hassan et al. 2021).

Under most flow conditions mountain rivers are often considered supply limited. This can change during infrequent large flood events when sediment supply overwhelms transport capacities (Turowski et al., 2013). Despite relatively high hillslope sediment productions rates (Curtis et al., 2015), sediment discontinuity in the study segment may limit this type of flood-based deposition, meaning finer sediments are mostly transported downstream (section 3.6.3). Increased roughness at steep plane bed and alluvial step dominated cross-sections may increase potential for flood deposition, but sedimentological observations are needed to support this supposition. LBEs mapped in the study segment by Wiener and Pasternack (2022) had minimum dimensions of 0.46 x 0.46 x 0.312 m. Thus, channel reformation associated with LBE mobilization and liberation of stored in-channel sediment supplies likely remains limited to large infrequent flood events (Turowski et al., 2013; Polvi, 2021).

Interpreting steep plane bed and alluvial step HM variables in the context of jammed-state hypothesis had mixed results. Consistent with the hypothesis, both units dominated where W_F was

narrower than expected and where formative channel widths were narrowing (i.e. negative ΔW_F). However, the comparatively large $W_{13.7}$ values at these units are not only more aligned with the keystone model of step formation, but slightly counterintuitive to the idea that jamming of large grains should occur at higher discharges when grains are increasingly mobile (Grant et al., 1990; Golly et al., 2019; Saletti & Hassan, 2020). Median $W_{13.7}$ values may be influenced by the fat upper tail of the distributions, and both steep plane bed and alluvial step sections occurred over a range of $W_{13.7}$ values (Figure 3.8). The keystone model also posits that expanding channel widths and decreasing downstream shear stress serve as mechanisms for keystone deposition. Neither of these conditions prevailed at steep plane bed or alluvial step cross-sections at the formative discharge. Greater uniformity of $W_{13.7}$ across MU types and preliminary evaluation of conditions at $Q_{13.7}$ indicate width changes still tend to be evenly distributed about zero and changes in τ to be positive. Calculating a representative step forming grain-size (D_{SFG}) for the study segment based on D_{SFG}/D_{90} ratios from Table 1 of Curran (2007) yields an average D_{SFG} of 0.7 m. Based on W_F values, this results in jamming-ratios at alluvial step cross-sections ranging from 34.7-78.7, which are ~6-13 times larger than the upper-bound of 6 commonly recognized as supporting step-pool channel morphologies (Chin & Wohl, 2005; Church & Zimmermann, 2007; Comiti & Mao, 2012). Notwithstanding, both jamming and keystone deposition appear to play relevant roles on the occurrence of steep plane bed and alluvial step units in the study segment. The wide range of W_F and $W_{13.7}$ values and both negative and positive $\Delta\tau_F$ values at our steep plane bed and alluvial step units require additional evaluation to determine at what flow(s) these formation models dominate and if models spatially overlap or occur more independently (section 3.6.2).

As a final interpretation of where steep plane bed and alluvial pool units were found to dominate, not only did these cross-sections have the highest median W/h_{Bf} and W/h_F, but only one

alluvial step and one steep plane bed dominated cross-section had W/h_{Bf} <10. This changed to 3 of 49 alluvial step, and 14 of 365 steep plane bed dominated cross-sections for the criteria that sections had W/h_F <10. The W/h value of 10 has been recognized as a lower threshold for bar instability and the formation of alluvial bars and coarse grained bedforms (Furbish, 1998; Wilkinson et al., 2008), thus bar instability appears to be a complimentary morphogenetic process influencing steep plane bed and alluvial step dominance in the study segment. Alternately, despite having comparatively low W/h_{Bf} and W/h_F values, many alluvial pool and forced pool cross-sections occurred where W/h_{Bf} and W/h_F were above 10. Therefore, the threshold served as a lower bound for the occurrence of steep plane bed and alluvial step, but did not prohibit pool and other units from dominating cross-sections with W/h_{Bf} and W/h_F values above the threshold.

With regard to transitional units such as glide and slackwater, cross-sections dominated by these units had HM variables with comparatively intermediate values. Between units, glide tended to occur in cross-sections that were slightly narrower at all flows, had higher WSS_{Bs}, and had less valley confinement than slackwater dominated cross-sections. Individual glide polygons were often mapped at steep plane bed to pool-head or pool exit-slope to steep plane bed transitions, whereas slackwater was ubiquitous along the periphery of low gradient portions of the baseflow channel (section 3.5.1). The abundance of slackwater dominated cross-sections and polygons provides some justification for the majority of the study segment being aligned with the 'plane bed' classification of Montgomery and Buffington (1997). However, the presence of other MU types conflicts with their description of plane bed lacking bedforms patterns. Based on the influence of LBEs and local variations in bed slope, the study segment appears to be better described as an intergraded mix of the channel morphologies that includes step-pool, cascade, forced morphologies, and intermediate morphologies (Thompson et al., 2006; Polvi, 2021).

Cross-sections dominated by chute, and to a lesser degree run, had similar HM variable attributes as steep plane bed and alluvial step sections with a few notable differences. Chute and run sections had much lower W/h_{Bf} and W/h_F, were less confined (i.e. lower W_{Bs}/W_v), and had typically higher Γ_{Bf}. High LBE concentrations persisted at chute sections at the formative discharge (i.e. high Γ_F), but not at run dominated sections. High Γ_{Bf} and Γ_F at chute sections may have been due to bank attached bedrock outcrops being included in the spatially explicit LBE dataset (Wiener & Pasternack, 2022). This is not taken as problematic as it aligns with the view that this unit occurs in highly confined steep sections of deeply eroded bedrock (Table A.3.2). Resistance borne from high Γ_{Bf} and Γ_F may balance the erosive capacity of chute cross-sections resulting from high bed and water surface slopes (e.g. S_{Bs}, WWS_{Bs}, and WSS_F), and promote stability of such units (Wiener & Pasternack, 2022). Lower W/h_{Bf} and W/h_F at chute and run cross-sections may result by proxy of the classification scheme, which specified *a priori* that these units have relative high baseflow depths and water speeds, which by mass conservation would likely require narrow flow widths.

Lastly, of the ~ 40% of channel cross-sections classified as mixed, ~ 96% were found to have a single sub-dominant MU type (section 3.4.4; Table A.3.3). Visual comparison found HM variable distributions from these section were similar to those with the same dominant MU type, but had greater dispersion and more overlap between MU types (Figure 3.8; Figure A.3.9). Several factors could be involved in the less distinct, more complex MU patterns in these locations. For example, high flow processes could be less effective at shaping the baseflow channel in these cross-sections, because these cross-sections had slightly higher average LBE concentrations and were often in locations of bifurcated flow. Such perturbations could drive greater baseflow hydraulic diversity and may also indicate portions of the channel that are prone to disturbance, in

disequilibrium, or more resistant (section 3.6.3). More research is needed to understand mountain river locations with a large number of MUs distributed across the baseflow channel.

3.6.2 Decoupling processes and morphological unit variability

The idea that comparable sets of morphogenetic processes were locally active throughout the study segment where specific MU types occurred is bolstered by three results. First, each MU type had a relatively large set of dominant cross-sections. Second, MU types had statistically unique HM variable combinations. Third, many HM variables had reasonable internal consistency within each set of MU dominated cross-sections (Figure 3.8) (Lane & Richards, 1996). While this type of local control does not explicitly conflict with the position held by hierarchical channel classification models that MU scale landforms are strongly dictated by larger scale (e.g. reach scale) physical channel attributes, it does highlight that local control can drive greater morphological variability than suggested by reach scale morphology alone (Wyrick et al., 2014; Byrne et al., 2020; Lane et al., 2021).

Decoupling local processes was complicated by several HM variables having multiple process-linkages (Table 3.1), several processes emerging as being relevant to formation/maintenance of the same MU type, and different processes emerging as being relevant to the same MU at different discharges (section 3.6.1). Establishment of combinations of HM variables values uniquely aligned with expectations for different process mechanisms associated with each MU type could serve as a first-order approach to decouple or elucidate the relevance of individual processes at individual MU locations. Further research is needed.

Another key finding of this study was that the sets of cross-sections dominated by each MU type had diverse and often overlapping ranges of HM variable values (Figure 3.8). An initial interpretation of these outcomes was the potential for multiple MU types to occur in locations with

similar HM variable conditions. This was certainly true for a number of MU types as illustrated by consistency between MU pairings that had relatively few differences in HM variables based on pairwise analysis (section 3.5.3.2) and those misclassified in the RF predictive analysis (section 3.5.5). While HM variable values mostly aligned with expectations from other MU studies, ranges of certain HM variables were outside those previously measured (Table A.3.9), and expectations were not met for the majority of variables (6 of 11) believed to have stronger process-morphology linkages (Table 3.1; Table 3.9). This resulted in MU dominated cross-sections that appear as 'outliers' (Figure 3.8), and/or cross-sections where HM variable expectations were not met. These locations may represent a variety of phenomena, and while it is outside this effort to address all examples, discussion of a limited set of these locations is provided in APPENDIX 3.

3.6.3 Morphological unit expectations not met

Study results confirmed that the four HM variables, W_{Bs}, S_{Bs}, WSS_{Bs}, and $\Delta W_{Bs,}$ viewed as being primarily for MU prediction (Table 3.1) were typically powerful at discriminating and/or predicting MU types and conformed to MU expectations derived from past studies (Table 3.9). To the contrary, expectations were not met for six of the other 11 HM variables associated with higher flow stages and presumed to have stronger process-morphological linkages. These variables also tended to have less discriminatory and predictive power. This brings up questions about what processes are active in the study segment and how study segment MU types are formed and/or maintained.

One commonality among MU types with the possible exception of alluvial step was that based on HM variables all units appear to occur in erosional, or at least not in strongly depositional settings, at high flow stages. Pasternack et al. (2021) also found that overall canyon confinement meant sediment moving down the study segment would only tend to deposit in local valley width

expansions or move quite far downstream to where the canyon finally widens. Sediment discontinuity in the watershed has also impacted the study segment's contemporary alluvial processes and it remains unclear if the channel is in a state of adjustment to historic changes in the basin rather than in some balance to the current flow and sediment regimes (James, 2005; YCWA, 2013). The result is that all MU types may be highly winnowed. Absent historical observations of the channel's alluvial state, this does not mean study segment morphologies are not self-formed (Whipple, 2004), and the topographic signature of currently morphologies are clearly sculpted into the channels bedrock in the form of semi-rhythmic undulations in the vertical dimension (Pasternack et al., 2021; Figure A.3.2). In this manner, channel morphology is more defined by undulations in the vertical dimension in response to variations in width at the highest flows and by differences in coarse-grained sedimentology, and channel adjustments are primarily through changes in resistance (Chin, 2002; Polvi, 2021; Wiener & Pasternack, 2022).

Drawing from the HM variable results, one broad process interpretation for the MU patterns is that valley-scale topography is responsible for creating zones of differential scour with pool units occurring in locations of greatest high flow scour, and steep plane bed and alluvial step units occurring where resistance is high, the valley is unconfined, and/or at locations of mass wasting. This concept is supported by the findings of Pasternack et al. (2021) who found that above ~161 m^3/s study segment topographic structure was increasingly associated with localized zones of laterally convergence and divergent flows being in-phase with topographic lows and topographic highs.

Because variables associated with $Q_{13.7}$ were more informative than those from the formative discharge in terms of explaining MU formation, analysis of HM variables at discharges higher than those currently available may further elucidate processes that explain MU patterns.

For instance, high potential for mass wasting provides abundant contemporary possibilities to supply LBEs to the study segment valley-bottom (Curtis et al., 2005). Wiener and Pasternack (2022) found study segment longitudinal LBE concentrations to be semi-oscillatory with sequences of LBE clustering suggesting some degree of historic fluvial transport. Given the size of LBEs in their study, mobilization and deposition would only occur during infrequent large flood events. Confined valley settings also have low capacity for planform channel adjustment over historic timescales (Fryirs, 2017), and a final plausibility is that contemporary channel morphology is inherited from past extreme flood events (Polvi, 2012) outside the current flow regime, such as landslide outburst floods or melting of Quaternary glaciers present in the easternmost portions of the Yuba ca. 10,000 yBP (James et al., 2002; James, 2004).

Separate interpretation on why expectations were not for several HM variables and how study segment MU types were formed are given in terms of the study design. Delineation of baseflow channel morphology using baseflow depths and velocities is a proven method used by the fluvial geomorphology community (van Rooijen et al., 2021; Woodworth & Pasternack, 2022), and the study's final set of MU polygons were mapped at a scale consistent with previous examples (e.g. Comiti & Mao, 2012; Wyrick & Pasternack, 2014; Wheaton et al., 2015). A potential issue arises when comparing these baseflow defined fluvial landforms to processes occurring at higher discharges. At baseflow, the spatial pattern of study segment hydraulics change rapidly leading to high subdivision of the channel into the selected MU types (Figure 3.6). For instance, glide and run units were commonly mapped at steep plane bed to pool-head and pool exit-slope to steep plane bed transitions, and given their location and relative topographic position may be part of residual pool areas (Figure A.3.2; section 3.5.1; Figure A.3.4).

Because baseflow hydraulics define MU locations and are intended to embody underlying

topography, baseflow HM variables in turn are strongly controlled by MU type. At higher flows, hydraulic controls present at low flow are drowned out and the scale of contiguous hydraulic characteristics expands across MU types. Thus, subdivisions present at baseflow vanish at high flow and leave room to question if such subdivisions are morphologically significant in the context of evaluating processes. This raises the question of what scale is appropriate to study governing processes (Thompson, 2018). The study's focus on the cross-sectional scale may have further compounded this issue, as analyses are made independent of adjacent MU types or even cross-sections dominated by the same MU type. Separating variables into those with stronger process-morphological linkages (e.g. $W_{13.7}$) and those viewed as responses to formative processes (e.g. S_{Bs}, W_{Bs}, and WSS_{Bs}) aided in interpreting how HM variables exert deterministic control, however this issue remains complicated by the inevitable 'chicken-egg' paradox of whether HM variable conditions precede MU occurrence or if morphodynamic processes driving MU formation and subsequent HM variable conditions occur more simultaneously (Brierley & Fryirs, 2005). These questions remain open problems. Nevertheless, it remains our view that MU dominated cross-sections in the study segment are strong representations of the form of each MU type and HM variables at these sections reflect local controls on MU formation and/or persistence or at least the channel's response to such processes.

3.6.4 Utility of HM variables and Random Forest predictive approach

The set of HM variables used in this study spanned a larger range of geometric, hydraulic, and geomorphic attributes than past studies performing bottom-up MU classification and/or analysis (Grant et al., 1990; Peterson & Rabeni, 2001; Halwas & Church, 2002; Wyrick & Pasternack, 2014; Helm et al., 2020). HM variables varied in terms of their ability to discriminate MU types, but together results of the pairwise and RF predictive model analyses determined

WSS_{Bs}, W_{Bs}, W/h_{Bf}, and W_{Bs}/W_v had the greatest power to discriminate/predict MU occurrence (Table 3.7; Figure 3.12). Combining variables together in a series of RF models achieved median predicative accuracies ranging from 80.5-81.6% compared to resampled independent test data. Misclassifications of the study's RF models were most commonly between MU pairings that had few differences in HM variables (Table 3.8) and/or occupied more of the channel. These accuracies are comparable to classification accuracies reported in similar studies made in comparison with training data, whereas this study's accuracies are based on comparison with independent test data (Table 3.10). Further, variables from the referenced studies are not always easily or meaningfully transferable between rivers (Peterson & Rabeni, 2001; Marcus et al. 2003), and typically provide only minimal interpretation in terms of process-based explanation for why MUs were accurately predicted.

When considering what makes a good prediction, the effort taken in this study to describe MU process-morphology linkages underlying the study's HM variables should enable better transferability for MU prediction across a range of river morphologies, even if it is most suitable for high-gradient, coarse-bedded rivers (Wheaton et al., 2015; Belletti et al., 2017). For instance, outside of directly applying the study's RF models in other settings, the set or a subset of the 9 HM variables that had their MU expectations met (Table 3.9) could theoretically serve as the basis for a top-down fuzzy MU classification system. Classification would occur as an inverse problem whereby raw HM variable measurements made at channel cross-sections would be converted into ordinal data (i.e. the expectations in Table 3.2 or Table 3.9) and then related back to the MU type that most closely aligns with the set of ordinal expectations. More generally, the study's top-down classification followed by bottom-up analysis experimental design provides an objective basis for evaluating channel morphology and developing unbiased MU predictive models (Helm et al.,

2020).

A key methodological advance in this study, even if it only yielded one predictor variable, was adaptation of Eq. 5 (e.g. Dingman, 2007) and use of Θ_3 in lieu of AHG exponents as a HM variable. Although Θ_3 had only moderate discriminatory capability compared to AHG exponents, the ability of Θ_3 to holistically describe channel cross-section shape without having to compute AHG metrics has geomorphic relevance that warrants further study. Similarly, equations, such as Eq. 5, that can produce a variety of cross-section shapes could prove useful in creating artificial river topographies (Brown & Pasternack, 2019) and in procedural river design (Pasternack & Zhang, 2021).

Lastly, the low predictive capacity of using models trained on cross-sections with a single dominant MU to predict subdominant MUs illustrates a potential shortcoming of applying an MU dominance approach in settings with a large relative abundance of high MU lateral diversity. A portion of this low predictive capability can be explained by the lateral distribution analysis (section 3.5.1), which found MU types were often adjacent to MUs having common HM attributes that were difficult to differentiate from each other (Table 3.8). For instance, slackwater, glide, alluvial pool, and forced pool units were often found in lateral succession, as were alluvial step, steep plane bed and glide units. The study's RF models can be modified to output the probability that each MU is predicted for each cross-section. These probabilities could potentially elucidate where predictions were confounded by similarity between MU types. A model trained on the subdominant cross-section dataset would also likely have performed better. However, both efforts are beyond the scope of this study.

Table 3.10. Classification accuracies of this study and other studies of bottom-up MU classification.

Study	Method	Variables	MU types	Accuracy	Site details
This study	Random forest	18 hydro-morphological variables	9: deep forced pool, forced pool, alluvial pool, slackwater, glide, run, chute, steep plane bed, alluvial step	80.5-81.6%	Steep boulder-bedded mountain river
Helm et al. (2020)	PCA-clustering	5: hydraulic radius, median grain size (D_{50}), local bed and water surface slope, and reach bed slope	5: riffle, slackwater, glide, run, and pool	85%†	Forested, gravel-bed stream
Marcus et al. (2003)	Maximum likelihood principal component	128-band hyperspectral imagery	4: glides, riffles, pools, and eddy drop zones	67.7-85.5%†	Three cobble-gravel bed streams
Peterson and Rabeni (2001)	Discriminant analysis	6: area, mean depth, velocity, and aerial coverage of aquatic vegetation, woody debris, and bedrock	11 'channel units'	75% and 80%‡	Headwater and downstream reaches of cobble-coarse sand bed Ozark stream
Jowett (1993)	Linear discriminant analysis	2: water surface slope and either velocity/depth ratio or Froude number	3: pool, run, and riffle	65-66%†	Braided gravel-bed river
Grant et al. (1990)	Linear discriminant analysis	slope	riffles	73%†	Two steep coarse-bedded mountain rivers

†Accuracy on training data

‡Average five-fold cross validation classification accuracy

3.6.5 Bespoke morphological units

Common definitions of MU types across the scientific community are helpful, but can be detrimental in their potential for inducing misclassification and a lack of recognition of fluvial diversity and variability in unique settings. Effort was taken to relate study MU types to the most representative MU type of those common in the scientific literature while still honoring local

landform diversity (Brierly et al., 2013). We believe study results corroborate these comparisons, but several differences require reconciliation. Our alluvial step units, which were more akin to a hybrid step-riffle (Table A.3.2), had HM variable values often outside ranges from the step-pool literature (Table A.3.9). Differences from traditional definitions make direct comparison difficult, nonetheless, many alluvial step units were identified as steps using the step-pool classification algorithm of Zimmermann et al. (2008) (APPENDIX 3) and HM variables at alluvial step cross-sections both followed expectations and were phenomologically consistent with models of step formation (Golly et al., 2019; Saletti & Hassan, 2021). This suggests either a broader reconceptualization of steps and where they can occur is warranted, or simply reinforces an important morphological difference between the alluvial step units in the study segment and more traditional step morphology.

Riffles are one of the mostly commonly defined channel features in alluvial and mixed bedrock-alluvial channels with bed slopes ranging between ~0.1-2% (Thompson, 2018). Steep plane bed was used as a riffle analog to provide comparison to this common feature, however, results question this relation (sections 3.6.1). Firstly, field observations found steep plane bed units lacked a defined crest and were comprised of semi-random configurations of very coarse substrates. HM variable results also question the idea that steep plane bed were depositional at high flows via the flow convergence routing mechanism, which is a common conceptualization for riffles. Certainly other processes have been associated with riffle formation and maintenance (e.g. Pasternack et al., 2018a; Thompson, 2018; Hassan et al., 2021), and HM variable interpretations support that jamming, instabilities related to channel geometry and LBE concentrations, and differential resistance due to high LBE concentrations play a role at steep plane bed dominated cross-sections.

These disconnects and the bespoke nature of study segment MU types may limit transferability of study findings to systems with similar segment or reach scale characteristics and anthropogenic influences. However, the study segment is not unique, and these conditions are often present in the northern Sierra Nevada range and globally (e.g. Guillon et al., 2020). Several of the processes presumed active in the study segment have been identified for their role in controlling channel morphology in lower gradient alluvial rivers (Table 3.1). Thus, despite differences in the study segment and the delineated MU types, study findings should still have applicability to a range of coarse-grained alluvial and mixed bedrock-alluvial rivers.

3.7 Conclusions

Organized in response to processes of water flow and sediment transport, river channel morphology at the MU scale exhibits complex patterns and morphodynamic feedbacks that drive local patterns of topographic variability (Pasternack & Zhang, 2021). Using a large dataset of nine baseflow channel MU types and a diverse set of 18 HM variables having either predictive capability or representing an array of possible hydraulic and geomorphic controls, this study describes physical conditions at cross-sections dominated by a single MU type in far more detail than has previously been completed. The study's rigorous, objective, and data-driven analyses addressed five key questions on MU diversity, HM variable control on where MU types tended to occur, and if locations dominated by single MU types were consistent with expectations based on previous observations and MU process-morphology linkages with HM variables. Although some MU types had similar HM variable attributes, multi-variate statistical analyses confirmed MU types were different. This not only aids in validating the top-down, supervised classification approach of Wyrick et al. (2014) used to classify and map MU types in the study segment, but aligns with geomorphic theory that MUs represent distinct local form–process associations

(Brierley & Fryirs, 2005; Belletti et al., 2017). Building on this, a key discovery was that MUs had diverse ranges of HM variable values often outside ranges reported by MU studies in other high-gradient, coarse-bedded rivers. Additional statistical and predictive analyses determined several of the 15 selected HM variables, WSS_{Bs}, W_{Bs}, W/h_{Bf}, and W_{Bs}/W_v, as well as all three AHG exponents (*b*, *f*, and *m*) were effective in discriminating and predicting MU locations. Although less instrumental, less common or novel variables like Θ_3, ΔW_{Bs}, ΔW_F, $\Delta\tau_F$ provided new insight into conditions supporting different MU types and methodological advances in how to describe channel morphology.

Though not all hypothesized HM variable expectations were met for each MU type, the majority (9 of 15) of expectations being met confirmed the studies hypothesis that MUs would be located in portions of the river valley with typical assemblages of HM attributes. Focus on describing MU-HM variable process-morphology linkages allowed analysis and identification of several morphogenetic processes likely active in the study segment, even if expectations for several HM variables were not met and decoupling the influence of different processes on specific MU locations remained a challenge. Viewed inversely, HM variables could prove useful in geomorphic assessment as first-order criteria for testing river restoration designs for the presence of processes known to create and/or maintain common fluvial landforms (Brown et al., 2016). For the geomorphic and river management communities, the study's top-down classification to bottom-up analysis approach provides a useful framework for verifying geomorphic classification, understanding factors relevant to supporting diverse set of MU types, and testing process-morphology linkages.

Finally, Random Forest models developed with all 15 selected HM variables and a reduced predictor model with only 10 variables achieved classification accuracies of 81.0% and 80.0%,

which are comparable to past studies but for a broader diversity of MU types. This accuracy was surpassed by an even simpler model with only AHG exponents as predictors (81.6%). Notably, each of these models did not perform well when attempting to predict subdominant MUs at cross-sections with more complex lateral MU configurations. While universality and transferability of these models requires further testing, they can serve as an immediate reference for studies wishing to better understand MU patterns in high-gradient, coarse-bedded rivers.

3.8 References

Anderson, M. J. (2001). A new method for non-parametric multivariate analysis of variance. *Austral Ecology, 26*(1), 32-46. doi:https://doi.org/10.1111/j.1442-9993.2001.01070.pp.x

Belletti, B., Rinaldi, M., Bussettini, M., Comiti, F., Gurnell, A. M., Mao, L., . . . Vezza, P. (2017). Characterising physical habitats and fluvial hydromorphology: A new system for the survey and classification of river geomorphic units. *Geomorphology, 283*, 143-157. doi:https://doi.org/10.1016/j.geomorph.2017.01.032

Bisson, P. A., J. L. Nielsen, R. A. Palmason, and L. E. Grove. (1982). A system of naming habitat types in small streams, with examples of habitat utilization by salmonids during low streamflow. Pages 62–73 in N. B. Armantrout (Ed.) Acquisition and Utilization of Aquatic Habitat Inventory Information. Symposium proceedings, October 28–30, 1981, Portland, Oregon. The Hague Publishing, Billings, MT.

Bisson, P. A., Montgomery, D. R., & Buffington, J. M. (2006). CHAPTER 2 - Valley Segments, Stream Reaches, and Channel Units Methods in Stream Ecology (Second Edition) (pp. 23-49). San Diego: Academic Press.

Booker, D.J., Sear, D.A., & Payne, A.J. (2001). Modelling three-dimensional flow structures and patterns of boundary shear stress in a natural pool–riffle sequence. *Earth Surf. Process. Landforms*, 26: 553-576. https://doi.org/10.1002/esp.210

Breiman, L. (2001). Random Forests. *Machine Learning* 45, 5–32. https://doi.org/10.1023/A:1010933404324

Brierley, G., Fryirs, K., Cullum, C., Tadaki, M., Huang, H. Q., & Blue, B. (2013). Reading the landscape:Integrating the theory and practice of geomorphology to develop place-based understandings of river systems. *Progress in Physical Geography: Earth and Environment, 37*(5), 601-621. doi:10.1177/0309133313490007

Brierley, G. J., & Fryirs, K. A. (2005). The River Styles Framework. *Geomorphology and River Management: Applications of the River Styles Framework*. Malden, MA: Blackwell Publishing.

Brown, R. A., & Pasternack, G. B. (2019). How to build a digital river. *Earth-Science Reviews, 194*, 283-305. doi:https://doi.org/10.1016/j.earscirev.2019.04.028

Brown, R. A., Pasternack, G. B., & Lin, T. (2016). The Topographic Design of River Channels for Form-Process Linkages. *Environmental Management, 57*(4), 929-942. doi:10.1007/s00267-015-0648-0

Buffington, J. M., Lisle, T. E., Woodsmith, R. D., & Hilton, S. (2002). Controls on the size and occurrence of pools in coarse-grained forest rivers. *River Research and Applications, 18*(6), 507-531. doi:https://doi.org/10.1002/rra.693

Buffington, J. M. & Montgomery, D. R. (2013). Geomorphic classification of rivers. In: Shroder, J.; Wohl, E., ed. Treatise on Geomorphology; Fluvial Geomorphology, Vol. 9. San Diego, CA: Academic Press. p. 730-767.

Burnham, K.P., Anderson, D.R. (2002). Information and Likelihood Theory: A Basis for Model Selection and Inference. In: Burnham, K.P., Anderson, D.R. (eds) Model Selection and Multimodel Inference. Springer, New York, NY. https://doi.org/10.1007/978-0-387-22456-5_2

Byrne, C. F., Pasternack, G. B., Guillon, H., Lane, B. A., & Sandoval-Solis, S. (2020). Reach-scale bankfull channel types can exist independently of catchment hydrology. *Earth Surf. Process. Landforms*, 45: 2179– 2200. https://doi.org/10.1002/esp.4874.

Byrne, C. F., Pasternack G. B., Guillon, H., Lane, B. A., & Sandoval-Solis, S. (2021). Channel constriction predicts pool-riffle velocity reversals across landscapes. *Geophysical Research Letters*. DOI: 10.1029/2021GL094378.

Caamaño, D., Goodwin, P., Buffington, J. M., Liou, J. C., & Daley-Laursen, S. (2009). Unifying Criterion for the Velocity Reversal Hypothesis in Gravel-Bed Rivers. *Journal of Hydraulic Engineering, 135*(1), 66-70. doi:doi:10.1061/(ASCE)0733-9429(2009)135:1(66)

Carbonari, C., Recking, A., & Solari, L. (2020). Morphology, Bedload, and Sorting Process Variability in Response to Lateral Confinement: Results From Physical Models of Gravel-bed Rivers. *Journal of Geophysical Research: Earth Surface, 125*(12), e2020JF005773. doi:https://doi.org/10.1029/2020JF005773

Chartrand, S. M., Hassan, M. A., & Radić, V. (2015). Pool-riffle sedimentation and surface texture trends in a gravel bed stream, *Water Resour. Res.*, 51, 8704– 8728, doi:10.1002/2015WR017840.

Chartrand, S. M., Jellinek, M., Whiting, P. J., & Stamm, J. (2011). Geometric scaling of step-pools in mountain streams: Observations and implications. *Geomorphology, 129*(1), 141-151. doi:https://doi.org/10.1016/j.geomorph.2011.01.020

Chin, A. (2002). The periodic nature of step-pool mountain streams. *American Journal of Science*, 302 (2) 144-167; DOI: 10.2475/ajs.302.2.144

Chin, A., & Wohl, E. (2005). Toward a theory for step pools in stream channels. *Progress in Physical Geography: Earth and Environment, 29*(3), 275-296. doi:10.1191/0309133305pp449ra

Church, M., & Zimmermann, A. (2007). Form and stability of step-pool channels: Research progress. *Water Resources Research, 43*(3), n/a-n/a. doi:10.1029/2006WR005037

Clarke, K. R. (1993). Non-parametric multivariate analyses of changes in community structure. *Australian Journal of Ecology*, 18: 117–143. DOI: 10.1111/j.1442-9993.1993.tb00438.x

Comiti, F., & Mao, L. (2012). Recent Advances in the Dynamics of Steep Channels *Gravel-Bed Rivers* (pp. 351-377).

Curran, J. C. (2007). Step–pool formation models and associated step spacing. *Earth Surface Processes and Landforms, 32*(11), 1611-1627. doi:10.1002/esp.1589

Curtis, J. A., Flint, L. E., Alpers, C. N., & Yarnell, S. M. (2005). Conceptual model of sediment processes in the upper Yuba River watershed, Sierra Nevada, CA. *Geomorphology*, 68(3-4), 149-166. doi:10.1016/j.geomorph.2004.11.019

Diaz-Gomez, R., Pasternack, G. B., Guillon, H., Byrne, C. F., Schwindt, S., Larrieu, K. G., Sandoval-Solis, S. (2021). Substrate map challenge: Airborne lidar and machine learning predicts subaerial sand-gravel-cobble fluvial sediment facies. Geomorphology 401. DOI: 10.1016/j.geomorph.2021.108106.

Dingman, S.L. (2007). Analytical derivation of at-a-station hydraulic–geometry relations. *Journal of Hydrology*, 334: 17– 27. https://doi.org/10.1016/j.jhydrol.2006.09.021

Donadio, C., Brescia, M., Riccardo, A. Giuseppe, A., Michele, D. V., & Guiseppe, R. (2021). A novel approach to the classification of terrestrial drainage networks based on deep learning and preliminary results on solar system bodies. *Sci Rep* 11, 5875. https://doi.org/10.1038/s41598-021-85254-x

Dunne, K. B. J., & Jerolmack, D. (2020). What sets river width?. *Science Advances* 6(41). DOI: 10.1126/sciadv.abc1505

Florsheim, J. L. (1985). Fluvial requirements for gravel bar formation in northwestern California [Master's Thesis, Hombolt State University].

Fryirs, K. A. (2017). River sensitivity: a lost foundation concept in fluvial geomorphology. Earth Surf. Process. Landforms, 42: 55– 70. doi: 10.1002/esp.3940.

Furbish, D. J. (1998). Irregular bed forms in steep, rough channels: 1. Stability analysis. *Water Resources Research, 34*(12), 3635-3648. doi:https://doi.org/10.1029/98WR02339

Games, P. A., Keselman, H. J., & Clinch, J. J. (1979). Tests for homogeneity of variance in factorial designs. *Psychological Bulletin*, 86(5), 978–984. https://doi.org/10.1037/0033-2909.86.5.978

Golly, A., Turowski, J. M., Badoux, A., & Hovius, N. (2019). Testing models of step formation against observations of channel steps in a steep mountain stream. *Earth Surface Processes and Landforms, 44*(7), 1390-1406. doi:https://doi.org/10.1002/esp.4582

Gonzalez, R. L., & Pasternack, G.B. (2015). Reenvisioning cross-sectional at-a-station hydraulic geometry as spatially explicit hydraulic topography. *Geomorphology*, 246: 394–406. http://dx.doi.org/10.1016/j.geomorph.2015.06.024

Grant, G. E., & Swanson, F. J. (1995). Morphology and Processes of Valley Floors in Mountain Streams, Western Cascades, Oregon *Natural and Anthropogenic Influences in Fluvial Geomorphology* (pp. 83-101): American Geophysical Union.

Grant, G. E., Swanson, F. J., & Wolman, M. G. (1990). Pattern and origin of stepped-bed morphology in high-gradient streams, Western Cascades, Oregon. *GSA Bulletin, 102*(3), 340-352. doi:10.1130/0016-7606(1990)102<0340:PAOOSB>2.3.CO;2

Guillon, H., Byrne, C. F., Lane, B. A., Sandoval Solis, S., & Pasternack, G. B. (2020). Machine Learning Predicts Reach-Scale Channel Types From Coarse-Scale Geospatial Data in a Large River Basin. *Water Resources Research, 56*(3), e2019WR026691. doi:https://doi.org/10.1029/2019WR026691

Halwas, K. L., & Church, M. (2002). Channel units in small, high gradient streams on Vancouver Island, British Columbia. *Geomorphology, 43*(3), 243-256. doi:https://doi.org/10.1016/S0169-555X(01)00136-2

Harrison, L. R., & Keller, E. A. (2007). Modeling forced pool–riffle hydraulics in a boulder-bed stream, southern California. *Geomorphology, 83*(3), 232-248. doi:https://doi.org/10.1016/j.geomorph.2006.02.024

Hassan, M. A., Radić, V., Buckrell, E., Chartrand, S. M., & McDowell, C. (2021). Pool-riffle adjustment due to changes in flow and sediment supply. *Water Resources Research*, 57, 2020WR028048. https://doi.org/10.1029/2020WR028048

Hawkins, C. P., Kershner, J. L., Bisson, P. A., Bryant, M. D., Decker, L. M., Gregory, S. V., . . . Young, M. K. (1993). A Hierarchical Approach to Classifying Stream Habitat Features. *Fisheries, 18*(6), 3-12. doi:10.1577/1548-8446(1993)018<0003:AHATCS>2.0.CO;2

Helm, C., Hassan, M. A., and Reid, D. (2020). Characterization of morphological units in a small, forested stream using close-range remotely piloted aircraft imagery, *Earth Surf. Dynam.*, 8, 913–929, https://doi.org/10.5194/esurf-8-913-2020

Holm, S. (1979). A Simple Sequentially Rejective Multiple Test Procedure. *Scandinavian Journal of Statistics, 6*(2), 65-70.

James, L. A., Harbor, J., Fabel, D., Dahms, D., & Elmore, D. (2002). Late Pleistocene Glaciations in the Northwestern Sierra Nevada, California. *Quaternary Research*, 57(3), 409-419. https://doi.org/10.1006/qres.2002.2335.

James, L.A. (2004), Tailings fans and valley-spur cutoffs created by hydraulic mining. *Earth Surf. Process. Landforms*, 29: 869-882. https://doi.org/10.1002/esp.1075

James, L. A. (2005). Sediment from hydraulic mining detained by Englebright and small dams in the Yuba basin. *Geomorphology*, 71(1–2), 202-226. doi:https://doi.org/10.1016/j.geomorph.2004.02.016

Jowett, I. G. (1993). A method for objectively identifying pool, run, and riffle habitats from physical measurements. *New Zealand Journal of Marine and Freshwater Research*, 27:2, 241-248, DOI: 10.1080/00288330.1993.9516563

Kasprak, A., Hough-Snee, N., Beechie, T., Bouwes, N., Brierley, G., Camp, R., . . . Wheaton, J. (2016). The Blurred Line between Form and Process: A Comparison of Stream Channel Classification Frameworks. *PLOS ONE, 11*(3), e0150293. doi:10.1371/journal.pone.0150293

Lai, Y. G. (2008). *"SRH-2D version 2: Theory and User's Manual Sedimentation and River Hydraulics – Two-Dimensional River Flow Modeling".* Retrieved from U.S. Department of the Interior, Bureau of Reclamation, Technical Service Center, Sedimentation and River Hydraulics Group. Denver, Colorado.: https://www.usbr.gov/tsc/techreferences/computer%20software/models/srh2d/index.html

Lane, B., Guillon, H., Byrne, C., Pasternack, G. B., Kasprak, A., & Sandoval-Solis, S. (2022). Channel-reach morphology and landscape properties are linked across a large

heterogeneous region. *Earth Surface Processes and Landforms, 47*(1), 257-274. doi:https://doi.org/10.1002/esp.5246

Lane, S. N., & Richards, K. S. (1997). Linking River Channel Form and Process: Time, Space and Causality Revisited. *Earth Surf. Process. Landforms*, 22: 249-260. https://doi.org/10.1002/(SICI)1096-9837(199703)22:3<249::AID-ESP752>3.0.CO;2-7

Legleiter, C. J., Roberts, D. A., Marcus, W. A., & Fonstad, M. A. (2004). Passive optical remote sensing of river channel morphology and in-stream habitat; physical basis and feasibility. *Remote Sensing of Environment, 93*(4), 493-510. doi:http://dx.doi.org/10.1016/j.rse.2004.07.019

Leopold, L. B., & Wolman, M. G. (1957). River channel patterns: Braided, meandering, and straight (282B). Retrieved from Washington, D.C.: http://pubs.er.usgs.gov/publication/pp282B

Lisle, T. E., Nelson, J. M., Pitlick, J., Madej, M. A., & Barkett, B. L. (2000). Variability of bed mobility in natural, gravel-bed channels and adjustments to sediment load at local and reach scales. *Water Resources Research, 36*(12), 3743-3755. doi:10.1029/2000WR900238

MacWilliams, M. L., Wheaton, J. M., Pasternack, G. B., Street, R. L., & Kitanidis, P. K. (2006). Flow convergence routing hypothesis for pool-riffle maintenance in alluvial rivers. *Water Resour. Res., 42*, W10427.

Mahdade, M., Le Moine, N., Moussa, R., Navratil, O., & Ribstein, P. (2020). Automatic identification of alternating morphological units in river channels using wavelet analysis and ridge extraction. *Hydrol. Earth Syst. Sci., 24*(7), 3513-3537. doi:10.5194/hess-24-3513-2020

Marcus, W. A., Legleiter, C. J., Aspinall, R. J., Boardman, J. W., Crabtree, R. L. (2003). High spatial resolution hyperspectral mapping of in-stream habitats, depths, and woody debris in mountain streams. *Geomorphology*, 55, 1-4, 363-380. https://doi.org/10.1016/S0169-555X(03)00150-8

Montgomery, D. R., & Buffington, J. M. (1997). Channel-reach morphology in mountain drainage basins. *Geological Society of America Bulletin, 109*(5), 596-611. doi:10.1130/0016-7606(1997)109<0596:CRMIMD>2.3.CO;2

Montgomery, D. R., Buffington, J. M., Smith, R. D., Schmidt, K. M., & Pess, G. (1995). Pool Spacing in Forest Channels. *Water Resources Research, 31*(4), 1097-1105. doi:https://doi.org/10.1029/94WR03285

Morris, H. (1959). Design methods for flow in rough channels. *Proc. ASCE, Journal of Hydraulics Division, 85*((HY7)), 43-62.

Nardini, A., Yépez, S., Mazzorana, B., Ulloa, H., Bejarano, M. D., Laraque, A. (2020). A Systematic, Automated Approach for River Segmentation Tested on the Magdalena River (Colombia) and the Baker River (Chile). *Water*, 12(10):2827. https://doi.org/10.3390/w12102827

Palucis, M. C., & Lamb, M. P. (2017). What controls channel form in steep mountain streams? *Geophysical Research Letters, 44*(14), 7245-7255. doi:https://doi.org/10.1002/2017GL074198

Pasternack, G. B., Baig, D., Weber, M. D., & Brown, R. A. (2018a). Hierarchically nested river landform sequences. Part 1: Theory. *Earth Surface Processes and Landforms, 43*(12), 2510-2518. doi:https://doi.org/10.1002/esp.4411

Pasternack, G. B., Baig, D., Weber, M. D., & Brown, R. A. (2018b). Hierarchically nested river landform sequences. Part 2: Bankfull channel morphodynamics governed by valley nesting structure. *Earth Surface Processes and Landforms, 43*(12), 2519-2532. doi:https://doi.org/10.1002/esp.4410

Pasternack, G. B., Ellis, C. R., Leier, K. A., Vallé, B. L., & Marr, J. D. (2006). Convergent hydraulics at horseshoe steps in bedrock rivers. *Geomorphology, 82*(1), 126-145. doi:https://doi.org/10.1016/j.geomorph.2005.08.022

Pasternack, G. B., Gore, J. L., & Wiener, J. S. (2021). Geomorphic covariance structure of a confined mountain river reveals landform organization stage threshold. *Earth Surface Processes and Landforms, 46*(13), 2582-2606. doi:https://doi.org/10.1002/esp.5195

Pasternack, G. B., & Zhang, M. (2021). River Builder User's Manual For Version 1.2.0. University of California, Davis, CA.

Peters, G. (2018). userfriendlyscience: Quantitative analysis made accessible. doi: 10.17605/osf.io/txequ (URL: https://doi.org/10.17605/osf.io/txequ), R package version 0.7.2, <URL: https://userfriendlyscience.com>.

Peterson, J.T., & Rabeni, C.F., (2001). Evaluating the Physical Characteristics of Channel Units in an Ozark Stream. *Transactions of the American Fisheries Society*, 130:5, 898-910, DOI: 10.1577/1548-8659(2001)130<0898:ETPCOC>2.0.CO;2

Polvi, L. E. (2021). Morphodynamics of boulder-bed semi-alluvial streams in northern Fennoscandia: A flume experiment to determine sediment self-organization. *Water Resources Research*, 57, e2020WR028859. https:// doi.org/10.1029/2020WR028859

Rabanaque, M. P., Martínez-Fernández, V., Calle, M., & Benito, G. (2022). Basin-wide hydromorphological analysis of ephemeral streams using machine learning algorithms. *Earth Surface Processes and Landforms*, 47(1), 328– 344. Available from: https://doi.org/10.1002/esp.5250

Radecki-Pawlik, A. (2002). Bankfull discharge in mountain streams: theory and practice. *Earth Surface Processes and Landforms, 27*(2), 115-123. doi:10.1002/esp.259

Richards, K. S. (1976a). Channel width and the riffle-pool sequence. *Geological Society of America Bulletin, 87*(6), 883-890. doi:10.1130/0016-7606(1976)87<883:cwatrs>2.0.co;2

Richards, K.S. (1976b). The morphology of riffle-pool sequences. Earth Surf. Process., 1: 71-88. https://doi.org/10.1002/esp.3290010108

Saletti, M., & Hassan, M. A. (2020). Width variations control the development of grain structuring in steep step-pool dominated streams: insight from flume experiments. *Earth Surface Processes and Landforms, 45*(6), 1430-1440. doi:https://doi.org/10.1002/esp.4815

Sawyer, A. M., Pasternack, G. B., Moir, H. J., & Fulton, A. A. (2010). Riffle-pool maintenance and flow convergence routing observed on a large gravel-bed river. *Geomorphology, 114*(3), 143-160. doi:10.1016/j.geomorph.2009.06.021

Strom, M. A., Pasternack, G. B., & Wyrick, J. R. (2016). Reenvisioning velocity reversal as a diversity of hydraulic patch behaviours. *Hydrological Processes, 30*(13), 2348-2365. doi:10.1002/hyp.10797

Szabó, C. Z., Mikita, T., Négyesi, G., Varga, O. G., Burai, P., Takács-Szilágyi, L., & Szabó, S. (2020). Uncertainty and Overfitting in Fluvial Landform Classification Using Laser Scanned Data and Machine Learning: A Comparison of Pixel and Object-Based Approaches. *Remote Sensing*, 12, no. 21: 3652. https://doi.org/10.3390/rs12213652

Thompson, C. J., Croke. J., Ogden, R., & Wallbrink, P. (2006). A morpho-statistical classification of mountain stream reach types in southeastern Australia. *Geomorphology*, 81 (1-2), 43-65. https://doi.org/10.1016/j.geomorph.2006.03.007

Thompson, D. M. (2011). The velocity-reversal hypothesis revisited. *Progress in Physical Geography, 35*(1), 123-132. doi:doi:10.1177/0309133310369921

Thompson, D. M. (2012). The challenge of modeling pool–riffle morphologies in channels with different densities of large woody debris and boulders. *Earth Surface Processes and Landforms, 37*(2), 223-239. doi:10.1002/esp.2256

Thompson, D.M. (2018). Pool-riffle Sequences. *Reference Module in Earth Systems and Environmental Sciences*. https://doi.org/10.1016/B978-0-12-409548-9.11029-2.

Thompson, D. M., & Fixler, S. A. (2017). Formation and maintenance of a forced pool-riffle couplet following loading of large wood. *Geomorphology, 296*, 74-90. doi:https://doi.org/10.1016/j.geomorph.2017.08.030

Turowski, J.M., Badoux, A., Leuzinger, J. & Hegglin, R. (2013). Large floods, alluvial overprint, and bedrock erosion. *Earth Surf. Process. Landforms*, 38: 947-958. https://doi.org/10.1002/esp.3341

Valle, B. L., & Pasternack, G. B. (2006). Field mapping and digital elevation modelling of submerged and unsubmerged hydraulic jump regions in a bedrock step-pool channel. *Earth Surface Processes and Landforms, 31*(6), 646-664. doi:10.1002/esp.1293

van Rooijen, E., Vanzo, D., Vetsch, D. F., Boes, R. M., & Siviglia, A. (2021). Enhancing an unsupervised clustering algorithm with a spatial contiguity constraint for river habitat analysis. *Ecohydrology, 14*(4), e2285. doi:https://doi.org/10.1002/eco.2285

Wang, J., Hassan, M. A., Saletti, M., Chen, X., Fu, X., Zhou, H., & Yang, X. (2021). On How Episodic Sediment Supply Influences the Evolution of Channel Morphology, Bedload Transport and Channel Stability in an Experimental Step-Pool Channel. *Water Resources Research, 57*(7), e2020WR029133. doi:https://doi.org/10.1029/2020WR029133

Wheaton, J. M., Fryirs, K. A., Brierley, G., Bangen, S. G., Bouwes, N., & O'Brien, G. (2015). Geomorphic mapping and taxonomy of fluvial landforms. *Geomorphology, 248*(Supplement C), 273-295. doi:https://doi.org/10.1016/j.geomorph.2015.07.010

White, J. Q., Pasternack, G. B., & Moir, H. J. (2010). Valley width variation influences riffle–pool location and persistence on a rapidly incising gravel-bed river. *Geomorphology, 121*(3–4), 206-221. doi:https://doi.org/10.1016/j.geomorph.2010.04.012

Whiting, P. J., & Bradley, J. B. (1993). A process-based classification system for headwater streams. *Earth Surface Processes and Landforms, 18*(7), 603-612. doi:https://doi.org/10.1002/esp.3290180704

Wiener, J., & Pasternack, G.B. (2016). Accretionary Flow Analysis- Yuba River from New Bullards Bar to Colgate Powerhouse. Prepared for Yuba County Water Agency. University of California, Davis, CA. Retrieved from http://pasternack.ucdavis.edu/research/projects/ncrs/mountain-river-eco-geo

Wiener, J. S., & Pasternack, G. B. (2019). Diversity and organization of mountain river morphological units challenge conceptions of riffle-pool, step-pool, and cascade channel types. Abstract EP51E-2129 presented at 2019 Fall Meeting, AGU, San Francisco, CA, 9-13 Dec.

Wiener, J. S., & Pasternack, G. B. (2022). Scale dependent spatial structuring of mountain river large bed elements maximizes flow resistance. Accepted. *Geomorphology*.

Wilkinson, S. N., Rutherfurd, I. D., & Keller, R. J. (2008). An experimental test of whether bar instability contributes to the formation, periodicity and maintenance of pool–riffle sequences. *Earth Surface Processes and Landforms, 33*(11), 1742-1756. doi:https://doi.org/10.1002/esp.1645

Williams, G. P. (1978). Bank-full discharge of rivers. *Water Resour. Res*. 14(6), 1141– 1154, doi:10.1029/WR014i006p01141.

Wolman, M. G. (1954). A method of sampling coarse river-bed material. *Eos, Transactions American Geophysical Union, 35*(6), 951-956. doi:https://doi.org/10.1029/TR035i006p00951

Wolman, M. G., & Eiler, J. (1958). Reconnaissance study of erosion and deposition produced by the flood of August 1955 in Connecticut. *Eos, Transactions American Geophysical Union, 39*(1), 1-14. doi:https://doi.org/10.1029/TR039i001p00001

Woodworth, K. A., & Pasternack, G. B. (2022). Are dynamic fluvial morphological unit assemblages statistically stationary through floods of less than ten times bankfull discharge? *Geomorphology, 403*, 108135. doi:https://doi.org/10.1016/j.geomorph.2022.108135

Woznicki, S. A., Baynes, J., Panlasigui, J., Mehaffey, M., & Neale, A. (2019). Development of a spatially complete floodplain map of the conterminous United States using random forest. *Science of the Total Environment*, 647: 942-953. https://doi.org/10.1016/j.scitotenv.2018.07.353

Wyrick, J. R., & Pasternack, G. B. (2012). *Landforms of the Lower Yuba River.* Prepared for the Yuba Accord River Management Team. University of California, Davis. Retrieved from: http://www.yubaaccordrmt.com/Annual%20Reports/Mapping%20and%20Modeling/LYR%20Landforms%20Report%20%285-9-2012%29.pdf

Wyrick, J. R., & Pasternack, G. B. (2014). Geospatial organization of fluvial landforms in a gravel–cobble river: Beyond the riffle–pool couplet. *Geomorphology, 213*(Supplement C), 48-65. doi:https://doi.org/10.1016/j.geomorph.2013.12.040

Wyrick, J. R., Senter, A. E., & Pasternack, G. B. (2014). Revealing the natural complexity of fluvial morphology through 2D hydrodynamic delineation of river landforms. *Geomorphology, 210*, 14-22. doi:10.1016/j.geomorph.2013.12.013

Yuba County Water Agency (YCWA). (2012). *Model Report. Appendix A. Hydrology Report. Yuba River Development Project FERC Project No. 2246*. Marysville, California: Yuba County Water Agency.

YCWA. (2013). *Technncal Memorandum 1-1. Channel Morphology Upstream of Englebright Reservoir. Yuba River Development Project FERC Project No. 2246.* Retrieved from http://www.ycwa-relicensing.com/Technical%20Memoranda/Forms/AllItems.aspx

Zimmermann, A. E., Church, M., & Hassan, M. A. (2008). Identification of steps and pools from stream longitudinal profile data. *Geomorphology, 102*(3), 395-406. doi:https://doi.org/10.1016/j.geomorph.2008.04.009

APPENDIX 1. Supporting Information for Scale dependent spatial structuring of mountain river large bed elements maximizes flow resistance

This appendix provide supplemental materials that include information on the following topics:

- Details on topographic and bathymetric data collection, processing, and mapping (A.1.3.1);
- Details of large bed element (LBE) mapping procedure including performance metrics, extraction algorithms, post-extraction filtering, and geometric assessment (A.1.3.3);
- Details of two-dimensional hydrodynamic modeling including model selection, parametrization and calibration, model validation, and model sensitivity to roughness parameterization (A.1.3.4);
- Details of LBE spatial analysis including cross-section polygon creation and path-based approach for streamwise spacing calculations (A.1.3.5)
- Additional LBE mapping results (A.1.4.1);
- Additional LBE spacing analysis results (A.1.4.3);
- Additional hydrodynamic regime comparison analysis results and discussion (4.4 and A.1.5.4); and
- References

The organization of this appendix uses the same outline and headings of the chapter to which this supplements. Subject headings followed by the word “none” indicate no supplemental information is provided for that section.

A.1.1 Introduction

Table A1.1. Summary of LBE influences on river channels and landscapes.

Topic	Summary	Selected references
Hydraulics and hydrodynamics	LBEs are a primary source of flow resistance in mountain rivers. Locally, LBEs generate complex wake and vortex structures that cause deviations from idealized logarithmic vertical velocity profiles. Collectively, LBEs act to influence flow patterns and the spatial distribution of hydraulic properties (depth, velocity, bed shear stress) that govern other fluvial processes such as sediment transport.	Baiamonte & Ferro, 1997; Bathurst, 1978, 1985, 1987; Byrd et al., 2000; Canovaro et al., 2007; Fang et al., 2017; Ferguson et al., 2017; Ferro, 1999; Gippel et al., 1996; Gomez, 1993; Groom & Friedich, 2019; Hardy et al., 2009; Lacey & Roy, 2008; Lamarre & Roy, 2005; Monsalve et al., 2017; Morris, 1959; Pagliara et al., 2008; Schneider et al., 2015a, 2015b
Sediment transport and retention dynamics	LBEs influence localized patterns of erosion and deposition. This in-turn effects the granular structure of the bed and the formation, stability, and sedimentological characteristics of sediment patches. The presence of LBEs can enhance bed stability through interlocking, imbrication, and hiding effects that therein influence the entrainment and transport of adjacent grains and patches. By extracting energy from the flow in the form of resistance and stabilizing the bed LBEs regulate the storage and export of sediments. So called LBE 'sticky spots' can even provide potential for long term storage (1000's of years) which contrasts with traditional views of mountain rivers as conveyor belts for sediment transport. Collectively, LBE interactions aggregate to exert primary control of sediment storage within and fluxes of sediment out of mountain rivers systems.	Billi, 1988; Faustini & Jones, 2003; Ghilardi et al., 2014; Kirchner et al., 1990; Lancaster et al., 2001; Laronne et al., 2001; Nitsche et al., 2011; Paola et al., 1992; Paola & Seal, 1995; Papanicolaou & Tsakiris, 2017; Reid & Hassan, 1992; Sear, 1992, 1995, 1996; Shamloo et al., 2001; Sutfin & Wohl, 2019; Thompson, 2001, 2008; Thompson et al., 2016; Yager et al., 2007, 2012
Channel stability and organization of fluvial landforms	LBEs comprise a key constituent of coarse-bedforms including stone clusters, transverse ribs, stone cells, and alluvial steps. These bedforms all tend to increase channel resistance which is hypothesized to directly correlate with conditions of maximum bed stability. LBEs specifically promote stability through interlocking and imbrication with surrounding substrates. Evidence suggests LBEs in natural rivers may organize in order to maximize flow resistance and promote channel stability.	Brayshaw, 1985; Buffington et al., 2002; Church et al., 1998; Church & Zimmermann, 2007; Grant et al., 1990; Hassan & Reid, 1990; Madej, 2001; Nowell & Church, 1979; Zimmermann & Church, 2001
Landscape evolution	LBEs are a product of landscape evolutions processes but also have direct autogenic feedbacks on channel and hillslope evolution due to their ability to mediate fluvial incision and shape channel morphology.	Attal et al., 2015; Benda & Dunne, 1997; Glade et al., 2019; Johnson et al., 2009; Shobe et al., 2016; Sklar & Dietrich, 2004; Turowski et al., 2007, 2008
Morphodynamic processes	Through their ability to steer the flow, influence hydraulics and sediment transport processes, regulate landscape evolution, and self-organize LBEs have first order control on the morphodynamic evolution of rivers channels.	MacKenzie & Eaton, 2017; Piedra et al. 2012; Tan & Curran, 2012; Williams et al., 2019; Wittenberg & Newson, 2005

Table A1.2. Existing definitions of LBEs.

Reference	LBE definition
Grant et al., 1990	Clasts with diameters on the same order as the depth of the bankfull channel; wood not included.
Grant et al., 1990	Clasts equaling or exceeding the 90th percentile of the bed material; wood not included.
Hassan et al., 2019	Clasts equaling or exceeding the 95th percentile of the bed material; wood not included.
Ferguson et al., 2017; Thompson, 2008	Clasts with b-axis equal to or greater than 0.256 m; wood not included.
Finnegan et al., 2019	Clasts with planform diameter equal to or greater than 0.3 m; wood not included.
Benda, 1990; Nitsche et al., 2011; Schneider et al., 2015a	Clasts with b-axis equal to or greater than 0.5 m; wood not included.
Shobe et al., 2016	Clasts with b-axis equal to or greater than 1 m; wood not included.
Grant & Swanson, 1995	Clasts that protrude from an otherwise relatively level surface by at least 1.5 m; wood not included.
Lisle, 1986; Thompson, 2001	Boulders or protrusions with the longest dimension larger than one-third bankfull width; wood included.
Weichert, 2006; (see also Bathurst, 1985; Shamloo et al., 2001)	Review of roughness length scale definitions where 'large-scale' features are generally defined as having relative submergence[a] values < 3; wood not included.
Fang et al., 2017; Monsalve et al., 2017; Papanicolaou & Tsakiris, 2017	Relative submergence threshold value of 3.5 used to define a 'low relative submergence regime' for replicating flows around LBE-like objects in flumes; wood not included.

[a]Relative submergence defined as ratio of flow depth to LBE diameter.

A.1.2 Study River Segment

None.

A.1.3 Methods

A.1.3.1 Topo-bathymetric mapping

This was the first time a detailed topographic map has been produced of the Yuba River between New Bullards Bar Dam and Colgate Powerhouse (study site). Position of the aircraft performing ALS collection was measured twice per second (2 Hz) by an onboard differential GPS

unit, and aircraft attitude was measured 200 times per second (200 Hz) as pitch, roll and yaw (heading) from an onboard inertial measurement unit (IMU). To allow for post-processing correction and calibration, aircraft and sensor position and attitude data are indexed by GPS time. The average overall ground classified density including bathymetric bottom was 3.96 points/m^2, while the bathymetric bottom return density alone was 2.30 points/m^2. Average discharge over this time period was estimated to be 1.19 m^3/s at the downstream study site boundary, which is hereafter referred to as the 'lidar baseline' flow condition.

Review of the initial bare-earth and sub-aqueous bathymetry lidar files (ground points) from Quantum Spatial indicated a significant number of true ground points associated with boulders, exposed bedrock, and other high variability terrain features had been erroneously rejected (i.e., Type I errors). Using a publically available ground classification algorithm (Isenburg, 2016) a procedure was developed to reclassify and reincorporate these Type I errors back into the ground point dataset (Wiener & Pasternack, 2016). The objective of this process was balancing proper classification of previous Type I errors without introducing new Type II errors (e.g. incorrectly classified ground points). Following processing, the revised lidar dataset was subjected to significant vetting through visualization methods and hand editing to remove lingering classification errors. The reclassification procedure increased average point density of the final ground point dataset from 9.0 to 13.9 pts/m^2 (Wiener & Pasternack, 2016).

In addition to (mis)classification issues, NIR and Green lidar have inherent coverage and water-depth penetration limitations. Despite overall excellent lidar penetration and coverage, the survey did not yield ground returns for ~ 40,873 m^2 of in-water areas representing ~ 22% of the open water area present at the time of the survey. Supplemental bathymetric observations at three locations within the study site were made between July 8 and 9, 2015 by kayak using a single-

beam echosounder coupled to a real-time kinematic global positioning system (RTK GPS) covering an area of ~13,530 m^2 (~ 33% of area missing data).

Limited access and rugged terrain within the river canyon largely prevented kayak and foot access to much of the remaining areas lacking bathymetric data. To fill these data gaps an approach developed by Legleiter et al. (2004) linking known water depths to an image-derived quantity 'X', defined as the natural logarithm of two multi-spectral imagery wavelengths, was used to predict water depths and derive additional bathymetric data (depth-derived data; Wiener & Pasternack, 2016). Source imagery for depth-to-X statistical models was obtained from the National Agricultural Inventory Program (NAIP). The source imagery, dated from 2014, was close to the date of lidar acquisition, and the 1-m resolution imagery included three spectral bands; green (460 nm, width 60 nm); red (635 nm, width 50 nm), and blue (560nm, width 50nm). Rasters of lidar intensity returns were used to georeference NAIP imagery with other topographic/bathymetric data to ensure proper alignment of depth-derived data.

Depth data for training depth-to-X statistical models was derived from water surface elevations (WSE) obtained during the lidar acquisition and final lidar ground points such that depths were approximated as: WSE minus ground surface elevation. Edge effects were minimized by only selecting points at least 2 meters from the georeferenced imagery's waters' edge. The training dataset consisted of 137,022 estimated depth points. For each depth point, underlying imagery band wavelength values were sampled and statistical relationships (linear and/or polynomial regression models) were created relating depth to all possible band ratio combinations (i.e., X values). Statistical models were evaluated based on goodness of fit criteria such as R^2 values. Models were also tested in a predictive mode against an independent depth dataset (i.e. the single-beam soundings) using three performance metrics: (i) lowest root mean square error

(RMSE); (ii) linear regression slope between predicted depths and observed sounding depths closest to unity; and (iii) R^2 between predicted depths and observed sounding depths closest to unity.

The depth-to-X method has typically been applied to lowland, shallow, relatively clear flowing, gravel-bottom rivers with higher resolution imagery (Legleiter et al., 2004). Locations within the study site where the method was implemented were characterized by complex and heterogeneous terrain and substrates, varying water turbidity, and generally high depths. Due to differences in statistical model performance, the final mapping approach included a suite of depth-to-X predictive models spatially distributed along the river. Use of one model over another was based on an analysis of localized fit using the same metrics above (Wiener & Pasternack, 2016). A total of 168,965 depth-derived ground points covering an area of ~ 15,783 m^2 were predicted and included in the final topographic map (~ 39% of area missing data). To fill remaining locations lacking topographic data all available data sources were used to strategically place "augmented points". Ground elevations at these locations were assigned manually based on best professional judgement and neighboring points. A total of 2,182 augmented ground points, many analogous to 'breaklines', were manually input and included in the final topographic map. Merging all data sources resulted in a total of 69,784,144 topographic points. Of these 21,279,867 points at an average spacing of 0.25 m and average density of ~ 16 pts/m^2 were located within the river corridor.

Lidar accuracy was assessed independently based on estimates of absolute accuracy, the error of the lidar derived ground surface compared to a more accurate survey method. Absolute accuracy was computed by comparison of the lidar ground surface to 23 ground check points and 24 bathymetric check points from an RTK-GPS survey. The Fundamental Vertical Accuracy

(FVA), a measure of error reported at the 95% confidence level (i.e. 1.96*RMSE), for ground points and bathymetric points were 0.037 m and 0.117 m, respectively. A full account of the mapping efforts, accuracy of mapping data, and post-processing of data is detailed in Wiener and Pasternack (2016).

A WSE point dataset was also provided by Quantum Spatial. Review of the WSE data indicated the presence of numerous erroneous points. Spuriously high and low water surface points were manually removed resulting in a final dataset of 147,644 points representing the lidar baseline flow condition water surface (Wiener & Pasternack, 2016). Triangular irregular network (TIN) based interpolation methods were used to generate a continuous surface from the verified WSE points where sufficient data was present.

A.1.3.2 Observed LBE dataset

None.

A.1.3.3 LBE mapping

A.1.3.3.1 Roughness surface model generation and testing question 1

This section presents additional details on the procedure for mapping LBEs from 3D topographic point clouds. In the procedure's first step, the "lasground_new.exe" ground classification algorithm of Isenburg (2016) was used to create a series of smoothed digital terrain models (DTMs) needed for creating roughness surface models (RSMs). As discussed in the main text the algorithm applies an adaptive TIN approach to iteratively classify ground points from an unclassified point cloud and requires input of a point cloud and six user-defined parameters. The approach for setting the algorithm's parameters is described below, focusing on the spike, offset, down-spike, and step parameters as these were found to disproportionally influence the algorithm's

performance.

To constrain the range of ground classification algorithm parameter values an initial 'larger' parameter space was informed by several physically based metrics. For example, roughness length scales such as a representative grain size or a minimum LBE height were considered when setting the range for spike, offset, and down-spike parameter values. These parameters control if points are classified as ground or removed from the algorithm's iteratively generated ground surfaces. Summarily, the specified length scale(s) define thresholds for ground point classification based on how much points extend below or protrude above an otherwise smooth but variable bed surface. Previously reported estimates of the study site's D_{50} and D_{16} values (D is particle diameter and the subscript is the percent of particles finer) of 0.128-0.256 m and 0.032-0.64 m, respectively, and two representative LBE sizes, 0.256 m and 0.5 m, were used to define the range of parameters (Table A1.3). The latter two values correspond to the diameter of boulders in the Udden-Wentworth scale (Wentworth, 1922) and a common length used to define LBEs (Table A1.2), respectively.

The algorithm's 'step' parameter, which controls the size of the search window used to add points to the ground surface was also informed by physical considerations. Larger window sizes function to remove increasingly larger terrain features such that cohesive terrain features bigger than the window-size are often preserved in the final ground classification. However, larger window sizes can also modify the underlying terrain through non-ground classification, especially where steep slopes or rapidly undulating terrain features are present (Zhang & Whitman, 2005). For RSM generation and LBE mapping purposes, where the goal is creating a smoothed ground surface that retains the dominant topographic features of the original ground surface, a reasonable recommendation is for window sizes to be larger than the typical planform diameter of LBEs

expected to be present or that are desired to be mapped but smaller than the expected/desired maximum LBE diameter or scale of dominate terrain features. For this study, step sizes ranged between 1.5 – 4.6 m (~3-9 DEM raster cell lengths).

Altogether, 14 unique parameter combinations were established and used to generate smoothed point clouds and associated DTMs (Table A1.3). The 14 smoothed DTMs were assessed qualitatively with *LAStools* 3D visualization software based on two visual criteria: i) removal of clearly discernable LBEs; and ii) retaining the dominant topographic character of the original ground surface (i.e., location of slope breaks, small-scale terrain undulations, meso-scale terrain features). As discussed in the main text, six DTMs were selected to create a series of unique RSMs and a binary threshold approach was used to map discrete sets of preliminary LBEs from each RSM. After assigning a random selection of 70% of the LBE_o data to a 'training' dataset the average RSM value of all raster cells located along the exterior boundary of each LBE_o polygon in the training set were calculated for each RSM, independently. The average of these values served as the vertical threshold for each RSM (Figure A.1.1). While thresholds were unique for each RSM, they were obtained through a numerically consistent approach to avoid introduction of bias.

To identify the preferred ground classification algorithm parameter combination and associated RSM, preliminary LBEs mapped from each smoothed DTM were quantitatively compared to the remaining 30% of the LBE_o data using the study's four performance metrics. Prior to conducting this analysis LBE_o training and test data subsets were compared for similarity to provide confidence that training LBE data characteristics did not differ significantly from LBE test data, and thus not bias the mapping process. Metrics selected for this comparison were LBE planform area and max RSM raster value (D_c) of each LBE in the respective datasets. Comparison

was performed using Welch's t-test and the Kolmogorov-Smirnov test. Testing concluded an inability to reject the null hypotheses that distributions of these metrics had equivalent means and came from the same family of distribution at the 95% confidence level ($p>>0.05$).

Quantitative assessment of predicted LBEs used four performance metrics. Details of each metric are described in the following paragraphs.

The first metric, Producers accuracy (PA), is the ratio of the number of predicted LBEs (N_p) spatially intersecting observed LBEs (N_o) to the number of observed LBEs:

$$PA = \frac{N_p \cap N_o}{N_o} \quad \text{(Eq. A.1.1)}$$

PA is widely applied across disciplines (Barsi et al., 2018; Labatut & Cherifi, 2011; Shao et al., 2019) and in this context simply measures the hit-rate of predicted LBEs relative to observed LBEs. Since PA does not penalize for over-mapping the metric is entirely focused on accuracy without consideration of precision or commission errors.

The next metric, Producers overlap (PO), is the ratio of the area of predicted LBEs (A_p) spatially overlapping the area of observed LBEs (A_o) to the area of observed LBEs from the set of observed LBEs that spatially intersect predicted LBEs:

$$PO = \frac{A_p \cap A_o}{A_o \in N_o \cap N_p} \quad \text{(Eq. A.1.2)}$$

This metric is simply the relative percent of total observed LBE area that is correctly predicted for the subset of observed LBEs that overlap with a predicted LBE. By constraining the denominator to only intersecting observed and predicted LBEs this metric focuses on the accuracy of how well those LBEs were predicted. Albeit similar to other metrics this formulation is believed to be unique.

Both PA and PO metrics range from 0-1 with higher values indicating better precision and

accuracy, respectively. One caveat is that both metrics benefit from more area being predicted as LBE and lack a penalty for commission errors. For example a rectangle covering the entire domain of observed LBEs would result in the max value of unity for both metrics. PO also does not penalize for omission errors and thus should be used in consideration with other metrics that do, such as PA.

Two other metrics, modified Jaccard similarity index (MJI) and missed-to-excess ratio (MER), penalize commission errors while being less sensitive to omission errors. The Jaccard similarity index is a common metric for comparing polygons that penalizes both omission and commission (Labatut & Cherifi, 2011). However, since the full set of observed LBEs was unknown the metric has been modified and is calculated as the ratio of the area of intersect between predicted LBEs and observed LBEs to the area of union between predicted LBEs and observed LBEs from the set of observed LBEs that spatially intersect predicted LBEs and the set of predicted LBEs that spatially intersect observed LBEs:

$$MJI = \frac{A_p \cap A_o}{A_p \cup A_o} \in (N_o \cap N_p \;\&\; N_p \cap N_o) \qquad \text{(Eq. A.1.3)}$$

The metric assumes that excess LBEs predicted in the vicinity of an observed LBE should be penalized. The MJI metric ranges from 0-1 with a value of unity indicating perfect mapping for the set of LBEs considered.

Lastly, MER is defined as the ratio of the area of observed LBEs less the area of intersection between observed and predicted LBEs (e.g., area of missed observed LBE mapping) to the area of predicted LBEs less the area of intersection between predicted and observed LBEs (e.g., area of excess predicted LBE mapping):

$$MER = \frac{A_o - A_p \cap A_o}{A_p - A_o \cap A_p} \qquad \text{(Eq. A.1.4)}$$

Here it is assumed that a greater extent of predicted LBE mapping should yield a high probability

of overlap with observed LBEs and penalizes the amount of observed LBE area that is missed scaled by excess predicted LBE mapping. The MER metric ranges from 0 - ∞. Larger MER values are presumed better for several reasons. First, it is more ideal for only small areas of observed LBEs to be missed resulting is less variation in the numerator between predictions. Second, preliminary analysis suggests excess LBE prediction tends to be much greater than missed area (denominator >> numerator) across predictions and excess area is more variable between predictions. Thus higher MER values are associated with less missed mapping per unit excess mapping and functionally MER values do not exceed unity under the above described circumstances. Though similar to miss rate we are not aware of other studies using the MER metric.

Table A1.3. Parameters and qualitative assessment of 14 smoothed DTMs. Selected DTMs marked with *.

ID	Step (m)	Bulge (m)	Spike (m)	Down spike (m)	Offset (m)	Intensity	Qualitative finding (LBE removal; Terrain modification)[ab]
P-LBE-1*	3.05	0.03	0.15	0.30	0.15	extra	Excellent; Moderate
P-LBE-2	1.52	0.03	0.15	0.30	0.15	extra	Moderate; Moderate
P-LBE-3*	4.57	0.03	0.15	0.30	0.15	extra	Excellent; Moderate
P-LBE-4	3.05	0.03	0.15	0.0	0.15	extra	Poor; Moderate
P-LBE-5	3.05	0.30	0.15	0.30	0.15	extra	Moderate; Moderate
P-LBE-6	3.05	0.03	0.15	0.30	0.15	hyper	Moderate; Moderate
P-LBE-7	3.05	0.03	0.50	0.25	0.50	extra	Poor; Excellent
P-LBE-8	3.05	0.03	0.25	0.25	0.25	extra	Poor; Excellent
P-LBE-9	3.05	0.03	0.13	0.50	0.13	extra	Moderate; Moderate
P-LBE-10*	3.05	0.03	0.13	0.25	0.13	extra	Excellent; Moderate
P-LBE-11*	3.05	0.03	0.03	0.13	0.03	extra	Excellent; Moderate
P-LBE-12*	3.05	0.03	0.06	0.13	0.06	extra	Excellent; Moderate
P-LBE-13*	4.57	0.03	0.06	0.13	0.06	extra	Excellent; Poor
P-LBE-14	4.57	0.03	0.13	0.25	0.13	extra	Excellent; Poor

[a]LBE removal performance increases from: poor to moderate to excellent.
[b]Terrain modification performance increases from: poor to moderate to excellent.

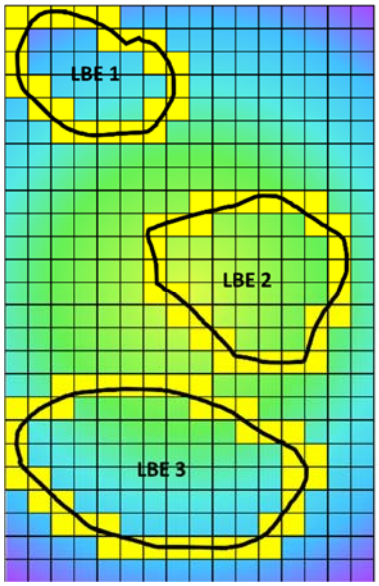

LBE ID	Average LBE boundary RSM
1	3.1
2	2.2
3	4.4
Vertical threshold (average)	3.23

Figure A.1.1. Conceptual depiction of how vertical threshold were calculated from LBE_o training data. The training data was constant but RSM heights would vary between smoothed DTMs.

A.1.3.3.2 LBE extraction and accuracy testing for question 1

Approaches for LBE extraction tested in this study were informed by methods for mapping tree-crowns from remotely-sensed imagery and/or topographic data. Tree-crown mapping methods can be broadly classified into those that apply mathematical morphology (Andersen et al., 2001; Koukoulas & Blackburn, 2005), object-based image analysis (Jakubowski et al., 2013; Sullivan et al., 2009), edge-detection, local-maxima filtering and detection (Argamosa et al., 2016; Popescu & Wynne, 2004), clustering (Culvenor, 2002; Morsdorf et al., 2004), valley-following (Leckie et al., 2003), region-growing (Barnes et al., 2017; Dalponte et al., 2019), watershed segmentation (Chen et al., 2006; Koch et al., 2006; Kwak et al., 2007), and graph based (Strîmbu & Strîmbu, 2015) approaches. Nearly all approaches use a canopy height model (CHM) as a starting point. Smoothing CHMs with low-pass mean or Gaussian filters prior to crown mapping is also typical (Kwak et al., 2007; Chen et al., 2006). Crown mapping approaches differ in their computational expense, number of parameters, and public availability. Given the goal of mapping LBEs at the

river segment scale, computational efficiency was a necessary consideration when testing approaches. Reproducibility using open-source software was also favored. Details on the five LBE extraction approaches used in this study are provided in the following paragraphs.

The simplest and most computationally efficient strategies, (i) RSM with vertical threshold and (ii) Gaussian filtered RSM with vertical threshold, involved applying a vertical threshold to the RSM or filtered RSM. Areas above the threshold were considered LBE and those below were masked out as non LBE. This is similar to Otsu's (1979) binary threshold approach, the only difference being how thresholds were specified. Conceptually, vertical thresholds could be data-driven based on LBE training data, optimized through comparison with LBE testing data using the study's performance metrics, based on representative length scales, be statistical (*sensu* Otsu, 1979), or set qualitatively. For approach (i) 12 thresholds were tested (Table A1.4). Eleven values between 0.1524-0.4572 m set in increments of 0.03048 m were tested as these covered a wide range of reasonable LBE length scales. The final threshold value of 0.283 m was derived from averaging the set of averaged RSM values for cells along the boundary of each observed LBE polygon (Figure A.1.1).

For approach (ii) three parameters were needed: two for the Gaussian filter (standard deviation of kernel [σ] and window-size) and the vertical threshold. A total of six parameter combinations were tested using three different sigma values (0.152, 0.305, and 1.524 m), two different window sizes (3 cells and 5 cells), and vertical thresholds calculated as the average of all averaged Gaussian filtered RSM values for cells along the boundary of each observed LBE polygon (Table A1.4). When applying a Gaussian filter to CHMs, Dralle and Rudemo (1996) found tree-crown mapping to be insensitive to the sigma parameter but that window-size did influence performance due to the effect on the smoothed CHMs. For tree-crown mapping they

recommended window sizes should be less than the crown size of the smallest tree of interest. Gaussian filtering was done in R code using the 'spatialEco' package (Evans, 2019). Raster masking using the vertical thresholds for approach (i) and (ii) were done with the ArcGIS spatial analyst extension tool suite and converted to polygons using the raster to polygon tool.

Marker-controlled watershed segmentation (MCWS) approaches: (iii) RSM with MCWS and constant window-size; (iv) RSM with MCWS and variable window-size; and (v) Gaussian filtered RSM with MCWS and constant window-size, were slightly more complex and computationally intensive. All MCWS approaches involved two steps: first, markers or "LBE tops" were detected from the RSM; and second, markers were used to delineate distinct LBEs from the RSM. The number of parameters for each approach varied and are listed in Table A1.4.

Markers were retrieved from the RSM using a variable-window local-maxima filter algorithm (*sensu* Popescu & Wynne, 2004) implemented in R code using the 'ForestTools' package (Plowright & Roussel, 2020). The algorithm requires input of an RSM, a parameter controlling the minimum RSM value for a pixel to be considered a marker, and a search window size. The window-size in the algorithm can be set as a constant or vary as a function of RSM pixel value. Both constant and variable window sizes were tested. Functions to define window-size can be based on observed data and/or assumptions of idealized relationships between feature height and area (Popescu & Wynne, 2004; Chen et al., 2006). Comparing the relationship between D_c and planform area for the observed LBE data with several functions for ideal spheroid objects found over 98% of LBEs to geometrically reside in-between models for an oblate (wide) spheroid and a prolate (tall) spheroid, in the domain of spherical objects (section A.1.3.3.2.2). Therefore, a spherical model where window-size was set equal to the pixel RSM value divided by two was used to define the variable window-size (e.g., window size was set equal to the planform radius of each

potential LBE based on RSM value). In order to control for very small window sizes that would add to computational time and also be inefficient at mapping LBEs (Chen et al., 2006), a constraint was placed requiring a minimum window-size. Two minimum sizes were tested, 3 and 5 m, respectively which equated to windows with radii of ~3 and ~5 raster cells.

In order to constrain the parameter spaces of approaches (iii-v) only data-driven parameterization methods were used when specifying other input parameters. Values for the minimum RSM value for a pixel to be considered a marker were based on five calculations from the observed LBE data using different approximations for the minimum height observed features protruded above the smoothed DTM raster:

- (1) the median of the set of averaged RSM values for cells within each observed LBE polygon;
- (2) the average of the set of averaged RSM values for cells within each observed LBE polygon;
- (3) the average of the set of maximum RSM values for cells within each observed LBE polygon;
- (4) the median of the set of averaged RSM values for points generated every 0.31 m along a border line located one raster cell inward of each observed LBE polygon's border; and
- (5) the average of the set of averaged RSM values for raster cells along each observed LBE polygon's border.

Following marker identification, LBE polygons were created using a watershed segmentation function (*sensu* Beucher & Meyer, 1993) implemented in R code using the 'ForestTools' package (Plowright & Roussel, 2020). The segmentation algorithm requires input of markers, a RSM raster, and a parameter that controls the minimum RSM value for a pixel to be included in the segmentation. Values for the minimum RSM parameter were based on six

calculations using the observed LBE data to approximate the minimum value that the edge of observed features protruded above the smoothed DTM raster:

- (1) the median of the set of median values of RSM values for points generated every 0.31 m along each observed LBE polygon's border;
- (2) the median of the set of averaged RSM values for points generated every 0.31 m along each observed LBE polygon's border;
- (3) the average of the set of averaged RSM values for points generated every 0.31 m along each observed LBE polygon's border;
- (4) the median of all RSM values for points generated every 0.31 m along each observed LBE polygon's border;
- (5) the average of the set of minimum RSM values for cells along each observed LBE polygon's border; and
- (6) the average of the set of minimum RSM values for cells within each observed LBE polygon.

Ultimately, 10 parameter combinations were tested for approach (iii), two combinations for approach (iv), and 14 combinations for approach (v) (Table A1.4).

Table A1.4. Parameters for 44 predicted LBE datasets.

ID	Parameters		
(i) RSM with vertical threshold: One parameter - vertical threshold (m)			
V-1	0.152		
V-2	0.183		
V-3	0.213		
V-4	0.244		
V-5	0.274		
V-6	0.305		
V-7	0.335		
V-8	0.366		
V-9	0.396		
V-10	0.427		
V-11	0.457		
V-12	0.283		
(ii) Gaussian filtered RSM with vertical threshold: Three parameters - vertical threshold (m); σ (m); window size (# of cells)			
GV-1	0.031	0.152	3
GV-2	0.031	0.305	3
GV-3	0.031	1.524	3
GV-4	0.011	0.152	5
GV-5	0.011	0.305	5
GV-6	0.011	1.524	5
(iii) RSM with MCWS algorithm and constant window size: Three parameter - minimum marker height (m); minimum crown height (m); window size (m)[a]			
MCWS-C-1	0.283 (5)	0.033 (5)	3
MCWS-C-2	0.297 (1)	0.118 (1)	3
MCWS-C-3	0.297 (1)	0.169 (4)	3
MCWS-C-4	0.423 (2)	0.07 (6)	3
MCWS-C-5	0.423 (2)	0.169 (4)	3
MCWS-C-6	0.423 (2)	0.272 (3)	3

ID	Parameters				
MCWS-C-7	0.312 (4)	0.192 (2)	3		
MCWS-C-8	0.312 (4)	0.272 (3)	3		
MCWS-C-9	0.283 (5)	0.033 (5)	6		
MCWS-C-10	0.423 (2)	0.07 (6)	6		
(iv) RSM with MCWS algorithm and variable window size: Three parameter - minimum marker height (m); minimum crown height (m); window size function[a]					
MCWS-V-1	0.312 (4)	0.272 (3)	{3 if (RSM/2) <3; else (RSM/2)}		
MCWS-V-2	0.312 (4)	0.272 (3)	{5 if (RSM/2) <5; else (RSM/2)}		
(v) Gaussian filtered RSM with MCWS and constant window size: Five parameter - σ (m); window size (# of cells); minimum marker height (m); minimum crown height (m); window size (m)[a]					
GV-MCWS-C-1	0.152	3	0.031 (1)	0.016 (1)	0.914
GV-MCWS-C-2	0.305	3	0.027 (1)	0.019 (1)	0.914
GV-MCWS-C-3	0.305	3	0.027 (1)	0.024 (4)	0.914
GV-MCWS-C-4	0.305	3	0.043 (2)	0.024 (4)	0.914
GV-MCWS-C-5	0.914	3	0.026 (1)	0.025 (4)	0.914
GV-MCWS-C-6	0.914	3	0.042 (2)	0.025 (4)	0.914
GV-MCWS-C-7	1.524	3	0.026 (1)	0.019 (1)	0.914
GV-MCWS-C-8	0.152	5	0.011 (1)	0.006 (1)	0.914
GV-MCWS-C-9	0.305	5	0.009 (1)	0.007 (1)	0.914
GV-MCWS-C-10	0.914	5	0.008 (1)	0.007 (1)	0.914
GV-MCWS-C-11	0.914	5	0.013 (2)	0.009 (4)	0.914
GV-MCWS-C-12	0.914	5	0.02 (3)	0.009 (4)	0.914
GV-MCWS-C-13	1.524	5	0.013 (2)	0.01 (4)	0.914
GV-MCWS-C-14	1.524	5	0.008 (1)	0.007 (1)	0.914

[a]Number in parenthesis next to minimum marker height and minimum crown height parameters corresponds to calculation method listed on pages 19-20 of supplement.

A.1.3.3.2.1 Filtering

As discussed in the main text, two steps were taken to address uncertainty and filter the preferred predicted LBE dataset (LBE_p). Topographic sources such as imagery-derived bathymetric estimates and augmented points were considered to have greater uncertainty than lidar. Therefore, a convex hull was generated surrounding areas where topographic information was derived from these data. Predicted LBE polygons with >50% of their area overlapping this area were removed. Remaining portions of LBE_p polygons overlapping the area of uncertain source topography were erased using the convex hull polygon. The resulting set of LBE polygons is referenced herein as LBE_{p-1}.

A second filtering process was used to remove additional LBE_{p-1} polygons in areas with low topographic point densities and low standard deviation in elevations. The belief that these factors would results in poor LBE predictions was supported by comparing metrics from polygons in the LBE_o dataset that were completely missed in the preferred LBE_p dataset versus those that were at-least partially mapped. To do this, each LBE_o polygon was defined as being matched or missed based on spatial intersection with the preferred LBE_p polygons. Lidar point densities (points/m^2) and the mean standard deviation of gridded elevations ($\overline{\sigma_z}$) were calculated for each LBE_o where local standard deviation (σ_z) was calculated individually for each raster cell using the bare-earth point cloud. Point densities and $\overline{\sigma_z}$ for LBE_o polygons matched by the predicted LBEs were generally greater than those for missed LBE_o polygons. Further, comparison of point density and $\overline{\sigma_z}$ from matched and missed LBE_o polygons using Welch's t-test and the Kolmogorov-Smirnov test concluded that the null hypotheses that distributions had equivalent means and came from the same family of distribution could both be rejected above the 95% confidence level ($p<<0.05$). Thresholds for point density and $\overline{\sigma_z}$ to filter the LBE_{p-1} data were generated by

maximizing the difference in relative frequency within the first break of histograms of missed and matched LBE_o polygons by iteratively adjusting histogram break values with the two constraints that matched and missed histograms had the same break values, and that frequencies of the first three breaks had a monotonic trend. The break values maximizing the difference in point density and $\overline{\sigma_z}$ were 2.9 points/m^2 and 0.03 m, respectively. These values were used to filter the LBE_{p-1} data by removing polygons with either point densities or $\overline{\sigma_z}$ values below the respective thresholds.

A.1.3.3.2.2 Geometry

Geometric analysis included comparing the D_c-to-LBE planform area relationship for each LBE in the final LBE dataset to that of several idealized spheroidal geometries (Figure A.1.2). For example, the top (planform) area of perfect sphere is $\pi 0.5 {D_c}^2$. Relations for oblate and prolate spheroids are shown in Figure A.1.2.

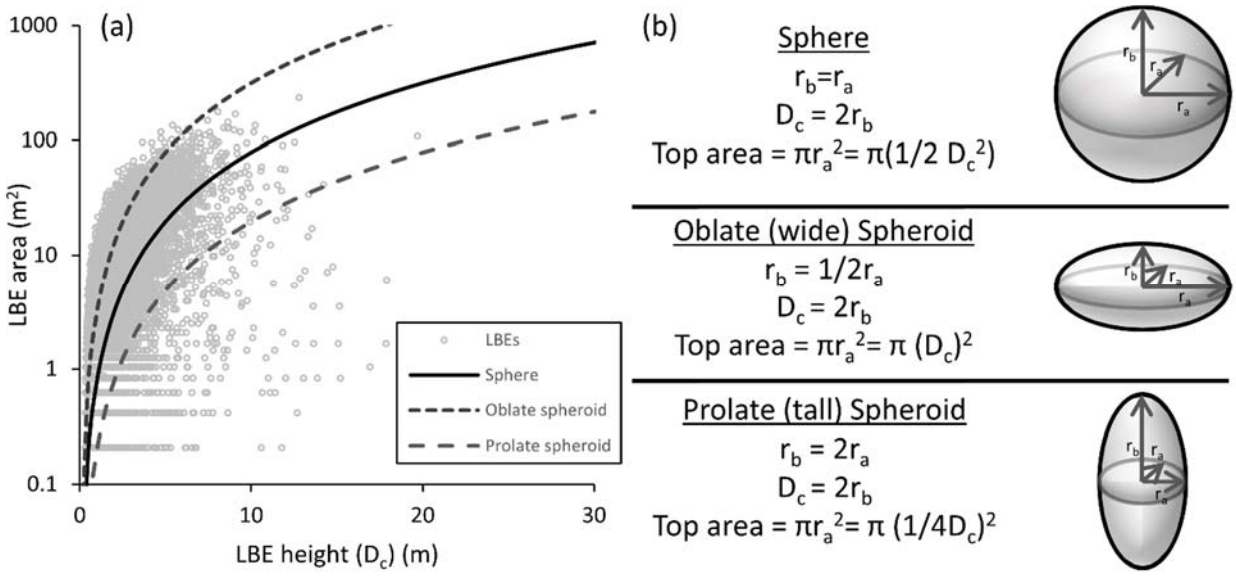

Figure A.1.2. (a) LBE planform area versus LBE height (D_c) overlain with relations for several idealized spheroidal geometries and (b) visual examples of idealized spheroids.

A.1.3.4 Two-dimensional hydrodynamic modeling

For this study, the 2D model known as Sedimentation and River Hydraulics—Two-

Dimensional model (SRH-2D) v. 2.2 was used to predict hydrodynamics. The Surface-water Modeling System (SMS) v. 11.2 graphical user interface (Aquaveo, Inc.) was used for pre- and post-processing model inputs, parameters, and outputs. SRH-2D v. 2.2 solves the 2D dynamic wave equations (i.e. the depth-averaged St. Venant equations) (Lai, 2008). The model uses a finite volume numerical scheme that can handle subcritical and supercritical flow. The model also incorporates seamless wetting-drying algorithms that results in fewer tuning parameters needed to generate solutions. Model outputs include WSE (m), water depth (h) (m), depth-averaged velocity components (longitudinal, U, and lateral, V) (m/s), depth-averaged water speed ($\overline{U}$) (m/s), Froude number, and shear stress (τ) (N/m^2). SRH-2D was developed by the U.S. Bureau of Reclamation and is freely available to the public. For more information, see https://www.usbr.gov/tsc/techreferences/computer%20software/models/srh2d/index.html. Model development followed the Pasternack (2011) textbook.

The model's finite-volume numerical solver requires input of a computational mesh. Three computational meshes with ~ 1 m internodal spacing were made to cover the extent of inundation associated with flows spanning two orders of magnitude (e.g. approximately 1.2–343.6 m^3/s) (Figure A.1.3). SMS software was used to build the final suite of meshes based on the approach described by Pasternack (2011).

The two primary model parameters in SRH-2D include bed roughness as approximated using variable Manning's n and isotropic kinematic eddy viscosity (E). For model development, unresolved roughness (e.g. not represented in the bare-earth topography) was initially estimated using a constant Manning's coefficient (n) of 0.1 (Pasternack & Senter, 2011). After simulating the lidar baseline flow condition for the whole river, predicted WSEs were compared to the 147,644 collocated WSE measurements from the lidar data. Initial WSE assessment showed the

model systematically over-predicted water depth. As a result, additional simulations were conducted with constant roughness coefficients values of 0.07, 0.08, and 0.09, respectively. Computational time limited the assignment and calibration of spatially based roughness values for this study. Testing found a uniform value of 0.09 worked best as this value minimized mean square error between measured and predicted WSE values, and observed and predicted velocity magnitudes. This calibrated value, which is physically realistic for the setting (Yochum et al., 2014), was used in all subsequent flow simulations. Sensitivity to large (> 0.01) variations in n values have been observed in 2D models and it is important to address this level of uncertainty (Pasternack, 2011). Sensitivity analysis testing the model's response to such incremental variations in n values found differences in predicted depths and velocities to be relatively minimal (section A.1.3.4.2).

The bed roughness parameter in a 2D model can vary spatially to account for variable bed sediment facies and several methods exist to estimate roughness (Pasternack, 2011). However, use of a constant roughness value is common in 2D modeling and has been shown to both perform well (L'Hommedieu et al., 2020**;** MacWilliams et al., 2006; Pasternack & Senter, 2011; Reid et al., 2020) and produce results similar to models with spatially varied roughness (Lisle et al., 2000). Further, 2D model hydraulic predictions are equally if not more sensitive to topographic inaccuracies than to typical model calibration parameters such as roughness (McKean et al., 2014; Pasternack, 2011; Pasternack et al., 2006). Available methods to estimate spatially varying roughness are generally qualitative (Yochum et al., 2014), empirical (Cienciala & Hassan, 2013; Lisle et al., 2000), or based on iterative numerical simulation (Pasternack, 2011). In addition to varying spatially, roughness may change with discharge. Numerical analysis, flume experiments, and observations in natural rivers suggest that roughness values decrease rapidly with increasing

discharge, especially at flows exceeding a channel's banks, prior to stabilizing (Ferguson et al., 2017; Richardson & Carling, 2006; Yang et al., 2007). Contrary to these findings, several 2D modeling studies in gravel-bed rivers have found that roughness does not decrease with increasing stage (Brown & Pasternack, 2008; Pasternack, 2008; Sawyer et al., 2010; Strom et al., 2017). In these studies, contact with new types of roughness elements such as boulder clusters, bedrock outcrops, vegetation, and valley width variations maintain high roughness values as discharge increases. Ferguson et al. (2017) also found resistance to increase at high discharges due to macro-roughness elements of rock walls in a bedrock confined river. It is also possible that selective transport and continued armoring of the bed during increasing discharge could result in near constant bed roughness over a wide range of discharges (Gomez, 1993). Abu-Aly et al. (2014) in applying a methodology to account for spatially distributed effects of riparian vegetation found overall roughness to increase with increasing discharge for a 28.3-km segment of a meandering gravel-bed river. Much like the rivers in these studies the study site was characterized by multiple scales of landform heterogeneity whereby increasing stage continuously encountered new forms of resistance, supporting that a decrease in roughness with increasing discharge was unwarranted. Undeniably, if the model roughness parameter had been allowed to vary spatially, the submergence of macro-roughness features in the low-flow channel with increasing stage would likely have been associated with a localized decrease in roughness. However, for the reasons previously described roughness was held spatially constant.

SRH-2D requires the user to select a turbulence closure scheme and the input of an eddy viscosity coefficient. These inputs are used in calculating the turbulent eddy viscosity term in the turbulent stress forces portion of the equation of motion and influence the degree of turbulent mixing incorporated into the solution process (Lai, 2008). 2D models are particularly sensitive to

the eddy viscosity parameterization used to cope with turbulence (Nelson et al., 2016). In the model used in this study, eddy viscosity (E) was a variable in the system of model equations, computed using the following standard equations developed from many studies of turbulence in rivers:

$$E = e^{*}h \cdot u_{*} \quad \text{(Eq. A.1.5)}$$

$$u_{*} = \overline{U}\sqrt{C_d} \quad \text{(Eq. A.1.6)}$$

$$C_d = \mathrm{g}\left(\frac{\mathrm{n}^2}{h^{1/3}}\right) \quad \text{(Eq. A.1.7)}$$

where e* is the non-dimensional eddy viscosity coefficient, u* is shear velocity, $\overline{U}$ is depth-averaged water velocity at a point, C_d is a drag coefficient, and g is the gravitational acceleration constant. Equation A.1.5 is a parabolic turbulent eddy model (Zero-Equation) common in hydraulic applications and has been shown to perform well within a variety of riverine settings compared to observed conditions and other turbulence models (Lai, 2008; Nelson et al., 2016). These equations allow E to vary throughout the model domain, yielding more accurate transverse velocity gradients. However, a comparison of 2D and 3D models for a shallow gravel-bed river demonstrated that, even with spatial variation in E, rapid lateral variations in velocity are not simulated to the degree that occur in natural channels, presenting a fundamental limitation of 2D models like SRH-2D (MacWilliams et al., 2006).

The eddy viscosity coefficient term is channel-geometry-dependent, typically varying between 0.3 and 1.0 in larger rivers. Two-dimensional modeling of carefully controlled shallow flumes found that an eddy viscosity coefficient value of 0.075-0.1 is better in shallow gravel/cobble settings (Pasternack & MacVicar, 2013). Subsequent application of a value of 0.1 in the Yuba River did well at capturing the relative size, shape, and flow direction of eddies, with this lower value also helping to decrease over-prediction of low velocities (Brown & Pasternack, 2012; Pasternack & Senter, 2011). An eddy viscosity coefficient of 0.1 was used for all simulations

in this study.

To run the 2D model, boundary conditions must be input at all inflow and outflow locations. For inflow locations, discharge must be specified across the face of all upstream boundaries as well as any additional tributary inflow junctions. A corresponding water surface elevation (WSE) must also be defined at the downstream boundary. The study site had two primary upstream inflow boundaries; flows originating from NBB dam into Reach 1 and inflow from the Middle Yuba; and one downstream boundary (Figure A.1.3). Several highly ephemeral tributaries also drain into the study site contributing appreciable flow during climate driven high flow events. In this study, model simulations were grouped into two classes based on input conditions, the methods used to specify model inputs, and reason for conducting the simulation. Specifically, these are (1) *calibration and validation flows*, and (2) *geomorphic synthetic flows*. These simulation classes are described next.

The first class, *calibration and validation flow simulations*, involved attempting to replicate hydraulic and hydrologic conditions in the study site associated with specific periods of data collection. These simulations were used to calibrate model parameters and assess performance of the calibrated model. For these simulations, boundary conditions were assigned to match gauged and/or estimated flow conditions during the associated period of data collection. Discharges at the upstream input boundary were based on USGS gaging station 11413517 or data provided by Yuba Water Agency (YWA). Discharges at the Middle Yuba River were based on USGS gaging stations 11408880 and 11409400 or data provided by YWA as well as estimated accretionary flow. WSEs at the downstream boundary were estimated from a site specific rating-curve or from field measured conditions using RTK-GPS.

The second class of simulation, *geomorphic synthetic flow simulations*, involved modeling

a range of hypothetical flow conditions of relevance to understanding the hydraulic mechanisms governing the channel's LBE patterns. Using the calibrated model parameters, a series of four discharges were simulated spanning a range of hydrologic conditions. The four selected discharges represent flows of potential geomorphic importance and are all referenced to the bankfull discharge (10.73 m^3/s) for non-dimensional scaling considerations. The *geomorphic synthetic flows* simulated include a representative baseflow condition of 0.14x bankfull flow, bankfull flow, and two multiples (7.7x and 32x) of the estimated bankfull flow. The 32x bankfull flow simulation corresponded to the peak value for which boundary conditions were available (i.e., availability of downstream stage measurement). The four selected discharges have estimated yearly recurrence intervals of 1.00, 1.06, 1.59, and 3.46, respectively.

Ultimately, simulated flows included two *calibration and validation flow simulations* and four *geomorphic synthetic flow simulations*. The complete array of all specific discharge inputs and downstream WSE values for every 2D model simulation are given in Table A1.5. Model input locations including tributary locations are depicted in Figure A.1.3. For all simulations, SRH-2D outputs raw hydraulic variable values computed at computational mesh nodes. For each model simulation, a number of steps were taken to process data for later analyses with certain calculations made using the raw (nodal) results and others using post-processed results (e.g. rasterized data). ArcGIS software (ESRI, Redlands, CA) was used to process and analyze 2D model outputs. Initially, wetted area polygons were created for each flow simulation *sensu* Pasternack (2011) using interpolated depths greater than zero as the minimum threshold. These wetted area polygons were then used as the interpolation boundaries for each respective flow simulation in the creation of hydraulic variable rasters. All rasters were derived from TIN-based surface models re-sampled to 0.46 m resolution grids to provide an equal-area basis for analysis.

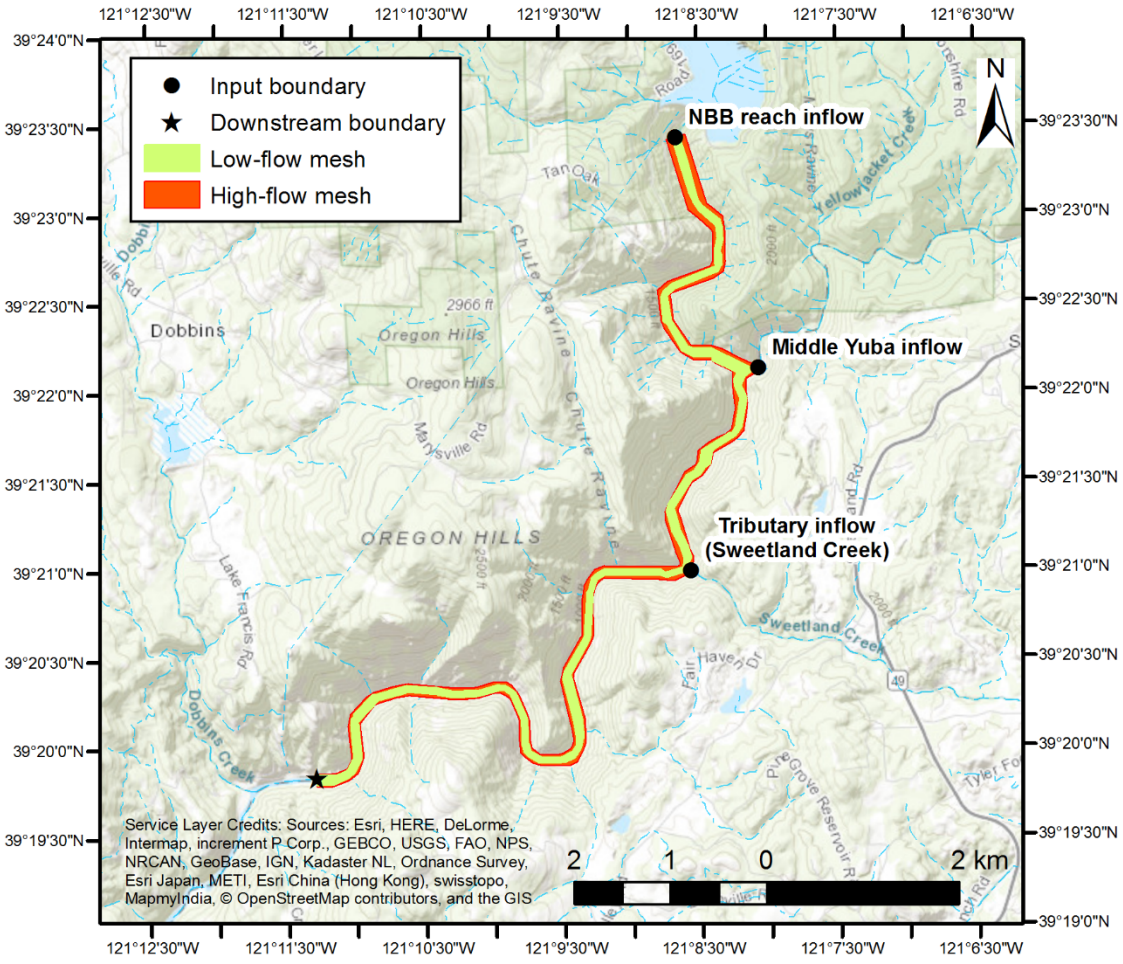

Figure A.1.3. Extent of 2D model low-flow and high-flow computational meshes and location of inflow/outflow boundaries.

Table A1.5. 2D Model input and parameter values

Total discharge (m^3/s)	Reach 1 input (m^3/s)	Middle Yuba input (m^3/s)	Number of tributary inputs (-)	Total tributary inputs (m^3/s)	Downstream WSE[a] (m)
Calibration and validation simulations					
1.19	0.16	1.02	1	0.01	169.60
3.51	n/a[b]	n/a[b]	1	0.19	169.61
Geomorphic synthetic flow simulation					
1.54	1.40	0.14	0	0	169.51
10.73	10.59	0.14	0	0	169.91
82.12	81.98	0.14	0	0	170.94
343.60	343.45	0.14	0	0	172.06

[a] Elevations referenced to North American Vertical Datum of 1988

[b] Simulation of lower 4.2 km of study site. Only required input of total discharge and tributary input.

A.1.3.4.1 2D Model Assessment

Two-dimensional hydrodynamic models have inherent strengths and weaknesses, thus there is need to assess a model's representation of reality and understand and accept uncertainty in the results. SRH-2D is a proven tool capable of simulating hydraulic conditions in natural rivers (Brown & Pasternack, 2014; Lai, 2008; Pasternack & Senter, 2011). However, there is still a risk of poor model performance. The scope of model assessment is outlined below. Table A1.6 provides a summary of model assessment testing.

A suite of tests typical of those carried out in the peer-reviewed journal literature for the assessment of 2D models were performed to characterize model performance and uncertainty (Pasternack, 2011). Tests included mass conservation checks, lidar baseline WSE assessment, and fixed-point depth and velocity assessment (Table A1.6). For the lidar baseline WSE and fixed-point depth and velocity assessment some tests were done using raw (i.e., signed) or absolute (i.e., unsigned) deviations between observed and predicted values, and some on the signed or unsigned

percent errors. WSE was analyzed in terms of deviations, not percent error (Brown & Pasternack, 2012). In contrast, percent error of depth and velocity are meaningful because deviations may be a substantial fraction of the observed values. Often percent error for low values of depth or velocity are not evaluated due to low values having inflated numerical errors. Regression and correlation analyses as well as the standard error of the regression slope (SES) and standard error of the regression intercept (SEI) between predicted vs. observed values were computed to add further statistical rigor. Descriptive statistics of model deviations and percent errors and the results of the regression analysis were all used to evaluate model performance. In addition to these metrics commonly used by the 2D hydrodynamic modeling community, three metrics: Nash-Sutcliffe efficiency (NSE), percent bias (PBIAS), and the root mean square error-observations standard deviation ratio (RSR), commonly used in the hydrological modeling community to assess performance of discharge prediction (Moriasi et al., 2007) were also computed.

Table A1.6. Summary of 2D model assessment testing

Total discharge (m^3/s)	Mass conservation	WSE	Fixed-point velocity magnitude	Fixed-point depth	Manning's n sensitivity
Calibration and validation simulations					
1.19	X	X			X
3.51	X		X	X	X
Geomorphic synthetic flow simulation					
1.54	X				X
10.73	X				X
82.12	X				X
343.60	X				

A.1.3.4.1.1 Mass Conservation

The first key model performance criteria, mass conservation, was evaluated by computing the percent difference between specified inflow and model-predicted outflow. Computationally,

mass conservation losses increase in the downstream direction as error accumulates, therefore good mass conservation should show little difference in discharge at the downstream model boundary from the total input discharge. Mass conservation error in a 2D model can be anywhere in the 0.01 – 2% range (Pasternack, 2011) with errors greater than ~ 2-3% a potential sign of poor model performance (Pasternack & Senter, 2011). This range is typically smaller than uncertainty associated with stream gauges and other discharge measurement methods such as flumes and weirs or stream stage-gauge relations that may be off by upwards of ~ 5-10% of actual values. Mass conservation losses at the downstream model boundary were all less than 1%, well within what is considered acceptable (Table A1.7).

Table A1.7. 2D model mass conservation performance summary

Total discharge (m^3/s)	Total outflow (m^3/s)	Percent error (%)
Calibration and validation simulations		
1.19	1.18	-0.60
3.51	3.50	-0.17
Geomorphic synthetic flow simulation		
1.54	1.54	-0.41
10.73	10.67	-0.60
82.12	82.11	-0.01
343.60	342.69	-0.27

A.1.3.4.1.2 WSE Evaluation

The next key test was ability of the 2D model lidar baseline simulation to match lidar-measured WSEs as this is a proxy for matching wetted area. Even though lidar-measured WSE values were used to calibrate Manning's n for this simulation, the final deviations between observed and predicted values were non-zero. Thus, deviations between observed and final calibrated WSE predictions were used to characterize uncertainty in water depth after calibration.

Longitudinal profiles of observed and predicted WSEs were used to evaluate the spatial distribution of error in WSE deviations. Profiles were generated by discretizing points along the lidar baseline thalweg at 0.91 m intervals. At each point, model predicted WSE and observed WSE were interpolated. The distribution of signed deviations between these values should be centered about zero as this demonstrates no bias in model predictions.

There are no formal standards for evaluating WSE deviations to indicate when a model is invalid, but the greater the deviation from zero the more unreliable the model. Topographic error is a dominant factor explaining 2D model depth prediction errors that warrants consideration in model evaluation. It is presumptuous to expect model prediction to be more accurate than topographic deviations, as such, best practices suggest that depth or WSE deviations should not exceed uncertainty in the topographic data (Brown & Pasternack, 2012; Pasternack, 2011; Pasternack & Senter, 2011). The FVA for ground points and bathymetric lidar points in this study were 0.037 m and 0.117 m, respectively (section A.1.3.1), but high topographic variability is likely to yield larger uncertainties. Generally, WSE deviations falling within the range of bathymetric lidar uncertainty were considered suitable for this study. The performance standards reported by Moriasi et al. (2007) for the additional discharge prediction metrics are NSE > 0.5, PBIAS within 25%, and RSR < 0.7, however the exact interpretation of these thresholds in this study remains unclear due to limited use of these metrics in 2D model assessment.

Comparison of lidar based WSEs to 2D model predictions consisted of 147,644 paired data points distributed throughout the 13.2 km study domain, a considerably larger sample size than studies relying solely on field measured WSEs. All deviation statistics were calculated as observed (lidar measured) minus predicted (2D model), meaning that positive deviations represent model WSE and depth under-prediction and negative deviations model WSE and depth over-prediction.

Mean signed WSE deviation error (ME) was -0.077 m and mean absolute error (MAE) was 0.162 m. Water surface deviations displayed a near equal balance of over-versus under-predictions with a slight tendency toward 2D model over-prediction, as reflected by the negative ME value Figure A.1.4a). A majority (53%) of the raw WSE point deviations had less absolute error than the 0.117 m FVA of the bathymetric lidar and 81.6% of the data within 0.25 m, which is close to two times the FVA of the bathymetric lidar (Table A1.8). Additional metrics from the regression and correlation assessment analysis as well as NSE, PBIAS, and RSR were all within the standards of satisfactory model performance (Table A1.9).

Locations with the largest WSE over-prediction were dispersed throughout the model domain, but were often clustered upstream of hydraulic controls, specifically in areas of relatively deep water immediately upstream of narrow channel constrictions. Comparison of the complete topographic surface with 2D model computational mesh surfaces revealed a smoothing effect present at many of these constrictions due to the resampling procedure used to create the up-scaled mesh surfaces. This smoothing resulted in reduced channel conveyance and artificially high bed elevations that, when modeled created a backwater effect over-elevating upstream conditions. These simulated backwater conditions help explain the WSE over-prediction in these settings. A qualitative review of the spatial distribution of WSE deviations also revealed that areas of large over-prediction (e.g. model predicted depths were too high) tended to be in locations with low WSE point densities, thus questioning the accuracy of the observed values and making quantitative review of these large errors more difficult.

Review of WSE deviations identified at least 15 locations displaying the physical conditions described above. These locations included 7,743 points with WSE over-prediction deviations greater than 0.1 m and represent ~ 5% of the total WSE comparison dataset. Removal

of these points from the WSE assessment dataset ('selected WSE dataset') and re-assessment of WSE deviations improved model predicted WSE descriptive statistics. The ME and MAE for the selected WSE dataset were -0.042 m and 0.132 m, respectively. Similar improvements were observed in the percentage of data meeting several deviation thresholds (Table A1.8) and other performance metrics (Table A1.9).

WSE deviations varied longitudinally, illustrating the spatially varying nature of water surface errors (Figure A.1.5). Black points in Figure A.1.5 represent locations of poor model prediction described above. These points coincide with nearly all regions of large model over-prediction and it is likely other areas of over-prediction have similar unidentified topographic controls. Visually, locations of both over- and under- prediction appear to be located in distinct spatially cohesive patches. This grouping of errors as well as the lack of systematic error in WSE deviations may in-part reflect the decision to use a constant roughness coefficient value rather than spatially varied roughness.

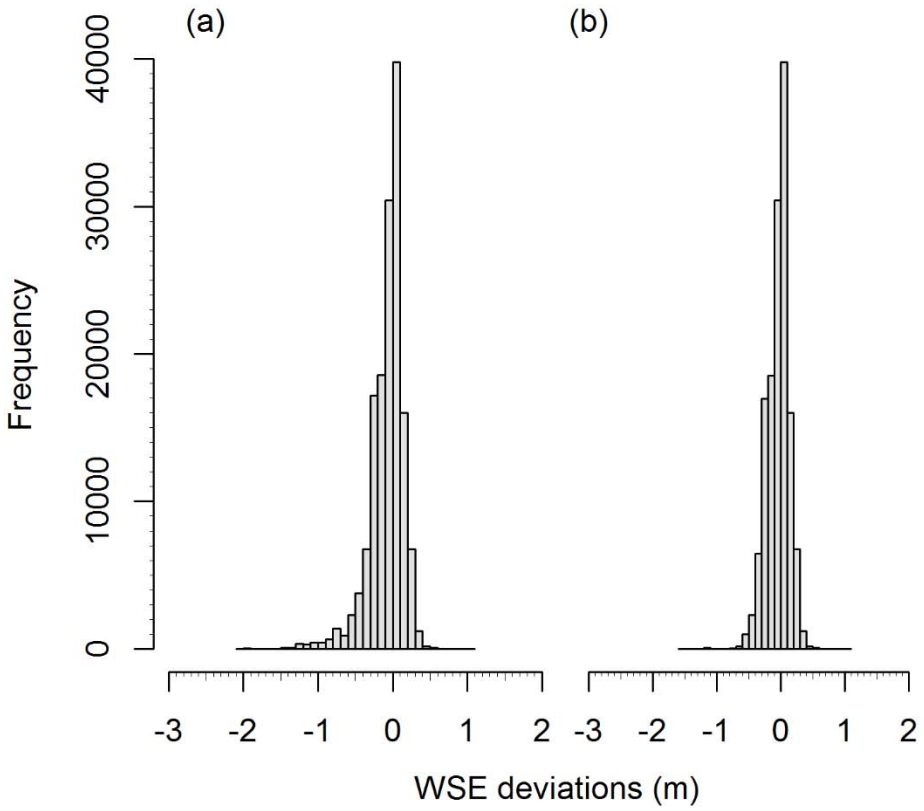

Figure A.1.4. Histograms of 2D model WSE deviations for the (a) entire WSE dataset and (b) selected WSE dataset.

Table A1.8. Non-exceedance probabilities of WSE deviations meeting different thresholds of performance for entire WSE dataset and selected WSE dataset.

All WSE dataset		Selected WSE dataset	
Absolute WSE deviation (m)	Non-exceedance probability (%)	Absolute WSE deviation (m)	Non-exceedance probability (%)
0.025	13.8	0.025	14.5
0.05	26.6	0.05	28.1
0.1	47.6	0.1	50.2
0.117[a]	52.7	0.117[a]	55.6
0.155[b]	61.7	0.155[b]	65.1
0.25	81.6	0.25	86.0
0.5	95.3	0.5	99.0

[a]Lidar bathymetric FVA

[b]Combined bathymetric and terrestrial lidar FVA

Table A1.9. Regression and hydrologic metrics for entire WSE dataset and selected WSE dataset assessment.

Test Statistic	All WSE dataset	Selected WSE dataset
n	147644	139901
Regression Slope	1.00	1.00
Regression Intercept	0.06	-0.03
R^2	1.00	1.00
SES	9.9E-06	7.4E-06
SEI	0.00	0.00
ME (m)	-0.08	-0.04
MAE (m)	0.16	0.13
PBIAS	0	0
RSR	3.8E-03	2.8E-03
NSE	1.00	1.00

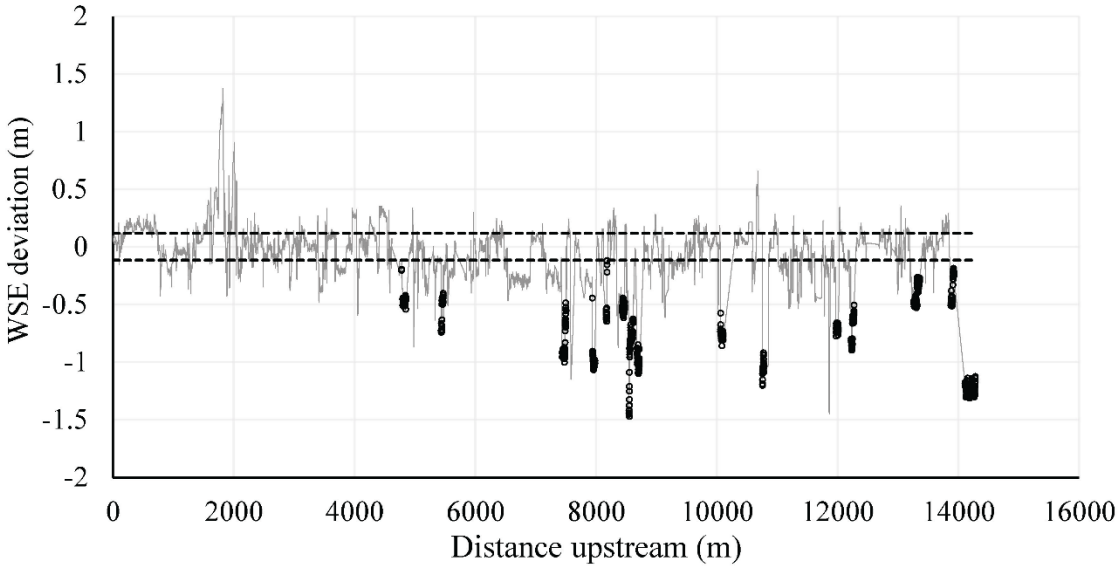

Figure A.1.5. Longitudinal profile of deviation between observed and predicted WSE. Positive deviation corresponds to model under-prediction and negative deviation to model over-prediction. Black dots are areas of poor performance potentially due to topographic uncertainty. Horizontal dashed lines are bathymetric lidar FVA (± 0.117m).

A.1.3.4.1.3 Fixed-point Depth and Velocity

The next test was assessment of the model for fixed-point depth and velocity performance. This test is less relevant toward the study purpose of accurately mapping wetted areas for the simulated discharges, but nonetheless provides a relevant check of model performance. Depth and velocity data were collected on April 8, 2016 at 61 independent locations in the downstream portion of the study site in a location with complex, shallow hydraulics. The discharge corresponding to the period of measurement was estimated as 3.51 m^3/s, herein referred to as the 'velocity assessment' discharge simulation. The data collection strategy used focused on sampling the range of velocities present in the river at this discharge opposed to more traditional cross-section based sampling strategies. This design allows quantitative testing of a model's ability to predict over a range of velocities (Pasternack & Senter, 2011). Measurements were made with no *a priori* knowledge of the spatial pattern of velocity and prior to model simulation to ensure no

sampling bias. Velocity measurements were made in wadable areas using a SonTek FlowTracker Handheld Acoustic Doppler Velocimeter (ADV) mounted to a depth setting wading rod. Depth measurement errors were ±1 cm. Velocity measurement error reported by the manufacturer is ±1% of measured velocity + 0.25 cm/s. Depth-averaged velocities were estimated by sampling velocity at 10 Hz averaged over 20 s at 0.6·depth from the water surface (Pasternack, 2011). The position of each measurement were simultaneously surveyed using RTK-GPS.

Correlation and regression analyses between predicted vs. observed depth and velocity values yielded several variables for evaluation. The coefficient of determination (R^2) metric describes variance about the best fit slope, an indicator of model precision. R^2 values of ~ 0.6 for water speed are common for 2D models with values in the ~ 0.7-0.85 range considered very good (Brown & Pasternack, 2012). R^2 values for depth are typically higher (~ 0.7-0.8) than those for velocity (~0.5-0.8) and values in these ranges are recommended as a minimum standard for model performance (Pasternack, 2011). The accuracy of model predictions is better described by the slope term in the regression equation than R^2 values. A value of unity represents no bias in the model predictions. The y-intercept of the regression equation also indicates potential model bias. Over prediction of low velocities and under prediction of high velocities have been reported in previous 2D modeling studies (Brown & Pasternack, 2012). Based on recommendations by Pasternack (2011) standards for demonstrating model suitability using comparison of predicted vs observed velocity data are a slope term >0.8 and a y-intercept <10% of the maximum observed velocity.

Model accuracy was also evaluated from statistical analysis of unsigned depth and velocity percent error. Mean and/or median velocity errors >50% suggest poor model performance whereas mean and median error values of ~ 10-15% for depth and ~ 15-30% for velocity are considered reasonable (Pasternack, 2011). Percent error for low values often exceed 200% due to the strong

influence of even small deviations. To address this issue separate velocity tests for low and high values may be performed with a threshold value between 0.3 m/s to 0.9 m/s used to differentiate velocities (Brown & Pasternack, 2012; Pasternack, 2011; Strom et al., 2016). Depth measurement with a depth setting wading rod as well as RTK-GPS topographic data have much greater point accuracy and probability of being measured directly from the river bed than lidar point data collection. Comparison of lidar derived vs. field observed elevations at the fixed-point depth observation sites were reviewed to address systematic differences that might influence depth measurement uncertainty.

Comparison of model predicted hydraulics (depth and depth-averaged velocity) with field measured estimates showed predicted values closely approximated observed conditions (Table A1.10). Coefficient of determination (R^2) values between predicted and observed hydraulics were 0.80 for depth and 0.84 for velocity ($p<0.001$ for both tests). Linear regression between predicted and observed values yielded regression slopes of 0.87 for both depth and velocity ($p<0.001$ for both tests) and y-intercepts of 0.04 ($p<0.001$) and 0.03 ($p=0.28$), respectively (Figure A.1.6 and Figure A.1.7). These y-intercept values scale to 2.9% and 2.4% of the maximum observed depth and depth-averaged velocity, consistent with acceptable performance standards.

Regression slopes and intercepts all indicate slight bias toward the model over-predicting depths and velocities. This precludes errors being associated with the selected roughness coefficient, as adjusting this value to improve prediction of one metric would have been at the detriment of the other. Residuals between predicted and observed velocity suggest over-prediction was somewhat more prevalent in slow flowing than faster areas (i.e., 63% of points with velocities less than 0.3 m/s were over-predicted versus only 45% of points with velocities greater than 0.3 m/s), a common occurrence in 2D model performance. Velocity residuals had slight

heteroscedasticity further suggesting error dependence on the magnitude of velocity, whereas depth residuals were relatively trendless (Figure A.1.7).

Descriptive statistics comparing observed and predicted values corroborated the findings described above including the tendency to over-predict slow velocities and slightly under-predict fast velocities. The mean percent error (MPE) of all velocity observations regardless of magnitude was -25% (median percent error of -5%), with the negative sign connoting model over-prediction. Velocity points were stratified into bins above and below 0.3 m/s. Low velocity points had a MPE of -48% (median percent error of -17%) and high velocity points a MPE of -1% (median percent error of 4%). Mean absolute percent velocity error (MAPE) for velocities below 0.3 m/s, velocities above 0.3 m/s, and all data were 64%, 20% and 43%, respectively. Median absolute percent error for these same subsets of data were 30%, 19% and 24%, respectively. With the exception of observations in the low velocity bin (i.e., fixed-point velocities < 0.3 m/s) nearly all metrics were within the 20–30% benchmark for this study. In addition to descriptive statistics comparing observed and predicted hydraulics and metrics from the regression and correlation analysis NSE, PBIAS, and RSR values were also all within the standards of satisfactory model performance (Table A1.10).

Table A1.10. Regression and hydrologic metrics for fixed-point depth and velocity assessment.

Test Statistic	Fixed-point depth	Fixed-point velocity
n	60	61
Regression Slope	0.87	0.87
Regression Intercept	0.04	0.03
R^2	0.80	0.84
SES	0.06	0.05
SEI	0.05	0.02
MPE (%)	-6.0	-25.4
MAPE (%)	9.0	43.1
PBIAS	8.8	6.1
RSR	0.54	0.43
NSE	0.70	0.82

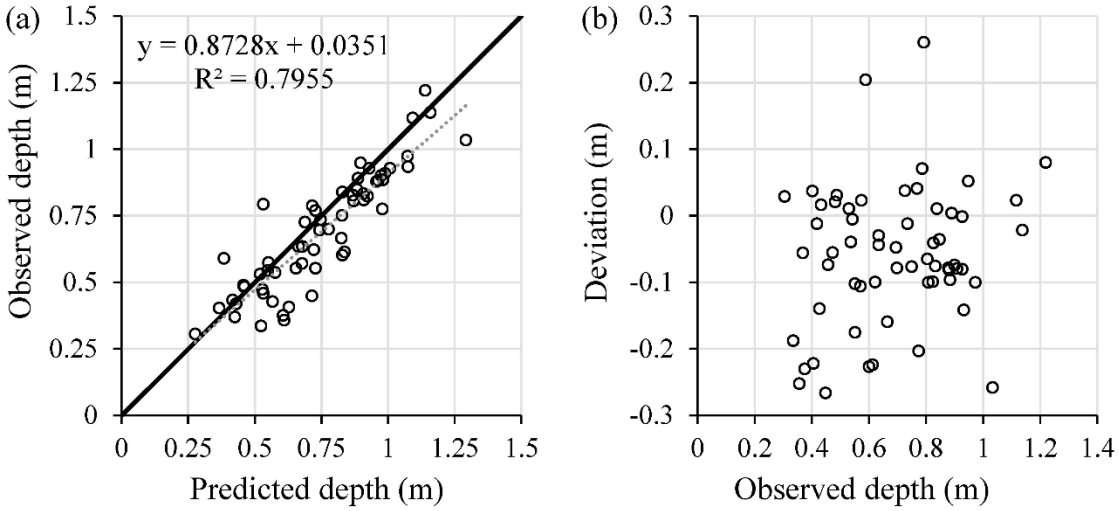

Figure A.1.6. (a) Scatter plot of observed versus 2D model predicted depth with 1:1 line (dark black line), line of best fit (gray dashed line) as well as equation of best fit line and coefficient of determination and (b) deviations between observed and predicted depth versus observed depth.

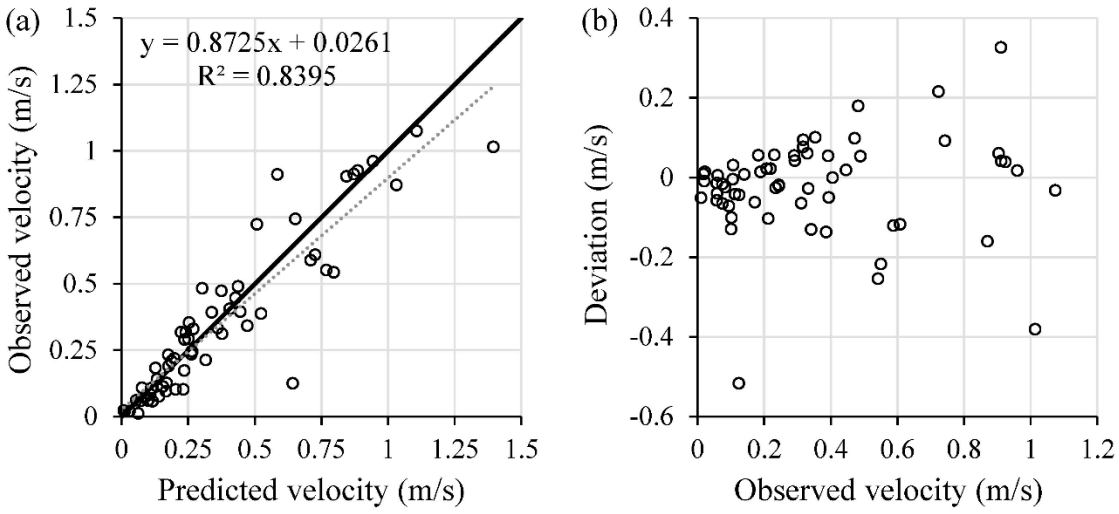

Figure A.1.7. (a) Scatter plot of observed versus 2D model predicted velocity with 1:1 line (dark black line), line of best fit (gray dashed line) as well as equation of best fit line and coefficient of determination and (b) deviations between observed and predicted depth versus observed depth.

A.1.3.4.2 2D Model Roughness Sensitivity

The scale of model sensitivity to large (> 0.01) variations in n values was tested through studying changes of model predicted depths and velocities. Lidar baseline flow simulation results were compared using variable roughness coefficient values of 0.07, 0.08, 0.09, and 0.10, respectively. For each pair of simulations (e.g. a simulation with n=0.07 was compared to simulations with n=0.08, n=0.09, and n=0.10), differences in predicted depths at all nodes that were wet in both simulations were computed. The same was done for velocity. Average deviations for both variables were computed for each simulation pairing and trends were assessed. This analysis was repeated for the velocity assessment discharge simulation and a more limited analysis comparing n values of 0.09 and 0.10 was performed for a wider range of discharges (those listed in Table A1.6 and 2.68, 32.20, and 160.98 m^3/s).

Average sensitivity of predicted depth and velocity at the lidar baseline discharge to the range of tested roughness values were well described by a linear model fit using least squares (R^2

values of 1.0 and 0.98, respectively, $p<0.10$). Similar linear scaling was also observed for the velocity assessment discharge simulation of 3.51 m^3/s (R^2 values of 1.0 and 0.98 for depth and velocity sensitivity, respectively, $p<0.10$). While these results are based on a small number of samples (six data points), the findings encourage the assumption that average model sensitivity to changes in Manning's n scaled linearly regardless of discharge (i.e., there was a constant magnitude change in average predicted depth and velocity per 0.01 unit change in Manning's n for each discharge). Average sensitivity of model predicted depths and velocities to increase in Manning's n of 0.01 (e.g. average change in hydraulics going from 0.08 to 0.09 or 0.09 to 0.1) for the range of simulated discharges are depicted in Figure A.1.8. Sensitivities are generally small and represent only a small portion of average hydraulic conditions. For example, although model sensitivity is greater at higher discharges, average depth and velocity conditions also increase with discharge and the ratio of sensitivity to predicted depths and velocities was between 2-3% of average conditions for all discharges. In essence it would take large changes in roughness values to markedly change bulk predicted hydraulics, though large local affects are certainly possible that were not captured by this limited analysis.

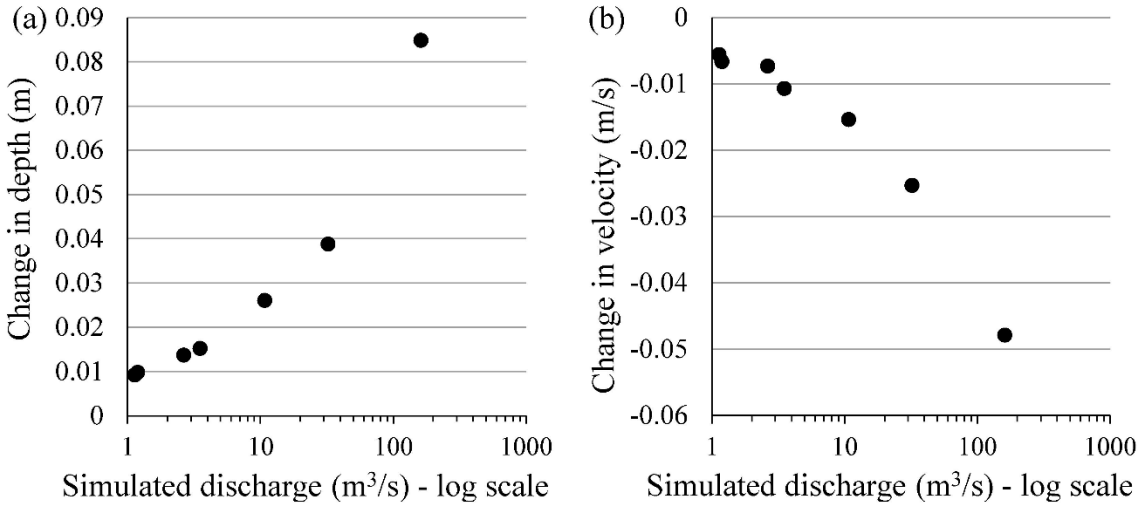

Figure A.1.8. Semi-log plot of 2D Model average (a) depth and (b) velocity sensitivity to an increase in Manning's n of 0.01 over various simulated discharges.

A.1.3.5 LBE spatial analysis

The heterogeneous and hierarchical nature of the study site, like essentially all rivers, required implementation of a disaggregation and aggregation procedure (Alber & Piegay, 2011) to allow longitudinal analysis of river characteristics at appropriate scales. Spatial disaggregation and aggregation was accomplished using a box counting procedure described by Wyrick and Pasternack (2012). Simplistically, the procedure involves generating points longitudinally along a river centerline, creating station-lines perpendicular to these points, and buffering the station lines into individual polygons that are then clipped to the wetted area or other boundary of interest.

The disaggregation and aggregation process is sensitive to the location and tortuosity of the alignment used to generate the longitudinal series of points. An overly tortuous path results in highly overlapping sections and polygons that also miss covering portions of the wetted area, while an overly simple alignment such as using a valley centerline for interpretation of all flows may result in clipped polygons that are not perpendicular to the main direction of flow, particularly at lower flows. To address this issue two longitudinal alignments were generated based on the

centerlines of the bankfull (10.73 m^3/s) and max flood flow (343.6 m^3/s) simulations. Centerlines were delineated using the Polygon Centerline Tool™ (https://www.beachbumgis.com/). The bankfull alignment was used to generate cross-sectional polygons for all simulated flows below bankfull (10.7 m^3/s) and the max flood flow alignment was used for all remaining flows. Prior to applying the box counting procedure the bankfull and flood flow centerlines were simplified using the ArcGIS simplify line (point remove algorithm with 4.6 m offset) and smooth line (Bezier interpolation) tools. Points were spaced along the revised alignments every 3 m, yielding a series of 3-m cross-sectional polygons distributed down the river for each simulated discharge. Notably there was some overlap or underlap of rectangles at locations of high channel curvature. These areas were determined to balance out and no manual adjustment of the polygons occurred.

As discussed in the main text, a path-based approach was developed for the LBE-to-LBE spacing analysis to estimate longitudinal distances (λ^l) between each LBE and downstream LBEs. In the first step, the unique centerline for each simulated wetted area was repeatedly offset by 1.5 m on each side until the entire wetted area of each discharge was covered with paths (e.g. a new offset would be completely outside the wetted area), thus creating a set of longitudinal paths parallel to the bulk flow direction for each flow simulation. Paths were clipped to each wetted area and vertices were added along paths to densify vertex spacing to a maximum of 0.25 m. Each vertex was assigned its projected coordinates (x,y) and a binary code if it fell within a LBE (1) or not (0). Distances along paths between each upstream LBE and all downstream LBEs where a contiguous path was present were computed. If no downstream LBE was encountered the calculation was left blank for that LBE. Other factors considered in the calculations included that an LBE could be downstream of itself and that multiple paths and associated spacing values could exist from an upstream LBE to one or more downstream LBEs. These were considered to

accurately reflect field conditions and not conflict with the goals of the analysis. Zero spacing values were not supported by the calculation. Instead, abutting LBEs were assigned the distance between sequential vertices resulting in a maximum error equal to the maximum spacing interval (0.25 m). The maximum error in λ^l values for non-abutting LBEs was twice the maximum vertex spacing (0.5 m). Both these errors were unlikely worst-case scenarios given vertex densities were often less than the maximum spacing. Very long spacings were also rare given that most paths either encountered an LBE or terminated at a channel margin.

A.1.4 Results

A.1.4.1 Question 1 results (LBE mapping)

As stated in the main text, qualitative assessment of the 14 smoothed ground surfaces determined certain parameter sets performed better than others. Generally, larger step sizes (~3 and 4.5 m), smaller spike and offset values (0.128 m [D_{50}] and 0.064 m [D_{16}] verses 0.5 m), and intermediate down-spike values (0.128 m, 0.256 m, and 0.15 m) in the ground classification algorithm were best at filtering-out LBEs while maintaining character of the overall terrain (Table A1.3).

Results of the quantitative assessment of preliminary LBEs mapped from the best six smoothed surfaces are depicted in Table A1.11. Based on the global performance metric, P-LBE-10 was found to perform best, making the associated RSM the study's preferred RSM. Performance metrics of all 44 LBE_p datasets from the five LBE extraction approaches are presented in Table A1.12.

Table A1.11. Performance metrics of predicted LBEs for six selected parameter combinations. Maximum values for each metric highlighted in light-gray and bolded and minimum values are italicized. Preferred dataset in red font.

ID	Minimum vertical threshold (m)	PA	PO	MJI	MER	Normalized mean
P-LBE-1	0.23	*0.794*	*0.680*	**0.212**	**0.017**	0.500
P-LBE-3	0.28	0.822	0.690	0.161	0.011	*0.349*
P-LBE-10	0.28	0.836	0.696	0.183	0.014	**0.552**
P-LBE-11	0.41	**0.864**	**0.737**	*0.107*	*0.009*	0.500
P-LBE-12	0.32	0.833	0.707	0.153	0.010	0.401
P-LBE-13	0.32	0.830	0.706	0.149	0.010	0.372

Table A1.12. Performance metrics of all 44 predicted LBE datasets. Maximum values for each metric for each approach are highlighted in light-gray and bolded while minimum values are italicized. Global maximum values for each metric are highlighted in dark-gray, bolded and underlined while global minimums are italicized and underlined. Preferred dataset in red font.

ID	PA	PO	MJI	MER	Normalized mean
(i) RSM with vertical threshold					
V-1	**0.894**	**0.774**	*0.269*	*0.030*	*0.445*
V-2	0.876	0.759	0.284	0.034	0.451
V-3	0.856	0.747	0.311	0.038	0.474
V-4	0.839	0.735	0.339	0.043	0.500
V-5	0.822	0.722	0.347	0.048	0.505
V-6	0.802	0.709	0.352	0.054	0.505
V-7	0.785	0.696	0.358	0.059	0.509
V-8	0.755	0.687	0.361	0.065	0.509
V-9	0.732	0.675	0.365	0.072	0.513
V-10	0.703	0.665	0.369	0.079	0.516
V-11	*0.669*	*0.659*	**0.371**	**0.086**	**0.521**
V-12	0.816	0.718	0.351	0.050	0.507
(ii) Gaussian filtered RSM with vertical threshold					
GV-1	**0.760**	*0.705*	**0.333**	0.054	**0.458**
GV-2	0.642	0.762	0.298	0.051	0.409
GV-3	0.611	0.779	*0.246*	0.051	*0.352*
GV-4	0.757	0.706	0.332	**0.054**	0.457
GV-5	0.600	0.789	0.309	0.049	0.423
GV-6	*0.514*	**0.842**	0.315	*0.045*	0.426
(iii) RSM with MCWS algorithm and constant window size					
MCWS-C-1	**0.901**	0.837	0.422	*0.018*	0.647
MCWS-C-2	0.760	0.789	0.445	0.046	0.645
MCWS-C-3	0.828	0.763	0.453	0.050	0.676

ID	PA	PO	MJI	MER	Normalized mean
MCWS-C-4	0.825	0.827	0.432	0.025	0.630
MCWS-C-5	0.772	0.774	0.455	0.061	0.700
MCWS-C-6	*0.742*	0.727	**0.469**	**0.087**	**0.740**
MCWS-C-7	0.819	0.752	0.456	0.063	0.708
MCWS-C-8	0.798	*0.715*	0.464	0.083	0.738
MCWS-C-9	0.879	**0.838**	*0.374*	0.019	0.586
MCWS-C-10	0.809	0.828	0.392	0.025	*0.581*
(iv) RSM with MCWS algorithm and variable window size					
MCWS-V-1	**0.760**	*0.715*	**0.460**	*0.083*	*0.714*
MCWS-V-2	*0.756*	**0.720**	*0.450*	**0.086**	**0.718**
(v) Gaussian filtered RSM with MCWS and constant window size					
GV-MCWS-C-1	0.886	0.854	0.402	0.017	0.629
GV-MCWS-C-2	0.847	0.858	0.384	0.019	0.600
GV-MCWS-C-3	0.712	*0.810*	0.436	0.057	**0.674**
GV-MCWS-C-4	0.608	0.838	**0.440**	0.063	0.673
GV-MCWS-C-5	0.691	0.815	0.431	0.058	0.665
GV-MCWS-C-6	0.593	0.842	0.433	0.063	0.663
GV-MCWS-C-7	0.840	0.859	0.379	0.019	0.594
GV-MCWS-C-8	**0.893**	0.863	0.393	*0.015*	0.627
GV-MCWS-C-9	0.829	0.870	0.358	0.018	0.570
GV-MCWS-C-10	0.657	**0.894**	0.361	0.035	0.572
GV-MCWS-C-11	0.501	0.870	0.399	0.065	0.614
GV-MCWS-C-12	*0.416*	0.887	0.393	**0.075**	0.617
GV-MCWS-C-13	0.479	0.860	0.403	0.074	0.627
GV-MCWS-C-14	0.780	0.874	*0.339*	0.020	*0.535*

A.1.4.2 LBE concentrations

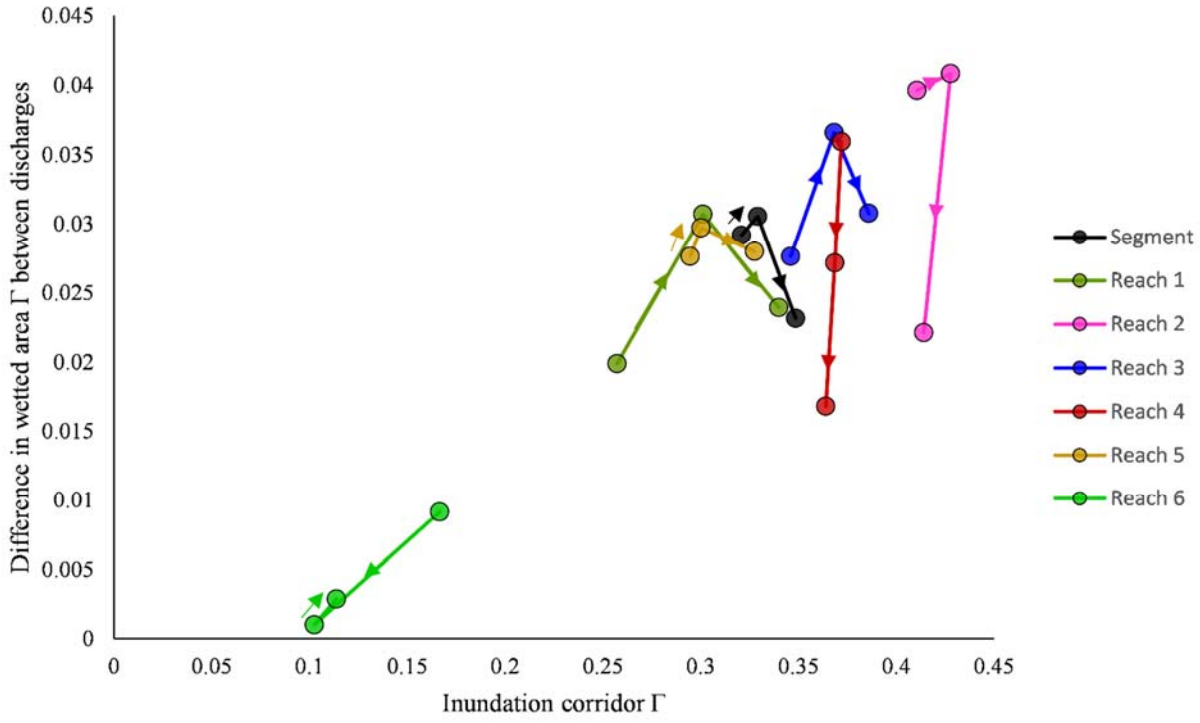

Figure A.1.9. Difference in wetted area Γ between discharges versus inundation corridor Γ. Data are colored by reach. Lines with arrows between points indicate direction of increasing discharges from data points associated with 10.73 to 82.12 to 343.6 m^3/s. Some arrows have been offset for visual purposes.

A.1.4.3 LBE spacings

As stated in the main text, distributions of discharge-dependent streamwise spacing metrics were positively skewed and indicated a strong tendency for closely spaced LBEs. Histograms of λ^l, λ_*^l, and $\widehat{\lambda_*^l}$ distributions are depicted in Figure A.1.10.

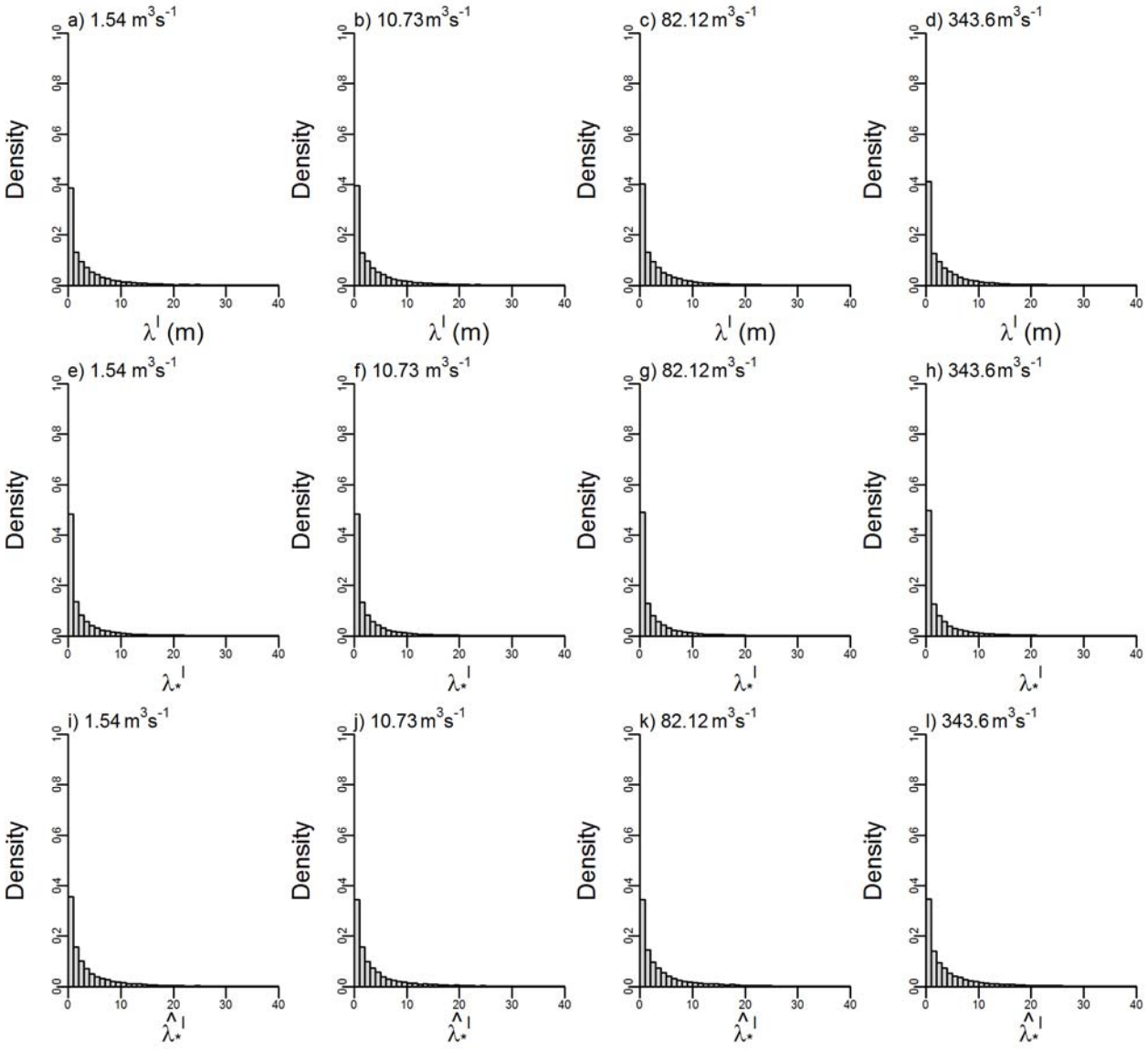

Figure A.1.10. Histograms of streamwise spacing metrics (a-d) $\boldsymbol{\lambda^l}$, (e-h) $\boldsymbol{\lambda_*^l}$, and (i-l) $\widehat{\boldsymbol{\lambda_*^l}}$ for discharge-dependent LBEs. For visual purposes X-axis values have been truncated to a maximum value of 40 despite higher values occurring.

A.1.4.4 Question 2 results (maximum resistance)

None.

A.1.4.5 Comparing Hydrodynamic Regimes from Concentration and Spacing Metrics

As stated in the main text, comparison of cross-sections classified into Morris's (1959) hydrodynamic regimes using $\overline{\lambda_*^l}$ and Γ found only 44% sections were classified the same by each

method. Table A1.13 depicts a complete confusion matrix of how cross-sections were classified according to each metric for each discharge-dependent LBE dataset.

Visualizing distributions of cross-sectional LBE counts found data were more distinct between hydrodynamic regimes classified by Γ compared to regimes classified by $\overline{\lambda_*^l}$, the former showing clear stepwise increases in the number of LBEs per cross-section when going from isolated flow to wake interference to skimming flow, whereas the latter had more uniform counts across regimes (Figure A.1.11). Similar, albeit more muted patterns, were observed comparing distributions of cross-sectional median LBE areas (Figure A.1.12).

Comparing LBE count and median LBE area distributions of similarly classified cross-sections with those having the three most common classification discrepancies (i.e., Γ-based wake interference sections classified as isolated roughness and skimming flow regimes according to $\overline{\lambda_*^l}$, and Γ-based skimming flow sections classified as wake interference according to $\overline{\lambda_*^l}$), several patterns emerged. Firstly, LBE counts of sections classified as wake interference by Γ but as isolated roughness or skimming flow by $\overline{\lambda_*^l}$ were lower than for similarly classified sections (i.e. both in wake interference regime) (Figure A.1.13). Median LBE areas were also lower for $\overline{\lambda_*^l}$-based isolated roughness sections and higher for $\overline{\lambda_*^l}$-based skimming flow sections compared to similarly classified sections (Figure A.1.14). This result is what would be expected, but together with LBE count data suggests $\overline{\lambda_*^l}$-based isolated roughness classification discrepancies might have been driven by lower numbers of smaller LBEs with longer downstream spacings compared to similarly classified sections, and that $\overline{\lambda_*^l}$-based skimming flow classification discrepancies might have been driven by lower numbers of larger LBEs with shorter downstream spacings.

Comparing Γ-based skimming flow sections classified as wake interference by $\overline{\lambda_*^l}$ found LBE counts to be higher and LBE medians areas to be lower than sections classified the same by

both metrics (i.e. both in skimming flow regime) (Figure A.1.13 and Figure A.1.14). This suggests larger numbers of smaller LBEs were present in dissimilar sections relative to similar sections, which does not point to clear reasons for the discrepancies. Notably these sections had higher LBE counts and median areas than sections classified in the wake regime by both metrics, which supports the Γ-based skimming flow classification and again suggests there may be uncertainty with the $\overline{\lambda_*^l}$ metric.

Table A1.13. Confusion matrix of the number of cross-sections classified into each of Morris's (1959) hydrodynamic regimes using $\overline{\boldsymbol{\lambda_*^l}}$ (columns) and Γ (rows) values for each discharge-dependent LBE dataset. Numbers along diagonals were classified the same by both metrics. Abbreviations are such that: IF – isolated roughness; WI – wake interference; and SF – skimming flow.

(a) 1.54 m^3/s		$\widehat{\lambda_*^l}$		
		IF	WI	SF
Γ	IF	509	165	182
	WI	780	743	619
	SF	203	381	654

(b) 10.79 m^3/s		$\widehat{\lambda_*^l}$		
		IF	WI	SF
Γ	IF	397	134	129
	WI	796	806	569
	SF	197	512	696

(c) 82.12 m^3/s		$\widehat{\lambda_*^l}$		
		IF	WI	SF
Γ	IF	279	83	48
	WI	891	875	468
	SF	216	661	668

(d) 343.6 m^3/s		$\widehat{\lambda_*^l}$		
		IF	WI	SF
Γ	IF	179	53	28
	WI	944	896	341
	SF	250	790	708

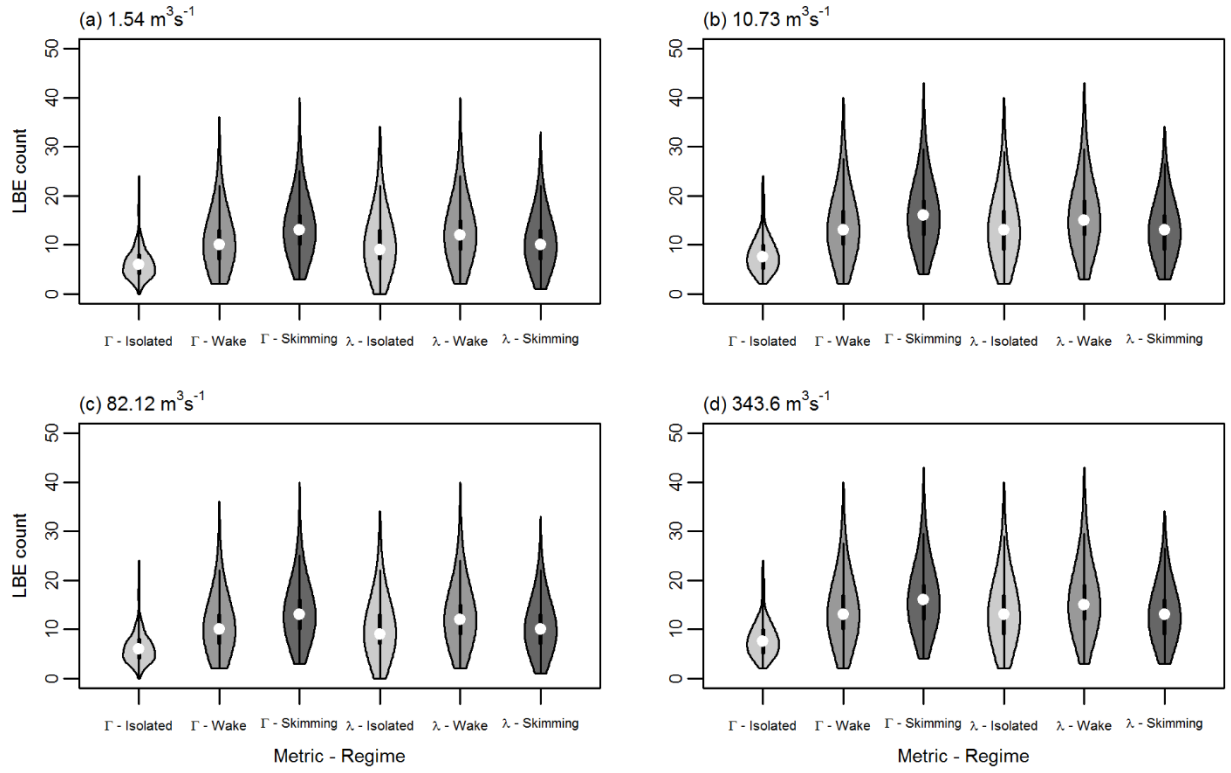

Figure A.1.11. Violin plots of LBE count distributions for cross-sections classified into each of the three hydrodynamic regimes using Γ and $\overline{\boldsymbol{\lambda}_*^{\boldsymbol{l}}}$ values for each discharge-dependent LBE dataset.

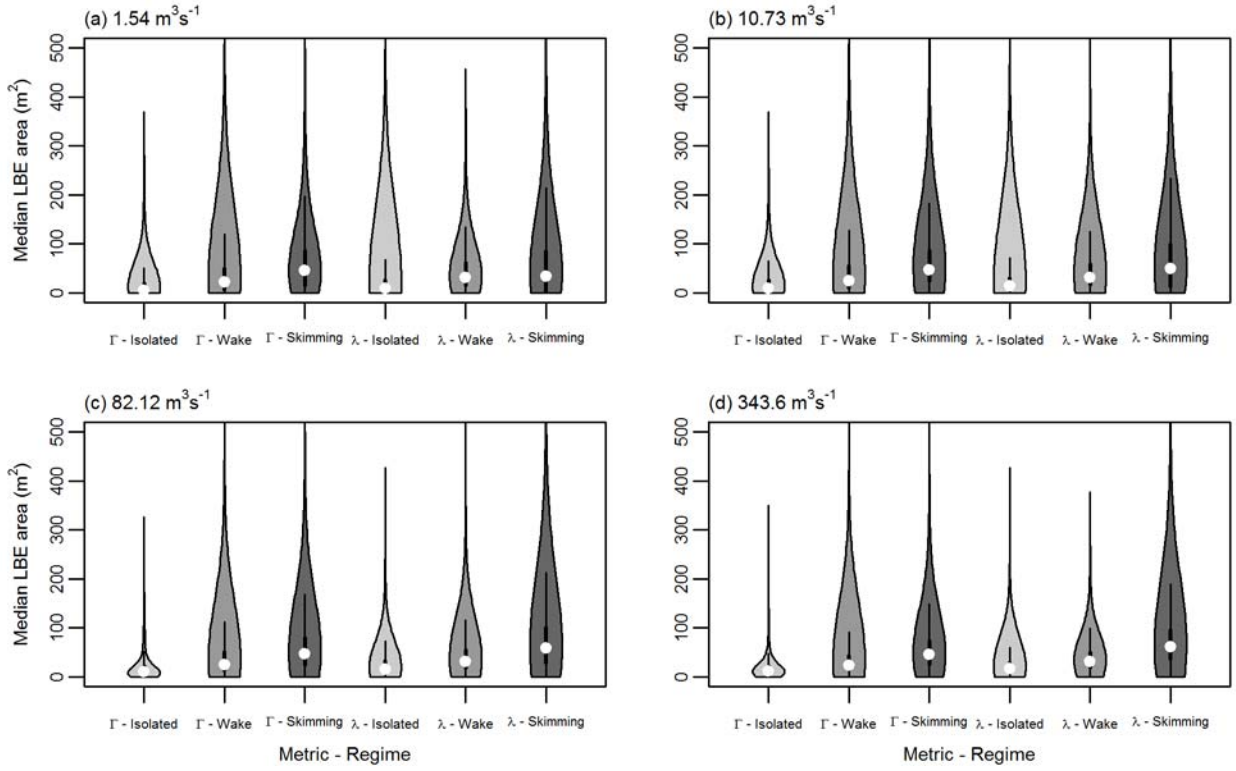

Figure A.1.12. Violin plots of median LBE area distributions for cross-sections classified into each of the three hydrodynamic regimes using Γ and $\overline{\boldsymbol{\lambda}_*^{\boldsymbol{I}}}$ values for each discharge-dependent LBE dataset.

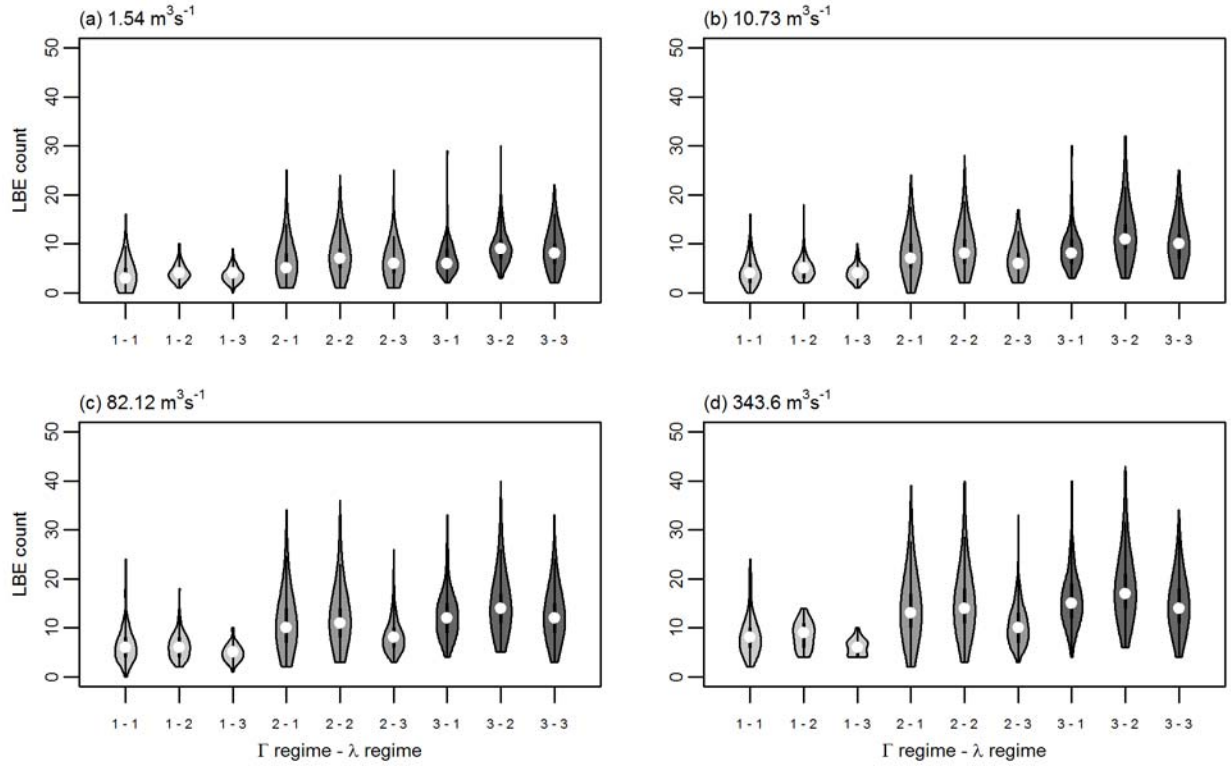

Figure A.1.13. Violin plots of cross-sectional LBE count distributions for each discharge-dependent LBE dataset stratified by how sections were classified into hydrodynamic regimes by both Γ and $\overline{\boldsymbol{\lambda}_*^{\boldsymbol{I}}}$ values. X-axis values are unique codes for all possible regime classification combinations. The first number corresponds to the Γ-based regime classification and the second number to the $\overline{\boldsymbol{\lambda}_*^{\boldsymbol{I}}}$-based regime classification. Values are coded as follows: 1 – isolated roughness; 2 – wake interference; and 3 – skimming flow.

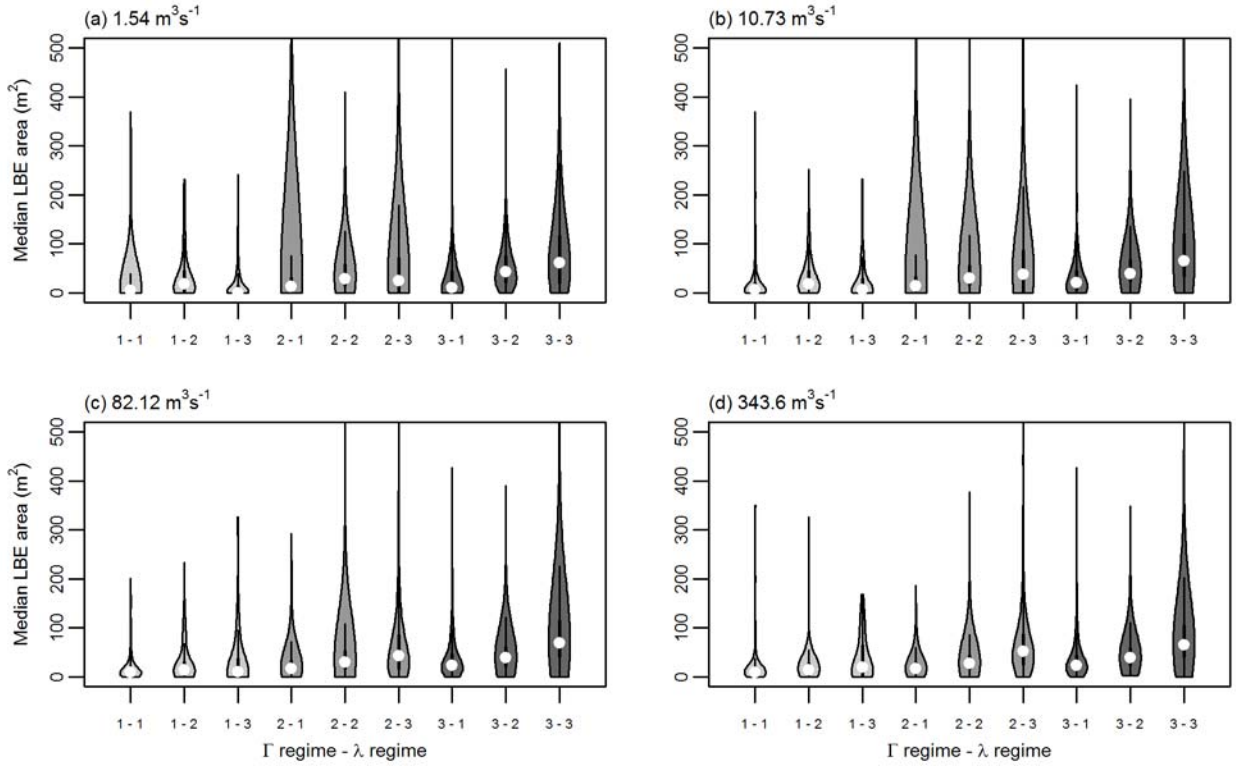

Figure A.1.14. Violin plots of cross sectional LBE median area distributions for each discharge-dependent LBE dataset stratified by how sections were classified into hydrodynamic regimes by both Γ and $\overline{\lambda_*^I}$ values. X-axis values are unique codes for all possible regime classification combinations. The first number corresponds to the Γ-based regime classification and the second number to the $\overline{\lambda_*^I}$-based regime classification. Values are coded as follows: 1 – isolated roughness; 2 – wake interference; and 3 – skimming flow.

A.1.4.6 Question 3 results (LBE lateral structure)

None.

A.1.5 Discussion

A.1.5.1 Mapping LBEs in a mountain river

None.

A.1.5.2 LBE lateral spatial structure and resistance

None.

A.1.5.3 Segment and reach resistance maximization

None.

A.1.5.4 Cross-section resistance maximization

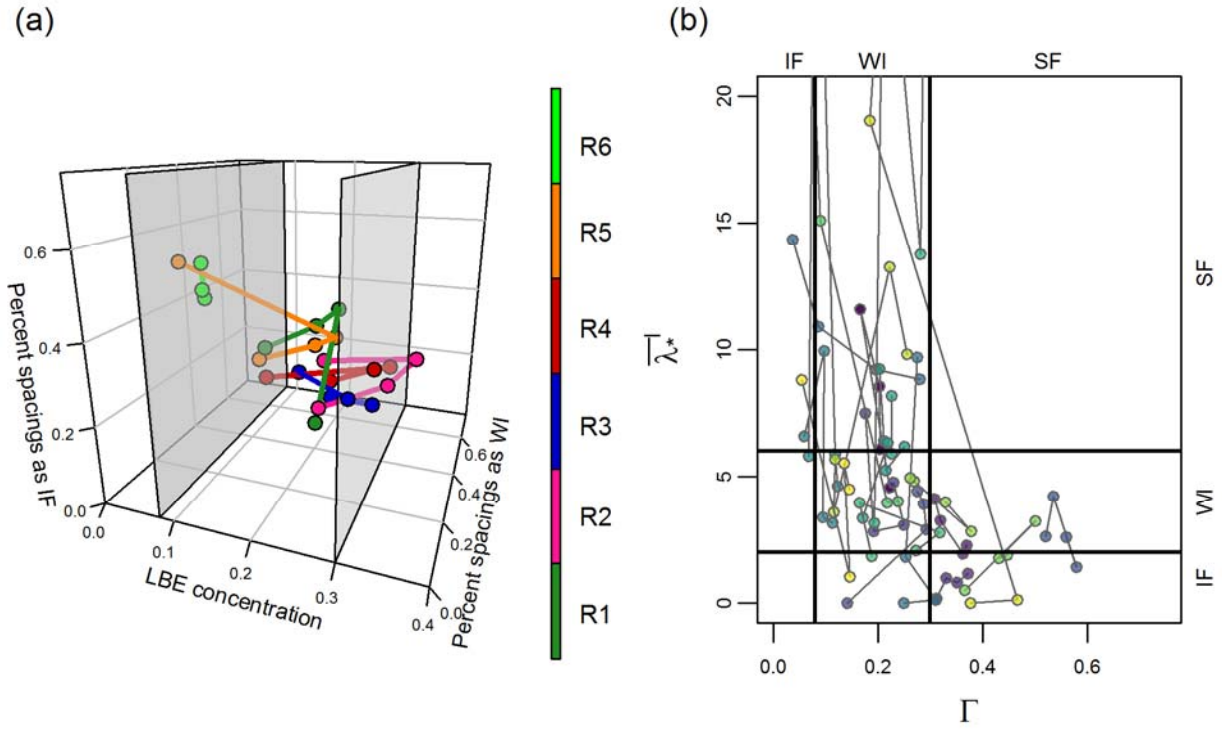

Figure A.1.15. (a) 3D phase-space showing reach-scale Γ (x-axis) and percentage of $\widehat{\lambda}_*^l$ values classified as WI (y-axis) and IF (z-axis). Vertical gray planes are Γ thresholds for Morris's hydrodynamic regimes. Regime thresholds for spacing were not able to be shown on this phase-phase, but can be inferred from the two spacing dimensions. (b) 2D phase-space showing cross-section scale Γ and $\overline{\lambda}_*^l$ values for 20 randomly selected cross-sections. Vertical and horizontal bold dark lines are thresholds for Morris's hydrodynamic regimes. Abbreviations are such that: R – Reach; IF – isolated roughness; WI – wake interference; and SF – skimming flow.

A.1.5.5 Resistance maximization as an attractor state

None.

A.1.6 Conclusions

None.

A.1.7 References

Abu-Aly, T. R., Pasternack, G. B., Wyrick, J. R., Barker, R., Massa, D., & Johnson, T. (2014). Effects of LiDAR-derived, spatially distributed vegetation roughness on two-dimensional hydraulics in a gravel-cobble river at flows of 0.2 to 20 times bankfull. *Geomorphology, 206*, 468-482. doi:http://dx.doi.org/10.1016/j.geomorph.2013.10.017

Alber, A., & Piégay, H. (2011). Spatial disaggregation and aggregation procedures for characterizing fluvial features at the network-scale: Application to the Rhône basin (France). *Geomorphology*, 125(3), 343-360. doi:https://doi.org/10.1016/j.geomorph.2010.09.009

Andersen, H. E., Reutebuch, S. E., & Schreuder, G. F. (2001). Automated individual tree measurement through morphological analysis of a lidar-based canopy surface model. Proceedings of the First International Precision Forestry Symposium, 11–22. June 17–20, 2001, Seattle, WA.

Argamosa, R. J. L., Paringit, E. C., Quinton, K. R., Tandoc, F. A. M., Faelga, R. A. G., Ibañez, C. A. G., . . . Zaragosa, G. P. (2016). Fully automated GIS-based individual tree crown delineation based on curvature values from a LIDAR derived canopy height model in a coniferous plantation. *Int. Arch. Photogramm. Remote Sens. Spatial Inf. Sci., XLI-B8*, 563-569. doi:10.5194/isprs-archives-XLI-B8-563-2016

Attal, M., Mudd, S. M., Hurst, M. D., Weinman, B., Yoo, K., & Naylor, M. (2015). Impact of change in erosion rate and landscape steepness on hillslope and fluvial sediments grain size in the Feather River basin (Sierra Nevada, California). *Earth Surf. Dynam., 3*(1), 201-222. doi:10.5194/esurf-3-201-2015

Baiamonte, G., & Ferro, V. (1997). The influence of roughness geometry and Shields parameter on flow resistance in gravel-bed channels. *Earth Surface Processes and Landforms, 22*(8), 759-772. doi:10.1002/(sici)1096-9837(199708)22:8<759::aid-esp779>3.0.co;2-m

Barnes, C., Balzter, H., Barrett, K., Eddy, J., Milner, S., Suárez, J.C. (2017). Individual Tree Crown Delineation from Airborne Laser Scanning for Diseased Larch Forest Stands. *Remote Sens*. 9, 231.

Barsi, Á., Kugler, Z., László, I., Szabó, G., & Abdulmutalib, H. M. (2018). Accuracy Dimensions in Remote Sensing. *ISPRS - International Archives of the Photogrammetry, Remote Sensing and Spatial Information Sciences, 42.3*, 61. doi:10.5194/isprs-archives-XLII-3-61-2018

Bathurst, J.C., (1978). Flow resistance of large-scale roughness. *J. Hydraul. Div*. ASCE 104, 1587–1603.

Bathurst, J. C. (1985). Flow Resistance Estimation in Mountain Rivers. *Journal of Hydraulic Engineering, 111*(4), 625-643. doi:doi:10.1061/(ASCE)0733-9429(1985)111:4(625)

Bathurst, J. C., Graf, W. H., & Cao, H. H. (1987), Bed load discharge equations for steep mountain rivers, in *Sediment Transport in Gravel-bed Rivers*, edited by Thorne et al., pp. 453–477, John Wiley, New York.

Benda, L. (1990). The influence of debris flows on channels and valley floors in the Oregon Coast Range, U.S.A. *Earth Surface Processes and Landforms, 15*(5), 457-466. doi:10.1002/esp.3290150508

Benda, L., & Dunne, T. (1997). Stochastic forcing of sediment routing and storage in channel networks. *Water Resources Research, 33*(12), 2865-2880. doi:10.1029/97wr02387

Beucher, S., & Meyer, F. (1993). The morphological approach to segmentation: the watershed transformation. *Mathematical morphology in image processing*, 433-481.

Billi, P. (1988). A note on cluster bedform behaviour in a gravel-bed river. *CATENA, 15*(5), 473-481. doi:https://doi.org/10.1016/0341-8162(88)90065-3

Brayshaw, A. C. (1985). Bed microtopography and entrainment thresholds in gravel-bed rivers. *GSA Bulletin, 96*(2), 218-223. doi:10.1130/0016-7606(1985)96<218:bmaeti>2.0.co;2

Brown, R. A., & Pasternack, G. B. (2008). Engineered channel controls limiting spawning habitat rehabilitation success on regulated gravel-bed rivers. *Geomorphology, 97*(3-4), 631-654. doi:10.1016/j.geomorph.2007.09.012

Brown, R.A., & Pasternack, G.B. (2012). *Monitoring and assessment of the 2010-2011 gravel/cobble augmentation in the Englebright Dam Reach of the lower Yuba River, CA. Prepared for the U.S. Army Corps of Engineers, Sacramento District.* Retrieved from University of California at Davis, Davis, CA.: http://pasternack.ucdavis.edu/files/5313/7692/9028/EDRreport_20121215_FINAL.pdf

Brown, R. A., & Pasternack, G. B. (2014). Hydrologic and topographic variability modulate channel change in mountain rivers. *Journal of Hydrology, 510*(Supplement C), 551-564. doi:https://doi.org/10.1016/j.jhydrol.2013.12.048

Buffington, J.M., Lisle, T.E., Woodsmith, R.D., & Hilton, S. (2002). Controls on the size and occurrence of pools in coarse-grained forest rivers. *River Res. Applic.*, 18: 507-531. doi:10.1002/rra.693

Byrd, T.C., Furbish, D.J., & Warburton, J. (2000). Estimating depth-averaged velocities in rough channels. *Earth Surf. Process. Landforms*, 25: 167-173. doi:10.1002/(SICI)1096-9837(200002)25:2<167::AID-ESP66>3.0.CO;2-G

Canovaro, F., Paris, E., & Solari, L. (2007). Effects of macro-scale bed roughness geometry on flow resistance. *Water Resources Research, 43*(10). doi:10.1029/2006wr005727

Chen, Q., Baldocchi, D., Gong, P., & Kelly, M. (2006). Isolating individual trees in a savanna woodland using small footprint lidar data. *Photogrammetric Engineering and Remote Sensing, 72*, 923-932.

Church, M., Hassan, M. A., & Wolcott, J. F. (1998). Stabilizing self-organized structures in gravel-bed stream channels: Field and experimental observations. *Water Resources Research, 34*(11), 3169-3179. doi:10.1029/98wr00484

Church, M., & Zimmermann, A. (2007). Form and stability of step-pool channels: Research progress. *Water Resources Research, 43*(3), n/a-n/a. doi:10.1029/2006WR005037

Cienciala, P., & Hassan, M. A. (2013). Linking spatial patterns of bed surface texture, bed mobility, and channel hydraulics in a mountain stream to potential spawning substrate for small resident trout. *Geomorphology, 197*(Supplement C), 96-107. doi:https://doi.org/10.1016/j.geomorph.2013.04.041

Culvenor, D. S. (2002). TIDA: an algorithm for the delineation of tree crowns in high spatial resolution remotely sensed imagery. *Computers & Geosciences, 28*(1), 33-44. doi:https://doi.org/10.1016/S0098-3004(00)00110-2

Dalponte, M., Frizzera, L., & Gianelle, D. (2019). Individual tree crown delineation and tree species classification with hyperspectral and LiDAR data. *PeerJ,* 6:e6227 DOI 10.7717/peerj.6227.

Dralle, K., & Rudemo, M. (1996). Stem number estimation by kernel smoothing of aerial photos. *Canadian Journal of Forest Research, 26*(7), 1228-1236. doi:10.1139/x26-137

Evans, J.S. (2020). *spatialEco*. R package version 1.3-1, https://github.com/jeffreyevans/spatialEco.

Fang, H. W., Liu, Y., & Stoesser, T. (2017). Influence of Boulder Concentration on Turbulence and Sediment Transport in Open-Channel Flow Over Submerged Boulders. *Journal of Geophysical Research: Earth Surface, 122*(12), 2392-2410. doi:10.1002/2017jf004221

Faustini, J. M., & Jones, J. A. (2003). Influence of large woody debris on channel morphology and dynamics in steep, boulder-rich mountain streams, western Cascades, Oregon. *Geomorphology, 51*(1), 187-205. doi:https://doi.org/10.1016/S0169-555X(02)00336-7

Ferguson, R. I., Sharma, B. P., Hardy, R. J., Hodge, R. A., & Warburton, J. (2017). Flow resistance and hydraulic geometry in contrasting reaches of a bedrock channel. *Water Resources Research, 53*(3), 2278-2293. doi:10.1002/2016WR020233.

Ferro, V. (1999). Friction Factor for Gravel-Bed Channel with High Boulder Concentration. *Journal of Hydraulic Engineering, 125*(7), 771-778. doi:doi:10.1061/(ASCE)0733-9429(1999)125:7(771)

Finnegan, N. J., Broudy, K. N., Nereson, A. L., Roering, J. J., Handwerger, A. L., & Bennett, G. (2019). River channel width controls blocking by slow-moving landslides in California's Franciscan mélange. *Earth Surf. Dynam., 7*(3), 879-894. doi:10.5194/esurf-7-879-2019

Ghilardi, T., Franca, M. J., & Schleiss, A. J. (2014). Bed load fluctuations in a steep channel. *Water Resources Research, 50*(8), 6557-6576. doi:10.1002/2013wr014449

Gippel, C. J., O'neill, I. C., Finlayson, B. L., & Schnatz, I. (1996). Hydraulic guidelins for the re-inroduction and management of large woody debris in lowland rivers. *Regulated Rivers: Research & Management, 12*(2-3), 223-236. doi:10.1002/(sici)1099-1646(199603)12:2/3<223::aid-rrr391>3.0.co;2-#

Glade, R. C., Shobe, C. M., Anderson, R. S., & Tucker, G. E. (2019). Canyon shape and erosion dynamics governed by channel-hillslope feedbacks. *Geology, 47*(7), 650-654. doi:10.1130/g46219.1

Gomez, B. (1993). Roughness of stable, armored gravel beds. *Water Resources Research, 29*(11), 3631-3642. doi:10.1029/93wr01490

Grant, G. E., & Swanson, F. J. (1995). Morphology and Processes of Valley Floors in Mountain Streams, Western Cascades, Oregon. *Natural and Anthropogenic Influences in Fluvial Geomorphology* (J. Costa, A. Miller, K. Potter and P. Wilcock ed.).

Grant, G. E., Swanson, F. J., & Wolman, M. G. (1990). Pattern and origin of stepped-bed morphology in high-gradient streams, Western Cascades, Oregon. *GSA Bulletin, 102*(3), 340-352. doi:10.1130/0016-7606(1990)102<0340:PAOOSB>2.3.CO;2

Groom, J., & Friedrich, H. (2019). Spatial structure of near-bed flow properties at the grain scale. *Geomorphology, 327*, 14-27. doi:https://doi.org/10.1016/j.geomorph.2018.10.013

Hardy, R. J., Best, J. L., Lane, S. N., & Carbonneau, P. E. (2009). Coherent flow structures in a depth-limited flow over a gravel surface: The role of near-bed turbulence and influence of Reynolds number. *Journal of Geophysical Research: Earth Surface, 114*(F1). doi:10.1029/2007jf000970

Hassan, M. A., Bird, S., Reid, D., Ferrer-Boix, C., Hogan, D., Brardinoni, F., & Chartrand, S. (2019). Variable hillslope-channel coupling and channel characteristics of forested mountain streams in glaciated landscapes. *Earth Surface Processes and Landforms, 44*(3), 736-751. doi:10.1002/esp.4527

Hassan, M. A., & Reid, I. (1990). The influence of microform bed roughness elements on flow and sediment transport in gravel bed rivers. *Earth Surface Processes and Landforms, 15*(8), 739-750. doi:10.1002/esp.3290150807

Isenburg, M. (2016). "LAStools - efficient LiDAR processing software" (version 160730, unlicensed), obtained from http://rapidlasso.com/LAStools.

Jakubowski, M.K., Li, W., Guo, Q., & Kelly, M. (2013). Delineating Individual Trees from Lidar Data: A Comparison of Vector- and Raster-based Segmentation Approaches. *Remote Sens*. 4163-4186.

Johnson, J. P. L., Whipple, K. X., Sklar, L. S., & Hanks, T. C. (2009). Transport slopes, sediment cover, and bedrock channel incision in the Henry Mountains, Utah. *Journal of Geophysical Research: Earth Surface, 114*(F2). doi:10.1029/2007jf000862

Kirchner, J. W., Dietrich, W. E., Iseya, F., & Ikeda, H. (1990). The variability of critical shear stress, friction angle, and grain protrusion in water-worked sediments. *Sedimentology, 37*(4), 647-672. doi:10.1111/j.1365-3091.1990.tb00627.x

Koch, B., Heyder, U., & Weinacker, H. (2006). Detection of individual tree crowns in airborne lidar data. *Photogramm. Eng. Remote Sens*, 72, 357–363. https://doi.org/10.14358/PERS.72.4.357

Koukoulas, S., & Blackburn, G. A. (2005). Mapping individual tree location, height and species in broadleaved deciduous forest using airborne LIDAR and multi-spectral remotely sensed data. *International Journal of Remote Sensing, 26*(3), 431-455. doi:10.1080/0143116042000298289

Kwak, D.-A., Lee, W.-K., Lee, J.-H., Biging, G. S., & Gong, P. (2007). Detection of individual trees and estimation of tree height using LiDAR data. *Journal of Forest Research, 12*(6), 425-434. doi:10.1007/s10310-007-0041-9

L'Hommedieu, W., Tullos, D., & Jones, J. (2020). Effects of an engineered log jam on spatial variability of the flow field across submergence depths. *River Res Applic,* 36: 383– 397. https://doi.org/10.1002/rra.3555

Labatut, V., & Cherifi, H. (2011). *Accuracy Measures for the Comparison of Classifiers.* Paper presented at the The 5th International Conference on Information Technology, amman, Jordan.

Lacey, R. W. J., & Roy, A. G. (2008). The spatial characterization of turbulence around large roughness elements in a gravel-bed river. *Geomorphology, 102*(3), 542-553. doi:https://doi.org/10.1016/j.geomorph.2008.05.045

Lai, Y. G. (2008). *"SRH-2D version 2: Theory and User's Manual Sedimentation and River Hydraulics – Two-Dimensional River Flow Modeling"*. Retrieved from U.S. Department of the Interior, Bureau of Reclamation, Technical Service Center, Sedimentation and River Hydraulics Group. Denver, Colorado.: https://www.usbr.gov/tsc/techreferences/computer%20software/models/srh2d/index.html

Lamarre, H., & Roy, A. G. (2005). Reach scale variability of turbulent flow characteristics in a gravel-bed river. *Geomorphology, 68*(1), 95-113. doi:https://doi.org/10.1016/j.geomorph.2004.09.033

Landcaster, S. T., Hayes, S. K., & Grant, G. E. (2001). Modeling Sediment and Wood Storage and Dynamics in Small Mountainous Watersheds *Geomorphic Processes and Riverine Habitat* (pp. 85-102).

Laronne, J. B., Garcia, C., & Reid, I. (2001). Mobility of patch sediment in gravel-bed streasm: Patch character and its implications for bedload, in *Gravel Bed Rivers V*, edited by M. P. Mosley, pp. 249–289, New Zealand Hydrological Society, Wellington, N. Z.

Leckie, D., Gougeon, F., Hill, D., Quinn, R., Armstrong, L., & Shreenan, R. (2003). Combined high-density lidar and multispectral imagery for individual tree crown analysis. *Canadian Journal of Remote Sensing, 29*(5), 633-649. doi:10.5589/m03-024

Legleiter, C. J., Roberts, D. A., Marcus, W. A., & Fonstad, M. A. (2004). Passive optical remote sensing of river channel morphology and in-stream habitat; physical basis and feasibility. *Remote Sensing of Environment, 93*(4), 493-510. doi:http://dx.doi.org/10.1016/j.rse.2004.07.019

Lisle, T. E. (1986). Stabilization of a gravel channel by large streamside obstructions and bedrock bends, Jacoby Creek, northwestern California. *GSA Bulletin, 97*(8), 999-1011. doi:10.1130/0016-7606(1986)97<999:soagcb>2.0.co;2

Lisle, T. E., Nelson, J. M., Pitlick, J., Madej, M. A., & Barkett, B. L. (2000). Variability of bed mobility in natural, gravel-bed channels and adjustments to sediment load at local and reach scales. *Water Resources Research, 36*(12), 3743-3755. doi:10.1029/2000wr900238

MacKenzie, L. G., & Eaton, B. C. (2017). Large grains matter: contrasting bed stability and morphodynamics during two nearly identical experiments. *Earth Surf. Process. Landforms*, 42: 1287– 1295. doi: 10.1002/esp.4122.

MacWilliams, M. L., Wheaton, J. M., Pasternack, G. B., Street, R. L., & Kitanidis, P. K. (2006). Flow convergence routing hypothesis for pool-riffle maintenance in alluvial rivers. *Water Resour. Res., 42*, W10427.

Madej, M. A. (2001). Development of channel organization and roughness following sediment pulses in single-thread, gravel bed rivers. *Water Resources Research, 37*(8), 2259-2272. doi:10.1029/2001wr000229

McKean, J., Tonina, D., Bohn, C., & Wright, C. W. (2014). Effects of bathymetric lidar errors on flow properties predicted with a multi-dimensional hydraulic model. *Journal of Geophysical Research-Earth Surface, 119*(3), 644-664. doi:10.1002/2013jf002897

Monsalve, A., Yager, E. M., & Schmeeckle, M. W. (2017). Effects of bed forms and large protruding grains on near-bed flow hydraulics in low relative submergence conditions. *Journal of Geophysical Research: Earth Surface, 122*, 1845– 1866. https://doi.org/10.1002/2016JF004152

Moriasi, D. N., Arnold, J. G., Van Liew, M. W., Bingner, R. L., Harmel, R. D., & Veith, T. L. (2007). Model Evaluation Guidelines for Systematic Quantification of Accuracy in Watershed Simulations. *Transactions of the ASABE, 50*(3), 885. doi:https://doi.org/10.13031/2013.23153

Morris, H. (1959). Design methods for flow in rough channels. *Proc. ASCE, Journal of Hydraulics Division, 85*((HY7)), 43-62.

Morsdorf, F., Meier, E., Kötz, B., Itten, K. I., Dobbertin, M., & Allgöwer, B. (2004). LIDAR-based geometric reconstruction of boreal type forest stands at single tree level for forest and wildland fire management. *Remote Sensing of Environment, 92*(3), 353-362. doi:https://doi.org/10.1016/j.rse.2004.05.013

Nelson, J.M., Shimizu, Y., Abe, T., Asahi, K., Gamou, M., Inoue, T., Iwasaki, T., Kakinuma, T., Kawamura, S., Kimura, I., Kyuka, T., McDonald, R.R., Nabi, M., Nakatsugawa, M., Simões, F.R., Takebayashi, H., & Watanabe, Y. (2016). The international river interface cooperative: Public domain flow and morphodynamics software for education and applications. *Advances in Water Resources 93*: 62–74. https://doi.org/10.1016/j.advwatres.2015.09.017.

Nitsche, M., Rickenmann, D., Turowski, J. M., Badoux, A., & Kirchner, J. W. (2011). Evaluation of bedload transport predictions using flow resistance equations to account for macro-roughness in steep mountain streams. *Water Resources Research, 47*(8). doi:10.1029/2011wr010645

Nowell, A. R. M., & Church, M. (1979). Turbulent flow in a depth-limited boundary layer. *Journal of Geophysical Research: Oceans, 84*(C8), 4816-4824. doi:10.1029/JC084iC08p04816

Otsu, N. (1979). "A Threshold Selection Method from Gray-Level Histograms," in *IEEE Transactions on Systems, Man, and Cybernetics*, vol. 9, no. 1, pp. 62-66, doi: 10.1109/TSMC.1979.4310076.

Pagliara, S., Das, R., & Carnacina, I. (2008). Flow resistance in large-scale roughness condition. *Canadian Journal of Civil Engineering, 35*(11), 1285-1293. doi:10.1139/L08-068

Paola, C., & Seal, R. (1995). Grain Size Patchiness as a Cause of Selective Deposition and Downstream Fining, *Water Resour. Res.*, 31(5), 1395– 1407, doi:10.1029/94WR02975.

Paola, C., Heller, P., & Angevine, C. (1992). The large-scale dynamics of grain-size variation in alluvial basins: 1. Theory, *Basin Res*., 4, 73–90.

Papanicolaou, A. N., & Tsakiris, A. G. (2017). Boulder Effects on Turbulence and Bedload Transport. In D. T. a. J. B. Laronne (Ed.), *Gravel-Bed Rivers*.

Pasternack, G. B. (2008). Spawning Habitat Rehabilitation: Advances in Analysis Tools. In D. A. Sear & P. DeVries (Eds.), *Salmonid Spawning Habitat in Rivers: Physical Controls, Biological Responses, and Approaches to Remediation* (Vol. 65, pp. 321-348). Bethesda: Amer Fisheries Soc.

Pasternack, G. B. (2011). *2D Modeling and Ecohydraulic Analysis*. Seatle, WA: Createspace.

Pasternack, G. B., Ellis, C. R., Leier, K. A., Vallé, B. L., & Marr, J. D. (2006). Convergent hydraulics at horseshoe steps in bedrock rivers. *Geomorphology, 82*(1), 126-145. doi:https://doi.org/10.1016/j.geomorph.2005.08.022

Pasternack, G. B., & MacVicar, B. J. (2013). *Gold-standard performance for 2D hydrodynamic modeling. Abstract EP51B-0708.* Paper presented at the 2013 Fall Meeting, AGU, San Francisco, Calif., 9-13 Dec.

Pasternack, G. B., & Senter, A. E. (2011). *21st Century instream flow assessment framework for mountain streams.* Retrieved from California Energy Commission, PIER. CEC-500-2013-059.: https://www.energy.ca.gov/2013publications/CEC-500-2013-059/CEC-500-2013-059.pdf

Piedra, M. M., Haynes, H., & Hoey, T. B. (2012). The spatial distribution of coarse surface grains and the stability of gravel river beds. *Sedimentology, 59*(3), 1014-1029. doi:10.1111/j.1365-3091.2011.01290.x

Plowright, A., & Roussel, J. (2020). ForestTools: Analyzing Remotely Sensed Forest Data. R package version 0.2.1. https://CRAN.R-project.org/package=ForestTools

Popescu, S. C., & Wynne, R. H. (2004). Seeing the Trees in the Forest. *Photogrammetric Engineering & Remote Sensing, 70*(5), 589-604. doi:10.14358/PERS.70.5.589

Reid, I. & Hassan, M.A. (1992). The influence of microform bed roughness elements on flow and sediment transport in gravel bed rivers: A reply. *Earth Surf. Process. Landforms*, 17: 535-538. doi:10.1002/esp.3290170512

Reid, D. A., Hassan, M. A., Bird, S., Pike, R., & Tschaplinski, P. (2020) Does variable channel morphology lead to dynamic salmon habitat?. *Earth Surf. Process. Landforms*, 45: 295–311. https://doi.org/10.1002/esp.4726.

Richardson, K., & Carling, P. A. (2006). The hydraulics of a straight bedrock channel: Insights from solute dispersion studies. *Geomorphology, 82*(1), 98-125. doi:https://doi.org/10.1016/j.geomorph.2005.09.022

Sawyer, A. M., Pasternack, G. B., Moir, H. J., & Fulton, A. A. (2010). Riffle-pool maintenance and flow convergence routing observed on a large gravel-bed river. *Geomorphology, 114*(3), 143-160. doi:10.1016/j.geomorph.2009.06.021

Schneider, J. M., Rickenmann, D., Turowski, J. M., & Kirchner, J. W. (2015a). Self-adjustment of stream bed roughness and flow velocity in a steep mountain channel. *Water Resources Research, 51*(10), 7838-7859. doi:10.1002/2015wr016934

Schneider, J. M., Rickenmann, D., Turowski, J. M., Bunte, K., & Kirchner, J. W. (2015b). Applicability of bed load transport models for mixed-size sediments in steep streams considering macro-roughness. *Water Resources Research, 51*(7), 5260-5283. doi:10.1002/2014wr016417

Sear, D.A. (1992). Impact of hydroelectric power release on sediment transport processes in pool-riffle sequences. In *Dynamics of Gravel Bed Rivers*, Billi, P., Hey, R.D., Thorne, C.R., & Tacconi, P. (eds). Wiley: Chichester; 629–650.

Sear, D.A. (1995). The effect of 10 years river regulation for hydropower on the morphology and sedimentology of a gravel-bed river. *Regulated Rivers* **10**: 247–264.

Sear, D.A. (1996). Sediment transport in riffle-pool sequences. *Earth Surface Processes and Landforms* **21**: 147–164.

Shamloo, H., Rajaratnam, N., & Katopodis, C. (2001). Hydraulics of simple habitat structures. *Journal of Hydraulic Research, 39*(4), 351-366. doi:10.1080/00221680109499840

Shao, G., Tang, L., & Liao, J. (2019). Overselling overall map accuracy misinforms about research reliability. *Landscape Ecology, 34*(11), 2487-2492. doi:10.1007/s10980-019-00916-6

Shobe, C. M., Tucker, G. E., & Anderson, R. S. (2016). Hillslope-derived blocks retard river incision. *Geophysical Research Letters, 43*(10), 5070-5078. doi:10.1002/2016gl069262

Sklar, L. S., & Dietrich, W. E. (2004). A mechanistic model for river incision into bedrock by saltating bed load. *Water Resources Research, 40*(6). doi:10.1029/2003wr002496

Strîmbu, V. F., & Strîmbu, B. M. (2015). A graph-based segmentation algorithm for tree crown extraction using airborne LiDAR data. *ISPRS Journal of Photogrammetry and Remote Sensing, 104*, 30-43. doi:https://doi.org/10.1016/j.isprsjprs.2015.01.018

Strom, M. A., Pasternack, G. B., Burman, S. G., Dahlke, H. E., & Sandoval-Solis, S. (2017). Hydraulic hazard exposure of humans swept away in a whitewater river. *Natural Hazards, 88*(1), 473-502. doi:10.1007/s11069-017-2875-6

Strom, M. A., Pasternack, G. B., & Wyrick, J. R. (2016). Reenvisioning velocity reversal as a diversity of hydraulic patch behaviours. *Hydrological Processes, 30*(13), 2348-2365. doi:10.1002/hyp.10797

Sullivan, A. A., McGaughey, R. J., Andersen, H.-E., & Schiess, P. (2009). Object-Oriented Classification of Forest Structure from Light Detection and Ranging Data for Stand Mapping. *Western Journal of Applied Forestry, 24*(4), 198-204. doi:10.1093/wjaf/24.4.198

Sutfin, N. A., & Wohl, E. (2019). Elevational differences in hydrogeomorphic disturbance regime influence sediment residence times within mountain river corridors. *Nature Communications, 10*(1), 2221. doi:10.1038/s41467-019-09864-w

Tan, L., & Curran, J. C. (2012). Comparison of Turbulent Flows over Clusters of Varying Density. *Journal of Hydraulic Engineering, 138*(12), 1031-1044. doi:doi:10.1061/(ASCE)HY.1943-7900.0000635

Thompson, C. J., Fryirs, K., & Croke, J. (2016). The Disconnected Sediment Conveyor Belt: Patterns of Longitudinal and Lateral Erosion and Deposition During a Catastrophic Flood in the Lockyer Valley, South East Queensland, Australia. *River Research and Applications, 32*(4), 540-551. doi:10.1002/rra.2897

Thompson, D. M. (2001). Random controls on semi-rhythmic spacing of pools and riffles in constriction-dominated rivers. *Earth Surface Processes and Landforms, 26*(11), 1195-1212. doi:10.1002/esp.265

Thompson, D. M. (2008). The influence of lee sediment behind large bed elements on bedload transport rates in supply-limited channels. *Geomorphology, 99*(1), 420-432. doi:https://doi.org/10.1016/j.geomorph.2007.12.004

Turowski, J. M., Lague, D., & Hovius, N. (2007). Cover effect in bedrock abrasion: A new derivation and its implications for the modeling of bedrock channel morphology, *J. Geophys. Res.*, 112, F04006, doi:10.1029/2006JF000697.

Turowski, J.M., Hovius, N., Meng-Long, H., Lague, D., & Men-Chiang, C. (2008). Distribution of erosion across bedrock channels. *Earth Surf. Process. Landforms*, 33: 353-363. doi:10.1002/esp.1559

Weichert, R. (2006). "*Bed Morphology and Stability of Steep Open Channels"*. In Mitteilung 192, Zürich: Versuchsanstalt fürWasserbau, Hydrologie und Glaziologie (VAW), ETH. https://doi.org/10.3929/ethz-a-005135522

Wentworth, C. (1922). A Scale of Grade and Class Terms for Clastic Sediments. *The Journal of Geology*, 30(5), 377-392. http://www.jstor.org/stable/30063207

Wiener, J., & Pasternack, G.B. (2016). 2014 Topographic Mapping Report- Yuba River from New Bullards Bar to Colgate Powerhouse. Prepared for Yuba County Water Agency. University of California, Davis, CA. Retrieved from http://pasternack.ucdavis.edu/index.php?cID=429

Williams, R. D., Reid, H. E., & Brierley, G. J. (2019). Stuck at the Bar: Larger-Than-Average Grain Lag Deposits and the Spectrum of Particle Mobility. *Journal of Geophysical Research: Earth Surface, 124*(12), 2751-2756. doi:10.1029/2019jf005137

Wittenberg, L., & Newson, M. D. (2005). Particle clusters in gravel-bed rivers: an experimental morphological approach to bed material transport and stability concepts. *Earth Surface Processes and Landforms, 30*(11), 1351-1368. doi:10.1002/esp.1184

Wyrick, J.R., & Pasternack, G.B., (2012). Specific sampling protocols for delineating morphological units and mesohabitats: methodology for classifying channel landforms. Prepared for the Lower Yuba River Accord, River Management Team. June 2011. 30p.

Yager, E. M., Dietrich, W. E., Kirchner, J. W., & McArdell, B. W. (2012). Prediction of sediment transport in step-pool channels. *Water Resources Research, 48*(1). doi:10.1029/2011wr010829

Yager, E. M., Kirchner, J. W., & Dietrich, W. E. (2007). Calculating bed load transport in steep boulder bed channels. *Water Resources Research, 43*(7). doi:10.1029/2006wr005432

Yang, K., Cao, S., & Liu, X. (2007). Flow resistance and its prediction methods in compound channels. *Acta Mechanica Sinica, 23*(1), 23-31. doi:10.1007/s10409-006-0043-4

Yochum, S. E., Comiti, F., Wohl, E., David, G. C. L., & Mao, L. (2014). *Photographic guidance for selecting flow resistance coefficients in high-gradient channels*. Retrieved from https://www.fs.usda.gov/treesearch/pubs/46250

Zhang, K., & Whitman, D. (2005). Comparison of Three Algorithms for Filtering Airborne Lidar Data. *Photogrammetric Engineering & Remote Sensing, 71*(3), 313-324. doi:10.14358/PERS.71.3.313

Zimmermann, A., & Church, M. (2001). Channel morphology, gradient profiles and bed stresses during flood in a step–pool channel. *Geomorphology, 40*(3), 311-327. doi:https://doi.org/10.1016/S0169-555X(01)00057-5

APPENDIX 2. Supporting Information for 'Process-based similarity' revealed by discharge-dependent relative submergence dynamics of thousands of large bed elements

This appendix provide supplemental materials that include information on the following topics:

- Details of statistical assessment of LBE relative submergence distributions and alternative methods used to calculate LBE relative submergence (1A.2.3.4);
- Details of LBE relative submergence analysis methods (1A.2.3.5 and 1A.2.3.6);
- Additional LBE relative submergence distribution results (1A.2.4.1);
- Additional LBE relative submergence distribution type and Style results (1A.2.4.2);
- Additional process-based similarity Style results (1A.2.4.3);
- Additional incremental inundation corridor relative submergence results (1A.2.4.4);
- Additional submergence trends and alternative relative submergence calculation results (1A.2.4.5);
- Additional discussion on relative submergence implications including resistance equations (1A.2.5.3); and
- References.

The organization of this appendix uses the same outline and headings of the chapter to which this supplements. Subject heading followed by the word "none" indicate no supplemental information is provided for that section.

A.2.1 Introduction

None.

A.2.1.1 Background

None.

A.2.1.2 Styles of LBE relative submergence response to discharge

As stated in the main text, the evolution of river channel h/D_c distributions from one discharge to another involves: (i) depth changes at previously wetted LBEs result in a new distribution of h/D_c values at just these LBEs; and (ii) new LBEs become wetted along the expanding channel margin (i.e. the incremental inundation corridor [IIC]) and their distribution is convolved with the new distribution of previously wetted LBEs. The assumption for this study is that h/D_c values at newly wetted LBEs would be relatively low compared to the set of previously wetted LBE and depth at most previously wetted LBEs would increase with increasing discharge. Both assumptions are realistic for partly-confined to confined rivers, but may not always be the case. For each change in discharge the two processes described above occur in tandem to form each unique set of discharged-dependent h/Dc values. Examples of how these processes could result in the conceptualized Style 2 and Style 3 conditions are described in the main text and graphically depicted in Figure A.2.1.

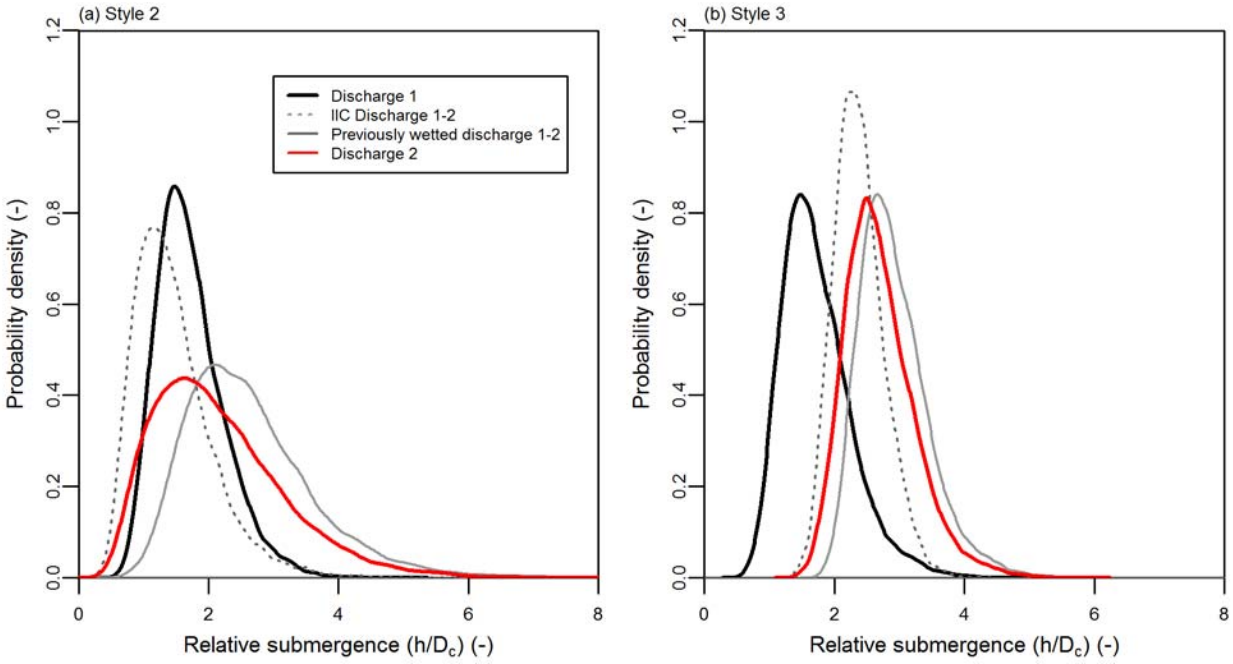

Figure A.2.1. Conceptual illustration showing how a h/D_c distribution at an initial discharge (solid dark line) can evolve to a new h/D_c distribution at a second discharge (solid red line) through combination of the new h/D_c distribution of previously wetted LBEs (solid gray line) and the incremental inundation corridor h/D_c distribution (dashed gray line) that result in conditions conceptualized in (a) Style 2 and (b) Style (3).

A.2.1.3 Study questions

None.

A.2.2 Study river segment

None.

A.2.3 Methods

A.2.3.1 Topographic and bathymetric mapping

None.

A.2.3.2 LBE mapping

None.

A.2.3.3 Two-dimensional hydrodynamic modeling

None.

A.2.3.4 Relative submergence calculations

As discussed in the main text, relative submergence calculations were not without potential issues and uncertainty, and thus one alternative method for calculating depth (h) as well as an alternative method for calculating LBE representative grain size (D_c) at each LBE were explored. The alternative grain size metric, $\overline{D}$, could be informative if LBEs have complex shapes that are poorly represented by a single maximum height. For reference, a perfect hemisphere would have $\overline{D} = \frac{2}{3}D_c$. If area was held equal, a wider spheroid would have a $\overline{D}$ that was a larger percentage of D_c, a taller spheroid would have a $\overline{D}$ that was a smaller percentage of D_c, and a cube or rectangle would have $\overline{D} = D_c$. Most of the predicted LBEs, resembled hemispherical to hemispheroidal objects such that 71 percent were in the range of $0.25D_c < \overline{D} < 0.75D_c$ (Wiener & Pasternack, 2022). Therefore, $\overline{D}$ is generally less than D_c for LBEs in the study segment. The alternative depth metric, $\hat{h}$, is always less than or equal to h. Using the two particle size metrics (D_c and $\overline{D}$) and two measures for depth (h and $\hat{h}$), four relative submergence values were calculated for each LBE for each discharge to address sensitivity of the calculation methods.

A.2.3.5 LBE relative submergence general hypothesis testing

Statistical properties of all 39 h/D_c distributions were calculated using the R programming language and included the arithmetic mean [$\bar{x}$], standard deviation [σ], mode [φ], coefficient of skewness [g], and coefficient of kurtosis [β_2] (R Core Team, 2021). Both g and β_2 were calculated using the 'EnvStat' package (Millard, 2013**)**. Modal values were calculated from frequency histograms using the midpoint of the bin with the highest count. The number of bins for each dataset followed the approach of Freedman and Diaconis, (1981) (Table A.2.1).

Table A.2.1. Segment- and reach-scale h/D_c histogram bin-widths (m) used for modal calculations.

Discharge (m^3/s)	Spatial Domain						
	Segment	Reach 1	Reach 2	Reach 3	Reach 4	Reach 5	Reach 6
1.54	0.05	0.1	0.05	0.1	0.05	0.05	0.1
10.73	0.05	0.1	0.1	0.1	0.1	0.1	0.1
82.12	0.1	0.2	0.2	0.5	0.2	0.2	0.5
343.6	0.2	0.5	0.5	0.5	0.5	0.5	0.5
1184.6	0.5	1	1	1	0.5	1	1

A.2.3.6 LBE relative submergence distribution and styles analysis

As discussed in the main text, statistical properties of h/D_c data (e.g. $\bar{x}$, σ, φ, g, and β_2) were compared within domains either qualitatively, or using non-parametric or appropriate parametric statistical tests. Comparison of φ, g, and, β_2 values was done qualitatively, simply comparing relative magnitudes and trends of how values changed between datasets. Comparison of $\bar{x}$ and σ values between datasets was done using Welch's t-test and F-test, respectively, for normally distributed h/D_c datasets and with the Mann-Whitney U and Levene's tests, respectively, for non-normally distributed h/D_c datasets (R Core Team, 2021; Fox & Weisberg, 2019). Normality was assessed based on the best fitting distribution for each dataset.

Six conceptual discharge-dependent h/D_c distribution behavior styles were presented in the main text (Section 2.2.2), additional details on hypothesis testing for Styles 2-4 not described in the main text are presented below. For all Styles central tendency was tested between datasets using either Welch's t-test or Mann-Whitney U test for normally and non-normally h/D_c datasets, respectively, and variance was tested using either F-test and Levene's test for normally and non-normally h/D_c datasets, respectively. As stated in the main text, Style 4 testing first required that within each given domain, central tendency and variance were both not equivalent between discharge-dependent h/D_c datasets. Next, to determine the rate that parametric and statistical properties changed between discharges statistical models were fit for each domain using discharge

as a dependent variable and h/D_c dataset properties (i.e. $\bar{x}$, σ, φ, g, β_2, and Θ values, where Θ is a placeholder for distribution parameters) as independent variables. Slopes of the fitted statistical models were compared to test if rates at which h/D_c dataset properties changed were equivalent (e.g. Paternoster et al., 1998). Notably, while comparing the rate of change of all dataset properties could be of general interest, the expectation that all properties would evolve at similar rates is not necessarily appropriate. For example, let us presume h/D_c distributions are positively skewed and leptokurtic, and thus may be reasonably modeled as having log-normal distributions. Applying the following system of discharge-specific linear scaling relationships:

$$F\left(\frac{h}{D_c}_{i+1,j}\right) = \lambda_i \cdot F\left(\frac{h}{D_c}_{i,j}\right) + C_i$$
$$F\left(\frac{h}{D_c}_{i+1,j+1}\right) = \lambda_i \cdot F\left(\frac{h}{D_c}_{i,j+1}\right) + C_i \qquad \text{(Eq. A.2.1)}$$

where F() is the frequency distribution of h/D_c values, i is and index for discharge, j is an index for domain, λ is a unique scalar for each discharge, and C is a unique constant for each discharge by definition only $\bar{x}$, σ, μ, and σ_{ln} would have equivalent discharge-dependent slopes between domains, where μ and σ_{ln} are the first and second parameters of the log-normal distribution estimated according to maximum likelihood, respectively. Values for g, and β_2 would be constant across discharges (i.e. zero slope for all domains) and non-linear scaling of φ values result in non-equivalent slopes between domains. While these between domain variable relationships are specific for log-normally distributed data, they remain true for several other distributions including Gamma distributed data. Scaling relationship in EQ. A.2.1 are much simpler than the complex convolution of previously wetted and newly wetted LBE h/D_c values that occur between discharges, but provide a basis for the Style 4 acceptance criteria that only $\bar{x}$, σ, and distribution parameters would have equivalent discharge-dependent slopes between domains.

A.2.4 Results

A.2.4.1 Question 1 (LBE relative submergence distributions) and general hypothesis results

Table A.2.2. Segment- and reach-scale h/D_c dataset statistical properties.

Discharge (m^3/s)	Spatial Domain							Reach-scale CV[a]
	Segment	Reach 1	Reach 2	Reach 3	Reach 4	Reach 5	Reach 6	
$\bar{x}$ (-)								
1.54	0.73	0.82	0.68	0.75	0.70	0.70	0.67	0.08
10.73	1.02	1.18	0.96	1.04	0.95	0.96	0.89	0.10
82.12	1.97	2.22	1.85	2.09	1.79	1.94	1.69	0.10
343.6	3.63	4.00	3.37	3.90	3.26	3.71	3.48	0.08
1184.6	6.78	7.17	6.33	7.06	6.22	6.93	7.99	0.09
s (-)								
1.54	0.53	0.69	0.44	0.58	0.44	0.44	0.29	0.29
10.73	0.81	1.04	0.71	0.84	0.67	0.65	0.41	0.29
82.12	1.67	1.99	1.58	1.76	1.41	1.55	1.03	0.21
343.6	3.15	3.54	3.01	3.49	2.63	3.16	2.11	0.18
1184.6	5.66	6.21	5.43	6.14	4.79	5.86	4.23	0.15
φ (-)								
1.54	0.53	0.55	0.53	0.55	0.53	0.73	0.75	0.17
10.73	0.68	0.55	0.65	0.45	0.65	0.75	0.85	0.22
82.12	0.85	0.70	0.70	0.75	0.70	0.70	0.75	0.04
343.6	0.70	0.75	0.75	0.75	0.75	0.75	3.25	0.87
1184.6	0.75	1.50	1.50	1.50	0.75	0.50	5.50	0.98
g (-)								
1.54	3.98	3.94	2.39	4.08	2.90	3.30	2.84	0.20
10.73	2.85	2.62	2.18	2.84	2.71	2.27	2.62	0.10
82.12	1.73	1.62	1.75	1.67	1.70	1.38	1.08	0.17
343.6	1.39	1.30	1.54	1.38	1.31	1.16	0.65	0.25
1184.6	1.24	1.18	1.38	1.40	1.08	1.10	0.36	0.35
β_2 (-)								
1.54	37.52	33.18	14.29	33.30	21.76	27.31	25.69	0.28
10.73	18.74	15.27	10.90	17.81	17.42	14.14	22.98	0.25
82.12	7.30	6.39	6.98	7.06	7.47	5.23	5.71	0.13
343.6	5.15	4.59	5.76	5.12	4.96	3.99	3.42	0.18
1184.6	4.50	4.07	5.03	5.13	4.01	3.73	2.73	0.22
α (-)								
1.54	2.53	2.05	2.75	2.30	2.93	2.92	5.75	0.43
10.73	2.05	1.65	2.09	1.95	2.52	2.33	4.72	0.44

Discharge (m^3/s)	Spatial Domain							Reach-scale CV[a]
	Segment	Reach 1	Reach 2	Reach 3	Reach 4	Reach 5	Reach 6	
82.12	1.53	1.33	1.55	1.48	1.77	1.58	2.51	0.25
343.6	1.31	1.22	1.31	1.21	1.50	1.28	2.16	0.25
1184.6	1.32	1.21	1.33	1.30	1.49	1.24	2.58	0.34
β (-)								
1.54	3.45	2.49	4.02	3.08	4.19	4.19	8.56	0.48
10.73	2.00	1.39	2.18	1.87	2.66	2.44	5.29	0.52
82.12	0.78	0.60	0.84	0.71	0.99	0.81	1.48	0.34
343.6	0.36	0.30	0.39	0.31	0.46	0.34	0.62	0.30
1184.6	0.19	0.17	0.21	0.18	0.24	0.18	0.32	0.26

[a]Coefficient of variation (CV) calculated as ratio of standard deviation and mean of reach-scale values.

Table A.2.3. Incremental inundation corridor h/D_c dataset statistics.

Discharge (m^3/s)	Value
$\bar{x}$ (-)	
1.54-10.73	0.75
10.73-82.12	1.14
82.12-343.6	1.55
343.6-1184.6	2.28
σ (-)	
1.54-10.73	0.33
10.73-82.12	0.70
82.12-343.6	1.14
343.6-1184.6	2.07
φ (-)	
1.54-10.73	0.63
10.73-82.12	0.75
82.12-343.6	0.75
343.6-1184.6	0.90
g (-)	
1.54-10.73	1.45
10.73-82.12	1.84
82.12-343.6	1.84
343.6-1184.6	1.64
β_2 (-)	
1.54-10.73	3.86
10.73-82.12	4.54
82.12-343.6	4.22
343.6-1184.6	2.79

Discharge (m^3/s)	Value
μ (-)	
1.54-10.73	-0.26
10.73-82.12	-0.37
82.12-343.6	-0.03
343.6-1184.6	0.22
σ_{ln} (-)	
1.54-10.73	0.48
10.73-82.12	0.42
82.12-343.6	0.55
343.6-1184.6	0.64

A.2.4.2 Question 2 results (distribution types and style testing)

A.2.4.2.1 Goodness-of-fit testing

All distribution goodness-of-fit testing was done in R code using a permutation based approach, whereby a random set of 500 values was selected from each dataset for use in each test. This process was repeated 500 time for each test. Fit was considered good if the arithmetic mean of *p* values from the set of 500 tests was > 0.05. The corrected Anderson-Darling test was performed using the 'ad.test' function from the Goftest package (Faraway et al., 2019**)**. Additional test results not reported directly in the main text are presented below.

As discussed in the main text, 24 of 30 reach-scale datasets were best fit by two-parameter Gamma distributions, and six were best fit by Weibull distributions (Figure A.2.2). The two-parameter Gamma distribution is parameterized by a shape parameter (α) and an inverse scale or rate (β) parameter with probability density function for random variable *x*:

$$f(x;\alpha,\beta) = \frac{\beta^{\alpha}}{\Gamma(\alpha)} x^{\alpha-1} e^{-\beta x} \quad for\ x > 0 \mid \alpha,\beta > 0 \qquad \text{(Eq. A.2.2)}$$

where $\Gamma()$ is the Gamma function. Equivalent α values but different β's correspond to distributions with similar overall shapes that scale such that the ratio of variances (σ^2) are roughly proportional

to the ratio of squared β values ($\frac{\sigma_1^2}{\sigma_2^2} \approx \frac{\beta_1^2}{\beta_2^2}$) and the ratio of mean ($\overline{x}$) and modal (φ) values are roughly proportional to the ratio of β values. Thus, α's being equal, lower β values result in similarly shaped distributions with larger variance and increasing central tendency and *vice versa* for larger β values. Alternately, when β is constant and α varies, distributions take different shapes and ratios of means and variances scale proportionally to the ratio of α values ($\frac{\sigma_1^2}{\sigma_2^2} \approx \frac{\alpha_1}{\alpha_2} \approx \frac{\bar{x}_1}{\bar{x}_2}$).

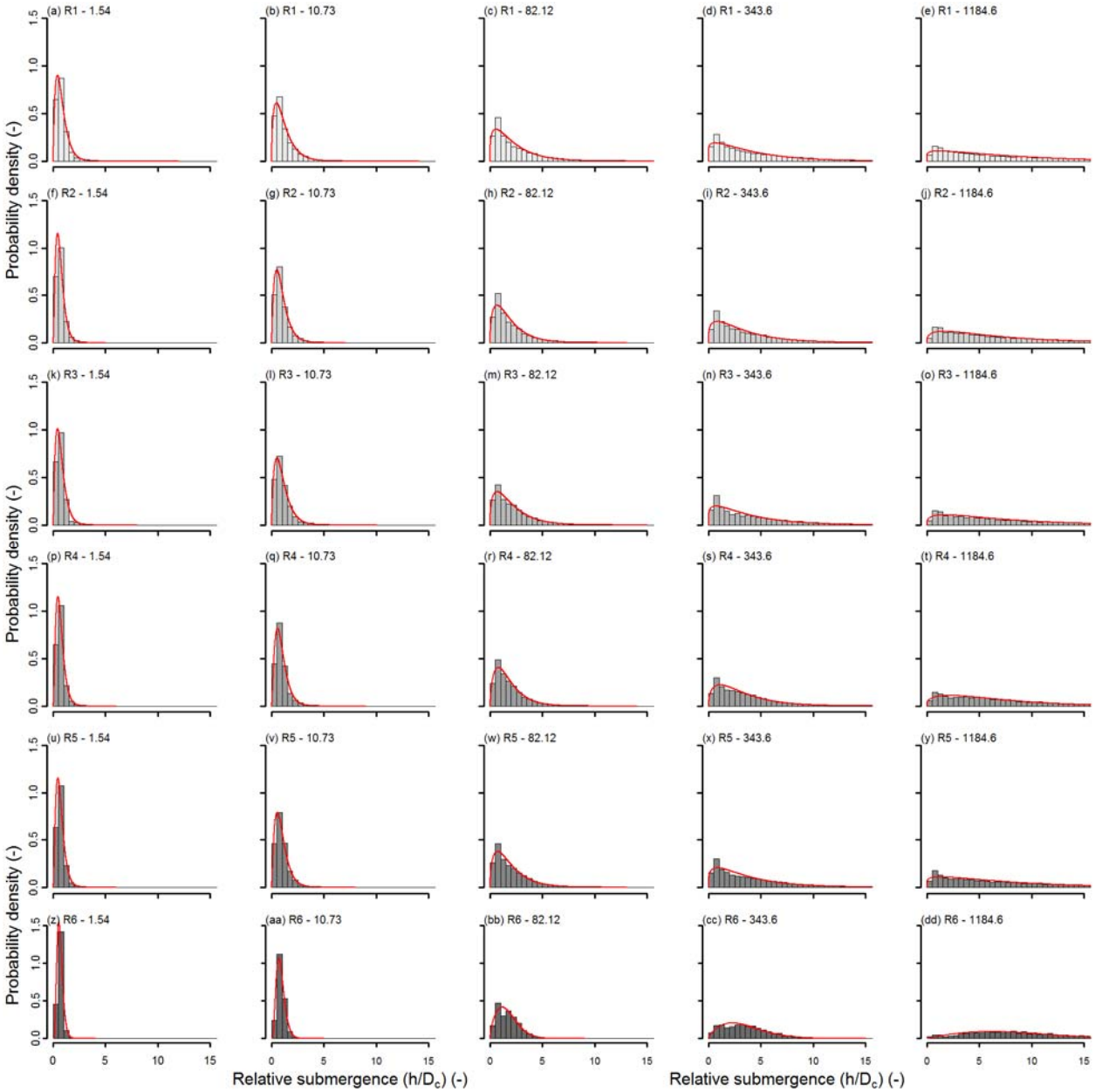

Figure A.2.2. Histograms of reach-scale discharge-dependent *h/Dc* probability densities (bars) overlain with best fitting distribution (red lines) (a-dd). The 'R' in plot titles denotes reach and the number next to R is the reach number. The next number in the plot titles is discharge in m^3/s. Panels are organized such that each row is a different geomorphic reach and each column is a different discharge.

A.2.4.2.2 Parameter and statistical testing

For comparing fitted Gamma distribution shape (α) and rate (β) parameters the likelihood-

ratio-test of Krishnamoorthy et al. (2015) returns two test statistics representing *p* values for each dataset for each individual test. If both test statistics were > 0.05 then equality of parameters was rejected above a 95% confidence level. Figure A.2.3.(a) depicts a network graph showing the 19 of 150 possible between segment and reach domain combinations with α values 'equal' above a 95% confidence level. Overall, 8 of 19 datasets with equivalent α values occurred for LBEs associated with the same discharge. Figure A.2.3.(b and c) depict network graphs of the between reach pair-wise combinations with equivalent α and β values, respectively. No segment-to-reach or reach-to-reach pairs had similar parameters across all discharge-dependent datasets. Figure A.2.4 depicts network graphs showing positive results (i.e. fail to reject null hypothesis) of the between segment- and reach-scale domain Mann-Whitney U and Levene's testing ($p > 0.05$). Only 12 and 5 of 150 between segment and reach datasets had positive Mann-Whitney U and Levene's tests, respectively. Of the 425 possible tests, between reach datasets had 24 and 13 positive Mann-Whitney U and Levene's tests, respectively. All but three of these between reach tests occurred at the same discharge.

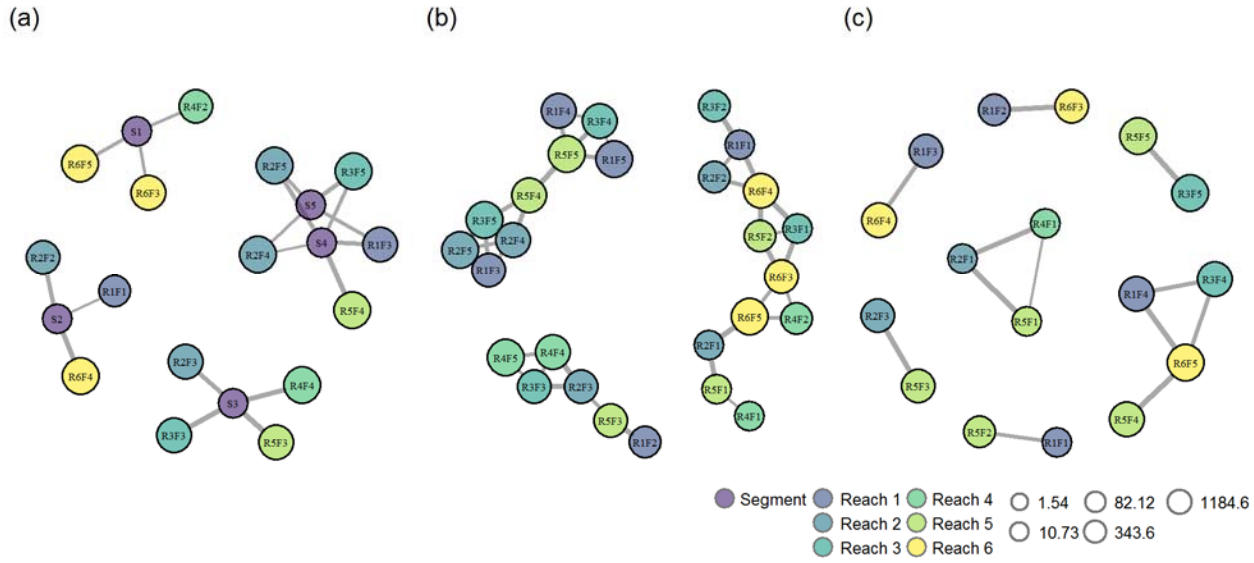

Figure A.2.3. Network graphs of spatial domains as nodes (colored circles) with links (lines) to other domains indicating equivalency between (a) segment- and reach-scale α values, (b) between reach-scale α values, and (c) between reach-scale β values. Nodes are colored by domain and sized by discharge. 'S' and 'R' are shorthand for segment and reach, respectively. The number next to R is the reach number. The number next to F is the discharge: 1 – 1.54; 2 – 1.73; 3 – 81.12; 4 – 343.6; and 5 – 1184.6 m^3/s. Domains or links that are absent did not have equivalent properties. Link line thicknesses are weighted by *p* values.

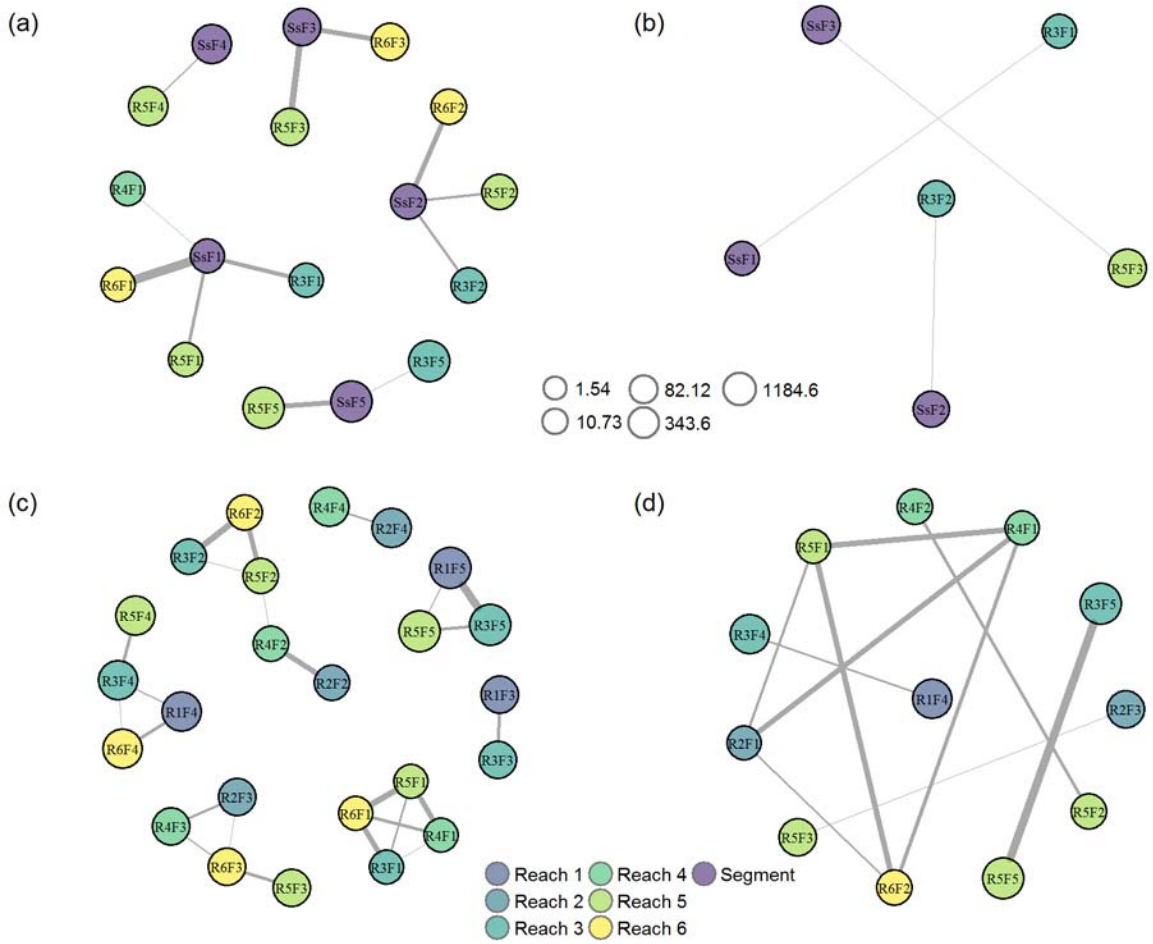

Figure A.2.4. Network graphs of (a) Mann-Whitney U and (b) Levene's tests between segment-scale and reach datasets and (c) Mann-Whitney U and (d) Levene's tests between reach-scale datasets. Nodes are colored by domain and sized by discharge. 'S' and 'R' are shorthand for segment and reach, respectively. The number next to R is the reach number. The number next to F is the discharge: 1 – 1.54; 2 – 1.73; 3 – 81.12; 4 – 343.6; and 5 – 1184.6 m^3/s. Domains or links that are absent did not have equivalent properties. Link line thicknesses are weighted by *p* values.

A.2.4.3 Processed-based similarity

Relationships between parametric and statistical properties versus discharge and associated power-law models are shown in Figure A.2.5. Details of the models, including model coefficients, adjusted-R^2 values, and F-test p-values are provided in Table A.2.4. . Of the 23 rejected slope comparisons five were comparing the φ model of Reach 5 to Reaches 1, 2, 3, 4, and 5; five were comparing the *g* model of Reach 6 to the Segment and to Reaches 1, 3, 4, and 5; six were comparing

the *g* model of Reach 2 to the Segment and to Reaches 1, 3, 4, 5, and 6; six were comparing the β_2 model of Reach 2 to the Segment and to Reaches 1, 3, 4, 5, and 6; and one was comparing the α model of Reach 1 to Reach 5.

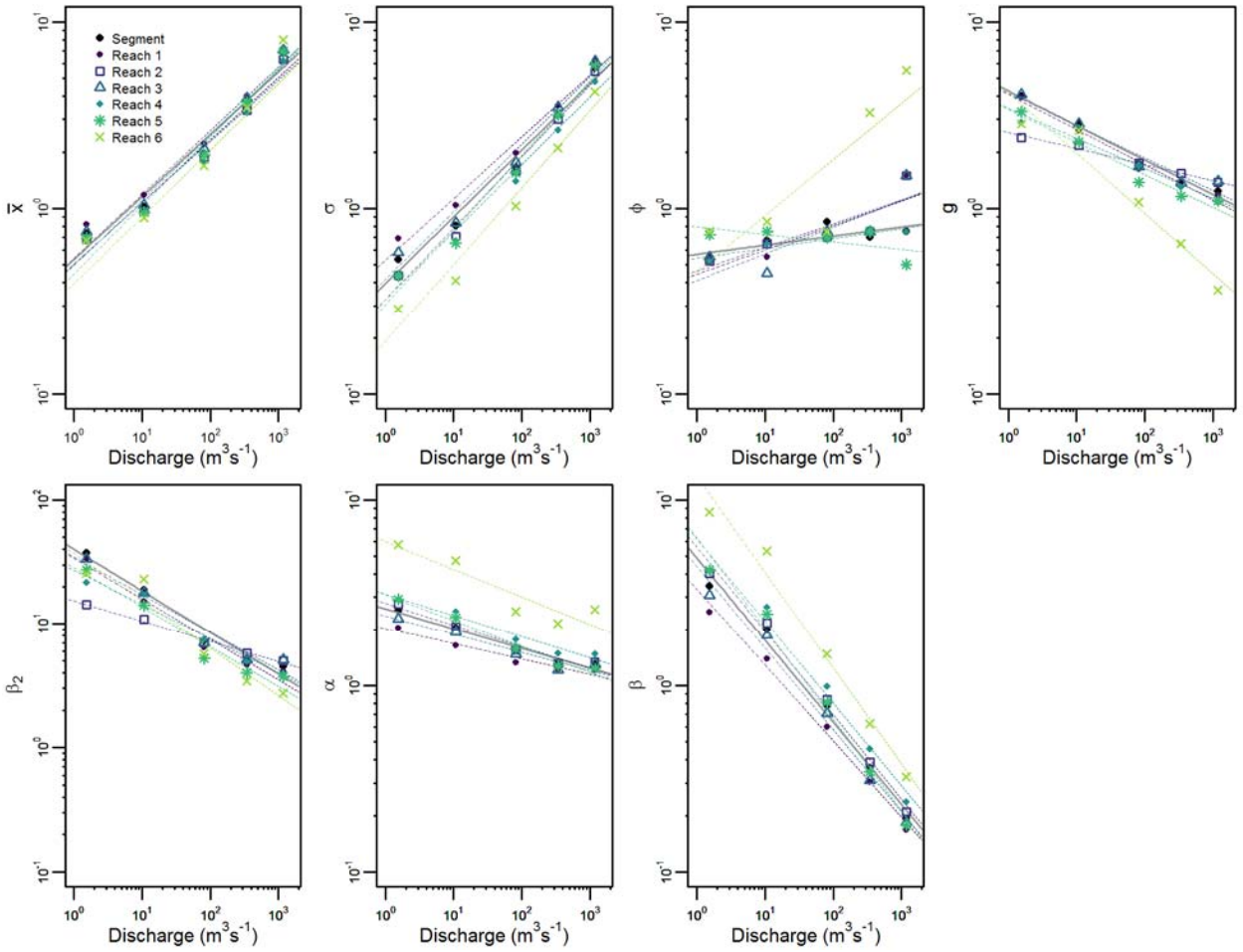

Figure A.2.5. Log-log plot of statistical and parametric properties ($\bar{x}$, σ, φ, g, β_2, α, and β values) versus discharge (points) and fitted power law models (dashed lines). Spatial domains are differentiated using point shape and color.

Table A.2.4. Summary of discharge (Q) vs h/D_c dataset property (Φ) power-law models of the form $\Phi = a'(Q)^b$ including model parameters (a',b), adjusted-R^2, and F-test p-values.

Spatial Domain	a'	b	adjusted-R^2	F-test p-value
$\bar{x}$ (-)				
Segment	0.53	0.3351	0.96	0.003
R1	0.61	0.3259	0.96	0.002
R2	0.50	0.3347	0.96	0.003
R3	0.54	0.3410	0.96	0.002
R4	0.50	0.3280	0.95	0.003
R5	0.49	0.3490	0.95	0.003
R6	0.44	0.3671	0.91	0.007
σ (-)				
Segment	0.39	0.36	0.97	0.001
R1	0.53	0.33	0.97	0.001
R2	0.32	0.38	0.98	0.001
R3	0.42	0.36	0.97	0.002
R4	0.32	0.36	0.97	0.001
R5	0.30	0.40	0.97	0.001
R6	0.19	0.41	0.96	0.002
φ (-)				
Segment	0.57	0.05	0.38	0.162
R1	0.44	0.13	0.62	0.070
R2	0.46	0.13	0.64	0.066
R3	0.41	0.14	0.60	0.077
R4	0.54	0.05	0.86	0.015
R5	0.80	-0.04	0.18	0.263
R6	0.46	0.30	0.62	0.070
g (-)				
Segment	4.25	-0.18	0.98	0.001
R1	4.08	-0.19	0.97	0.001
R2	2.56	-0.09	0.98	0.001
R3	4.17	-0.17	0.92	0.006
R4	3.44	-0.16	0.94	0.004
R5	3.39	-0.17	0.95	0.003
R6	4.18	-0.32	0.92	0.006
β_2 (-)				
Segment	40.10	-0.34	0.96	0.002
R1	33.98	-0.33	0.95	0.003
R2	15.37	-0.16	0.98	0.001
R3	34.80	-0.30	0.93	0.005
R4	27.26	-0.28	0.96	0.002

R5	28.60	-0.32	0.93	0.005
R6	37.16	-0.38	0.91	0.007
α (-)				
Segment	2.59	-0.11	0.95	0.004
R1	2.04	-0.08	0.93	0.005
R2	2.77	-0.12	0.94	0.004
R3	2.38	-0.10	0.90	0.009
R4	3.11	-0.11	0.94	0.004
R5	3.10	-0.14	0.97	0.002
R6	5.96	-0.15	0.78	0.031
β (-)				
Segment	4.87	-0.44	0.98	0.001
R1	3.32	-0.41	0.99	0.000
R2	5.56	-0.45	0.99	0.000
R3	4.38	-0.44	0.98	0.001
R4	6.16	-0.44	0.97	0.001
R5	6.27	-0.49	0.98	0.001
R6	13.40	-0.52	0.97	0.001

A.2.4.4 Incremental inundation corridor relative submergence

As discussed in the main text, comparison of D_c values within each incremental inundation corridor were found to have greater similarity than h values across the four corridors (Figure A.2.6).

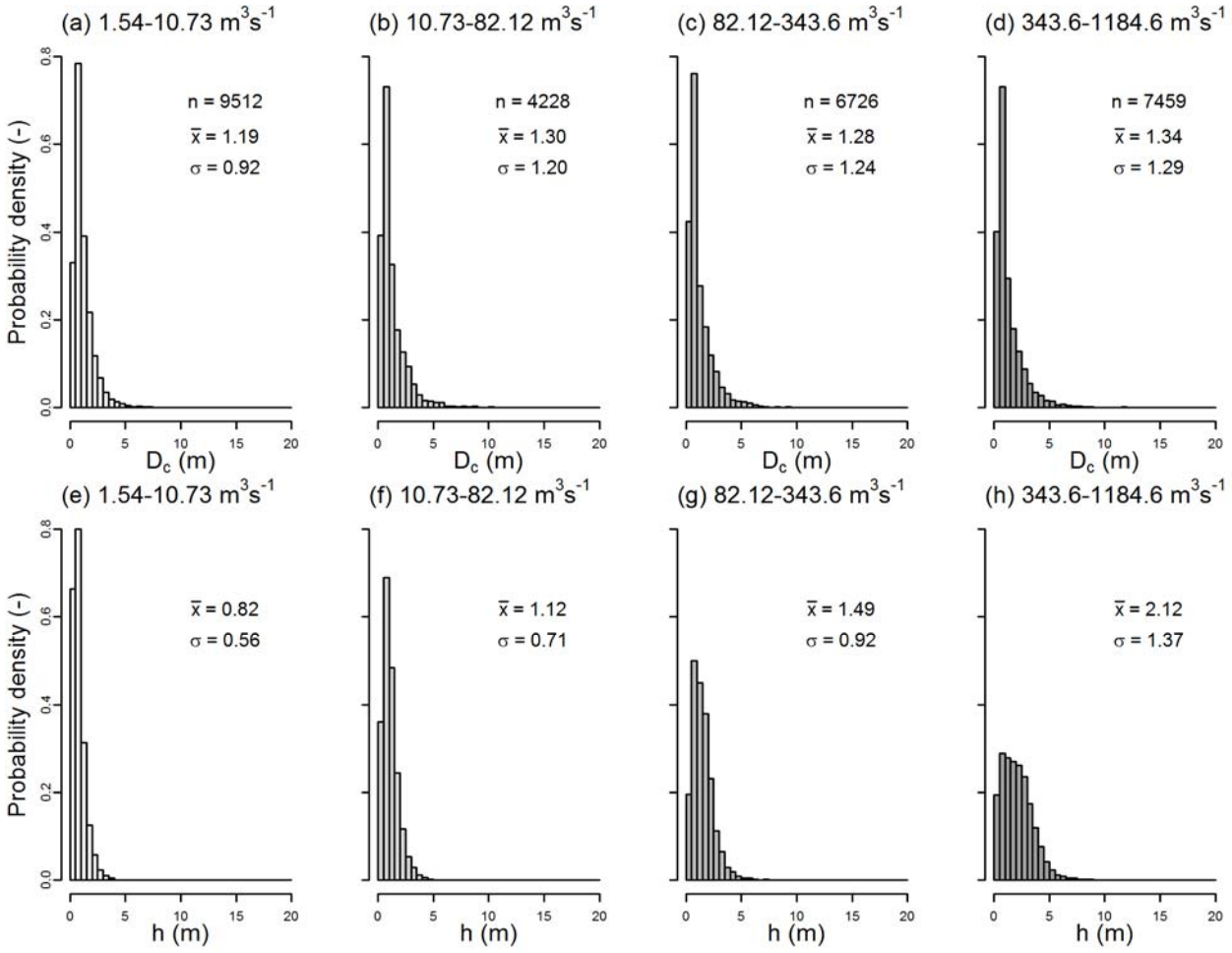

Figure A.2.6. Histograms of (a-d) D_c values and (e-h) h values at LBEs within each incremental inundation corridor. Note greater similarity of D_c values between datasets compared to h values.

A.2.4.5 Submergence trends and alternate calculations

To isolate sets of h/D_c values at newly wetted LBEs between discharges, only those LBEs that were not wetted at lower discharges were included (e.g. for 10.73-82.12 m^3/s dataset only LBEs not wetted at 10.73 m^3/s considered). In order to isolate how depths changed at previously wetted LBEs between discharges, differences in h/D_c values between successive discharges (e.g. h/D_c at 10.73 m^3/s minus h/D_c at 1.54 m^3/s) were calculated for each LBE. From these data only those LBEs that were wetted at lower discharges were included (e.g. for 10.73-82.12 m^3/s dataset only LBEs wetted at 10.73 m^3/s considered), essentially the opposite of the incremental inundation

corridor and the set of newly wetted LBE.

Differences in h/D_c dataset means resulting solely from the addition of newly wetted LBEs ($\Delta\bar{x}_n$) were calculated for each change in discharge by subtracting the mean of the set of h/D_c values resulting from combining h/D_c values at newly wetted LBEs with h/D_c values of previously wetted LBEs from the prior discharge (e.g. for 10.73-82.12 m^3/s this comprised combining h/D_c values from the 82.12 m^3/s dataset for LBEs that were not wetted at 10.73 m^3/s and h/D_c values from the 10.73 m^3/s dataset) from the mean of the complete h/D_c dataset of the higher discharge (e.g. using the same example, the 82.12 m^3/s dataset). Differences in h/D_c dataset means due solely to depth changes at previously wetted LBEs ($\Delta\bar{x}_p$) were calculated for each change in discharge by subtracting the mean of h/D_c values from each subsequently higher discharge for the set of LBEs that were wetted at the prior discharge (e.g. for 10.73-82.12 m^3/s h/D_c values came from the higher discharge but were limited to the set of LBEs that were wetted at 10.73 m^3/s) from the mean of the complete h/D_c dataset.

As discussed in the main text, comparison of reach-scale discharge-dependent D_c values were found to be visually similar within each reach, independently (Figure A.2.7). Overlap index values from comparing all possible reach-scale D_c datasets within each independent reach varied between 0.69-0.98 versus between 0.07-0.73 for h comparisons.

As discussed in the main text, LBE submergence did not occur equally within each laterally nested discharge-dependent portion of the river corridor, such that LBEs located in the baseflow channel were often more submerged at any given discharges relative to LBEs in other portions of the river corridor. The percent of LBEs intersecting each wetted area that exceeded relevant h/D_c thresholds at each higher discharge are presented in Table A.2.5..

Lastly, as discussed in the main text discharge-dependent distributions of relative

submergence were consistent in their shape and how they changed between datasets regardless of method for calculating h and D_c. For instance, segment-scale distributions of h/D_c, $h/\overline{D}$, $\hat{h}/D_c$, and $\hat{h}/\overline{\mathrm{D}}$ were all positively skewed and predominantly leptokurtic (Figure A.2.8). The majority of datasets (8 of 15) were best fit by Gamma distributions with the rest best fit by Weibull distributions. Calculations using h/D_c had the lowest average values as $D_c > \overline{D}$ and $h < \hat{h}$. Alternately, $\hat{h}/\overline{\mathrm{D}}$ had the highest average values.

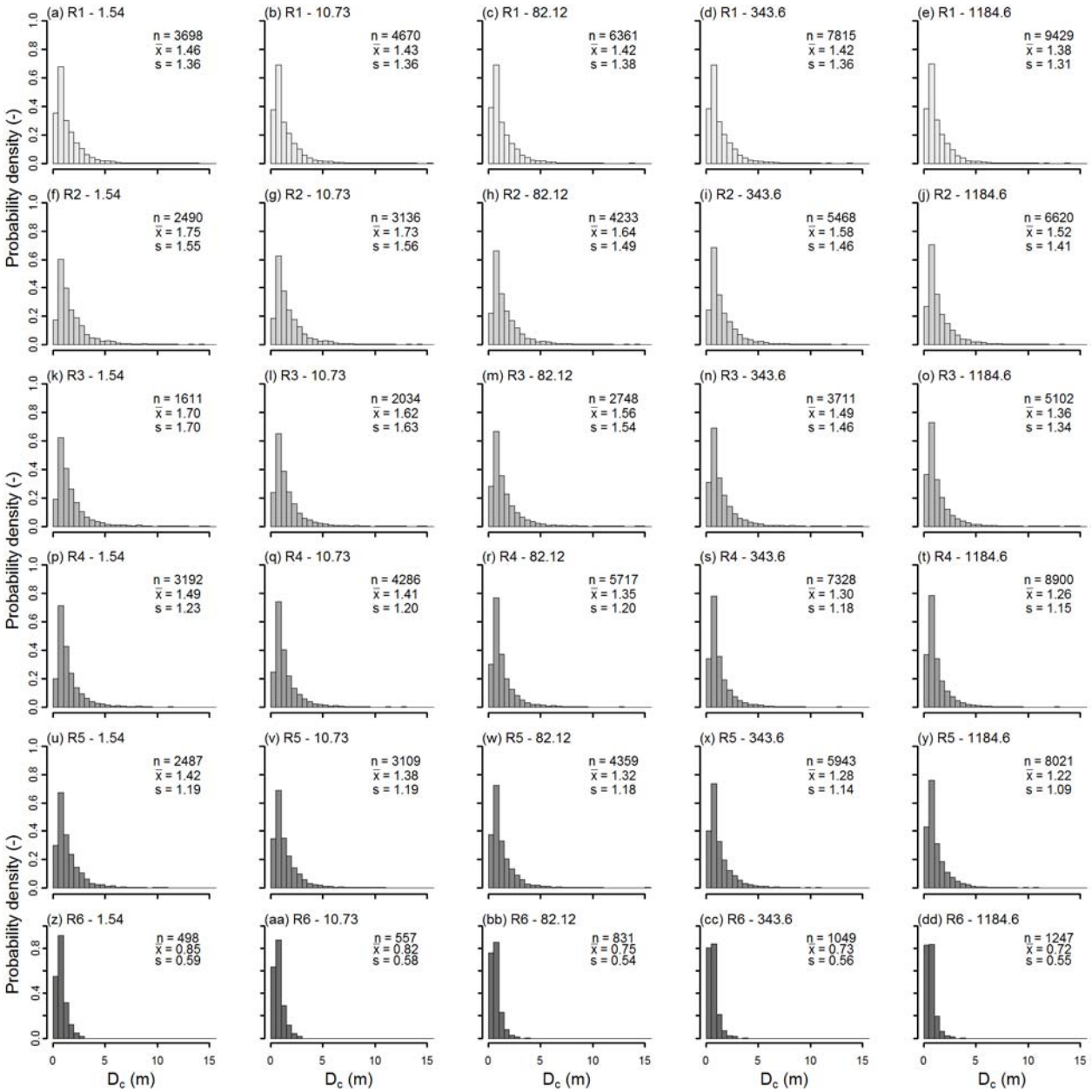

Figure A.2.7. Histograms of LBE heights (D_c) for reach-scale discharge-dependent LBEs (a-dd). Panels are organized such that each row is a different geomorphic reach and each column is a different discharge.

Table A.2.5. Percentage of segment-scale h/D_c values for just those LBEs within each discharges wetted area exceeding certain thresholds at each higher discharge.

Simulated Discharge (m^3/s)	Threshold					
	1	2	3	3.5	4	10
LBEs in 1.54 m^3/s wetted area						
10.73	45.9	11.8	3.8	2.2	1.3	0.0
82.12	81.4	52.7	31.0	23.6	17.9	0.4
343.6	94.6	79.8	64.8	57.6	51.3	9.3
1184.6	98.6	93.4	86.0	81.4	76.9	35.9
LBEs in 10.73 m^3/s wetted area						
82.12	77.8	48.9	27.9	20.9	15.5	0.3
343.6	93.5	78.4	63.7	56.8	50.6	8.4
1184.6	98.5	92.8	85.5	81.1	76.8	36.7
LBEs in 82.12 m^3/s wetted area						
343.6	90.0	73.3	58.3	51.5	45.3	6.4
1184.6	98.0	91.3	83.6	79.3	75.1	35.3
LBEs in 343.6 m^3/s wetted area						
1184.6	96.7	88.0	79.5	75.0	70.6	30.3

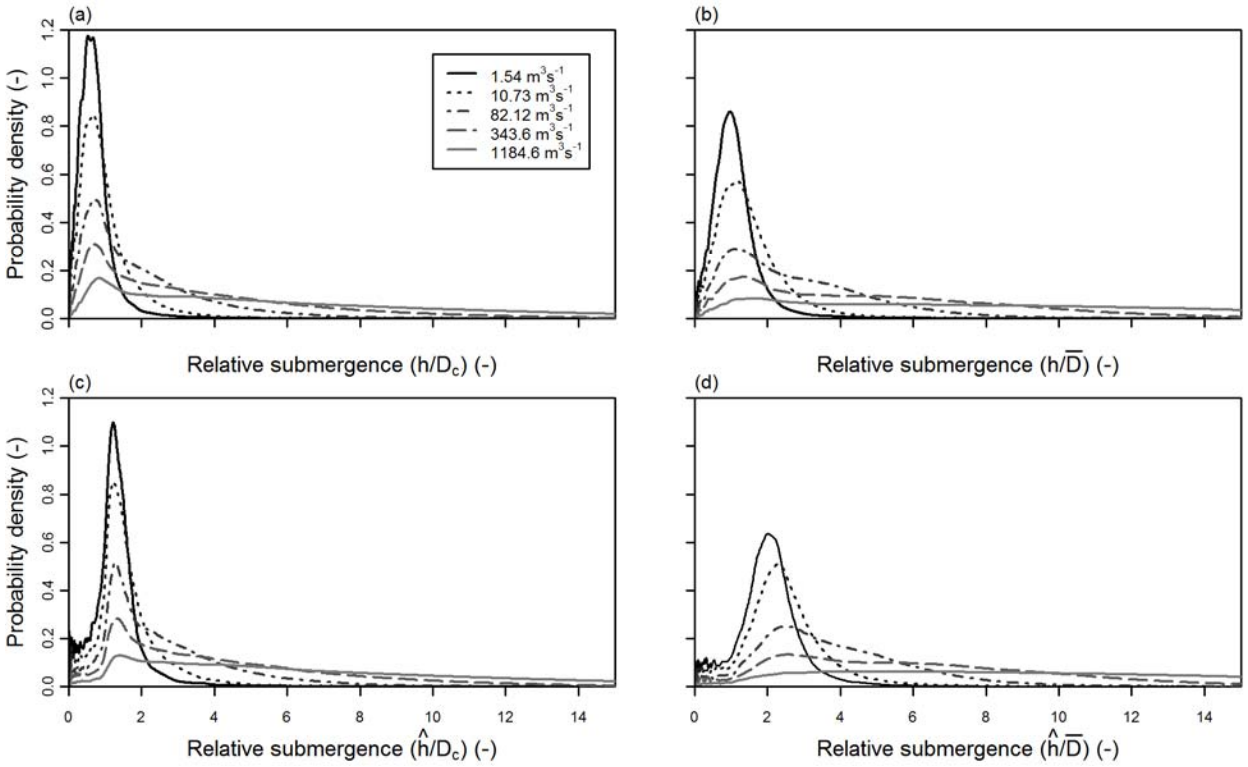

Figure A.2.8. Overlain kernel densities of segment-scale relative submergence probability densities for all five discharge-dependent LBE datasets based on relative submergence calculated according to (a) h/D_c, (b) $h/\overline{\boldsymbol{D}}$, (c) $\hat{h}/D_c$, and (d) $\hat{h}/\overline{\mathbf{D}}$.

A.2.5 Discussion

A.2.5.1 LBE relative submergence styles

None.

A.2.5.2 Evolution toward steady-state relative submergence

None.

A.2.5.3 Implications of relative submergence distributions

As discussed in the main text, the resistance equations of Bathurst (1985), Ferguson (2007), Katul et al. (2002), and Thompson & Campbell (1979) were used to estimate reach-scale flow resistance (f):

Bathurst (1985):

$$\sqrt{\frac{8}{f}} = 4 + 5.62 \log\left(\frac{h}{D_{84}}\right) \quad \text{(Eq. A.2.3)}$$

Ferguson (2007):

$$\sqrt{\frac{8}{f}} = \frac{a_1 a_2 \left(\frac{h}{D_{84}}\right)}{\sqrt{a_1^2 + a_2^2 \left(\frac{h}{D_{84}}\right)^{5/3}}} \quad \text{(Eq. A.2.4)}$$

Katul et al. (2002) [from Ferguson, 2007]:

$$\sqrt{\frac{8}{f}} = 1 + \frac{k}{h} \log\left[0.65 \cosh\left(\frac{h}{k} - 1\right)\right] \quad \text{(Eq. A.2.5)}$$

Thompson & Campbell (1979) [from Ferguson, 2007]:

$$\sqrt{\frac{8}{f}} = 2.5\left(1 - \frac{0.1k}{R}\right) \ln\left(\frac{12R}{k}\right) \quad \text{(Eq. A.2.6)}$$

Equation (A.2.5) of Katul et al. (2002) is the result of integration of a mixing layer type equation with a vertical velocity profile represented by a hyperbolic tangent function and mixing layer thickness *k*. In (A.2.5) *k* is set equal to $1 \cdot D_{84}$ Ferguson's (2007). In Thompson and Campbell's (1979) modified Keulegan equation (A.2.6) *k* is set equal to $2.37 \cdot D_{84}$. In Ferguson's (2007) variable-power equation (A.2.4) value for a_1 and a_2 are 6.5 and 2.5, respectively as recommended by Rickenmann and Recking (2011). For calculations, the assumption that $h \sim R$ is applied.

The expected value of a continuous distribution of random variable x is defined as:

$$E[x] = \int_{-\infty}^{\infty} x \cdot f(x) dx \quad \text{(Eq. A.2.7)}$$

which can be simplified and solved with numerical integration as:

$$E[x] = \sum_i x_i \cdot p(x_i) \quad \text{(Eq. A.2.8)}$$

Thus, substituting (A.2.8) into (A.2.3) for instance with x = h/D_c yields:

$$\sqrt{\frac{8}{f}} = \sum_i p\left(\frac{h}{D_{ci}}\right)\left(4 + 5.62 \log\left(\frac{h}{D_{ci}}\right)\right) \quad \text{(Eq. A.2.9)}$$

The same was done when solving equations A.2.4-A.2.6 using expected values of each reach-scale h/D_c dataset as input for h/D_{84}.

A.2.5.4 Resistance trends and fixed roughness coefficients

None.

A.2.5.5 Dynamism of relative submergence

None.

A.2.6 Conclusions

None.

A.2.7 References

Bathurst, J. C. (1985). Flow Resistance Estimation in Mountain Rivers. *Journal of Hydraulic Engineering, 111*(4), 625-643. doi:doi:10.1061/(ASCE)0733-9429(1985)111:4(625)

Faraway, J., Marsaglia, G., Marsaglia, J., & Baddeley, A., (2019). goftest: Classical Goodness-of-Fit Tests for Univariate Distributions. R package version 1.2-2. https://CRAN.R-project.org/package=goftest

Ferguson, R. (2007). Flow resistance equations for gravel- and boulder-bed streams. *Water Resources Research, 43*(5). doi:10.1029/2006wr005422

Fox, J., & Weisberg, S. (2019). An R Companion to Applied Regression, Third edition. Sage, Thousand Oaks CA. https://socialsciences.mcmaster.ca/jfox/Books/Companion/.

Freedman, D., & Diaconis, P. (1981). On the histogram as a density estimator:L 2 theory. Z. *Wahrscheinlichkeitstheorie verw Gebiete* 57, 453–476. https://doi.org/10.1007/BF01025868

Katul, G., Wiberg, P., Albertson, J., & Hornberger, G. (2002). A mixing layer theory for flow resistance in shallow streams. *Water Resources Research, 38*(11), 32-31-32-38. doi:https://doi.org/10.1029/2001WR000817

Krishnamoorthy, K., Lee, M., & Xiao, W. (2015). Likelihood ratio tests for comparing several gamma distributions. *Environmetrics, 26*(8), 571-583. doi:10.1002/env.2357

Millard, S. P. (2014). EnvStats, an R Package for Environmental Statistics *Wiley StatsRef: Statistics Reference Online*.

Paternoster, R. Brame, R. Mazerolle, P, & Piquero A. (1998). Using the correct statistical test for the equality of regression coefficients. *Criminology, 36*(4), 859-866. doi:https://doi.org/10.1111/j.1745-9125.1998.tb01268.x

R Core Team (2021). R: A language and environment for statistical computing. R Foundation for Statistical Computing, Vienna, Austria. URL https://www.R-project.org/.

Rickenmann, D., & Recking, A. (2011). Evaluation of flow resistance in gravel-bed rivers through a large field data set. *Water Resources Research, 47*(7). doi:10.1029/2010wr009793

Thompson, S. M., & Campbell, P. L. (1979). Hydraulic of a large channel paved with boulders. *Journal of Hydraulic Research, 17*(4), 341-354. doi:10.1080/00221687909499577

Wiener, J. S., & Pasternack, G. B. (2022). Scale dependent spatial structuring of mountain river large bed elements maximizes flow resistance. Unpublished.

APPENDIX 3. Supporting Information for Hydro-morphological variable linkages with morphological unit scale fluvial landforms in a boulder-bedded mountain river

This appendix provide supplemental materials that include information on the following topics:

- Details of generalized MU types and literature review of the selected HM variables (1A.3.1.2);
- Details of two-dimensional hydrodynamic modeling including parametrization and calibration, and model validation (1A.3.3.1);
- Details of morphological unit (MU) classification, delineation, assessment, and analysis methods (1A.3.3.1);
- Details of hydro-morphological (HM) variable calculations (1A.3.3.1);
- Details of heuristic assessment methods (1A.3.3.2.3);
- Details of at-a-station hydraulic-topography exponent calculations (1A.3.3.3);
- Details of random forest model parameterization (1A.3.3.4);
- Additional MU analysis results (1A.3.4.1);
- Additional HM variable results (1A.3.4.2);
- Additional MU-HM variable statistical relationship results (1A.3.4.3);
- Additional MU-HM variable pairwise analysis results (1A.2.4.3.2);
- Additional MU-HM variable heuristic expectation analysis results (1A.2.4.3.3);
- Additional at-a-station hydraulic-topography results (1A.3.4.4);
- Additional random forest model results (1A.3.4.5);
- Comparison of HM variable ranges in this study to past studies (1A.3.5.2); and
- References.

The organization of this appendix uses the same outline and headings of the chapter to which this supplements. Subject heading followed by the word “none” indicate no supplemental information is provided for that section.

A.3.1 Introduction

None.

A.3.1.1 Scientific questions

A.3.1.2 Generalized in-channel MU types, selected hydro-morphological variables, and MU expectations for coarse-bedded rivers

As discussed in the main text MU types can be coarsely simplified into five end-member groups based on relative combinations of collocated, low flow water depth and water speed (velocity). At one quadrant lies pool type MUs that have relatively high flow depths and low flow speeds. Opposite this quadrant are units that have relatively low flow depths and high flow speeds (riffle type and step type). Riffle and step type units are further differentiated based on step type units having higher water speeds and bed slopes, and coarser grain sizes. Pools, riffles, and steps are by far the most commonly referenced MUs in the scientific literature, and are often defined using characteristics beyond low flow depth and water speed (Wheaton et al., 2015). For instance, pools typically occur in lower gradient channel sections than rifles, which occur in lower gradient sections than steps (Grant et al., 1990; Halwas & Church, 2002; Wyrick & Pasternack, 2014). The other two end-members contain less common MU types that function as transitional units between pools and riffles/steps. The first of these are units with both relatively low baseflow flow depths and flow speeds (slackwater type). Common MUs in this quadrant include slackwater and glide. Opposite these units are those that have both relatively high baseflow flow depths and flow speeds, which include run, chute, and rapid units (chute type).

A total of 18 HM variables were considered for this study based on the concept that HM variables measured at the MU scale exert local control on the formation and/or persistence of specific MU types through associated process-morphology linkages or at least reflect the channel's

response to such processes (Grant et al., 1990; Belletti et al., 2017; Byrne et al., 2020; Lane et al., 2022). Non-local factors such as downstream hydraulic controls and MU-to-MU interactions (i.e. scour pools downstream of steps) also influence MU occurrence (Lisle, 1986; Harrison & Keller, 2007; Chartrand et al., 2011; Wheaton et al., 2015). Thus, three longitudinal change HM variables were included to capture a subset of non-local factors including changes in channel width and shear stress upstream of MUs (Golly et al., 2019). A comprehensive review of the selected HM variables including process-morphology linkages for the generalized set of MU types for each variable is provided in the subsections below organized by the following 6 groups: channel-size variables, channel-shape variables, channel-obstruction/roughness variables, gradient variables, longitudinal change variables, and at-a-station hydraulic geometry (AHG) exponent variables.

Channel-size variables:

Wetted widths are indirectly linked to several morphogenetic processes associated with the formation and/or persistence of several MU types. Width is a component of jamming ratio, defined as the ratio of channel width to step forming grain diameter. Jamming ratio describes the probability that stable force chains will be established across the channel via granular interactions and arrangements (e.g. Church & Zimmermann, 2007; Golly et al., 2019), which are the basis of the jammed-state hypothesis, a popular step formation model. Ratios of 2-6 are suggested as being critical for step formation (Church & Zimmermann, 2007). If the jamming ratio's representative grain size is uniform in a study domain then wetted width alone is the main determinant of step formation potential. Wetted width and multi-stage downstream width variability also figure prominently in the flow convergence routing mechanism (MacWilliams et al., 2006; Pasternack et al., 2018), which for this study is assumed to be interchangeable with the velocity reversal hypothesis (Thompson, 2011). This process of stage-dependent scour and deposition within

longitudinally sequenced zones of laterally convergent and divergent flow whereby scour shifts from topographic highs (riffles) to topographic lows (pools) with increasing discharge is believed to play a critical role in the formation and maintenance of riffle-pool couplets (MacWilliams et al., 2006; Brown et al., 2016; Hassan et al., 2021). Under the flow convergence routing mechanism, shifts in scour typically arise due to changes in flow width and bed elevation, and field observations, numerical modeling, and one-dimensional (1D) mass and energy conservation suggest maintenance and/or formation of riffle-pool couplets is generally achieved if flow widths at riffles are wider than pools at some channel-forming flow (Caamaño et al., 2009; Brown et al., 2016). Empirical observations have also found MUs to be differentiated by baseflow width measurements (Halwas & Church, 2002; Wyrick & Pasternack, 2014). Wetted width's dependence on stage makes the question of which width measurements to include as HM variable(s) challenging. Consistent with the dual-stage nature of the flow convergence routing mechanism we have included width measurements at three representative stages as HM variables: baseflow width (W_{Bs}), width at a formative discharge (W_F), and width at highest discharge for which measurements were available, which corresponds to a valley-filling flood event with an ~13.7-yr recurrence interval ($W_{13.7}$). The inclusion of W_F and $W_{13.7}$ reflect uncertainty in terms of which stage may have the strongest, if any, control on MU formation processes. Despite its relevance to the flow convergence routing mechanism, W_{Bs} has limited control on MU formation, which takes place at higher discharges, and is primarily included for predictive purposes.

Channel-shape variables:

A channel's width-to-depth ratio (W/h) serves as a proxy for how bed shear stress (τ) is portioned between the channel bed and banks, is an indicator of channel stability, and has been widely used to characterize channel morphology (Florsheim, 1985; Church & Jones, 1982; Wyrick

& Pasternack, 2014). W/h has been linked to the formation of fluvial landforms (e.g. alluvial bars as well as more coarse grained irregular bedforms) via the process of bar instability (Furbish, 1998; Wilkinson et al., 2008). Bar instability involves longitudinal variations in sediment transport that arise due to instabilities in motion of water and sediment flowing over erodible beds (Nelson, 1990; Furbish, 1998). Topographic steering of flow around bed and/or bank attached obstacles is key to generating initial instabilities in the flow field that drive bar formation (Nelson, 1990). The view of riffles and step landforms as a manifestation of alluvial bar forms is not uncommon, thus facilitating a link between bar instability and MUs (Furbish, 1998; Venditti et al., 2017). Findings for gravel-bed rivers suggest bar instability occurs when $W/h>10$. However, observation of bars and bedforms in coarse-grained rivers with $W/h<10$ remain (Florsheim, 1985; Wilkinson et al., 2008). While factors such as high transverse velocities, topographically induced flow deflections, coarse sediment and hydraulically rough channels, width variations, and large-scale turbulent eddies that influence deposition and explain bar and bedform formation complicate the connection between bar instability and MU formation (Furbish, 1998; Wilkinson et al., 2008), W/h still has explanatory power in differentiating between MU types and which MUs may occur (Wyrick & Pasternack, 2014). Bankfull and formative width-depth ratios (W/h_{Bf} and W/h_F) are included as HM variables with the expectation that pool units have the lowest W/h values followed by transitional units followed by riffles/step units.

Width-to-valley width ratios (W/W_V), a measure of hillslope connectivity, have been related to the potential for mass wasting deposits to enter the bankfull channel (Whiting & Bradley, 1983), were found to correspond to general patterns of flood scour and deposition (Wolman & Eiler, 1958), and were found to corresponded with boulder densities and spatial patterns of hillslope landforms (Grant & Swanson, 1995). The ratio is also a proxy for entrenchment ratio, a

measure of valley confinement and lateral channel adjustment (Rosgen, 2001; Beechie & Imaki, 2014). While, MU process-morphology linkages with W/W_V are less developed, hillslope connectivity and delivery of coarse sediment to the channel are relevant to jammed state and keystone step formation models (Golly et al., 2019). Local valley expansions, that can be captured by W/W_V measurement, have also been found to support persistence of riffles across river types with inferred connection to the flow convergence routing mechanism (White et al., 2010). For this study we use the ratio of baseflow width-to-valley width (W_{Bs}/W_V) as a means to capture large multi-scale width variability. Expectations for W_{Bs}/W_V are for pool units to have higher W_{Bs}/W_V values than riffles/step units and transitional MUs to have intermediate values.

Cross-sectional channel geometry is a primary control on hydraulics and morphodynamic processes (Ferguson, 1986; Dingman, 2007; Pasternack et al., 2021; Byrne et al., 2021), and observations support that MUs are associated with certain cross-section shapes (Lane & Richards, 1996; Caamaño et al., 2009; Wheaton et al., 2015; Hassan et al. 2021). However, variables that holistically describe channel cross-section shape, such as whether sections are U-shaped, V-shaped, or convex-up shaped, and their confinement, remain somewhat lacking, and have not been directly used to discriminate MU types. Several mathematical functions exist to model cross-section geometry but are often limited to simple shapes such as triangles, rectangles, trapezoids, and parabolas, and have limited flexibility to fit multiple shapes (e.g. Brown & Pasternack, 2019; Ohara and Yamatani, 2019). More parametrically flexible functions such as power-laws, sigmoids, and ellipsoids may offer opportunity to fill this gap. For instance, equation 11 in Dingman (2007), which is of a power-law form, was able to produce a variety of cross-section shapes by modifying a single parameter. Parameters of this nature are referred to herein as cross-section geometry index variables. Canonical AHG relations, which can be interpreted in the context of archetypical cross-

section shapes, provide a framework for establishing expectations between MU type and this kind of geometric variable (Ferguson, 1986; Rhodes, 1977; Gleason, 2015). For instance, Hopkins and Pasternack (2017) separate the classic ternary diagram of AHG exponents (i.e. *b-f-m*) into five representative shapes with varying degrees of confinement, concavity, and convexity (Figure A.3.1). The flow convergence routing mechanism suggests certain MU types should plot in distinct portions of the AHG ternary diagram, such that pools have low rates of width increase (*b*), high rates of velocity increase (*m*), and low-to-intermediate rates of depth increase (*f*), whereas riffles are essentially the opposite (Richards, 1976). These behaviors were confirmed by Gonzalez and Pasternack (2015) for riffle and pool MU types in a partially-confined wandering gravel-bed river. Thus, the connections between AHG exponents and MU type, and AHG exponents and cross-section shape enable expectations to be drawn between MU type and cross-section shape. For this study we explore the use of a bankfull cross-section geometry index (Θ) based on equation 11 in Dingman (2007) as an HM variable. Expectations for Θ were based on expert judgment and the limited references documented above.

Channel obstruction/roughness variables:

Macro-roughness elements such as boulders and bedrock outcrops, collectively referred to as large bed elements (LBEs), exert resistance and steer the flow. LBEs are a basic building block of alluvial steps and are linked to the formation of forced pool morphologies (Buffington et al., 2002; Church & Zimmermann, 2007; Harrison & Keller, 2007; Chartrand et al., 2011; Thompson, 2012). Flow resistance tends to increase with LBE concentration (Γ), defined as the ratio of planform LBE area to wetted channel area (Wiener & Pasternack, 2022). Higher flow resistance can promote deposition of keystones or promote particle jamming in-line with step formation models and the process of bar instability (Golly et al., 2019). Higher Γ are also associated with

increasing transverse velocities and other flow instabilities needed for bar and coarse bedform formation (Furbish, 1998). However, like other GSD metrics, there is uncertainty whether Γ patterns are more a cause of MU formation or result from processes associated with MU morphology after formation (Thompson & Fixler, 2017; Hassan et al., 2021). Bankfull and formative LBE concentrations (Γ_{Bf} and Γ_F) are included as HM variables with the expectation that Γ is highest for riffle/step units followed by transitional and then pool units.

Gradient variables:

Channel-bed slope ('slope') is perhaps the most common HM variable that has been use to discriminate channel morphologies at both MU and reach scales (Grant et al., 1990; Rabeni & Jacobson, 1993; Halwas & Church, 2002; Montgomery & Buffington, 1997; Byrne et al., 2020). The general view presented in these studies is that slope represents a continuum along which typical MUs occur. We view slope as a variable that influences contemporary geomorphic processes such as sediment transport capacity and is an important boundary condition for certain MUs, but that other causal mechanisms are needed to influence MU formation (Montgomery et al., 1995). For instance, the references above support that MUs tend to occur in discrete slope ranges, but such ranges can be relatively large, there is often overlap between ranges associated with certain MUs, and slope alone is not descriptive or diagnostic of a specific MU formation process (Montgomery et al., 1995; Byrne et al., 2020). Local measurements of baseflow slope (S_{Bs}) was included as a HM variable. In addition to slope, local baseflow water surface slope (WSS_{Bs}) and formative water surface slope (WSS_F) are included as HM variables. Our view is that differences in WSS_{Bs} occur purely in response to presence of different MU types with little process-based control, but the variable has been included due to use in other studies to discriminate MU types (Wyrick & Pasternack, 2014). Similar to previous studies the expectation is for MUs to

occur along a low-to-high continuum of these gradient variables from pool-to-transitional-to-riffle and step units. At formative discharge differences in WSS are expected to decrease between units relative to WSS_{Bs} (Richards, 1976; Thompson, 2018).

Longitudinal change variables:

Non-local factors can play a significant role in MU formation and persistence (Grant et al., 1990; Caamaño et al., 2009; Pasternack et al., 2018). For example, the jammed-state hypothesis posits that downstream narrowing should increase potential for step formation, and the keystone step formation model highlights decreasing downstream shear stress as a mechanism for deposition of keystones (Golly et al., 2019; Saletti & Hassan, 2020; Wang et al., 2021). Local width and bed shear stress changes also figure prominently in the flow convergence mechanism whereby at baseflow, pools are expected to be located where widths are expanding (divergent flow) and riffles in locations of channel narrowing (convergent flow), and as stage increases above some formative discharge these tendencies switch (MacWilliams et al., 2006; Thompson, 2011; Brown et al., 2016). Thus, longitudinal changes in baseflow width (ΔW_{Bs}), formative width (ΔW_F) and formative bed shear stress ($\Delta\tau_F$) were included as HM variables. To be consistent with Golly et al. (2019) and Saletti & Hassan (2020), these variables reflect longitudinal changes occurring at a constant stage rather than changes occurring between stages. Based on observations from the references above the expectation is for ΔW_{Bs} to increase (positive) toward pool units, decrease (negative) toward riffle and step units, and stay relatively constant (near-zero) for transitional units. Expectations for ΔW_F are the opposite as those for ΔW_{Bs}, with the exception for step units to be in locations with both increasing (keystone model) and decreasing (jammed-state) values. Expectations for $\Delta\tau_F$ are to increase toward pool units, decrease to riffle units, stay relative uniform toward transitional units, and increase or decrease to step units.

AHG exponent variables:

Canonical AHG relations provide a simple mathematical framework to describe discharge-dependent hydraulics (i.e. width, depth, and velocity) (e.g. Gleason, 2015). As discussed above in the section describing cross-section geometry index variables, theory and observation support that riffle and pool MU types have typical and distinct AHG exponents (Richards, 1976; Gonzalez & Pasternack, 2015), whereas *b-f-m* expectations for other MU types are less defined. One issue using AHG exponents as HM variables is the potential for spurious connection if MUs are mapped from 2D hydraulics as proposed by several approaches (Legleiter & Goodchild, 2005; Hauer et al., 2009; Wyrick et al., 2014; Tamminga et al., 2015). Nonetheless, the AHG exponents *b*, *f*, and *m* were considered for use as HM variables.

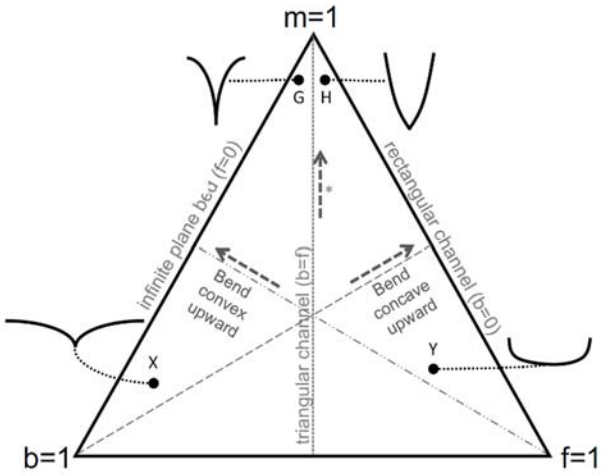

Figure A.3.1. Conceptual ternary diagram of canonical at-a-station hydraulic geometry exponents and associated cross-section archetypes (Hopkins & Pasternack, 2017).

A.3.2 Study river segment

None.

A.3.3 Methods

None.

A.3.3.1 Experimental design and data generation

Topographic and bathymetric mapping

Conducting 2D modeling for MU classification and mapping and determining HM variables both required topographic data as an input. Between September 27-29, 2014 Airborne Light Detection and Ranging (LiDAR) data were collected within the study segment by a professional surveying firm (Quantum Spatial, https://www.quantumspatial.com/) using a Riegl VQ-820-G bathymetric sensor system and a Leica ALS50 Phase II system (near infrared) mounted in a Cessna Grand Caravan. ALS collection was conducted during a period of low discharge estimated at 1.19 m^3/s at the downstream study site boundary. These data were supplemented with boat-based bathymetric observations, imagery-derived bathymetric estimates (*sensu* Legleiter et al., 2004), and systematically placed augmented points (Valle & Pasternack, 2006). Through verification and merging of each individual dataset, an extremely detailed and accurate topographic dataset was created (Wiener & Pasternack, 2022). The final bare Earth mapping included > 21 million points at an average point-spacing of 0.25 m (~ 16 pts/m^2). Points were used to create a 0.46 m x 0.46 m resolution digital terrain model (DTM) raster, the final map product used in the study.

Two-dimensional hydrodynamic modeling

Steady-state hydrodynamics were simulated at ~ 1-m resolution using the free, public 2D model known as Sedimentation and River Hydraulics—Two-Dimensional model (SRH-2D) v. 2.2 (Lai, 2008). This is a proven code capable of simulating complex hydraulic conditions in mountain

rivers (Brown & Pasternack, 2014; Strom et al., 2016). The decision to use 2D modeling represented a compromise between performance and accuracy compared to simpler 1D models and more complex 3D modeling (Benjankar et al., 2015). It also reflected the study's need for spatially explicit simulation of hydraulic conditions, specifically the delineation of wetted areas and flow-depth and velocity predictions aggregated at 10^0-10^2 m^2 scales. Simulations were run for four geomorphically or otherwise relevant discharges (1.54, 10.73, 161.0, and 1184.6 m^3/s) from an approximate baseflow to an ~13.7-yr flood. A summary of model development, parameterization, and performance assessment is provided in Table A.3.1. Additional details of depth and velocity prediction performance, which were most relevant to this study are below.

Depth and depth-averaged velocity predictions were assessed using a suite of tests and standard model performance metrics (Pasternack, 2011; Moriasi et al., 2007). First, deviations between observed and predicted water-surface elevations (WSEs) were assessed at 147,644 discrete point locations distributed throughout the 13.2-km domain. Observed WSE measurements were obtained as part of LiDAR data collection. Discharge during the period of LiDAR collection was estimated at 1.19 m^3/s. Simulation of this discharge was used to generate the set of predicted WSE values at the observation locations. The mean absolute deviation between measured and predicted WSE was 0.162 m. The majority (53%) of absolute deviations were less than the independently reported 0.117 m vertical accuracy uncertainty of the bathymetric LiDAR, which aligns with the expectation that 2D model WSE deviations should not exceed uncertainty in the topographic data (Pasternack, 2011; Brown & Pasternack, 2012).

For a second test, depth and depth-averaged velocity measurements made at 61 independent locations with a standard wading rod during a period of discharge of 3.51 m^3/s were compared to collocated model predictions for this same flow. Mean absolute deviation between

measured and predicted depths and velocities were 0.09 m and 0.08 m/s, respectively. Coefficient of determination (R^2) values for predicted versus observed fixed-point depths and depth-averaged velocities were 0.80 and 0.84 ($p<0.001$), respectively, and linear regression slopes were both 0.87 ($p<0.001$). These values are considered very good amongst 2D models (Brown & Pasternack, 2012) and certainly exceed recommended minimum norms for model performance (Pasternack, 2011). Among hydrologist-preferred metrics, depth predictions significantly outperformed standards for Nash-Sutcliffe efficiency, percent bias, and the root mean square error-observations standard deviation ratio.

Table A.3.1. Summary of two-dimensional hydrodynamic model development, parameterization, and performance.

Model Parameter	Description
Mesh Generator and Modeling Interface	Surface-water Modeling System (SMS) v. 11.2 graphical user interface (Aquaveo, Inc.)
2D Hydrodynamic Model Numerical Code	Sedimentation and River Hydraulics—Two-Dimensional model (SRH-2D) v. 2.2
Model domains	For the whole river, there were 4 overlapping model domains used to simulate incrementally larger ranges of discharge. The 'low-flow' domain was used to simulate discharges <10.73 m^3/s, the 'bankfull' domain was used to simulate discharges between 10.73-32.2 m^3/s, the 'high-flow' domain was used to simulate discharges between 82.12-343.6 m^3/s, and a final 'flood' domain was used to simulate a discharge of 1184.6 m^3/s. A portion of the low-flow domain was clipped to the downstream 1.2 km of the study site for the purpose of simulating a discharge of 3.51 m^3/s, which corresponded to flow during the period of wading depth and velocity measurement collection. For maps and details about them, see (Wiener & Pasternack, 2022).
Computational mesh resolution	Internodal spacing for all computational meshes was ~0.96 m.
Discharge range of model	For the whole river the range was 1.19-1184.6 m^3/s. The latter corresponding to a flow with an ~13.7 annual recurrence interval.

Model Parameter	Description
Downstream WSE data/model source	WSEs at the downstream boundary were estimated from a site specific rating-curve or from field measured conditions using RTK-GPS.
River roughness specification	Because the scientific literature reports no consistent variation of Manning's n as a function of stage-dependent relative roughness for the whole wetted area of a river (i.e., roughness/depth), a calibrated constant value of 0.09 was used for all simulations (Wiener & Pasternack, 2022). This calibrated value was physically realistic for the setting (Yochum et al., 2014) and sensitivity analysis testing the model's response to small (< 0.01) incremental variations in n values found differences in predicted depths and velocities to be relatively minimal (Wiener & Pasternack, 2022).
Eddy viscosity specification	Parabolic turbulence closure with an eddy velocity that scales with depth, shear velocity, and an on-dimensional eddy viscosity coefficient (e*) that can be selected between ~0.05 to 1 based on expert knowledge and local data indicators. An eddy viscosity coefficient of 0.1 was used for all simulations in this study.
Hydraulic validation range	Lidar point observations of WSE were collected at 1.19 m^3/s. Wading depth, velocity, and WSE fixed-point observations were collected at 3.51 m^3/s.
Model mass conservation (Calculated vs Given Q)	0.01-0.6%
WSE prediction accuracy	At 1.19 m^3/s there are 147,644 lidar-based discrete WSE point locations distributed throughout the 13.2-km domain. Mean raw deviation is -0.08 m. 27% of deviations within 0.05 m, 48% of deviations within 0.1 m', 82% within 0.25 m, and 95% within 0.5 m. 53% of deviations were less than 1.96*(root mean square error) of the bathymetric lidar points.
Wading depth prediction accuracy	From 61 independent locations, predicted vs observed depths yielded a coefficient of determination (R^2) of 0.84 and linear regression slope of 0.87. Mean absolute deviation between observed and predicted depths was 0.092 m.
Wading velocity magnitude prediction accuracy	From 61 independent locations, predicted vs observed velocities yielded a coefficient of determination (R^2) of 0.80 and linear regression slope of 0.87. Median error of 5%. Percent error metrics include all velocities (including V<0.3 m/s, which tends to have high error percents) yielding a rigorous standard of reporting.

Baseflow morphological unit delineation

Morphological units were delineated using the hydraulics-based landform classification

method of Wyrick et al. (2014). MU mapping concepts, details of Wyrick's method, and example applications of the method for MU mapping purposes are exhaustively described in Wyrick et al. (2014), Wyrick & Pasternack (2014,) and Woodworth & Pasternack (2022). To avoid unnecessary repetition of details found in these references, this section is limited to providing a brief summary of the Wyrick et al. (2014) method and how it was used to map MUs in the study segment.

Wyrick's method is founded on the established theory that baseflow hydraulics conform to topographic controls and thus reveal overlying landforms that are created at higher stages (Keller & Melhorn, 1978; Aadland, 1993; Rabeni & Jacobson, 1993; Coarer, 2007), and that MUs occupy discrete combinations of baseflow depth and velocity that can be quantitatively delineated using 2D model outputs (Wyrick & Pasternack, 2014; Woodworth & Pasternack, 2022). Summarily, the method involves two steps. First, a supervised classification approach (i.e. decision tree) is used to discriminate a river's bivariate baseflow depth-velocity phase-space into a set number of MUs with discrete bivariate ranges created on an expert basis using knowledge about a particular fluvial setting, statistical analysis of baseflow hydraulics, and hydraulic thresholds from other MU studies (Pasternack & Senter, 2011, Wyrick & Pasternack, 2014). Second, the phase-space classification is applied to 2D model output rasters to classify each cell. Adjacent cells of the same MU type are then agglomerated into contiguous MU patches.

The selected baseflow condition of 1.54 m^3/s was calculated from the study segment's estimated unimpaired historic flow record (October 1, 1930 to September 30, 2015) as the arithmetic mean of all daily flows occurring during the dry season (July 1 – September 30) and is ~ 0.14 of the estimated bankfull discharge (Wiener & Pasternack, 2016). This is consistent with baseflow recommendations from other studies for delineating MUs (Wyrick & Pasternack, 2014). Further, Wyrick and Pasternack (2012) found MU mapping is not sensitive to the selected baseflow

discharge for discharge variations within ~ ±15%.

Trial MU patches were generated from baseflow model predicted depth and velocity hydraulic rasters with 0.48 m resolution using ArcGIS Spatial Analyst. Hydraulic thresholds and the number of initial MUs were informed by previous studies (Grant et al., 1990; Hauer et al., 2009; Pasternack & Senter, 2011; Wyrick & Pasternack, 2014). Expert judgment from field experience was used to adjust MU names and descriptions as well as to iteratively evaluate depth and velocity threshold values. Statistical analysis was also used to differentiate MU types and set thresholds.

Final hydraulic thresholds delineated nine baseflow channel MUs covering the entire extent of the baseflow river channel's wetted area. This diversity is consistent with recommendations to identify units beyond the common riffle, step, and pool MUs associated with steep channels (Comiti & Mao, 2012). Despite potential challenges in delineating thresholds, the approach is at least open to review/re-evaluation by all stakeholders; it is fully objective for the majority of the river not used to "calibrate" the thresholds; it is superior to ground-based delineation by individuals (which is not even possible in this remote mountain segment) that result in subjective and highly variable classifications (Roper & Scarnecchia, 1995); the 'place-based' framework upholds relevant localized landform diversity (Brierly et al., 2013); and supervision offers advantages over 'black-box' statistical clustering approaches for reasons explained by Wyrick et al. (2014). The 2D delineation of MUs over the entire baseflow wetted area also honors lateral variability in channel morphology that is ignored by many common top-down 1D delineation techniques reliant on topographic differences measured along a single longitudinal profile, such as the Richard's (1976) zero-crossing method or bedform differencing technique of O'Neill and Abrahams (1984) (e.g. Wyrick & Pasternack, 2014; Mahdade et al., 2020). The ultimate result was a transparent,

objective, and continuous mapping of 2D MU polygons within the entirety of the baseflow wetted area. While units were delineated purely on the basis of simulated baseflow depths and velocities, Table A.3.2 provides qualitative descriptions of the delineated units, including where they generally occurred in the channel and how these slightly bespoke units relate to the diversity of previously described in-channel MU types. Unit types also largely conformed to the common conceptualization that pool units types occur at topographic lows, alluvial step and steep plane bed units occur at topographic highs, and other units have more intermediate topographic positions (Thompson, 2018) (Figure A.3.2).

The final MU set included three separate types of pool units: deep forced pools, forced pools, and alluvial pools. All pools occur in topographic lows (Figure A.3.2), and are characterized by high baseflow depths and low baseflow velocities. At the highest distinction, pools are separated as being free-formed or forced (Montgomery and Buffington, 1997), where forced pools are deepened relative to the rest of the channel due to scouring induced by an adjacent hard obstruction that causes localized high flow convergence and convective acceleration for a range of flows that can be different in each case. Pool types have been found to be difficult to automatically distinguish using hydraulics alone (Wyrick and Pasternack 2014). In this study, a qualitative-statistical based approach was used to differentiate more alluvial vs forced pool types. Firstly, differentiation of alluvial vs forced pool types was made based on observation of distinct slope breaks in a depth histogram of hydraulic raster cells with velocities below the 0.112 m/s threshold for pool units. A minimum raster cell depth of 1.22 m was specified for all pools and depth breaks at 1.98 and 3.86 m were used to classify the other pool subclasses (i.e., forced pool and deep forced pool). This depth stratification resulted in a bathtub ring effect with shallower pool units (alluvial pool and forced pool) encircling deeper pool units.

The final MU set also included delineation of alluvial step units, which occurred in topographic highs (Figure A.3.2). The peer-reviewed literature generally defines steps as composed of transverse, channel spanning accumulations of cobbles, boulders, wood, or other debris that occur in sequence with pools (Chin & Wohl, 2005; Church & Zimmermann, 2007). The alluvial step units delineated in this study differ from the traditional definition since there was no requirement to span the channel or be adjacent to a pool. In this sense they may be more akin to 'rapid steps' and 'stone lines/stone cells' (Church & Zimmermann, 2007). The complex and vertical nature of step morphology makes automated delineation difficult, and past examples are rare (Cavalli et al., 2008; Zimmermann et al., 2008; Trevisani et al., 2010). In order to verify our delineation, alluvial step locations ('MU Steps') were compared to an independent set of steps mapped using the step-pool classification algorithm of Zimmermann et al. (2008) ('Zimmermann steps'). Summarily, the Zimmermann et al. (2008) algorithm works as follows: based on input of a longitudinal profile of channel bed elevations the algorithm uses geometric relations from the step-pool literature to classify input points along the profile as 'step', 'pool', or 'other'. The model is sensitive to the alignment of the profile as well as the density of input point elevations (Zimmermann et al. 2008). To address these limitations a total of seven longitudinal profiles of channel bed elevations were used as inputs to the algorithm. Alignments for the profiles were based on thalweg profiles derived from simulations of the following discharges: 1.54, 2.68, 10.73, 32.2, 82.12, 161.0, and 343.6 m^3/s (Wiener & Pasternack, 2022). This decision was based on the assumption that thalweg profiles from a range of flow simulations would increase the likelihood of encountering steps along the channel profile, if present. All profiles were evaluated by the algorithm with point spacings of 0.30 m and 0.91 m, respectively, resulting in classifying a total of 478,116 points along 14 profiles. No changes to the default setting of the algorithm were made.

While Zimmermann et al. (2008) define steps as having to span the channel, the algorithm does not make this distinction.

The resulting Zimmermann step locations were compared to the MU step mapping to determine the percentage of steps classified as step by the other method, respectively. Based on areal intersection with all MU polygons, ~53% of the Zimmermann steps occurred within MU step polygons. The remaining ~47% of Zimmermann steps were split evenly as being mapped steep plane bed and chute MU polygons. Of the 504 individual MU step polygons that intersected with the input profiles used to map the Zimmermann steps, 104 (21%) intersected steps mapped by the Zimmermann et al. (2008) algorithm. Neither classification method is without uncertainty and the inclusion of buffers of ~3 m and ~6.1 m around the MU step polygons increased positive intersection with the Zimmermann steps to 211 (42%) and 310 (62%) of MU steps, respectively. The majority of step locations being classified the same by both methods is reassuring, but underscores that many of our alluvial step units may differ from the traditional definition.

Once mapped, MU polygons were further processed to obtain additional data products needed specifically for this study. To address rasterization artifacts of the delineation process small MU polygons were eliminated based on a minimum MU size threshold of 8.6 m^2 (41 pixels, or ~9x10 m^2). This corresponds to the minimum polygon size that would retain at least ~ 90% of the baseflow channel's wetted area (*sensu* Wyrick &Pasternack, 2014). Because HM variables were designed to be measured at river cross-sections the box counting procedure of Wyrick and Pasternack (2012) was used to generate a baseflow series of longitudinally abutting 3-m wide, cross-sectional polygons ('cross-sections') stationed along the river corridor (Wiener & Pasternack, 2022). Baseflow cross-sections were then assigned to a specific 'dominant' MU if at least 50% of a cross-sectional polygons area was occupied by a single MU types polygons. Cross-

sections without a singular dominant MU were labeled as 'mixed'. Of the 4236 baseflow cross-sections, 2539 were found to be dominated by a single MU type, meaning ~40% of cross-sections did not have a single dominant MU type. Dominance by individual MU types varied, resulting in strong class imbalance in MU dominated cross-sections. For instance, ~83% of dominant cross-sections consisted of three MU types: slackwater, forced pool, and steep plane bed.

Lastly, as discussed in the main text, the final set of processed MU polygons were analyzed in the context of their abundance (counts and areal coverage), lateral diversity, adjacency probabilities, and longitudinal spacing. These analyses were conducted using the methods of Wyrick and Pasternack (2014) and are briefly summarized in the subsections below.

Spatial abundance

The total number (counts) and areal coverage of each MU type were quantified and percentages were calculated reflecting each unit's occurrence probability. Methods did not differ from those of Wyrick and Pasternack (2014).

Lateral diversity

Lateral diversity was assessed by counting the number of distinct MU polygons at each cross-section. Methods did not diverge from those of Wyrick and Pasternack (2014).

Adjacency probability

MU adjacency tendencies were evaluated using an updated version of the transition probability analysis method of Grant et al. (1990) (Wyrick & Pasternack, 2014). For each MU type, the total number of adjacencies were summed and individual unit adjacencies were represented as percentages of the total. MU adjacency probabilities were compared to the concept that randomly occurring MUs would exhibit equal probability of occurrence, which equates to

each MU having an occurrence probability equal to 100/N, where N is the total number of MU types. Normalizing MU adjacency probabilities by the random probability indicates where certain MUs exhibit 'preference' (normalize probability >1) or if they can be thought of as geomorphically 'avoided'. Adjacencies within 20% of unity (i.e., 0.8–1.2) were considered near-random (Wyrick & Pasternack, 2014).

Longitudinal spacing

Spacing of like MU types were determined by relocating the centroid of MU polygons to the nearest (i.e., perpendicular) point along the channel's baseflow thalweg (Wiener & Pasternack, 2022). Point-to-point distances along the thalweg of like MUs were calculated. Spacing distances were normalized by dividing by the average bankfull channel width ($\overline{W_{Bf}}$), consistent with the literature (Keller 1972; Chin and Wohl 2005). The analysis was limited to the streamwise dimension meaning laterally adjacent units of the same type were not counted separately. A manual evaluation and 'cleaning' of the aligned centroids was performed to address locations where multiple MU polygons occurred, but were clearly part of a single landform such as at cross-sections where the same MU was present separately along opposite banks and locations where a larger MU community was separated by pixilation. The three pool MU types were also aggregated to allow more homogenous comparison of pool spacing with other studies. Furthermore, MUs that occurred ubiquitously along the channel, plane bed and glide, were not included, meaning the focus was on those MUs that were primarily longitudinally distributed: run, steep plane bed, alluvial step, chute, and aggregated pools.

Table A.3.2. Qualitative descriptions of baseflow channel morphological units.

Unit Name	Definition and Description
Deep Forced Pool	Occur where plunging or highly concentrated, high velocity (jet) flow from upstream vertical drops or channel constrictions scours into bedrock and/or alluvial deposits formed due to downstream backwater control. High velocity jet flow may be present at low stage due to drops but most scour likely occurs at high stage. These excessively deepened areas often occur where bedrock canyon walls impinge on pool areas.
Forced Pool	Similar to deep forced pools, these features occur where plunging or highly concentrated jet flow from upstream vertical drops or channel constrictions scour alluvium or bedrock. The magnitude of the force involved is less than in deep forced pools such that these are not scoured nearly as deep. Impinging bedrock canyon walls that function to limit width expansion also aid in scour.
Alluvial Pool	Alluvial pools also occur in erosional zones, but those less associated with the strong scour involved in forced pool formation. Alluvial pools in this setting occur in less laterally confined areas of flow convergence, at pool-tail locations downstream of forced pools, adjacent to the thalweg in zones of recirculating flow, in moderately deep and slow-moving baseflow waters upstream of topographic highs, as shallow baseflow plunge pools in step-pool complexes, and along the channel periphery where higher flows activate new flow paths. It is unclear if locations along the channel periphery are more reflective of a forced pool setting associated with less frequently occurring higher flows.
Slackwater	Areas with shallow-to-moderately deep baseflow depths with low gradient, variable bed roughness, and low baseflow water speeds often occurring along the periphery of the channel and other units, especially pools, glides, and runs. Analogous with terms such as “plane bed” or “pocket water”. Aside from the criteria to span the channel and potentially lower gradients, these areas, at least locally, conform to the general plane bed channel description provided by Montgomery et al. (1997), by lacking bar forms, having high relative roughness, and lacking rhythmic bedforms except where local flow obstructions result in forced forms (pools/riffles/steps). Encompass zones of recirculating flow at baseflow discharges due to channel boundaries and LBEs.
Glide	Transitional units of low-to-moderate baseflow depths and moderate baseflow water speeds representing areas of changing slope or convergent/divergence flow patterns, and acceleration changes based on morphological forcing (e.g. lateral and/or vertical flow changes). Often located at steep plane bed to pool-head or pool exit-slope to steep plane bed

Unit Name	Definition and Description
	transitions, in intermediate locations within cascades/step-pool sections, and around forcing elements.
Run	Areas of deep, moderate baseflow water speeds with steeper, smooth relatively unbroken baseflow water surface slope (e.g. low Froude number). Occur in the channel center or locations of most flow momentum in relatively wide channel areas or adjacent to LBE forcing elements due to topographic steering and scour. Often follow chutes in transition to lower baseflow velocity features.
Chute	Areas of deep, high velocity flow at baseflow with smooth relatively unbroken baseflow water surface slope (e.g. low Froude number). Occur in abrupt channel expansions where increased cross-sectional area causes concentrated flow in the form of a hydraulic jet, or adjacent to LBE forcing elements where flow has been steered. Also occur in highly confined steep sections of deeply eroded bedrock (e.g. gorge) or convergent constrictions adjacent/downstream of shallow high velocity baseflow units.
Steep Plane Bed	Topographic highs with areas of shallow, high baseflow water speeds. Similar to slackwater but with rougher water surface textures and steeper bed and baseflow water surface slopes. Areas envisioned to be depositional at high flow stages or at least have stable accumulations of coarse substrates. These areas encompass various channel morphologies that could not be individually distinguished from each other using only hydraulics, such as riffles, forced riffles, cascading flow, and rapids. While areas may lack defined crests they are the most representative riffle analog of all MU types.
Alluvial Step	Areas with shallow, very high baseflow water speeds, characterized by rough water surface textures and steep bed and baseflow water surface slopes. Generally occur where low flows are cascading over a transverse LBE resulting in an abrupt/rapid drop in water surface elevation. Unit differs somewhat from traditional definition of a step due to limitation in mapping approach. Mapped areas have highly convergent flow during baseflow conditions.

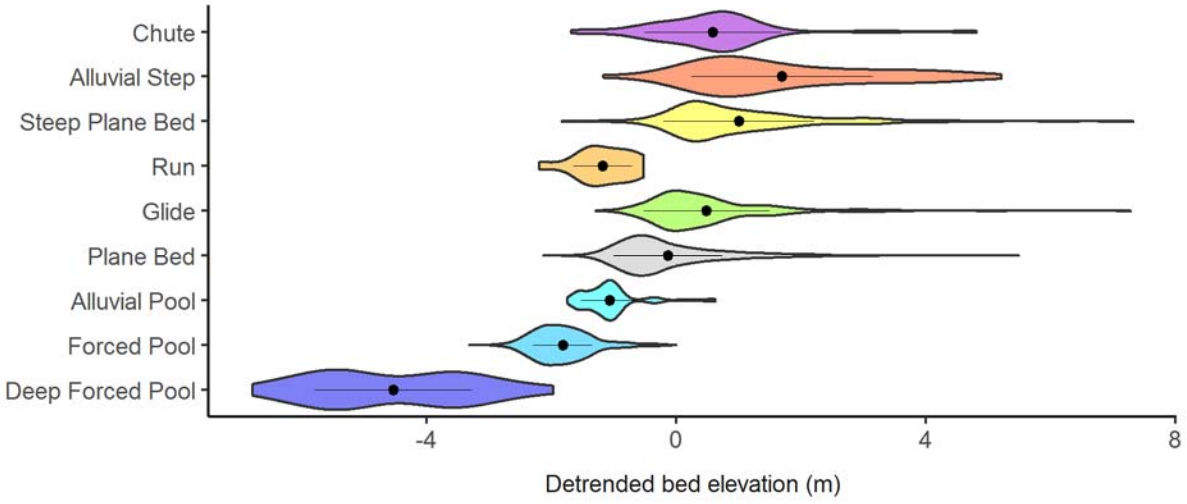

Figure A.3.2. Violin plot of detrended bed elevations by morphological unit (MU) type for dominant MU cross-sections. Violins represent kernel density of each variable. Points in each violin are mean values and lines in each violin show one standard deviation from mean. Detrended bed elevation data is from Pasternack et al. (2021).

Hydro-morphological variables

A total of 15 HM variables having either predictive capability or representing an array of possible geometric, hydraulic, and geomorphic controls on baseflow channel fluvial landforms were selected from the set of 18 HM variables to address the first three study questions. Focus was put on selecting HM variables reflecting purely topographic or morphological aspects of the riverscape that were decoupled from hydraulics such as depth and velocity, as these form the basis of the Wyrick et al. (2014) MU classification and mapping scheme. This required removing the three AHG variables from initial consideration. HM variables were determined directly at or numerically related to the same set of 4236 baseflow cross-sectional polygons used when defining dominant MUs. The process for calculating HM variable values is described below.

Firstly, the box counting procedure of Wyrick and Pasternack (2012) was used to generate several discharge-dependent series of longitudinally abutting 3-m wide, cross-sectional polygons

stationed along the river corridor (Wiener & Pasternack, 2022). Simplistically, the procedure involves generating points longitudinally along a river centerline, creating station-lines perpendicular to these points, buffering the station lines into individual polygons, and clipping the polygons using a wetted area or other boundary of interest. However, the process is sensitive to the location and tortuosity of the alignment used to generate the longitudinal series of points. An overly tortuous path results in highly overlapping sections and polygons that also miss covering portions of the wetted area, while an overly simple alignment such as using a valley centerline for interpretation of all flows may result in clipped polygons that are not perpendicular to the main direction of flow, particularly at lower flows. To address this issue, two longitudinal alignments were generated based on the centerlines of the bankfull (10.73 m^3/s) and 343.6 m^3/s flood flow simulations. Centerlines were delineated using the Polygon Centerline Tool™ (https://www.beachbumgis.com/). The bankfull alignment was used to generate cross-sectional polygons for all simulated flows below bankfull (10.7 m^3/s) and the flood flow alignment was used for all remaining flows.

Prior to applying the box counting procedure, the bankfull and flood flow centerlines were simplified using the ArcGIS simplify line (point remove algorithm with 4.6 m offset) and smooth line (Bezier interpolation) tools. Points were spaced along the revised alignments every 3 m, yielding a series of 3-m long cross-sectional polygons distributed down the river for each alignment. These polygons were then clipped using wetted area polygons of the baseflow (1.54 m^3/s), bankfull (10.73 m^3/s), formative (161.0 m^3/s), and $Q_{13.7}$ (1184.7 m^3/s) flow simulations to create a unique set of cross-sectional polygons for each discharge. Wetted area polygons were created for each flow simulation *sensu* Pasternack (2011) using interpolated depths greater than zero as the minimum threshold. Notably there was some overlap or underlap of polygons at

locations of high channel curvature. These areas were determined to balance out and no manual adjustment of the polygons occurred.

The next step was to calculate HM variables using the appropriate set of discharge-dependent cross-sectional polygons. Wetted widths ($W_{Bs,}$ W_F, and $W_{13.7}$), width-to-depth ratios (W/h_{Bf} and W/h_F), and water surface slopes (WSS_{Bs} and WSS_F) were determined using wetted areas and hydraulic rasters derived from 2D model outputs following the approaches of Wyrick and Pasternack (2012, 2014). For instance, baseflow width (W_{Bs}) was simply calculated as the average width of each baseflow cross-sectional polygon, whereas formative width (W_F) was the average width of each formative cross-sectional polygon since polygons were clipped using wetted areas from these respective discharges (Wyrick & Pasternack, 2014). Cross-sectionally average hydraulic values such as depth (h), water surface elevation (WSE), and bed shear stress (τ) needed to calculate bankfull and formative width-to-depth ratios (W/h_{Bf} and W/h_F), water surface slopes (WSS_{Bs} and WSS_F), and formative shear stress change ($\Delta\tau_F$) were calculated using the ArcGIS zonal statistics tool with the appropriate set of discharge-dependent cross-sectional polygons and 0.46 m resolution hydraulic rasters generated from raw SRH-2D outputs as inputs (Pasternack, 2011; Wyrick & Pasternack, 2012, 2014; Wiener & Pasternack, 2022). Valley width, needed for determining W_{Bs}/W_V, was delineated as the detrended elevation corresponding to the contact between the soil-mantled, vegetated hillside and the river corridor (White et al., 2010; Pasternack et al., 2021). With specific regard to estimation of τ, values were calculated at each node in the 2D model using manning's equation (Lai, 2008):

$$\begin{pmatrix}\tau_x\\ \tau_y\end{pmatrix} = \rho C_f \begin{pmatrix}U\\ V\end{pmatrix}\sqrt{U^2+V^2};\quad C_f = \frac{gn^2}{h^{1/3}} \qquad \text{(Eq. A.3.1)}$$

where τ_x and τ_y are bed shear stresses in the x and y horizontal Cartesian coordinate directions, ρ

is the density of water, U and V are depth-averaged velocity components in x and y directions, g is acceleration due to gravity, and *n* is manning's coefficient. Like other hydraulics, raw SRH-2D output τ values were used to generate discharge-dependent 0.46 m resolution rasters.

Water surface slopes (WSS_{Bs} and WSS_F) were determined following the approach described by Wyrick and Pasternack (2012, 2014). Specifically, for each relevant discharge, mean WSEs were calculated at each cross-section from 0.43 m WSE rasters generated from SRH-2D outputs as described above. WSS was then calculated as the difference in mean WSE between upstream and downstream sections lagged two sections apart divided by the 12-m longitudinal distance. Local variability in channel bed elevations and WSS are known to make estimates of WSS and slope in mountain rivers challenging (Nitsche et al., 2012). The study's averaging and smoothing techniques help address, but do not alleviate uncertainty. To quantify expected estimation errors in WSS_{Bs} and WSS_F resulting due to variability in simulated WSE values, the standard error of the mean WSEs (SEM_{wse}) was calculated for each cross-section according to:

$$SEM_{wse} = \frac{\sigma_{wse}}{\sqrt{n_{wse}}} \quad \text{(Eq. A.3.2)}$$

where σ_{wse} is the standard deviation of WSEs in each cross-section and n_{wse} is the count of WSE measurements in each cross-section. The maximum absolute expected error in WSS at each cross-section (WSS_e) were then obtained by recalculating WSS by adding the SEM_{wse} of the upstream cross-section ($SEM_{wse\text{-}u}$) to the mean WSE of the upstream cross-section ($\overline{WSE}_u$) and subtracting the SEM_{wse} of the downstream cross-section ($SEM_{wse\text{-}d}$) to the mean WSE of the downstream cross-section ($\overline{WSE}_d$) and then differencing this from the original WSS measurement:

$$WSS_e = \left|\left(\frac{[(\overline{WSE}_u + SEM_{wse-u}) - (\overline{WSE}_d - SEM_{wse-d})]}{12}\right) - \left(\frac{\overline{WSE}_u - \overline{WSE}_d}{12}\right)\right| \quad \text{(Eq. A.3.3)}$$

Since, WSS_e represents error magnitude, absolute percent estimation errors were calculated by dividing each WSS_e by WSS from the same cross-section. Both error statistics were calculated for

all WSS_{Bs} and WSS_F cross-sections, respectively, and stratified and summarized by cross-sections dominated by a single MU type. Beyond this scale of uncertainty, simulated WSEs are not without error. The mean deviation between 139,901 paired simulated and observed WSEs distributed throughout the 13.2 km study domain was 0.042 m. However, these deviations were found to have a near equal balance of over-versus under-predictions (Wiener & Pasternack, 2022), which complicates how such errors would propagate into cross-sectionally averaged WSE and WSS calculations. WSE simulation error is acknowledged but not addressed further at this time.

Channel-bed slope (S_{Bs}) was determined similar to the approach for WSS_{Bs} whereby the mean bed elevation of each baseflow cross-section was calculated from the DTM and then slope was calculated as the difference in mean bed elevation between upstream and downstream sections lagged two section apart divided by the 12-m longitudinal distance (Wyrick & Pasternack, 2014). In order to calculate S_{Bs} without the influence of macro-roughness features (Nitsche et al., 2012), a 'smoothed' DTM was created by removing LBEs from the DTM prior to calculating cross-sectional mean bed elevations. The first step in making the smoothed DTM was to use LBE polygons to create a multi-part polygon 'deletion mask', whereby topographic/bathymetric points inside the mask were removed from the bare Earth point cloud ('preliminary smoothed point cloud'). Only LBEs with 90% of their planform area inside the baseflow simulated wetted area were included in the deletion mask. A small buffer equal to ½ the DTM cell resolution (~0.23 m) was added around each of these LBEs to account for edge effects. Bank attached LBE points were retained in each preliminary smoothed point cloud by creating a ~0.46 m buffer region along the simulated baseflow wetted edge and removing any LBE in this region from the deletion mask. To densify regions where points had been deleted, new points were randomly placed within each polygon of the deletion mask at a density equal to the density of the original bare Earth point cloud

(16 pts/m^2). Elevations at these new points were interpolated with ordinary kriging using the preliminary smoothed point cloud data as input. To add surface texture to these points consistent with their surroundings, random noise was added to each point elevation by drawing from a normal distribution with mean of zero and standard deviation of 0.064 m, which corresponds to the study segment's estimated D_{16}. Lastly, smoothed point cloud data were converted to a DTM using TIN-based surface models re-sampled to a 0.46 m resolution grid.

Expected S_{Bs} estimation error metrics including the maximum absolute expected error and maximum absolute percent error in S_{Bs} at each cross-section were calculated the same as for WSS variables but using bed elevations from the smoothed DTM instead of WSEs. Error in bed elevation measurements also propagate to create uncertainty in S_{Bs} estimates. Reported root means square error (RMSE) between co-located lidar and RTK GPS bed measurements were 0.02 m for near-infrared laser lidar ground points and 0.06 m for green lidar bathymetric points (Wiener & Pasternack, 2022). Like WSS simulation errors it is not straightforward to determine how this measurement error influences S_{Bs} estimates.

Regarding, bankfull and formative LBE concentrations (Γ_{Bf} and Γ_F), these data were previously calculated in the study segment by Wiener and Pasternack (2022). Summarily, their procedure applied a ground classification algorithm to the study segment's bare Earth point cloud to create a 'smoothed' DTM raster. The smoothed DTM raster was differenced from the bare Earth DTM to generate a roughness surface model (RSM) raster. A marker-controlled watershed segmentation algorithm was used to extract LBEs from the RSM. Mapping performance was comparable to or better than benchmark values from forestry research for mapping tree crowns, which is a reasonable proxy given the absence of performance metrics for mapping LBEs. The study segment census yielded a total of 42,176 LBEs. Minimum LBE size was a single raster cell

(0.46 m x 0.46 m). For this study Γ is defined as the areal proportion of LBE polygons within any larger domain. Γ_{Bf} and Γ_F were geospatially quantified by clipping the LBE polygons with the associated discharge's wetted area polygon.

Determination of longitudinal change variables (ΔW_{Bs}, ΔW_F, and $\Delta\tau_F$) followed the approaches described by Golly et al. (2019). Specifically, ΔW_{Bs} and ΔW_F were calculated as the slope ($\Delta W/\Delta x$, where x is distance) of how these variables changed upstream of each dominant MU cross-section using linear regression. As such, negative values correspond to the channel narrowing toward an MU and positive values to the channel expanding. $\Delta\tau_F$ was similarly calculated as the slope ($\Delta\tau/\Delta x$) of cross-sectionally averaged τ value changes upstream of each dominant MU cross-section. Negative $\Delta\tau_F$ values indicate shear stress decreasing toward an MU and positive values as shear stress increasing. A fixed upstream distance of 52 m (17 cross-sections), corresponding to $2\cdot\overline{W_{Bf}}$, was used as the spatial scale over which all longitudinal change variable calculations were made (Golly et al., 2019). Cross-sectionally averaged τ values were derived from model generated τ rasters as described above. We acknowledge there is uncertainty in τ predicted from the 2D model. However, we consider this uncertainty no greater than τ estimates derived from the DuBois equation (i.e. depth-slope product) which are ubiquitous in studies of geomorphic classification and analysis (e.g. Buffington & Montgomery, 2013; Golly et al., 2019; Saletti & Hassan, 2020). For instance, in a 2D model with larger average depth and velocity percent errors Pasternack et al. (2006) found 56% of tested 2D model shear velocity predictions were within the 95% confidence limit of the best field-based estimation method and at least as accurate as field measurements.

Lastly, Θ_3, which served as a proxy for hydraulic geometry exponents was derived by fitting observed cross-sectional elevations (z) with a mathematical model for cross-section

geometry. Elevations were obtained by stationing points at 0.25 m increments along the centerline of each cross-sectional polygon and sampling elevations from the DTM. The extent of each cross-section centerline was determined by the wetted area from the 2D model bankfull simulation (10.73 m^3/s). Note that this differs from the spatial domain used for MU delineation which included only the baseflow wetted area. Elevations and cross-stream distances at each cross-section were independently rescaled from 0-1 using min-max and max normalization, respectively. For each section, normalized elevations (z_n) were fit using a power function of the form:

$$z_n = \theta_1(|x - \theta_2|)^{\theta_3} \quad \text{(Eq. A.3.4)}$$

where x is normalized cross-stream distance and $\{\Theta_i\}$ are three fitting parameters. The function is symmetrical about Θ_2, and can take on various shapes depending on combinations of Θ_1 and Θ_3. The Θ_3 parameter primary determines the shape of the cross-section. For Θ_3=1, the equation produced a perfect V-shaped section. As Θ_3 increases above unity sections become increasingly concave-up (U-shaped) approaching a rectangular cross-section as Θ_3 goes to infinity, whereas for Θ_3 less than unity sections are convex. In this manner, the equation allows for cross-sectional geometries consistent with the hypothesized expectations for different MU types. The Θ_1 parameter dictates the vertical scaling of predicted z_n values and is somewhat inversely correlated with Θ_3 in order to constrain z_n values in the 0-1 range. Thus, only Θ_3 was included as an HM variable. Despite its flexibility, Eq. A.3.4 only produces smooth, symmetric cross-section shapes. In this manner, cross-section models are unable to account for in-channel topographic variability associated with roughness features, bedforms, and channel asymmetries. The function may also have difficulty fitting multi-thread channels.

Fitting was performed by non-linear least squares regression with the 'minpack.lm' R package which employs a modification of the Levenberg-Marquardt algorithm (Elzhov et al.,

2016), yielding a unique model and Θ_3 value for each cross-section. We are not aware of performance standards with which to assess the goodness of model fits. In this absence, the ability to model cross-sectional topography with Eq. A.3.4 was heuristically assessed with four metrics. First, the best fit slope and coefficient of determination (R^2) were calculated for each cross-section by regressing observed vs model predicted z_n. These metrics describe model precision and accuracy, respectively. Slopes closer to unity and higher R^2 values are generally considered better. Linear correlation between observed and predicted z_n was assessed using Pearson's correlation coefficient (r). Lastly, the percentage of observed z_n falling outside of each model's 95% prediction interval, an indicator of poor model fit, were calculated for each cross-section. Fits were considered satisfactory if each of the following criteria were met: i) the majority of slope values were between 0.5-1.5, ii) the majority of R^2 values exceeded 0.5; iii) the majority of r values exceeded 0.7, a common benchmark for high correlation (Mukaka, 2012); and iv) the majority of cross-sections had at least 95% of observed z_n within 95% prediction intervals. Use of Eq. A.3.4 and the bankfull wetted area relative to other options were determined based on preliminary evaluation of several potential mathematical cross-section models [e.g. parabolic, catenary, sigmoid, and ellipsoid; *sensu* Brown and Pasternack (2019) and Ohara and Yamatani (2019)] and wetted extents on the basis of goodness-of-fit and heuristic assessment of how well MUs were differentiated by fitting parameters of tested mathematical models.

Once HM variables were calculated for the appropriate set of discharge-dependent cross-sectional polygons the final step was to relate all calculations to the set of baseflow cross-sectional polygons. This was necessary as it was this set of cross-sections that were classified as having dominant MUs. Transferring baseflow and bankfull HM variables was easy as these sections overlap since they are both based on the bankfull centerline. Transferring formative HM variables

and valley widths (W_v) needed to calculate baseflow-to-valley width ratios (W_{Bs}/W_V) was slightly more involved and involved two transference schemes. In the first scheme, the set of formative/valley cross-sectional polygons that occupied at least 10% of each baseflow cross-section polygon area based on spatial overlap were initially identified. Next, the average of HM variables from these sets of formative/valley cross-sectional polygons were calculated and transferred to the associated baseflow cross-section polygon. This scheme was used to transfer W_F, $W_{13.7}$, W/h_F, W_v, WSS_F, and Γ_F to the set of baseflow cross-section polygon. The second scheme used to transfer formative wetted width change (ΔW_F) and $\Delta\tau_F$ to the set of baseflow cross-section polygon involved first identifying the downstream-most formative cross-section polygon with the greatest amount of spatial overlap with each baseflow cross-section polygon. Next, ΔW_F and $\Delta\tau_F$ values calculated for the identified formative cross-section polygon were transferred to the associated baseflow cross-section polygon.

Covarying adjustment of river channel morphology (e.g. planform, gradient, bed roughness, etc.; Palucis et al., 2017), and similarity between certain HM variables meant there was potential for high correlation between HM variables. Thus, pairwise correlations were calculated for all possible HM variable pairings. High correlation ($r > 0.7$ or < -0.7) was not viewed as reason to remove variables from use in addressing study questions, but is relevant for interpretative purposes.

A.3.3.2 Statistical analysis linking MUs and HM variables

None.

A.3.3.2.1 Question 1: multivariate differences methods

PERMANOVA analysis was conducted on the basis of a Euclidian dissimilarity matrix at an alpha of $p \leq 0.05$ (Anderson, 2001). NMDS and PCA were conducted using the 'metaMDS'

and ‘rda’ functions from the ‘vegan’ R package (Oksanen et al., 2019). Analyses were calculated based upon Euclidean distance with HM variables that were rescaled using min-max normalization.

A.3.3.2.2 Question 2: pairwise analysis methods

Welch's ANOVA determines if statistically significant differences exist in population means for each variable between MU types. The test accounts for heterogeneity of variance and unbalanced sample sizes between MUs better than traditional analysis of variance (ANOVA) and the non-parametric Kruskal-Wallis test (Liu, 2015). Further, the test is robust against the assumption of normality, which is invalidated for nearly all variables.

Post-hoc analysis for each HM variable found significant by Welch’s ANOVA was performed using the Games-Howell (GH) test at the 95% confidence level adjusted for multiple inference following Holm (1979). This analysis identifies distinct MU types for each variable, and is proven to be valid for unbalanced samples with heterogeneous variance that do not meet the normality assumption (Games et al., 1979). HM variables were also ranked based on the number of significant GH pairwise tests to compare their relative discriminatory capabilities.

A.3.3.2.3 Question 3: heuristic expectation assessment methods

As shown in Table 2 in the main text expectations for generalized MU types were defined along a fuzzy gradient: low (L), intermediate (I), and high (H). In addition to the main categories, multiple expectations, such as low-to-intermediate (L-I) or intermediate-to-high (I-H), reflect higher uncertainty and potential for variable to span a wider range of value. To compare HM variable results from the set of study segment MUs to the generalized set of MU types ranked median HM variable values were ordered from low (1) to high (9) and related to ordinal

expectations and colored using the following fuzzy classification: low (1-4), low-intermediate (2-5), intermediate (4-6), intermediate-high (5-8), and high (6-9). The ordination scheme for Θ_3 values was interpreted as follows: <1 convex, ~1 V-shaped, >1 U-shaped, and >2.5 rectangular. Comparisons to these values was made heuristically based on visualizing distributions of Θ_3 values for each MU and based on performance of a two-sided t.test relative to unity. The expectation for WSS_F was for differences in median WSS between units to reduce relative to differences at baseflow. Differences for each variable were calculated as the sum of absolute differences in median WSS between all unit combinations. The ordination scheme for longitudinal change variables (ΔW_{Bs}, ΔW_F, and $\Delta\tau_F$) was based on whether values were negative, positive, or near-zero. Comparisons to these values was made heuristically based on visualizing distributions HM variable values for each MU and based on performance of a two-sided t.test relative to zero.

Figure A.3.3 depicts the transference scheme to map the final set of MU types to the generalized MU types list in section 3.2.2 of the main text.

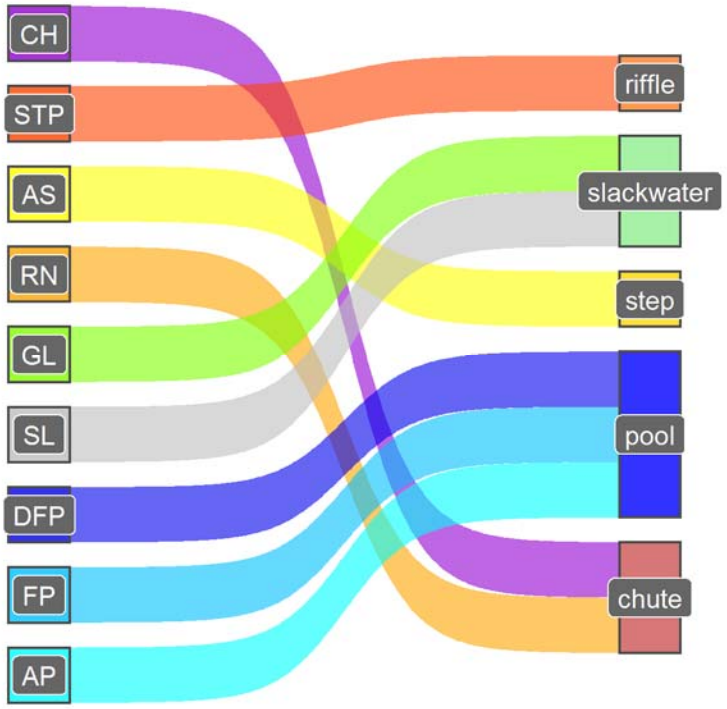

Figure A.3.3. Scheme to relate study segment morphological units (MUs) to generalized MU types. Each study segment MU (on left) is connected via a path to one generalized MU type (on right).

A.3.3.3 Question 4: hydraulic topography as alternative to topographic HM variables

methods

The *b*, *f*, and *m* exponent of each cross-section were calculated following the hydraulic topography approach of Gonzalez & Pasternack (2015) using the canonical hydraulic geometry equations for width, depth, and velocity. Specifically, average width, depth, and velocity were calculated at the set of flood flow cross-sectional polygons (section A.3.3.1) clipped to the wetted area extents from the following eight discharge simulations: 1.54, 2.68, 10.73, 32.2, 82.12, 161.0, 343.6, and 1184.6 m^3/s. Average hydraulics were calculated from 2D model hydraulic rasters (Wiener & Pasternack, 2022) using the ArcGIS zonal statistics tool. Hydraulic topography goodness-of-fit relationships were evaluated the same as Eq. A.3.4 (Section A.3.3.1).

A.3.3.4 Question 5: random forest prediction models

Matthews's correlation coefficient (MCC) is considered more robust compared to accuracy (i.e., ratio of number of accurately predicted classes to total classes) when class imbalance is high (Chicco et al., 2021). MCC ranges from -100 to 100%, with values at the extremes corresponding to cases of perfect misclassification and perfect classification, respectively, and an MCC of zero 0 being the expected value for a Bernoulli trial of equal probability. Overall model performance was based on the median MCC from all resampling events.

As discussed in the main text, RF models require tuning of four hyperparameters: number of trees to ensemble (ntree), number of variables randomly sampled as candidates at each split (mtry), the fraction of observations to sample (sample.fraction), and the maximum depth of each tree (Breiman, 2001). First, the number of trees was determined by fitting each model on the full dataset with ntree values between 500 and 3000 in increments of 20. The mtry hyperparameter for these preliminary models was set to the default of the square-root of the number of predictors. Models were evaluated based on classification accuracy on the trained samples and ntree values were selected as the minimum value where classification accuracy was both relatively low and stable. Remaining hyperparameter tuning for each model followed a grid search approach whereby mtry varied from 2 to the max number of predictors in increments of 1, sample.fraction varied between 0.5 and 0.9 in increments of 0.5, there was no limit on max tree depth, and ntree was specified as described. Each hyperparemeter combination was evaluated based on classification accuracy on the trained samples, and the set of hyperparemeter with the best classification accuracy were selected. All model development and testing was done using the 'Ranger' R package (Wright & Ziegler, 2017).

Of the 1697 baseflow cross-sections not dominated by a single MU type, 1633 were found

to have a single sub-dominant MU (Table A.3.3).

Table A.3.3. Cross-sections previously classified as mixed (n = 1697) but with a single sub-dominant morphological unit (MU) type.

MU Type	Number of cross-section
Alluvial Pool	110
Forced Pool	183
Deep Forced Pool	7
Slackwater	748
Glide	223
Run	29
Steep Plane Bed	248
Alluvial Step	49
Chute	36
Total	1633

A.3.4 Results

A.3.4.1 Morphological unit types

None.

Adjacency probability

Results of the adjacency probability analysis are presented in Table A.3.4 and Figure A.3.4.

Table A.3.4. Adjacency probabilities between the starting unit (top row) to all other units (left column). Grayed boxes represent values that are much larger than random (≳1.2), i.e., a 'collocation'. Values much less than random (≲0.2) represent an 'avoidance'.

	Alluvial Pool	Forced Pool	Deep Forced Pool	Slackwater	Glide	Run	Chute	Steep Plane Bed	Alluvial Step
Alluvial Pool	-	1.6	0.0	4.8	0.1	2.4	0.0	0.0	0.0
Forced Pool	4.7	-	0.1	2.2	0.0	2.0	0.0	0.0	0.0
Deep Forced Pool	0.0	6.5	-	0.0	0.0	2.5	0.0	0.0	0.0
Slackwater	2.9	0.4	0.0	-	3.9	1.5	0.2	0.1	0.0
Glide	0.3	0.0	0.0	4.0	-	1.7	0.9	1.4	0.7
Run	2.5	1.0	0.0	2.7	1.7	-	1.0	0.0	0.0
Chute	0.0	0.0	0.0	0.5	3.6	1.5	-	2.5	0.9
Steep Plane Bed	0.0	0.0	0.0	0.1	5.0	0.0	2.0	-	1.9
Alluvial Step	0.0	0.0	0.0	0.0	0.0	0.0	2.7	6.3	-

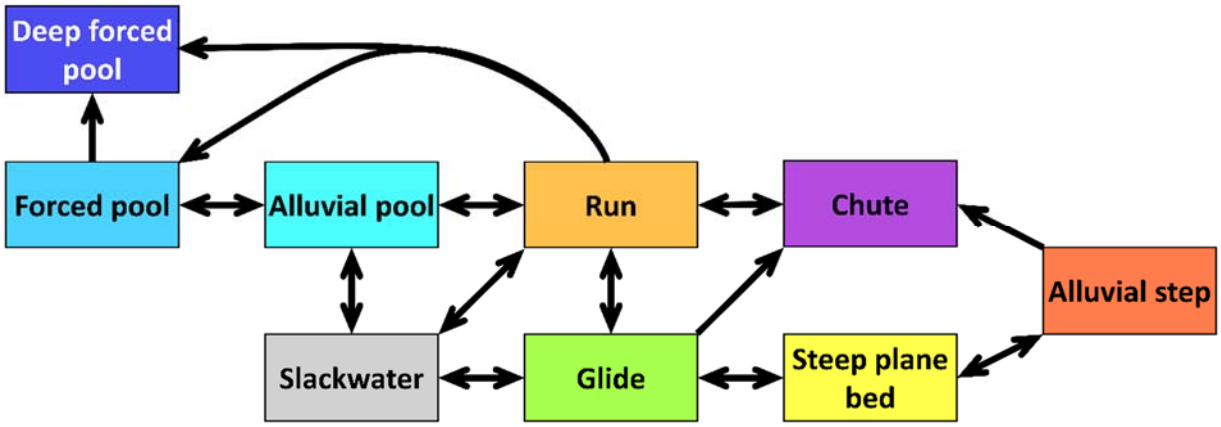

Figure A.3.4. Collocation adjacency diagram between MUs.

Longitudinal spacing

Results of the longitudinal spacing analysis are presented in Figure A.3.5.

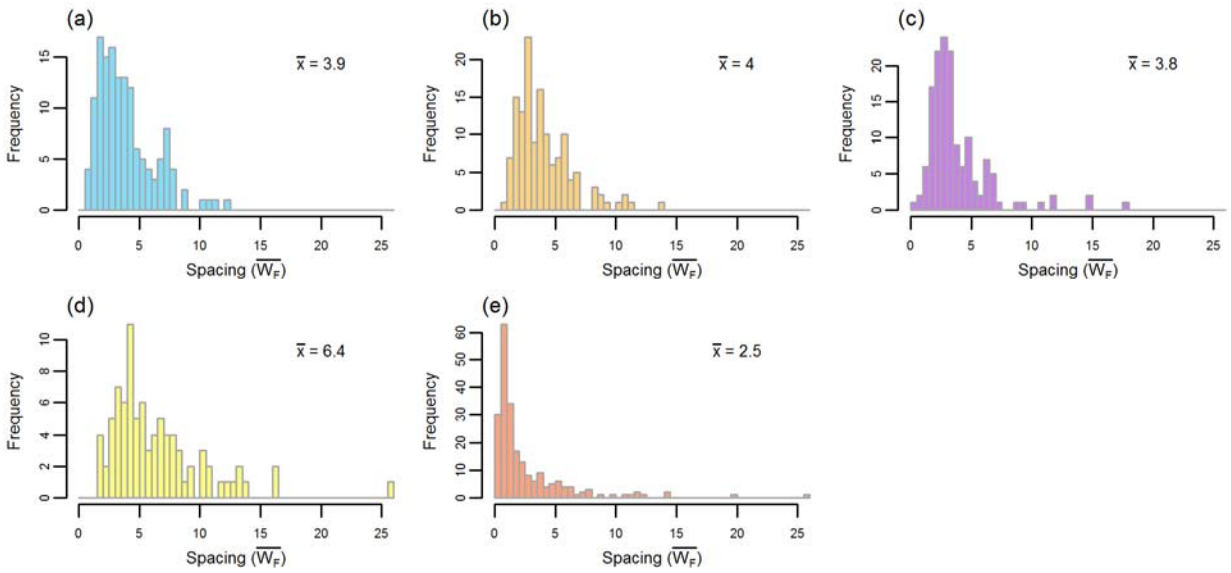

Figure A.3.5. Histograms of unit-to-unit non-dimensional spacings for (a) aggregated pool, (b) run, (c) chute, (d) steep plane bed, and (e) alluvial step units. All spacings have been normalized by dividing spacing by average bankfull width ($\overline{W_{Bf}}$). For each MU the average spacing ($\bar{x}$) is shown.

A.3.4.2 Hydro-morphological variables

Additional details of HM variables are provided below.

Visual comparison found HM variable ranges and distribution shapes were similar between the 2539 cross-sections with a single dominant MU and the complete set of 4236 baseflow cross-sections, indicating the set of cross-sections with dominant MUs were representative of the range of HM variable conditions present in the entire study segment.

As discussed in the main text, HM variables exhibited diverse ranges of values and levels of dispersion (Table A.3.5). Specifically, channel-obstruction/roughness variables (Γ_{Bf} and Γ_F), channel-size variables (W_{Bs}, W_F, and W_F), certain gradient variables (S_{Bs} and WSS_{Bs}), and certain channel-shape variables (W/h_F and W_{Bs}/W_V) had greater dispersion than longitudinal change variables (ΔW_{Bs}, ΔW_F, and $\Delta\tau_F$) and the remaining variables (W/h_{Bf}, Θ_3, and WSS_F). Comparing unscaled variables, only 5 of 105 pairs of HM variables were highly correlated ($r > 0.7$): W_{Bs} and

W_{Bs}/W_V, W_F and $W_{13.7}$, W_F and W/h_F, $W_{13.7}$ and W/h_F. and W/h_{Bf} and W/h_F (Figure A.3.6).

Goodness-of-fit metrics used to assess Eq. 1 exceeded the study's performance criteria (section A.3.3.1) indicating the function performed satisfactorily at fitting cross-section geometry (Figure A.3.7). Specifically, 60.8% of observed vs predicted z_n regression slope values were between 0.5-1.5, exceeding the 50% benchmark. The median R^2 from regressing observed vs predicted z_n values at all cross-sections was 0.60, which was above the specified 0.5 benchmark. The median r value between observed vs predicted z_n values for all cross-sections was 0.78, exceeding the 0.7 benchmark. For the final benchmark, over 63% of cross-sections had at least 95% of observed z_n values within their model's 95% prediction interval, thus exceeding the specified majority (>50%) criteria.

Maximum expected estimation errors in WSS_{Bs}, WSS_F, and S_{Bs} due to variability in smoothed bed elevations and simulated WSS values had mean values of 0.0004, 0.0005, and 0.0044 m/m across all cross-section, respectively. While the magnitude of these errors is relatively small, they result in mean percent errors in WSS_{Bs}, WSS_F, and S_{Bs} across all cross-section of 25.5, 13.4, and 55.9% due to the small magnitude of estimated WSS_{Bs}, WSS_F, and S_{Bs} values. Both error metrics varied by MU type, meaning MU types with low WSS_{Bs}, WSS_F, and S_{Bs} values often had high percent errors even if error magnitude was comparatively small (Table A.3.6). Mean SEM values for baseflow WSEs, formative WSEs, and smoothed bed elevations were 0.004, 0.005, and 0.04 m, respectively (4, 5, and 40 mm). As described in section A.3.3.1, mean deviation in simulated versus observed WSE was 0.042 m and RMSE between lidar and RTK GPS bed measurements was 0.02 m for exposed ground points and 0.06 m for bathymetric points. These values are roughly the same magnitude as the mean SEM for smoothed bed elevations and thus may be expected to contribute a similar magnitude of uncertainty. Ultimately, bed elevation

measurement and WSE simulation errors are likely to contribute additional uncertainty, but are outside the scope of this effort to fully quantify given complications in how these localized and often balanced errors (i.e. measurement/prediction over and under observed) propagate into WSS_{Bs}, WSS_F, and S_{Bs} values).

Table A.3.5. Summary statistics of hydro-morphological (HM) variables. For each HM variable, values are shown in the following order: arithmetic mean, standard deviation, inter-quartile range, minimum, and maximum. Numbers in parentheses are standard deviation and inter-quartile range of rescaled variables. Dashed lines separate groups of HM variables.

HM Variable	Summary statistic						
	Arithmetic mean	Minimum	Maximum	Standard deviation	Interquartile-range	Standard deviation (rescaled)	Interquartile-range (rescaled)
Baseflow wetted width (W_{Bs})	20.6	4.2	76.1	8.5	9.4	0.1	0.1
Formative wetted width (W_F)	40.2	16.7	86.9	11.4	13.5	0.2	0.2
$Q_{13.7}$ wetted width ($W_{13.7}$)	60.2	26.4	112.2	14.5	16.5	0.2	0.2
Bankfull width-to-depth (W/h_{Bf})	26.4	2.3	163.8	17.7	18.0	0.1	0.1
Formative width-to-depth (W/h_F)	16.4	3.5	62.6	9.0	9.0	0.1	0.1
Baseflow-to-valley width (W_{Bs}/W_V)	0.3	0.1	0.9	0.1	0.2	0.1	0.2
Bankfull cross-section geometry index (Θ_3)	1.1	0.0	10.0	1.0	1.0	0.1	0.1
Bankfull LBE concentration (Γ_{Bf})	0.2	0.0	0.9	0.2	0.2	0.2	0.3
Formative LBE concentration (Γ_F)	0.3	0.0	0.8	0.1	0.2	0.2	0.2
Baseflow bed-slope (S_{Bs})	0.0	-0.2	0.3	0.1	0.1	0.1	0.1

HM Variable	Summary statistic						
	Arithmetic mean	Minimum	Maximum	Standard deviation	Interquartile-range	Standard deviation (rescaled)	Interquartile-range (rescaled)
Baseflow water surface slope (WSS_{Bs})	0.0	0.0	0.2	0.0	0.0	0.1	0.1
Formative water surface slope (WSS_F)	0.0	0.0	0.2	0.0	0.0	0.1	0.1
Baseflow wetted width change (ΔW_{Bs})	0.0	-1.2	1.1	0.2	0.2	0.1	0.1
Formative wetted width change (ΔW_F)	0.0	-0.8	1.6	0.2	0.3	0.1	0.1
Formative shear stress change ($\Delta\tau_F$)	-0.2	-21.4	47.9	3.6	3.2	0.1	0.0

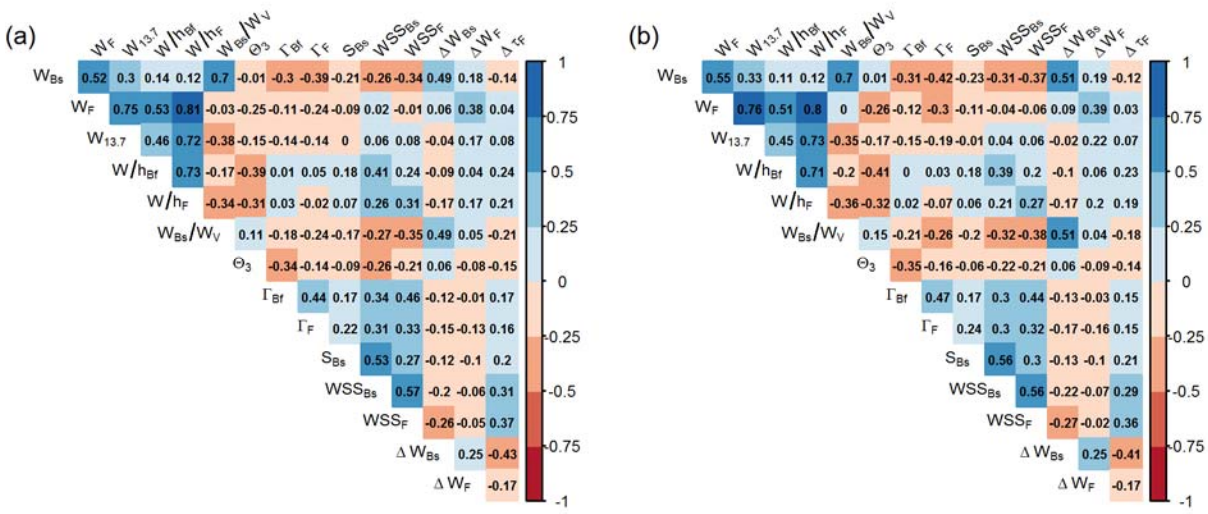

Figure A.3.6. Upper-triangular matrix showing Person's correlation coefficient between all combinations of hydro-morphologic (HM) variables for (a) all channel cross-section, and (b) only those cross-section with a single dominant morphological unit.

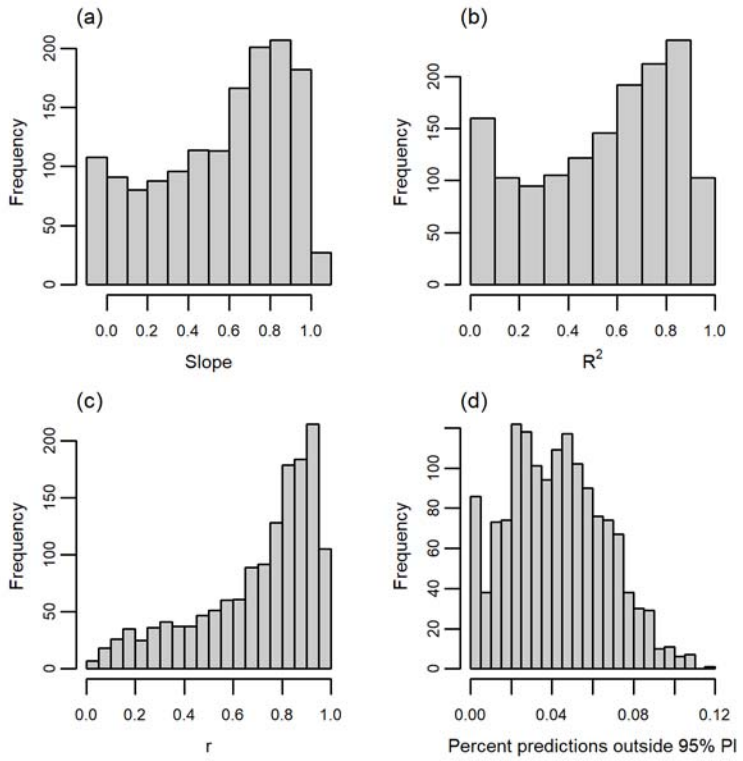

Figure A.3.7. Histograms of goodness-of-fit metrics between observed zn values and those predicted with Eq. A.3.4, including: (a) best-fit slope, (b) coefficient of determination (R^2), (c) Pearson's correlation coefficient (r), and (d) the percentage of observed z_n falling outside of each model's 95% prediction interval.

Table A.3.6. Maximum expected estimation errors and percent errors in baseflow water surface slope (WSS_{Bs}), formative water surface slope (WSS_F), and baseflow bed-slope (S_{Bs}) calculations stratified and averaged across cross-sections dominated by a single morphological unit (MU) type.

MU type	WSS_{Bs}		WSS_F		S_{Bs}	
	Magnitude	Percent	Magnitude	Percent	Magnitude	Percent
Alluvial Pool	1.1E-05	36.3	2.0E-04	4.0	0.004	208.8
Forced Pool	1.4E-05	92.1	1.6E-04	16.5	0.007	55.2
Deep Forced Pool	2.7E-06	25.4	1.5E-05	11.3	0.013	33.1
Slackwater	2.8E-04	8.4	4.3E-04	27.5	0.004	83.2
Glide	3.9E-04	3.7	5.3E-04	5.0	0.003	47.2
Run	3.2E-05	5.4	9.5E-04	3.1	0.012	61.9
Chute	7.8E-04	2.8	1.3E-03	3.2	0.008	18.4
Steep Plane Bed	1.0E-03	1.9	7.5E-04	3.5	0.003	26.5
Alluvial Step	1.4E-03	1.4	1.3E-03	3.0	0.004	5.9

A.3.4.3 Morphological unit-hydro-morphological variable relations

Summary statistics including the mean, standard deviation, minimum, and maximum of each HM variable for each MU type are reported in Table A.3.7.

As discussed in section A.3.4.2, goodness-of-fit metrics indicated performance of Eq. A.3.4 was satisfactory and yielded a range of Θ_3 values representing a variety of cross-section shapes. These same goodness-of-fit metrics varied by MU type, but with the exception of the regression slope, R^2, and r metrics for cross-sections dominated by steep plane bed performance remained satisfactory when stratified by MU type (Table A.3.8).

Table A.3.7. Summary statistics of hydro-morphological (HM) variables stratified by morphological unit (MU) type. For each MU and HM variable, values are shown in the following order: arithmetic mean, standard deviation, minimum, and maximum. Dashed lines separate groups of HM variables.

HM variable	Alluvial Pool	Forced Pool	Deep Forced Pool	Slackwater	Glide	Run	Steep Plane Bed	Alluvial Step	Chute
Baseflow wetted width (W_{Bs})	24.56	23.62	53.89	21.70	16.62	8.79	14.90	9.65	7.95
	6.87	6.23	19.46	6.99	4.78	2.28	4.89	2.68	2.10
	13.00	8.99	16.38	7.60	6.79	5.42	5.98	5.86	4.23
	40.97	51.01	76.12	53.97	41.63	13.84	39.89	18.06	13.90
Formative wetted width (W_F)	42.12	35.15	61.77	41.96	38.64	32.01	38.79	36.19	35.57
	9.49	9.91	19.54	11.53	9.41	9.05	9.39	7.14	10.29
	27.87	16.73	20.53	18.02	19.21	22.98	19.41	24.35	23.07
	69.17	84.76	81.58	86.89	75.25	53.25	76.99	55.08	57.62
$Q_{13.7}$ wetted width ($W_{13.7}$)	63.33	54.24	78.36	60.95	59.43	49.05	63.15	60.67	51.77
	13.17	12.91	9.72	14.81	12.53	10.53	13.83	13.51	10.26
	37.80	28.55	51.17	26.35	37.61	36.04	36.75	38.35	36.14
	92.09	93.22	87.04	112.20	110.57	67.07	111.44	89.08	75.99
Bankfull width-to-depth (W/h_{Bf})	16.62	10.58	8.54	27.19	31.81	7.63	41.23	35.80	18.86
	5.72	3.27	2.14	15.82	18.55	4.69	19.75	13.45	15.48
	7.85	3.74	4.26	5.50	6.63	2.33	8.41	9.25	4.79
	31.03	21.76	11.86	163.85	123.27	16.20	159.95	65.52	64.77
Formative width-to-depth (W/h_F)	15.11	9.29	7.47	17.51	17.54	12.30	19.76	19.87	17.33
	5.98	4.16	1.72	9.19	8.54	6.16	9.20	7.42	9.22
	7.31	3.64	3.48	4.72	5.04	7.13	6.15	8.60	8.79
	30.65	36.77	10.36	59.93	62.58	28.34	58.06	36.84	41.33

HM variable	Alluvial Pool	Forced Pool	Deep Forced Pool	Slackwater	Glide	Run	Steep Plane Bed	Alluvial Step	Chute
Baseflow-to-valley width (W_{Bs}/W_V)	0.34	0.39	0.63	0.32	0.26	0.18	0.23	0.17	0.16
	0.10	0.12	0.20	0.10	0.07	0.07	0.08	0.06	0.06
	0.15	0.16	0.22	0.10	0.08	0.10	0.07	0.08	0.08
	0.61	0.92	0.85	0.74	0.46	0.28	0.53	0.36	0.37
Bankfull cross-section geometry index (Θ_3)	1.99	2.15	1.30	0.82	0.84	1.20	0.78	0.78	0.89
	1.13	1.15	0.73	0.82	0.80	1.08	0.98	0.65	0.94
	0.09	0.00	0.61	0.00	0.00	0.33	0.00	0.00	0.00
	4.85	5.28	3.17	5.50	6.10	3.27	10.00	3.00	4.22
Bankfull LBE concentration (Γ_{Bf})	0.14	0.15	0.06	0.24	0.21	0.46	0.24	0.30	0.46
	0.10	0.11	0.04	0.15	0.15	0.19	0.15	0.19	0.16
	0.00	0.00	0.01	0.00	0.00	0.03	0.00	0.00	0.10
	0.49	0.48	0.17	0.87	0.84	0.68	0.67	0.67	0.82
Formative LBE concentration (Γ_F)	0.16	0.19	0.07	0.25	0.30	0.29	0.31	0.33	0.36
	0.09	0.09	0.08	0.12	0.13	0.23	0.13	0.18	0.12
	0.01	0.00	0.02	0.01	0.05	0.09	0.00	0.03	0.12
	0.38	0.60	0.44	0.81	0.70	0.77	0.77	0.68	0.66
Baseflow bed-slope (S_{Bs})	0.00	0.00	0.01	0.00	0.01	-0.03	0.06	0.10	0.06
	0.03	0.05	0.13	0.05	0.04	0.07	0.04	0.04	0.08
	-0.08	-0.15	-0.19	-0.14	-0.08	-0.13	-0.06	-0.02	-0.12
	0.08	0.17	0.25	0.21	0.17	0.09	0.20	0.21	0.25
Baseflow water surface slope (WSS_{Bs})	0.00	0.00	0.00	0.01	0.01	0.00	0.05	0.10	0.04
	0.00	0.00	0.00	0.02	0.02	0.00	0.03	0.04	0.04
	0.00	0.00	0.00	0.00	0.00	0.00	0.00	0.03	0.00
	0.00	0.03	0.00	0.15	0.13	0.00	0.18	0.21	0.17
Formative water surface slope (WSS_F)	0.01	0.00	0.00	0.02	0.02	0.05	0.03	0.05	0.05
	0.01	0.01	0.00	0.02	0.02	0.02	0.03	0.03	0.03
	0.00	0.00	0.00	0.00	0.00	0.00	0.00	0.01	0.01
	0.04	0.08	0.00	0.11	0.08	0.07	0.22	0.15	0.13
Baseflow wetted width change (ΔW_{Bs})	0.05	0.08	0.40	0.03	-0.06	-0.08	-0.09	-0.18	-0.18
	0.18	0.18	0.43	0.18	0.18	0.09	0.16	0.14	0.22
	-1.04	-0.27	-0.45	-1.25	-0.85	-0.26	-0.62	-0.43	-1.09
	0.52	1.04	1.15	0.80	0.28	0.03	0.34	0.09	0.10
Formative wetted width change (ΔW_F)	-0.04	-0.01	0.09	0.03	0.01	0.00	-0.04	0.06	-0.04
	0.24	0.25	0.28	0.21	0.19	0.23	0.23	0.46	0.21
	-0.52	-0.71	-0.33	-0.75	-0.52	-0.44	-0.63	-0.63	-0.66
	0.60	0.77	0.55	0.90	0.63	0.34	1.10	1.58	0.51
Formative bed shear stress change ($\Delta\tau_F$)	-0.62	-1.34	-1.07	-0.44	0.76	-2.16	1.38	2.77	1.41
	1.66	2.30	1.52	3.04	2.86	4.23	5.03	8.78	4.69
	-5.41	-10.12	-6.12	-16.79	-10.04	-9.04	-20.05	-21.41	-5.25
	2.79	4.74	0.01	12.27	9.85	2.54	47.87	35.60	10.23

Table A.3.8. Goodness-of-fit metrics between observed z_n values and those predicted with Eq. A.3.4 stratified by cross-sections dominated by a single morphological unit (MU) type. Values not meeting performance criteria are highlighted in gray.

MU	Slope	Coefficient of determination (R^2)	Pearson correlation coefficient (r)	Percent of observed z_n in 95% prediction interval
Alluvial Pool	0.87	0.76	0.88	66.7
Forced Pool	0.94	0.82	0.91	70.2
Deep Forced Pool	1.00	0.89	0.94	61.8
Slackwater	0.53	0.53	0.73	61.2
Glide	0.57	0.54	0.74	63.8
Run	0.73	0.71	0.84	81.8
Chute	0.59	0.59	0.77	78.4
Steep Plane Bed	0.48	0.46	0.68	64.1
Alluvial Step	0.59	0.65	0.81	59.2
Performance criteria	0.50	0.50	0.70	50.0

A.2.4.3.1 Question 1: multivariate differences results

None.

A.2.4.3.2 Question 2: pairwise analysis results

As discussed in the main text, not all HM variables discriminated the same MU types from one another. Complete results of the pairwise Games-Howell (GH) tests are depicted as 'heatmaps' in Figure A.3.8.

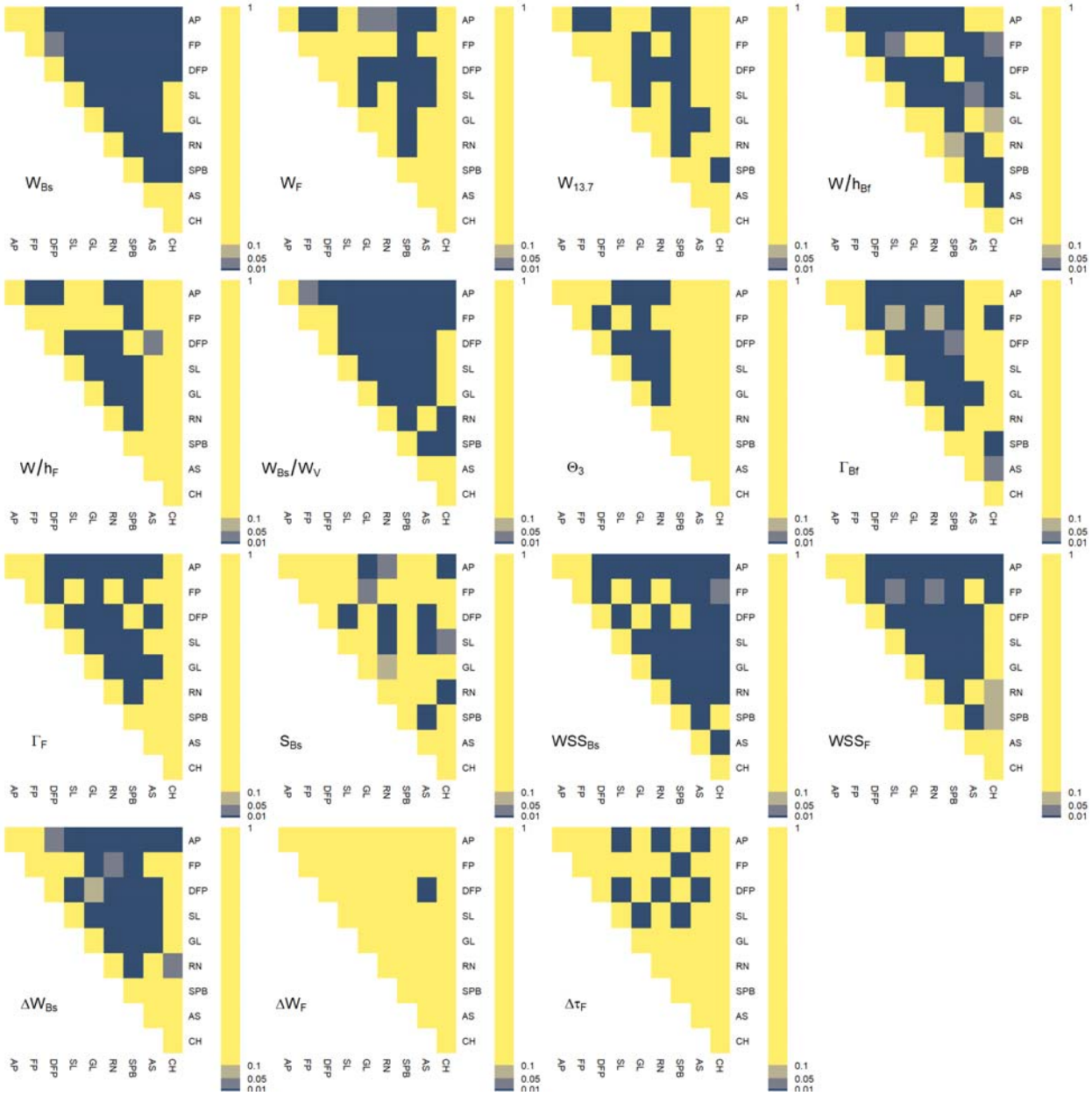

Figure A.3.8. Heatmaps of adjusted p-values from pairwise Games-Howell tests between all unique morphological unit (MU) comparisons for each hydro-morphological variable. Color scaling is such that the yellow fill corresponds to MU pairs with adjusted p-values between 0.1-1, light-gray fill to pairs with adjusted p-values between 0.05-0.1, and darker-gray and dark blue fills to pairs with adjusted p-values <0.05. Acronyms for MUs are as follows: alluvial pool (AP), forced pool (FP), deep forced pool (DFP), slackwater (SL), glide (GL), run (RN), steep plane bed (SPB), alluvial step (AS), and chute (CH).

A.2.4.3.3 Question 3: heuristic expectation assessment results

As reported in the main text, of the six HM variables where MU expectations were not met, W_F, $W_{13.7}$, Θ_3, and ΔW_F had 6 of 9 MU expectations met, while only 5 of 9 MU expectations were met for Γ_{Bf}, and $\Delta\tau_F$. Both W_F and $W_{13.7}$ were slightly narrower than expected at run units and wider than expected at alluvial pool and deep forced pool units. Unsurprisingly, there was much greater overlap of W_F and $W_{13.7}$ between all MU types compared to W_{Bs} as higher flow stages likely inundated local topographic controls. With regard to the flow convergence routing mechanism's expectation that pool type units would become narrower than riffle type units at higher flow stages and have lower W_F and/or $W_{13.7}$ values (section A.3.1.2), one explanation is that neither the formative or $Q_{13.7}$ discharge were high enough to elicit such a switch. Alternately, for forced pools, narrowing would be expected upstream of the pool, not necessarily in the pool itself, which was partly corroborated by the majority (57%) of ΔW_F values being negative for alluvial pool and forced pool units. The possibility also remains whether such a switch would ever occur in the study segment's confined and high roughness setting (Pasternack et al., 2021). As discussed in section A.3.1.2 expectations for Θ_3 were based on expert judgment largely in the absence of substantive examples. In addition to knowledge gaps and other limitations discussed in the main text, the inability of Eq. 1 to effectively represent confinement may have contributed to why expectations for this variable were not met. With regard to ΔW_F, all MUs had high dispersion and overlap in their distributions, which complicated interpretations. The two main ΔW_F expectations not met were that, first upstream formative channel widths decreased toward cross-section dominated by steep plane bed more often than they increased, the latter being associated with conditions promoting high flow deposition common to riffles, and second was that formative channel widths tended to increase leading into deep forced pool units. For Γ_{Bf}, steep plane bed had

slightly lower and run and chute had higher than expected concentrations. High concentrations at chute and run units are likely due to bedrock outcrops being mapped as LBE and included in concentration calculations (Wiener & Pasternack, 2022). Lastly, contrary to expectations, $\Delta\tau_F$ was predominantly positive (increasing) immediately upstream and leading into steep plane bed units and was negative or constant (decreasing or near-zero) when leading into pool units. The latter may result from backwater conditions upstream of forced pools.

A.3.4.4 Question 4: hydraulic topography variable results

Metrics used to assess AHG relationship goodness-of-fit (section A.3.3.3) exceeded the study's specified criteria for all metrics. Specifically, 99.8, 99.0, and 100% of observed vs predicted width, depth, and velocity regression slope values were between 0.5-1.5, respectively, which all exceed the 50% benchmark. The median R^2 from regressing observed vs predicted width, depth, and velocity values at all cross-sections were 0.95, 0.97, and 0.98, which are above the specified 0.5 benchmark. The median r value between observed vs predicted width, depth, and velocity values for all cross-sections were 0.97, 0.98, and 0.99, exceeding the 0.7 benchmark. Lastly, over 70.2, 67.9, and 97.2% of cross-sections had at least 95% of observed width, depth, and velocity values within their model's 95% prediction interval, thus exceeding the specified majority (>50%) criteria. While not one of the study's specified goodness-of-fit metrics, mean pseudo-R^2 of the fit hydraulic topography relationships were 0.93, 0.95, and 0.98 for width, depth, and velocity.

Results also generally aligned with hypothesized expectations across MU types such that pool units had higher *m* values, lower *b* values, and lower *f* values than units with high baseflow velocities (section A.3.1.2). The lower *f* values in pools compared to steep high baseflow velocity units indicates that as discharge increased momentum transfer in pool units primarily occurred via

stronger increases in velocity than depth, but occurred via stronger increases in width and depth compared to velocity in steep high baseflow velocity units. These latter units also had greater LBE concentrations. Other units such as slackwater, glide, and run had intermediate *b*, *f*, and *m* values. Chute units, which tended to be very narrow at baseflow, increased in width rapidly but had relatively low increases in velocity likely due to depth increases and relatively high LBE roughness.

A.3.4.5 Question 5: random forest model results

As discussed in the main text, distributions of HM variables at cross-sections with only a single sub-dominant MU type appeared similar to distributions with a single dominant MU Figure A.3.9).

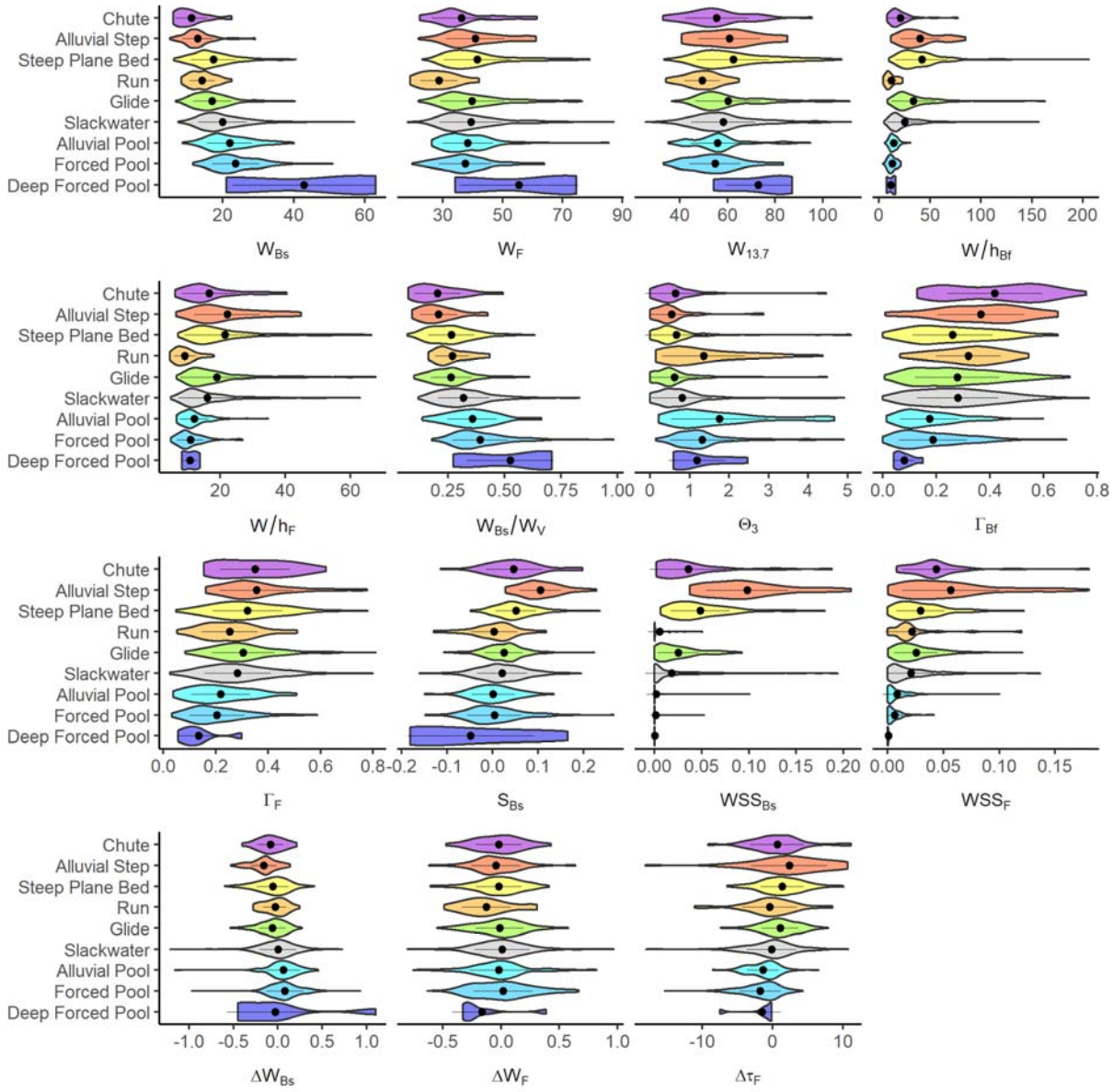

Figure A.3.9. Violin plots of hydro-morphological variables by morphological unit (MU) type for sub-dominant MU cross-sections. Violins represent kernel density of each variable. Points in each violin are mean values and lines in each violin show one standard deviation from mean.

A.3.5 Discussion

None.

A.3.5.1 Synthesis of hydro-morphological links with morphological unit spatial patterns

None.

A.3.5.2 Decoupling processes and morphological unit variability

As noted in the main text, several MU dominated cross-sections appear as either statistical 'outliers', and/or did not meet HM variable expectations. These locations may represent a variety of phenomena including: variability in how the form of each MU manifested in the study segment (Phillips, 2014); channel morphologies that have not adjusted to changes in water flow and sediment transport or recent disturbances (Lane & Richards, 1996; Tooth & Nanson, 2013); influence of non-local factors or factors not included in the study (Buffington et al., 2002; Carbonari et al., 2020); competition, exclusion, merging, cannibalization among MUs during formation (Furbish, 1998); the influence of multiple processes (Pasternack et al., 2018); or simply errors or uncertainty in HM variable calculations (Table A.3.6; section A.3.3.1). While it is the scope of this effort to address all outliers or examples where expectations were not met, some notable examples warrant discussion.

Firstly, several deep forced pool cross-sections had comparatively low W_{Bs}, W_F, and $W_{13.7}$. These locations also had lower W_{Bs}/W_v, ΔW_{Bs}, and ΔW_F than other deep forced pool cross-sections. Thus, our interpretation is that increased valley confinement and width convergence served to balance the lower W_F and $W_{13.7}$ values in terms of maintaining conditions that promote scour associated with deep forced pool units. A separate subset of deep forced pool cross-sections was also found to have relatively high S_{Bs}, with some values exceeding 0.2 m/m. These values were specifically associated with the entrance slope to a large scour pool formed immediately at the base of the New Bullards Bar Dam emergency spillway. While these data were not removed from the analysis, it is clear this location was formed by spillway operations. A final subset of

outliers to highlight, were several steep plane bed, alluvial step, and chute dominated cross-sections that had high W_F values relative to cross-sections dominated by the same MU type. Comparatively, these sections had higher W/h_{Bf} and W/h_F, lower W_{Bs}/W_v (i.e. less confined), and had lower ΔW_{Bs} and higher ΔW_F. This meant that wider steep plane bed, alluvial step, and chute dominated cross-sections were nested in wider portions of the river valley and experienced greater width expansion at formative discharge.

Table A.3.9. Comparison of the range of hydro-morphological (HM) variables for each morphological unit (MU) type in this study (values in top row next to each HM variable) with values available from past studies for similar MU types (values in bottom row next to each HM variable)[†].

HM variable	Alluvial Pool	Forced Pool	Deep Forced Pool	Slackwater
Baseflow wetted width (W_{Bs})[‡]	0.698 - 2.041	0.507 - 2.09 0.245 - 0.93	0.816 - 3.791	0.476 - 2.546 1.58
Bankfull width-to-depth (W/h_{Bf})	8.591 - 30.294	3.743 - 18.543 26.00	4.257 - 11.619	8.755 - 143.945 90.00
Baseflow bed-slope (S_{Bs})	-0.064 - 0.048	-0.137 - 0.123 -0.145 - 0.2	-0.194 - 0.255	-0.124 - 0.158 0.01 - 0.05
Baseflow water surface slope (WSS_{Bs})	0 - 0	0 - 0.021 -0.092 - 0.072	0 - 0	0 - 0.125 0.03
Baseflow wetted width change (ΔW_{Bs})	-1.038 - 0.499 -	-0.255 - 0.674 -	-0.445 - 0.948 -	-1.246 - 0.732 -
Formative wetted width change (ΔW_F)	-0.3 - 0.604 -	-0.711 - 0.715 -	-0.332 - 0.551 -	-0.752 - 0.831 -
Formative shear stress change ($\Delta \tau_F$)	-4.819 - 1.69 -	-9.525 - 4.745 -	-2.258 - 0.012 -	-16.794 - 11.685 -

HM variable	Glide	Run	Steep Plane Bed	Alluvial Step	Chute
Baseflow wetted width (W_{Bs})‡	0.403 - 2.073	0.27 - 0.427	0.306 - 1.308	0.292 - 0.769	0.211 - 0.524
	0.96 - 1	0.78	0.94 - 1.14	0.21	0.47
Bankfull width-to-depth (W/h_{Bf})	7.043 - 123.266	2.512 - 9.799	9.746 - 159.955	11.111 - 65.524	4.846 - 64.774
	64 - 73	82.00	89 - 114	-	113.00
Baseflow bed-slope (S_{Bs})	-0.062 - 0.069	-0.127 - 0.004	-0.022 - 0.177	0.027 - 0.208	-0.05 - 0.25
	-0.162 - 0.1	-0.025 - 0.147	-0.075 - 0.25	0.019 - 0.697	0.02 - 0.29
Baseflow water surface slope (WSS_{Bs})	0.001 - 0.105	0 - 0.004	0.01 - 0.159	0.044 - 0.209	0.002 - 0.169
	-0.046 - 0.088	-0.042 - 0.78	-0.016 - 0.765	-	0.42
Baseflow wetted width change (ΔW_{Bs})	-0.849 - 0.137	-0.177 - 0.022	-0.597 - 0.337	-0.433 - 0.095	-0.491 - 0.054
	-	-	-	-0.582 - 0.584	-
Formative wetted width change (ΔW_F)	-0.516 - 0.632	-0.218 - 0.337	-0.626 - 1.1	-0.393 - 1.452	-0.271 - 0.169
	-	-	-	-0.582 - 0.584	-
Formative shear stress change ($\Delta\tau_F$)	-7.732 - 9.48	-9.043 - 2.42	-19.134 - 47.872	-21.405 - 35.6	-4.69 - 8.437
	-	-	-	-2326.9 - 2484.2	-

†Ranges from past studies were derived from Grant et al. (1990); Jowett (1993); Halwas and Church (2002); Wyrick and Pasternack (2014); Golly et al. (2019); and Helm et al. (2020). Comparative values were not available for all HM variables for all MU types. Ranges of comparative values are shown where available, otherwise singular values typically represent availability of mean values only.

‡W_{Bs} values were normalized by dividing by segment average baseflow wetted width to allow comparison with other studies.

A.3.5.3 Morphological unit expectations not met

None.

A.3.5.4 Utility of HM variables and Random Forest predictive approach

None.

A.3.5.5 Bespoke morphological units

None.

A.3.6 Conclusion

None.

A.3.7 References

Aadland, L. P. (1993). Stream Habitat Types: Their Fish Assemblages and Relationship to Flow. *North American Journal of Fisheries Management, 13*(4), 790-806. doi:10.1577/1548-8675(1993)013<0790:SHTTFA>2.3.CO;2

Anderson, M. J. (2001). A new method for non-parametric multivariate analysis of variance. *Austral Ecology, 26*(1), 32-46. doi:https://doi.org/10.1111/j.1442-9993.2001.01070.pp.x

Beechie, T., & Imaki, H. (2104). Predicting natural channel patterns based on landscape and geomorphic controls in the Columbia River basin, USA. *Water Resour Res*. 50: 39–57.

Belletti, B., Rinaldi, M., Bussettini, M., Comiti, F., Gurnell, A. M., Mao, L., . . . Vezza, P. (2017). Characterising physical habitats and fluvial hydromorphology: A new system for the survey and classification of river geomorphic units. *Geomorphology, 283*, 143-157. doi:https://doi.org/10.1016/j.geomorph.2017.01.032

Benjankar, R., Tonina, D., & McKean, J. (2015). One-dimensional and two-dimensional hydrodynamic modeling derived flow properties: impacts on aquatic habitat quality predictions. *Earth Surface Processes and Landforms, 40*(3), 340-356. doi:10.1002/esp.3637

Breiman, L. (2001). Random Forests. *Machine Learning* 45, 5–32. https://doi.org/10.1023/A:1010933404324

Brierley, G., Fryirs, K., Cullum, C., Tadaki, M., Huang, H. Q., & Blue, B. (2013). Reading the landscape:Integrating the theory and practice of geomorphology to develop place-based understandings of river systems. *Progress in Physical Geography: Earth and Environment, 37*(5), 601-621. doi:10.1177/0309133313490007

Brown, R.A., & Pasternack, G.B. (2012). *Monitoring and assessment of the 2010-2011 gravel/cobble augmentation in the Englebright Dam Reach of the lower Yuba River, CA. Prepared for the U.S. Army Corps of Engineers, Sacramento District.* Retrieved from University of California at Davis, Davis, CA.: http://pasternack.ucdavis.edu/files/5313/7692/9028/EDRreport_20121215_FINAL.pdf

Brown, R. A., & Pasternack, G. B. (2014). Hydrologic and topographic variability modulate channel change in mountain rivers. *Journal of Hydrology, 510*(Supplement C), 551-564. doi:https://doi.org/10.1016/j.jhydrol.2013.12.048

Brown, R. A., & Pasternack, G. B. (2019). How to build a digital river. *Earth-Science Reviews, 194*, 283-305. doi:https://doi.org/10.1016/j.earscirev.2019.04.028

Brown, R. A., Pasternack, G. B., & Lin, T. (2016). The Topographic Design of River Channels for Form-Process Linkages. *Environmental Management, 57*(4), 929-942. doi:10.1007/s00267-015-0648-0

Buffington, J. M., Lisle, T. E., Woodsmith, R. D., & Hilton, S. (2002). Controls on the size and occurrence of pools in coarse-grained forest rivers. *River Research and Applications, 18*(6), 507-531. doi:https://doi.org/10.1002/rra.693

Buffington, J. M. & Montgomery, D. R. (2013). Geomorphic classification of rivers. In: Shroder, J.; Wohl, E., ed. Treatise on Geomorphology; Fluvial Geomorphology, Vol. 9. San Diego, CA: Academic Press. p. 730-767.

Byrne, C. F., Pasternack, G. B., Guillon, H., Lane, B. A., & Sandoval-Solis, S. (2020). Reach-scale bankfull channel types can exist independently of catchment hydrology. *Earth Surf. Process. Landforms*, 45: 2179– 2200. https://doi.org/10.1002/esp.4874.

Byrne, C. F., Pasternack G. B., Guillon, H., Lane, B. A., & Sandoval-Solis, S. (2021). Channel constriction predicts pool-riffle velocity reversals across landscapes. *Geophysical Research Letters*. DOI: 10.1029/2021GL094378.

Caamaño, D., Goodwin, P., Buffington, J. M., Liou, J. C., & Daley-Laursen, S. (2009). Unifying Criterion for the Velocity Reversal Hypothesis in Gravel-Bed Rivers. *Journal of Hydraulic Engineering, 135*(1), 66-70. doi:doi:10.1061/(ASCE)0733-9429(2009)135:1(66)

Carbonari, C., Recking, A., & Solari, L. (2020). Morphology, Bedload, and Sorting Process Variability in Response to Lateral Confinement: Results From Physical Models of Gravel-bed Rivers. *Journal of Geophysical Research: Earth Surface, 125*(12), e2020JF005773. doi:https://doi.org/10.1029/2020JF005773

Cavalli, M., Tarolli, P., Marchi, L., & Dalla Fontana, G. (2008). The effectiveness of airborne LiDAR data in the recognition of channel-bed morphology. *CATENA, 73*(3), 249-260. doi:https://doi.org/10.1016/j.catena.2007.11.001

Chartrand, S. M., Jellinek, M., Whiting, P. J., & Stamm, J. (2011). Geometric scaling of step-pools in mountain streams: Observations and implications. *Geomorphology, 129*(1), 141-151. doi:https://doi.org/10.1016/j.geomorph.2011.01.020

Chicco, D., Tötsch, N., & Jurman, G. (2021). The Matthews correlation coefficient (MCC) is more reliable than balanced accuracy, bookmaker informedness, and markedness in two-class confusion matrix evaluation. *BioData Mining, 14*(1), 13. doi:10.1186/s13040-021-00244-z

Chin, A., & Wohl, E. (2005). Toward a theory for step pools in stream channels. *Progress in Physical Geography: Earth and Environment, 29*(3), 275-296. doi:10.1191/0309133305pp449ra

Church, M., & Jones, D. (1982). Channel bars in gravel-bed rivers. In Gravel-Bed Rivers, Hey RD, Bathurst JC, Thorne CR (eds). Wiley: New York; 291–338.

Church, M., & Zimmermann, A. (2007). Form and stability of step-pool channels: Research progress. *Water Resources Research, 43*(3), n/a-n/a. doi:10.1029/2006WR005037

Coarer, Y. L. (2007). Hydraulic signatures for ecological modelling at different scales. *Aquatic Ecology, 41*(3), 451-459. doi:10.1007/s10452-005-9005-3

Comiti, F., & Mao, L. (2012). Recent Advances in the Dynamics of Steep Channels *Gravel-Bed Rivers* (pp. 351-377).

Dingman, S.L. (2007). Analytical derivation of at-a-station hydraulic–geometry relations. *Journal of Hydrology*, 334: 17– 27. https://doi.org/10.1016/j.jhydrol.2006.09.021

Elzhov, T.V., Mullen, K.M., Spiess A., & Bolker, B. (2016). minpack.lm: R Interface to the Levenberg-Marquardt Nonlinear Least-Squares Algorithm Found in MINPACK, Plus Support for Bounds. R package version 1.2-1. https://CRAN.R-project.org/package=minpack.lm

Ferguson, R. I. (1986). Hydraulics and hydraulic geometry. *Progress in Physical Geography: Earth and Environment*, 10(1), 1–31. https://doi.org/10.1177/030913338601000101

Florsheim, J. L. (1985). Fluvial requirements for gravel bar formation in northwestern California [Master's Thesis, Hombolt State University].

Furbish, D. J. (1998). Irregular bed forms in steep, rough channels: 1. Stability analysis. *Water Resources Research, 34*(12), 3635-3648. doi:https://doi.org/10.1029/98WR02339

Games, P. A., Keselman, H. J., & Clinch, J. J. (1979). Tests for homogeneity of variance in factorial designs. *Psychological Bulletin*, 86(5), 978–984. https://doi.org/10.1037/0033-2909.86.5.978

Gleason, C. J. (2015). Hydraulic geometry of natural rivers: A review and future directions. *Progress in Physical Geography: Earth and Environment*, 39(3), 337–360. https://doi.org/10.1177/0309133314567584

Golly, A., Turowski, J. M., Badoux, A., & Hovius, N. (2019). Testing models of step formation against observations of channel steps in a steep mountain stream. *Earth Surface Processes and Landforms, 44*(7), 1390-1406. doi:https://doi.org/10.1002/esp.4582

Gonzalez, R. L., & Pasternack, G.B. (2015). Reenvisioning cross-sectional at-a-station hydraulic geometry as spatially explicit hydraulic topography. *Geomorphology*, 246: 394–406. http://dx.doi.org/10.1016/j.geomorph.2015.06.024

Grant, G. E., & Swanson, F. J. (1995). Morphology and Processes of Valley Floors in Mountain Streams, Western Cascades, Oregon *Natural and Anthropogenic Influences in Fluvial Geomorphology* (pp. 83-101): American Geophysical Union.

Grant, G. E., Swanson, F. J., & Wolman, M. G. (1990). Pattern and origin of stepped-bed morphology in high-gradient streams, Western Cascades, Oregon. *GSA Bulletin, 102*(3), 340-352. doi:10.1130/0016-7606(1990)102<0340:PAOOSB>2.3.CO;2

Halwas, K. L., & Church, M. (2002). Channel units in small, high gradient streams on Vancouver Island, British Columbia. *Geomorphology, 43*(3), 243-256. doi:https://doi.org/10.1016/S0169-555X(01)00136-2

Harrison, L. R., & Keller, E. A. (2007). Modeling forced pool–riffle hydraulics in a boulder-bed stream, southern California. *Geomorphology, 83*(3), 232-248. doi:https://doi.org/10.1016/j.geomorph.2006.02.024

Hassan, M. A., Radić, V., Buckrell, E., Chartrand, S. M., & McDowell, C. (2021). Pool-riffle adjustment due to changes in flow and sediment supply. *Water Resources Research*, 57, 2020WR028048. https://doi.org/10.1029/2020WR028048

Hauer, C., Mandlburger, G., & Habersack, H. (2009). Hydraulically related hydro-morphological units: description based on a new conceptual mesohabitat evaluation model (MEM) using

LiDAR data as geometric input. *River Research and Applications, 25*(1), 29-47. doi:10.1002/rra.1083

Helm, C., Hassan, M. A., and Reid, D. (2020). Characterization of morphological units in a small, forested stream using close-range remotely piloted aircraft imagery, *Earth Surf. Dynam.*, 8, 913–929, https://doi.org/10.5194/esurf-8-913-2020

Holm, S. (1979). A Simple Sequentially Rejective Multiple Test Procedure. *Scandinavian Journal of Statistics, 6*(2), 65-70.

Hopkins, C. E., & Pasternack, G. B. (2017). Near-census Delineation of Laterally Organized Geomorphic Zones and Associated Sub-width Fluvial Landforms. Abstract EP43A-1876 presented at 2017 Fall Meeting, AGU, New Orleans, LA., 11-15 Dec.

Jowett, I. G. (1993). A method for objectively identifying pool, run, and riffle habitats from physical measurements. *New Zealand Journal of Marine and Freshwater Research*, 27:2, 241-248, DOI: 10.1080/00288330.1993.9516563

Keller, E. A. 1972. 'Development of alluvial stream channels: A five stage model', *Geological Society of America Bulletin*, 83, 1531-1536.

Keller, E. A., & Melhorn, W. N. (1978). Rhythmic spacing and origin of pools and riffles. GSA Bulletin; 89 (5): 723–730. doi: https://doi.org/10.1130/0016-7606(1978)89<723:RSAOOP>2.0.CO;2

Lai, Y. G. (2008). *"SRH-2D version 2: Theory and User's Manual Sedimentation and River Hydraulics – Two-Dimensional River Flow Modeling"*. Retrieved from U.S. Department of the Interior, Bureau of Reclamation, Technical Service Center, Sedimentation and River Hydraulics Group. Denver, Colorado.: https://www.usbr.gov/tsc/techreferences/computer%20software/models/srh2d/index.html

Lane, B., Guillon, H., Byrne, C., Pasternack, G. B., Kasprak, A., & Sandoval-Solis, S. (2022). Channel-reach morphology and landscape properties are linked across a large heterogeneous region. *Earth Surface Processes and Landforms, 47*(1), 257-274. doi:https://doi.org/10.1002/esp.5246

Lane, S. N., & Richards, K. S. (1997). Linking River Channel Form and Process: Time, Space and Causality Revisited. *Earth Surf. Process. Landforms*, 22: 249-260. https://doi.org/10.1002/(SICI)1096-9837(199703)22:3<249::AID-ESP752>3.0.CO;2-7

Legleiter, C. J., & Goodchild, M. F. (2005). Alternative representations of in-stream habitat: classification using remote sensing, hydraulic modeling, and fuzzy logic. *International Journal of Geographical Information Science, 19*(1), 29-50. doi:10.1080/13658810412331280220

Legleiter, C. J., Roberts, D. A., Marcus, W. A., & Fonstad, M. A. (2004). Passive optical remote sensing of river channel morphology and in-stream habitat; physical basis and feasibility. *Remote Sensing of Environment, 93*(4), 493-510. doi:http://dx.doi.org/10.1016/j.rse.2004.07.019

Lisle, T. E. (1986). Stabilization of a gravel channel by large streamside obstructions and bedrock bends, Jacoby Creek, northwestern California. *Geological Society of America Bulletin, 97*, 999-1011.

Liu, H. (2015). Comparing Welch ANOVA, a Kruskal-Wallis test, and traditional ANOVA in case of heterogeneity of variance [Master's Thesis, Virginia Commonwealth University]. Biostatistics Commons. https://doi.org/10.25772/BWFP-YE95

MacWilliams, M. L., Wheaton, J. M., Pasternack, G. B., Street, R. L., & Kitanidis, P. K. (2006). Flow convergence routing hypothesis for pool-riffle maintenance in alluvial rivers. *Water Resour. Res., 42*, W10427.

Mahdade, M., Le Moine, N., Moussa, R., Navratil, O., & Ribstein, P. (2020). Automatic identification of alternating morphological units in river channels using wavelet analysis and ridge extraction. *Hydrol. Earth Syst. Sci., 24*(7), 3513-3537. doi:10.5194/hess-24-3513-2020

Montgomery, D. R., & Buffington, J. M. (1997). Channel-reach morphology in mountain drainage basins. *GSA Bulletin, 109*(5), 596-611. doi:10.1130/0016-7606(1997)109<0596:CRMIMD>2.3.CO;2

Montgomery, D. R., Buffington, J. M., Smith, R. D., Schmidt, K. M., & Pess, G. (1995). Pool Spacing in Forest Channels. *Water Resources Research, 31*(4), 1097-1105. doi:https://doi.org/10.1029/94WR03285

Moriasi, D. N., Arnold, J. G., Van Liew, M. W., Bingner, R. L., Harmel, R. D., & Veith, T. L. (2007). Model Evaluation Guidelines for Systematic Quantification of Accuracy in Watershed Simulations. *Transactions of the ASABE, 50*(3), 885. doi:https://doi.org/10.13031/2013.23153

Mukaka, M. M. (2012). Statistics corner: A guide to appropriate use of correlation coefficient in medical research. *Malawi medical journal : the journal of Medical Association of Malawi*, 24(3), 69–71.

Nelson, J. M. (1990). The initial instability and finite-amplitude stability of alternate bars in straight channels. *Earth-Science Reviews, 29*(1), 97-115. doi:https://doi.org/10.1016/0012-8252(0)90030-Y

Nitsche, M., Rickenmann, D., Kirchner, J. W., Turowski, J. M., & Badoux, A. (2012). Macroroughness and variations in reach-averaged flow resistance in steep mountain streams. *Water Resources Research, 48*(12). doi:https://doi.org/10.1029/2012WR012091

Ohara, N., & Yamatani, K. (2019). Theoretical Stable Hydraulic Section based on the Principle of Least Action. *Scientific Reports, 9*(1), 7957. doi:10.1038/s41598-019-44347-4

Oksanen J., Blanchet F.G., Friendl, F., Kindt R., Legendre, P., McGlinn, D., Minchin, P.R., O'Hara,, R. B. Simpson, G.L., Solymos, P., Stevens, M. H., Szoecs, E., & Wagner, H. (2020). vegan: Community Ecology Package. R package version 2.5-7. https://CRAN.R-project.org/package=vegan

Pasternack, G. B. (2011). *2D Modeling and Ecohydraulic Analysis*. Seatle, WA: Createspace.

Pasternack, G. B., Gilbert, A. T., Wheaton, J. M., & Buckland, E. M. (2006). Error Propagation for Velocity and Shear Stress Prediction Using 2D Models For Environmental Management. *Journal of Hydrology*, 328:227-241. https://doi.org/10.1016/j.jhydrol.2005.12.003

Palucis, M. C., & Lamb, M. P. (2017). What controls channel form in steep mountain streams? *Geophysical Research Letters, 44*(14), 7245-7255. doi:https://doi.org/10.1002/2017GL074198

Pasternack, G. B., Baig, D., Weber, M. D., & Brown, R. A. (2018). Hierarchically nested river landform sequences. Part 1: Theory. *Earth Surface Processes and Landforms, 43*(12), 2510-2518. doi:https://doi.org/10.1002/esp.4411

Pasternack, G. B., Gore, J. L., & Wiener, J. S. (2021). Geomorphic covariance structure of a confined mountain river reveals landform organization stage threshold. *Earth Surface Processes and Landforms, 46*(13), 2582-2606. doi:https://doi.org/10.1002/esp.5195

Pasternack, G. B., & Senter, A. E. (2011). *21st Century instream flow assessment framework for mountain streams.* Retrieved from California Energy Commission, PIER. CEC-500-2013-059.: https://www.energy.ca.gov/2013publications/CEC-500-2013-059/CEC-500-2013-059.pdf

Phillips, J. D. (2014). Badass geomorphology. *Earth Surf. Process. Landforms*, 40, 22– 33, doi: 10.1002/esp.3682.

Rabeni, C. F., & Jacobson, R. B. (1993). The importance of fluvial hydraulics to fish-habitat restoration in low-gradient alluvial streams. *Freshwater Biology, 29*(2), 211-220. doi:10.1111/j.1365-2427.1993.tb00758.x

Richards, K. S. (1976). Channel width and the riffle-pool sequence. *Geological Society of America Bulletin, 87*(6), 883-890. doi:10.1130/0016-7606(1976)87<883:cwatrs>2.0.co;2

Rhodes, D. D. (1977). The b-f-m diagram; graphical representation and interpretation of at-a-station hydraulic geometry. *American Journal of Science, 277*(1), 73-96. doi:10.2475/ajs.277.1.73

Roper, B. B., & Scarnecchia, D. L. (1995). Observer Variability in Classifying Habitat Types in Stream Surveys. *North American Journal of Fisheries Management, 15*(1), 49-53. doi:10.1577/1548-8675(1995)015<0049:OVICHT>2.3.CO;2

Rosgen, D.L. (2001). A stream channel stability assessment methodology. Proceedings of the 7th Federal Interagency Sedimentation Conference; Reno, Nevada.

Saletti, M., & Hassan, M. A. (2020). Width variations control the development of grain structuring in steep step-pool dominated streams: insight from flume experiments. *Earth Surface Processes and Landforms, 45*(6), 1430-1440. doi:https://doi.org/10.1002/esp.4815

Strom, M. A., Pasternack, G. B., & Wyrick, J. R. (2016). Reenvisioning velocity reversal as a diversity of hydraulic patch behaviours. *Hydrological Processes, 30*(13), 2348-2365. doi:10.1002/hyp.10797

Tamminga, A., Hugenholtz, C., Eaton, B., & Lapointe, M. (2015). Hyperspatial Remote Sensing of Channel Reach Morphology and Hydraulic Fish Habitat Using an Unmanned Aerial Vehicle (UAV): A First Assessment in the Context of River Research and Management. *River Res. Applic.*, 31, pages 379– 391, doi: 10.1002/rra.2743

Thompson, D. M. (2011). The velocity-reversal hypothesis revisited. *Progress in Physical Geography, 35*(1), 123-132. doi:doi:10.1177/0309133310369921

Thompson, D. M. (2012). The challenge of modeling pool–riffle morphologies in channels with different densities of large woody debris and boulders. *Earth Surface Processes and Landforms, 37*(2), 223-239. doi:10.1002/esp.2256

Thompson, D.M. (2018). Pool-riffle Sequences. *Reference Module in Earth Systems and Environmental Sciences*. https://doi.org/10.1016/B978-0-12-409548-9.11029-2.

Thompson, D. M., & Fixler, S. A. (2017). Formation and maintenance of a forced pool-riffle couplet following loading of large wood. *Geomorphology, 296*, 74-90. doi:https://doi.org/10.1016/j.geomorph.2017.08.030

Tooth, S., & Nanson, G. C. (2000). Equilibirum and nonequilibirum conditins in dryland rivers. *Physical Geography*, 21:3, 183-211, DOI: 10.1080/02723646.2000.10642705

Trevisani, S., Cavalli, M., & Marchi, L. (2010). Reading the bed morphology of a mountain stream: a geomorphometric study on high-resolution topographic data. *Hydrol. Earth Syst. Sci., 14*(2), 393-405. doi:10.5194/hess-14-393-2010

Valle, B. L., & Pasternack, G. B. (2006). Field mapping and digital elevation modelling of submerged and unsubmerged hydraulic jump regions in a bedrock step-pool channel. *Earth Surface Processes and Landforms, 31*(6), 646-664. doi:10.1002/esp.1293

Venditti, J. G., Nelson, P. A., Bradley, R. W., Haught, D., & Gitto, A. B. (2017). Bedforms, Structures, Patches, and Sediment Supply in Gravel-Bed Rivers *Gravel-Bed Rivers* (pp. 439-466).

Wang, J., Hassan, M. A., Saletti, M., Chen, X., Fu, X., Zhou, H., & Yang, X. (2021). On How Episodic Sediment Supply Influences the Evolution of Channel Morphology, Bedload Transport and Channel Stability in an Experimental Step-Pool Channel. *Water Resources Research, 57*(7), e2020WR029133. doi:https://doi.org/10.1029/2020WR029133

Wheaton, J. M., Fryirs, K. A., Brierley, G., Bangen, S. G., Bouwes, N., & O'Brien, G. (2015). Geomorphic mapping and taxonomy of fluvial landforms. *Geomorphology, 248*(Supplement C), 273-295. doi:https://doi.org/10.1016/j.geomorph.2015.07.010

White, J. Q., Pasternack, G. B., & Moir, H. J. (2010). Valley width variation influences riffle–pool location and persistence on a rapidly incising gravel-bed river. *Geomorphology, 121*(3–4), 206-221. doi:https://doi.org/10.1016/j.geomorph.2010.04.012

Whiting, P. J., & Bradley, J. B. (1993). A process-based classification system for headwater streams. *Earth Surface Processes and Landforms, 18*(7), 603-612. doi:https://doi.org/10.1002/esp.3290180704

Wiener, J., & Pasternack, G.B. (2016). Accretionary Flow Analysis- Yuba River from New Bullards Bar to Colgate Powerhouse. Prepared for Yuba County Water Agency. University of California, Davis, CA. Retrieved from http://pasternack.ucdavis.edu/research/projects/ncrs/mountain-river-eco-geo

Wiener, J. S., & Pasternack, G. B. (2022). Scale dependent spatial structuring of mountain river large bed elements maximizes flow resistance. Accepted. *Geomorphology*.

Wilkinson, S. N., Rutherfurd, I. D., & Keller, R. J. (2008). An experimental test of whether bar instability contributes to the formation, periodicity and maintenance of pool–riffle sequences. *Earth Surface Processes and Landforms, 33*(11), 1742-1756. doi:https://doi.org/10.1002/esp.1645

Wolman, M. G., & Eiler, J. (1958). Reconnaissance study of erosion and deposition produced by the flood of August 1955 in Connecticut. *Eos, Transactions American Geophysical Union, 39*(1), 1-14. doi:https://doi.org/10.1029/TR039i001p00001

Woodworth, K. A., & Pasternack, G. B. (2022). Are dynamic fluvial morphological unit assemblages statistically stationary through floods of less than ten times bankfull

discharge? *Geomorphology, 403*, 108135. doi:https://doi.org/10.1016/j.geomorph.2022.108135

Wright, M.N., & Ziegler, A. (2017). ranger: A Fast Implementation of Random Forests for High Dimensional Data in C++ and R. Journal of Statistical Software, 77(1), 1-17. doi:10.18637/jss.v077.i01

Wyrick, J. R., & Pasternack, G. B. (2012). *Landforms of the Lower Yuba River.* Prepared for the Yuba Accord River Management Team. University of California, Davis. Retrieved from: http://www.yubaaccordrmt.com/Annual%20Reports/Mapping%20and%20Modeling/LYR%20Landforms%20Report%20%285-9-2012%29.pdf

Wyrick, J. R., & Pasternack, G. B. (2014). Geospatial organization of fluvial landforms in a gravel–cobble river: Beyond the riffle–pool couplet. *Geomorphology, 213*(Supplement C), 48-65. doi:https://doi.org/10.1016/j.geomorph.2013.12.040

Wyrick, J. R., Senter, A. E., & Pasternack, G. B. (2014). Revealing the natural complexity of fluvial morphology through 2D hydrodynamic delineation of river landforms. *Geomorphology, 210*, 14-22. doi:10.1016/j.geomorph.2013.12.013

Yochum, S. E., Comiti, F., Wohl, E., David, G. C. L., & Mao, L. (2014). *Photographic guidance for selecting flow resistance coefficients in high-gradient channels*. Retrieved from https://www.fs.usda.gov/treesearch/pubs/46250

Zimmermann, A. E., Church, M., & Hassan, M. A. (2008). Identification of steps and pools from stream longitudinal profile data. *Geomorphology, 102*(3), 395-406. doi:https://doi.org/10.1016/j.geomorph.2008.04.009